

Gas-Water-Rock Interactions and Implications for Geoenvironmental Issues

Special Issue Editor in Chief: Liangping Li
Guest Editors: Meijing Zhang and Ming Zhang





Gas-Water-Rock Interactions and Implications for Geoenvironmental Issues

Gas-Water-Rock Interactions and Implications for Geoenvironmental Issues

Special Issue Editor in Chief: Liangping Li

Guest Editors: Meijing Zhang and Ming Zhang



Copyright © 2018 Hindawi. All rights reserved.

This is a special issue published in “Geofluids.” All articles are open access articles distributed under the Creative Commons Attribution License, which permits unrestricted use, distribution, and reproduction in any medium, provided the original work is properly cited.

Editorial Board


Carmine Apollaro, Italy
Baojun Bai, USA
Maurizio Barbieri, Italy
Julien Bourdet, Australia
Andrea Brogi, Italy
David A. Butterfield, USA
Mauro Cacace, Germany
Isabelle Chambeft, New Zealand
Shengnan Nancy Chen, Canada
Paola Cianfarra, Italy
Daniele Cinti, Italy
Timothy S. Collett, USA
Nicoló Colombani, Italy
Mercè Corbella, Spain
Carlos R. De Souza Filho, Brazil
Henrik Drake, Sweden
Lionel Esteban, Australia
Cinzia Federico, Italy
Paulo Fonseca, Portugal
Francesco Frondini, Italy
Paolo Fulignati, Italy
Paola Gattinoni, Italy
Mauro Giudici, Italy

Fausto Grassa, Italy
Salvatore Inguaggiato, Italy
Francesco Italiano, Italy
Jaewon Jang, Republic of Korea
Luchao Jin, USA
Shinsuke Kawagucci, Japan
Karsten Kroeger, New Zealand
Cornelius Langenbruch, USA
Huazhou Li, Canada
Liangping Li, USA
Marcello Liotta, Italy
Stefano Lo Russo, Italy
Constantinos Loupasakis, Greece
Lin Ma, USA
Paolo Madonia, Italy
Fabien Magri, Germany
Andrew H. Manning, USA
Micòl Mastrocicco, Italy
Lucie Mathieu, Canada
John A. Mavrogenes, Australia
Agnes Mazot, New Zealand
Yuan Mei, Australia
Jean-Luc Michelot, France

Ferenc Molnar, Finland
Julie K. Pearce, Australia
Daniele Pedretti, Finland
Marco Petitta, Italy
Christophe Renac, France
Reza Rezaee, Australia
Mohammad Sarmadivaleh, Australia
Christian Siebert, Germany
Ricardo L. Silva, Canada
Craig T. Simmons, Australia
Ondra Sracek, Czech Republic
Andri Stefansson, Iceland
Richard E. Swarbrick, UK
Pietro Teatini, Italy
Svetlana G. Tessalina, Australia
Rene Therrien, Canada
Umberta Tinivella, Italy
Tivadar M. Tóth, Hungary
Zhenjiang You, Australia
Keni Zhang, China
Ling-Li Zhou, Ireland

Contents

Gas-Water-Rock Interactions and Implications for Geoenvironmental Issues

Liangping Li , Meijing Zhang, and Ming Zhang 

Editorial (4 pages), Article ID 6847392, Volume 2018 (2018)

Sources Identification of Nitrogen Using Major Ions and Isotopic Tracers in Shenyang, China

Huan Huang , Mingzhu Liu , Junjie Wang, Jiangtao He, and Honghan Chen

Research Article (11 pages), Article ID 8683904, Volume 2018 (2018)

A Statistical Constitutive Model considering Deterioration for Brittle Rocks under a Coupled Thermal-Mechanical Condition

Meiben Gao , Tianbin Li , Tao Wei, and Lubo Meng 


Research Article (10 pages), Article ID 3269423, Volume 2018 (2018)

Integration of an Iterative Update of Sparse Geologic Dictionaries with ES-MDA for History Matching of Channelized Reservoirs

Sungil Kim, Baehyun Min , Kyungbook Lee, and Hoonyoung Jeong

Research Article (21 pages), Article ID 1532868, Volume 2018 (2018)

The Monitoring-Based Analysis on Deformation-Controlling Factors and Slope Stability of Reservoir Landslide: Hongyanzi Landslide in the Southwest of China

Bing Han , Bin Tong , Jinkai Yan, Chunrong Yin, Liang Chen, and Deying Li


Research Article (14 pages), Article ID 7391517, Volume 2018 (2018)

Hydrochemical Characteristics and Formation of the Madeng Hot Spring in Yunnan, China

Ren Zhenhua, Zhou Xun , Yang Miaolin, Wang Xiaocui, Zheng Yuhui, Li Xiaolu, and Shen Ye

Research Article (11 pages), Article ID 2368246, Volume 2018 (2018)

Fluid Geochemistry of Fault Zone Hydrothermal System in the Yidun-Litang Area, Eastern Tibetan Plateau Geothermal Belt

Yanyan Hou, Zheming Shi , and Wenqing Mu

Research Article (13 pages), Article ID 6872563, Volume 2018 (2018)

Investigation on the Relationship between Wellhead Injection Pressure and Injection Rate for Practical Injection Control in CO₂ Geological Storage Projects

Bing Bai , Haiqing Wu , and Xiaochun Li

Research Article (14 pages), Article ID 4927415, Volume 2018 (2018)

Numerical Investigation into the Evolution of Groundwater Flow and Solute Transport in the Eastern Qaidam Basin since the Last Glacial Period

Qichen Hao , Chuan Lu , Yuchen Zhu , Yong Xiao , and Xiaomin Gu

Research Article (12 pages), Article ID 9260604, Volume 2018 (2018)

Characterization of Microscopic Pore Structures of Rock Salt through Mercury Injection and Nitrogen Absorption Tests

Jianwen Chen, Erbing Li, and Jin Luo 

Research Article (7 pages), Article ID 9427361, Volume 2018 (2018)

Interaction between Vetiver Grass Roots and Completely Decomposed Volcanic Tuff under Rainfall Infiltration Conditions

Ling Xu , Chongyang Gao, and Dongdong Yan

Research Article (8 pages), Article ID 5219592, Volume 2018 (2018)

A Measured Method for In Situ Viscosity of Fluid in Porous Media by Nuclear Magnetic Resonance

Zhengming Yang , Zhuangzhi Ma, Yutian Luo , Yapu Zhang, Hekun Guo, and Wei Lin 

Research Article (8 pages), Article ID 9542152, Volume 2018 (2018)

Stability Analysis of Partially Submerged Landslide with the Consideration of the Relationship between Porewater Pressure and Seepage Force

Yang Wang , Le Yu, Tianci Yin, Lanbing Yu, and Zhitao Huo

Research Article (9 pages), Article ID 9145830, Volume 2018 (2018)

CO₂ Leakage-Induced Contamination in Shallow Potable Aquifer and Associated Health Risk Assessment

Chan Yeong Kim , Weon Shik Han , Eungyu Park, Jina Jeong, and Tianfu Xu 

Research Article (19 pages), Article ID 4834601, Volume 2018 (2018)

Hydrochemical Characteristics and Evolution of Geothermal Fluids in the Chabu High-Temperature Geothermal System, Southern Tibet

X. Wang, G. L. Wang , H. N. Gan, Z. Liu, and D. W. Nan







Research Article (15 pages), Article ID 8532840, Volume 2018 (2018)

Impact of Redox Condition on Fractionation and Bioaccessibility of Arsenic in Arsenic-Contaminated Soils Remediated by Iron Amendments: A Long-Term Experiment

Quan Zhang, Lixin Pei, Chunyan Liu, Mei Han, and Wenzhong Wang 

Research Article (7 pages), Article ID 5243018, Volume 2018 (2018)

Effects of Dissolved Organic Matter on Sorption of Oxytetracycline to Sediments

Zongzhou Wang , Qianli Jiang , Runze Wang, Xiaoyu Yuan , Shengke Yang , Wenke Wang , and Yaqian Zhao 



Research Article (12 pages), Article ID 1254529, Volume 2018 (2018)

A Regional Scale Investigation on Groundwater Arsenic in Different Types of Aquifers in the Pearl River Delta, China

Qinxuan Hou, Jichao Sun, Jihong Jing, Chunyan Liu, Ying Zhang, Jingtao Liu , and Mengjian Hua

Research Article (9 pages), Article ID 3471295, Volume 2018 (2018)

A Coupled One-Dimensional Numerical Simulation of the Land Subsidence Process in a Multilayer Aquifer System due to Hydraulic Head Variation in the Pumped Layer

Ye Wang , Mao-sheng Zhang, Fu-sheng Hu , Ying Dong, and Kun Yu

Research Article (12 pages), Article ID 4083439, Volume 2018 (2018)

Editorial

Gas-Water-Rock Interactions and Implications for Geoenvironmental Issues

Liangping Li¹, Meijing Zhang² and Ming Zhang³

¹Department of Geology and Geological Engineering, South Dakota School of Mines and Technology, Rapid City, SD, USA

²Department of Agricultural and Biological Engineering, University of Florida, Gainesville, USA

³Faculty of Engineering, China University of Geosciences, Wuhan, China

Correspondence should be addressed to Liangping Li; liangping.li@sdsmt.edu

Received 12 September 2018; Accepted 12 September 2018; Published 8 October 2018

Copyright © 2018 Liangping Li et al. This is an open access article distributed under the Creative Commons Attribution License, which permits unrestricted use, distribution, and reproduction in any medium, provided the original work is properly cited.

1. Motivation and Background

Water and gas, as the two most common fluids and primary geologic forces, are crucial components in various geological processes. Gas-water-rock interactions play indispensable roles in the evolution of geoenvironmental issues. For example, the accurate prediction of groundwater flow and contaminant transport requires a profound understanding of physicochemical processes that occur among liquid, solid, and gas phases [1]. At present, more attention should be paid to gas-water-rock interactions related to the transport and retention of toxic contaminants such as heavy metals and organic contaminants in aquifers and vadose zones, due to the release of toxic contaminants from intensive human activities [2]. In addition, a gas-water-rock reaction might change the stress field, groundwater seepage field, and properties of rocks and soils, which subsequently leads to the instability of slope and landslide hazards [3]. A rapid sliding rock mass is likely to trigger waves or stir the atmosphere generating air blasts and facilitating its transport, both aggravating the hazards.

2. Contents of the Special Issue

In the paper “Sources Identification of Nitrogen Using Major Ions and Isotopic Tracers in Shenyang, China,” H. Huang et al. used multiproxy analysis in their research (stable isotope analyses in combination with chemical and hydrogeological data of the study area) to investigate the interactions between surface water and groundwater, as well as to

identify the source of nitrogen contamination in groundwater in Shenyang City, China. $\delta^{18}\text{O}_{\text{water}}$ and $\delta^2\text{H}_{\text{water}}$ were used to determine the amount of surface water that was discharged into groundwater, while $\delta^{18}\text{O}_{\text{nitrate}}$ and $\delta^{15}\text{N}_{\text{nitrate}}$ were employed to determine the sources of nitrate and ammonium in groundwater, which are the main contaminants in the study area. According to the results, the reducing environment in groundwater may result from the prevailing iron and manganese, occurring from the weathering of minerals and rocks, which prevents the ammonium being oxidized into nitrate. The ratios of the recharge from the Hun River into groundwater were also identified. Multiproxy analysis also indicated that human activities, such as manure and sewage discharge, are the prevailing source of nitrogen in the waters.

In the paper “A Statistical Constitutive Model considering Deterioration for Brittle Rocks under a Coupled Thermal-Mechanical Condition,” M. Gao et al. investigated constitutive behaviors of rocks under thermal-mechanical coupling conditions. A statistical damage constitutive model was firstly established on the basis of Weibull’s distribution, by considering the thermal effects and crack initiation strength. Then, the parameters of the model were determined and expressed according to the characteristics of the stress-strain curve. Finally, the model was verified by conventional triaxial experiments of granite under thermal-mechanical actions (25 MPa, 40°C–60°C). The results show a relatively good coincidence between experimental curves and theoretical curves in the case studies. The validity of the model was therefore confirmed.

In the paper “Integration of an Iterative Update of Sparse Geologic Dictionaries with ES-MDA for History Matching of Channelized Reservoirs,” S. Kim et al. proposed to couple an iterative sparse coding in a transformed space with an ensemble smoother with multiple data assimilation (ES-MDA) for dealing with the non-Gaussian problem. In this approach, discrete cosine transform (DCT) is followed by the repetition of K-singular value composition (K-SVD) for constructing sparse geologic dictionaries that preserve geological features of the channelized reservoir. Two channelized gas reservoirs were used to validate the proposed algorithm and the results show that the integration of DCT and iterative K-SVD improves the matching performance of gas rate, water rate, bottom-hole pressure, and channel properties with geological plausibility.

In the paper “The Monitoring-Based Analysis on Deformation-Controlling Factors and Slope Stability of Reservoir Landslide: Hongyanzi Landslide in the Southwest of China,” B. Han et al. conducted a comprehensive analysis to improve the understanding on the deformation characteristics and controlling factors of the Hongyanzi landslide in the Southwest of China. The results indicated that significant deformation occurred during the drawdown period; otherwise, the landslide remained stable. The major reason of the reservoir landslide deformation was the generation of seepage water pressure caused by the rapidly growing water-level difference between inside and outside of the slope. The influences of precipitation and earthquake were insignificant.

In the paper “Hydrochemical Characteristics and Formation of the Madeng Hot Spring in Yunnan, China,” Z. Ren et al. investigated the hydrochemical characteristics and formation of the Madeng hot spring. Through field data collection and studies, the temperature of the hot spring is 42.1°C. The spring water has a pH value of 6.41, TDS of 3.98 g/L, F contents of 3.08 mg/L, and H_2SiO_3 of 35.6 mg/L. Stable hydrogen and oxygen isotopes indicate that the hot water is of meteoric origin. Groundwater is recharged from the infiltration of precipitation in the mountain regions, undergoes a deep circulation, obtains heat from the heat flow, flows upward along fractures, and emerges as an upflow spring through the Quaternary sand and gravel in the central low-lying river valley.

In the paper “Fluid Geochemistry of Fault Zone Hydrothermal System in the Yidun-Litang Area, Eastern Tibetan Plateau Geothermal Belt,” Y. Hou et al. investigated the chemical and isotopic compositions of thermal water in an underexploited geothermal belt in the eastern Tibetan Plateau. By analyzing water samples from 24 hot springs, mostly taken from locations in fault zones, it was revealed that the water chemical types of the hot springs are mainly Na-HCO_3 -type water. Besides, water-rock interaction and cation exchange and mixture are the dominant hydrogeochemical processes in the hydrothermal evolution. According to the results, the hydrothermal systems are recharged by the meteoric water and are heated by the different deep, thermally and topographically driven convection heat along faults undergoing subsurface boiling before going back to the surface.

In the paper “Investigation on the Relationship between Wellhead Injection Pressure and Injection Rate for Practical Injection Control in CO_2 Geological Storage Projects,” B. Bai et al. proposed the complete constraint conditions of wellbore injection and used it to investigate the relationship between wellhead injection pressure and injection rate. The results show that these two parameters were mutually constrained. For a certain injection project, the allowable wellhead injection pressure and injection rate separately formed a continuous interval. A change of one parameter within its allowable interval could also change the other, both forming a closed region. Thus, controlling the wellhead injection parameters in this closed region could simultaneously ensure the effectiveness and the safety of injection.

In the paper “Numerical Investigation into the Evolution of Groundwater Flow and Solute Transport in the Eastern Qaidam Basin since the Last Glacial Period,” Q. Hao et al. utilized TOUGHREACT to perform a reactive solute transport simulation and considered the influence of water-soluble components on the fluid density in the arid-semiarid Qaidam basin in the northeastern Tibetan Plateau since the last glacial period. A three-level nested groundwater flow system was developed in the study area. Based on the simulation results, there are significant differences in the flow ranges and velocities of the different groundwater flow systems. The seepage velocity of the local water flow system is significantly higher than that of the intermediate and regional water flow systems. Since the last glacial period, the groundwater in the eastern part of the Qaidam Basin has experienced solute concentration and enrichment. The distributions of the groundwater flow system and solutes have been greatly affected by climate variations in different geological periods. The groundwater in the discharge region is currently in the stage of carbonate precipitation and is far from gypsum and halite precipitation. The findings in this study are useful for sustainable utilization of local groundwater resources and for coping with climate change.

In the paper “Characterization of Microscopic Pore Structures of Rock Salt through Mercury Injection and Nitrogen Absorption Tests,” J. Chen et al. collected rock salt samples from the Yunying salt mine of Hubei province in China and implemented high pressure mercury injection, rate-controlled mercury penetration, and nitrogen absorption tests with them. The pore size distribution was evaluated based on fractal analysis. The results showed that the pore size of rock salt varied from 0.01 to 300 μm with a major concentration of pore sizes smaller than 1.00 μm . The pore's radiuses were mainly distributed within a range between 15 and 50 nm. The research further revealed that the pore channel size of rock salt was randomly distributed, but the distribution of pore throat radius fitted very well with fractal law. By analysis of permeability, it was found that the maximum and medium radiuses of the pore throat had significant impacts while porosity was not apparently related to the permeability of rock salt. The higher the fractal dimension, the higher impacts on the permeability of the small throat was detected and the lower influence on the permeability of the big throat was exhibited. Therefore, the small throat determined majorly the permeability of rock salt.

In the paper “Interaction between Vetiver Grass Roots and Completely Decomposed Volcanic Tuff under Rainfall Infiltration Conditions,” L. Xu et al. identified and clarified the influence of vetiver grass roots on soil properties and slope stability through planting vetiver grass at the Kadoorie Farm in Hong Kong and leaving it to grow without artificial maintenance. Under the natural conditions of Hong Kong, growth of the vetiver grass roots can reach 1.1 m in depth after one-and-a-half year from planting. The percentage of grain size which is less than 0.075 mm in rooted soil is more than that of the nonrooted soil. The rooted soil of high finer grain content has a relatively small permeability. As a result, the increase in water content is therefore smaller than that of nonrooted soil in the same rainfall conditions. Shear box test reveals that the vetiver grass roots significantly increased the peak cohesion of the soil. The combined effects of grass roots on hydrological responses and shearing strength significantly stabilized the slope in local rainfall conditions.

In the paper “A Measured Method for In Situ Viscosity of Fluid in Porous Media by Nuclear Magnetic Resonance,” Z. Yang et al. established a method for determining the in situ viscosity of fluids in porous media and tested the in situ viscosity spectra of water in tight cores under different displacement conditions. The results show that the in situ viscosity distribution of water in porous media was inhomogeneous, and it was not a constant but was related to the distance between water and rock walls. If the distance was small enough, the viscosity would increase rapidly and be greater than the bulk viscosity.

In the paper “Stability Analysis of Partially Submerged Landslide with the Consideration of the Relationship between Porewater Pressure and Seepage Force,” Y. Wang et al. presented a modified mathematical expression for the stability analysis of a partially submerged landslide, based on the relationship between porewater pressures and buoyancy acting on the underwater zone of a partially submerged landslide, and the relationship between porewater pressures, seepage force, and buoyancy acting on the partially submerged zone. The resultant porewater pressures acting on the underwater slice equaled the buoyancy, and the porewater pressures acting on the partially submerged slice were equivalent to the seepage force and the buoyancy. The result showed that there were two equivalent approaches for considering the effect of water on landslide stability in the limit equilibrium method. One was based on total unit weight and porewater pressures, and the other was in terms of the buoyant weight and the seepage force. The study provided a good opportunity for simplifying the complex boundary porewater pressures in limit equilibrium analysis for the stability of the partially submerged landslide.

In the paper “CO₂ Leakage-Induced Contamination in Shallow Potable Aquifer and Associated Health Risk Assessment,” C. Y. Kim et al. focused on the risk assessment of CO₂ leakage in a shallow aquifer. 2D reactive transport models were developed and used to simulate the groundwater contamination. The results show that the movement of leaked CO₂ was mainly governed by local flow fields within the shallow aquifer. The dissolution of aquifer minerals and increased permeabilities of the aquifer are caused by the

induced low-pH plume. The distribution of the total arsenic plume was similar to the one for the arsenopyrite dissolution. Authors conclude that the shape of the arsenic plume impacts the human health risk.

In the paper “Hydrochemical Characteristics and Evolution of Geothermal Fluids in the Chabu High-Temperature Geothermal System, Southern Tibet,” X. Wang et al. presented reasonable reservoir temperatures and cooling processes of subsurface geothermal fluids in the Chabu high-temperature geothermal system in Southern Tibet. It investigated the hydrochemical characteristics of a geothermal spring by analyzing 36 geothermal spring samples, and combining this analysis with cluster analysis of multivariate statistical analysis to reveal the cooling processes of subsurface geothermal fluids. According to the results, the geothermal waters of the research area are generally mixed with the shallow cooler waters from the reservoirs. The major cooling processes of the subsurface geothermal fluids gradually transform from adiabatic boiling to conduction from the central part to the peripheral belt.

In the paper “Impact of Redox Condition on Fractionation and Bioaccessibility of Arsenic in Arsenic-Contaminated Soils Remediated by Iron Amendments: A Long-Term Experiment,” Q. Zhang et al. focused on the water-soil interactions related to the transport and retention of heavy metal(loid)s such as arsenic in soils. It investigated the effect of redox condition on arsenic fractions and bioaccessibility in arsenic-contaminated soils remediated by iron grit. Specifically, it investigated arsenic fractions in soils under the anoxic condition and aerobic condition before or after the addition of iron grit. According to the results, the labile fractions of As in soils decreased significantly after the addition of iron grit, while the unlabile fractions of As increased rapidly, and the bioaccessibility of As was negligible after 180 d incubation. More labile fractions of As in iron-amended soils were transformed into less mobilizable or unlabile fractions with the contact time. The increase of crystallization of Fe oxides, decomposition of organic matter, molecular diffusion, and the occlusion within Fe-(hydr)oxides cocontrolled the transformation of As fractions in iron-amended soils under different redox conditions.

In the paper “Effects of Dissolved Organic Matter on Sorption of Oxytetracycline to Sediments,” Z. Wang et al. investigated the effect of two representative dissolved organic matters (DOMs) on the adsorption of oxytetracycline (OTC) to three typical sediments (first terrace sediment, river floodplain sediment, and riverbed sediment). Two typical DOMs were derived from corrupt plants (PDOM) and chicken manure (MDOM). Elemental analysis and three-dimensional fluorescence were deployed to elucidate the mechanism of the effect of DOM on the adsorption of OTC to sediments. The samples subjected for testing were collected from the Weihe River, Northwest China. According to the results, the humus-like DOM can promote the adsorption of OTC while the protein-like DOM can inhibit the adsorption of OTC to sediments, which is determined by the aromaticity, hydrophilicity, and polarity of the DOMs.

In the paper “A Regional Scale Investigation on Groundwater Arsenic in Different Types of Aquifers in the Pearl

River Delta, China,” Q. Hou et al. focused on groundwater arsenic and other hydrochemical compositions in various aquifers in the Pearl River Delta. It investigated the source and driving forces of arsenic in different types of aquifers in the Pearl River Delta. Specifically, 399 groundwater samples were collected from various aquifers in the Pearl River Delta, 20 chemical compositions of groundwater samples were analyzed, and the relationship between arsenic and other hydrochemical compositions was evaluated by the principal component analysis (PCA). According to the results, about 9.4% and 2.3% of the samples with high concentrations (>0.01 mg/L) of arsenic were in granular and fissured aquifers, respectively, but no samples with a high concentration of arsenic were in karst aquifers. The source and mobilization of groundwater arsenic in granular aquifers are likely controlled by the following mechanism: organic matter in marine strata was mineralized and this provided electrons for electron acceptors, resulting in the release of NH_4^+ and I^- and the reduction of Fe/Mn and NO_3^- , which was accompanied with the mobilization of arsenic from sediments into groundwater.

In the paper “A Coupled One-Dimensional Numerical Simulation of the Land Subsidence Process in a Multilayer Aquifer System due to Hydraulic Head Variation in the Pumped Layer,” Y. Wang et al. focused on a case study of land subsidence modeling in China. A numerical model of a coupled one-dimensional multilayer aquifer system is developed. The results show that the pressure head in layers does not rise immediately after pumping ceases. Also, the results show that there is a transition period between land subsidence and rebound. In this transition period, land could continue to subside while the head in the pumped layer starts to recover.

Conflicts of Interest

The authors declare that there is no conflict of interest regarding the publication of this article.

Acknowledgments

The guest editorial team would like to thank all the authors for their contributions to this special issue. We also thank anonymous reviewers for their constructive comments which have greatly improved the quality of those papers. We hope that you enjoy reading this special issue that highlights the geoenvironmental issues of gas-water-rock interactions.

Liangping Li
Meijing Zhang
Ming Zhang

References

- [1] L. Li, H. Zhou, and J. J. Gómez-Hernández, “A comparative study of three-dimensional hydraulic conductivity upscaling at the macro-dispersion experiment (MADE) site, Columbus Air Force Base, Mississippi (USA),” *Journal of Hydrology*, vol. 404, no. 3–4, pp. 278–293, 2011.
- [2] G. Huang, M. Zhang, C. Liu, L. Li, and Z. Chen, “Heavy metal(-loid)s and organic contaminants in groundwater in the Pearl River Delta that has undergone three decades of urbanization and industrialization: distributions, sources, and driving forces,” *Science of the Total Environment*, vol. 635, pp. 913–925, 2018.
- [3] M. Zhang and M. J. McSaveney, “Is air pollution causing landslides in China?,” *Earth and Planetary Science Letters*, vol. 481, pp. 284–289, 2018.

Research Article

Sources Identification of Nitrogen Using Major Ions and Isotopic Tracers in Shenyang, China

Huan Huang¹,^{ORCID} Mingzhu Liu¹,^{ORCID} Junjie Wang,² Jiangtao He,¹ and Honghan Chen¹

¹Beijing Key Laboratory of Water Resources & Environmental Engineering, China University of Geosciences (Beijing), Beijing, China

²Development Research Center of the Ministry of Water Resources of P.R. China, Beijing, China

Correspondence should be addressed to Mingzhu Liu; liumz@cugb.edu.cn

Received 17 October 2017; Revised 30 April 2018; Accepted 3 July 2018; Published 23 August 2018

Academic Editor: Meijing Zhang

Copyright © 2018 Huan Huang et al. This is an open access article distributed under the Creative Commons Attribution License, which permits unrestricted use, distribution, and reproduction in any medium, provided the original work is properly cited.

Stable isotopes are natural tracers that can provide quantitative information about the surface water/groundwater interactions and sources of pollutants in water. In this study, we measured $\delta^{18}\text{O}_{\text{water}}$ and $\delta^2\text{H}_{\text{water}}$ and $\delta^{18}\text{O}_{\text{nitrate}}$ and $\delta^{15}\text{N}_{\text{nitrate}}$ of the samples from the Hun River and groundwater in Shenyang City, China, where the water from the Hun River has a strong discharge and recharge connection with the groundwater. $\delta^{18}\text{O}_{\text{water}}$ and $\delta^2\text{H}_{\text{water}}$ were used to determine the amount of surface water that was discharged into groundwater, while $\delta^{18}\text{O}_{\text{nitrate}}$ and $\delta^{15}\text{N}_{\text{nitrate}}$ were employed to determine the sources of nitrate and ammonium in groundwater, which are the main contaminants in the study area. The reducing environment in groundwater may result from the prevailing iron and manganese, occurring from weathering of minerals and rocks, which prevents the ammonium being oxidized into nitrate. Results show that the amount of recharge from the Hun River into groundwater accounts for around 55.56–86.60% of the total groundwater in the dry season, and the ratio changed to 30.97–63.79% in the wet season. Multiproxy analysis (stable isotope analyses in combination with chemical and hydrogeological data of the study area) indicates that human activities, such as manure and sewage discharge, are the prevailing source of nitrogen in the waters.

1. Introduction

Nitrogen pollution is an increasingly serious problem of groundwater in the riparian wellhead area of the Hun River. On the basis of the monitoring data of groundwater quality, nitrogen pollution has been found in most monitoring wells. Some water source wells have to be suspended, because the nitrogen content in groundwater exceeds the threshold in the Standard for Groundwater Quality (GB/T14848-93) in China. There are many sources of nitrogen pollution, and different sources cause different degrees of nitrogen pollution to groundwater. The groundwater source near the river plays an important role in the water supply in Shenyang. Therefore, it is of great significance to identify the source of groundwater nitrogen pollution and its contribution level and to carry out the targeted pollution control work and protect the groundwater resources.

Groundwater and surface water (such as rivers and lakes) are important components of the hydrological cycle, and they

interact with each other in a variety of physiographic and climatic landscapes in the hydrologic system. Water quality and quantity from one component may have an influence on the other component in the hydrological cycle. Therefore, it is necessary to understand the basic principles of interactions between them, as well as spatial and temporal transformation rules of water quantity and quality between groundwater and surface water. These understandings will be of theoretical and practical significance with regard to assessment of water quantity and quality and further lead to the remediation, treatment, and prevention of water pollution [1–4].

The interaction between river water and groundwater is related to factors such as geography, landform, and rock characteristics of the water-bearing stratum, which are changing with seasons. In time and space, the transformation of groundwater and river water forms an indivisible complex system. Therefore, the chemical composition of water may be due to its long-term interaction with the surrounding

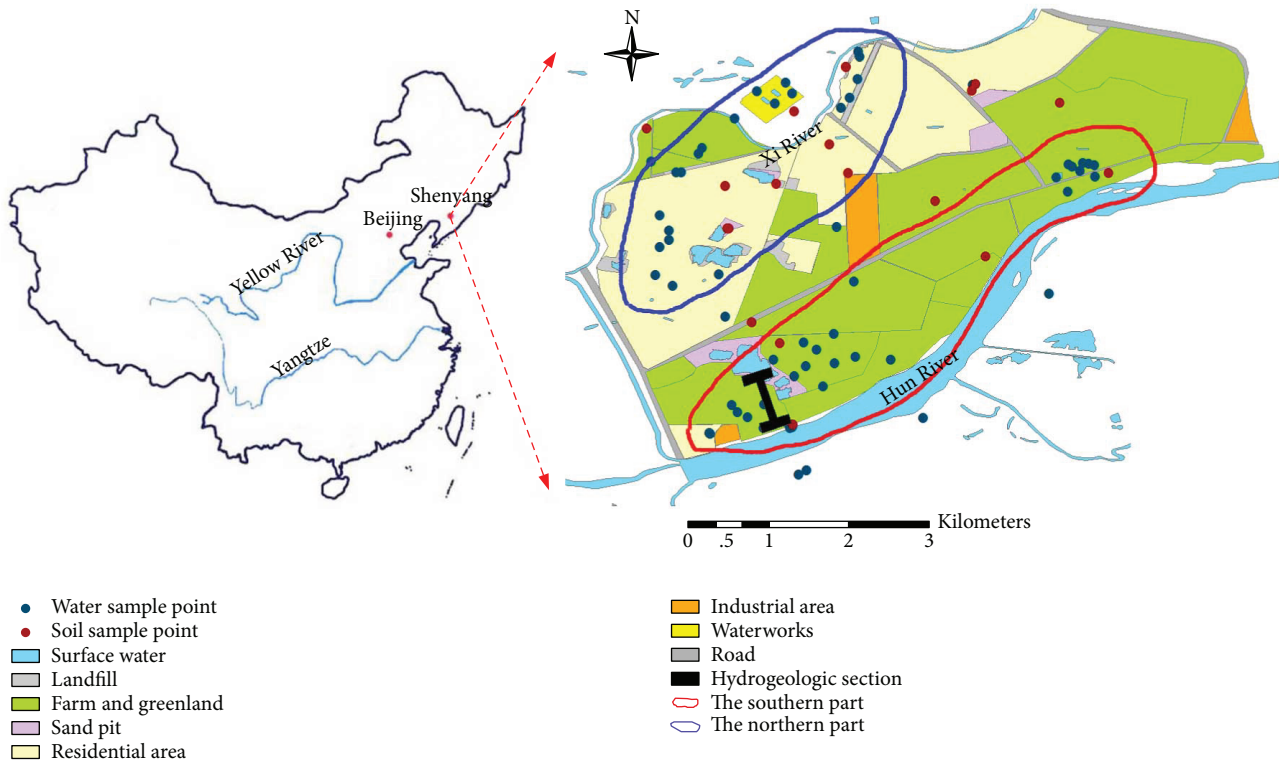


FIGURE 1: Location map of the study area. Modified from L. Y. Liu et al. [20].

environment in the water cycle. Moreover, water quality changes are usually caused by more complex interactions [3, 5–10]. Accordingly, the chemical composition of water can reflect its source information and evolution history to a certain extent, which will provide an effective tracing method for the study of the interaction between groundwater and surface water [11, 12]. Researchers in different disciplines, such as geologists, hydrologists, and ecologists, are developing a more comprehensive conceptualization of groundwater and surface water interactions [13]; for example, Levy and Xu [14] review and compare methods to describe groundwater and surface water interactions at different scales and show typical applications in South Africa. Hayashi and Rosenberry [15] provide a comprehensive review for the effect of groundwater exchange on the hydrology and ecology of surface water. This work attempts to investigate the broader, multi-disciplinary perspective of groundwater and surface water interactions, starting from some underlying prerequisites for comprehending environmental systems. To this end, we evaluate the hydrologic and water quality data for the Hun River basin, Shenyang city, China, to better understand the interactions between groundwater and surface water.

The main objective of the study was to identify the source(s) of nitrogen contamination in groundwater along the Hun River, Shenyang, China. To this end, the interactions between the Hun River and groundwater are analyzed with respect to the hydrogeology conditions of the site. $\delta^{18}\text{O}_{\text{water}}$ and $\delta^2\text{H}_{\text{water}}$ and $\delta^{18}\text{O}_{\text{nitrate}}$ and $\delta^{15}\text{N}_{\text{nitrate}}$ were measured from the Hun River and groundwater to determine the

amount of surface water that was discharged into groundwater as well as to track back the sources of the main contaminant. The approaches presented in this paper provide a framework for evaluating the importance of the interactions between groundwater and surface water in a human-natural coupled watershed.

2. Geological Setting

2.1. Description of Site. The study area lies in Shenyang city, Liaoning province, China, within latitudes $41^{\circ}42'00'' \sim 41^{\circ}47'30''$ and longitudes $123^{\circ}15'00'' \sim 123^{\circ}30'00''$ in the northeast of China. It is located between the Xi River and the Hun River and covers an area of about 36 km^2 (Figure 1). The northern part of the study area was mainly residential and industrial land, which has a high intensity of contaminating sources. The south of the research area was the farmland and the green land with a relatively high intensity of contamination source.

2.2. Geology and Hydrogeology Conditions. The study area is located in the first terrace of the Hun River alluvial-proluvial fan. The groundwater system consists of the phreatic aquifer and the leaky confined aquifer (Figure 2). The phreatic aquifer is composed mainly of medium sand and medium-coarse sand (hydraulic conductivity of ca. $7 \times 10^{-4} \text{ m}\cdot\text{s}^{-1}$ [16]). The thickness of the phreatic aquifer is ca. 15 m. The leaky confined aquifer is located below ca. 16 m from the surface, mainly composed of medium sand

and medium-fine sand, with a thickness of ca. 15 m. For the aquitard, it is located ca. 40 m below ground surface and composed mainly of clay and silty clay (hydraulic conductivity of ca. $8 \times 10^{-11} \text{ m} \cdot \text{s}^{-1}$ [16]). The groundwater table ranges from 10 to 12 m below ground surface, and the thickness of the aquitard is 4–6 m.

3. Sampling and Methodology

Sampling conditions were shown in Table 1. The shallow well refers to the sampling well located in the phreatic aquifer, and the deep well refers to the sampling well located in the leaky confined aquifer. All water samples were collected in 50 mL high-density polyethylene bottles which were cleaned with detergent first, then with 10% nitric acid, and finally rinsed several times with distilled water. This procedure was carried out to ensure that the sample bottles we used were all free from contaminants.

In order to obtain the fresh aquifer samples for analysis, every borehole at the sampling point was pumped for about 5 minutes to purge the aquifer of stagnant water. Samples were initially collected in a sterilized bucket immediately after purging the aquifer and quickly transferred into the sampling bottles. Samples were taken in duplicate for major ion and stable isotope analyses. Some basic parameters of groundwater were measured directly in the field, including the temperature, pH, dissolved oxygen (DO), total dissolved solid (TDS), and electrical conductivity (EC). Samples earmarked for major ion analyses were filtered on-site through 0.45 mm cellulose filters with the aid of a hand-operated vacuum pump. The samples were kept in the refrigerator until they were transported to the laboratory for chemical analysis.

The major ions in the water at each sampling point were analyzed using a Dionex-120 ion chromatograph from the Laboratory of Environmental Chemistry, China University of Geosciences (Beijing). The accuracy of the analyses was estimated from the charge balance error (Freeze and Cherry, 1979), which is within $\pm 5\%$ for all samples.

The stable hydrogen (^2H) and oxygen (^{18}O) isotopes in water collected in June 2011 (47 water samples) and September 2012 (54 water samples) were measured by a Picarro Isotopic Water Analyzer in the Water and Water-Rock Reactions Isotope Laboratory, Institute of Geology and Geophysics, Chinese Academy of Sciences. The isotopic results of $^2\text{H}_{\text{water}}$ and $^{18}\text{O}_{\text{water}}$ were reported as $\delta^2\text{H}_{\text{water}}$ and $\delta^{18}\text{O}_{\text{water}}$ ($\delta = (R_{\text{sample}}/R_{\text{standard}} - 1) \times 1000$) in per mil (‰) data with the Vienna Standard Mean Ocean Water (VSMOW) standard. The analytical precision is $\pm 0.2\text{‰}$ and $\pm 0.02\text{‰}$ for $\delta^2\text{H}_{\text{water}}$ and $\delta^{18}\text{O}_{\text{water}}$, respectively.

The stable isotopes of nitrogen (^{15}N) and oxygen (^{18}O) of nitrate in 26 water samples collected in June 2011 were analyzed in the Ministry of Land and Resources of Karst Geology Environmental Supervision and Testing Center using the anion exchange technique. The method for removing all O-bearing compounds from samples except NO_3^- and for removing the interference from other components to nitrogen measurement were based on a former paper reported by Silva et al. [17]. The stable isotopes of nitrogen

(^{15}N) and oxygen (^{18}O) of nitrate in 28 water samples and 11 soil samples collected in September 2012 were measured with the Isotope Mass Spectrometer MAT253 at the Soil and Environment Analysis and Testing Center, Nanjing Institute of Soil Sciences, Chinese Academy of Sciences, according to the method of Brand [18]. The ^{15}N results were reported as $\delta^{15}\text{N}_{\text{nitrate}}$ relative to air in per mil (‰) data. The analytical precision of $\delta^{15}\text{N}_{\text{nitrate}}$ and $\delta^{18}\text{O}_{\text{nitrate}}$ was about 0.05‰ and 0.5‰, respectively.

4. Results and Discussion

4.1. Hydrochemistry Analysis. The statistical results of the chemical index of the samples of groundwater and surface water are shown in Tables 2 and 3. The variation range of pH in groundwater (both the southern and northern side of the study area) was 5.94–7.41, and the majority of the samples were within natural pH range of 6.50–8.50. The pH of surface water (Hun River) varied from 7.14 to 8.20 with a mean of 7.60, which was generally higher than the values in the groundwater. Lower pH of the water in the study area might be associated with CO_2 produced by microbial respiration in the surface soil [19] or associated with local precipitation infiltration [20, 21]. The EC results in groundwater ranged from 511.50 to 1783.00 $\mu\text{S} \cdot \text{cm}^{-1}$, while the values for surface water ranged from 877.20 to 1231.90 $\mu\text{S} \cdot \text{cm}^{-1}$. The standard of drinking water for EC values in the World Health Organization (WHO) was between 500 and 1500 $\mu\text{S} \cdot \text{cm}^{-1}$ (Rodier, 1996), and some samples in both groundwater and the Hun River were higher than the standard value. From 2001 to 2005, nearly 400,000 tons of domestic sewage water and a portion of industrial waste water were discharged into the Shenyang section of the Hun River without treatment every day (Lin et al., 2007); the polluted river recharged the aquifer and may lead to the increase of EC value. The relative errors of charge balance for all the elements in groundwater and river in June 2011 were -1.53% and -1.49% , respectively, and those for March 2011 were 4.71% and 5.67%, respectively.

From 2001 to 2005, the concentration of ammonium nitrogen (abbreviated as NH_4^+-N) in the river water was as high as 9.72 $\text{mg} \cdot \text{L}^{-1}$ to 22.35 $\text{mg} \cdot \text{L}^{-1}$ (Lin et al., 2007). A high level of NH_4^+-N in moving water indicated some kind of contaminant entering the water. The Hun River of the study area was characterized by high levels of ammonium nitrogen concentrations, and all surface water samples exceeded the 0.5 $\text{mg} \cdot \text{L}^{-1}$ limit specified by the WHO drinking water standard. The Hun River was close to heavily fertilized fields, and therefore, the manure and sewage discharged into the Hun River might contain a higher ammonium nitrogen.

In March 2011, the content of NH_4^+-N in the water samples of the southern part was larger than that in the northern part. The content of NH_4^+-N in the Hun River had reached 6.09–12.12 $\text{mg} \cdot \text{L}^{-1}$, and the groundwater sampling points of high concentration were located at the riverside. The groundwater level is lower than the river level due to the exploitation of water source wells. Therefore, it can be speculated that the ammonia in groundwater comes from the Hun River. In addition, fertilizers containing ammonium

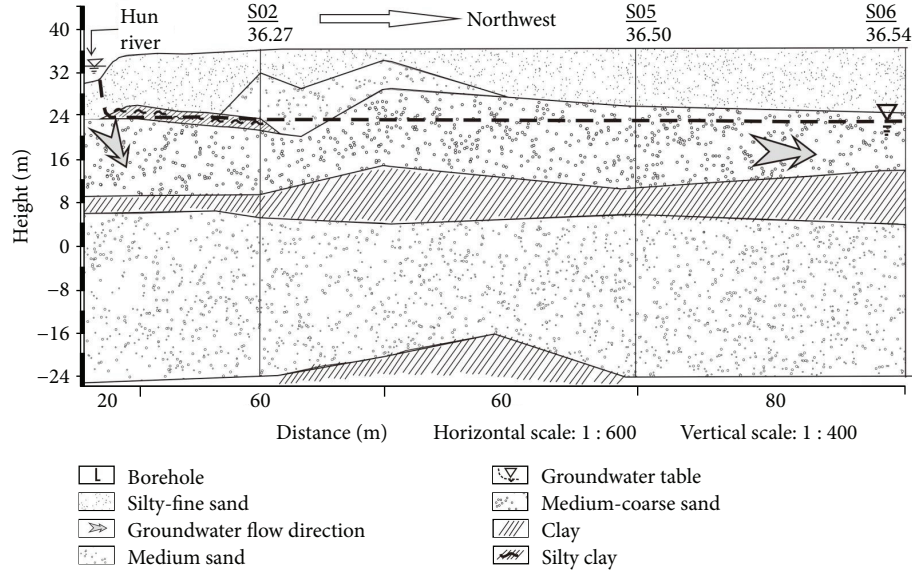


FIGURE 2: Hydrogeologic profile of the region near the Hun River. Modified from Hou et al. [16].

sulfate, $(\text{NH}_4)_2\text{SO}_4$, or ammonium nitrate, NH_4NO_3 , might also result in a high level of ammonium ions in the samples. The most serious contaminants in the groundwater were $\text{NH}_4^+\text{-N}$, ranging from 0.02 to $24\text{ mg}\cdot\text{L}^{-1}$, which was followed by $\text{NO}_3^-\text{-N}$ ($0.16\text{--}71.50\text{ mg}\cdot\text{L}^{-1}$), TFe ($0.05\text{--}12.92\text{ mg}\cdot\text{L}^{-1}$), and Mn^{2+} ($0.15\text{--}9.92\text{ mg}\cdot\text{L}^{-1}$). $\text{NH}_4^+\text{-N}$, $\text{NO}_3^-\text{-N}$, TFe, and Mn^{2+} concentrations at some locations exceeded the $0.5\text{ mg}\cdot\text{L}^{-1}$ ($\text{NH}_4^+\text{-N}$), $11\text{ mg}\cdot\text{L}^{-1}$ ($\text{NO}_3^-\text{-N}$), $0.3\text{ mg}\cdot\text{L}^{-1}$ (TFe), and $0.1\text{ mg}\cdot\text{L}^{-1}$ (Mn^{2+}) limits specified by the WHO drinking water standard. The study area was a primary high iron and manganese groundwater zone [22]. The iron and manganese minerals in the study area were goethite, siderite, and rhodochrosite and contained a small amount of pyrite, magnetite, and pyrolusite [23]. The most common sources of Fe^{2+} , Fe^{3+} , and Mn^{2+} in groundwater were likely occurring naturally, from weathering of iron and manganese oxide minerals. However, industrial effluent, sewage, and landfill leachate might also contribute to Fe^{2+} , Fe^{3+} , and Mn^{2+} in groundwater [24, 25].

4.2. Groundwater Recharge. The geophysical investigation results showed that there was a close hydraulic connection between the phreatic aquifer in the study area and the Hun River. About 1 million cubic meters of groundwater were pumped every day from the Hun River aquifer for urban water supply, and a groundwater depression cone was formed, which causes continuous recharge of the river water to the phreatic aquifer. The phreatic aquifer and leaky confined aquifer are the main layers for groundwater exploitation in the area, and there is close hydraulic connection between the two aquifers [26]. The geophysical investigation results also revealed that there was a connection between the Hun River and the aquifer 60m below the surface in the riverside area. As for the water quality, the Hun River, with a long history of pollution, also had a close relationship with groundwater. For example, the nitrogen concentration in groundwater was high, and a large portion was from the

TABLE 1: Sampling conditions in different periods.

Sampling time	March 2011	June 2011	September 2012
Deep wells	29	49	27
Shallow wells	9	20	24
Surface water	7	10	7
Soil samples	0	0	13

seepage of the Hun River, which had already been polluted by the manure and sewage and runoff from heavily fertilized fields, causing the river water to continuously recharge the phreatic aquifer.

4.3. Isotopic Compositions of Groundwater and the Hun River. Differences in the content of $\delta^2\text{H}_{\text{water}}$ and $\delta^{18}\text{O}_{\text{water}}$ of groundwater, rainfall, and surface water were used to determine the mixing processes in the groundwater flow system in the study area. $\delta^2\text{H}_{\text{water}}$ and $\delta^{18}\text{O}_{\text{water}}$ data typically were plotted on a diagram showing $\delta^2\text{H}_{\text{water}}$ versus $\delta^{18}\text{O}_{\text{water}}$ relative to VSMOW. Mean annual values of $\delta^2\text{H}_{\text{water}}$ and $\delta^{18}\text{O}_{\text{water}}$ in precipitation collected at many locations around the world plot along a line with a slope of 8 and an intercept of +10 ($\delta^2\text{H} = 8\delta^{18}\text{O} + 10$), commonly referred to as the global meteoric water line (GMWL) [27]. The variability in isotopic composition of rainfall from one site to another is a function of several factors, including storm-track origin, rainfall amount and intensity, atmospheric temperature, and the number of evaporation and condensation cycles [28]. The stable isotopic composition of water relative to the GMWL revealed important information on groundwater recharge patterns, the origin of waters in hydrologic systems, and mixing of groundwater and surface water.

The exchange of water between river and aquifer could be traced by the difference in stable isotope composition between the regional groundwater and the river water. The

TABLE 2: Statistical summary of hydrochemical data in the Shenyang areas, March 2011. All units are in $\text{mg}\cdot\text{L}^{-1}$, except for electrical conductivity (EC, $\mu\text{S}\cdot\text{cm}^{-1}$).

Parameter	Groundwater						The Hun River		
	Mean	Southern side Max	Min	Mean	Northern side Max	Min	Mean	Max	Min
pH	7.08	7.41	6.45	6.44	6.85	5.94	7.60	8.20	7.14
EC	628.86	1035.00	511.50	1170.53	1783.00	650.60	1231.90	1652.00	877.20
Ca	61.79	111.00	34.00	4.13	9.00	1.50	81.81	91.00	70.00
Mg	19.16	35.00	1.00	41.53	85.00	18.00	25.54	32.00	20.00
Na	48.09	70.83	29.92	71.13	113.90	33.43	110.84	182.20	50.69
K	3.66	5.86	2.49	4.04	6.92	2.24	7.22	8.48	4.20
Fe	1.13	5.16	0.06	2.62	23.86	0.13	1.59	4.93	0.99
Mn	1.25	2.46	0.15	2.00	4.04	0.21	0.45	2.29	0.45
$\text{NH}_4\text{-N}$	2.55	12.11	0.03	0.14	0.68	0.03	12.12	19.00	6.09
Cl	55.58	83.00	30.00	126.73	204.00	53.00	175.18	271.00	102.00
HCO_3	189.77	259.16	98.13	153.97	236.47	70.45	201.29	228.97	178.65
$\text{NO}_3\text{-N}$	9.11	76.27	0.71	137.73	401.02	13.55	2.70	5.61	1.20
SO_4	86.96	55.69	154.47	147.86	201.07	75.98	122.70	150.03	96.39

TABLE 3: Statistical summary of hydrochemical data in the Shenyang areas, June 2011. All units are in $\text{mg}\cdot\text{L}^{-1}$, except for electrical conductivity (EC, $\mu\text{S}\cdot\text{cm}^{-1}$).

Parameter	Groundwater						The Hun River		
	Mean	Southern side Max	Min	Mean	Northern side Max	Min	Mean	Max	Min
pH	6.86	7.32	6.15	6.61	7.06	6.22	7.26	7.36	7.02
EC	690.18	1033.00	546.50	1356.37	2871.00	619.7	962.15	1399.0	474.8
Ca	72.59	114.20	47.65	130.67	270.20	59.93	53.99	59.62	49.97
Mg	17.34	27.75	11.77	34.78	52.64	12.98	12.86	15.96	11.77
Na	52.19	67.34	33.66	81.89	132.10	38.98	30.71	35.48	27.61
K	4.84	6.90	2.72	7.00	40.41	1.92	4.87	5.38	4.12
Fe	0.89	6.49	0.02	1.21	11.79	0.03	0.35	0.61	0.19
Mn	1.68	3.17	0.02	3.36	9.48	0.04	2.12	6.39	0.43
$\text{NH}_4\text{-N}$	1.10	4.79	0.06	2.51	17.53	0.03	0.07	0.12	0.05
Cl	61.01	104.60	44.88	136.87	287.62	48.66	46.26	55.33	40.38
HCO_3	214.38	281.14	123.17	268.22	527.50	93.71	143.27	123.20	179.40
$\text{NO}_3\text{-N}$	38.71	102.71	2.58	135.29	338.24	6.23	2.79	4.37	1.77
SO_4	92.34	142.32	58.13	174.44	500.32	28.56	75.21	78.19	73.39

results of stable isotope (Tables 4 and 5) showed clear mixing between shallow groundwater and surface water in the basin. In groundwater, the mean values of $\delta^2\text{H}_{\text{water}}$ and $\delta^{18}\text{O}_{\text{water}}$ for the dry season (June 2011) were -8.87 and -65.12‰ , respectively, and those for the wet season (September 2012) were -8.79 and -65.64‰ , respectively; because of the lag of river and precipitation recharge, the isotope content in the dry and wet periods is not significantly different. But in the Hun River, the mean values of $\delta^2\text{H}_{\text{water}}$ and $\delta^{18}\text{O}_{\text{water}}$ for the dry season (June 2011) were -9.16 and -65.79‰ , respectively, and those for the wet season (September 2012) were -9.54 and -70.25‰ , respectively. The values of $\delta^2\text{H}_{\text{water}}$ and $\delta^{18}\text{O}_{\text{water}}$ in the wet season were -0.38‰ and -4.46‰

higher, respectively, than those in the dry season. Generally, the stable isotopic compositions of precipitation decrease with decreasing temperature and with increasing rainfall amount [29]. The results showed that the effect of precipitation amount was significant, and the stable isotope composition of precipitation decreased with the increase of rainfall amount and air temperature.

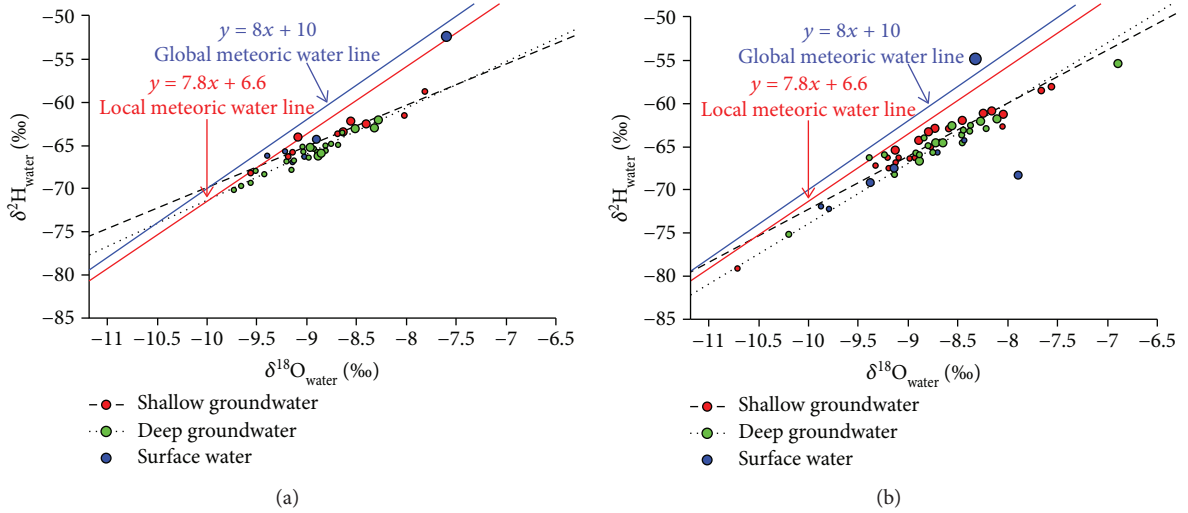
In Figures 3(a) and 3(b) (the size of the symbols represents the perpendicular distance of the sampling site measured from the Hun River), both $\delta^{18}\text{O}_{\text{water}}$ and $\delta^2\text{H}_{\text{water}}$ of the groundwater and surface water were located slightly lower than the local meteoric water line (LMWL), these suggesting that there was evaporation in the basin, and the

TABLE 4: Statistical summary of $\delta^{18}\text{O}_{\text{water}}$ (‰) and $\delta^2\text{H}_{\text{water}}$ (‰) values of groundwater and river water in the study area.

	Groundwater				The Hun River			
	Dry season		Wet season		Dry season		Wet season	
	$\delta^{18}\text{O}$ (‰)	$\delta^2\text{H}$ (‰)	$\delta^{18}\text{O}$ (‰)	$\delta^2\text{H}$ (‰)	$\delta^{18}\text{O}$ (‰)	$\delta^2\text{H}$ (‰)	$\delta^{18}\text{O}$ (‰)	$\delta^2\text{H}$ (‰)
Mean	-8.87	-65.12	-8.79	-65.64	-9.16	-65.79	-9.54	-70.25
Maximum	-7.82	-58.77	-6.90	-55.30	-8.90	-64.3	-9.14	-67.60
Minimum	-9.73	-70.24	-13.85	-103.2	-9.39	-66.92	-9.87	-72.30

TABLE 5: Statistical summary of $\delta^{18}\text{O}_{\text{nitrate}}$ (‰) and $\delta^{15}\text{N}_{\text{nitrate}}$ (‰) values of groundwater and river water in the study area.

	Groundwater				The Hun River			
	Dry season		Wet season		Dry season		Wet season	
	$\delta^{18}\text{O}$ (‰)	$\delta^{15}\text{N}$ (‰)	$\delta^{18}\text{O}$ (‰)	$\delta^{15}\text{N}$ (‰)	$\delta^{18}\text{O}$ (‰)	$\delta^{15}\text{N}$ (‰)	$\delta^{18}\text{O}$ (‰)	$\delta^{15}\text{N}$ (‰)
Mean	10.87	6.17	5.04	9.74	13.05	3.25	3.16	5.70
Maximum	14.08	13.22	15.02	24.85	15.96	3.87	13.31	7.26
Minimum	7.36	-3.14	-18.36	-7.26	10.13	2.63	-10.36	3.80

FIGURE 3: Plot of $\delta^2\text{H}_{\text{water}}$ and $\delta^{18}\text{O}_{\text{water}}$ for shallow groundwater, deep groundwater, and surface water samples collected in the study region: (a) dry season; (b) wet season.

groundwater was a mixture of river water and precipitation, and the influence of the river water recharge was greater than that of the infiltration.

In Figure 3, the distribution of deep groundwater and shallow groundwater was approximately the same, which was further consistent with the closely hydraulic connection between the two layers of aquifer. The points representing shallow groundwater were closer to the LMWL, and the phenomenon was more obvious in Figure 3(b) (wet season). This means that the phreatic aquifer was more affected by rainfall than the leaky confined aquifer. The values of $\delta^{18}\text{O}_{\text{water}}$ and $\delta^2\text{H}_{\text{water}}$ of the points far away from the river bank (larger symbols) were higher than those near the Hun River (smaller symbols). This indicates that the groundwater in the riverside area is more affected by the river. It receives the recharge of the Hun River, and the isotopic enrichment occurs at a distance from the river.

4.4. Mass Balance of Isotopic Compositions of Groundwater. Different stable isotopic compositions of $^2\text{H}_{\text{water}}$ and $^{18}\text{O}_{\text{water}}$ in groundwater were used to identify the mixing progress in the study area. The variability in isotopic composition of rainfall from one site to another is a function of several factors, including storm-track origin, rainfall amount and intensity, atmospheric temperature, and the number of evaporation and condensation cycles [28]. The stable isotopic composition of water relative to the GMWL revealed important information on groundwater recharge patterns, the origin of waters in hydrologic systems, and mixing of groundwater and surface water [30, 31].

The isotopic composition of groundwater is equivalent to the average weighted value of recharge sources. Therefore, there are deviations in isotope ratios between groundwater and precipitation. Understanding the transfer function of precipitation to groundwater is crucial to the study of

TABLE 6: The recharge ratios of the Hun River to the groundwater.

Section	Point	Distance from Hun River (km)		G (‰)	R (‰)	P (‰)	θ (%)
I	LG18	1.02	$\delta^{18}\text{O}$	-8.69	-9.14	-7.59	70.97
			$\delta^2\text{H}$	-52.44	-66.92	-64.98	86.60
II	ZK05	0.66	$\delta^{18}\text{O}$	-8.49	-9.21	-7.59	55.56
			$\delta^2\text{H}$	-52.44	-65.7	-63.45	83.03
III	JS23-1	0.41	$\delta^{18}\text{O}$	-8.80	-9.87	-8.32	30.97
			$\delta^2\text{H}$	-54.90	-71.90	-64.90	58.82
IV	LG42-2	0.47	$\delta^{18}\text{O}$	-8.88	-9.79	-8.32	38.10
			$\delta^2\text{H}$	-54.90	-72.30	-66.00	63.79

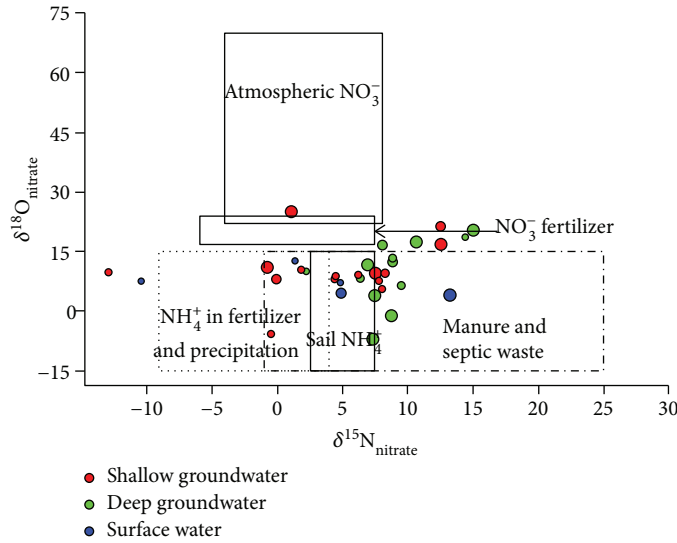


FIGURE 4: Dual-isotope method for nitrate source attribution in groundwater, September 2012. Modified from Fenech et al. [33].

groundwater sources. The transfer function can provide basic information of recharge mechanism [32].

Groundwater in the study area was recharged by rainfall and river water. In the study of basin water balance, it was important to assess the actual recharge of groundwater by rainfall and river water. The stable isotopes of groundwater were determined by the percentage of recharge from the relevant sources. It is assumed that the groundwater in the vicinity of the study area is a mixture of the Hun River and the precipitation. Based on the mass balance calculation of oxygen and hydrogen isotopes, the contribution percentage of each recharge source to groundwater in the study area could be evaluated by the following equation:

$$\begin{aligned}
 G(V_P + V_R) &= PV_P + RV_R, \\
 G &= P \frac{V_P}{V_P + V_R} + R \frac{V_R}{V_P + V_R} = P(1 - X) + RX, \\
 X &= \frac{G - P}{R - P} \times 100\%,
 \end{aligned} \tag{1}$$

where P is the precipitation stable isotope value, R is the river water stable isotope value, G is the groundwater

stable isotope value, V_P is the amount of precipitation, V_R is the amount of river water, X is the recharge proportion of river water, and $(1 - X)$ is the recharge proportion of precipitation.

According to the groundwater level in June 2011, two profiles were chosen to calculate the recharge of groundwater from the Hun River. The values of $\delta^2\text{H}_{\text{water}}$ and $\delta^{18}\text{O}_{\text{water}}$ in river water and rain were used as the endpoints for calculating groundwater recharge. Using the results of $\delta^2\text{H}_{\text{water}}$ and $\delta^{18}\text{O}_{\text{water}}$ in groundwater, river, and rain samples (Section I and II in Table 6), the recharge ratios of the Hun River to the groundwater are 55.56%–86.60%, respectively, and average value is 74.04%.

For September 2012, two profiles were chosen according to the groundwater level. Using the results of $\delta^2\text{H}_{\text{water}}$ and $\delta^{18}\text{O}_{\text{water}}$ in groundwater, river, and rain samples (Section III and IV in Table 6) the recharge ratios of the Hun River to groundwater are 30.97%–63.79%, respectively, and average value is 47.92%.

The recharge ratios of the Hun River to the groundwater in the dry season were about 55.56%–86.60%, and the ratio in the wet season was about 30.97%–63.79%. The difference in recharge ratio between the two seasons may be caused by seasonal variations and changes in groundwater exploitation

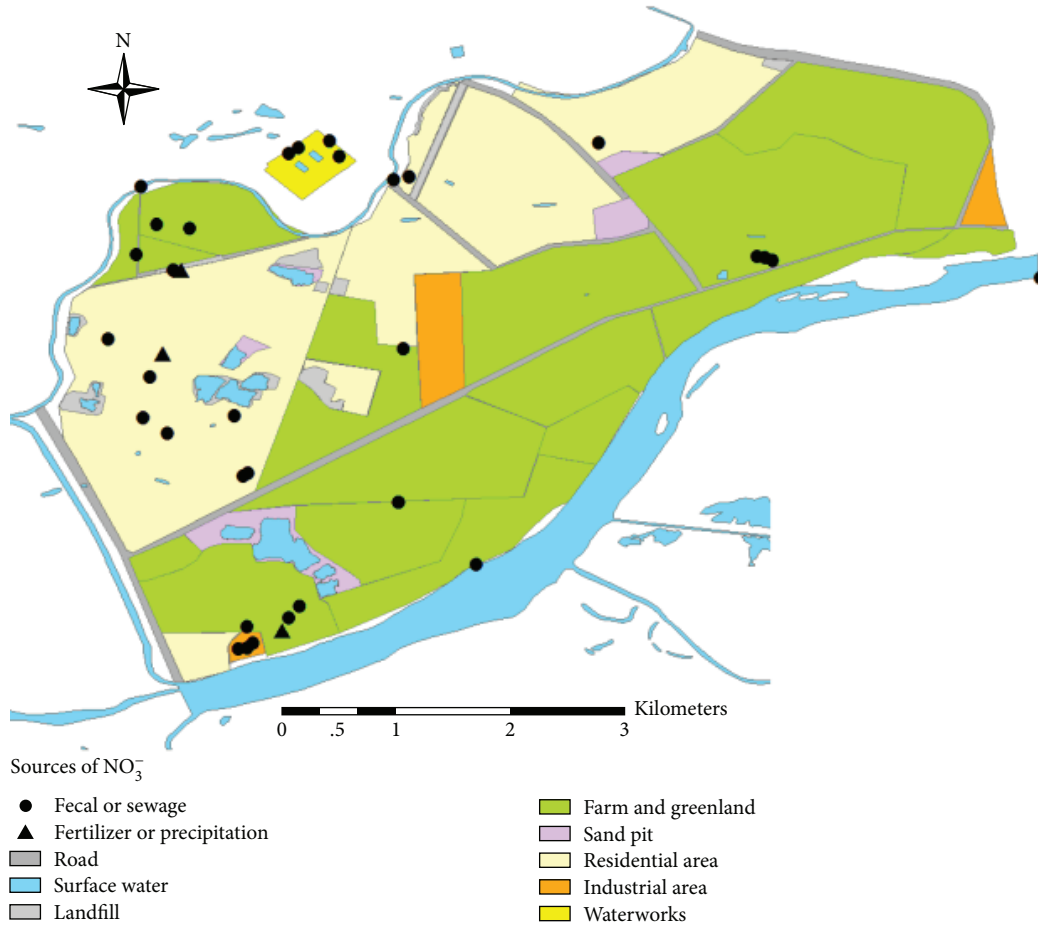


FIGURE 5: Nitrogen source spatial distribution in groundwater, September 2012.

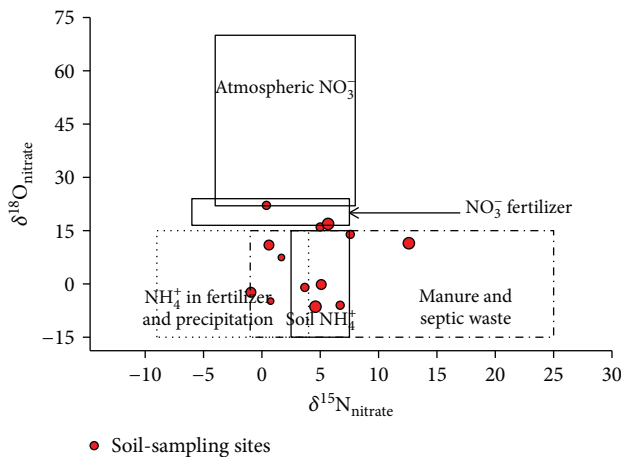


FIGURE 6: Dual-isotope method for nitrate source attribution in soil, September 2012. Modified from Fenech et al. [33].

intensity in the water source wells. In June 2011, the water source wells were in the mining state, and when the sample was taken in September 2012, the water source wells were almost not in use.

4.5. Source Identification of Groundwater Nitrogen Contamination. A key objective was to identify the sources of nitrogen pollution in the groundwater. Isotopic composition can be used to identify sources of groundwater contamination. Because different sources of NO_3^- have different $\delta^{15}\text{N}_{\text{nitrate}}$ and $\delta^{18}\text{O}_{\text{nitrate}}$ values, we identified the major contaminant source of NO_3^- in groundwater by detecting the NO_3^- isotopic composition in this study. Figure 4 shows the $\delta^{15}\text{N}_{\text{nitrate}}$ and $\delta^{18}\text{O}_{\text{nitrate}}$ values for the sample in the study area and the typical ranges for the major possible sources of NO_3^- [33, 34]. The main source of nitrogen could be attributed to the manure and septic waste by human activities, and the distribution of various nitrogen sources is shown in Figure 5. By using an isotopic source apportionment model based on the bias analysis of SIAR, Wang (2016) also found that the contribution rate of manure and sewage contamination is much higher than that of the other sources, reaching 76%–86% in the northern part of the study area.

In addition, soil samples were collected for the analysis of nitrogen and oxygen isotopes. Figure 6 shows the $\delta^{15}\text{N}_{\text{nitrate}}$ versus $\delta^{18}\text{O}_{\text{nitrate}}$ values for soil samples and different sources. It indicates that in the soil, $\delta^{15}\text{N}_{\text{nitrate}}$ values range from -10‰ to $+15\text{‰}$.

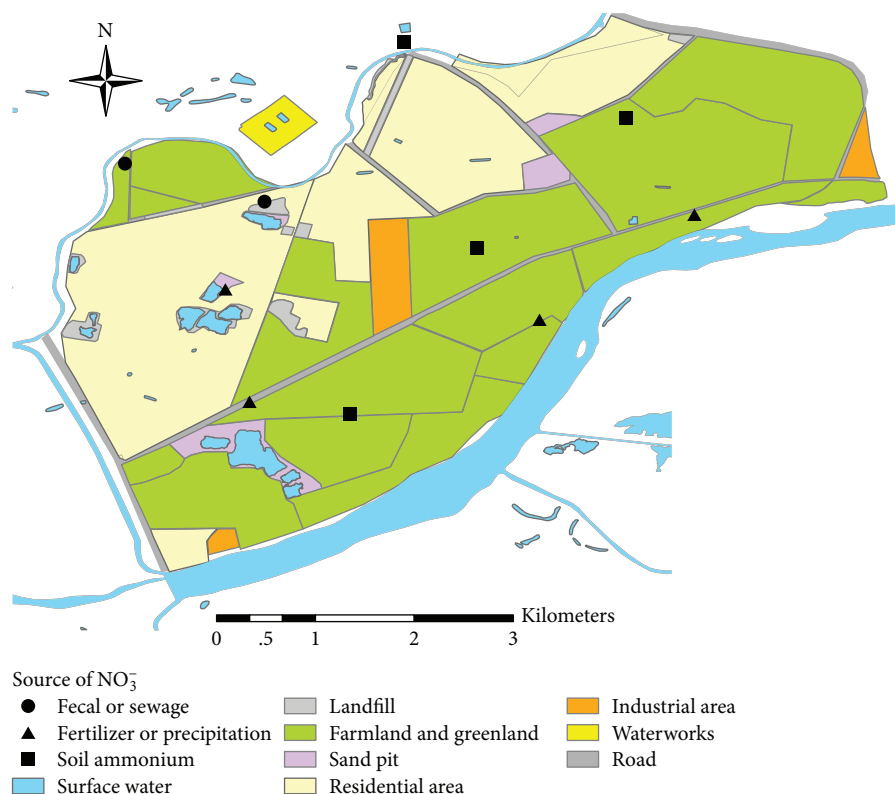


FIGURE 7: Sample point distribution and its nitrate source of soil samples in September 2012.

The location of the soil samples and the actual utilization of land showed in Figure 7 indicates that soil samples affected by manure and sewage were mainly distributed in the north-west of the study area. This was consistent with the analysis above; that is, groundwater pollution mainly results from manure and sewage infiltration [20, 21]. Nitrate in soil, originating from ammonium contained in soil input by fertilizers and precipitation, is mainly located in the southern part of the study area. This is consistent with the actual situation in the south area, mainly for farmland and green land.

5. Conclusions

In this paper, we used multiproxy analysis encompassing environmental isotopes and hydrochemical data to investigate the interactions between surface water and groundwater, as well as to identify the source of nitrogen contamination in groundwater in Shenyang city, China. Our work leads to the following major conclusions.

- (1) Water from the Hun River with an enriched isotopic signature moves downwards and laterally and mixes with the lower-gradient groundwater. The use of $\delta^2\text{H}_{\text{water}}$ and $\delta^{18}\text{O}_{\text{water}}$ in surface water and groundwater indicated that river water accounted for around 55.56%–86.60% of the total groundwater recharge in the dry season, and the ratio changed to 30.97%–63.79% in the wet season. The huge supply of

groundwater indicates that groundwater is highly susceptible to contamination from land surface activities.

- (2) Stable isotope analyses combined with the chemical and hydrogeological data from this study site indicate that the human activities, such as manure and sewage discharge, are the prevailing source of nitrogen in the waters. This will be useful for future management and decisions to control pollution sources and protect groundwater quality.

Conflicts of Interest

The authors declare that there is no conflict of interest regarding the publication of this paper.

Acknowledgments

The studies described in this paper were funded jointly by the 863 Program (2007AA06A410) of the Chinese Ministry of Science and Technology, the National Natural Science Foundation of China (no. 41572225), and the Studies of Safety Evaluation and Pollution Prevention Technology and Demonstration for Groundwater Resources in Beijing (D07050601510000).

Supplementary Materials

The original data of Table 2 are listed in Table S1. The original data of Table 3 are listed in Table S2. The original data of

Table 4 are listed in Table S3 for the dry season and in Table S4 for the wet season. The original data of Table 5 are listed in Table S5 for the dry season and in Table S6 for the wet season. The $\delta^{15}\text{N}_{\text{nitrate}}$ and $\delta^{18}\text{O}_{\text{nitrate}}$ values for soil samples are listed in Table S7. (*Supplementary Materials*)




References

- [1] M. Brunke and T. Gonser, "The ecological significance of exchange processes between rivers and groundwater," *Freshwater Biology*, vol. 37, no. 1, pp. 1–33, 1997.
- [2] S. Krause, A. Bronstert, and E. Zehe, "Groundwater–surface water interactions in a north German lowland floodplain—implications for the river discharge dynamics and riparian water balance," *Journal of Hydrology*, vol. 347, no. 3–4, pp. 404–417, 2007.
- [3] M. Sophocleous, "Interactions between groundwater and surface water: the state of the science," *Hydrogeology Journal*, vol. 10, no. 2, pp. 348–348, 2002.
- [4] D. O. Whittemore, M. S. Tsou, and C. McElwee, *Arkansas River Salinity and Contamination of the High Plains Aquifer. Challenges Facing Irrigation and Drainage in the New Millennium*, Proceedings Us Committee on Irrigation and Drainage, Fort Collins, Colorado, USA, 2000.
- [5] S. W. Chapman, B. L. Parker, J. A. Cherry, R. Aravena, and D. Hunkeler, "Groundwater–surface water interaction and its role on TCE groundwater plume attenuation," *Journal of Contaminant Hydrology*, vol. 91, no. 3–4, pp. 203–232, 2007.
- [6] R. S. Gabor, S. J. Hall, D. P. Eiriksson et al., "Persistent urban influence on surface water quality via impacted groundwater," *Environmental Science & Technology*, vol. 51, no. 17, pp. 9477–9487, 2017.
- [7] D. W. Rassam, D. E. Pagendam, and H. M. Hunter, "Conceptualisation and application of models for groundwater–surface water interactions and nitrate attenuation potential in riparian zones," *Environmental Modelling & Software*, vol. 23, no. 7, pp. 859–875, 2008.
- [8] K. E. Schilling, Z. Li, and Y. K. Zhang, "Groundwater–surface water interaction in the riparian zone of an incised channel, Walnut Creek, Iowa," *Journal of Hydrology*, vol. 327, no. 1–2, pp. 140–150, 2006.
- [9] J. Tóth, "Groundwater as a geologic agent: an overview of the causes, processes, and manifestations," *Hydrogeology Journal*, vol. 7, no. 1, pp. 1–14, 1999.
- [10] T. C. Winter, "Relation of streams, lakes, and wetlands to groundwater flow systems," *Hydrogeology Journal*, vol. 7, no. 1, pp. 28–45, 1999.
- [11] K. E. Bencala, V. C. Kennedy, G. W. Zellweger, A. P. Jackman, and R. J. Avanzino, "Interactions of solutes and streambed sediment: 1. An experimental analysis of cation and anion transport in a mountain stream," *Water Resources Research*, vol. 20, no. 12, pp. 1797–1803, 1984.
- [12] T. C. Winter, "Recent advances in understanding the interaction of groundwater and surface water," *Reviews of Geophysics*, vol. 33, no. S2, pp. 985–994, 1995.
- [13] R. Barthel and S. Banzhaf, "Groundwater and surface water interaction at the regional-scale—a review with focus on regional integrated models," *Water Resources Management*, vol. 30, no. 1, pp. 1–32, 2016.
- [14] J. Levy and Y. Xu, "Review: groundwater management and groundwater/surface-water interaction in the context of South African water policy," *Hydrogeology Journal*, vol. 20, no. 2, pp. 205–226, 2012.
- [15] M. Hayashi and D. O. Rosenberry, "Effects of ground water exchange on the hydrology and ecology of surface water," *Groundwater*, vol. 40, no. 3, pp. 309–316, 2002.
- [16] G. Hou, F. Liu, M. Liu et al., "Performance of a permeable reactive barrier for in situ removal of ammonium in groundwater," *Water Science & Technology: Water Supply*, vol. 14, no. 4, p. 585, 2014.
- [17] S. R. Silva, C. Kendall, D. H. Wilkison, A. C. Ziegler, C. C. Y. Chang, and R. J. Avanzino, "A new method for collection of nitrate from fresh water and the analysis of nitrogen and oxygen isotope ratios," *Journal of Hydrology*, vol. 228, no. 1–2, pp. 22–36, 2000.
- [18] W. A. Brand, "Precon: a fully automated interface for the pre-GC concentration of trace gases on air for isotopic analysis," *Isotopes in Environmental and Health Studies*, vol. 31, no. 3–4, pp. 277–284, 1995.
- [19] H. Koizumi, T. Nakadai, Y. Usami, M. Satoh, M. Shiyomi, and T. Oikawa, "Effect of carbon dioxide concentration on microbial respiration in soil," *Ecological Research*, vol. 6, no. 3, pp. 227–232, 1991.
- [20] L. Y. Liu, J. T. He, and J. J. Wang, "China ordnance industry survey and Geotechnical Institute Beijing Key Laboratory of Water Resources and Environmental Engineering," in *Contributions to the Source of Groundwater Nitrogen Pollution in Hun River Riparian Zone*, Geotechnical Engineering Technique, 2015.
- [21] Y. C. Liu, H. B. Yang, X. D. Zou et al., "Ph value in Shenyang area from 2005 to 2012," *Environmental Science & Technology*, vol. 38, no. 12Q, pp. 116–119, 2015.
- [22] D. Su, X. S. Su, L. H. Zhang et al., "Redox zonation in the process of river water infiltration in the Huangjia riverside well field, Shenyang City," *China Environmental Science*, vol. 36, no. 7, pp. 2043–2050, 2016.
- [23] W. Z. Yuan, *Biogeochemical Process of Fe and Mn during River Bank Infiltration Affected by Groundwater Exploiting*, Doctoral dissertation, Jilin University, 2017.
- [24] M. M. Abd El-Salam, E. M. El-Ghitany, and M. M. Kassem, "Quality of bottled water brands in Egypt part i: physico-chemical analyses," *The Journal of the Egyptian Public Health Association*, vol. 83, no. 5–6, pp. 369–388, 2008.
- [25] X. S. He, H. Yu, B. D. Xi, D. Y. Cui, H. W. Pan, and D. Li, "Difference of contaminant composition between landfill leachates and groundwater and its reasons," *Science*, vol. 35, no. 4, pp. 1399–1406, 2014.
- [26] N. Shan, *Research on Nitrogen Numerical Simulation of Typical Riverside Source Field*, Dissertation, China University of Geosciences (Beijing), 2011.
- [27] H. Craig, "Isotopic variations in meteoric waters," *Science*, vol. 133, no. 3465, pp. 1702–1703, 1961.
- [28] W. Dansgaard, "Stable isotopes in precipitation," *Tellus*, vol. 16, no. 4, pp. 436–468, 1964.
- [29] T. Coplen, "Stable isotope hydrology: deuterium and oxygen-18 in the water cycle," *Eos, Transactions American Geophysical Union*, vol. 63, no. 45, pp. 861–862, 1982.
- [30] D. A. Streletskiy, N. I. Tananaev, T. Opel et al., "Permafrost hydrology in changing climatic conditions: seasonal variability of stable isotope composition in rivers in discontinuous permafrost," *Environmental Research Letters*, vol. 10, no. 9, article 095003, 2015.

- [31] Q. Yang, H. Xiao, L. Zhao et al., “Hydrological and isotopic characterization of river water, groundwater, and groundwater recharge in the Heihe River basin, northwestern China,” *Hydrological Processes*, vol. 25, no. 8, pp. 1271–1283, 2011.
- [32] I. D. Clark and P. Fritz, *Environmental Isotopes in Hydrology*, vol. 80, no. 5, 1998, Boca Raton Fla Lewis Publishers, 1998, .
- [33] C. Fenech, L. Rock, K. Nolan, J. Tobin, and A. Morrissey, “The potential for a suite of isotope and chemical markers to differentiate sources of nitrate contamination: a review,” *Water Research*, vol. 46, no. 7, pp. 2023–2041, 2012.
- [34] C. Kendall, “Tracing nitrogen sources and cycling in catchments,” in *Isotope Tracers in Catchment Hydrology*, pp. 519–576, Elsevier, Amsterdam, 1998.

Research Article

A Statistical Constitutive Model considering Deterioration for Brittle Rocks under a Coupled Thermal-Mechanical Condition

Meiben Gao ^{1,2} Tianbin Li ^{1,2} Tao Wei,^{1,2} and Lubo Meng ^{1,2}

¹State Key Laboratory of Geohazard Prevention and Geoenvironment Protection, Chengdu University of Technology, Chengdu, Sichuan 610059, China

²College of Environment and Civil Engineering, Chengdu University of Technology, Chengdu, Sichuan 610059, China

Correspondence should be addressed to Tianbin Li; ltb@cdut.edu.cn

Received 2 March 2018; Revised 16 April 2018; Accepted 30 April 2018; Published 30 July 2018

Academic Editor: Ming Zhang

Copyright © 2018 Meiben Gao et al. This is an open access article distributed under the Creative Commons Attribution License, which permits unrestricted use, distribution, and reproduction in any medium, provided the original work is properly cited.

Due to active actions of groundwater and geothermal, the stability of underground engineering is important during geological structure active area. The damage mechanical theory and statistical mesoscopic strength theory based on Weibull distribution are widely used to discuss constitutive behaviors of rocks. In these theories, a statistical method is used to capture mesoscopic properties of rocks in order to generate a realistic behavior at a macroscopic scale. Based on the above theories, this paper aims at establishing a constitutive relation of brittle rocks under thermal-mechanical coupling conditions. First, a statistical damage constitutive model was established by considering the thermal effects and crack initiation strength. Subsequently, the parameters of the model were determined and expressed according to the characteristics of stress-strain curve. Third, the model was verified by conventional triaxial experiments under thermal-mechanical actions, and the experimental data and theoretical results were compared and analyzed in the case study. Finally, the physical meaning of the parameters and their effects on the model performance were discussed.

1. Introduction

With this longer, larger, and deeper underground engineering's construction, the rock deterioration caused by groundwater and geothermal has become increasingly prominent. Constitutive modeling of rocks, as a key in the theory development and numerical analysis of rock mechanics, has become a topic of everlasting interest to researchers and practitioners working on geosciences and geotechnics. In addition, many factors affect rock behaviors, such as water-rock interactions and temperature, which would lead to its deterioration. With the deterioration of rocks and soil, the state of the geoenvironment would be changed resulting in landslide [1, 2], rock avalanche [3, 4], and rock burst [5]. For brittle rocks, the deterioration process in laboratory samples is a consequence of microscale and macroscale fracturing that occurs in several stages. Recent research suggests that crack initiation stress can be used as an estimate for in situ spalling strength, which is commonly observed in brittle rocks around underground openings [6–10]. Additionally,

under high-temperature and high-pressure conditions, the mechanical characteristics of deep rocks exhibit different behaviors compared to those at more mild temperatures at lower depths. A reasonable constitutive model considering thermal action and crack initiation is the key to accurate prediction and judgment of the reliability and stability of those works such as the exploitation of deep mining resources and geothermal resources. Therefore, the constitutive behaviors of rocks considering thermal effects and crack initiation strength are significant to be studied and explored in order to better solve rock engineering problems in thermal-mechanical coupling conditions.

During the preceding four decades, various rock constitutive models have been established from theoretical, experimental approaches (e.g., [11–15]). Based on the traditional continuum mechanics and damage theory, thermoplastic and thermoelastic brittle models were proposed [16, 17]. However, these models failed to reflect the damage features of brittle rocks. For rock materials, numerous microscopic cracks, ranging from 0.01 to 1.0 mm in length, are statistically

distributed, which have significant influences on the damage processes and failure characteristics of rocks. The nucleation and growth of microcracks would lead to a concentration of these microcracks into a narrow zone and produce a visible macroscopic fissure wider than 1.0 mm [18], so the process from damage to fracture could be studied on a mesoscopic scale. Since the statistical damage-based approach has been used successfully to address rock constitutive behaviors [19–21], as a quite attractive tool for investigating deformation processes and failure mechanisms in the mechanics of geomaterial community, it has been especially favored by many researchers. However, these previous statistical models did not reflect the residual strength of rocks. By introducing a coefficient into the damage variable, the statistical damage-based model will be able to describe the residual strength [22, 23]. For thermal effects, Zhang et al. [24] proposed a three-parameter Weibull distribution to express the rock constitutive behavior under a uniaxial compression test, which considers the thermal-mechanical coupling conditions.

In the present study, a mesoscopic element is considered to be isotropically elastic and its properties are defined by Young's modulus or Poisson's ratio. The stress-strain relationship is linearly elastic until given damage threshold (crack initiation strength) is attained [17]. Thus, the macroscopic strength and the properties of rock depend on the statistical mechanical properties of individual mesoscopic elements, which could be described by a phenomenological model through a statistical method. A previous research work showed that continuum damage models can effectively simulate the elastic degradation caused by preexisting microcracks in rocks. Although rocks always exhibit anisotropy after macroscopic fissures occur, an isotropic damage model is still an effective method to estimate the gross damage of rocks subjected to external loading.

This paper aims at exploring a statistical damage constitutive model considering crack initiation strength, deterioration, and thermal effects. Based on a statistical damage approach, the statistical constitutive model is established by introducing a three-parameter Weibull distribution, which describes a brittle constitutive behavior of rocks under thermal-mechanical coupling conditions.

2. Constitutive Model

2.1. Thermal-Mechanical-Damage Evolution Equations

2.1.1. Thermal Damage. Under the thermal-mechanical coupling effect, numerous microcracks and considerable damage occur in the rock, which changes the mechanical properties. Macroscopically, the elastic modulus is usually chosen as the damage variable. According to Liu et al. [17], the thermal damage D_T can be given by

$$D_T = 1 - \frac{E_T}{E_0}, \quad (1)$$

where E_T and E_0 are the elastic moduli at $T^\circ\text{C}$ and room temperature, respectively.

2.1.2. Damage Evolution Equation considering the Thermal Effect. The randomly distributed preexisting microcracks in rocks are the main factors leading to the damage of the rock.

Suppose that a microunit within the rock is sufficiently large to contain numerous cracks and defects and adequately small in dimension compared with the whole rock structure. Obviously, the strengths of these microunits vary randomly according to a Weibull distribution. The rock damage level can be expressed by the ratio of the number of damaged microunits to total units. On the microscopic level, the rock damage evolution process includes three stages, that is, crack initiation, propagation, and coalescence. Based on this, the coupled thermal-mechanical constitutive model of the complete failure process of the rock is proposed from a damage statistical point.

Next, before the damage evolution equation presented, some assumptions are given in the following [22]:

- (a) Rock is an isotropic homogenous geomaterial on a macroscale.
- (b) Microunits conform to Hooke's law, prior to failure.
- (c) Rock damage occurs continuously and is the gradual accumulation of failures on the mesoscopic level.
- (d) Heat diffusion in a rock is only in the form of heat transfer, without considering convection and radiation.
- (e) Microunit strength follows a Weibull distribution, where the three-parameter density and distribution functions are given by the following:

Density function :

$$f(k) = \begin{cases} \frac{m}{F} \left(\frac{k-\gamma}{F} \right)^{m-1} \exp \left[- \left(\left(\frac{k-\gamma}{F} \right)^m \right) \right], & k \in [\gamma, \infty), \\ 0, & k \in (-\infty, \gamma), \end{cases}$$

Distribution function :

$$F(k) = 1 - \exp \left[- \left(\left(\frac{k-\gamma}{F} \right)^m \right) \right], \quad k \in [\gamma, \infty), \quad (2)$$

where k is the microunit strength and m , F , and γ are the mean uniformity, peak strength, and damage evolution threshold, respectively, which represent the shape, scale, dimension, and position (as shown in Figure 1).

Considering the thermal effects, the Weibull parameters can be given by

$$\begin{aligned} m(T) &= m_0(1 - D_T), \\ F(T) &= F_0(1 - D_T), \\ \gamma(T) &= \gamma_0(1 - D_T), \end{aligned} \quad (3)$$

where m_0 , F_0 , and γ_0 are the Weibull parameters at room temperature and m , F , and γ are as defined previously.

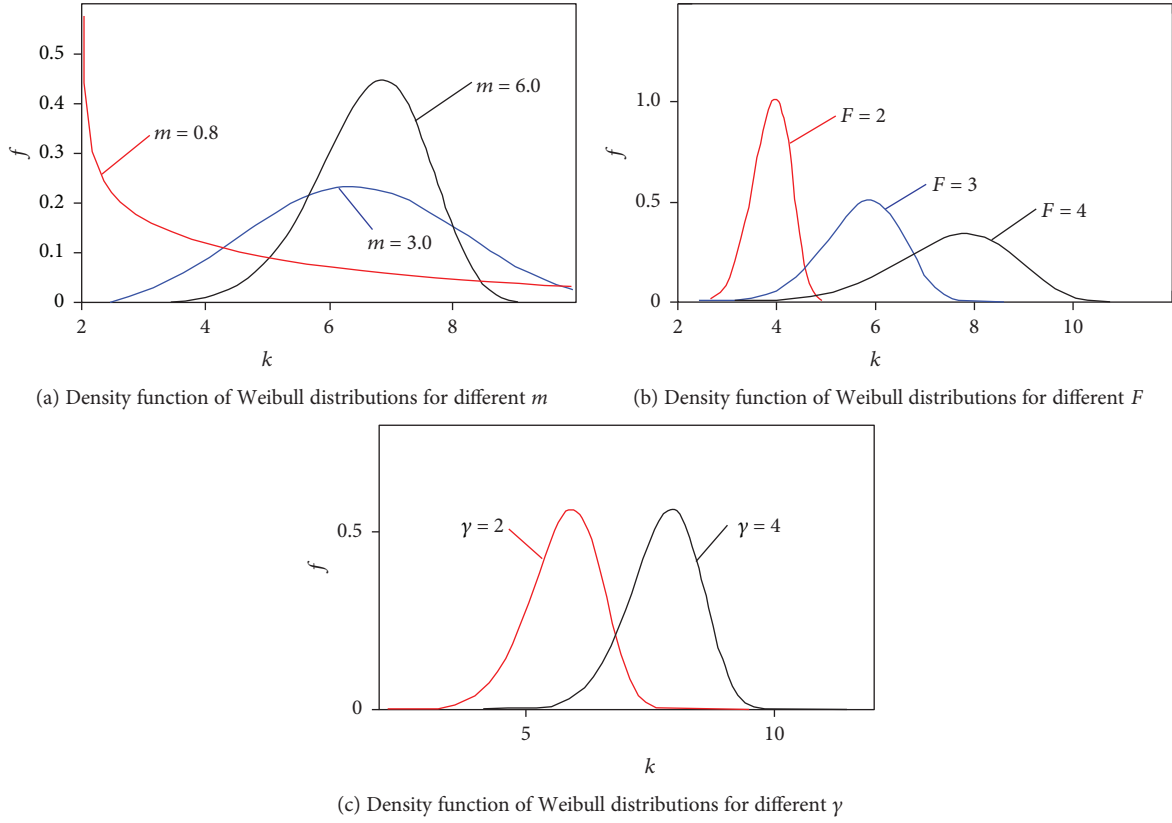


FIGURE 1: Density function of Weibull distributions for each parameter.

Rock damage is caused by the continuous failure of the microunits within the rock. Assuming that there are N_f failed microunits at a single load level, the statistic damage is defined as the ratio of the failure number to the total number (N) of microunits, namely,

$$D = \frac{N_f}{N}. \quad (4)$$

Then, at stress $f(\sigma)$, the failure number N_f is

$$N_f = \int_0^{f(\sigma)} N_f(\sigma) d\sigma. \quad (5)$$

Substituting (2) and (4) into (3) yields

$$\begin{aligned} D &= \frac{N_f}{N} = \frac{\int_0^{f(\sigma)} N_f(\sigma) d\sigma}{N} = \int_0^{f(\sigma)} f(\sigma) d\sigma \\ &= 1 - \exp \left[- \left(\frac{(f(\sigma) - \gamma_0(1 - D_T))}{F_0(1 - D_T)} \right)^{m_0(1 - D_T)} \right], \end{aligned} \quad (6)$$

Using the Drucker-Prager criterion as the unit's yield criterion,

$$f(\sigma) = k = \alpha_0 I_1 + \sqrt{J_2}, \quad (7)$$

where $\alpha_0 = \sin \varphi / \sqrt{9 + 3 \sin^2 \varphi}$, I_1 is the first stress invariant, and J_2 is the second invariant of deviator stress. These are expressed as follows:

$$\begin{aligned} I_1 &= \sigma_x^* + \sigma_y^* + \sigma_z^* = \sigma_1^* + \sigma_2^* + \sigma_3^*, \\ J_2 &= \frac{1}{6} \left[(\sigma_1^* - \sigma_2^*)^2 + (\sigma_2^* - \sigma_3^*)^2 + (\sigma_3^* - \sigma_1^*)^2 \right]. \end{aligned} \quad (8)$$

Therefore, (5) can be written as follows:

$$D = 1 - \exp \left[- \left(\frac{(\alpha_0 I_1 + \sqrt{J_2} - \gamma_0(1 - D_T))}{F_0(1 - D_T)} \right)^{m_0(1 - D_T)} \right]. \quad (9)$$

Rock damage evolution does not occur until the damage threshold is reached, at which time the rock damage value is considered to be zero. When the stress surpasses the threshold, the rock damage value is given by (8), and for the whole stress state, the hard rock damage evolution equation considering the thermal effect can be expressed as follows:

$$D(\sigma, T) = \begin{cases} 0, & \sigma < \sigma_{ci}, \\ 1 - \exp \left[- \left(\frac{(\alpha_0 I_1 + \sqrt{J_2} - \gamma_0(1 - D_T))}{F_0(1 - D_T)} \right)^{m_0(1 - D_T)} \right], & \sigma \geq \sigma_{ci}, \end{cases} \quad (10)$$

where $D(\sigma, T)$ is the damage value considering the thermal effect and σ_{ci} is the crack initiation strength.

2.2. Rock Damage Deterioration Statistical Constitutive Model. According to the concept of the theories of Lemaitre [25] strain equivalence and effective stress principle, the damage variable D is the ratio of the number of the failure units to total units; then, the relationship between nominal stress σ and effective stress σ^* in three-dimensional isotropy damage can be expressed by

$$[\sigma^*] = \frac{[\sigma]}{1 - [D]} = \frac{[C][\epsilon]}{1 - [D]}, \quad (11)$$

where $[\sigma]$ is the nominal stress matrix, $[\sigma^*]$ is the effective stress matrix, $[\epsilon]$ is the strain matrix, $[C]$ is the elastic flexibility matrix, and $[D]$ is the damage matrix.

During the compression process, rock retains the ability to pass a certain level of compressive stress and shear stress after the peak strength owing to a change in friction and confining pressure. Residual strength can be observed over the whole stress-strain curve. In most cases, the experimental curve of the residual strength is approximately horizontal after the peak strength. However, (10) does not take into account the rock residual strength; therefore, it has been

revised by introducing the damage variable correction coefficient δ , and its value is between 0 and 1.

By introducing the damage variable correction coefficient, the effective stress can be expressed by

$$[\sigma^*] = \frac{[\sigma]}{1 - \delta[D]}. \quad (12)$$

Then,

$$\sigma_i^* = \frac{\sigma_i}{1 - \delta[D]}, \quad i = 1, 2, 3. \quad (13)$$

According to the generalized Hooke's law, we have

$$\epsilon_i = \frac{1}{E} [\sigma_i^* - \mu(\sigma_j^* + \sigma_k^*)], \quad i, j, k = 1, 2, 3. \quad (14)$$

Substituting (12) into (15), we obtain

$$\epsilon_i = \frac{1}{E(1 - \delta[D])} [\sigma_i - \mu(\sigma_j + \sigma_k)], \quad i, j, k = 1, 2, 3. \quad (15)$$

Substituting $D = 1 - \exp[-((\alpha_0 I_1 + \sqrt{J_2} - \gamma_0(1 - D_T))/F_0(1 - D_T))^{m_0(1 - D_T)}]$ into (14) leads to

$$\sigma_i = E\epsilon_i \left\{ 1 - \delta + \delta \exp \left[- \left(\frac{\alpha_0 I_1 + \sqrt{J_2} - \gamma_0(1 - D_T)}{F_0(1 - D_T)} \right)^{m_0(1 - D_T)} \right] \right\} + \mu(\sigma_j + \sigma_k). \quad (16)$$

According to (1), the elastic modulus of hard rock under different temperatures is given as follows:

$$D_T = 1 - \frac{E_T}{E_0}. \quad (17)$$

Substituting (16) into (15), the hard rock damage constitutive equation considering thermal effects is obtained (after the damage threshold point):

$$\sigma_i = E_0(1 - D_T)\epsilon_i \left\{ 1 - \delta + \delta \exp \left[- \left(\frac{\alpha_0 I_1 + \sqrt{J_2} - \gamma_0(1 - D_T)}{F_0(1 - D_T)} \right)^{m_0(1 - D_T)} \right] \right\} + \mu(\sigma_j + \sigma_k). \quad (18)$$

The hard rock constitutive equation considering the thermal-mechanical coupling is given by (17) after the damage threshold point. The constitutive equation can be fitted by a polynomial before the damage threshold point. Because the rock stress-strain curve covers the coordinate origin, its function is given as follows:

$$\sigma_i = A\epsilon_i^2 + B\epsilon_i. \quad (19)$$

Integrating (17) and (18), the hard rock constitutive equation with the thermal-mechanical coupling is given as follows:

$$\sigma_i = \begin{cases} A\epsilon_i^2 + B\epsilon_i, & 0 \leq \epsilon \leq \epsilon_{ci}, \\ E_0(1 - D_T)\epsilon_i \left\{ 1 - \delta + \delta \exp \left[- \left(\frac{\alpha_0 I_1 + \sqrt{J_2} - \gamma_0(1 - D_T)}{F_0(1 - D_T)} \right)^{m_0(1 - D_T)} \right] \right\} + \mu(\sigma_j + \sigma_k), & \epsilon > \epsilon_{ci}, \end{cases} \quad (20)$$

where ε_{ci} is the strain value at the damage threshold point.

2.3. Model Parameters. The determination of the model parameters is closely related to the rock macroparameters. Thus, the determined model parameters have certain physical meaning and a wider applicability. Therefore, the strain

values at the damage threshold point ($\sigma_{ci}, \varepsilon_{ci}$) and the peak strength (σ_c, ε_c) are introduced as the macroparameters to determine the model parameters.

To simplify the calculation, (19) is rewritten in the following form:

$$\sigma_i = \begin{cases} A\varepsilon_i^2 + B\varepsilon_i, & 0 \leq \varepsilon \leq \varepsilon_{ci}, \\ E\varepsilon_i \left\{ 1 - \delta + \delta \exp \left[- \left(\left(\frac{\alpha_0 I_1 + \sqrt{J_2} - \gamma}{F} \right)^m \right) \right] \right\} + \mu(\sigma_j + \sigma_k), & \varepsilon > \varepsilon_{ci}. \end{cases} \quad (21)$$

2.3.1. Determination of m , F , and γ . In the rock triaxial tests, the nominal stress $\sigma_1, \sigma_2, \sigma_3$ ($\sigma_2 = \sigma_3$) and strain ε_1 can be measured. Based on Hooke's Law and the effective stress theory, we have

$$\begin{aligned} \varepsilon_1 &= \frac{1}{E}(\sigma_1^* - 2\mu\sigma_3^*), \\ \sigma_2^* &= \sigma_3^* = \frac{\sigma_2}{1 - \delta D}, \\ \sigma_1^* &= \frac{\sigma_1}{1 - \delta D}. \end{aligned} \quad (22)$$

Solving (21), $\sigma_1^*, \sigma_2^*, \sigma_3^*$ can be obtained. Then, $I_1, J_2, \sqrt{J_2}$ is solved:

$$\begin{aligned} I_1 &= \frac{(\sigma_1 + 2\sigma_3)E\varepsilon_1}{\sigma_1 - 2\mu\sigma_3}, \\ J_2 &= \frac{[(\sigma_1 - \sigma_3)E\varepsilon_1]^2}{3(\sigma_1 - 2\mu\sigma_3)^2}, \\ \sqrt{J_2} &= \frac{(\sigma_1 - \sigma_3)E\varepsilon_1}{\sqrt{3}(\sigma_1 - 2\mu\sigma_3)}. \end{aligned} \quad (23)$$

In the conventional triaxial test ($\sigma_2 = \sigma_3$) and when $\varepsilon > \varepsilon_D$, (20) can be abbreviated as follows:

$$\sigma_1 = E\varepsilon_1 \left\{ 1 - \delta + \delta \exp \left[- \left(\left(\frac{\alpha_0 I_1 + \sqrt{J_2} - \gamma}{F} \right)^m \right) \right] \right\} + 2\mu\sigma_3. \quad (24)$$

Similarly, parameter γ determines the starting point of the rock damage evolution, that is, the damage evolution threshold point ($\sigma_{ci}, \varepsilon_{ci}$). According to $f([\sigma]) - \gamma \geq 0$ and assuming the damage value is zero here, we obtain

$$\begin{aligned} \gamma &= \lim_{\sigma \rightarrow \sigma_{ci}} (\alpha_0 I_1 + \sqrt{J_2}) \\ &= \left[\alpha_0 \frac{(\sigma_{ci} + 2\sigma_3)E\varepsilon_{ci}}{\sigma_{ci} - 2\mu\sigma_3} + \frac{(\sigma_{ci} - \sigma_3)E\varepsilon_{ci}}{\sqrt{3}(\sigma_{ci} - 2\mu\sigma_3)} \right]. \end{aligned} \quad (25)$$

By referring the rock stress-strain curve geometry (as shown in Figure 2), we know that ① $\sigma = \sigma_c, \varepsilon = \varepsilon_c$; ② $\sigma = \sigma_c, d\sigma_c/d\varepsilon_c = 0$.

Combining boundary ① $\sigma = \sigma_c, \varepsilon = \varepsilon_c$, we obtain

$$\sigma_c = E\varepsilon_c \left\{ 1 - \delta + \delta \exp \left[- \left(\left(\frac{\alpha_0 I_1 + \sqrt{J_2} - \gamma}{F} \right)^m \right) \right] \right\} + 2\mu\sigma_3. \quad (26)$$

Substituting boundary ② $\sigma = \sigma_c, d\sigma_c/d\varepsilon_c = 0$ into the partial derivative of (23), we have

$$\frac{\partial \sigma_1}{\partial \varepsilon_1} \Big|_{\varepsilon = \varepsilon_c} = 0. \quad (27)$$

Integrating (26) and (27) yields

$$\left(\frac{\alpha_0 I_1 + \sqrt{J_2} - \gamma}{F} \right)^m = \ln \frac{\delta E \varepsilon_c}{\sigma_c - 2\mu\sigma_3 + (\delta - 1)E\varepsilon_c}, \quad (28)$$

$$\frac{m(\alpha_0 I_1 + \sqrt{J_2} - \gamma)^{m-1}}{F^m} = \frac{\sigma_c - 2\mu\sigma_3}{\varepsilon_c Y (\sigma_c - 2\mu\sigma_3 + (\delta - 1)E\varepsilon_c)}. \quad (29)$$

Solving (28) and (29), the parameters m and F can be obtained:

$$\begin{aligned} m &= \frac{X(\sigma_c - 2\mu\sigma_3)}{\varepsilon_c Y [\sigma_c - 2\mu\sigma_3 + (\delta - 1)E\varepsilon_c] \ln(\delta E \varepsilon_c / \sigma_c - 2\mu\sigma_3 + (\delta - 1)E\varepsilon_c)}, \\ F &= \left(\frac{X^m}{\ln(\delta E \varepsilon_c / \sigma_c - 2\mu\sigma_3 + (\delta - 1)E\varepsilon_c)} \right), \end{aligned} \quad (30)$$

where $X = \alpha_0((\sigma_c + 2\sigma_3)E\varepsilon_c / \sigma_c - 2\mu\sigma_3) + ((\sigma_c - \sigma_3)E\varepsilon_c / \sqrt{3}(\sigma_c - 2\mu\sigma_3)) - \gamma$ and $Y = \alpha_0((\sigma_c + 2\sigma_3)E / \sigma_c - 2\mu\sigma_3) + ((\sigma_c - \sigma_3)E / \sqrt{3}(\sigma_c - 2\mu\sigma_3))$.

2.3.2. Determination of A and B . As the stress is continuous in the compression and damage evolution section of the rock stress-strain curve, we obtain

$$\begin{aligned} E\varepsilon_{ci} \left\{ 1 - \delta + \delta \exp \left[- \left(\left(\frac{\alpha_0 I_1 + \sqrt{J_2} - \gamma}{F} \right)^m \right) \right] \right\} + 2\mu\sigma_3 \\ = A\varepsilon_{ci}^2 + B\varepsilon_{ci}. \end{aligned} \quad (31)$$

In addition, the first derivative is also continuous at these two sections; then,

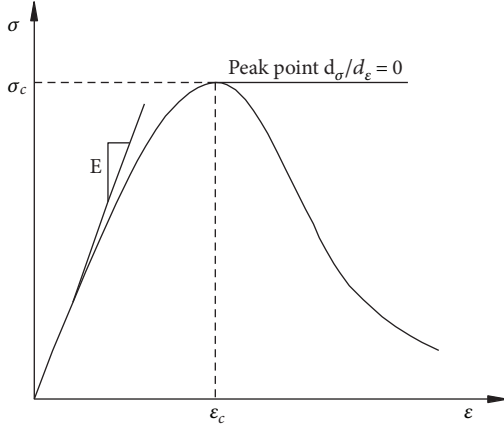


FIGURE 2: Typical stress-strain curve in conventional triaxial compressive test (E is the elastic modulus of rock, σ is the axial stress, and ϵ is the axial strain).

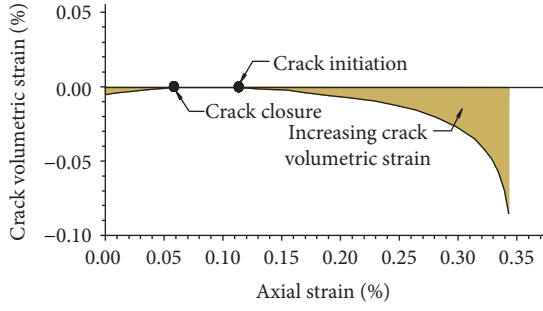


FIGURE 3: Crack volumetric strain method (Martin and Chandler [26]).

$$\left. \frac{\partial \sigma_1}{\partial \epsilon_1} \right|_{\epsilon=\epsilon_{ci}} = 2A\epsilon_{ci} + B. \quad (32)$$

Dividing (31) by ϵ_{ci} on both sides and integrating,

$$E \left\{ 1 - \delta + \delta \exp \left[- \left(\frac{\alpha_0 I_1 + \sqrt{J_2} - \gamma}{F} \right)^m \right] \right\} + \frac{2\mu\sigma_3}{\epsilon_{ci}} = A\epsilon_{ci} + B. \quad (33)$$

By supposing $R|_{\epsilon=\epsilon_{ci}} = E \{ 1 - \delta + \delta \exp [- (\frac{\alpha_0 I_1 + \sqrt{J_2} - \gamma}{F})^m] \} + (2\mu\sigma_3/\epsilon_{ci})$, $Z = (\partial \sigma_1 / \partial \epsilon_1)|_{\epsilon=\epsilon_{ci}}$.

Equations (32) and (33) can be rewritten as follows:

$$\begin{aligned} Z &= 2A\epsilon_{ci} + B, \\ R &= A\epsilon_{ci} + B. \end{aligned} \quad (34)$$

Solving (34), we have

$$\begin{aligned} A &= \frac{Z - R}{\epsilon_{ci}}, \\ B &= 2R - Z. \end{aligned} \quad (35)$$

2.3.3. Determination of Damage Threshold Point (Crack Initiation Point). In the compression, the original cracks in

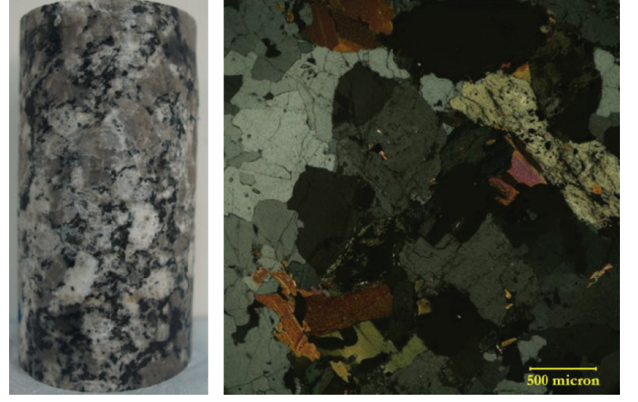


FIGURE 4: Examples of samples and a generalized photomicrograph of the granite.

TABLE 1: Mineralogical composition of the tested material (weight %).

Plagioclase	Quartz	Biotite	K-feldspar	Chlorite	Tremolite	Pyrite
29	25	20	15	4	4	3

the rock sample close first under loading. This refers to the key issue in the crack evolution section of the crack initiation and propagation, that is, the damage threshold point. Obviously, it is not easy to obtain the crack initiation stress on a rock stress-strain curve. By researching Lac du Bonnet granite, Martin and Chandler [26] proposed a method to determine the granite initiation point (shown in Figure 3) assuming a crack initiation strength of approximately 40% of the peak strength ($\sigma_{ci}=40\%\sigma_c$).

3. Verification of the Constitutive Model

The validity of the constitutive model was verified by the biotite granite triaxial experiment results under a confining pressure of 25 MPa and at varying temperatures (i.e., 40°C, 60°C, and 130°C).

The samples of granite were obtained from the Dali to Ruili railway at the depth 677–682 m (lithology is mainly biotite granite). The average density of the samples was 2.65 g/cm³ at room temperature. Cylindrical specimens were used (diameter: 50 mm, height: 100 mm, Figure 4). The constituent mineralogical components and their compositions were examined by an X-ray diffraction test, and the results are listed in Table 1. The samples did not have distinct, macroscopic heterogeneities (e.g., veins) at the specimen scale. The particle size distribution of various mineral particles is between 0 and 3 mm and mainly in 1 mm (Figure 4).

The granite triaxial compression tests were carried out on a MTS815 Teststar programmable servo stiffness test machine in the Material Mechanics Laboratory in the Institute of Water Resources and Hydropower, Sichuan University. The heating equipment is a KSW-5D-12 high-temperature box resistance furnace and resistance temperature controller, using a silicon carbon rod as the heating

TABLE 2: Values to calculate constitutive model parameters at different temperatures (25 MPa).

Temperature (T ($^{\circ}\text{C}$))	Peak strength (σ_c (MPa))	Strain at peak strength (ϵ_c (10^{-6}))	Crack initiation strength (σ_{ci} (MPa))	Strain at crack initiation (ϵ_{ci} (10^{-6}))	Elastic modulus (E (GPa))	Poisson's ratio (μ)	Constant (α_0)
40 $^{\circ}\text{C}$	253.3	4.9	101.3	1.9	5.9	0.27	0.23
60 $^{\circ}\text{C}$	229.5	5.1	91.8	1.6	6.1	0.34	0.21
130 $^{\circ}\text{C}$	263.7	6.2	105.5	1.9	5.6	0.34	0.22

TABLE 3: Parameter values at different temperatures (25 MPa).

Temperature (T ($^{\circ}\text{C}$))	Quadratic function coefficient		Average strength (F (MPa))	Uniformity coefficient (m)	Damage evolution threshold point (γ)	Damage variable correction coefficient (δ)
	A (10^6)	B				
40 $^{\circ}\text{C}$	-3.87	73468.5	233.6	3.18	99.39	0.800
60 $^{\circ}\text{C}$	-6.87	82808.2	229.7	1.87	88.43	0.781
130 $^{\circ}\text{C}$	-4.48	74223.2	274.0	2.09	100.40	0.890

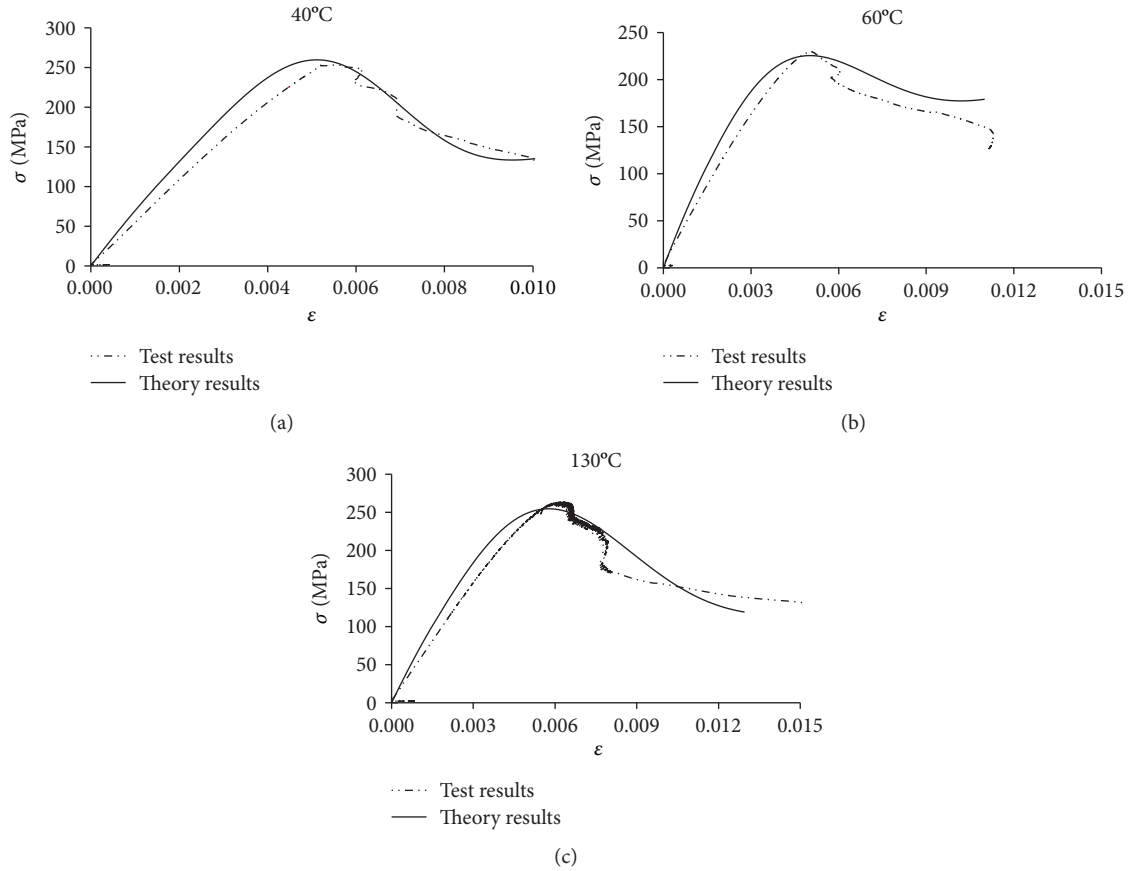


FIGURE 5: Experimental and theoretical stress-strain curves at different temperatures (25 MPa).

sensor and high-performance fiber as the insulation material. The heating and loading methods are described as follows:

- Heating method: heat the samples to the predetermined temperature at a speed of $2^{\circ}\text{C}/\text{min}$ and maintain a constant temperature for 5 h.
- Loading method: apply lateral pressure and axial pressure at the predetermined values simultaneously

at a speed of 0.005 mm/s ; then, use a 5 mm displacement sensor to measure the axial and circular displacements, and apply an axial load at a speed of 0.005 mm/s until the sample fails completely.

The constitutive model parameter values are obtained by combining the granite triaxial compression tests results and the constitutive model parameter expressions (Tables 2 and 3).

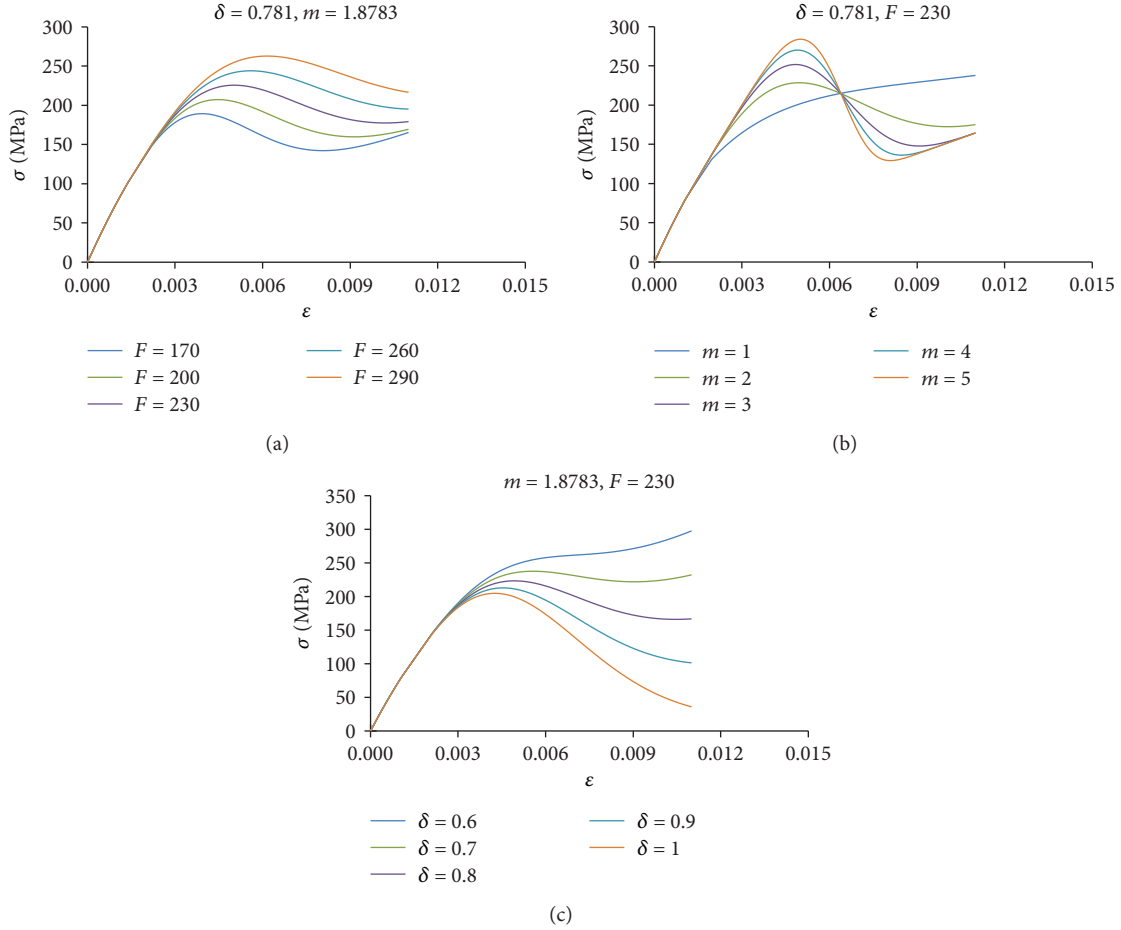


FIGURE 6: Stress-strain curves under different parameter values (25 MPa): (a) features of stress-strain curves with change in parameter F ; (b) features of stress-strain curves with change in parameter m ; (c) features of stress-strain curves with change in parameter δ (m is the mean uniformity of rock, F is the peak strength of rock, and δ is the damage variable correction coefficient).

The graphs are generated according to the constitutive model expression. Comparisons are made between the theoretical and experimental curves of the granite under different temperatures (40°C, 60°C, and 130°C) under a confining pressure of 25 MPa (Figure 5).

As shown in Figure 5, the theory curves fit well to the test curves. This effectively demonstrates the features of the whole process of rock stress-strain, with a good fitting to the curves of different temperatures. This reflects the characteristics of the deterioration and the residual strength of the rock. Adopting the effective stress, which better fits the rock damage rule, the peak strength and its corresponding strain in the theoretical curves are basically identical to those of the experimental curves.

4. Discussion

In this section, we would like to explore the relationship between the stress-strain curve and its parameters, as well as understanding the physical meaning of each parameter; we use the constitutive model of brittle granite at 25 MPa and 60°C as an example.

A and B are the coefficients of the quadratic function. The larger the A , the greater the degree of curvature of the concave curve, which means that the compaction stage of the stress-strain curve is more obvious. In these curves, B is the initial modulus of the rock sample; γ is the rock damage evolution threshold point; F reflects the rock average strength; m determines the shape of the stress-strain curve and reflects the homogeneity of rock mineral particles, also known as the uniformity coefficient; and δ reflects the residual strength. The complete stress-strain curves under different values of F , m , and δ are shown in Figure 6. The peak stress increases with increasing F . When $m = 1$, no peak point is observed on the curve, whereas both maximum and minimum values are observed at $m = 3$. With increasing δ , the residual declines.

The excavation of the deeply buried underground openings, the heat generated by decay of radioactive wastes after their emplacements, or the hydraulic fracturing stimulation in geothermal reservoirs may induce damage and progressive failure of the surrounding brittle rocks. The damage accumulation caused by microcracking is therefore considered the main mechanism that leads to the inelastic behavior of stress-strain relation, deterioration of strength and stiffness, and evolution of transport properties (e.g., permeability,

diffusivity, and thermal conductivity) of the host rocks. The proper model of coupled thermo-mechanical processes (TM) considering deterioration is hence of paramount importance for analyzing the rock mass response to excavation, thermal loading, and fluid flow. The model could be widely used in underground engineering, such as nuclear waste isolation, production of fossil fuels, underground gas storage, geothermal energy, and deep-buried tunnel.

5. Conclusions

The following conclusions can be drawn from this study:

- (a) Based on previous works, a statistical damage constitutive model was proposed by a three-parameter Weibull distribution, which considers the crack initiation strength, deterioration, and thermal effects.
- (b) By introducing the boundary conditions and macroscopic parameters, the parameters of the model were established and expressed. The physical significance of the parameters and its effects on the model performance were discussed.
- (c) The model is verified by conventional triaxial experiments under thermal-mechanical actions. A relatively good coincidence between experimental data and theoretical results was found in case studies, which confirms the validity of the model in considering brittle constitutive relations under thermal-mechanical action.

It is necessary to point out that our work does not intend to replace any of the existing models because the selection and application of models usually depend on a specific area or purpose. We want to check the possibility of applying this statistical damage model to describe the constitutive behavior of brittle rocks under thermal-mechanical coupling action. The results provide an alternative way of describing similar thermal-mechanical coupling properties of brittle rocks.

Data Availability

The data used to support the findings of this study are available from the corresponding author and first author upon request.

Conflicts of Interest

The authors declare that they have no conflicts of interest.

Acknowledgments

This study was supported by the National Natural Science Foundation of China (nos. 41772329, 41572283, and 41230635), and SKLGP (nos. SKLGP2017Z001 and SKLGP2013Z004) is gratefully acknowledged. This work is also supported by the Department of Science and Technology of Sichuan Province (Grant nos. 2015JQ0020 and 2017TD0018).

References

- [1] G. Q. Chen, R. Q. Huang, Q. Xu, T. B. Li, and M. L. Zhu, "Progressive modelling of the gravity-induced landslide using the local dynamic strength reduction method," *Journal of Mountain Science*, vol. 10, no. 4, pp. 532–540, 2013.
- [2] M. Zhang and M. J. McSaveney, "Is air pollution causing landslides in China?," *Earth and Planetary Science Letters*, vol. 481, pp. 284–289, 2018.
- [3] M. Zhang and Y. Yin, "Dynamics, mobility-controlling factors and transport mechanisms of rapid long-runout rock avalanches in China," *Engineering Geology*, vol. 167, pp. 37–58, 2013.
- [4] M. Zhang, Y. P. Yin, and M. J. McSaveney, "Dynamics of the 2008 earthquake-triggered Wenjiagou Creek rock avalanche, Qingping, Sichuan, China," *Engineering Geology*, vol. 200, pp. 75–87, 2016.
- [5] G. Q. Chen, T. B. Li, G. F. Zhang, H. Y. Yin, and H. Zhang, "Temperature effect of rock burst for hard rock in deep-buried tunnel," *Natural Hazards*, vol. 72, no. 2, pp. 915–926, 2014.
- [6] J. C. Andersson and C. D. Martin, "The äspö pillar stability experiment: part I-experiment design," *International Journal of Rock Mechanics and Mining Sciences*, vol. 46, no. 5, pp. 865–878, 2009.
- [7] G. Q. Chen, T. B. Li, W. Wang, F. Guo, and H. Y. Yin, "Characterization of the brittleness of hard rock at different temperatures using uniaxial compression tests," *Geomechanics and Engineering*, vol. 13, no. 1, pp. 63–77, 2017.
- [8] M. S. Diederichs, "The 2003 Canadian geotechnical colloquium: mechanistic interpretation and practical application of damage and spalling prediction criteria for deep tunnelling," *Canadian Geotechnical Journal*, vol. 44, no. 9, pp. 1082–1116, 2007.
- [9] C. D. Martin, "Seventeenth Canadian geotechnical colloquium: the effect of cohesion loss and stress path on brittle rock strength," *Canadian Geotechnical Journal*, vol. 34, no. 5, pp. 698–725, 1997.
- [10] C. D. Martin and R. Christiansson, "Estimating the potential for spalling around a deep nuclear waste repository in crystalline rock," *International Journal of Rock Mechanics and Mining Sciences*, vol. 46, no. 2, pp. 219–228, 2009.
- [11] A. Demirci, K. Görgülü, and Y. S. Durutürk, "Thermal conductivity of rocks and its variation with uniaxial and triaxial stress," *International Journal of Rock Mechanics and Mining Sciences*, vol. 41, no. 7, pp. 1133–1138, 2004.
- [12] K. Görgülü, Y. S. Durutürk, A. Demirci, and B. Poyraz, "Influences of uniaxial stress and moisture content on the thermal conductivity of rocks," *International Journal of Rock Mechanics and Mining Sciences*, vol. 45, no. 8, pp. 1439–1445, 2008.
- [13] L. Jing, "A review of techniques, advances and outstanding issues in numerical modelling for rock mechanics and rock engineering," *International Journal of Rock Mechanics and Mining Sciences*, vol. 40, no. 3, pp. 283–353, 2003.
- [14] N. Sultan, P. Delage, and Y. J. Cui, "Temperature effects on the volume change behaviour of Boom clay," *Engineering Geology*, vol. 64, no. 2–3, pp. 135–145, 2002.
- [15] P. V. Drnevich, M. Tidfors, and G. Sällfors, "Temperature effect on preconsolidation pressure," *Geotechnical Testing Journal*, vol. 12, no. 1, pp. 93–97, 1989.

- [16] T. Hueckel, A. Peano, and R. Pellegrini, "A thermo-plastic constitutive law for brittle-plastic behavior of rocks at high temperatures," *Pure and Applied Geophysics*, vol. 143, no. 1–3, pp. 483–510, 1994.
- [17] Q. S. Liu, S. Huang, Y. S. Kang, and X. W. Liu, "A prediction model for uniaxial compressive strength of deteriorated rocks due to freeze–thaw," *Cold Regions Science and Technology*, vol. 120, pp. 96–107, 2015.
- [18] M. Cerrolaza and R. Garcia, "Boundary elements and damage mechanics to analyze excavations in rock mass," *Engineering Analysis with Boundary Elements*, vol. 20, no. 1, pp. 1–16, 1997.
- [19] J. Deng and D. S. Gu, "On a statistical damage constitutive model for rock materials," *Computers & Geosciences*, vol. 37, no. 2, pp. 122–128, 2011.
- [20] C. A. Tang, "Numerical simulation of progressive rock failure and associated seismicity," *International Journal of Rock Mechanics and Mining Sciences*, vol. 34, no. 2, pp. 249–261, 1997.
- [21] Z. L. Wang, Y. C. Li, and J. G. Wang, "A damage-softening statistical constitutive model considering rock residual strength," *Computers & Geosciences*, vol. 33, no. 1, pp. 1–9, 2007.
- [22] W. G. Cao, H. Zhao, X. Li, and Y. J. Zhang, "Statistical damage model with strain softening and hardening for rocks under the influence of voids and volume changes," *Canadian Geotechnical Journal*, vol. 47, no. 8, pp. 857–871, 2010.
- [23] X. Li, W. G. Cao, and Y. H. Su, "A statistical damage constitutive model for softening behavior of rocks," *Engineering Geology*, vol. 143–144, pp. 1–17, 2012.
- [24] L. Y. Zhang, S. J. Zhang, X. B. Mao, T. Z. Li, R. X. Liu, and X. Q. Guo, "Experimental research on thermal damage properties of mudstone at a high temperature," *Journal of Mining & Safety Engineering*, vol. 29, no. 6, pp. 852–858, 2012.
- [25] J. Lemaitre, "A continuous damage mechanics model for ductile fracture," *Journal of Engineering Materials and Technology*, vol. 107, no. 1, pp. 83–89, 1985.
- [26] C. D. Martin and N. A. Chandler, "The progressive fracture of lac du bonnet granite," *International Journal of Rock Mechanics and Mining Sciences & Geomechanics Abstracts*, vol. 31, no. 6, pp. 643–659, 1994.

Research Article

Integration of an Iterative Update of Sparse Geologic Dictionaries with ES-MDA for History Matching of Channelized Reservoirs

Sungil Kim,¹ Baehyun Min ,² Kyungbook Lee,³ and Hoonyoung Jeong⁴

¹Severe Storm Research Center, Ewha Womans University, 52 Ewhayeodae-gil, Seodaemun-gu, Seoul 03760, Republic of Korea

²Department of Climate and Energy Systems Engineering, Ewha Womans University, 52 Ewhayeodae-gil, Seodaemun-gu, Seoul 03760, Republic of Korea

³Petroleum and Marine Research Division, Korea Institute of Geoscience and Mineral Resources, 124 Gwahak-ro, Gajeong-dong, Yuseong-gu, Daejeon 34132, Republic of Korea

⁴Department of Energy Resources Engineering, Seoul National University, 599 Gwanak-gu, Seoul 151-744, Republic of Korea

Correspondence should be addressed to Baehyun Min; bhmin01@ewha.ac.kr

Received 9 March 2018; Revised 11 May 2018; Accepted 23 May 2018; Published 29 July 2018

Academic Editor: Meijing Zhang

Copyright © 2018 Sungil Kim et al. This is an open access article distributed under the Creative Commons Attribution License, which permits unrestricted use, distribution, and reproduction in any medium, provided the original work is properly cited.

This study couples an iterative sparse coding in a transformed space with an ensemble smoother with multiple data assimilation (ES-MDA) for providing a set of geologically plausible models that preserve the non-Gaussian distribution of lithofacies in a channelized reservoir. Discrete cosine transform (DCT) of sand-shale facies is followed by the repetition of K-singular value decomposition (K-SVD) in order to construct sparse geologic dictionaries that archive geologic features of the channelized reservoir such as pattern and continuity. Integration of ES-MDA, DCT, and K-SVD is conducted in a complementary way as the initially static dictionaries are updated with dynamic data in each assimilation of ES-MDA. This update of dictionaries allows the coupled algorithm to yield an ensemble well conditioned to static and dynamic data at affordable computational costs. Applications of the proposed algorithm to history matching of two channelized gas reservoirs show that the hybridization of DCT and iterative K-SVD enhances the matching performance of gas rate, water rate, bottomhole pressure, and channel properties with geological plausibility.

1. Introduction

Calibration of a subsurface system is an essential process to forecast fluid behaviors in a variety of geoenvironments such as aquifers, geothermal reservoirs, and petroleum reservoirs. History matching is an inverse process to find reservoir model parameters honoring observations by integration of static (e.g., core, logging, and seismic) and dynamic data (e.g., oil and gas rate, water cut, bottomhole pressure, and subsidence/uplift) [1]. Ensemble-based data assimilation approaches have been successfully utilized for history matching to provide subsurface models that are well conditioned to observations. For example, the ensemble Kalman filter (EnKF) [2–5], ensemble smoother (ES) [6, 7], and ES with

multiple data assimilation (ES-MDA) [8–10]. However, the ensemble-based data assimilation approaches have difficulty in preserving non-Gaussian distributions of model parameters such as lithofacies [11–14]. In the ensemble-based data assimilation approaches, model parameters lose the non-Gaussianity of their original distributions that are initially constrained and the distributions of the model parameters get close to Gaussian ones.

Shin et al. [14] and Zhou et al. [15] suggested using normal score transform in the ensemble-based data assimilation approaches to preserve non-Gaussian distributions of model parameters. Non-Gaussian model parameters are transformed into Gaussian model parameters using normal score transform, and then finally, updated model parameters

are backtransformed. Moreover, transformation can take advantage of parameterization if the number of essential transformed parameters is smaller than the number of original parameters in terms of saving computational cost and figuring out main features of parameters. For example, the discrete cosine transform (DCT) [16–21], fast Fourier transform [22, 23], grid connectivity transform [24], level set [13, 25], and sparse geologic dictionaries [26, 27] have been applied to reservoir characterization. In particular, Fourier transform-based methods such as DCT are capable of capturing essential traits such as main shapes and patterns of a facies channel reservoir [16, 17] but reveal a deficiency in describing a crisp contrast among different facies because of data loss from inverse transformation [28].

Sparse coding refers to the process of computing representation coefficients based on the given signal and dictionaries [29]. In sparse coding, the dictionaries indicate groups of features capable of brief expressions to represent various phenomena in the environment [30]. In geological modeling, sparse geologic dictionaries are used to represent models with sparse linear combinations of basis vectors that are essential geologic features of a reservoir [29]. Extracting essential geologic features and reducing the number of reservoir variables can be accomplished using sparse coding, thereby facilitating ensemble-based history matching [27]. Aharon et al. [29] showed the efficacy of K-singular value decomposition (K-SVD) resulting from the accelerated convergence for image reconstruction, which led Sana et al. [31] to build an archive of essential geologic features called sparse geologic dictionaries from thousands of static reservoir models using K-SVD and calibrate reservoir models with the dictionaries using EnKF. One drawback of K-SVD is its large size of sparse geologic dictionaries. References showed that sparse coding with a transformation of parameter space could reduce both computational complexity and costs that are simultaneously required for model calibration [26, 27, 32]. In this study, we note that the previous works have not considered the quality of sparse geologic dictionaries. The quality indicates how well reservoir models can be properly reconstructed by prototypes of dictionaries. Also, we expect an improvement in the history-matching performance by enhancing the quality of sparse geologic dictionaries.

This study proposes a hybridized ES-MDA algorithm that implements sparse coding in a transformed space to outperform previous history-matching methods by providing more accurate reconstructions of highly non-Gaussian model parameters. The proposed algorithm transforms multimodal facies into coefficients of discrete cosine functions using DCT. Invoking DCT is followed by iterating K-SVD for updating sparse geologic dictionaries. In each assimilation of ES-MDA, the combination of DCT and iterative K-SVD is performed to update the dictionaries and improve the quality of reservoir models. For brevity, the proposed algorithm with updated sparse geologic dictionaries is called ES-MDA-DCT-i-K-SVD in this paper. The performance of ES-MDA-DCT-i-K-SVD is tested with applications for channelized gas reservoirs and is compared with those of four ES-MDA algorithms: conventional ES-MDA, ES-MDA coupled with DCT (called ES-MDA-DCT in this paper), ES-MDA

coupled with K-SVD (called ES-MDA-K-SVD in this paper), and ES-MDA coupled with DCT and K-SVD (called ES-MDA-DCT-K-SVD in this paper).

2. Methodology

The novelty of the proposed algorithm ES-MDA-DCT-i-K-SVD is the integration of ES-MDA (Section 2.1), the dimensionality reduction of the parameter space using DCT (Section 2.2), and construction (Section 2.3) and updating (Section 2.4) of geologic dictionaries using sparse coding in the reduced space. Section 2.5 describes how the methods operate in the framework of ES-MDA-DCT-i-K-SVD in a complementary manner.

2.1. ES-MDA. The goal of history matching can be formulated as

$$\min J(\mathbf{m}), \quad (1)$$

where J is the objective function of history matching and \mathbf{m} is the state vector composed of reservoir variables (e.g., permeability and facies).

The typical form of $J(\mathbf{m})$ for ensemble-based history matching is presented as [33]

$$J(\mathbf{m}) = (\mathbf{m} - \mathbf{m}^b)^T \mathbf{B}^{-1} (\mathbf{m} - \mathbf{m}^b) + (\mathbf{d}^{\text{obs}} - \mathbf{d})^T \mathbf{R}^{-1} (\mathbf{d}^{\text{obs}} - \mathbf{d}), \quad (2)$$

where \mathbf{m}^b is the state vector before update and the superscript b refers to background; \mathbf{B} is the covariance matrix of \mathbf{m}^b ; \mathbf{d}^{obs} is the observed responses; $\mathbf{d} = f(\mathbf{m})$ is the dynamic vector composed of simulated responses obtained by running a reservoir simulator f for the state vector \mathbf{m} ; and \mathbf{R} is the covariance matrix of observation error. Note that the right-hand side of (2) is the addition of background and observation error terms [33]. Because \mathbf{m} can contain any unknown variables such as facies indexes, coefficients of discrete cosine functions or dictionary coefficients depending on the type of algorithms were used in this study.

$\partial J(\mathbf{m})/\partial \mathbf{m} = 0$ can be used to derive the update equation for \mathbf{m} as [8, 33]

$$\mathbf{m}_i = \mathbf{m}_i^b + \mathbf{C}_{\text{md}} (\mathbf{C}_{\text{dd}} + \alpha_p \mathbf{C}_{\text{D}})^{-1} (\mathbf{d}_i^{\text{unc}} - \mathbf{d}_i) \quad \text{for } i = 1, \dots, N_{\text{ens}}, \quad (3)$$

where the subscript i refers to the i th ensemble member; \mathbf{C}_{md} is the cross-covariance matrix of \mathbf{m} and \mathbf{d} ; \mathbf{C}_{dd} is the autocovariance matrix of \mathbf{d} ; α_p is the coefficient to inflate \mathbf{C}_{D} , which is the covariance matrix of the observed data measurement error [8]; \mathbf{d}^{unc} is the observation data perturbed by the inflated observed data measurement error; and N_{ens} is the ensemble size (i.e., number of reservoir models in the ensemble). Conventionally, ensemble-based history matching updates N_{ens} reservoir models simultaneously. In (3), $\mathbf{C}_{\text{md}} (\mathbf{C}_{\text{dd}} + \alpha_p \mathbf{C}_{\text{D}})^{-1}$ refers to Kalman gain K , which is computed with regularization by SVD using 99.9% of the total energy in singular values [8].

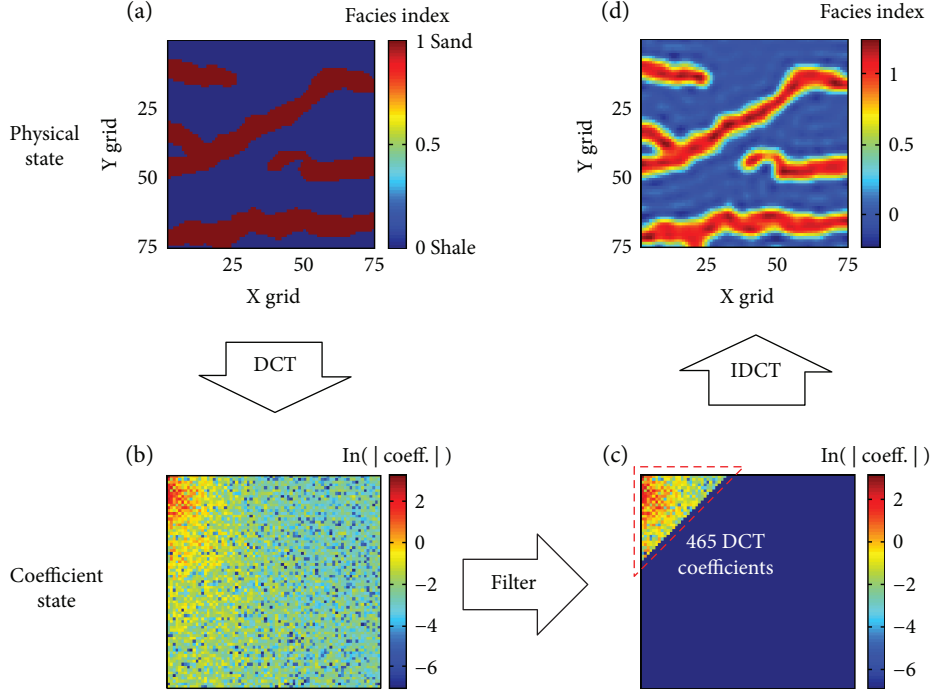


FIGURE 1: Example of discrete cosine transform (DCT) and inverse DCT (IDCT) applied to the reproduction of shale and sand facies of a channelized reservoir.

The main difference between ES and ES-MDA is the update process of the state vector \mathbf{m} . ES updates the state vector of each ensemble member using observation data measured at all time steps (Emerick and Reynolds, 2011). Compared to the single assimilation of ES, ES-MDA assimilates every state vector N^a times using an inflated covariance matrix of measurement error [8, 9]. Here, N^a is the number of assimilations in ES-MDA.

Definitions of \mathbf{C}_{md} and \mathbf{C}_{dd} are as follows:

$$\mathbf{C}_{\text{md}} = \frac{1}{N_{\text{ens}} - 1} \sum_{i=1}^{N_{\text{ens}}} (\mathbf{m}_i - \bar{\mathbf{m}})(\mathbf{d}_i - \bar{\mathbf{d}})^T, \quad (4)$$

$$\mathbf{C}_{\text{dd}} = \frac{1}{N_{\text{ens}} - 1} \sum_{i=1}^{N_{\text{ens}}} (\mathbf{d}_i - \bar{\mathbf{d}})(\mathbf{d}_i - \bar{\mathbf{d}})^T,$$

where $\bar{\mathbf{m}}$ is the mean of state vectors and $\bar{\mathbf{d}}$ is the mean of dynamic vectors.

In ES-MDA, α_p is constrained to

$$\sum_{p=1}^{N^a} \frac{1}{\alpha_p} = 1. \quad (5)$$

In ES, $N^a = 1$ and $\alpha_{p=1} = 1$ due to its single assimilation.

The perturbed observation data d^{unc} shown in (3) is computed as

$$d_i^{\text{unc}} = d_i^{\text{obs}} + \sqrt{\alpha_p} \mathbf{C}_{\text{D}}^{1/2} \mathbf{z}_{\text{d},i} \quad \text{for } i = 1, \dots, N_{\text{ens}}. \quad (6)$$

The second term on the right-hand side of (6) is the perturbation term, which reflects the uncertainty associated with

data measurement, processing, and interpretation. Stochastic characteristics of \mathbf{C}_{D} are reflected by $\mathbf{z}_{\text{d}} \sim N(0, I_{N_{\text{d}}})$. \mathbf{z}_{d} is the random error matrix to observations, which is generated with a mean of zero and a standard deviation of $I_{N_{\text{d}}}$, where N_{d} is the number of time steps in observations.

2.2. Extraction of Geologic Features Using Discrete Cosine Transform. Discrete cosine transform (DCT) has been utilized as an image-processing tool for characterization of channelized reservoirs due to the periodicity of cosine functions [34]. DCT converts parameters into coefficients of discrete cosine functions. The coefficients are sorted in descending order from the top left, capturing the overall trend of channel patterns, to bottom right, delineating details in channel patterns. Previous studies have shown that non-Gaussian channel patterns can be reproduced sufficiently via inverse transform of essential DCT coefficients [18, 28, 35]. Updating the truncated DCT coefficients can yield a calibrated model set. Another advantage of DCT is the improvement in computational efficiency resulting from data compression, which is effective in constructing sparse geologic dictionaries described in Section 2.3.

Figure 1 illustrates how to extract geologic features from an image of a target channelized reservoir using a truncated DCT and reproduce the target reservoir through an inverse DCT (IDCT). Two images in the first row represent the physical state of sand and shale facies in the target reservoir, that is, the original image on the left and the reproduced image on the right. Let N_{grid} and N_{DCT} denote the number of grid-blocks of the reservoir model and the number of essential DCT coefficients, respectively. Applying DCT to the original

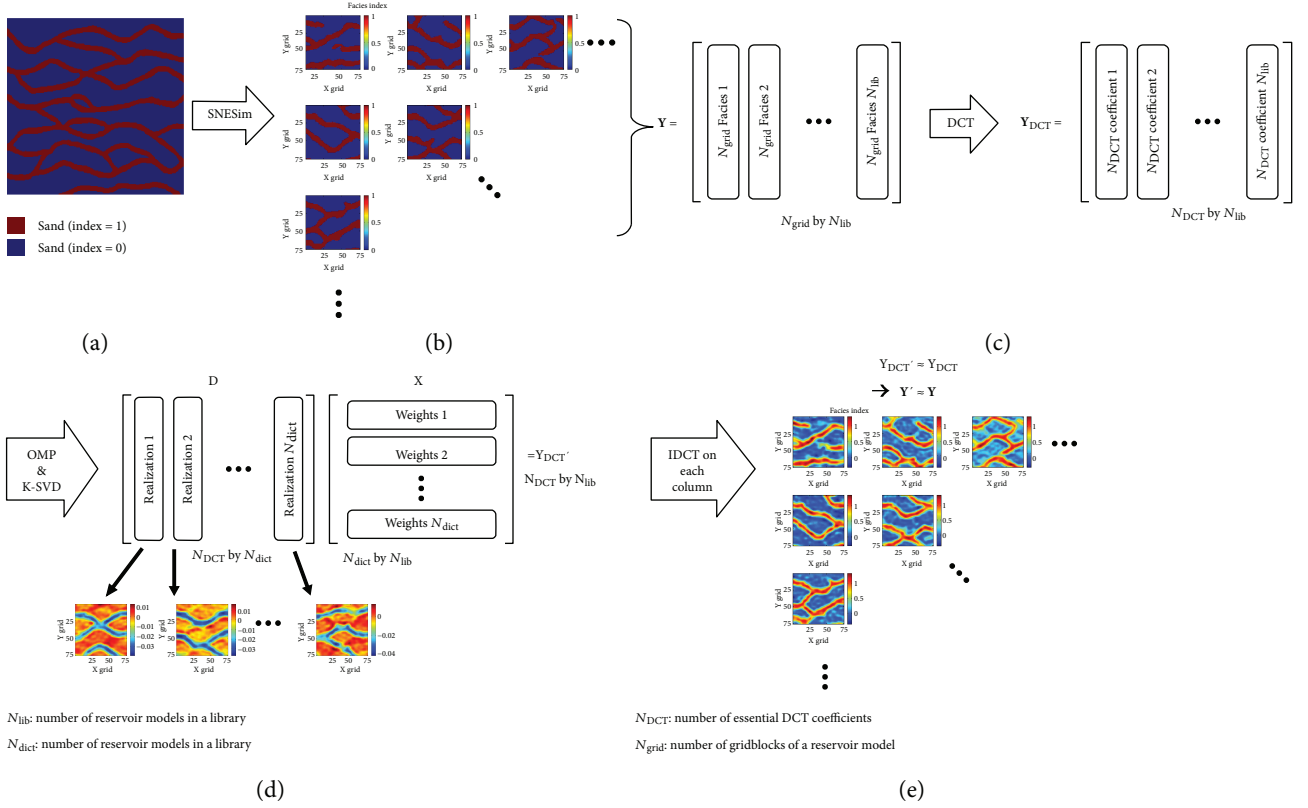


FIGURE 2: Construction of sparse geologic dictionaries using DCT and K-SVD: (a) training image, (b) generation of initial channel models (Y) using SNESim, (c) transformation of Y into DCT coefficients, (d) construction of D and X from Y using K-SVD in DCT domain, and (e) reconstruction of Y from D and X .

75 by 75 image yields an image composed of DCT coefficients, as shown in the bottom-left corner of Figure 1. In the bottom-right corner of Figure 1, filtering the coefficient state selects 465 components in the dotted triangle as essential ones. It seems that this small number of components is sufficient to restore the original image of the physical state (i.e., channel patterns) when comparing the two subfigures in the first row.

2.3. Construction of Geologic Dictionaries Using Sparse Coding. Figure 2 presents a procedure of sparse coding to construct geologic dictionaries using static data in the DCT domain. Sparse coding starts from building a library matrix Y , which is a N_{para} by N_{lib} matrix. N_{para} is the number of parameters in each reservoir model, and N_{lib} is the number of reservoir models in Y . Equiprobable reservoir models are generated using a geostatistical technique. Figure 2(a) shows a training image used for creating initial channelized reservoir models (see Figure 2(b)) by invoking single normal equation simulation (SNESim) [36]. In Figures 2(a) and 2(b), each reservoir model consists of two facies: shale and sand with 0 and 1 indexes, respectively. Each column vector of Y corresponds to either a reservoir model or an encoded reservoir model because N_{para} is determined depending on the type of assimilation algorithms in this study. $N_{para} = N_{grid}$ (e.g., Y in Figure 2(b)) in the conventional ES-MDA, while $N_{para} = N_{DCT}$ (e.g., Y_{DCT} in Figure 2(c)) if DCT is

applied to ES-MDA. In Figure 2(c), each column vector of Y_{DCT} consists of DCT coefficients filtered from the corresponding column vector in Y . That is, the data compression ratio is N_{grid}/N_{DCT} . In Figure 2, $N_{grid}/N_{DCT} = 75 \times 75/465 \approx 12.1$. Data compression using DCT reduces the dimension of the parameter space, thereby saving computing time required for sparse coding [37]. Meanwhile, a sufficiently large N_{lib} needs to be chosen to cover a variety of geologically plausible scenarios in Y . Previous investigators adopted N_{lib} in the range of 1000 to 2000 [31, 37]. In this paper, N_{lib} is a constant of 3000 for maintaining the diversity of library models. Note that generating N_{lib} models is computationally inexpensive because all the models are static. No dynamic reservoir simulation is required for any static model.

Library matrix Y is numerically decomposed into dictionary matrix D and weight matrix X using K-SVD: $Y \approx DX$. D and X are an N_{para} by N_{dict} matrix and an N_{dict} by N_{lib} matrix, respectively, where N_{dict} is the number of reservoir models in D . Thus, both Y and D are sets of reservoir models. Each column vector of D , called a realization in this paper, represents either an original or an encoded reservoir model. We expect that every realization exhibits distinguishable geological features in a well-organized dictionary. N_{dict} is to be predetermined considering computational costs associated with the sparse coding process. In this paper, N_{dict} is fixed as one third of N_{lib} . As a rule of thumb, $N_{lib} \gg N_{dict} \gg N_{ens}$.

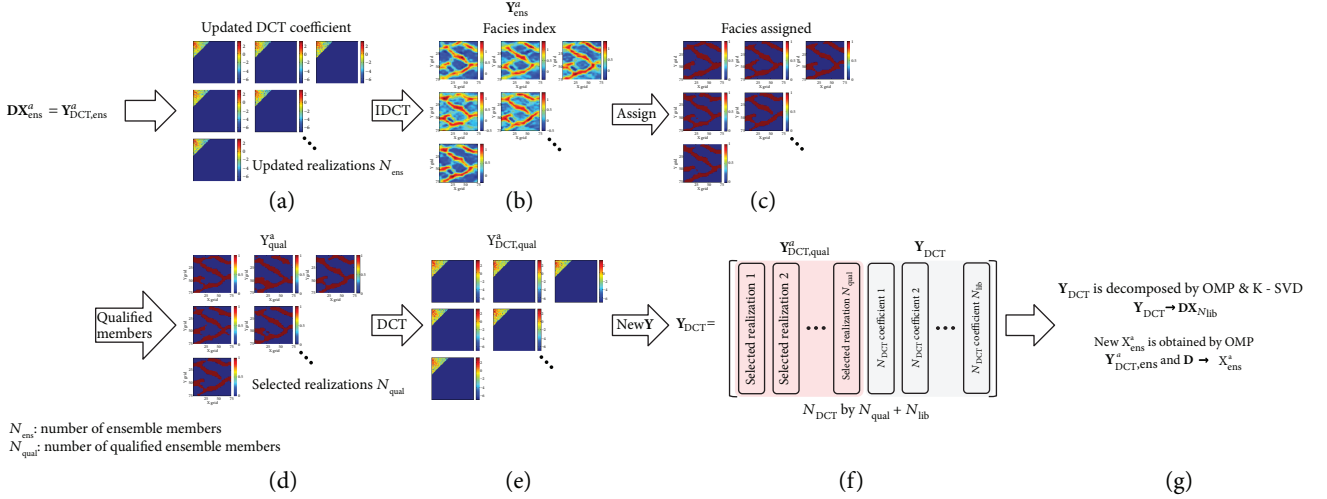


FIGURE 3: Update of sparse geologic dictionaries during assimilations.

Figure 2(d) illustrates how to decompose \mathbf{Y} into \mathbf{D} and \mathbf{X} using K-SVD in the DCT coefficient domain. Note that column vectors in \mathbf{Y} are sorted at random, while column vectors in \mathbf{D} are sorted from left to right in descending order of energy to help us conveniently check the reservoir model quality. The term *energy* indicates the norm of a row vector in \mathbf{X} corresponding to the realization in \mathbf{D} . Greater norms in \mathbf{X} indicate more essential principal components in \mathbf{D} .

The next task is how to decompose \mathbf{D} and \mathbf{X} from \mathbf{Y} . Due to the large size of the three matrices, matrix decomposition is conducted numerically to minimize the discrepancy between \mathbf{Y} and \mathbf{DX} . In other words,

$$\min \|\mathbf{Y} - \mathbf{Y}'\|_F, \quad (7)$$

where $\|\cdot\|_F$ is the Frobenius norm and $\mathbf{Y}' = \mathbf{DX}$.

More specifically, matrix decomposition is performed by iterating sparse coding that is an orthogonal matching pursuit (OMP) [38, 39] followed by K-SVD [29], as described by Sana et al. [31]. The first step of matrix decomposition is to initialize \mathbf{D} and \mathbf{X} . The second step is to compute \mathbf{X} with a fixed \mathbf{D} using OMP. The third step is update \mathbf{D} and \mathbf{X} simultaneously using K-SVD through the following three equations.

$$\min \|\mathbf{Y} - \mathbf{Y}'\|_F = \min \left\| \mathbf{Y} - \sum_{i=1}^{N_{dict}} \mathbf{d}_i^r \mathbf{x}_i \right\|_F, \quad (8)$$

where \mathbf{d}_i^r is the i th column vector (i.e., realization) in \mathbf{D} and \mathbf{x}_i is the i th row vector in \mathbf{X} .

The right-hand side of (8) is rearranged as follows:

$$\begin{aligned} \min & \left\| \left(\mathbf{Y} - \sum_{i \neq j} \mathbf{d}_i^r \mathbf{x}_i \right) - \mathbf{d}_j^r \mathbf{x}_j \right\|_F \\ & = \min \left\| E_j - \mathbf{d}_j^r \mathbf{x}_j \right\|_F \quad \text{for } j = 1, \dots, N_{dict}, \end{aligned} \quad (9)$$

where the subscript $j \in \{1, \dots, N_{dict}\}$ indicates the pivot and E_j is the discrepancy term.

To achieve (9), optimal \mathbf{d}_j^r and \mathbf{x}_j are explored from $j = 1$ to $j = N_{dict}$. The right-hand side of (9) is rearranged as

$$\begin{aligned} \min & \left\| E_j \Omega_j - \mathbf{d}_j^r \mathbf{x}_j \Omega_j \right\|_F \\ & \cong \min \left\| \mathbf{U} \Delta \mathbf{V}^T - \mathbf{d}_j^r \mathbf{x}_j \Omega_j \right\|_F \quad \text{for } j = 1, \dots, N_{dict}, \end{aligned} \quad (10)$$

where Ω_j is the matrix of which every element is either zero or one. At each j , \mathbf{x}_j multiplied by Ω_j returns a row vector of nonzero elements in \mathbf{x}_j . The size of Ω_j is N_{lib} by the number of nonzero elements in \mathbf{x}_j . $E_j \Omega_j$ is decomposed using SVD for determining \mathbf{d}_j^r and \mathbf{x}_j at each j , which results in $\mathbf{U} \Delta \mathbf{V}^T$, where \mathbf{U} is the first column vector from the left-singular vectors' matrix, Δ is the first element of the singular values' matrix, and \mathbf{V} is the first column vector from the right-singular vectors' matrix of $E_j \Omega_j$, respectively. As a consequence, \mathbf{d}_j^r is the first column vector of \mathbf{U} and $\mathbf{x}_j \Omega_j$ is the first column vector of \mathbf{V} multiplied by the first diagonal element of Δ . \mathbf{x}_j is obtained by multiplying the inverse Ω_j . Note that the updated \mathbf{d}_j^r and \mathbf{x}_j are used for the calculation of (9) at the subsequent j s. Performing (10) at all j s completes the update of \mathbf{D} and \mathbf{X} .

After the update of the dictionary matrices, the second step of matrix decomposition is reinvented to tune \mathbf{X} for further achieving (7). Then, the tuned \mathbf{X} and \mathbf{D} are reimported to (8) for conducting the third step again. This sequence of the second and third steps is iterated until a convergence criterion is satisfied. The criterion could be sparsity of \mathbf{X} , a threshold to accept the discrepancy shown in (7) or the maximum number of iterations. In this study, the criterion is the maximum number of iterations (set to ten) for all experiments.

In summary, Figures 2(a)–2(d) describe how to construct the original sparse geologic dictionary matrices \mathbf{Y} , \mathbf{D} , and \mathbf{X} using static data. Figure 2(e) is an example to show that performing an IDCT yields \mathbf{Y}_{DCT} while capturing geological features of the original \mathbf{Y}_{DCT} despite a diffusion in facies

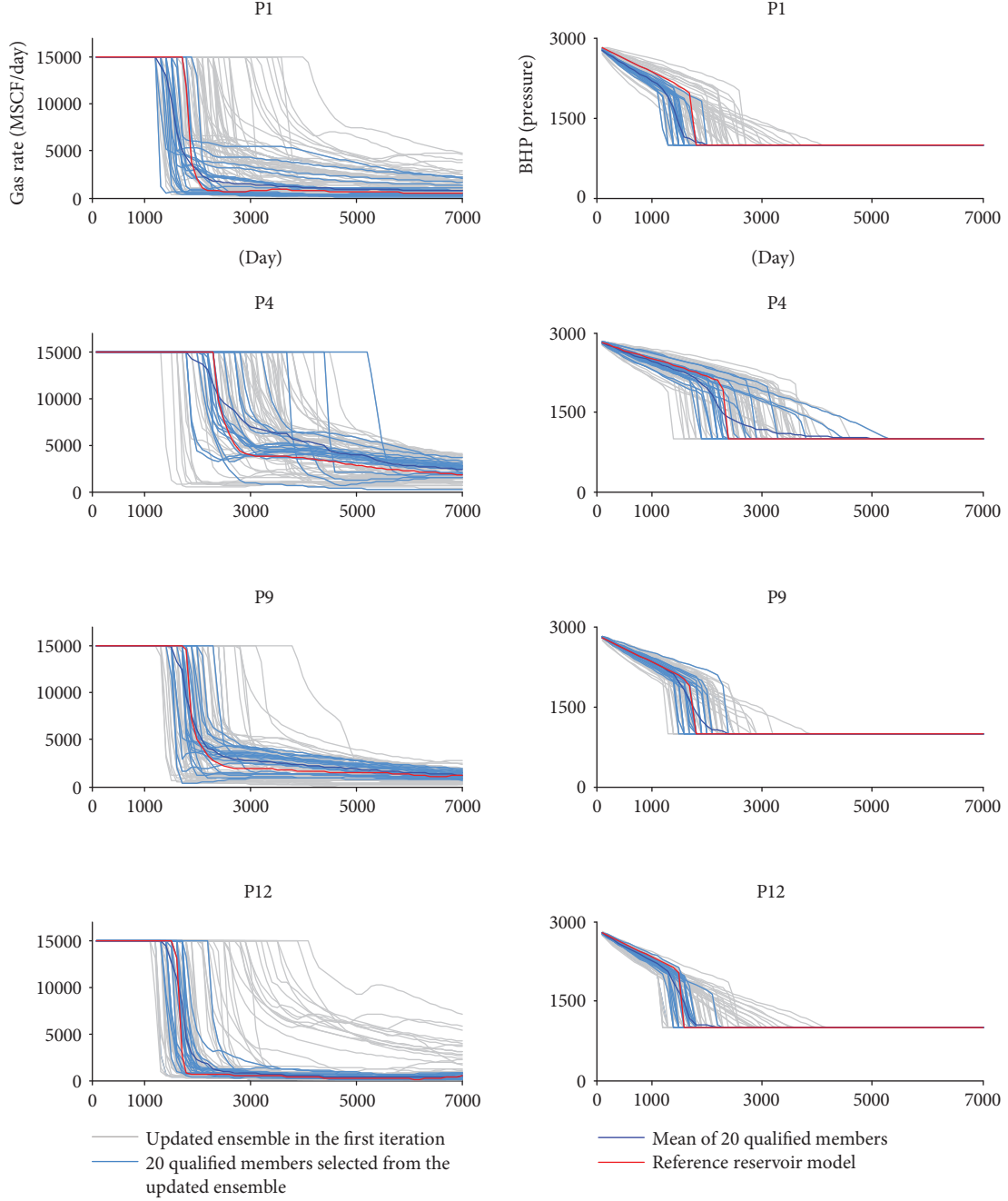


FIGURE 4: Gas rate and BHP profiles of 20 qualified realizations selected from the updated ensemble after the first assimilation.

designation. Note that the diffusion is filtered out using a cutoff method in this study. We employ the arithmetic mean of the two facies indexes (i.e., 0.5) as the threshold to determine either shale (if facies index < 0.5) or sand (if facies index ≥ 0.5) in each gridblock.

2.4. Update of Sparse Geologic Dictionaries during Multiple Data Assimilation. Once original sparse geologic dictionary matrices \mathbf{Y} , \mathbf{D} , and \mathbf{X} are constructed using static data, the proposed algorithm updates the dictionary matrices by conditioning dynamic observations (e.g., gas rate and bottom-hole pressure (BHP)) to the ensemble. Figure 3 explains

how to update the dictionary matrices during assimilations of the proposed algorithm. Let $N_{\text{para}} = N_{\text{DCT}}$ and $\mathbf{Y} = \mathbf{Y}_{\text{DCT}}$ in the proposed algorithm.

The weight matrix \mathbf{X}_{ens} is the state vector of the proposed algorithm. Only for the first assimilation, N_{ens} realizations are randomly selected from \mathbf{X} in order to compose the initial \mathbf{X}_{ens} . Thus, \mathbf{X}_{ens} is a N_{dict} by N_{ens} matrix while \mathbf{X} is a N_{dict} by N_{lib} matrix. Let the superscript a denotes *assimilation*. Then, $\mathbf{X}_{\text{ens}}^a$ denotes the updated weight matrix after assimilation. Using \mathbf{D} from Section 2.3 (Figure 3(a)),

$$\mathbf{Y}_{\text{DCT,ens}}^a = \mathbf{D}\mathbf{X}_{\text{ens}}^a, \quad (11)$$

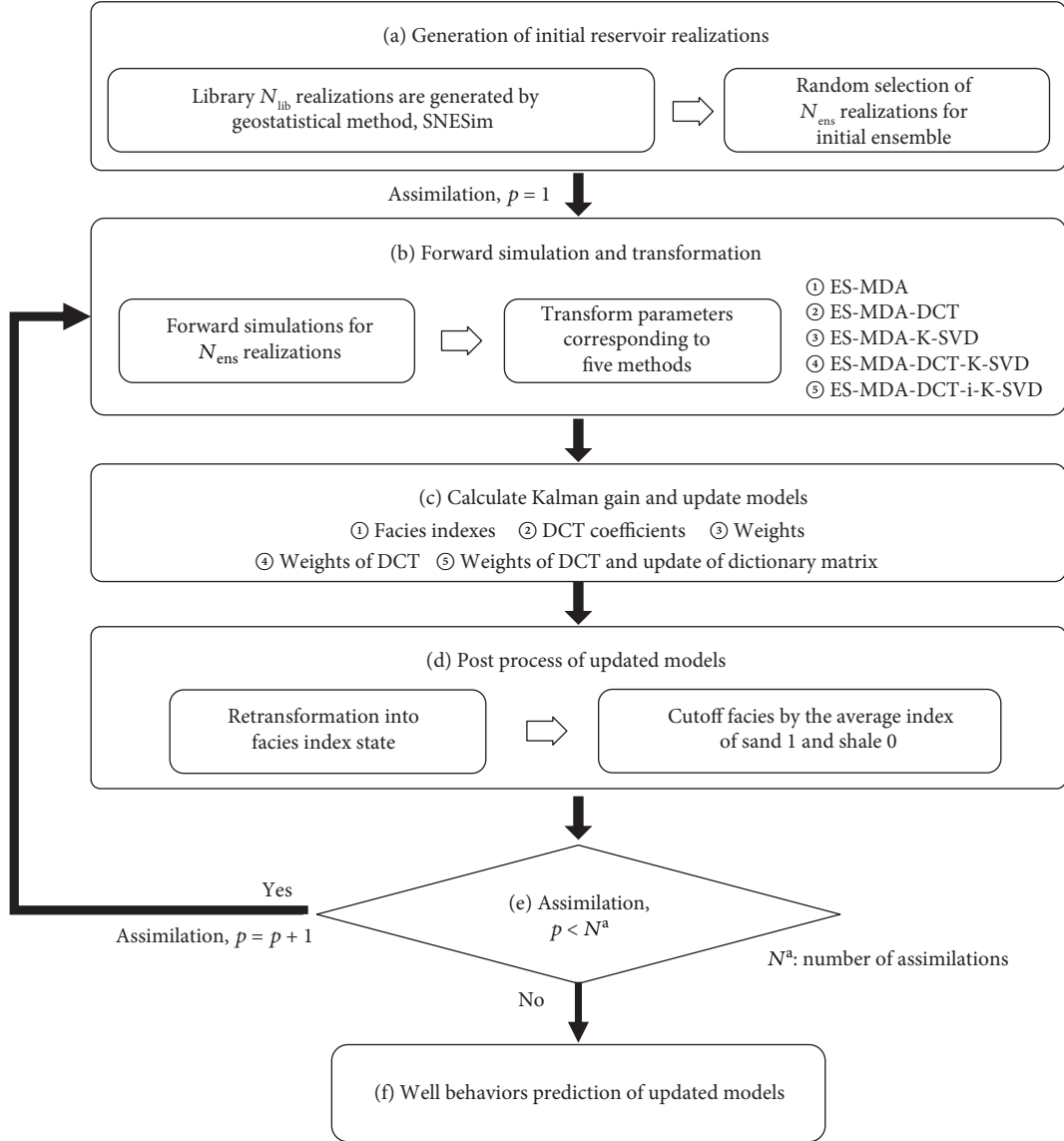


FIGURE 5: Flow chart of five ES-MDA algorithms investigated in this study. The proposed algorithm corresponds to the number five in the boxes (b) and (c).

where $\mathbf{Y}_{DCT,ens}^a$ is the N_{DCT} by N_{ens} matrix composed of DCT coefficients of ensemble members.

Through IDCT, the updated DCT coefficients of $\mathbf{Y}_{DCT,ens}^a$ are restored to facies indexes (Figure 3(b)). Each facies index map is transformed into its facies distribution map using a cutoff (Figure 3(c)): $\mathbf{Y}_{DCT,ens}^a \rightarrow \mathbf{Y}_{ens}^a$. The facies models are converted into petrophysical models and used for reservoir simulation. The simulation results are compared with observations for checking a quality of each reservoir model in \mathbf{Y}_{ens}^a . The quality is quantified in terms of ε_{qual} , which indicates the discrepancy between observation and simulation results of an ensemble member:

$$\varepsilon = \frac{1}{N_d} \sum_{i=1}^{N_d} \left(\frac{d_i - d_i^{obs}}{d_i^{obs}} \right)^2, \quad (12)$$

$$\varepsilon_{qual,i} = \frac{1}{N_{type}} \sum_{j=1}^{N_{type}} \varepsilon_j \quad \text{for } i = 1, \dots, N_{ens}, \quad (13)$$

where N_{type} is the number of data types.

Let N_{qual} be the number of qualified models selected from the ensemble. N_{qual} models are selected among N_{ens} models: $\mathbf{Y}_{ens}^a \rightarrow \mathbf{Y}_{qual}^a$, as seen in Figure 3(d). Figure 4, for example, shows to select $N_{qual} = 20$ realizations from $N_{ens} = 100$ realizations regarding gas rate and BHP. It seems that the simulated responses of the selected models are closer to the reference results than the rest of the ensemble members. Figure 3(e) shows that facies of the N_{qual} models are transformed into DCT coefficients: $\mathbf{Y}_{qual}^a \rightarrow \mathbf{Y}_{DCT,qual}^a$, where $\mathbf{Y}_{DCT,qual}^a$ is the N_{DCT} by N_{qual} matrix composed of DCT coefficients of qualified ensemble members.

TABLE 1: State vectors and update processes of sparse geologic dictionaries for five ES-MDA algorithms investigated in this study.

ES-MDA algorithm	State vector \mathbf{m}	Update of sparse geologic dictionaries
ES-MDA	Facies index	N/A
ES-MDA-DCT	DCT coefficients in facies domain	N/A
ES-MDA-K-SVD	Weight matrix \mathbf{X} in facies domain	Single K-SVD before ES-MDA
ES-MDA-DCT-K-SVD	\mathbf{X} in DCT domain	Single K-SVD before ES-MDA
ES-MDA-DCT-i-K-SVD	\mathbf{X} in DCT domain	Iterative K-SVD during ES-MDA

After obtaining the qualified models, the library matrix \mathbf{Y}_{DCT} is updated as (Figure 3(f))

$$\mathbf{Y}_{\text{DCT}} = \left[\mathbf{Y}_{\text{DCT,qual}}^a \mathbf{Y}_{\text{DCT}} \right]. \quad (14)$$

Note that (14) enhances both the quantity and quality of geologic libraries by conditioning \mathbf{Y}_{DCT} (which is conditioned to static observation data initially) to dynamic observation data with a relatively small number of reservoir simulation runs ($N_{\text{qual}} \ll N_{\text{lib}}$) for qualified ensemble members.

The updated \mathbf{Y}_{DCT} is decomposed to obtain newly updated \mathbf{D} and \mathbf{X} using OMP and K-SVD, as addressed in Section 2.3 (Figure 3(g)). With the new \mathbf{D} and $\mathbf{Y}_{\text{DCT,ens}}^a$ in (11), $\mathbf{X}_{\text{ens}}^a$ is reupdated using OMP: $\mathbf{Y}_{\text{DCT,ens}}^a = \mathbf{D}\mathbf{X}_{\text{ens}}^a$. This reupdated $\mathbf{X}_{\text{ens}}^a$ is used as \mathbf{m}^b in (2) as the state vector of the next assimilation.

2.5. Framework of ES-MDA-DCT-i-K-SVD. Figure 5 is a flowchart of the proposed ES-MDA algorithm that is compared with those of the other four ES-MDA algorithms investigated in this study. The general operating procedure for the algorithms is as follows: generation of an initial ensemble, reservoir simulation and selection of the qualified ensemble, Kalman-gain calculation and model update, facies designation, iteration of the above processes until the iteration number reaches the number of assimilations N^a , and acquisition of qualified reservoir models. Differences between the algorithms are found in the types of state vectors and model update processes, as presented in Figures 5(b) and 5(c).

Table 1 compares state vectors and sparse geologic dictionaries for the algorithms. ES-MDA updates gridblock facies indexes (originally assigned 0 and 1 for shale and sand, resp.). ES-MDA-DCT updates filtered DCT coefficients in the facies domain. ES-MDA-K-SVD tunes weights in facies domain with only one application of K-SVD before ES-MDA, while ES-MDA-DCT-K-SVD tunes weights in the DCT domain with only one application of K-SVD before ES-MDA. Finally, the proposed ES-MDA-DCT-i-K-SVD updates weights in the DCT domain with iterative K-SVD during ES-MDA.

3. Results and Discussions

The performance of the proposed algorithm (i.e., ES-MDA-DCT-i-K-SVD) is tested with applications to history matching of two channelized gas reservoirs. The algorithm performance is compared to those of four ES-MDA algorithms described in Table 1 to investigate coupling effects of dimensionality reduction and iterative sparse coding. Note

TABLE 2: Experimental setting of reservoir parameters used in Case 1 and Case 2.

Parameter	Value
Number of gridblocks in the x-direction (N_x) (dimensionless)	75
Number of gridblocks in the y-direction (N_y) (dimensionless)	75
Number of gridblocks in the z-direction (N_z) (dimensionless)	1
Grid size (ft ³)	200 × 200 × 100
Initial gas saturation (fraction)	0.75
Initial water saturation (fraction)	0.25
Initial reservoir pressure (psia)	3000
Porosity (fraction)	0.2
Permeability of sand facies (md)	300
Permeability of shale facies (md)	0.1
Index of sand facies (dimensionless)	1
Index of shale facies (dimensionless)	0

that the developed algorithm updates dictionaries with dynamic data in each assimilation of ES-MDA. Neither ES-MDA nor ES-MDA-DCT adopts dictionaries. Dictionaries generated using static data are unchanged during data assimilation for ES-MDA-K-SVD and ES-MDA-DCT-K-SVD.

3.1. Field Description. Table 2 summarizes gas reservoir properties used in Case 1 and Case 2. For each case, the gas reservoir consists of sand and shale facies. Each facies has its relative permeability curves and absolute permeability value; permeabilities of sand and shale facies are 300 and 0.1, respectively. Reservoir boundaries are surrounded by numerical aquifers modeled by employing pore volume multipliers.

Figure 6 compares training images and reference models of the two cases. The size of the reservoir domain, well location, and well name are the same in both cases; eight vertical wells (P1, P4, P6, P7, P9, P12, P14, and P15) are drilled in the sand formation, and the other eight vertical wells (P2, P3, P5, P8, P10, P11, P13, and P16) are drilled in the shale formation. These 16 facies data at the well locations are regarded as hard data used for model generation. Both the reference model and N_{lib} reservoir models are generated with hard data using SNESim that employs the training image shown in Figure 6(a) for Case 1.

The main differences between Case 1 and Case 2 are the shapes and widths of the channels. First, the reference model

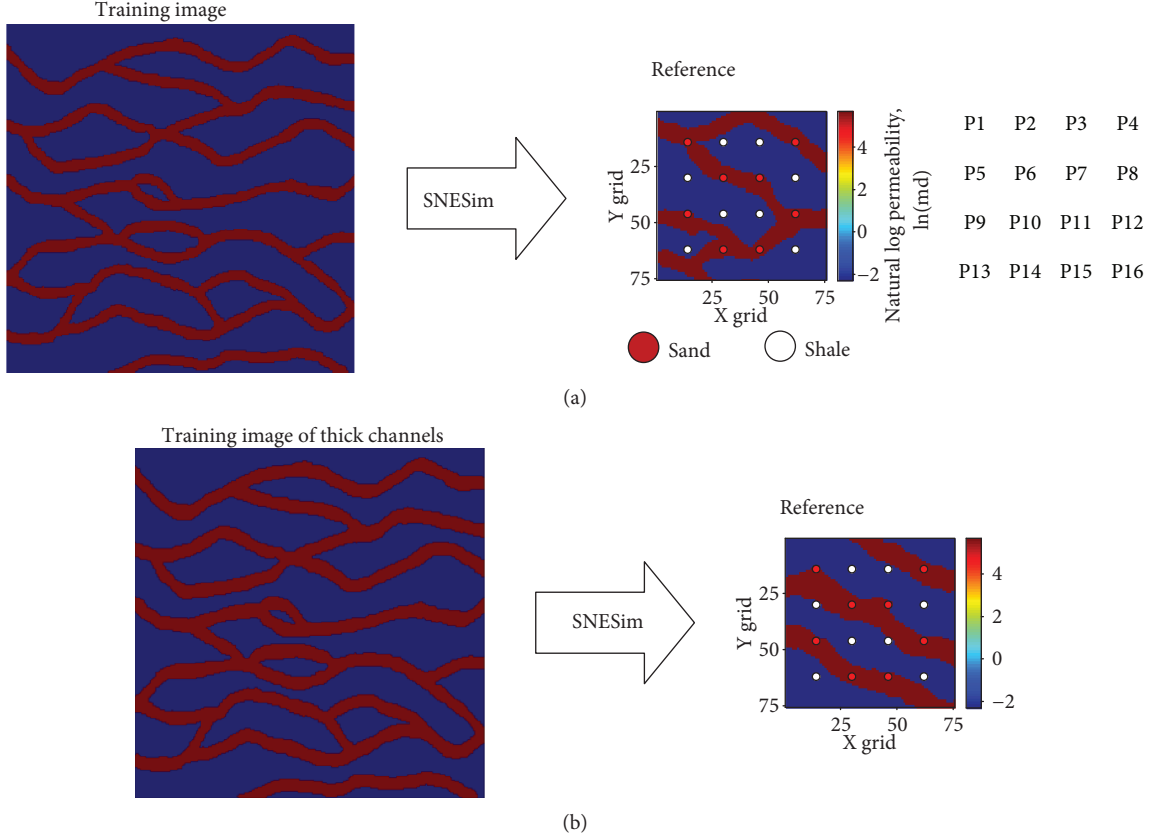


FIGURE 6: Training images and reference models adopted for history matching of (a) Case 1 and (b) Case 2.

TABLE 3: Experimental data for well parameters used in Case 1 and Case 2.

Parameter	Value
Observed well data	Gas rate and BHP
Maximum well gas production rate (MSCF/day)	15000
Minimum well BHP (psia)	1000
Total simulation period (day)	7000
History matching period (day)	3500
Prediction period (day)	3500
Coordinates of well locations in sand facies	(14, 14), (62, 14), (30, 30), (46, 30), (14, 46), (62, 46), (30, 62), (46, 62)
Coordinates of well locations in shale facies	(30, 14), (46, 14), (14, 30), (62, 30), (30, 46), (46, 46), (14, 62), (62, 62)

of Case 1 contains an S-shaped sand channel in the shale background, while the reference model of Case 2 has three parallel channels for which the orientation is NW-SE direction. Secondly, the channel width of the training image of Case 2 is 1.2 times thicker than that of Case 1, making that the channel width of the reference model of Case 2 is 1.2 times thicker as well. Despite the differences, this study intentionally reuses the initial ensemble designed for Case 1 as the initial ensemble of Case 2. The manipulation of an initial

TABLE 4: Number of parameters used for construction and update of sparse geologic dictionaries.

Parameter	Symbol	Value
Number of static reservoir models for constructing an initial library matrix \mathbf{Y}	N_{lib}	3000
Number of static reservoir models for constructing an initial dictionary matrix \mathbf{D}	N_{dict}	1000
Number of gridblocks in each reservoir model	N_{grid}	5625
Number of filtered DCT coefficients in each reservoir model	N_{DCT}	465
Number of ensemble members	N_{ens}	100
Number of qualified ensemble members	N_{qual}	20

ensemble amplifies intrinsic reservoir uncertainty that is hard to infer from prior information (i.e., training image) for Case 2.

Table 3 describes operating conditions of 16 wells (from P1 to P16), the well coordinates of which are shown in Figure 6(a). Table 4 presents the number of parameters used in the five ES-MDA algorithms. Implementing DCT yields the data compression ratio $N_{\text{grid}}/N_{\text{DCT}} = 12.1$. All experiments were set up such that $N^a = 4$ and $\alpha_p = 4$ according to (5). The proportion of the ensemble update in sparse geologic dictionaries $N_{\text{qual}}/N_{\text{lib}}$ is 0.67%.

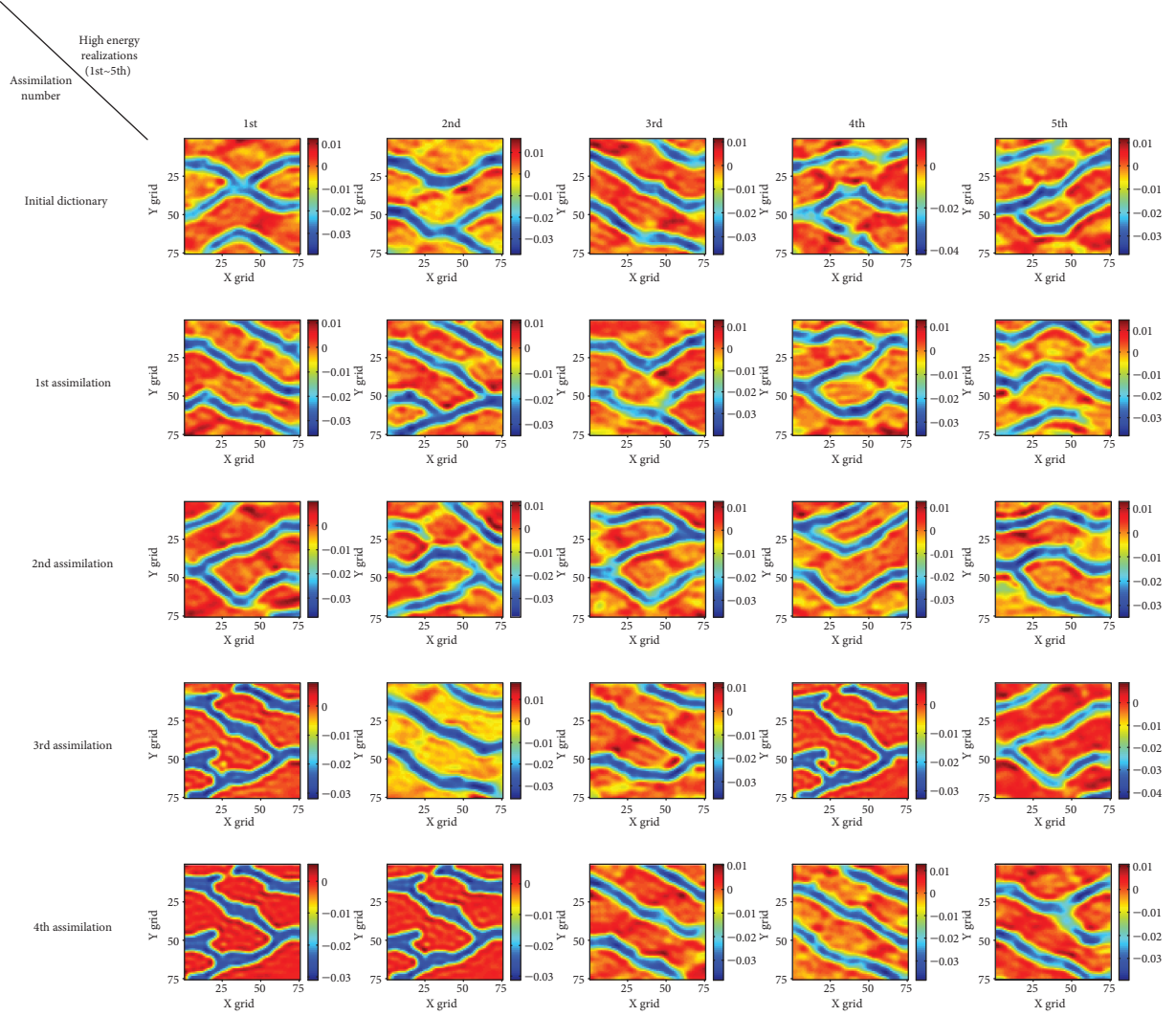


FIGURE 7: Evolution of realizations in the dictionary matrix \mathbf{D} during multiple data assimilation (Case 1).

3.2. Case 1. Figure 7 shows the evolution of realizations in \mathbf{D} achieved by invoking the proposed algorithm. We present five realizations having higher energy than the others, which are the first to the fifth column vectors in \mathbf{D} , in each assimilation. Qualified realizations vary until the second assimilation is complete, implying a deficiency in the assimilation process due to a large dispersion of realizations. In the third assimilation, it seems that the first and fourth realizations conform to the reference model (Figure 6(a)). The first and second realizations in the fourth assimilation capture the S-shaped channel pattern of the reference model. This increase in the similarity among realizations implies an increase in the probability that sparse geologic dictionaries sufficiently represent the target gas reservoir.

Figure 8 compares history-matching results (day 1–day 3500) and prediction results (day 3501–day 7000) of the initial and updated ensembles against the reference results. Gas production rate and BHP are matching parameters of each ES-MDA algorithm. Water production rate is excluded from the matching dataset because it is a watch parameter. The three data types measured at wells P1, P4, P9, and P15 are

shown because these wells installed in sand facies exhibit larger uncertainty than the other wells. In particular, water breakthrough does not occur at well P15 during the history-matching period. Thus, well P15 has the largest uncertainty in this case study. Solid gray, blue, dark blue, and red lines present well behaviors of the initial ensemble, the updated ensemble, the mean of the updated ensemble, and the reference model, respectively. The same initial ensemble is provided for each ES-MDA algorithm for a fair comparison. ES-MDA and ES-MDA-DCT expose a weakness in matching the reference results (Figures 8(a) and 8(b)). Improvements in matching accuracy are accomplished in the simulation results of the updated ensembles obtained using ES-MDA coupled with sparse coding (Figures 8(c)–8(e)). Executing sparse coding in the reduced parameter space has the result that most subfigures include the reference results within the bandwidth of the simulation results of the updated ensembles (Figures 8(d) and 8(e)), thereby improving the matching accuracy. Figure 8(d) results from the execution of ES-MDA-DCT-K-SVD of which the library matrix \mathbf{Y} is constructed using static data only. In Figure 8(d),

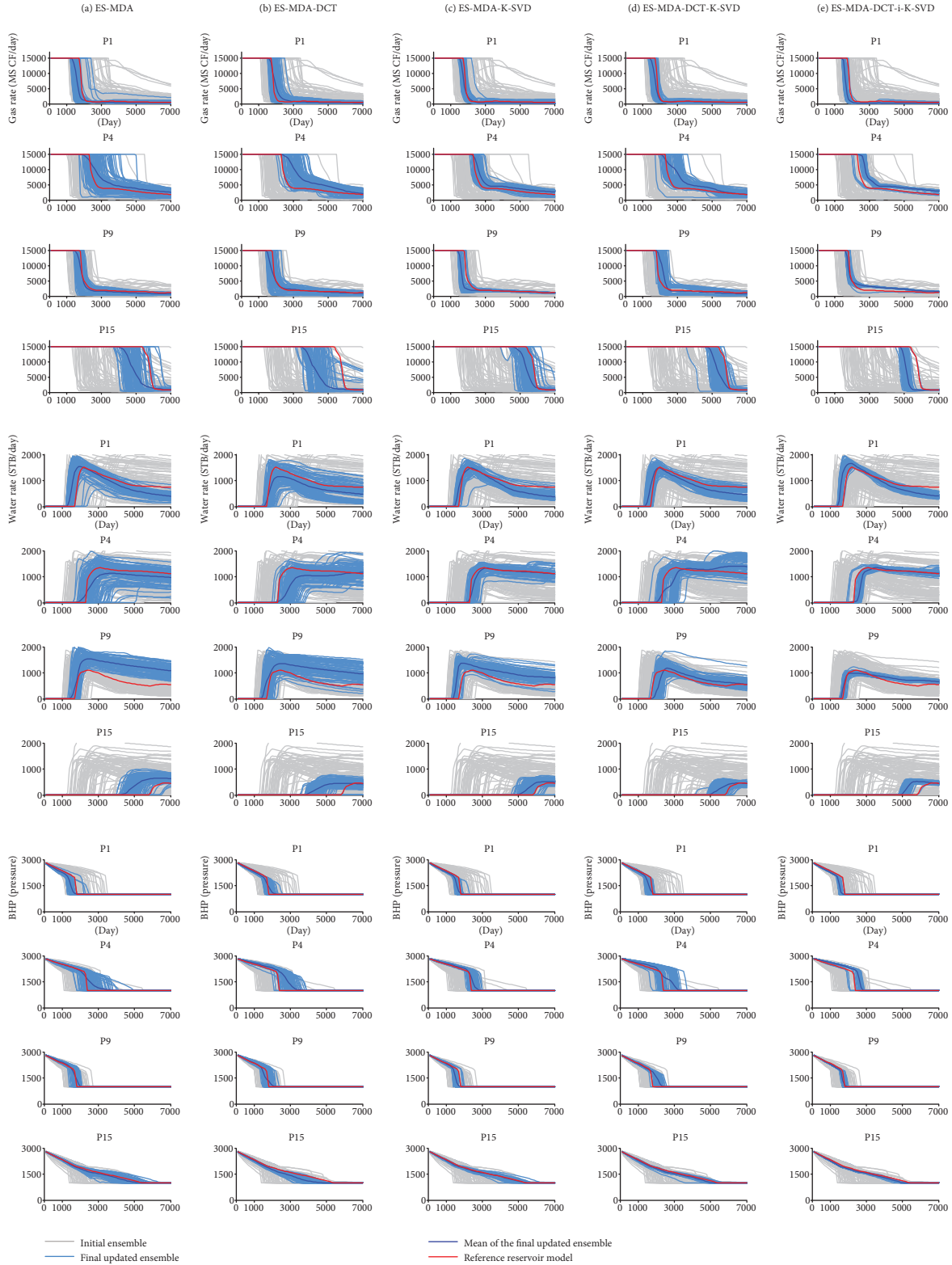


FIGURE 8: History matching results of Case 1: gas production rate, water production rate, and BHP measured at wells P1, P4, P9, and P15.

simulation results of some updated ensemble members deviate from the reference results at wells P4 and P9. It can be said that the update of \mathbf{Y} described in Section 2.4 yields an increase in matching accuracy and a reduction in dispersion

of simulation results (Figure 8(e)). For water breakthrough, underestimation of reservoir uncertainty is seen at well P15 in the simulation results obtained using the proposed algorithm. P15 showed the worst matching results among the

TABLE 5: Statistical parameters of history matching (HM) and prediction (PD) errors in terms of gas rate, water rate, and BHP (Case 1). μ_ϵ and σ_ϵ refer to the mean and standard deviation of ensemble error, respectively.

ES-MDA algorithm	μ_ϵ (%)	σ_ϵ (%)	μ_ϵ (%)	σ_ϵ (%)	μ_ϵ (%)	σ_ϵ (%)
	Gas rate (HM)		Water rate (HM)		BHP (HM)	
ES-MDA	46.44	122.79	18.61	20.99	55.84	53.01
ES-MDA-DCT	195.30	257.77	4.91	6.31	99.01	67.86
ES-MDA-K-SVD	11.83	34.88	6.04	2.94	27.72	29.78
ES-MDA-DCT-K-SVD	5.75	54.78	5.39	4.51	68.11	73.71
ES-MDA-DCT-i-K-SVD	0.98	1.69	6.29	2.40	39.36	16.54
	Gas rate (PD)		Water rate (PD)		BHP (PD)	
ES-MDA	37.05	48.74	13.11	10.24	27.85	27.70
ES-MDA-DCT	134.51	151.60	13.91	8.22	47.83	30.78
ES-MDA-K-SVD	26.03	16.08	2.54	0.01	8.13	11.79
ES-MDA-DCT-K-SVD	22.97	33.58	3.16	0.01	12.84	14.49
ES-MDA-DCT-i-K-SVD	24.68	13.39	4.62	0.01	13.15	3.54

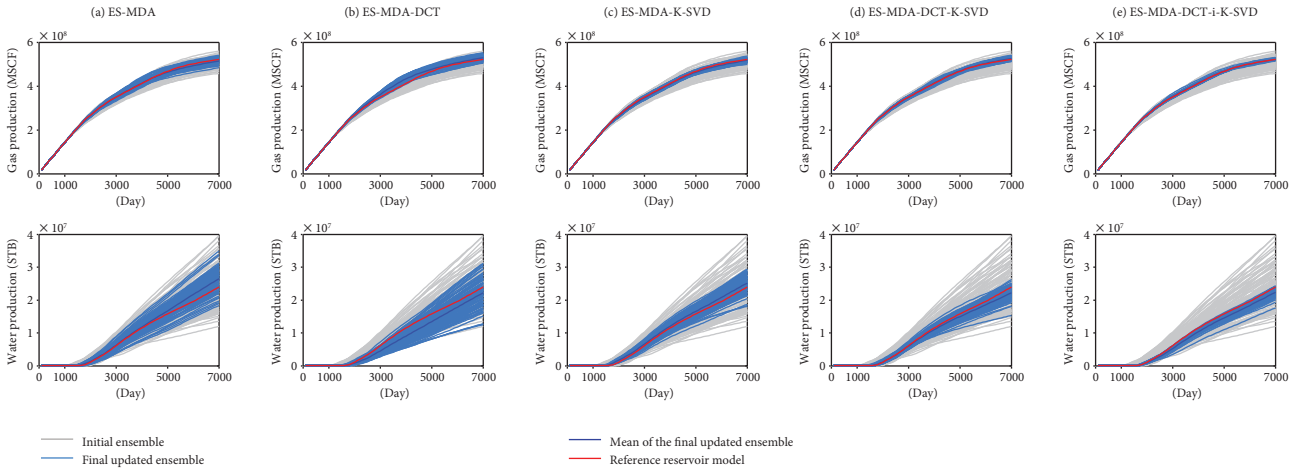


FIGURE 9: History matching results of Case 1: cumulative gas production and cumulative water production in the field.

16 wells as the breakthrough time is not detected during the matching period. It is reasonable to have moderate results at some matching targets despite the overall good matching performance [40, 41].

The performances of the algorithms in terms of both history-matching (HM) and prediction (PD) periods are summarized in Table 5. The quality of the updated ensembles was assessed using the following:

$$\mu_\epsilon = \frac{(1/N_{\text{ens}}) \sum_{i=1}^{N_{\text{ens}}} \epsilon_i^{\text{upd}}}{(1/N_{\text{ens}}) \sum_{i=1}^{N_{\text{ens}}} \epsilon_i^{\text{init}}} \times 100 (\%),$$

$$\sigma_\epsilon = \frac{\sqrt{(1/N_{\text{ens}} - 1) \sum_{i=1}^{N_{\text{ens}}} (\epsilon_i^{\text{upd}} - \overline{\epsilon_i^{\text{upd}}})^2}}{\sqrt{(1/N_{\text{ens}} - 1) \sum_{i=1}^{N_{\text{ens}}} (\epsilon_i^{\text{init}} - \overline{\epsilon_i^{\text{init}}})^2}} \times 100 (\%), \quad (15)$$

where μ_ϵ is the normalized average of error ϵ (see (12)) and σ_ϵ is the normalized standard deviation of ϵ . The superscripts upd and init refer to the updated ensemble member and the

initial ensemble member, respectively. Smaller values of μ_ϵ indicate a more accurate updated ensemble. Smaller values of σ_ϵ indicate a smaller degree of reservoir uncertainty associated with the ensemble. Any value larger than 100% indicates deterioration of the ensemble quality, as revealed in the results obtained using ES-MDA and ES-MDA-DCT. In terms of gas rate, for example, the updated ensemble of ES-MDA-DCT amplifies the degree of dispersion compared to the initial ensemble. Furthermore, the behaviors of its ensemble mean do not follow those of the reference model. The proposed algorithm yields acceptable μ_ϵ values and σ_ϵ values that are smaller than those of the other ES-MDA algorithms. Most observations are included within the bandwidths of the simulated profiles. The inclusion is also captured in the field cumulative production profiles of gas and water (Figure 9). Nonetheless, a remaining task is the construction of more robust dictionary matrices to improve the matching quality at every well target.

Figure 10 compares ensemble mean maps and histograms of permeability obtained using the five ES-MDA algorithms. A task herein is to investigate whether the ES-MDA

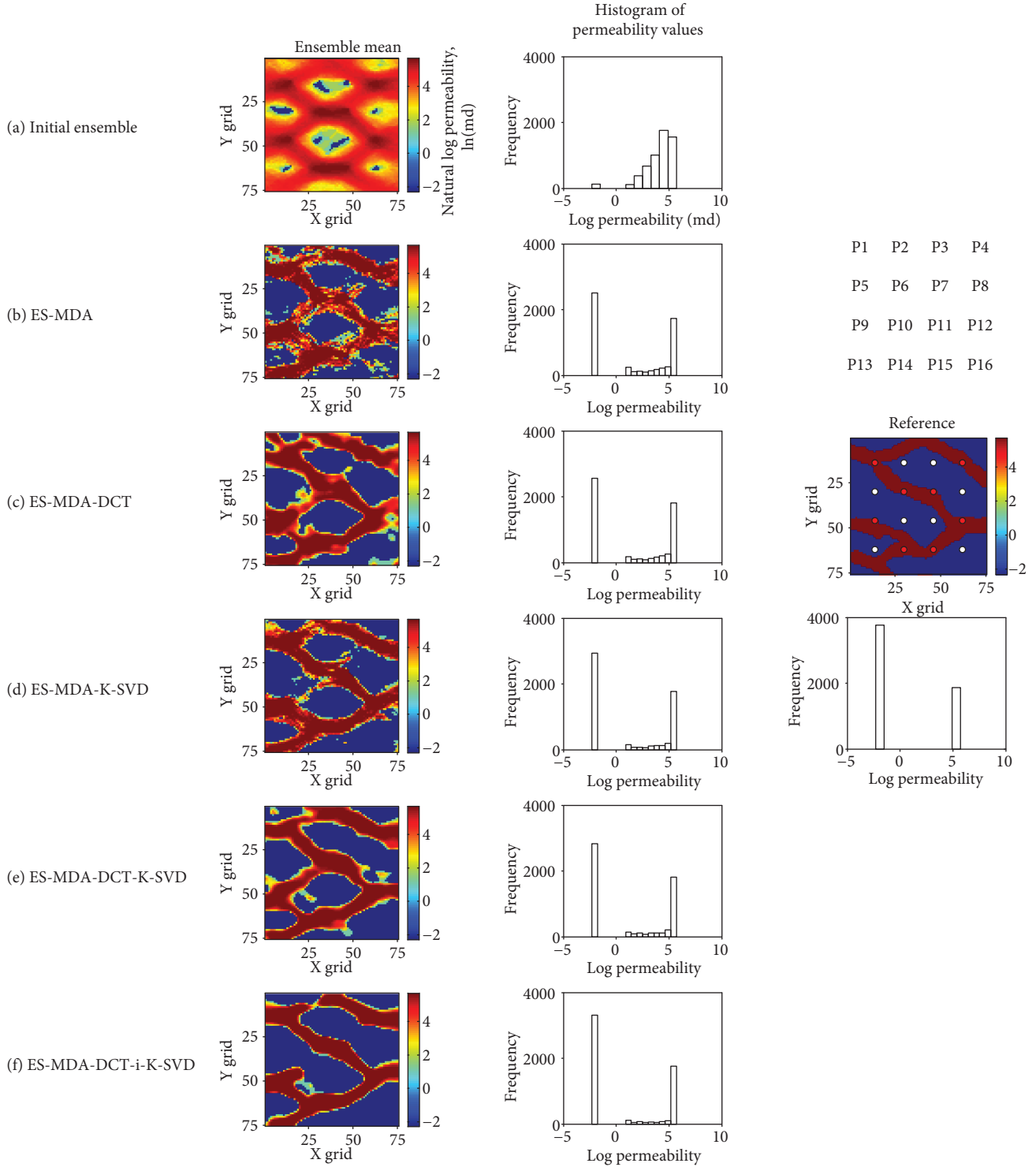


FIGURE 10: Permeability distribution of the ensemble means and their histogram of permeabilities obtained after history matching of Case 1.

algorithms can capture the overall trend of the sand channel while preserving shale facies in the background. In the reference model, for example, the shortest path between wells P6 and P9 is filled with shale. Each ensemble member consists of sand facies with a permeability of 300 md and shale facies with a permeability of 0.1 md. However, the histogram of the initial ensemble mean (Figure 10(a)) does not follow

the bimodal distribution. On the other hand, it seems that the histogram of each updated ensemble follows the bimodal distribution. The ensemble mean maps obtained using ES-MDA and ES-MDA-DCT (Figures 10(b) and 10(c)) conform less to the reference model than those obtained using the algorithms coupled with K-SVD. When comparing the log-scale permeability histograms, it seems

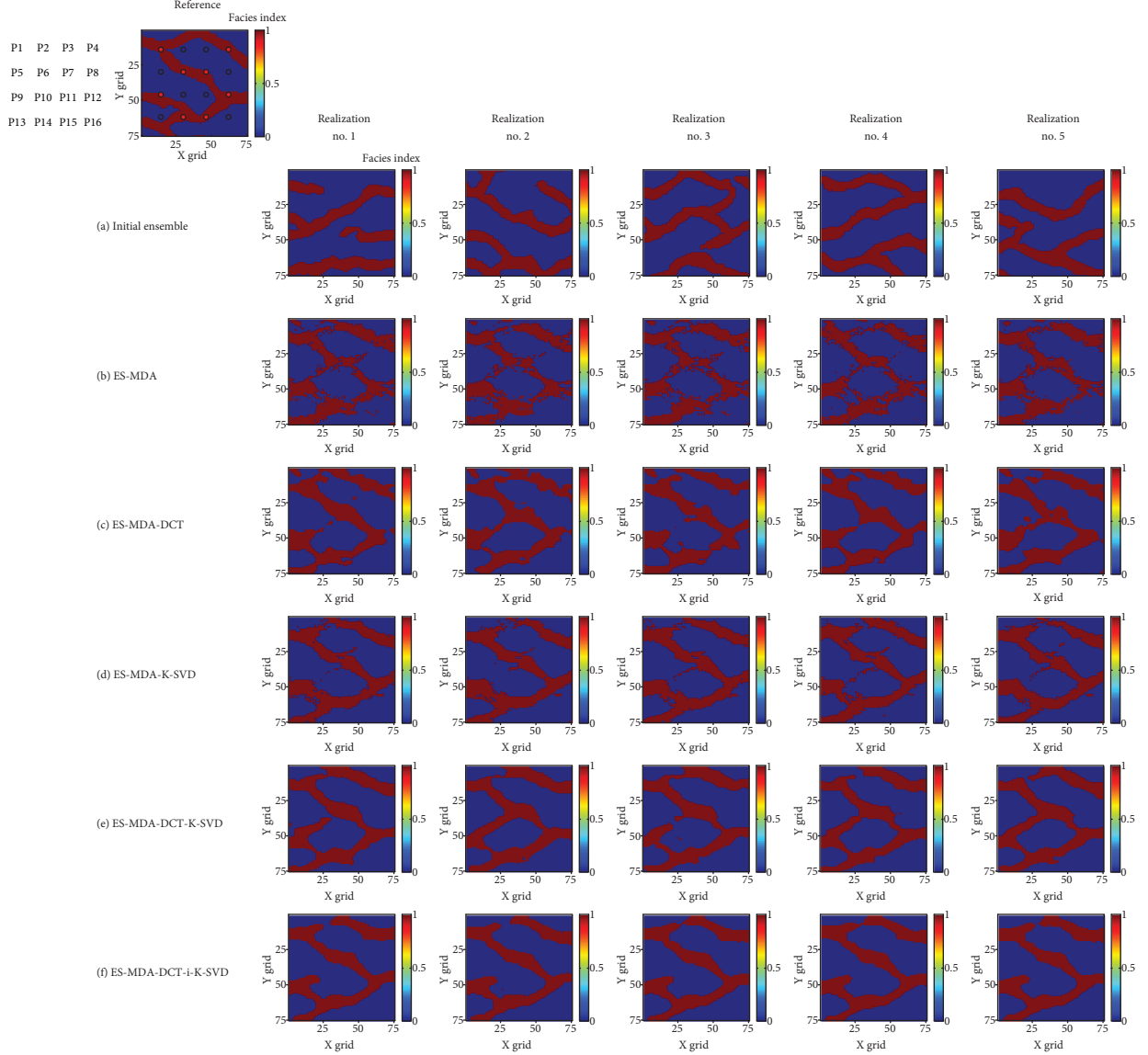


FIGURE 11: Permeability distribution of five qualified reservoir models obtained after history matching of Case 1.

TABLE 6: Comparison of computational costs required for dictionary construction and update.

ES-MDA algorithm	Computational costs (min)
ES-MDA	0.0
ES-MDA-DCT	0.0
ES-MDA-K-SVD	218.0
ES-MDA-DCT-K-SVD	5.7
ES-MDA-DCT-i-K-SVD	21.4 (=5.7 + 15.7)

that the unconformity is proportional to the frequencies of undesirable permeabilities between $\ln 0.1$ (≈ -2.3) md and $\ln 300$ (≈ 5.7) md in the histograms. DCT is advantageous for preserving channel connectivity; however, an artificial sand channel connects wells P6 and P9. In addition, truncated DCT coefficients smooth out borders between the sand

channel and background shale, as shown in Figure 10(c). ES-MDA-K-SVD, ES-MDA-DCT-K-SVD, and ES-MDA-DCT-i-K-SVD reproduce channel patterns and the connectivity of the reference model (Figures 10(d)–10(f)), although Figure 10(e) contains undesirable sand facies between wells P6 and P9. A crisp contrast between shale and sand facies is observed in the outcome of the assimilation algorithms coupling DCT and K-SVD (Figures 10(e) and 10(f)). The developed algorithm reveals clearer shale facies in the path than the other algorithms (Figure 10(f)).

Figure 11 compares characterization results of a channelized reservoir with regards to sand-shale facies distribution. The initial five realizations reveal diverse channel patterns in terms of orientation and shape (Figure 11(a)). Pixel-based perturbation using ES-MDA delivers a broken channel with a low-channel connectivity after assimilation (Figure 11(b)). In Figure 11(c), the shortest path between wells P6 and P9 is filled not with shale but sand in the

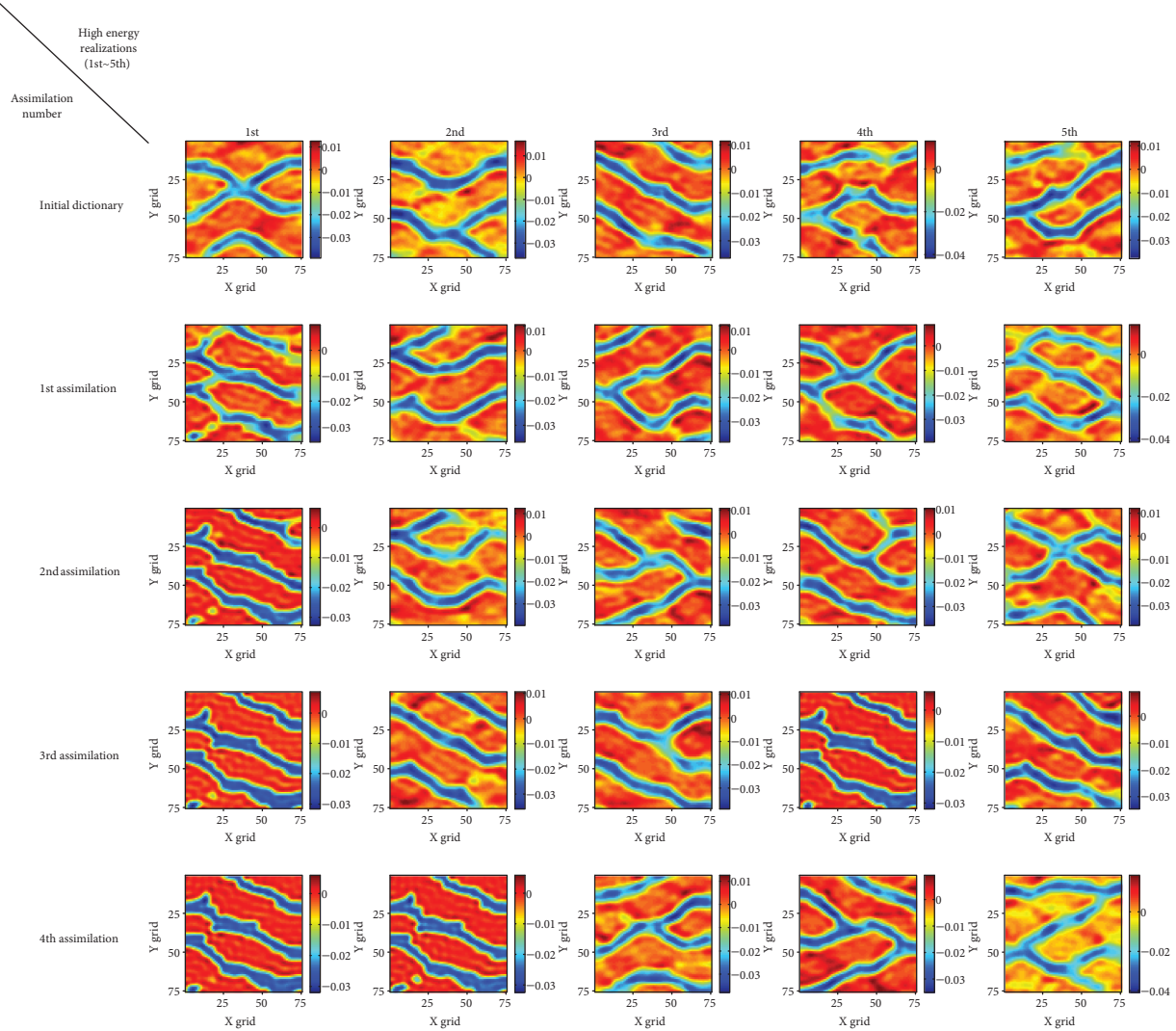


FIGURE 12: Evolution of realizations in the dictionary matrix \mathbf{D} during multiple data assimilation (Case 2).

second and fifth realizations, while part of the channel is disconnected in the first and third realizations. Interestingly, data loss during DCT made the channel width irregular. K-SVD helps conserve the connectivity and pattern of the channel (Figure 11(d)). Parameterization followed by sparse coding delivers satisfactory results in preserving overall channel characteristics (Figures 11(e) and 11(f)). Figure 11(e) connects well P6 and well P9 with an artificial sand channel, but Figure 11(f) does not. That is, conditioning dictionaries to dynamic data through the iterative sparse coding provides opportunities to calibrate the rock facies distribution between well P6 and well P9. The five realizations of the proposed algorithm keep the channel patterns similar to the reference, while maintaining shale facies on the shortest path between well P6 and well P9 (Figure 11(f)). Most realizations have a broken sand channel near the upper left corner of the domain. This phenomenon would be an intrinsic limitation of geostatistical methods arising from a lack of observation data.

Table 6 compares computational costs paid for the construction and update of dictionaries. The hardware

specification utilized for comparison was Intel® Core™ i5-7200U @ 2.5 GHz with 8 GB RAM. The runtime of the reservoir simulation was excluded from the comparison. ES-MDA and ES-MDA-DCT cost nothing for dictionary construction. ES-MDA-K-SVD was a relatively costly algorithm. It took 218 minutes to obtain the original dictionary matrices \mathbf{D} and \mathbf{X} via \mathbf{Y} despite the matrix construction one time. DCT helped save computational costs required for sparse coding. ES-MDA-DCT-K-SVD was the cheapest algorithm (taking 5.7 minutes) thanks to the reduced number of parameters due to DCT. Updating sparse geologic dictionaries in each assimilation resulted in an additional 15.7 minutes in the subsequent four assimilations. Nevertheless, it seems this amount of extra cost is within a reasonable range. ES-MDA-DCT-K-SVD was 38.2 times as fast as ES-MDA-K-SVD, and ES-MDA-DCT-i-K-SVD was 10.2 times faster than ES-MDA-K-SVD.

3.3. Case 2. This case study checks whether the updated ensemble can describe the shape and orientation of three parallel sand channels under uncertainty associated with the

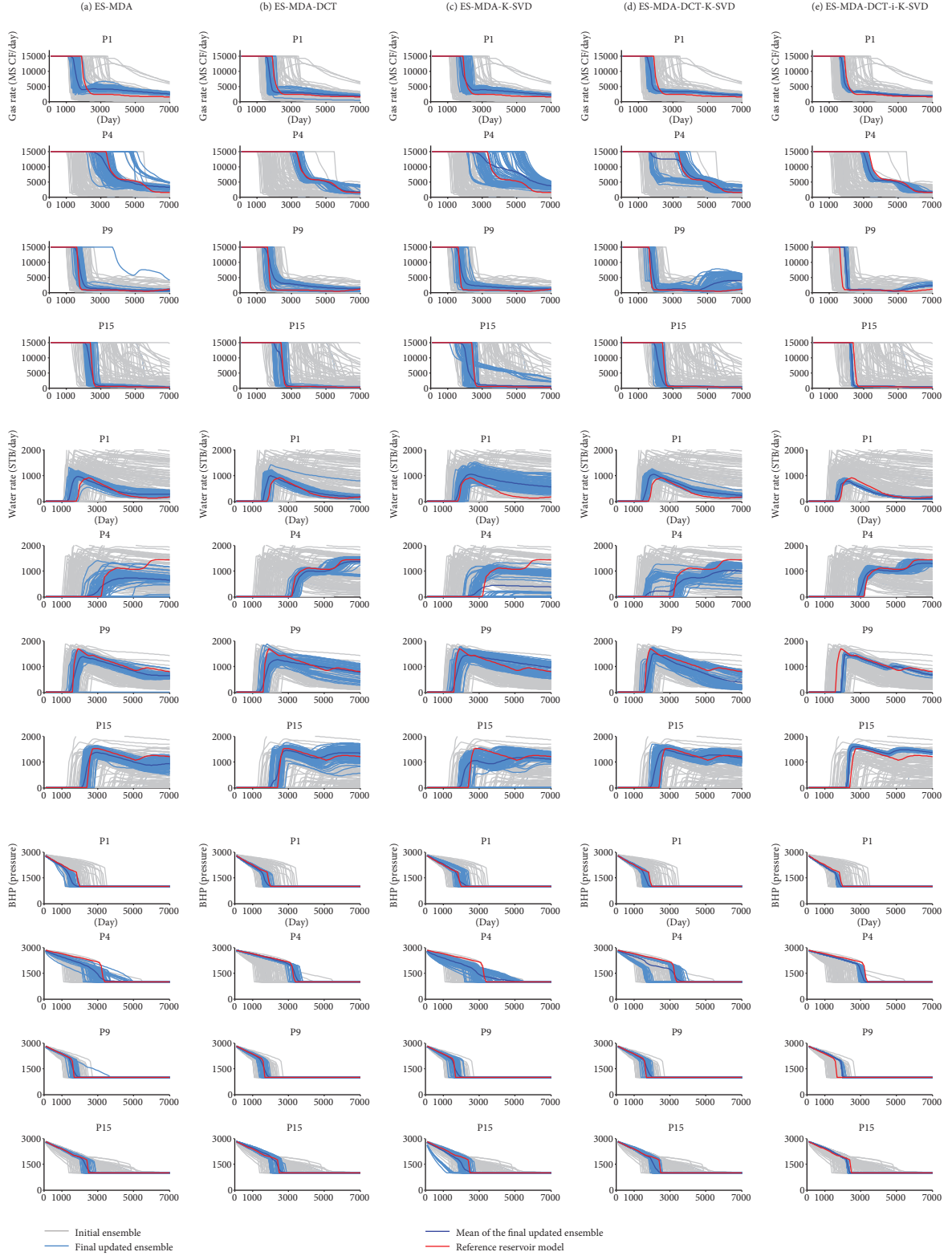


FIGURE 13: History matching results of Case 2: gas production rate, water production rate, and BHP measured at wells P1, P4, P9, and P15.

underestimated channel width. Figure 12 shows the evolution of realizations in the dictionary matrix \mathbf{D} obtained using the proposed algorithm during multiple data assimilation. The trend of evolution is consistent with that presented in

Case 1 (Figure 7). For example, the first and second realizations in the fourth assimilation sufficiently resemble the reference model. This similarity implies that the quality of geologic dictionaries is improved by adding N_{qual} models

TABLE 7: Statistical parameters of history matching (HM) and prediction (PD) errors in terms of gas rate, water rate, and BHP (Case 2). μ_ϵ and σ_ϵ refer to mean and standard deviation of the ensemble error, respectively.

ES-MDA algorithm	μ_ϵ (%)	σ_ϵ (%)	μ_ϵ (%)	σ_ϵ (%)	μ_ϵ (%)	σ_ϵ (%)
	Gas rate (HM)		Water rate (HM)		BHP (HM)	
ES-MDA	2.00	8.07	5.99	7.63	23.38	16.12
ES-MDA-DCT	6.64	27.96	2.44	3.12	19.70	16.00
ES-MDA-K-SVD	3.28	7.35	7.52	11.04	39.48	44.94
ES-MDA-DCT-K-SVD	1.66	2.48	15.25	24.38	29.09	34.30
ES-MDA-DCT-i-K-SVD	4.15	1.45	1.04	0.94	32.15	4.51
	Gas rate (PD)		Water rate (PD)		BHP (PD)	
ES-MDA	4.39	3.74	14.19	5.66	28.54	26.98
ES-MDA-DCT	2.67	0.64	8.38	6.17	25.48	12.27
ES-MDA-K-SVD	5.53	8.71	35.74	24.21	101.10	63.86
ES-MDA-DCT-K-SVD	10.02	6.90	20.23	12.09	23.95	26.59
ES-MDA-DCT-i-K-SVD	1.53	0.28	12.20	2.36	29.77	2.49

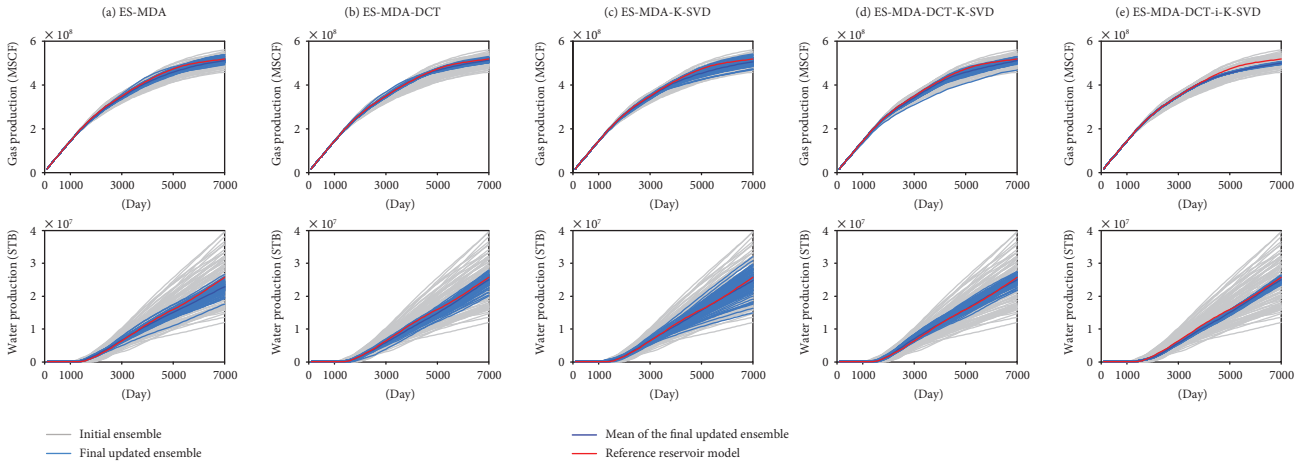


FIGURE 14: History matching results of Case 2: cumulative gas production and cumulative water production in the field.

conditioned to dynamic observations to the initially static library pool in each assimilation.

Figure 13 compares production profiles obtained using the five ES-MDA algorithms. Each algorithm reuses the initial ensemble introduced in Case 1, as mentioned in Section 3.1. The proposed algorithm yields smaller standard deviations than the other algorithms and reduces reservoir uncertainty with reasonable matching accuracy (Table 7). The matching accuracy is comparable to those of the algorithms coupling sparse coding. Matches and prediction results for gas and water rate are decent. In terms of BHP, the proposed method shows the best conformance to observations except for well P9. The overestimated BHP is related to the underestimation of the water rate at well P9. Our inference is that this happens because of incorrect prior knowledge of the channel width. Field cumulative production profiles of gas and water are presented in Figure 14. Figure 15 compares averaged permeability distribution of the updated ensemble obtained using the five algorithms. The proposed algorithm outperforms the other algorithms by preserving the separation among the channels with NW-SE orientation and a distinct contrast at the borders between the shale background and

sand channels. Facies index maps of individual ensemble members obtained after history matching also support the reliability of the proposed algorithm (Figure 16).

4. Conclusions

The hybridized ES-MDA algorithm coupled with iterative sparse coding in reduced parameter space was able to calibrate channelized reservoir models using and updating the repository of geologic features called sparse geologic dictionaries. The first library composed of thousands of reservoir models generated using SNESim was only conditioned to static data. Dimensionality reduction performed using DCT was effective in reducing the size of the library by converting gridblock facies into coefficients of discrete cosine functions. The weight matrix obtained by decomposing the library was imported to ES-MDA as a state vector. In each assimilation of ES-MDA, update of weights resulted in reservoir models that were well conditioned to both static and dynamic data. Adding the history-well-matched reservoir models as new members in the existing library was the critical factor for attaining improved matching accuracy and reduced model

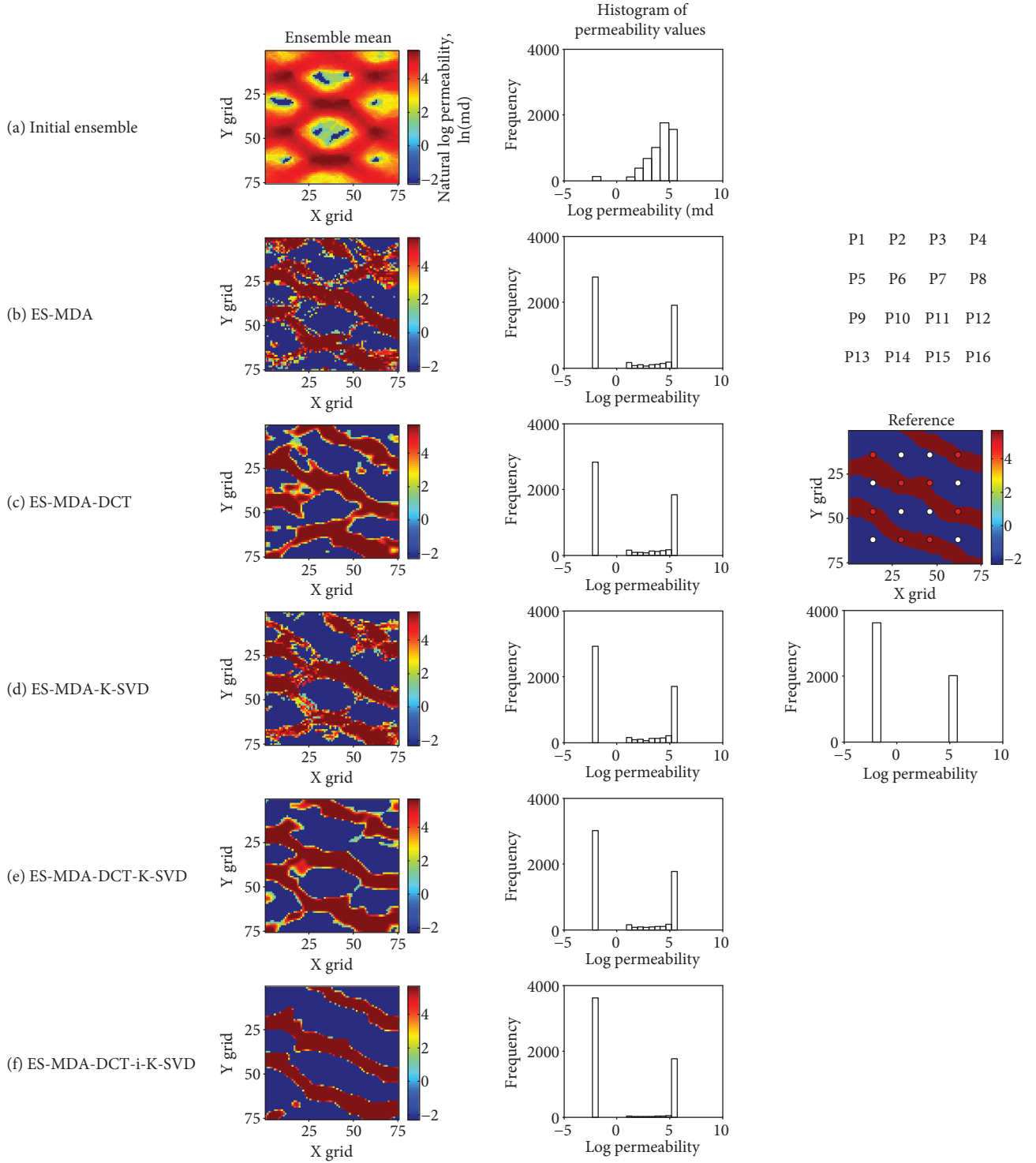


FIGURE 15: Permeability distribution of the ensemble means and their histogram of permeabilities obtained after history matching of Case 2.

dispersion because of the reflection of dynamic data in the updated dictionaries. The unprecedented consideration of dictionary update was the originality of this study and the contribution to researches about combinations of machine learning and ensemble-based data assimilation methods.

History-matching results of two channelized gas reservoirs (i.e., the S-shaped channel for Case 1 and three parallel

channels for Case 2) indicated that the achievements arose from an iterative update of dictionaries of the proposed algorithm: the improved matching accuracy in both history and forecast in terms of well and total production, the reduced dispersion of production behaviors and permeability distribution, and the well-connected channel body of reservoir models with geological plausibility. ES-MDA with the

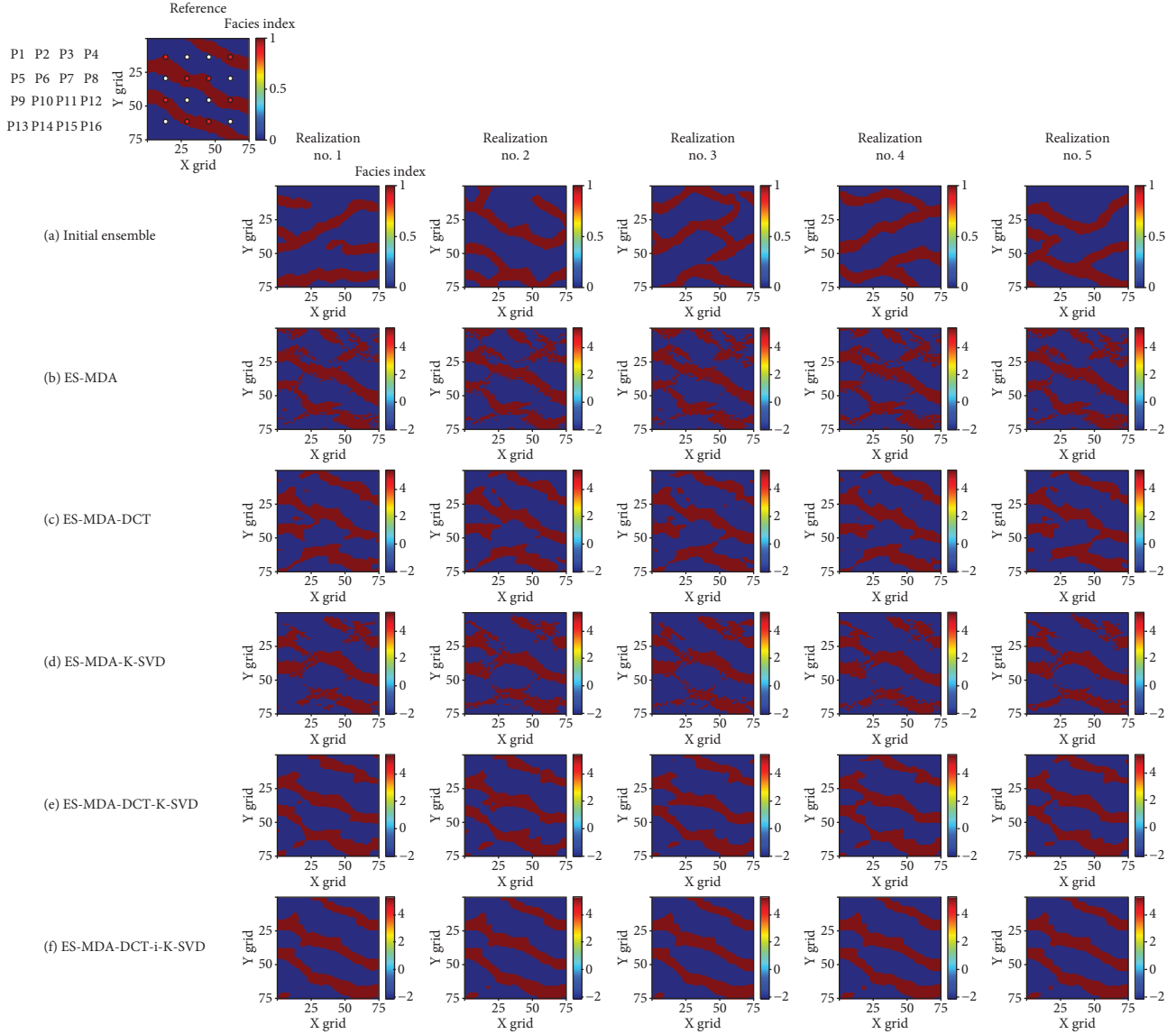


FIGURE 16: Permeability distribution of five qualified reservoir models obtained after history matching of Case 2.

dictionary update yielded higher matching accuracy values and lower dispersion values than ES-MDA incorporated with a fixed dictionary matrix. The increase in computational costs paid during the dictionary update was affordable compared to the assimilation algorithms not coupled with sparse coding. Improving the matching accuracy at some well-based levels remains as an outstanding task for the proposed technique despite the overall enhanced matching quality. We also anticipate that future works will adopt a more generalized sparse coding for diversifying the utility of the proposed framework in a variety of geoenvironments (e.g., naturally fractured reservoirs).

Nomenclature

B: Covariance matrix of state vectors
C_D: Covariance matrix of observed measurement error
C_{dd}: Autocovariance matrix of simulation data **d**

C_{md}: Cross-covariance matrix of state vector **m** and simulation data **d**
d: Simulation data
d^{obs}: Observation data
d^{unc}: Perturbed observation data
d^r: Column vector of the dictionary matrix **D** (i.e., realization)
 $\bar{\mathbf{d}}$: Mean of simulation data
D: Dictionary matrix
E_j: Discrepancy between the library matrix **Y** and the reconstructed library matrix **Y'** except the *j*th **d^r_j**
f: Reservoir simulator
J: Objective function
m: State vector of a reservoir model
 $\bar{\mathbf{m}}$: Mean of state vectors
m^b: State vector of a reservoir model before update
I_{N_d}: *N_d* by *N_d* identity matrix

K : Kalman gain
 N^a : Number of assimilations
 N_d : Number of time steps in observations
 N_{DCT} : Number of essential DCT coefficients
 N_{dict} : Number of reservoir models in the dictionary matrix D
 N_{ens} : Number of ensemble members
 N_{grid} : Number of gridblocks in a reservoir model
 N_{lib} : Number of reservoir models in the library matrix Y
 N_{para} : Number of parameters in a reservoir model
 N_{qual} : Number of qualified ensemble members
 N_{type} : Number of data types
 R : Covariance matrix of observation error
 x : Row vector of the weight matrix X
 X : Weight matrix
 Y : Library matrix
 Y' : Reconstructed library matrix
 z_d : Random error to observations
 α_p : Inflation coefficients of C_D
 ε : Error
 $\varepsilon_{\text{qual}}$: Discrepancy between observation and simulation results of an ensemble member
 μ : Average
 σ : Standard deviation.

Subscripts

DCT: Discrete cosine transform
 dict: Dictionary
 ens: Ensemble
 lib: Library
 qual: Qualified
 para: Parameter.

Superscripts

a : Assimilation
 init: Initial
 obs: Observation
 upd: Update.

Data Availability

The data used to support the findings of this study are available from the corresponding author upon request.

Conflicts of Interest

The authors declare no conflict of interest.

Acknowledgments

Dr. Baehyun Min was funded by the National Research Foundation of Korea (NRF) grants (no. NRF-2017R1C1B5017767 and no. NRF-2017K2A9A1A01092734). Dr. Kyungbook Lee was supported by the Korea Institute of Geoscience and Mineral Resources (GP2017-024) and MOTIE projects (NP2017-021, 20172510102090). Dr. Hoonyoung Jeong is thankful to the Research Institute of Energy and Resources,

Seoul National University. The authors are grateful for the support of Korea Gas Corporation (KOGAS).

References

- [1] B. Min, J. M. Kang, S. Chung, C. Park, and I. Jang, "Pareto-based multi-objective history matching with respect to individual production performance in a heterogeneous reservoir," *Journal of Petroleum Science and Engineering*, vol. 122, pp. 551–566, 2014.
- [2] G. Evensen, "Sequential data assimilation with a nonlinear quasi-geostrophic model using Monte Carlo methods to forecast error statistics," *Journal of Geophysical Research*, vol. 99, no. C5, pp. 10143–10162, 1994.
- [3] S. Kim, C. Lee, K. Lee, and J. Choe, "Aquifer characterization of gas reservoirs using ensemble Kalman filter and covariance localization," *Journal of Petroleum Science and Engineering*, vol. 146, pp. 446–456, 2016.
- [4] L. Li, M. Zhang, and K. Katzenstein, "Calibration of a land subsidence model using InSAR data via the ensemble Kalman filter," *Groundwater*, vol. 55, no. 6, pp. 871–878, 2017.
- [5] Æ. Geir, T. Mannseth, and E. H. Vefring, "Near-well reservoir monitoring through ensemble Kalman filter," in *SPE/DOE Improved Oil Recovery Symposium*, pp. 1–9, Tulsa, OK, USA, April 2002, SPE-75235-MS.
- [6] K. Lee, S. Jung, and J. Choe, "Ensemble smoother with clustered covariance for 3D channelized reservoirs with geological uncertainty," *Journal of Petroleum Science and Engineering*, vol. 145, pp. 423–435, 2016.
- [7] D. S. Oliver and Y. Chen, "Recent progress on reservoir history matching: a review," *Computational Geosciences*, vol. 15, no. 1, pp. 185–221, 2011.
- [8] A. A. Emerick and A. C. Reynolds, "History matching time-lapse seismic data using the ensemble Kalman filter with multiple data assimilations," *Computational Geosciences*, vol. 16, no. 3, pp. 639–659, 2012.
- [9] A. A. Emerick and A. C. Reynolds, "Ensemble smoother with multiple data assimilation," *Computers & Geosciences*, vol. 55, pp. 3–15, 2013.
- [10] X. Luo, A. S. Stordal, R. J. Lorentzen, and G. Nævdal, "Iterative ensemble smoother as an approximate solution to a regularized minimum-average-cost problem: theory and applications," *SPE Journal*, vol. 20, no. 5, pp. 962–982, 2015.
- [11] K. Lee, H. Jeong, S. Jung, and J. Choe, "Improvement of ensemble smoother with clustered covariance for channelized reservoirs," *Energy Exploration & Exploitation*, vol. 31, no. 5, pp. 713–726, 2013.
- [12] K. Lee, S. Jung, H. Shin, and J. Choe, "Uncertainty quantification of channelized reservoir using ensemble smoother with selective measurement data," *Energy Exploration & Exploitation*, vol. 32, no. 5, pp. 805–816, 2014.
- [13] R. J. Lorentzen, K. M. Flornes, and G. Nævdal, "History matching channelized reservoirs using the ensemble Kalman filter," *SPE Journal*, vol. 17, no. 1, pp. 137–151, 2012.
- [14] Y. Shin, H. Jeong, and J. Choe, "Reservoir characterization using an EnKF and a non-parametric approach for highly non-Gaussian permeability fields," *Energy Sources, Part A: Recovery, Utilization, and Environmental Effects*, vol. 32, no. 16, pp. 1569–1578, 2010.

- [15] H. Zhou, L. Li, and J. J. Gómez-Hernández, "Characterizing curvilinear features using the localized normal-score ensemble Kalman filter," *Abstract and Applied Analysis*, vol. 2012, Article ID 805707, 18 pages, 2012.
- [16] B. Jafarpour and D. B. McLaughlin, "History matching with an ensemble Kalman filter and discrete cosine parameterization," *Computational Geosciences*, vol. 12, no. 2, pp. 227–244, 2008.
- [17] B. Jafarpour and D. B. McLaughlin, "Estimating channelized-reservoir permeabilities with the ensemble Kalman filter: the importance of ensemble design," *SPE Journal*, vol. 14, no. 2, pp. 374–388, 2009.
- [18] H. Jung, H. Jo, S. Kim, K. Lee, and J. Choe, "Recursive update of channel information for reliable history matching of channel reservoirs using EnKF with DCT," *Journal of Petroleum Science and Engineering*, vol. 154, pp. 19–37, 2017.
- [19] S. Kim, C. Lee, K. Lee, and J. Choe, "Characterization of channelized gas reservoirs using ensemble Kalman filter with application of discrete cosine transformation," *Energy Exploration & Exploitation*, vol. 34, no. 2, pp. 319–336, 2016.
- [20] S. Kim, C. Lee, K. Lee, and J. Choe, "Characterization of channel oil reservoirs with an aquifer using EnKF, DCT, and PFR," *Energy Exploration & Exploitation*, vol. 34, no. 6, pp. 828–843, 2016.
- [21] Y. Zhao, F. Forouzanfar, and A. C. Reynolds, "History matching of multi-facies channelized reservoirs using ES-MDA with common basis DCT," *Computational Geosciences*, vol. 21, no. 5–6, pp. 1343–1364, 2017.
- [22] B. Min, M. F. Wheeler, and A. Sun, "Parallel multiobjective optimization for the coupled compositional/geomechanical modeling of pulse testing," in *SPE Reservoir Simulation Symposium*, pp. 1–25, Montgomery, TX, USA, February 2017, SPE-182641-MS.
- [23] A. Y. Sun, J. Lu, B. M. Freifeld, S. D. Hovorka, and A. Islam, "Using pulse testing for leakage detection in carbon storage reservoirs: a field demonstration," *International Journal of Greenhouse Gas Control*, vol. 46, pp. 215–227, 2016.
- [24] E. W. Bhark, B. Jafarpour, and A. Datta-Gupta, "A generalized grid connectivity-based parameterization for subsurface flow model calibration," *Water Resources Research*, vol. 47, no. 6, 2011.
- [25] R. J. Lorentzen, G. Nævdal, and A. Shafieirad, "Estimating facies fields by use of the ensemble Kalman filter and distance functions-applied to shallow-marine environments," *SPE Journal*, vol. 3, no. 1, pp. 146–158, 2012.
- [26] M. R. Khaninezhad and B. Jafarpour, "Sparse geologic dictionaries for field-scale history matching application," in *SPE Reservoir Simulation Symposium*, pp. 1–17, Houston, TX, USA, February 2015, SPE-173275-MS.
- [27] L. Li and B. Jafarpour, "Effective solution of nonlinear subsurface flow inverse problems in sparse bases," *Inverse Problems*, vol. 26, no. 10, article 105016, 2010.
- [28] S. Kim, H. Jung, K. Lee, and J. Choe, "Initial ensemble design scheme for effective characterization of three-dimensional channel gas reservoirs with an aquifer," *Journal of Energy Resources Technology*, vol. 139, no. 2, article 022911, 2017.
- [29] M. Aharon, M. Elad, and A. Bruckstein, "K-SVD: an algorithm for designing overcomplete dictionaries for sparse representation," *IEEE Transactions on Signal Processing*, vol. 54, no. 11, pp. 4311–4322, 2006.
- [30] K. Kreutz-Delgado, J. F. Murray, B. D. Rao, K. Engan, T. W. Lee, and T. J. Sejnowski, "Dictionary learning algorithms for sparse representation," *Neural Computation*, vol. 15, no. 2, pp. 349–396, 2003.
- [31] F. Sana, K. Katterbauer, T. Y. Al-Naffouri, and I. Hoteit, "Orthogonal matching pursuit for enhanced recovery of sparse geological structures with the ensemble Kalman filter," *IEEE Journal of Selected Topics in Applied Earth Observations and Remote Sensing*, vol. 9, no. 4, pp. 1710–1724, 2016.
- [32] M. M. Khaninezhad, B. Jafarpour, and L. Li, "Sparse geologic dictionaries for subsurface flow model calibration: part I. Inversion formulation," *Advances in Water Resources*, vol. 39, pp. 106–121, 2012.
- [33] F. Bouttier and P. Courtier, "Data assimilation concepts and methods," in *Meteorological Training Course Lecture Series*, pp. 1–59, European Centre for Medium-Range Weather Forecasts, 2002.
- [34] B. Jafarpour and D. B. McLaughlin, "Efficient permeability parameterization with the discrete cosine transform," in *SPE Reservoir Simulation Symposium*, pp. 1–9, Houston, TX, USA, February 2007, Paper No. 106453.
- [35] H. Jo, H. Jung, J. Ahn, K. Lee, and J. Choe, "History matching of channel reservoirs using ensemble Kalman filter with continuous update of channel information," *Energy Exploration & Exploitation*, vol. 35, no. 1, pp. 3–23, 2017.
- [36] S. Strebelle, "Conditional simulation of complex geological structures using multiple-point statistics," *Mathematical Geology*, vol. 34, no. 1, pp. 1–21, 2002.
- [37] E. Liu and B. Jafarpour, "Learning sparse geologic dictionaries from low-rank representations of facies connectivity for flow model calibration," *Water Resources Research*, vol. 49, no. 10, pp. 7088–7101, 2013.
- [38] T. T. Cai and L. Wang, "Orthogonal matching pursuit for sparse signal recovery with noise," *IEEE Transactions on Information Theory*, vol. 57, no. 7, pp. 4680–4688, 2011.
- [39] J. A. Tropp and A. C. Gilbert, "Signal recovery from random measurements via orthogonal matching pursuit," *IEEE Transactions on Information Theory*, vol. 53, no. 12, pp. 4655–4666, 2007.
- [40] B. Min, C. Park, I. Jang, J. M. Kang, and S. Chung, "Development of Pareto-based evolutionary model integrated with dynamic goal programming and successive linear objective reduction," *Applied Soft Computing*, vol. 35, pp. 75–112, 2015.
- [41] A. Nwachukwu, B. Min, and S. Srinivasan, "Model selection for CO₂ sequestration using surface deformation and injection data," *International Journal of Greenhouse Gas Control*, vol. 56, pp. 67–92, 2017.

Research Article

The Monitoring-Based Analysis on Deformation-Controlling Factors and Slope Stability of Reservoir Landslide: Hongyanzi Landslide in the Southwest of China

Bing Han ¹, Bin Tong ¹, Jinkai Yan,¹ Chunrong Yin,¹ Liang Chen,¹ and Deying Li²

¹China Institute of Geo-Environmental Monitoring, Beijing, China

²Faculty of Engineering, China University of Geosciences, Wuhan, China

Correspondence should be addressed to Bin Tong; tongb@mail.cigem.gov.cn

Received 28 February 2018; Accepted 8 May 2018; Published 10 July 2018

Academic Editor: Liangping Li

Copyright © 2018 Bing Han et al. This is an open access article distributed under the Creative Commons Attribution License, which permits unrestricted use, distribution, and reproduction in any medium, provided the original work is properly cited.

Reservoir landslide is a type of commonly seen geological hazards in reservoir area and could potentially cause significant risk to the routine operation of reservoir and hydropower station. It has been accepted that reservoir landslides are mainly induced by periodic variations of reservoir water level during the impoundment and drawdown process. In this study, to better understand the deformation characters and controlling factors of the reservoir landslide, a multiparameter-based monitoring program was conducted on a reservoir landslide—the Hongyanzi landslide located in Pubugou reservoir area in the southwest of China. The results indicated that significant deformation occurred to the landslide during the drawdown period; otherwise, the landslide remained stable. The major reason of reservoir landslide deformation is the generation of seepage water pressure caused by the rapidly growing water level difference inside and outside of the slope. The influences of precipitation and earthquake on the slope deformation of the Hongyanzi landslide were insignificant.

1. Introduction

Landslide induced by reservoir impoundment and drawdown is a commonly seen geological hazard in reservoir area and has caused significant impacts and damages on the operation and function of hydropower stations all over the world. Historical statistics show that in general, over 90% of reservoir-induced landslides are caused by the fluctuations of reservoir water level, and approximately 50% occurred during the period of impoundment [1–4]. More than 80% occurred during the first 3 to 5 years after the construction of the dam [1]. Regarding the influences of reservoir water level fluctuation, 40% occurred with the declination of reservoir water level [2, 3]. The large landslides of the sizes greater than ten million cubic meters were normally triggered by the rapid declination of the reservoir water level. Also, approximately 75% of triggered landslides were due to the revivification of ancient landslides

[5]. In summary, the significant and instant reservoir water level fluctuations normally cause negative influences on the global stability of the reservoir slopes through influencing their hydrological conditions and reducing the slope strength [6].

The failure mechanisms and resulted chain of disasters (such as the impulse of wave) by reservoir landslides have been extensively studied in previous studies [5–7]. Erosions of loose debris at the slope toe by flow, instant pore water pressure generation in the slope by the drawdown of reservoir water level, and structural and strength reduction of the hydrofluctuation belt are the main reasons of triggering reservoir landslides [1, 4–6]. By conducting numerical analysis [6, 7], the risk management of potential impulse wave by the slope movement also draws more attentions. The majority of these researchers are intent to provide a complete overview/analysis on the whole process of the disaster chain, including the deformation triggering of the landslide to the

generation of impulse wave, as well as the resulted potential hazard to the properties in the reservoir or on the opposite bank [2, 3]. The full-process analysis offers valuable insights into the planning of prevention, control of geological hazards, and guidance on estimation of landslide-generated impulse waves in reservoirs.

Studies [7, 8] on reservoir landslide deformation characters indicated that the global deformation always started at the front part of the slope and mainly composed of the deformation of the slip band. The potential negative influences caused by the reservoir-induced landslides mainly include two aspects: (1) the significant reduction of reservoir storage capacity and water conservancy facilities operation due to the entrance of sliding material into reservoirs; (2) the formation of impulsive waves induced by sliding materials reaching the reservoir water with large dynamic energy and cause significant safety issues on the dam and the operation of hydropower stations [7, 9, 10].

The slope monitoring technology developed rapidly over the past several decades. At the beginning of 21th century, the optical fiber monitoring system became more extensively used, and advancements of higher accuracy, greater speed, and higher automation in monitoring technology have occurred. Meanwhile, one of the important problems to be solved is to improve the coordination and integration of the monitoring system of involving different types of monitoring devices for various monitoring parameters. Currently, the data communication and compatibility of the data processing software for comprehensive slope dynamic performance is a major research issue.

Therefore, it is important in theory and engineering practice to study the impact and casual correlations among reservoir water level fluctuation, hydrodynamic, and deformation characters of reservoir landslides. Conducting the comprehensive monitoring program on reservoir landslides is the key issue of obtaining the in situ data, which set the basis for conducting the more comprehensive analysis and simulations. The periodic geological inspections are recommended to monitor the deformation and hydrogeological condition of the slope during the process of reservoir water level fluctuation [4, 11].

In this paper, a multiparameter monitoring program was conducted to record the change of ground water level, surface deformation, and deep-seated displacement at various locations on the Hongyanzi landslide, located in Pubugou Hydropower Station reservoir area, Sichuan province, Southwest China, during the period of reservoir impoundment and drawdown from 2013 to 2014.

Based on the measurements, the temporal correlations among reservoir water level fluctuation, slope groundwater level, surface displacements, crack propagations, and deep-seated displacement are interpreted. The preliminary recommendations are made to help control the negative influences of reservoir water level fluctuation on the slope stability of reservoir landslides. The findings presented in this paper could also offer the valuable insights into the planning of prevention and control of geological hazards in the Pubugou Hydropower Station reservoir area and relevant studies on reservoir induced landslides in the world.

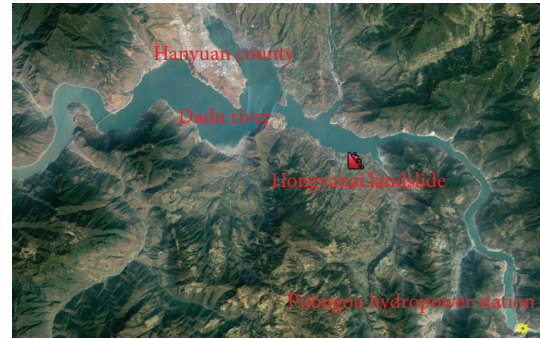


FIGURE 1: Location map of the Hongyanzi landslide (source: Google Earth).



FIGURE 2: 3D view of the Hongyanzi landslide.

2. Overview of the Hongyanzi Landslide

The Hongyanzi landslide is located in the right bank of the Dadu River, a secondary tributary of the Yangtze River in Hanyuan County, Sichuan province in the Southwest of China (Figure 1). It is 23 km away from the Pubugou Hydropower Station in the downstream region. According to the previous investigations, the overall slope of the Hongyanzi landslide is 27 degrees. The slope magnitude varies significantly along the surface the landslide from the scarp to the toe.

The plan view of the Hongyanzi landslide is approximately semicircular (Figure 2). The sliding direction is 340 degrees. The elevation of the slope toe and back-scarp is 810 m and 954 m, respectively, and the overall elevation difference between the toe and the slope is approximately 150 m. The total length and width are 600 and 580 m, respectively [10].

Prior to the installations of monitoring devices, the large deformations have occurred to both left and right boundaries, and the magnitude reached 1.7 m and 1.5 m, respectively, due to the reservoir water fluctuation during the same period. According to the in situ investigation [10], the thickness of sliding material is nonuniform, and the thickness varies from 20 to 50 m over the entire slope area. Since the Hongyanzi landslide is an ancient landslide, the thickness of sliding material in the front is greater than that in the rear. Geomorphologically, the plain area of Hongyanzi landslide is

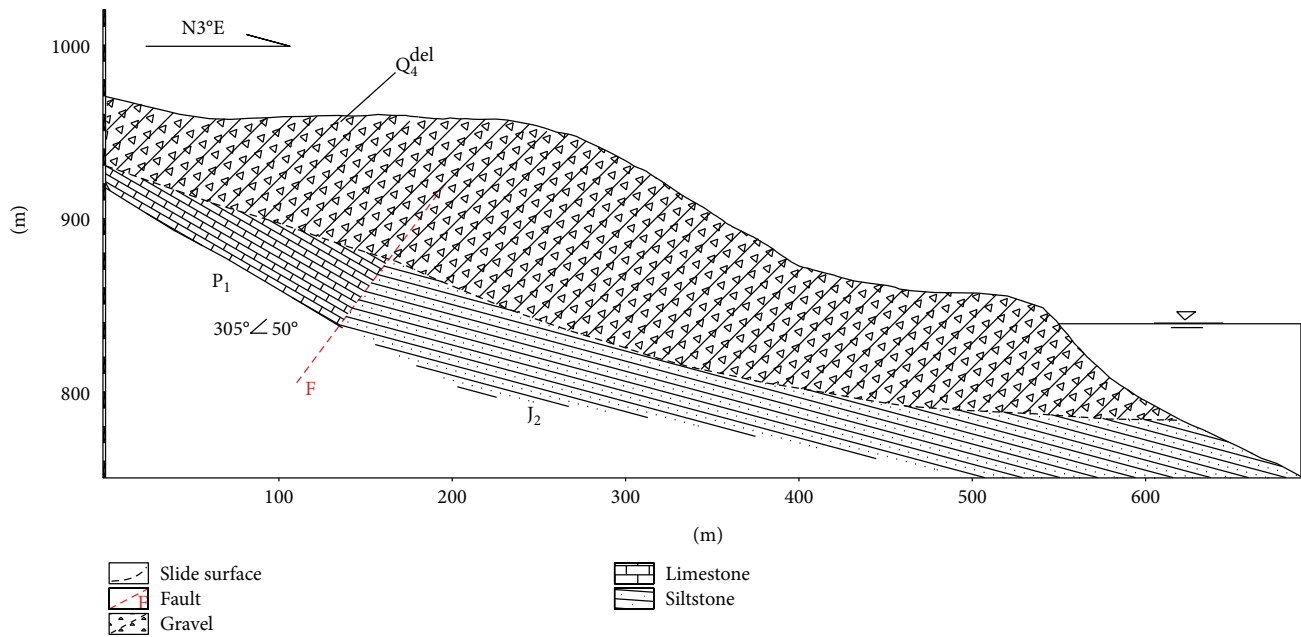


FIGURE 3: Main geological profile of the Hongyanzi landslide.

about $1.80 \times 10^5 \text{ m}^2$, and the total volume is approximately 7.7 million m^3 . The sliding surface is flatter in the front and steeper in the rear, and slope difference is about 20 degrees [10]. Due to the large distortions occurred to the pavements on the slope, the boundary of the Hongyanzi landslide can be easily identified in the field.

Based on field investigation, the Hongyanzi landslide is an ancient accumulation landslide (Figure 3), and the sliding material is mainly composed of the quaternary silty clay, cobble, or gravel, and the stones of diameter from 1 to 3 meters can be observed locally. The primary composition of cobble and gravel is limestone with a densely compact structure. The stratum of sliding bed is Jurassic reddish sandstone in the footwall of Hanyuan-Zhaojue fault and Permian limestone in hanging wall of the fault [10].

The hydrogeological condition of the Hongyanzi landslide is relatively simple. The groundwater is mainly the pore phreatic water in loose rock mass, and the major supply is atmospheric precipitation. The Hongyanzi landslide faces the Dadu River in the north and gullies in the east and west. The steep topography and large elevation differences from the scarp to the toe provide a great potential for groundwater to discharge into the Dadu River. During the operation of the Pubugou Hydropower Station, the reservoir water level varied from 790 m to 850 m, and the range of water-level-fluctuating zone was approximately 60 m. The fluctuation of reservoir water level had a vital impact on the ground water table of the reservoir bank slopes.

Based on the historical records [10], the Hongyanzi landslide remained stable before the construction of the hydropower station. After the impoundment, large deformation occurred to the Hongyanzi landslide during the declination period of the reservoir water level. The impoundment and power generation started on June and November 2010, respectively. In February 2011, after 8 months of

impoundment, large deformations occurred to the Hongyanzi landslide and the accumulated downward deformation reached up to 1 m by the end of 2011 depending on the local topography. Simultaneous deformation continued to occur with the declination of reservoir water level in 2012. From 2013 to 2014, the maximum deformation reached to 2.7 meters, and the accumulated deformation since the beginning of hydropower station operation is more than 4 meters. The majority of the deformations occurred during the declination of the reservoir water level, and no large deformations were observed when the reservoir water level remains stable or increases. Similar observations were also made by previous studies [12–18]. Due to the extensive deformation of the Hongyanzi landslide, a multiparameter monitoring program was conducted on the Hongyanzi landslide to advance the understanding on the deformation characters and its major influencing factors.

3. The Multiparameter Monitoring

Since 2012, various monitoring equipment (Figure 4 and Table 1) were employed to conduct a continuous monitoring program on the simultaneous developments of surface deformation, deep-seated deformation, ground water table in the slope, crack propagations on the left and right boundaries, and the atmospheric precipitations. Reservoir level was measured by the water gauge. The distribution of the installed monitoring devices is shown in Figure 4. The monitoring program started in January 2013, and this study mainly focuses on the monitoring data received prior to December 2014.

3.1. Slope Ground Water Table. As shown in Figure 5, a strong correlation exists between slope water level in ZK-5-w and reservoir water level. The reservoir water level declined

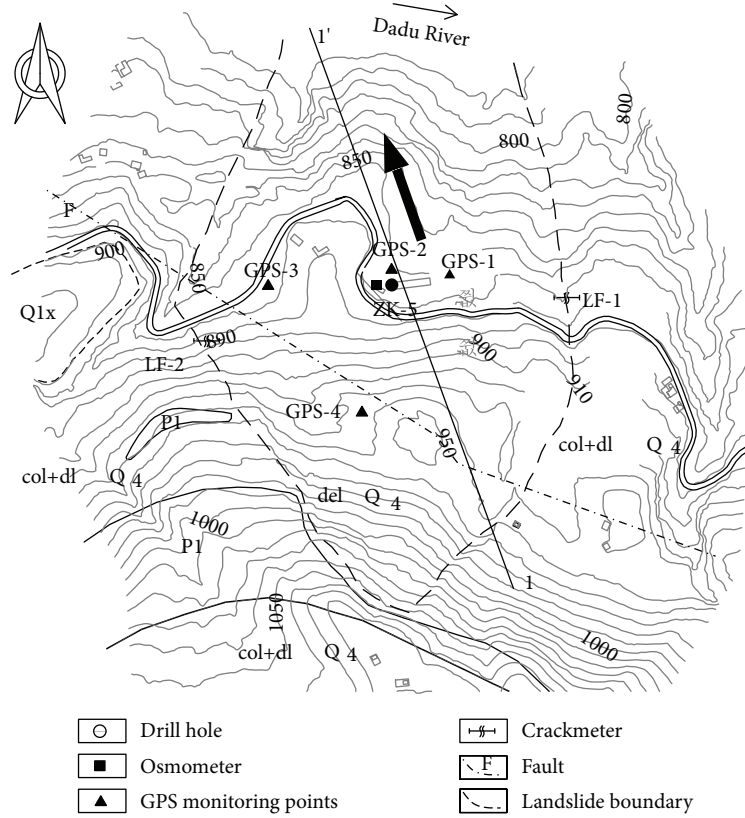


FIGURE 4: Distribution of monitoring devices on Hongyanzi landslide.

TABLE 1: Monitoring devices employed in this study.

Device ID	Measuring data and installed location
GPS-1	Surface displacement (on the right of the center)
GPS-2	Surface displacement (middle part of landslide)
GPS-3	Surface displacement (on the left of the center)
GPS-4	Surface displacement (near the scarp)
LF-1	Surface crack propagation (on the right boundary)
LF-2	Surface crack propagation (on the left boundary)
ZK-5-d	Deep-seated displacement (middle part of landslide)
ZK-5-w	Ground water table (middle part of landslide)

gradually from January to April 2013 from 850 m to 792 m. Meanwhile, the slope water level measured in ZK-5-w also decreased from 853 m to 825 m. In May, the reservoir water level started rising and reached 842 m in July. At the same time, the slope water level returned to 846 m. In August, the reservoir water level decreased from 842 m to 819 m, and the slope water level also decreased from 847 m to 834 accordingly. During the initial of the drawdown period, the declination rate of the slope water level is roughly the same with the value of reservoir water level. However, when the reservoir water level declined with increased speed, the declination of slope water level lags behind.

3.2. Surface Displacement. Four GPS monitoring stations were installed on the slope surface, and the measuring results showed that large slope deformations, which mainly

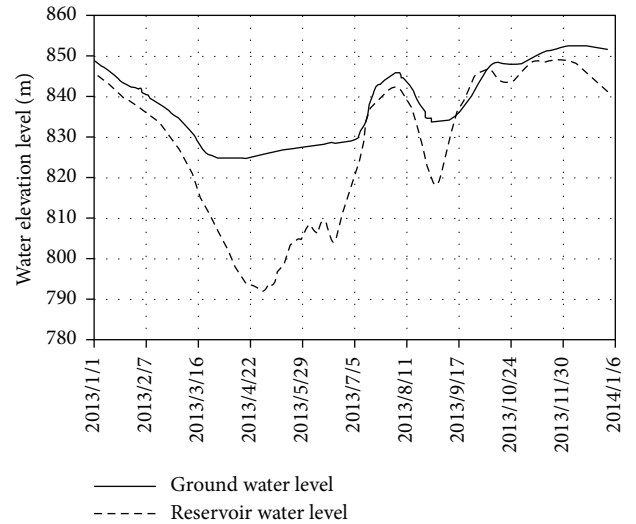


FIGURE 5: Reservoir water level versus ground water level.

occurred to from March to June, were captured from 2013 to 2014. The directions of the horizontal displacements measured by GPS-1, GPS-2, and GPS-3 that were located in the mid to front of the slope were approximately the same (NW 22 to 24 degrees). The magnitude of displacements also increased from left to the right on the slope. The maximum horizontal and vertical displacement was 2690 mm (GPS-1) and 760 mm (GPS-3), respectively. GPS-4 was located near a steep scarp in the midrear part of the slope. Therefore,

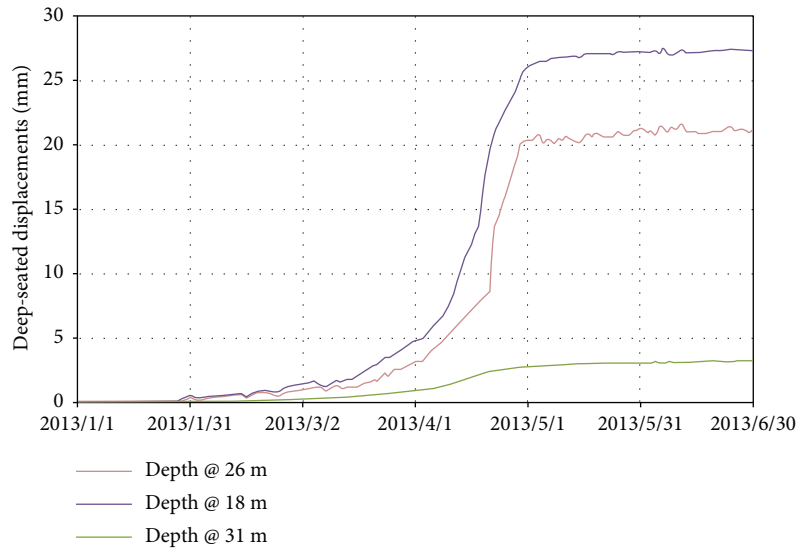


FIGURE 6: Reservoir water level versus deep-seated resultant displacement (ZK-7-d).

due to the influence of microtopography on the measurements, the deformation characters captured by GPS-4 were different from the other three stations. The direction of horizontal displacement at GPS-4 was NW 16 degrees, and the horizontal and vertical displacements were measured to be 1780 mm and 2000 mm, respectively.

Crack propagations were also monitored on the east and west boundaries of the Hongyanzi landslide. From January to July 2013, especially from April to July 2013, the crack development (LF-1) on the east boundary was significant, and the magnitude reached 1400 mm. On the contrast, crack propagated (LF-2) much lower on the west boundary, and the magnitude reached only 180 mm. Above measurements received good agreements with the surface displacements measured by GPS receivers, which clearly showed that the surface compression and tension occurred on the west and east boundaries, respectively. Also, the recording on both boundaries showed a consistent temporal correlation with surface displacement recorded by GPS stations.

3.3. Deep-Seated Displacement. The measuring depths for deep-seated displacement at ZK-7-d are 18 m, 26 m, and 31 m. Figure 6 shows that small magnitude of deformation of less than 5 mm occurred at a depth of 31 m, and the deformations at the depths of 18 m and 26 m were much larger. This could provide a good support for determining the elevation of sliding surface and volume of sliding material. Similar to the surface displacement and ground water table, a clear and consistent temporal correlation exists between the deep-seated displacement and fluctuation of reservoir water level as shown in Figure 7. Similar to the occurrence time of surficial deformation, the large deep-seated displacement started to increase in ZK-7-d from March to May.

3.4. Precipitation. According to the precipitation record at the Hongyanzi landslide, the average annual precipitation is approximately 400 mm and mainly concentrates from May to August, as shown in Figure 8. Based on the correlations

among the 1-day precipitation (Figure 9), 3-day accumulative precipitation (Figure 10), and slope deformation, it was found that significant deformation occurred during the period from March to April while no intensive precipitation was observed. In June, however, no large deformation was captured while intensive precipitation was recorded. Therefore, based on the above observations, the influence of rainfall on the development of landslide deformation could be fairly insignificant. Additional monitoring is being conducted currently to further analyze the influence of precipitation on the Hongyanzi landslide deformation.

3.5. Influence of Earthquake Events on Deformation of Hongyanzi Landslide. On April 20, 2013, an earthquake event of magnitude 7.0 hit the Lushan country, Sichuan province, and the distance from Hongyanzi landslide to the epicenter is about 100 km and the magnitude of intensity is VI. The recorded peak acceleration by the seismic station closest to Hongyanzi landslide was $0.4g$. A postearthquake field investigation was conducted, and the deformations on the boundaries were found larger than the routine deformation magnitudes induced by reservoir water fluctuations. The surface distortions of 50 mm and 10 mm were observed on the right and left boundaries, respectively. No obvious increases in the surface and deep-seated displacements were recorded by the monitoring devices.

4. Influence of Reservoir Water Level Fluctuation on Slope Stability

As shown in Figure 11, the primary deformations occurred during the drawdown period from March to April, especially when the declination rate was large. Other than that, no deformation was recorded during the impoundment period. Among the GPS measuring stations, the maximum deformation recorded by GPS-1 was the greatest and the magnitude reached 1823 mm in 2013, of which 1526 mm occurred from March to April. Meanwhile, the reservoir water level declined

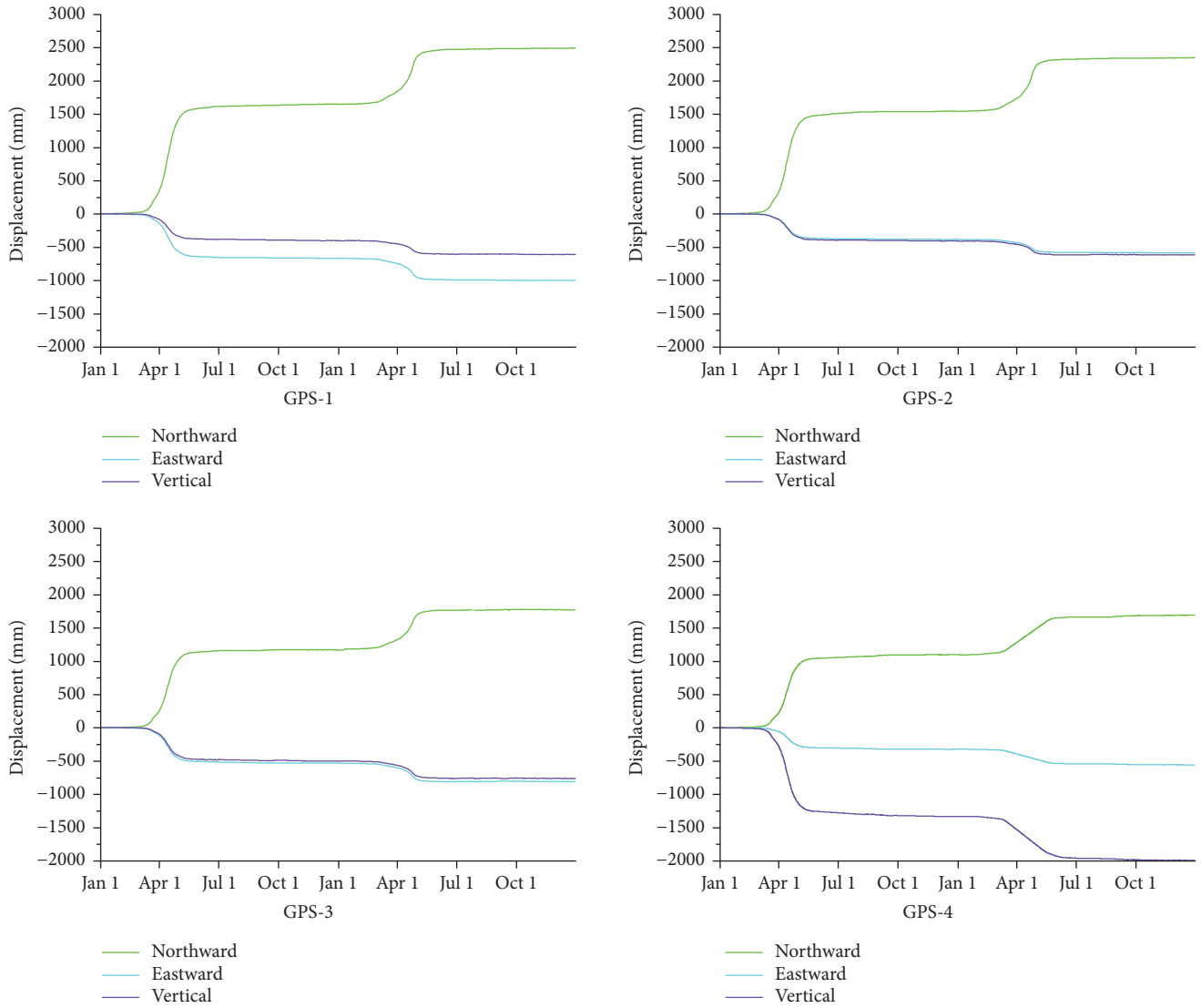


FIGURE 7: Surface displacement measurements at various GPS stations.

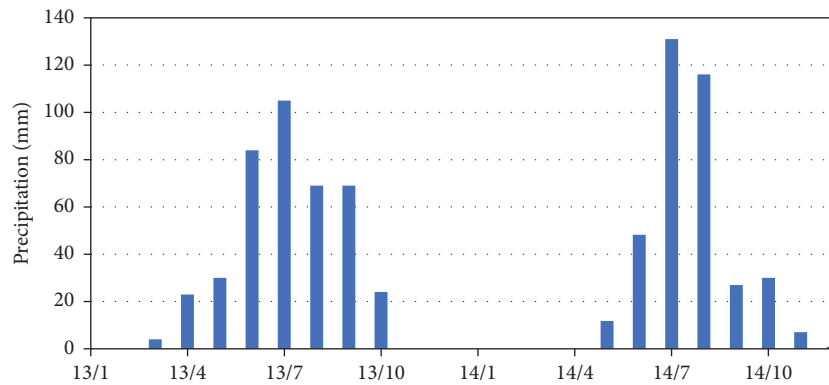


FIGURE 8: The monthly average precipitation amount from Jan. to Oct. in 2013 and 2014.

to 35.9 m. The overall deformation occurred in 2014 was approximately 932 mm, of which 730 mm occurred from March to April. Meanwhile, the reservoir water level declined to 30.6 m. The similar correlation between reservoir water

level and slope deformations was captured by the other GPS stations.

Based on the correlation between the magnitude of daily drawdown of reservoir water level and the slope deformation

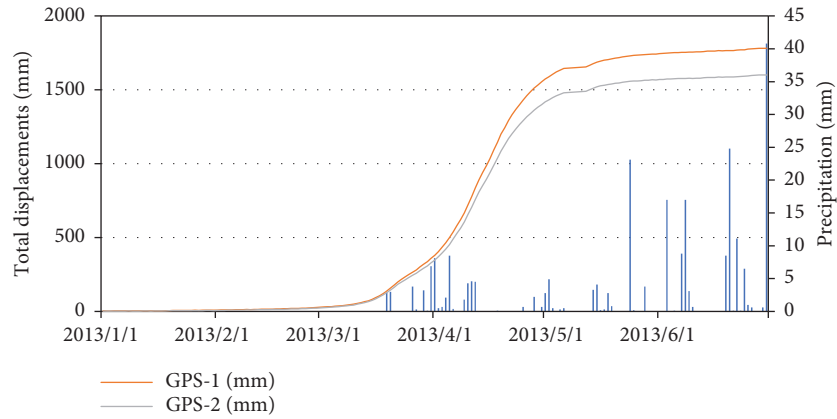


FIGURE 9: Total displacements measured by GPS versus daily precipitation.

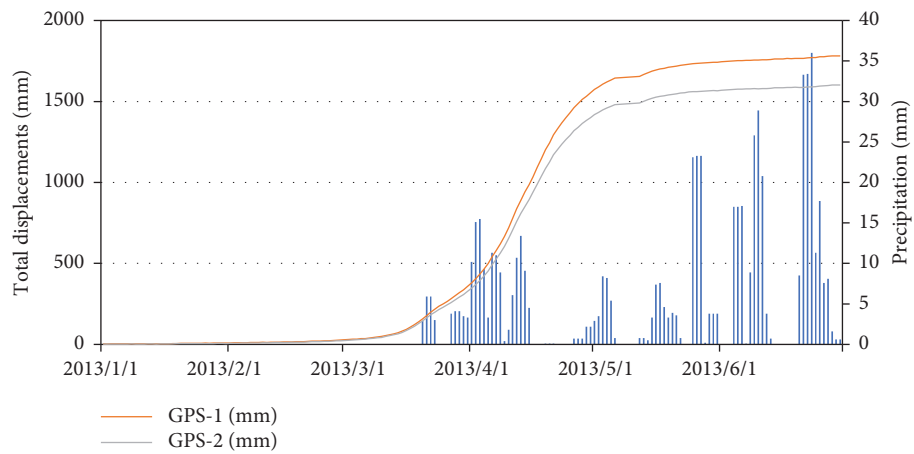


FIGURE 10: Total displacements measured by GPS versus precipitation in accumulative 3 days.

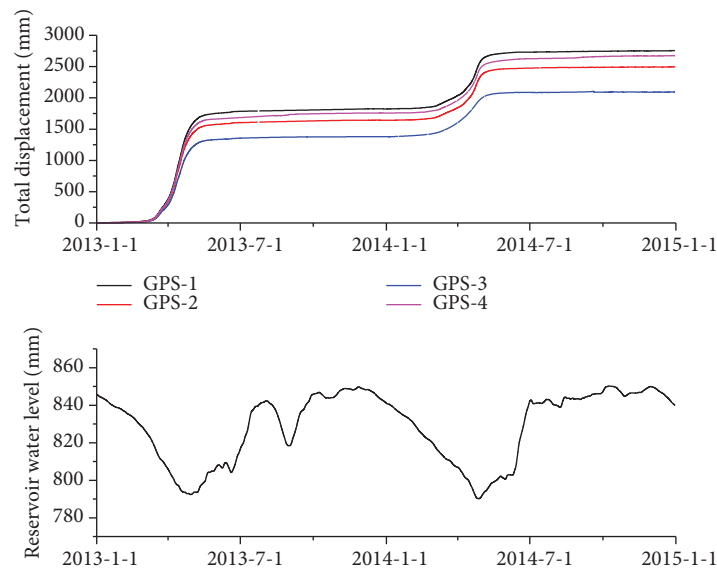


FIGURE 11: Surface displacements by GPS measuring stations versus reservoir water level fluctuations.

captured by GPS station (Figures 12 and 13), the deformation was insignificant from January to February when the draw-down rate was less than 0.5 m/day. From March to April,

the drawdown rate increased rapidly, and the magnitude exceeded 0.5 m/d. Meanwhile, significant slope deformations were captured by all GPS measuring positions, and the

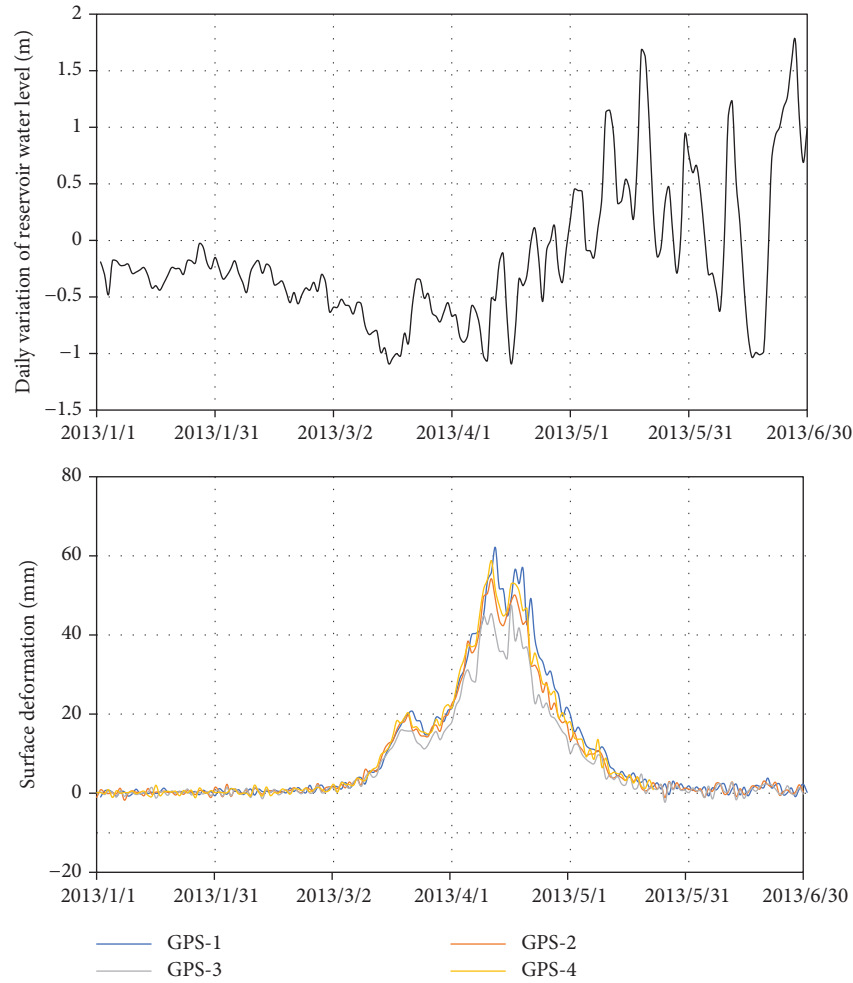


FIGURE 12: The magnitude of daily drawdown of reservoir water level from January to June 2013 versus surface deformation measured by GPS.

deformation rate showed an acceleration trend in an overall stable condition. From March 22 to 24 and April 13 to 14, the drawdown rate magnitude of reservoir water level decreased slightly, and also the deformation rate at all GPS measuring positions showed the declined trend.

From May, the reservoir water level started to rise, and daily rate of deformation decreased rapidly accordingly. After June, the deformation measurements at all GPS stations became stable gradually. Therefore, the deformation of the Hongyanzi landslide is related to the drawdown rate of Pubugou reservoir water level, and the magnitude of 0.5 m/day can be regarded as critical value based on the correlation between the slope deformation and drawdown magnitude.

A groundwater gauge was installed at ZK-5 to capture the correlation between the magnitude of water level difference (slope ground water minus reservoir water level) and deformation measurements. As seen from the correlation in Figure 14, before February 2013, the water level difference remains stable with slight increases, and similarly, during the same period, the slope deformation was

also insignificant; from the beginning of February to the mid of March, with the increase of water level difference inside and outside the slope, the slope deformations measured at all GPS positions increased; after the mid of March, significant increase occurred to all the measurements when the water level difference was approximately 10 m. Therefore, the increased water level difference between slope ground water level and reservoir water level has significant influence on the slope deformation.

The recordings indicated deformation mechanism that the rapid declination of reservoir water level increased the hydraulic gradient of groundwater and seepage in the slope, which further change the pore water pressure, decrease effective strength, and reduce the slope stability by decreasing the buoyant force acting on the slope.

To further quantify the influence of controlling factors on slope deformation, the SPSS software was utilized to conduct the correlation analysis among slope groundwater level, surface displacement (measured at GPS-2), reservoir water level, and precipitation. The results indicated that the difference between slope groundwater level and reservoir

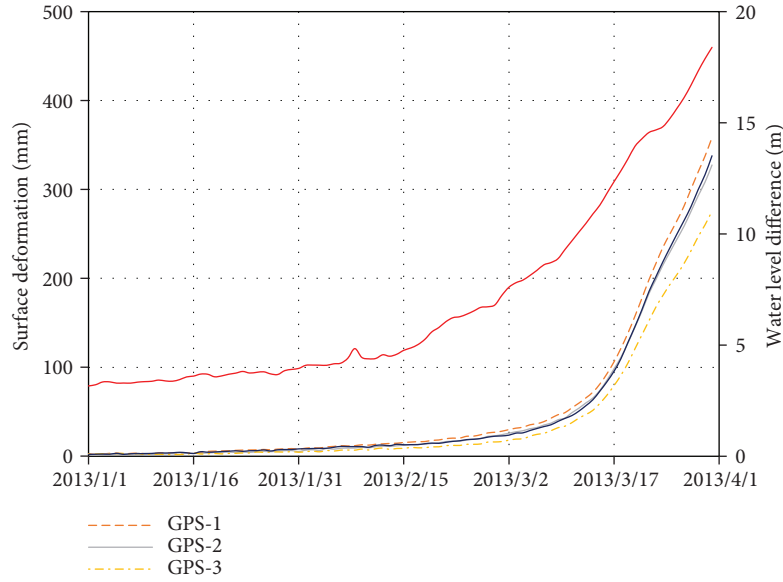


FIGURE 13: Water level difference inside and outside the slope versus surface measurements by GPS.

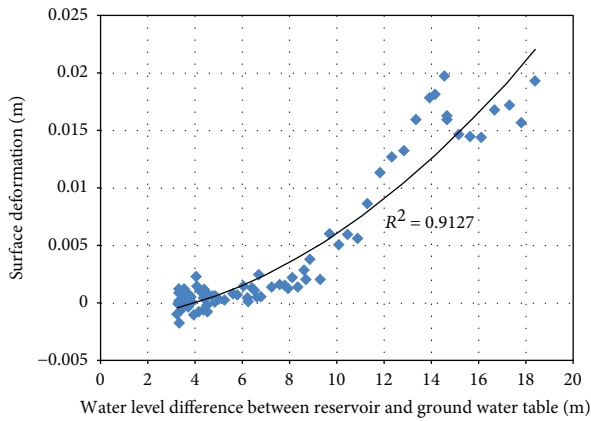


FIGURE 14: Correlation between the water level difference inside and outside the slope versus daily slope deformation in ZK-5.

water level showed the most statistical importance to the slope surface displacement (correlation coefficient=0.926) and followed by reservoir water table (coefficient=0.785). The correlation between precipitation and slope surface displacement is the lowest.

Based on the correlation between slope daily deformation and water level difference, a good consistency between can be observed. When the water head level difference was less than 7 m, the slope remained approximately stable and the deformation magnitude was insignificant. When the water level difference exceeded 7 m, the slope deformation also increased with the increases of water level difference, and the result can be fitted with quadratic function with determination of coefficient of 0.91.

Based on the above analysis, the major triggering mechanism of deformation is the rapid drawdown of reservoir water level, which caused the insufficient drainage of the

water in the slope and increased water level difference inside and outside the slope. The increased water level difference inside and outside the slope also leads the increase of seepage force. Then the seepage force reaches the threshold value; the slope deformation would be triggered.

4.1. Slope Model Establishment. Based on the field survey data, the two dimensional model of the Hongyanzi landslide was produced and the dimensions of the model is 670×210 m (in Figure 15). The base of the model was set as impermeable, and the left boundary was set to the fixed water head level of 850 m. When calculating the slope stability during the drawdown period, the right boundary above the reservoir water level is set as the zero flux. Below the reservoir water level, it was set as flexible flux boundary, and the water head equalled to the reservoir water level. When calculating the slope stability during the rise of the reservoir water level, the right boundary above 845 m is set as zero flux, and below 845 m was set as flexible flux, which the water head level equalled to the reservoir water level. The surface of the slope was set as the boundary of fixed flow, and the magnitude was set to be the amount of precipitation. The entire model consists of 1031 nodes and 990 meshes.

4.2. Parameters. According to the field investigation results, the major parameters used in simulation are presented in Table 2. The parameters being used in the numerical simulation is based on the experimental results conducted on the soil samples obtained in the field and the average value for each parameter was employed to eliminate the potential errors.

The slope ground water in natural condition is above the slip surface, and the saturated hydraulic coefficient is assumed to be 0.45 m/day; the characteristic curve between soil and water and permeability function for the upper part

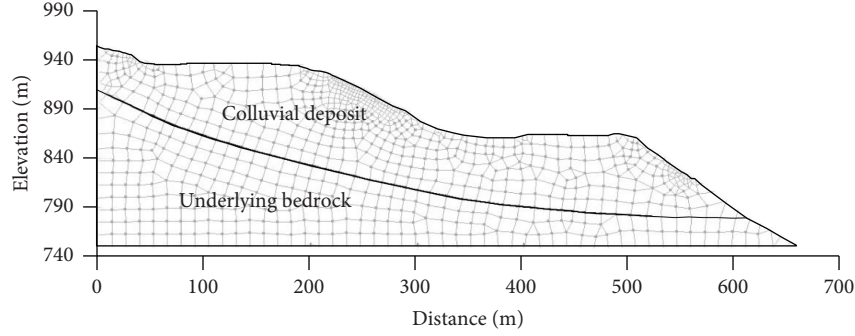


FIGURE 15: The established model of Hongyanzi landslide (unit: m).

TABLE 2: Physical parameters used in numerical simulation.

Zone	Saturated hydraulic coefficient (m/d)	Effective cohesive force (kPa)	Internal friction force (degree)	Dry density (g/cm ³)	Saturated density (g/cm ³)
Debris flow deposit	0.45	22	12.9	2.3	2.7
Underlying bedrock	0.001	3200	44	2.6	3.0

of the slope (unsaturated) was generated using the module in Seep/W, which was based on Fredlund-Xing theory.

4.3. Mathematical Model for Seepage Calculation of the Unsaturated Condition. The slope seepage analysis is one of the main issues in this study. Considering the homogeneous formation and uniform conductivity properties in various direction of the Hongyanzi landslide, the plane seepage theory based on saturated and unsaturated soils could be considered in this analysis.

Based on Morgenstern and Fredlund's theory, the non-steady seepage condition always involves the variation of flow rate, water level pressure head, and quality of flux with time. Therefore, the following equation could be produced based on two stress variables to calculate the volume water content θ_w , and the two stress variables are normal stress $(\sigma - u_a)$ and matric suction $(u_a - u_w)$.

$$d\theta_w = -P_1^w d(\sigma - u_a) - P_2^w d(u_a - u_w). \quad (1)$$

In the equation, σ is the total pressure; u_a and u_w is the pore air pressure and pore water pressure, respectively; P_1^w and P_2^w are the correlation coefficients related to $(\sigma - u_a)$ and $(u_a - u_w)$ for the water volume.

Within the infinite short time period, the P_1^w and P_2^w can be regarded as constants in the calculation; therefore, (2) can be rewritten as follows:

$$\frac{\partial}{\partial t} \theta_w = -P_1^w \frac{\partial}{\partial t} (\sigma - u_a) - P_2^w \frac{\partial}{\partial t} (u_a - u_w). \quad (2)$$

Then, the mathematical expression for the nonsteady seepage condition is

$$\begin{aligned} \frac{\partial}{\partial x} \left(k_x \frac{\partial h}{\partial x} \right) + \frac{\partial}{\partial z} \left(k_z \frac{\partial h}{\partial z} \right) = & -P_1^w \frac{\partial}{\partial t} (\sigma - u_a) \\ & - P_2^w \frac{\partial}{\partial t} (u_a - u_w). \end{aligned} \quad (3)$$

Considering that the pore air pressure is continuous and constant within the infinite short time period, and no external load was applied during the seepage condition, then,

$$\begin{aligned} \frac{\partial \sigma}{\partial t} &= 0, \\ \frac{\partial u_a}{\partial t} &= 0. \end{aligned} \quad (4)$$

Therefore,

$$\frac{\partial}{\partial x} \left(k_x \frac{\partial h}{\partial x} \right) + \frac{\partial}{\partial z} \left(k_z \frac{\partial h}{\partial z} \right) = -P_2^w \frac{\partial}{\partial t} (u_a - u_w), \quad (5)$$

where $P_2^w (\partial/\partial t)(u_a - u_w)$ is the slope magnitude of the soil-water characteristic curve.

Considering the total pressure head can be expressed as follows:

$$\begin{aligned} h &= y + \frac{u_w}{\gamma_w}, \\ \frac{\partial y}{\partial t} &= 0, \\ \frac{\partial u_a}{\partial t} &= 0. \end{aligned} \quad (6)$$

Therefore, the total pressure head can be expressed using u_w as follows:

$$\frac{\partial}{\partial x} \left(k_x \frac{\partial h}{\partial x} \right) + \frac{\partial}{\partial z} \left(k_z \frac{\partial h}{\partial z} \right) = \rho_w g P_2^w \frac{\partial h}{\partial t}. \quad (7)$$

In conclusion, the definite conditions of the unsaturated seepage condition can be expressed using the above mathematical equations. Based on the theoretical derivations, the correlations between the water content and matric suctions and the hydraulic conductivity and matric suctions of the Hongyanzi landslide can be plotted using the calculation module in Seep/W, and the results are presented in

Figures 16 and 17, respectively. The curves show the general characters of the soil-water characteristic and nonsaturated permeability of the analyzed landslide.

$h(x, y, t) = H_1(x, y, t)$, the boundary of the pressure head is known,

$$\begin{aligned} K_x \frac{\partial h}{\partial x} \cos \left(\vec{n}, x \right) + K_z \frac{\partial h}{\partial z} \cos \left(\vec{n}, z \right) &= q, \\ h(x, y, t) &= y(x, y, t), \\ h(x, y, t_0) &= H_0(x, y, t_0). \end{aligned} \quad (8)$$

$$F_s = \frac{\sum \left(c' l_i + \left[N - u_w l_i \left(\tan \varphi_b / \tan \varphi' \right) - u_a l_i \left(1 - \tan \varphi_b / \tan \varphi' \right) \right] \tan \varphi' \right)}{\sum W_i \sin \theta_i}, \quad (9)$$

where τ_f is the shear strength of unsaturated soil; c' is the effective cohesive force of the saturated soil; φ' is the effective friction angle; φ^b friction angle based on the matric suction. The value of φ^b can be regarded as regional value

4.4. Slope Stability Analysis. In this study, the slope/w module was applied to calculate the slope stability based on Morgenstern-Price limit equilibrium state theory. Morgenstern-Price theory is regarded as the most comprehensive limit equilibrium state theory by considering the mechanical and moment equilibrium currently [12, 14]. The method assumes the functional relationship between the tangential and normal stress among the soil slices. The mathematical expression of the factor of safety calculation is as follows:

φ and constant for saturated and nonsaturated conditions, respectively.

And, the parameter N in above equation can be expressed as follows:

$$N = \frac{W - (X_R - X_L) - \left(\left(c' l_i \sin \theta_i / F_s \right) + \left(u_w l_i \sin \theta_i \tan \varphi^b / F_s \right) \right)}{P_{\theta i}}, \quad P_{\theta i} = \cos \theta_i + \frac{\sin \theta_i \tan \varphi'_i}{F_s}. \quad (10)$$

where W is the weight of soil slice; X_L and X_R are the shear stress applied on the soil slices on the left and right boundaries, respectively; r is the radius of slicing surface; S_{mi} is the antisliding force on the base on the soil slice; θ_i is the angle between the tangent line of the soil slice base center and horizontal line.

A two-dimensional landslide stability analysis was conducted using the Geostudio software. The analytical module Seep/W was used to analyse the slope seepage condition changing with the fluctuations of reservoir water level and precipitation, and the slope ground water table, pore water pressure, and water head distribution of the seepage condition could be generated; then, apply the simulation results of seepage analysis into the slope stability analysis by the slice method using the module Slope/W, and the slope stability under different fluctuation rate of reservoir water level can be produced.

4.5. Numerical Simulation Verification. In this simulation, the monitoring data of the reservoir water level fluctuations and precipitation was used as input, and the results, as shown in Figure 18, indicated that the simulated slope ground water level of ZK-5 is approximately the same with the monitoring data, which provide good support for the set of the boundary conditions and parameters of the numerical simulation.

4.6. Landslide Slope Stability Analysis. Based on the simulation results, the Hongyanzi landslide remained stable under the condition without impounding, and the safety of factor is calculated to be 1.22 approximately (in Figure 19).

To understand the influence of reservoir water level fluctuations on slope stability, numerical simulation was conducted to calculate the slope stability when the fluctuation rate of reservoir water level equals from 0.1 to 0.7 m/day. The results show that during the impounding period, the slope ground water and pore pressure increased accordingly. A greater rising rate of reservoir water level could lead to the increased pore water pressure within a fixed time, which would further reduce the slope stability. When the rising rate equals to 0.7 m/d, the slope safety factor becomes 1.1 and the slope remains stable. During the drawdown period, when the drawdown rate of reservoir water level gradually increased, the slope ground water may not be dissipated sufficiently, which would lead to an increased water level difference and reduced slope stability. At the drawdown rate of 0.7 m/d, the minimum safety factor of the slope is 0.995 based on calculation results (Table 3).

As shown in Figure 20, when the drawdown rate of the reservoir water level equals to 0.1 and 0.3 m/d, the safety factor of the Hongyanzi landslide increased gradually after a slightly increasing trend. When the drawdown rate exceeded 0.4 m/d, the slope stability continued decreasing. The major

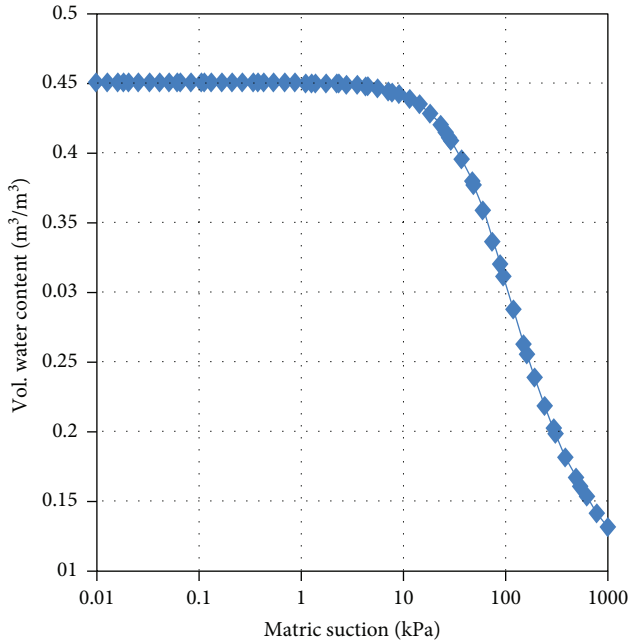


FIGURE 16: Soil-water characteristic curve of the Hongyanzi landslide.

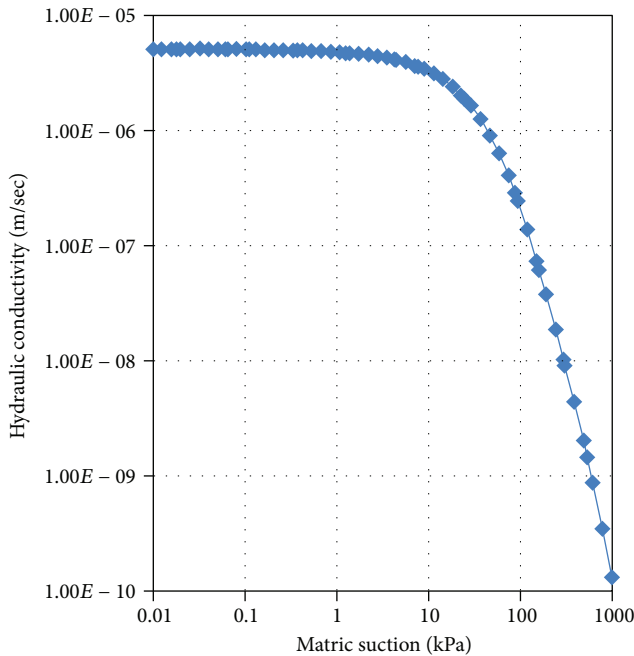


FIGURE 17: Nonsaturated permeability curve of the Hongyanzi landslide.

reason is that when the drawdown rate of the reservoir water level is fairly low, the stability was reduced due to the increased seepage force. On the other hand, the drawdown of reservoir water level caused the reduction of slope weight, which could increase the slope stability. When the drawdown rate is fairly large, the influences of seepage force play significant and negative impact on the slope stability.

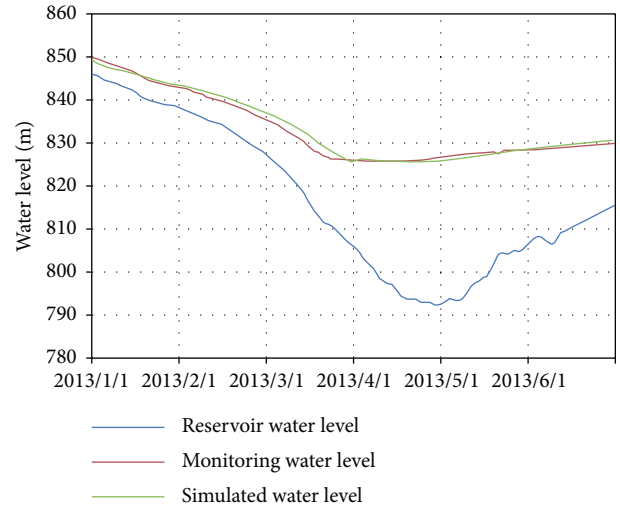


FIGURE 18: Comparison between simulated and monitored slope water level.

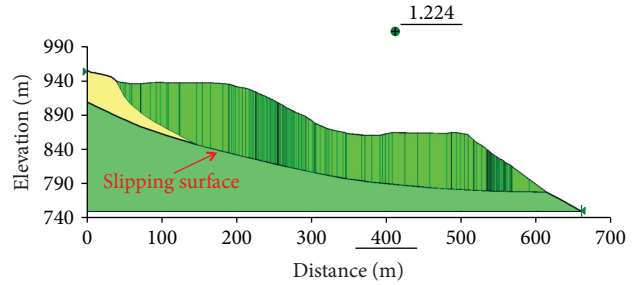


FIGURE 19: The stability calculation results without impounding of the reservoir water level (unit: m).

TABLE 3: The calculation results of FOS during the rise and decline of the reservoir water level.

Rate of fluctuation	0.1 m/d	0.3 m/d	0.4 m/d	0.5 m/d	0.7 m/d
Rising period	1.180	1.169	1.156	1.119	1.105
Decline period	1.119	1.091	1.077	1.013	0.0995

When the drawdown rate of reservoir water level equals to 0.1 to 0.4 m/d, the slope safety factor is greater than 1.05, and the slope remains stable; when the rate increased to be 0.5 m/d from 0.4 m/d, the slope safety factor reduced rapidly. The monitoring stations also indicated that when the drawdown rate of reservoir water exceeded 0.5 m/d, the slope deformation increased significantly.

The saturated hydraulic coefficient of Hongyanzi landslide is 0.45 m/d, between 0.4 m/d and 0.5 m/d. Based on the initial analysis, when the drawdown rate of reservoir water level is greater than the saturate hydraulic conductivity of the slope, the increase of water level difference and seepage pressure would lead to the reduction of slope stability. On the contrast, when the declination rate of reservoir water level is lower than the slope hydraulic conductivity, the influence of reservoir water level decline is fairly limited to the slope stability.

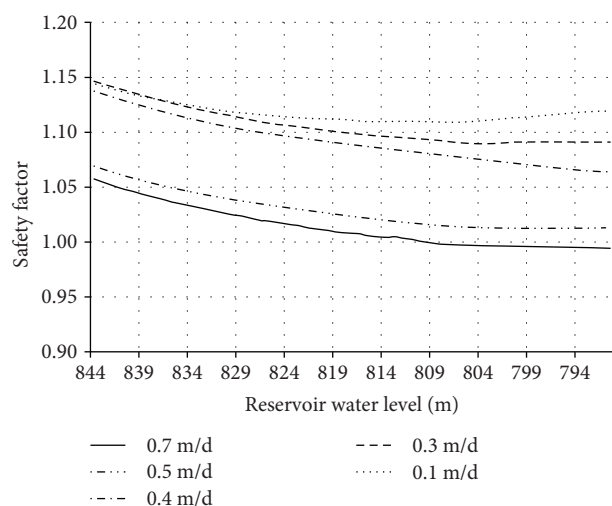


FIGURE 20: The variations of slope safety factor under different reservoir water level declination rate.

5. Conclusions

By conducting the multiparameter monitoring program on a reservoir landslide—the Hongyanzi landslide, the controlling factors of slope deformation were analysed and safety factor was calculated when the slope was hypothetically subjected to different rising rate of reservoir water level. The major conclusions are listed as below:

- (1) The Hongyanzi landslide was more prone to deformation during the rapid reservoir water level declination period, and otherwise, the slope remained stable. The slope deformation was insignificant under the intensive rainfall and earthquake conditions (e.g., Lushan earthquake) based on the captured data as presented in this study. It is recommended to conduct further monitoring on the influence of intensive rainfall and earthquake loadings on the deformation of the Hongyanzi landslide for further analysis.
- (2) The primary triggering mechanism of slope deformation is due to the increased seepage force generated by the increasing water level difference inside and outside the slope during the rapid declination of the reservoir water level. Roughly, there was a quadratic function relationship between the magnitude of slope water level difference and slope deformation.
- (3) The declination rate of reservoir water level has a vital impact on slope stability. The increasing of declination rate would lead to the decreased slope stability. When the declination rate exceeded 0.7 m/day, the slope stability factor would become less than 1.
- (4) The major characters of slope monitoring technology system are automation, wireless sensing, distributed arrangement, and high accuracy. It is anticipated that the multiparameter-based monitoring as used in this

study can be helpful to improve the coordination and integration of slope monitoring system.

Data Availability

The authors welcome the other researchers to cite and analyse the data of this paper in their studies. If you need the data, please send an e-mail to hanb@mail.cigem.gov.cn.

Conflicts of Interest

The authors wish to confirm that there are no known conflicts of interest associated with this publication.

Acknowledgments

The research data of this study is mainly from the “Sichuan Ya’an Geological Hazard Monitoring and Warning Field Scientific Observation and Research Base of the Ministry of Land and Resources of China.” The study was funded by China Geological Survey Projects (Grant nos. 1212011140016 and DD20160273), Chinese Key Science and Technology Project (Grant no. 2010ZX03006-007), and China Geological Environment Monitoring and Forecasting Project.


References

- [1] H. Tang, C. Li, X. Hu et al., “Deformation response of the Huangtupo landslide to rainfall and the changing levels of the Three Gorges Reservoir,” *Bulletin of Engineering Geology and the Environment*, vol. 74, no. 3, pp. 933–942, 2015.
- [2] Y. Yin, B. Huang, W. Wang et al., “Reservoir-induced landslides and risk control in Three Gorges project on Yangtze River, China,” *Journal of Rock Mechanics and Geotechnical Engineering*, vol. 8, no. 5, pp. 577–595, 2016.
- [3] J. B. Wei and H. C. Zheng, “Deformation characteristics of a preexisting landslide in reservoir area during reservoir filling and operation,” *Advanced Materials Research*, vol. 518–523, pp. 4675–4679, 2012.
- [4] Y. Y. Jiao, H. Q. Zhang, H. M. Tang, X. L. Zhang, A. C. Adoko, and H. N. Tian, “Simulating the process of reservoir-impoundment-induced landslide using the extended DDA method,” *Engineering Geology*, vol. 182, pp. 37–48, 2014.
- [5] F. C. Dai, J. H. Deng, L. G. Tham, K. T. Law, and C. F. Lee, “A large landslide in Zigui County, Three Gorges area,” *Canadian Geotechnical Journal*, vol. 41, no. 6, pp. 1233–1240, 2004.
- [6] J. Jiang, D. Ehret, W. Xiang et al., “Numerical simulation of Qiaotou landslide deformation caused by drawdown of the Three Gorges Reservoir, China,” *Environmental Earth Sciences*, vol. 62, no. 2, pp. 411–419, 2011.
- [7] G. Y. Liu, “Influence of water table fluctuation on stability of colluvial landslide in Three Gorges Reservoir,” *Safety and Environmental Engineering*, vol. 18, no. 5, pp. 26–28, 2011.
- [8] B. Huang, Y. Yin, and C. Du, “Risk management study on impulse waves generated by Hongyanzi landslide in Three Gorges Reservoir of China on June 24, 2015,” *Landslides*, vol. 13, no. 3, pp. 603–616, 2016.
- [9] J. M. Duncan, S. G. Wright, and K. S. Wong, “Slope stability during rapid drawdown,” in *Proceedings of the H. Bolton Seed Memorial Symposium*, pp. 235–272, Berkeley, CA, USA, 1990.

- [10] B. Han, *Research on Landslide Monitoring and Early Warning in Ya'an Area*, [Ph.D. thesis], China University of Geosciences, Beijing, China, 2016.
- [11] F. Wang, Y. Zhang, Z. Huo, X. Peng, K. Araiba, and G. Wang, "Movement of the Shuping landslide in the first four years after the initial impoundment of the Three Gorges Dam Reservoir, China," *Landslides*, vol. 5, no. 3, pp. 321–329, 2008.
- [12] W. Riemer, "Landslides and reservoirs," in *Proceedings of the 6th International Symposium on Landslide*, pp. 1373–2004, Christchurch, New Zealand, 1992.
- [13] Committee on Reservoir Slope Stability, *Reservoir Landslides: Investigation and Management*, International Commission on Large Dams, 2002.
- [14] X. Hu, M. Zhang, M. Sun, K. Huang, and Y. Song, "Deformation characteristics and failure mode of the Zhujiadian landslide in the Three Gorges Reservoir China," *Bulletin of Engineering Geology and the Environment*, vol. 74, no. 1, pp. 1–12, 2015.
- [15] D. Li, K. Yin, and C. Leo, "Analysis of Baishuihe landslide influenced by the effects of reservoir water and rainfall," *Environmental Earth Sciences*, vol. 60, no. 4, pp. 677–687, 2010.
- [16] M. Zhang, Y. Yin, and B. Huang, "Mechanisms of rainfall-induced landslides in gently inclined red beds in the eastern Sichuan Basin, SW China," *Landslides*, vol. 12, no. 5, pp. 973–983, 2015.
- [17] M. Zhang and M. J. McSaveney, "Is air pollution causing landslides in China?," *Earth and Planetary Science Letters*, vol. 481, no. 1, pp. 284–289, 2018.
- [18] M. Zhang and M. J. McSaveney, "Rock avalanche deposits store quantitative evidence on internal shear during runout," *Geophysical Research Letters*, vol. 44, no. 17, pp. 8814–8821, 2017.

Research Article

Hydrochemical Characteristics and Formation of the Madeng Hot Spring in Yunnan, China

Ren Zhenhua,¹ Zhou Xun ^{1,2} Yang Miaolin,¹ Wang Xiaocui,¹ Zheng Yuhui,¹ Li Xiaolu,¹ and Shen Ye^{1,2}

¹School of Water Resources and Environment, China University of Geosciences (Beijing), Beijing, China

²MOE Key Laboratory of Groundwater Circulation and Environmental Evolution, China University of Geosciences (Beijing), Beijing, China

Correspondence should be addressed to Zhou Xun; zhouxun@cugb.edu.cn

Received 26 October 2017; Revised 7 January 2018; Accepted 30 April 2018; Published 2 July 2018

Academic Editor: Liangping Li

Copyright © 2018 Ren Zhenhua et al. This is an open access article distributed under the Creative Commons Attribution License, which permits unrestricted use, distribution, and reproduction in any medium, provided the original work is properly cited.

The Madeng hot spring emerges in the central river valley in the northeastern Lanping Basin in Jianchuan county of Yunnan Province in China. Quaternary sand and gravel occur in the valley which is underlain by the red beds consisting of sandstone and mudstone. The temperature of the hot spring is 42.1°C. The spring water has a pH value of 6.41, TDS of 3.98 g/L, F contents of 3.08 mg/L, and H₂SiO₃ of 35.6 mg/L. The hot water is of SO₄•Cl-Na•Ca type. There is a slight hydrogen sulfide odor in the spring water. Stable hydrogen and oxygen isotopes indicate that the hot water is of meteoric origin. It is estimated that the elevation of the recharge area of the hot spring is approximately 3800 m, the age of the hot water is some 140 years, the temperature of the geothermal reservoir is 75°C–80°C, the mixture ratio of cold water is approximately 80%, and the circulation depth of the thermal groundwater is 1870 m. After receiving recharge from infiltration of precipitation in the mountainous recharge areas, the groundwater undergoes a deep circulation, obtains heat from the heat flow, flows upward along the fractured zone, and emerges as an upflow spring through the Quaternary sand and gravel in the central low-lying river valley.

1. Introduction

Hot springs display the thermal energy in the internal earth, and they can provide us important information on groundwater circulation and hydrochemistry at depth [1]. There are about 2800 hot springs in China [2], and more than 1000 of them are discharging in the Yunnan region [3] where a significant geothermal anomaly is present in the collision zone between the Indian Ocean Plate and the Eurasian Plate. For this reason, Yunnan is called “the hometown of hot springs” [4]. The Madeng hot spring in Jianchuan country of Yunnan is located in a river valley in the Yunnan-Tibet geothermal zone and is rich in several trace elements critical to the human body [5]. Hot springs such as the Madeng hot spring which discharges thermal groundwater from deep geothermal reservoirs and emerges through a shallow aquifer of unconsolidated sediments are seldom encountered in

Western Yunnan. The present work focuses on the hydrochemical aspects and formation of the hot spring.

Hydrogeochemical studies of hot springs were carried out by many researchers. For example, Ellis and Mahon [6] considered that most of the dissolved constituents of thermal water are from the reactions between surrounding rocks and water and elaborated the origins of hot water, thermal water isotope physicochemical characteristics, mineral precipitation in thermal water, and so on. Favara et al. [7] studied the chemical characteristics of thermal groundwater of the Sicily region in Italy and found that the geothermal water in this area is a mixture of two kinds of groundwater that one is rich in gypsum and the other is rich in carbonate. Cidu and Bahaj [8] examined the chemical characteristics of geothermal water in Morocco and reported that the thermal groundwater contains high concentrations of B, Li, and Sr and the hot water is of Na-Cl type. Frengstad et al. [9] carried

out hydrochemical research on groundwater in Norway and revealed the elements in the groundwater as the root of the increased pH value. By studying the chemical characteristics of the geothermal water in Portuguese Azores, Cruz and Franca [10] found that the hot springs are affected by the local volcanism, and they used multivariate analysis to divide the hydrochemical type of the geothermal water in this area. Davraz [11] used the hydrogeochemical methods to analyze the local geothermal water in Turkey and found that the geothermal water was mixed with the surface water in this region.

Stable ^2H and ^{18}O isotopes are often used to examine the origin of groundwater since Craig [12] established the global meteoric water line between $\delta^2\text{H}$ and $\delta^{18}\text{O}$ of precipitation. Payne [13] pointed out that stable isotopes can also be used for groundwater recharge and age determination. Favara et al. [14] studied the stable isotopes $\delta^2\text{H}$, $\delta^{18}\text{O}$, and ^{13}C of hot and cold springs in the western Sicily and revealed that the groundwater in this region is a mixture of the groundwater and the sea water. Majumdar et al. [15] suggested that the hot springs in the eastern India were originated from meteoric precipitation, and the values of $\delta^2\text{H}$ and $\delta^{18}\text{O}$ of the geothermal water in this region would be increased during the winter. Radioactive isotopes are mainly used for estimating the residence time (age) of groundwater. Cherdyntsev [16] proposed a method of using ^{226}Ra and ^{222}Rn to estimate the residence time of thermal groundwater. Liu et al. [17] estimated the age of the Jifei hot spring in Western Yunnan by using contents of ^{226}Ra and ^{222}Rn .

Geothermometers are used to estimate temperature of deep geothermal reservoirs. In the 1970s–1980s, several geothermometers were established to estimate the temperature of geothermal reservoirs [18–22] which are widely used in the development and utilization of geothermal resources. From 1988 to 1992, a series of triangular figures were created for the study of the origin and formation mechanism of geothermal fluids [23–25].

In this paper, on the basis of field investigation and sample detection, we analyze the occurrence of the Madeng hot spring, examine the hydrochemical characteristics, and summarize the isotopic signature of the hot water. The origin of the geothermal water, residence time of the geothermal water, circulation depth, reservoir temperature, elevation and temperature of the recharge area, and mixture ratio of the hot water and cold water are also identified and estimated. The formation of the hot spring is further proposed.

2. Materials and Methods

2.1. Geological Setting. The Madeng hot spring is located at the southeast of the Houdian village in Jianchuan County of Yunnan (Figure 1). The hot spring emerges in the central river valley in the eastern Lanping Basin. The elevation of the valley ranges from 2350 m in the southeast to 2400 m in the northwest [26]. The Mishahe river and groundwater in the Quaternary sediment flow from northwest to southeast in the valley. The Madeng hot spring is located in the western flank of Mt. Xueban, whose peak is 4295 m high and almost permanently covered by a glacier.

The mean annual precipitation in Jianchuan county is 731.1 mm (1990–2010). The main outcropping formations in the study area are related to the Devonian dolomitic limestone and dolomite, Permian tuff, Triassic siltstone, basaltic sandstone, limestone sandstone and carbonaceous shale, Jurassic red mudstone, marl, siltstone and fine sandstone, Cretaceous amaranth mudstone and feldspar quartz sandstone, Paleogene amaranth mudstone, siltstone, sandstone and conglomerate, and Quaternary sandy clay, gravel and grit (Figure 1). In the surrounding areas of Madeng hot spring, red beds consisting of Jurassic, Cretaceous, and Paleogene sedimentary deposits occur [27]. The red beds exist in the western, southern, and central Yunnan, which mainly consist of the purple mudstone and small amounts of feldspar quartz sandstone, and occupy around one-third of the area of Yunnan Province [28].

Tectonically, Yunnan Province is located in the Indian Ocean Plate and Eurasian Plate collision zone and its affected area. From east to west, Yunnan and Tibet geothermal zone can be divided into the Ailaoshan anticlinorium, Lanping-Simao depression, Changning-Lancang anticlinorium, Baoshan synclinorium, and Tengchong-Gaoligong mountain anticlinorium [29]. The Jianchuan region is located in the composite part of the “Dai” type tectonic system consisting of the Qinghai-Tibet and Yunnan-Myanmar tectonic systems, which belongs to the Sanjiang fold belt in the conjunctive part of the Tangua-Changdu-Simao fold belt and the Yangtze Paraplatform. The deep and huge faults in the region trend nearly in NNW and NS directions, including from east to west the Jinshajiang fault, Weixi-Qiaohou fault, Duosong-Ludian fault, Lanping-Simao central fault, Jinshajiang-Ailaoshan fault, Zhongdian-Jianchuan fault, Annan-Jianchuan fault, Honghe fault, Heqing-Eryuan fault, and Jianchuan-Lijiang fault. The study area lies in a trigonal belt bounded by the nearly SN-trending Annan-Jianchuan fault in the east and the nearly NNW-trending Weixi-Qiaohou fault in the west. The Jinshajiang-Ailaoshan fault, Honghe fault, Duosong-Ludian fault, and Jianchuan-Lijiang fault occur in the study area, forming the main body of a regional complex tectonic framework consisting of NNW and SN-trending tectonic belts with frequent magmatic activities in the geological history (Figure 1) [27].

Special geological and geographical conditions make the Yunnan Province abundant in geothermal resources in China. There is a very close relationship between the formation of geothermal resources and the geological background. From the point of view of geothermal geology background, Yunnan Province can be divided into two areas by the Jinshajiang-Ailaoshan fault zone. The west is a high-temperature hydrothermal area where some boiling hot springs and hot springs of low to moderate temperature occur, and the east is a low-temperature hydrothermal area where boiling hot springs are seldom encountered. High-temperature hydrothermal activities in the Western Yunnan are in the south band of the Yunnan and Tibet geothermal band. The high-temperature geothermal systems in the region are obviously controlled by the distribution of the activity of the basement and depression layout and the tectonic uplift.

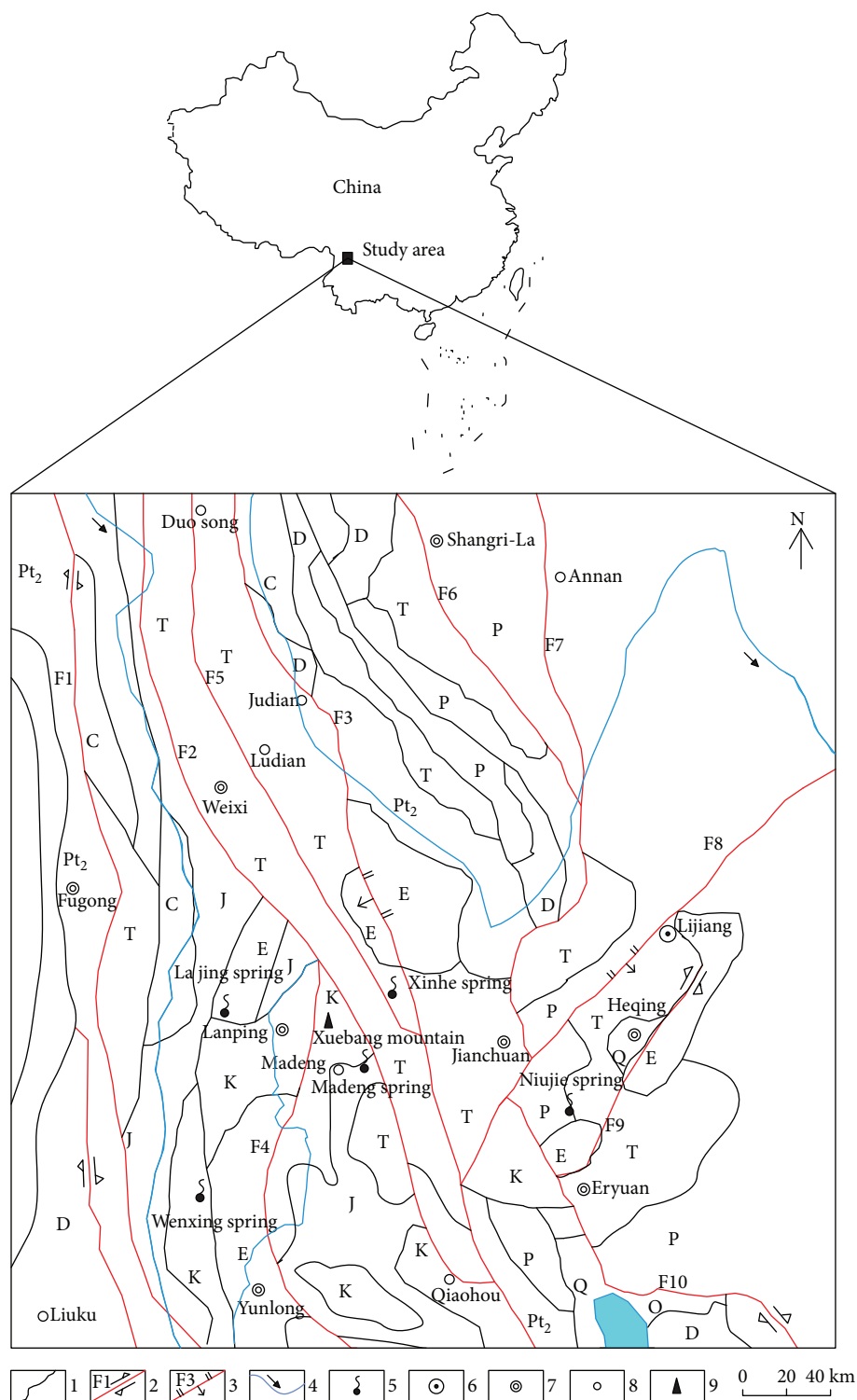


FIGURE 1: Geological sketch map near the Madeng hot spring in Jianchuan of Yunnan Q—Quaternary gravel and sand; E—Eogene purple mudstone, siltstone, sandstone, and conglomerate; K—Cretaceous fine-grained sandstone, amaranth mudstone, and feldspar quartz sandstone; J—Jurassic red mudstone, siltstone; T—Triassic limestone, siltstone; P—Permian basalt and tuff breccia; C—Carboniferous quartz sandstone, limestone; D—Devonian dolomitic limestone and dolomite; O—Ordovician quartz sandstone; Pt₂—Mesoproterozoic mica schist, dark cloud flash schist; F1—Lancangjiang river fault; F2—Weixi-Qiaohou fault; F3—Jinshajiang-Ailaoshan fault; F4—Lanping-Simao middle fault (Bijiang fault); F5—Duosong-Ludian fault; F6—Zhongdian-Jianchuan fault; F7—Annan-Jianchuan fault; F8—Jianchuan-Lijiang fault; F9—Heqing-Eryuan fault; F10—Honghe fault; 1—stratigraphic boundary; 2—strike-slip faults; 3—reverse fault; 4—rivers; 5—spring; 6—city; 7—county; 8—village and town; 9—mountain.

2.2. Brief Description of the Hot Spring. The Madeng hot spring (YJ2) is located in the west of Jianchuan county of Yunnan with an elevation of 2356 m. There are six vents in the hot spring, and the hot spring is an upflow spring. The upflow spring is a kind of genetic types of springs when the aquifer is covered by unconsolidated sediments of poor permeability or buried under an aquitard and when the hydraulic head in the aquifer is higher than the ground surface. Groundwater will flow through the upper unconsolidated sediments or aquitard and emerges on the land surface [30]. According to the “Hot Springs’ Records in Yunnan Province’ Records,” the discharge of the hot spring was approximately about 10 L/s, the water temperature is 42°C, and TDS of hot water is 2.82 g/L [5]. According to the measurements by Yu [26], the discharge of the spring was 3.24 L/s with the water temperature of 43°C and TDS of 3.647 g/L. The hot spring is situated in the central river valley, and the vents occur on the northeastern side of the Mishahé river in a circular area with the diameter of about 50 m. There are a few bathhouses near the springs’ vents. The water in the bottom pours with bubbles, and there is a slight hydrogen sulfide odor in the spring water. A shallow well and two drilling holes are located in three vents for pumping hot water for bathing, and the remaining three vents are still in a natural state. On August 19, 2014, the spring water temperature was measured as 42.1°C, pH as value 6.41, and TDS as 3.98 g/L and water samples were taken from the shallow well with the highest temperature of 42.1°C. The hot spring can also be regarded as a brackish spring according to TDS. In addition, there are 4 hot springs near the Madeng hot spring (Figure 1), including the Xinhe hot spring (Jianchuan county, 51.2°C), Wenxing hot spring (Yunlong county, 51.6°C), Lajing hot spring (Lanping county, 46.1°C), and Niujie hot spring (Eryuan county, 76.1°C).

2.3. Sampling and Chemical Analyses. Sampling was conducted for the Madeng hot spring in Jianchuan county of Yunnan on August 19, 2014. The chemical analyses were conducted at the laboratory of the Beijing Brigade of Hydrogeology and Engineering Geology, using the following methods: K, Na, Li, Sr, Zn, and Mn by the flame atomic absorption; Ba, Al, Pb, Cd, and Ag by the atomic absorption of the plumbago furnace; Cl, SO₄, and NO₃ by the ion chromatogram; NH₄, Fe²⁺, Fe³⁺, NO₂, F, Br, I, Cr(6), H₂SiO₃, HBO₂, and HPO₃ by the spectrophotometer; Hg, Se, and HAsO₃ by the atomic fluorescence; Ca, Mg, and hardness by the volumetric method (EDTA titration); HCO₃, CO₃, and total alkalinity by the volumetric method (HCl titration); total acidity by the volumetric method (NaOH titration); H₂S by the volumetric method (sodium hyposulfite titration); and ²²⁶Ra and ²²²Rn with the radioactive radon-thorium analyzer. ²H and ¹⁸O were detected at the Analysis Center of the Beijing Research Institute of Uranium Geology by the zinc reduction method for hydrogen isotopes and the carbon dioxide—water equilibrium method for oxygen isotopes. The chemical constituents were tested for accuracy by calculating the normalized inorganic charge balance which was less than 2.22% for the YJ2 sample and 0.17% for the YJ2-A sample, respectively.

TABLE 1: Chemical analyses of the Madeng hot spring (mg/L).

Composition	YJ2	YJ2-A
K	11.4	17.9
Na	802	733
Ca	378	185
Mg	37.9	35.5
NH ₄	<0.02	0.701
Fe	0.116	/
HCO ₃	663	287
Cl	810	595
SO ₄	1.24 × 10 ³	1.05 × 10 ³
F	3.08	2.32
NO ₃	3.7	/
²²⁶ Ra (Bq/L)	0.420	/
²²² Rn (Bq/L)	7.21	/
Ba	0.051	/
Cr (6)	<0.001	/
Pb	<0.0008	/
Mn	0.024	/
Al	0.060	/
Li	0.246	0.25
Sr	12.4	/
Br	0.17	/
I	<0.02	/
Zn	0.026	/
Se	0.0003	/
Ag	<0.0005	/
H ₂ SiO ₃	35.6	/
HAsO ₃	0.016	/
HBO ₂	3.60	2.75
HPO ₃	<0.01	/
NO ₂	0.078	/
Free CO ₂	91.5	/
TDS	3.98 × 10 ³	2.82 × 10 ³
Total alkalinity	543	/
Total acidity	104	/
Total hardness	1.10 × 10 ³	/
H ₂ S	<0.05	/
pH	6.41	7.65
Temperature (°C)	42.1	42

YJ2 represents the sample collected in August 2014; YJ2-A represents the data recorded in the “Hot Springs’ Records in Yunnan Province’ Records” in 1999.

3. Results and Discussion

3.1. Hydrochemical Characteristics. The chemical analyses of the hot spring (YJ2) and those reported in the “Hot Springs’ Records in Yunnan Province’ Records” (YJ2-A) are listed in Table 1. The ion concentrations except K are higher in the year 2014 than in 1999. The minor ions in the water are predominated by NH₄, NO₃, and Fe, and their contents are less than 0.02 mg/L, 3.7 mg/L, and 0.116 mg/L, respectively. Trace

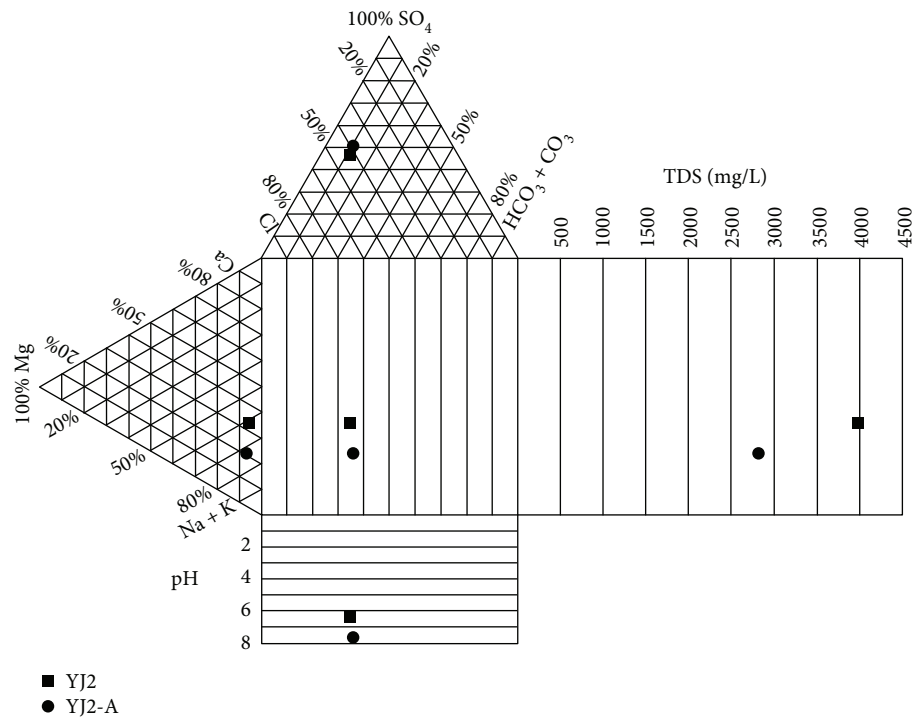


FIGURE 2: Durov diagram showing the Madeng hot spring water samples—YJ2: water sample of the hot spring taken in 2014; YJ2-A: water sample of the hot spring from Local Chronicles Compilation Committee of Yunnan Province [5].

elements mainly include I, Br, Sr, Li, Al, Zn, Ba, and Mn. The content of Sr in the hot spring water is 12.4 mg/L, and H_2SiO_3 is 35.6 mg/L, which means Sr water and H_2SiO_3 water, according to the Standards of “Chinese drinking natural mineral water” (GB8537-2008) ($\text{Sr} \geq 0.20$ mg/L for Sr water and $\text{H}_2\text{SiO}_3 \geq 25.0$ mg/L for H_2SiO_3 water).

The content of F in the hot spring water is 3.08 mg/L, which is greater than that in the “Hot Springs’ Records in Yunnan Province’ Records” (2.23 mg/L) (Figure 2) and is beyond the standard of fluoride (<1.5 mg/L) in the Standards of “Chinese drinking natural mineral water” (GB8537-2008). The hot spring water always contains fluorine, and bathing with the hot water can be used to the treatment of skin disease and rheumatism. The H_2SiO_3 content of the Madeng hot spring water is greater than that of the standards of “Chinese drinking natural mineral water.” The mineral water rich in H_2SiO_3 is useful for the treatment of nervous system disease and has certain effect on the disease of the heart, head, and blood vessel [31].

The pH of the hot spring water is 6.41, and the hot water is weakly acidic. As shown in Table 1, the Durov diagram is plotted in Figure 2. From the perspective of the data of 2014, we can see that the main cations are Na and Ca. Their corresponding milligram equivalent percentages are more than 60% and 35%, respectively. The main anions are SO_4 and Cl, and their corresponding milligram equivalent percentages are over 40%. The hot water is of $\text{SO}_4\text{-Cl-Na-Ca}$ type. As described in the “Hot Springs’ Records in Yunnan Province’ Records,” the hot spring water is of $\text{SO}_4\text{-Cl-Na}$ type. Comparison shows that pH of the hot springs changes from 7.65 to 6.41, salinity increases from 2.82 g/L to 3.98 g/L,

and the change of these two indicators results in the change in hydrochemical type from $\text{SO}_4\text{-Cl-Na}$ type into $\text{SO}_4\text{-Cl-Na-Ca}$ type. The source of the salinity of the hot water may be attributed to the subsurface incongruent dissolution of the red beds (containing salts to a larger or lesser degree) [28]. The pH of the hot spring water tends to reduce, causing the thermal groundwater to dissolve more Ca.

3.2. Isotopic Analysis

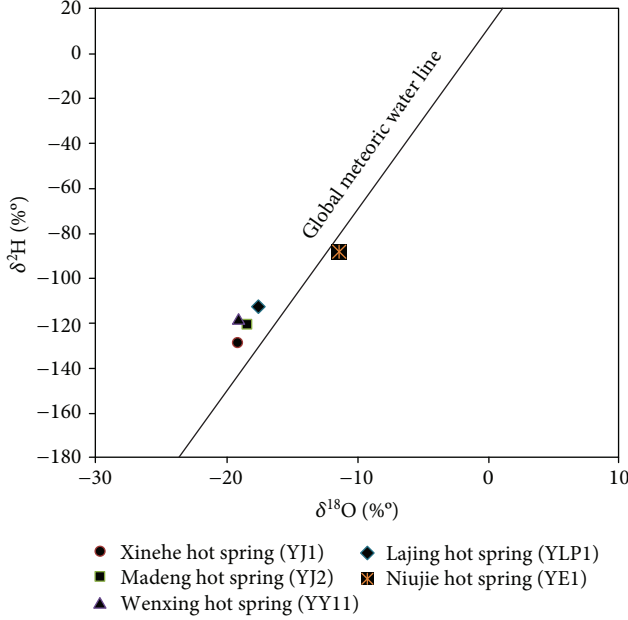
3.2.1. Recharge Source. Craig [32] summarized the values of $\delta^2\text{H}$ and $\delta^{18}\text{O}$ of the global meteoric water and established a linear relation between the values of $\delta^2\text{H}$ and $\delta^{18}\text{O}$, which is called the Craig precipitation line (global meteoric water line):

$$\delta^2\text{H} = 8\delta^{18}\text{O} + 10. \quad (1)$$

In order to examine the recharge source of the Madeng hot spring, we took the nearby hot springs (Xinhe, Wenxing, Lajing, and Niujie) into consideration. In August 2014, the five hot springs were analyzed for $\delta^2\text{H}$ and $\delta^{18}\text{O}$ (Table 2). We can see that the values of $\delta^2\text{H}$ and $\delta^{18}\text{O}$ of the hot springs in the region are mainly caused by the altitude effect. Figure 3 shows that the $\delta^2\text{H}$ and $\delta^{18}\text{O}$ data points of the water samples in the study area deviate slightly from the global meteoric water line, but overall fall near the line, indicating that the groundwater is of meteoric origin. At the same time, obvious ^{18}O shift cannot be found, reflecting that the deep thermal storage temperature is not high and the spring water belongs to geothermal water of low temperature [33]. On the contrary, slightly negative ^{18}O shift of the samples of Xinhe,

TABLE 2: Data of $\delta^2\text{H}$ and $\delta^{18}\text{O}$ of the hot spring water samples.

Name of hot spring	Madeng hot spring	Xinhe hot spring	Wenxing hot spring	Lajing hot spring	Niujie hot spring
Serial number	YJ2	YJ1	YY11	YLP1	YE1
T (°C)	42.1	42.7	40	46.1	76.1
$\delta^2\text{H}$ (‰)	-120.4	-128.6	-118	-112.4	-88.5
$\delta^{18}\text{O}$ (‰)	-18.5	-19.2	-19.1	-17.6	-11.4

FIGURE 3: Plot of $\delta^2\text{H}$ - $\delta^{18}\text{O}$ of the hot water samples.

Madeng, Lajing, and Wenxing hot springs exists, which cannot be explained at present and will be a future subject of isotope studies.

3.2.2. Recharge Elevation. As mentioned previously, the geothermal water was originated from meteoric water in the study area. On the mainland, the $\delta^2\text{H}$ and $\delta^{18}\text{O}$ values of the precipitation increases with the increasing terrain elevation (i.e., altitude effect). Altitude effects of $\delta^2\text{H}$ and $\delta^{18}\text{O}$ values are the most important for the hot water samples [34–36]. When the elevation increases by every 100 m, the value of $\delta^2\text{H}$ reduces from -1‰ to -4‰ and the value of $\delta^{18}\text{O}$ from -0.15‰ to -0.5‰ [2]. Altitude effect can be used to roughly estimate the recharge elevation of geothermal water [2, 26, 36] through the following equations.

The relationship between the values of the isotope and the altitude in Sichuan, Guizhou, and Tibetan areas in China [26] is used.

$$\delta^{18}\text{O} = -0.0031H - 6.19. \quad (2)$$

$$\delta^2\text{H} = -0.026H - 30.2, \quad (3)$$

where H is the infiltration height of isotopes (m).

The equation describing the relationship between the values of $\delta^2\text{H}$ and $\delta^{18}\text{O}$ and the local elevation [36, 37] is used.

$$H = \frac{\delta G - \delta P}{K} + h, \quad (4)$$

where H is the infiltration height of isotopes (m), h is the elevation of the sampling point (m), δG is the value of $\delta^{18}\text{O}$ or $\delta^2\text{H}$ of the hot spring water, δP is the value of $\delta^{18}\text{O}$ or $\delta^2\text{H}$ of the precipitation, and K is the altitude gradient of isotopes (‰/100 m).

Yu [26] proposed that the average values of $\delta^{18}\text{O}$ and $\delta^2\text{H}$ about the rainwater of Tengchong of Yunnan Province in 1985 are -9.3‰ and -62.6‰. The values of $\delta^{18}\text{O}$ and $\delta^2\text{H}$ about the rainwater of Kunming are -10.13‰ and -76.1‰ in 1980. The precipitation in the study area of the elevation gradient (k) about $\delta^2\text{H}$ is 3.2‰/100 m, and the value of the $\delta^2\text{H}$ about the rainwater in the study area is -69.35‰. As we have known, the elevation of the Madeng hot spring is 2356 m, the value of the $\delta^2\text{H}$ is -120.4‰, and the value of the $\delta^{18}\text{O}$ is -18.5‰. Equations (2), (3), and (4) are used, and the recharge altitudes are 3971 m, 3469 m, and 3951 m, respectively. Thus, the average value of elevation of approximately 3800 m is reasonably obtained, which is close to that of the Xueban mountain to the west of the Madeng spring.

3.2.3. Temperature of the Recharge Area. The temperature effect of the values of $\delta^2\text{H}$ and $\delta^{18}\text{O}$ of meteoric water can be used to estimate the water temperature of the recharge area (or average temperature). According to the data in high latitudes in the northern hemisphere, Dansgaard [38] established the relationship between the annual average value of $\delta^{18}\text{O}$ and the annual average temperature.

$$\delta^{18}\text{O} = 0.69t - 13.6, \quad (5)$$

where t is the monthly average temperature (°C). Yurtsever [39] summarized the relationship between the value of $\delta^{18}\text{O}$ and the average temperature of precipitation in the northern hemisphere.

$$\delta^{18}\text{O} = (0.521 \pm 0.014)t - (14.96 \pm 0.21), \quad (6)$$

where t is the monthly average temperature (°C) and the correlation coefficient of the formula is 0.893.

According to (5) and (6), the temperature of the recharge area is estimated as -7.1°C and -6.2°C, respectively. In general, the temperature of the recharge area of most hot springs is above 0°C. However, the Xueban mountain covered with ice and snow is located to the northwest of the Madeng spring. This mountain could be the highest recharge area of the hot spring. The average temperature -6.6°C is thought to be the lowest air temperature of the recharge area of the hot spring.

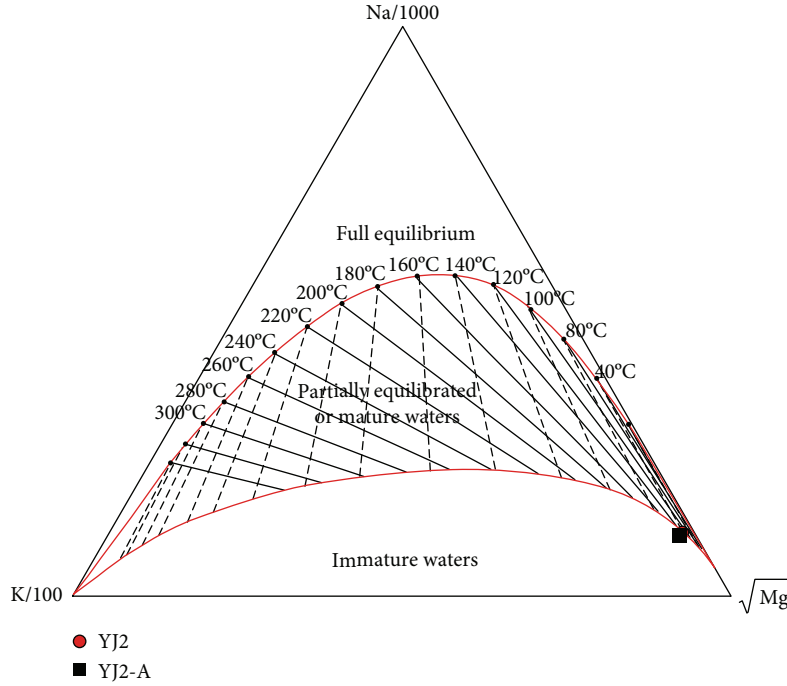


FIGURE 4: Triangular diagram of Na-K-Mg^{1/2}. YJ2: water sample of the hot spring taken in 2014; YJ2-A: water sample of the hot spring from Local Chronicles Compilation Committee of Yunnan Province [5].

3.2.4. Resident Time of the Thermal Groundwater. ²²⁶Ra and ²²²Rn are of uranium series isotopes. ²²⁶Ra is formed after the decay of uranium, and it becomes ²²²Rn after further decay of ²²⁶Ra. According to the contents of ²²⁶Ra and ²²²Rn in the hot water, the resident time (age) of the thermal water can be estimated by using the following equation [16]:

$$t = -\frac{1}{\lambda_{Ra}} \ln \left(1 - \frac{N_{Ra}}{N_{Rn}} \right), \quad (7)$$

where λ_{Ra} is the decay constant of ²²⁶Ra (0.00043) and N_{Ra} and N_{Rn} are contents of ²²⁶Ra and ²²²Rn (in Bq/L).

The contents of ²²⁶Ra and ²²²Rn of the hot water are 0.42 Bq/L and 7.21 Bq/L, respectively. According to (7), it is estimated that the age of the thermal water of the Madeng hot spring is approximately 140 years.

3.3. Genesis of the Thermal Groundwater

3.3.1. Estimation of the Reservoir Temperature. Surface temperature of hot water usually can be observed in the field, but the surface temperature does not stand for the reservoir temperature of the thermal water [40]. Silica geothermometers, cation ratio geothermometers and multimineral equilibrium geothermometers, and so on are widely used to estimate the temperature of a geothermal reservoir (Wang et al. 1993). The Na-K-Mg^{1/2} diagram (Figure 4) shows that the hot water samples of the Madeng hot spring is in the area of immature water, that is, cation geothermometers are not suitable [25]. Therefore, the silica geothermometers are considered in the present work.

SiO₂ mineral is widespread in geothermal water. When the hot water temperature drops, the process of SiO₂

deposition is very slow. When the temperature is lower than 300°C, the pressure and salinity have little impact on the solubility of quartz and amorphous SiO₂, and the dissolved SiO₂ in the water is generally not affected by other ions. These characteristics of SiO₂ make it suitable as a geothermometer and extensive applications. There are five commonly used silica geothermometer equations as follows [18, 41]:

- (1) Quartz geothermometer—without steam separation or mixing action:

$$t(^{\circ}\text{C}) = -42.198 + 0.28831\text{SiO}_2 - 3.6686 \times 10^{-4}(\text{SiO}_2)^2 + 3.1665 \times 10^{-7}(\text{SiO}_2)^3 + 77.0341\lg \text{SiO}_2. \quad (8)$$

- (2) Quartz geothermometer—without steam loss (0–250°C):

$$t(^{\circ}\text{C}) = \frac{1309}{5.19 - \lg \text{SiO}_2} - 273.15. \quad (9)$$

- (3) Quartz geothermometer—largest steam loss at 100°C (0–250°C):

$$t(^{\circ}\text{C}) = \frac{1522}{5.75 - \lg \text{SiO}_2} - 273.15. \quad (10)$$

- (4) α -christobalite geothermometer:

$$t(^{\circ}\text{C}) = \frac{1000}{4.78 - \lg \text{SiO}_2} - 273.15. \quad (11)$$

TABLE 3: Relationship between the hot water temperature, enthalpy, SiO_2 content, and ratio of cold water (X).

T (°C)	$S_h (\times 4.1868 \text{ J/g})$	$\text{SiO}_{2h} (\text{mg/L})$	X1	X2
50	50	13.5	0.255	-3.966
75	75	26.6	0.588	-0.047
100	100.1	48	0.715	0.543
125	125.1	80	0.782	0.752
150	151	125	0.825	0.849
175	177	185	0.854	0.901
200	203.6	265	0.875	0.932
225	230.9	365	0.891	0.951
250	259.2	486	0.904	0.963
275	289	614	0.914	0.971
300	321	692	0.924	0.975

The relationship between the hot water temperature, enthalpy, and SiO_2 content is quoted from Fournier and Truesdell [44].

(5) Chalcedony geothermometer—without steam loss (0–250°C):

$$t(^{\circ}\text{C}) = \frac{1032}{4.69 - \lg \text{SiO}_2} - 273.15. \quad (12)$$

The reservoir temperature is estimated as 76.2°C, 75.7°C, 79.8°C, 26°C, and 44.1°C by using (8), (9), (10), (11), and (12), respectively (content of H_2SiO_3 is approximately equal to 1.3 times that of SiO_2). The results show that the reservoir temperature by using quartz geothermometer is higher than that using christobalite geothermometer. The results with (11) and (12), which are lower than the temperature of the hot spring, are unreasonable and should be ignored. The result with the quartz geothermometer conforms to the actual situation. The reservoir temperature of the Madeng hot spring in Yunnan is in the range 75°C–80°C. The reason why this temperature is slightly lower than expected may be the mixture with the cold groundwater in the Quaternary sand and gravel in the valley, when the hot water rises to the land surface.

3.3.2. Circulation Depth. After receiving recharge from infiltration of precipitation, the groundwater is heated during a deep circulation, flows upward to the surface, and emerges in the form of the hot spring. The temperature of the geothermal water is mainly derived from geothermal heating in the process of deep circulation. The geothermal water often can reach as deep as thousands of meters [2]. If the temperature of the geothermal water relies on the deep circulation through normal geothermal heating, one can use the following equation to estimate the depth of geothermal water circulation [2, 33, 42]:

$$Z = G(T_z - T_0) + Z_0, \quad (13)$$

where Z is the depth of geothermal water circulation, G is the reciprocal of the geothermal gradient ($\text{m}/^{\circ}\text{C}$), T_z is the geothermal reservoir temperature ($^{\circ}\text{C}$), T_0 is the annual average temperature of the recharge area ($^{\circ}\text{C}$), and Z_0 is the depth of the local constant-temperature zone (m).

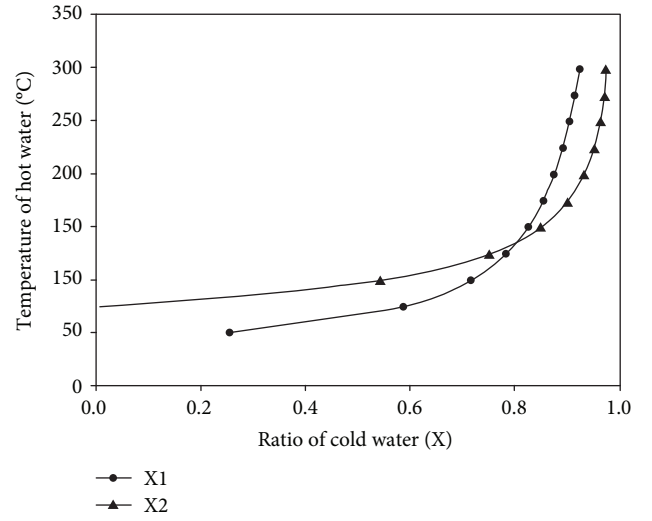


FIGURE 5: Relationship between temperature of hot water and ratio of cold water $X1 = (S_h - S_s)/(S_h - S_c)$; $X2 = (\text{SiO}_{2h} - \text{SiO}_{2s})/(\text{SiO}_{2h} - \text{SiO}_{2c})$.

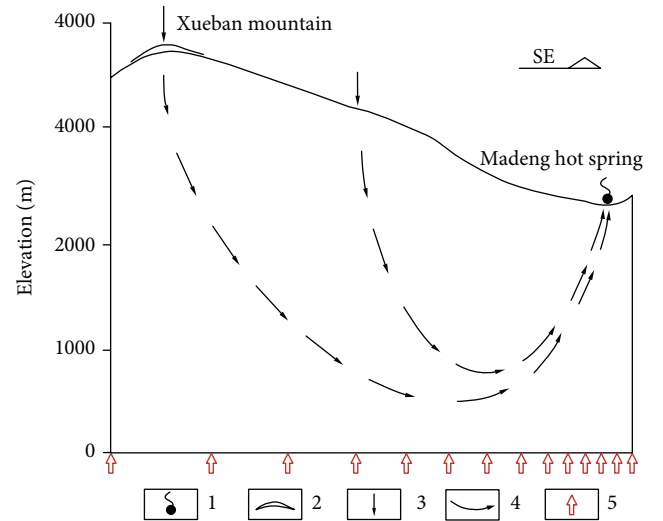


FIGURE 6: Schematic diagram showing the formation (a regional scale) of the Madeng hot spring in Jianchuan county, Yunnan. 1—hot spring; 2—snow and ice; 3—meteoric water; 4—flow line; 5—heat flow.

According to the “Jianchuan County Annals” published in 1999, we can obtain $G = 28.57 \text{ m}/^{\circ}\text{C}$, $T_0 = 12.3^{\circ}\text{C}$, and $Z_0 = 20 \text{ m}$ and the estimated underground averaged reservoir temperature $T_z = 77.2^{\circ}\text{C}$. Circulation depth of the thermal water in the research region is estimated as approximately 1870 m by using (13).

3.3.3. Mixture between the Hot Water and the Cold Water. The mixing between hot water and cold water in geothermal systems is very common, which may occur in the whole process of the geothermal fluid circulation. It is very important to recognize the formation conditions and the reservoir temperature of geothermal water by examining the mixing effect [43]. The exposed geologic background near the Madeng hot

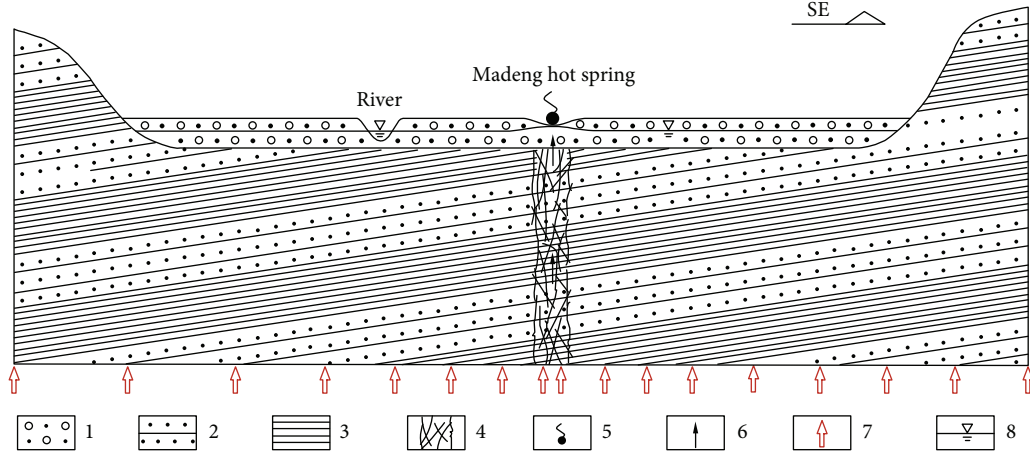


FIGURE 7: Schematic profile showing the formation (near the vent) of the Madeng hot spring in Jianchuan county, Yunnan. 1—sand and gravel; 2—sandstone; 3—mudstone; 4—fracture zone; 5—hot spring; 6—thermal ground water flow; 7—heat flow; 8—water table.

spring indicates that the geothermal water has the possibility of mixing with the shallow cold water in the sand and gravel while rising towards the ground.

Assuming that the dissolved SiO_2 of the deep geothermal water is in a saturated state, the initial enthalpy and SiO_2 content in the deep hot water at the beginning are inevitably converted into final enthalpy and SiO_2 content of hot spring water at last during the process of cold water and hot water mixing [17, 41, 44]. According to the law of conservation of mass, assuming that X is the cold water mixing ratio, then the relationship between the initial content of thermal groundwater SiO_2 and enthalpy and the final content of thermal groundwater SiO_2 and enthalpy can be expressed by the following equations [44]:

$$S_c X + S_h (1 - X) = S_s, \quad (14)$$

$$\text{SiO}_{2c} X + \text{SiO}_{2h} (1 - X) = \text{SiO}_{2s}, \quad (15)$$

where S_c is the enthalpy of the cold water, S_s is the final enthalpy of the spring water, S_h is the enthalpy of the deep thermal groundwater, SiO_{2c} is the SiO_2 concentration in the cold water, SiO_{2s} is the SiO_2 concentration in the spring hot water, and SiO_{2h} is the initial SiO_2 concentration in the deep thermal groundwater and is a function of S_h . The mixing ratio X of cold groundwater with deep thermal groundwater and the enthalpy of the deep thermal groundwater S_h are not known. The average temperature of the surface cold water in the Jianchuan area is 19°C , the corresponding content of SiO_2 is 10 mg/L , and the enthalpy is 79.55 J/g . The measured spring temperature is 42.1°C , SiO_2 content is 27.38 mg/L , and the corresponding heat enthalpy is 176.26 J/g .

Substituting the enthalpy of different temperatures and the content of SiO_2 (Table 3) into the (14) and (15), respectively, we can get a series value of X_1 and X_2 (Table 3), and the figure with the relationship between temperature of hot water and ratio of cold water in two curves can be drawn. The proportion corresponding to the intersection point is the required cold water ratio (Figure 5). The mixing ratio of the Madeng hot spring is approximately 80%, which

indicates that the hot spring water is mixed with surface cold water. Since the selection of cold water enthalpy and SiO_2 content are empirically estimated and other factors are not considered, the mixing ratio may be higher than the actual result.

3.3.4. Formation of the Hot Spring. Tectonically, the Madeng area in Jianchuan county is located in the west of the Weixi-Qiaohou fault zone and in the east of the Lanping-Simao fracture (Bijiang fault), which formed an inverted triangle. Fractured zones are observed in the red beds in the western of Yunnan and could provide good circulation conditions for the formation of the hot spring. The Madeng hot spring emerges in the center of the river valley in the northeastern Lanping Basin. Quaternary sand and gravel occur in the valley, and the underlying strata are the red beds of sandstone and mudstone. After receiving recharge from infiltration of precipitation in the recharge area in the surrounding mountains (Figure 6), the groundwater undergoes a deep circulation and obtains heat from heat flow. The hot water flows upward along the fractured zone and through the Quaternary sand and gravel (Figure 7) and emerges in the central low-lying river valley. This kind of spring is called an upflow spring [30] for the hot spring does not issue directly from the bed rocks, that is, the red beds.

4. Summary

The Madeng hot spring emerges in the central river valley in the eastern Lanping Basin of Yunnan in China. Temperature of the hot spring water is 42.1°C , belonging to geothermal water of low temperature. The total hardness is 1100 mg/L belonging to the especially hard water according to the classification of hardness. The TDS is 3.98 g/L , indicating the brackish water. The hot water has a pH value of 6.41, belonging to weakly acidic water, which can express that the ability to neutralize the alkali is greater than the acid in the hot spring water in the study area.

The cations of the hot water are predominated by Na, K, Ca, and Mg and the anions of the hot water by SO_4 , HCO_3 ,

and Cl. The minor ions of the hot water include NH_4 , NO_3 , and Fe. H_2SiO_3 of the hot water is 35.6 mg/L and F content is 3.08 mg/L, which are greater than the drinking water standard of China and are not suitable for drinking. The hot water is of $\text{SO}_4\text{-Cl-Na-Ca}$ type.

The values of the $\delta^2\text{H}$ and $\delta^{18}\text{O}$ are -120.4‰ and -18.5‰ , indicating that the hot water is of meteoric origin. Obvious ^{18}O shift phenomenon is not observed, inflecting that the deep thermal reservoir temperature is not high, and the hot water belongs to thermal groundwater of low temperature. The recharge altitude of the hot water is estimated as approximately 3800 m, which may indicate the Xueban mountain. The lowest temperature of the recharge area, the Xueban mountain covered with ice and snow to the northwest of the Madeng spring, is estimated as -6.6°C . The values of the N_{Ra} and N_{Rn} are 0.042 Bq/L and 7.21 Bq/L. The age of the hot water is estimated with the Ra and Rn contents as approximately 140 years.

SiO_2 geothermometer is used to estimate the thermal reservoir temperature of the hot spring in the study area, and the temperature of the geothermal reservoir in the study area ranges from 75°C to 80°C . The mixing ratio of cold water is approximately 80%, and the circulation depth of the hot water, approximately 1870 m. After receiving recharge from infiltration of precipitation in the recharge area, the groundwater is heated during a deep circulation, flows upward along the fractured zone, and emerges as an upflow spring through the Quaternary sand and gravel in the central low-lying river valley.

Given the key information of hydrochemistry and formation hypothesis of the Madeng hot spring in this article, it could provide some insights into the potential and development of thermal groundwater resources in Western Yunnan. Future studies of further explanation of the solutes and isotopic features of the hot spring are required to better understand the substance migration of thermal groundwater occurring in red bed areas.

Conflicts of Interest

The authors declare that they have no conflicts of interest.

Acknowledgments

This work was cooperatively supported by the Natural Science Foundation of China (41572223, 41772261) and the Fundamental Research Funds for the Central Universities of China (2652015245). The authors want to thank Dr. Haiyan Zhou and Dr. Juan Guo for their help in improving the manuscript. The authors are also grateful for the critical comments and suggestions by the editors and anonymous reviewers.

References

- [1] S. Huang, *China's Hot Spring Resources (The Specification of China's Hot Spring Distribution for A-Six Million)*, China Map Publishing House, Beijing, China, 1993.
- [2] X. Zhou, X. Jin, S. Liang, Y. Shen, and H. Zhang, *Special Topics on Groundwater Sciences*, Geological Publishing House, Beijing, China, 2010.
- [3] N. Liang, *Introduction to the Hot Springs in Yunnan*, Yunnan People's Publishing House, Kunming, China, 2000.
- [4] M. Chen, J. Wang, and X. Deng, *Geothermal Resources in China: Formation Characteristics and Potential Evaluation*, Science Press, Beijing, China, 1994.
- [5] Local Chronicles Compilation Committee of Yunnan Province, *Hot Springs' Records in the Yunnan Province's Records*, vol. 25, Yunnan People's Publishing House, Kunming, China, 1999.
- [6] A. J. Ellis and W. A. J. Mahon, "Natural hydrothermal systems and experimental hot-water/rock interactions," *Geochimica et Cosmochimica Acta*, vol. 28, no. 8, pp. 1323–1357, 1964.
- [7] R. Favara, F. Grassa, S. Inguaggiato, and F. D'Amore, "Geochemical and hydrogeological characterization of thermal springs in Western Sicily, Italy," *Journal of Volcanology and Geothermal Research*, vol. 84, no. 1–2, pp. 125–141, 1998.
- [8] R. Cidu and S. Bahaj, "Geochemistry of thermal waters from Morocco," *Applied Geochemistry*, vol. 29, no. 3, pp. 407–430, 2000.
- [9] B. Frengstad, A. K. Midtgård Skrede, D. Banks, J. Reidar Krog, and U. Siewers, "The chemistry of Norwegian groundwaters: III. The distribution of trace elements in 476 crystalline bed-rock groundwaters, as analysed by ICP-MS techniques," *The Science of the Total Environment*, vol. 246, no. 1, pp. 21–40, 2000.
- [10] J. V. Cruz and Z. Franca, "Hydrogeochemistry of thermal and mineral water springs of the Azores archipelago (Portugal)," *Journal of Volcanology and Geothermal Research*, vol. 151, no. 4, pp. 382–398, 2006.
- [11] A. Davraz, "Hydrogeochemical and hydrogeological investigations of thermal waters in the Usak area (Turkey)," *Environmental Geology*, vol. 54, no. 3, pp. 615–628, 2008.
- [12] H. Craig, "Isotopic variations in meteoric waters," *Science*, vol. 133, no. 3465, pp. 1702–1703, 1961.
- [13] B. R. Payne, "The status of isotope hydrology today," *Journal of Hydrology*, vol. 100, no. 1–3, pp. 207–237, 1988.
- [14] R. Favara, F. Grassa, S. Inguaggiato, and M. Valenza, "Hydrogeochemistry and stable isotopes of thermal springs: earthquake-related chemical changes along Belice Fault (Western Sicily)," *Applied Geochemistry*, vol. 16, no. 1, pp. 1–17, 2001.
- [15] N. Majumdar, R. Majumdar, A. Mukherjee, S. Bhattacharya, and R. Jani, "Seasonal variations in the isotopes of oxygen and hydrogen in geothermal waters from Bakreswar and Tantloi, Eastern India: implications for groundwater characterization," *Journal of Asian Earth Sciences*, vol. 25, no. 2, pp. 269–278, 2005.
- [16] V. V. Cherdynstev, *Uranium-234*, Keter Press, Jerusalem, Israel, 1971.
- [17] Y. Liu, X. Zhou, Z. Deng et al., "Hydrochemical characteristics and genesis analysis of the Jifei hot spring in Yunnan, southwestern China," *Geothermics*, vol. 53, pp. 38–45, 2015.
- [18] R. O. Fournier and R. W. Potter II, "A revised and expanded silica (quartz) geothermometer," *Geothermal Resources Council Bulletin*, vol. 11, pp. 3–12, 1982.
- [19] R. O. Fournier and R. W. Potter II, "Magnesium correction to the Na-K-Ca chemical geothermometer," *Geochimica et Cosmochimica Acta*, vol. 43, no. 9, pp. 1543–1550, 1979.

- [20] R. O. Fournier and A. H. Truesdell, "An empirical Na-K-Ca geothermometer for natural waters," *Geochimica et Cosmochimica Acta*, vol. 37, no. 5, pp. 1255–1275, 1973.
- [21] R. O. Fournier, "Silica in thermal waters: laboratory and field investigations," in *Proceedings of the International Symposium on Hydrogeochemistry and Biogeochemistry*, pp. 122–139, Tokyo, Japan, 1973.
- [22] R. O. Fournier, "Geochemical and hydrologic considerations and the use of enthalpy-chloride diagrams in the prediction of underground conditions in hot-spring systems," *Journal of Volcanology and Geothermal Research*, vol. 5, no. 1-2, pp. 1–6, 1979.
- [23] W. F. Giggenbach, "Chemical compositions of volcanic gases," in *Monitoring and Mitigation of Volcano Hazards*, R. Scarpa and R. I. Tilling, Eds., pp. 221–256, Springer-Verlag, New York, NY, USA, 1996.
- [24] W. F. Giggenbach and R. L. Goguel, "Collection and analysis of geothermal and volcanic water and gas discharge," Report No. 2401, Chemistry Division, Department of Scientific and Industrial Research, Petone, New Zealand, 1989.
- [25] W. F. Giggenbach, "Geothermal solute equilibria. Derivation of Na-K-Mg-Ca geothermometers," *Geochimica et Cosmochimica Acta*, vol. 52, no. 12, pp. 2749–2765, 1988.
- [26] X. Yu, "The tracking studies of Madeng hot spring CO_3^{2-} isotope in composition in Lanping Basin, the west of Yunnan," *Journal of Chengdu University of Technology*, vol. 24, pp. 70–77, 1997.
- [27] The Annals Compilation Committee in Jianchuan County of Yunnan province, *Jianchuan County Annals*, Yunnan People's Publishing House, Kunming, China, 1999.
- [28] Y. Luo, C. Zhang, C. Rao, and G. Yang, "Occurrence characters and development way of groundwater in Yunnan red stratum," *Investigation of Science and Technology*, vol. 2, pp. 46–49, 2006.
- [29] X. Cheng, *The Accumulation Rule and Genetic Mode about Geothermal Resources in the East of Yunnan Province*, Kunming University of Science and Technology, 2008.
- [30] X. Zhou, F. Hu, J. He, X. Wang, and B. Fang, *Introduction to Groundwater Sciences*, Geological Publishing House, Beijing, China, Second edition, 2014.
- [31] Y. Yao, "The analysis about geological characteristics and formation of the Midu hot spring," *Kunming University of Science and Technology*, p. 111, 2010.
- [32] H. Craig, "Standard for reporting concentrations of deuterium and oxygen-18 in natural waters," *Science*, vol. 133, no. 3467, pp. 1833–1834, 1961.
- [33] Z. Xun, F. Bin, Z. Haiyan, L. Juan, and W. Ying, "Isotopes of deuterium and oxygen-18 in thermal groundwater in China," *Environmental Geology*, vol. 57, no. 8, pp. 1807–1814, 2009.
- [34] I. D. Clark and P. Fritz, *Environmental Isotopes in Hydrogeology*, Lewis Publishers, New York, NY, USA, 1997.
- [35] P. G. Cook and L. H. Herczeg, *Environmental Tracers in Subsurface Hydrology*, Kluwer Academic Publishers, London, UK, 2000.
- [36] H. Wang, *Isotope Hydrology Geology Survey*, Geological Publishing House, Beijing, China, 1991.
- [37] C. Liu and H. Wang, *Foundation of Environmental Isotope Hydrogeology*, 1984.
- [38] W. Dansgaard, "Stable isotopes in precipitation," *Tellus*, vol. 16, no. 4, pp. 436–468, 1964.
- [39] Y. Yurtsever, "Worldwide survey of stable isotopes in precipitation," *Isotope Hydrology International Atomic Energy Agency*, 1975.
- [40] Q. Guo and Y. Wang, "Geochemistry of hot springs in the Tengchong hydrothermal areas, Southwestern China," *Journal of Volcanology and Geothermal Research*, vol. 215–216, pp. 61–73, 2012.
- [41] R. O. Fournier, "Chemical geothermometers and mixing models for geothermal systems," *Geothermics*, vol. 5, no. 1–4, pp. 41–50, 1977.
- [42] Z. Xun, L. Juan, Z. Haiyan, F. Bin, Y. Lan, and L. Shijun, "Increase in thermal groundwater due to a flowing well near the Songshan hot spring in Beijing, China," *Environmental Geology*, vol. 53, no. 7, pp. 1405–1411, 2008.
- [43] X. Zheng and J. Guo, "Studies of mixing and its application in geothermal systems," *Journal of Xi'an College of Geology*, vol. 18, pp. 53–57, 1996.
- [44] R. O. Fournier and A. H. Truesdell, "Geochemical indicators of subsurface temperature part 2, estimation of temperature and fraction of hot water mixed with cold water," *United States Geology Survey Research*, vol. 2, pp. 263–270, 1974.

Research Article

Fluid Geochemistry of Fault Zone Hydrothermal System in the Yidun-Litang Area, Eastern Tibetan Plateau Geothermal Belt

Yanyan Hou,¹ Zheming Shi ,^{1,2} and Wenqing Mu²

¹State Key Laboratory of Biogeology and Environmental Geology & MOE Key Laboratory of Groundwater Circulation and Environmental Evolution, China University of Geosciences, Beijing 100083, China

²School of Water Resources and Environment, China University of Geosciences, Beijing 100083, China

Correspondence should be addressed to Zheming Shi; szm@cugb.edu.cn

Received 3 December 2017; Revised 31 March 2018; Accepted 2 May 2018; Published 27 June 2018

Academic Editor: Meijing Zhang

Copyright © 2018 Yanyan Hou et al. This is an open access article distributed under the Creative Commons Attribution License, which permits unrestricted use, distribution, and reproduction in any medium, provided the original work is properly cited.

The geochemical and geothermal characteristics of hydrothermal systems in an area are useful information to appropriately evaluate the geothermal potential. In this paper, we investigated the chemical and isotopic composition of thermal water in an underexploited geothermal belt, Yidun-Litang area, in eastern Tibetan Plateau. 24 hot spring samples from the Yidun and Litang area were collected and analyzed. The water chemical types of the hot springs are mainly Na-HCO₃-type water. Water-rock interaction and cation exchange and mixture are the dominant hydrogeochemical processes in the hydrothermal evolution. The significant shift of D and ¹⁸O isotopes from the GMWL indicates that these springs have undergone subsurface boiling before rising to the surface. Different ratios of Cl to other conservation species can be found for the springs in Litang and Yidun areas, suggesting the different heat sources of the two hydrothermal systems. The reservoir temperature in the Yidun area is around 230°C while the reservoir temperature in the Litang area is around 200°C. Both hydrothermal systems are recharged by the meteoric water and are heated by the different deep, thermally and topographically driven convection heat along faults and undergoing subsurface boiling before going back to the surface.

1. Introduction

As one source of clean and renewable energy, geothermal energy has been developed worldwide. Investigating and evaluating the potential of geothermal fields is an important process prior to geothermal exploitation. Hydrogeochemical and isotopic information can be effective for identifying the source of heat, circulation process, and hydrochemical evolution [1–5]. Understanding the hydrochemical characteristics and geochemical evolution of thermal waters will provide useful information in protecting and developing these resources [6]. As an important part of the eastern Tibetan plateau geothermal belt, fumaroles, geysers, and boiling springs with many other hot springs occurred in the Yidun-Litang area. Due to the high altitude, complex terrain, and low density of population, geothermal energy in this area has not been well exploited. The only utilization of this geothermal energy is for bathing in some areas [7]. Although some basic physical and chemical properties of the hot

springs have been investigated by a few studies [8, 9], little has been done in detail describing the geochemical characteristic and reservoir temperature of these geothermal fields. Such studies, however, are important to understanding the genesis and evolution of the geothermal field and also providing insight views for evaluating the geothermal potential.

On the other hand, hot springs occur most commonly at the fault zones and their evolution depends on the interaction between heat sources, circulating fluids, and permeable pathways [10], and they tend to occur in high-permeability areas of fault zone and have a close relationship with seismic activities [11, 12]. Several previous studies also have documented that the chemical components in the hot springs are influenced by tectonic activity, especially by earthquakes [13–15]. Therefore, hot springs in the fault zone provide a unique opportunity for studying the interaction between tectonic activities and the hydrological systems. In addition to the hydrothermal activity, the Yidun-Litang area has a high level of seismic activity, as demonstrated by the Litang

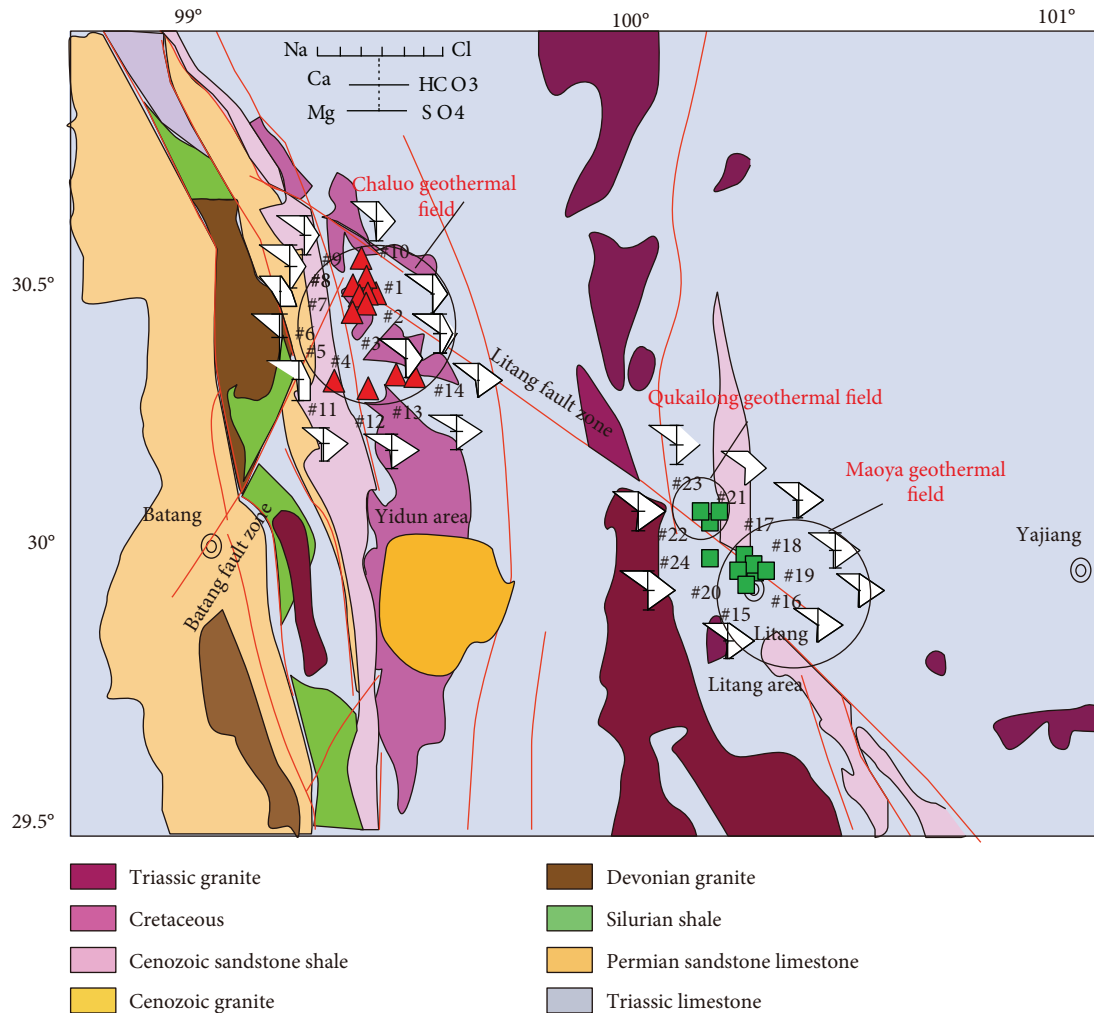


FIGURE 1: Geological setting of the study area.

Ms 5.1 earthquake on September 23, 2016 [16], and several large ($7.0 < M < 7.5$) earthquakes since 1700 [16].

In this study, we collected water samples from 24 hot springs located in the Yidun-Litang area, most of which were taken from locations coinciding with mapped fault zones. Hydrochemical evolution, groundwater circulation, and the reservoir temperature of these springs are discussed. The study will provide useful information for appropriately evaluating geothermal potential in this area and the thermal evolution process of the eastern Tibetan Plateau as well.

2. Geological Setting

The study is located between the Songpan-Ganzi fold belt and the Qiangtang Block, with the Ganzi-Litang suture to its east and the Jinsa suture to its west, with an average elevation of 3000~4000 m [17]. The area is covered by widespread Triassic limestone, with multistage magmatic activity. Early magmatic rocks are primarily diorites, and late magmatic rocks are primarily granites. The main eruption activity was from the Variscan to Indosinian, while intrusions occurred from the Yanshanian to Himalayan. The influence of

magmatic activity on the present geothermal activity is primarily related to age and scale, which means that less heat is retained by the older intruded or ejected magma and magma intrusions will dissipate heat faster with smaller volume. Generally, residual heat caused by some small-scale magmatic activity prior to the Quaternary has disappeared. The Triassic is the most widespread strata in this area (Figure 1); Devonian, Permian, and Cenozoic strata are sporadic. Limestone, sandstone, granite, siltstone, slate, and phyllite are the major lithologies that are exposed in the study area.

Fault systems are well developed in this area with frequent earthquakes. The Litang fault zone and the Batang fault zone are the two major fault zones in the area (Figure 1). The Batang fault is also a dextral fault, which strikes N30°E, dipping northwest with a steeply dipping angle, with a total length of about 200 km. The Litang fault zone comprises four subfaults: Cuopu fault, Maoya fault, Litang fault, and Dewu fault. All of the four subfaults are dominated by a left-lateral strike-slip with a reverse dip-slip component on different segments [18]. Three large earthquakes with magnitude > 7.0 had occurred since 1700, and small to moderate seismic events occurred frequently in this

TABLE 1: Concentrations of major and trace chemical constituents in hot spring sample in the Yidun-Litang area (mg/L).

Sample name	Alt (m)	T (°C)	pH	Li	Na	K	Ca	Mg	SiO ₂	B	Cl	F	SO ₄	HCO ₃	CO ₃	Rb	Cs	Cond us/cm	$\delta^{18}\text{O}$	δD	Tritium (TU)	CBE
1	3580	83.2	9.4	3.16	357.00	28.00	1.35	0.04	448.00	1.39	47.68	19.97	19.94	498.90	118.20	0.59	1.09	1440	-19.26	-152.96	<1.0	1.2%
2	3587	88.2	9.9	2.45	359.00	29.30	0.60	0.03	520.00	1.17	50.85	21.38	22.64	176.47	271.00	0.76	1.09	1430	-18.83	-152.09	—	0.78%
3	3562	88.0	9.2	2.84	368.80	30.10	0.52	0.07	460.00	1.37	53.19	22.25	24.64	560.80	114.60	0.78	1.22	1530	-18.44	-151.99	—	-1.58%
4	3561	89.0	9.7	3.48	380.50	30.55	0.30	0.03	528.00	1.46	53.28	21.93	22.56	367.80	218.50	0.69	1.32	1530	-18.75	-151.95	<1.0	-0.61%
5	3544	87.1	9.0	2.13	303.10	23.37	4.10	0.30	304.00	1.16	46.68	18.34	74.49	491.60	45.56	0.58	0.85	1240	-18.24	-148.91	—	-1.95%
6	3568	84.8	8.9	1.49	225.00	17.60	11.50	0.53	168.00	0.70	24.66	7.74	206.90	254.20	7.53	0.33	0.28	1030	-17.47	-150.84	—	1.64%
7	3564	88.2	9.5	1.09	127.80	14.64	66.31	0.49	100.00	0.24	9.30	3.42	208.40	183.75	—	0.30	0.50	1440	-17.25	-151.46	<1.0	7.66%
8	3566	87.8	8.4	3.45	370.50	31.40	1.28	0.03	440.00	1.48	51.59	20.15	31.54	411.50	164.80	0.70	1.09	820	-18.57	-151.94	<1.0	1.26%
9	3555	85.7	9.6	2.68	400.10	33.98	0.97	0.06	412.00	1.29	56.99	23.75	31.03	513.40	164.80	0.88	1.28	1560	-19.17	-152.65	—	-1.13%
10	3591	50.1	8.3	0.18	119.80	3.32	9.25	0.65	54.00	0.16	8.79	13.72	15.43	225.80	7.16	0.04	0.08	490	-20.74	-154.53	2.4	8.02%
11	3304	64.4	7.7	0.45	294.20	19.95	26.63	17.83	116.00	0.03	14.36	3.14	98.99	876.10	—	0.12	0.30	1580	-19.17	-151.22	—	-4.18%
12	3958	70.0	8.3	1.19	279.30	22.01	27.28	1.84	105.00	0.63	16.18	8.90	6.11	738.40	—	0.39	0.46	1180	-19.40	-155.35	<1.0	3.1%
13	3941	65.4	7.1	1.13	278.30	21.44	4.09	1.65	106.00	0.01	16.80	9.01	5.10	692.50	—	0.35	0.43	1200	-20.16	-155.85	<1.0	1.34%
14	3918	65.4	8.0	0.81	277.90	21.37	27.87	1.81	74.00	0.07	16.93	9.18	5.04	710.10	—	0.38	0.43	1160	-20.11	-155.16	—	4.33%
15	3946	34.6	6.9	1.96	726.10	33.17	7.39	18.59	68.00	3.13	30.36	3.96	8.96	1766.10	125.40	0.16	0.61	3400	-18.80	-158.36	—	-1.63%
16	3948	25.6	7.3	2.17	758.30	35.17	12.47	19.26	49.38	3.51	31.88	3.49	6.76	2070.00	—	0.08	0.66	3010	-18.86	-159.61	<1.0	-0.33%
17	3989	42.8	7.3	1.69	608.90	29.27	12.13	16.98	70.00	2.82	24.92	3.11	6.66	1713.90	—	0.11	0.53	3040	-18.15	-155.53	—	-1.27%
18	3965	46.9	6.8	2.04	746.40	35.40	42.30	18.44	55.77	3.34	31.37	3.08	16.82	1944.00	86.60	0.08	0.62	3110	-19.23	-161.33	—	-0.45%
19	3970	47.0	6.7	2.11	723.70	33.47	16.07	19.04	51.69	3.44	30.70	3.50	7.40	2123.30	—	0.07	0.62	3070	-18.89	-161.39	—	-3.35%
20	3965	50.7	7.0	2.20	729.00	34.09	11.75	18.64	59.62	3.71	33.61	3.45	7.39	2092.70	—	0.08	0.61	3040	-18.74	-161.99	—	-2.98%
21	4124	78.3	8.1	6.63	514.90	59.76	7.28	10.89	84.00	6.61	74.00	4.90	10.86	1154.30	93.12	0.71	1.68	2420	-18.25	-157.20	<1.0	-3.88%
22	4130	81.3	8.6	6.70	491.00	57.45	15.60	11.20	84.00	6.50	71.08	4.73	13.26	1415.50	—	0.71	1.66	2270	-17.64	-156.62	<1.0	-6.78%
23	4133	81.3	8.4	5.31	497.90	58.65	10.75	10.74	78.00	5.59	68.55	4.59	11.64	1430.80	—	0.74	1.63	2270	-17.95	-156.17	—	-7.08%
24	3980	48.9	6.6	2.04	395.00	25.70	5.77	16.02	59.00	3.50	41.27	2.95	16.60	1041.40	—	0.13	1.07	1860	-18.81	-150.02	—	-2.48%

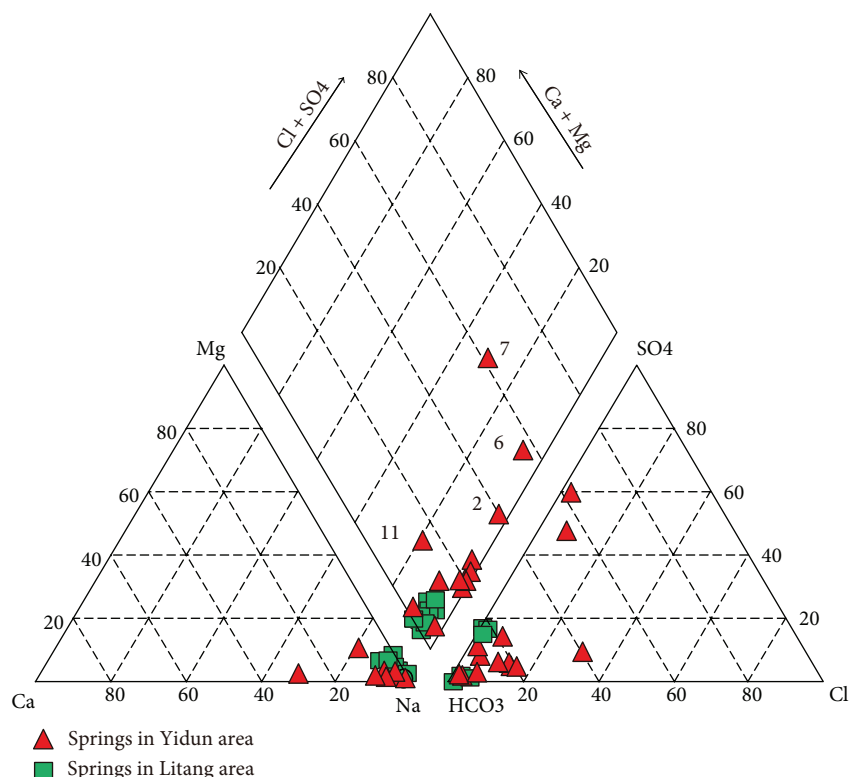


FIGURE 2: Piper diagram of the hot springs.

area [16]. Also, fault scarps, triangular facets, beheaded channels, and shutter ridges are widely observed in the Litang fault zone. Hot springs with temperature ranges from 25 to 89°C are distributed along the Litang fault zone and the intersection area of the Litang and Batang fault zones (Figure 1). Hot springs are mainly concentrated in Chaluo, Qukailong, and Maoya areas, especially high-temperature springs with temperature higher than 80°C which are found in Chaluo and Qukailong geothermal fields.

3. Sampling and Analysis

24 water samples were collected from hot springs during July 2016 in the Yidun-Litang area: 14 samples from the Chaluo area, 6 samples from the Maoya area, and 4 samples from the Qukailong area (Table 1). Temperature, pH, ORP, DO, and EC were measured on-site by a Clean M30 pen-type tester. At each site, we collect two 250 mL water samples for water chemical analysis and 50 mL for stable isotope analysis. Also, we collect 17 samples for tritium analysis, each with 500 mL volume, and stored in polyethylene bottles (Table 1). All the water chemical samples were filtered through 0.45 μm membranes on-site. For cation analysis, reagent-grade HNO_3 with a molar concentration up to 14 M was added to the samples at each site to bring the pH below 1. The major ions were analyzed by means of ion chromatography (Dionex-900). Stable isotopes of oxygen-18 and deuterium were analyzed with the liquid-water isotope analyzer LGR, with accuracy of 0.2‰ for $\delta^{18}\text{O}$ and 0.3‰ for δD . The CO_3^{2-} and HCO_3^- concentrations were measured by a

potentiometric titrator. The SO_4^{2-} and Cl^- concentrations were determined on an unacidified sample by ion chromatography. The Ca^{2+} , Mg^{2+} , Na^+ , and K^+ concentrations were analyzed by ICP-AES, the other metal elements by ICP-MS within 2 weeks after sampling. All of the chemical analyses were completed at the Sinomine Rock & Mineral Analysis Co. Ltd. The hydrochemistry of all water samples is summarized in Table 1. The tritium analysis of the samples was measured by an ultra-low background liquid scintillation mass spectrometer at the Key Laboratory of Groundwater Sciences and Engineering, Ministry of Land and Resources. The result of all the water samples is listed in Table 1.

4. Results

4.1. General Hydrogeochemistry. The water chemistry of the 24 hot springs is presented with a Piper diagram, where HCO_3^- -Na-type water dominated in these springs (Figure 2). Only number 6 and number 7 springs show Na- SO_4 - HCO_3 type. The pH ranges from 6.6 to 9.8 with TDS ranging from 0.29 mg/L to 1.9 mg/L. The springs that show a higher TDS (>1.0 g/L) are located in the Maoya and Qukailong geothermal fields, whereas other springs in the Chaluo geothermal field exhibit low TDS (<1.0 g/L). High-temperature springs ($T > 80^\circ\text{C}$) can be found in Chaluo and Qukailong geothermal fields. From the Stiff plot (Figure 1), we can find that Na^+ is the predominant cation, ranging from 127.8 to 758.0 mg/L. The HCO_3^- is the predominant anion, ranging from 176.47 to 2123.0 mg/L; Cl^- and SO_4^{2-} are the second highest anions ranging from 8.79 to 74

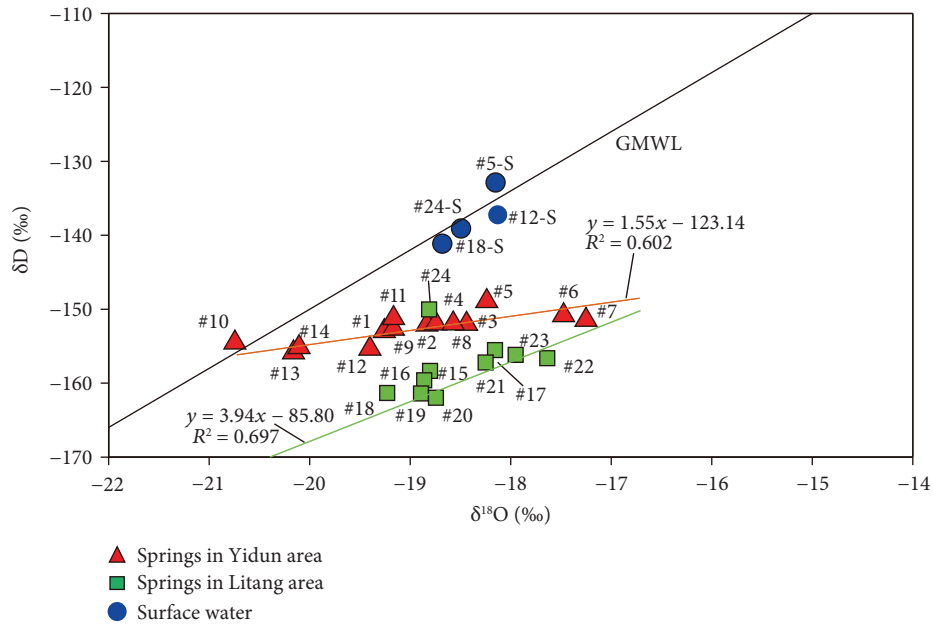


FIGURE 3: $\delta^2\text{H}$ - $\delta^{18}\text{O}$ plot of hot springs in the Yidun-Litang area.

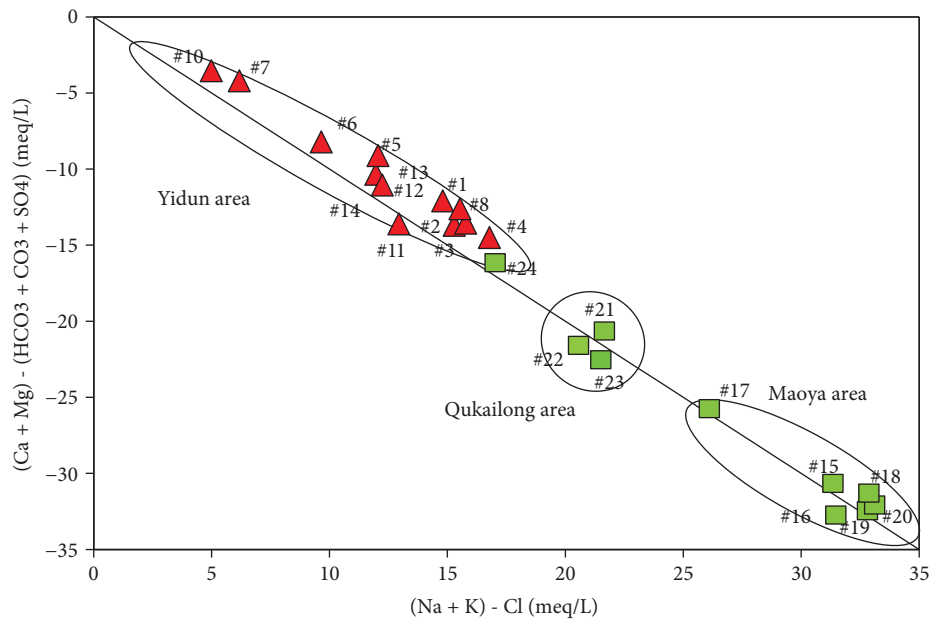


FIGURE 4: Relation between $(\text{Na} + \text{K})\text{-Cl}$ and $(\text{Ca} + \text{Mg})\text{-(HCO}_3 + \text{CO}_3 + \text{SO}_4)$.

and 5.04 to 208.4 mg/L, respectively. Li, B, Rb, and Cs can also be found from dozens to thousands of $\mu\text{g/L}$. HCO_3^- concentrations are high in the Litang area and low in Chaluo geothermal fields (Figure 1).

4.2. Isotope Composition. The stable oxygen isotope composition of the hot spring water samples ranges from -20.74‰ to -17.25‰ and deuterium from -161.99‰ to -148.91‰ (Table 1). All the hot springs (except for the number 10 spring) are falling below and away from the GMWL, and the springs in the Litang area show more negative δD and $\delta^{18}\text{O}$ than those in the Yidun area (Figure 3). For the surface

water collected from nearby, the $\delta^{18}\text{O}$ ranges from -18.52‰ to -15.52‰ , with δD ranging from -139.08‰ to -123.78‰ .

Tritium values of thermal water vary from <1 TU to 2.4 ± 1.2 TU. Tritium concentration can be used to qualitatively determine whether groundwater is modernly recharged or not (Clark and Fritz, 1997). Tritium concentrations below 1 TU indicate that groundwater is at least 50 years old (premodern) and tritium values equal to or greater than 1 TU are considered as modern groundwater. Values of tritium of about 3 TU indicate a residence time of the water of about 30–40 years. The ^3H concentration ranging from 1 to 8 TU could be attributed to an admixture of recent

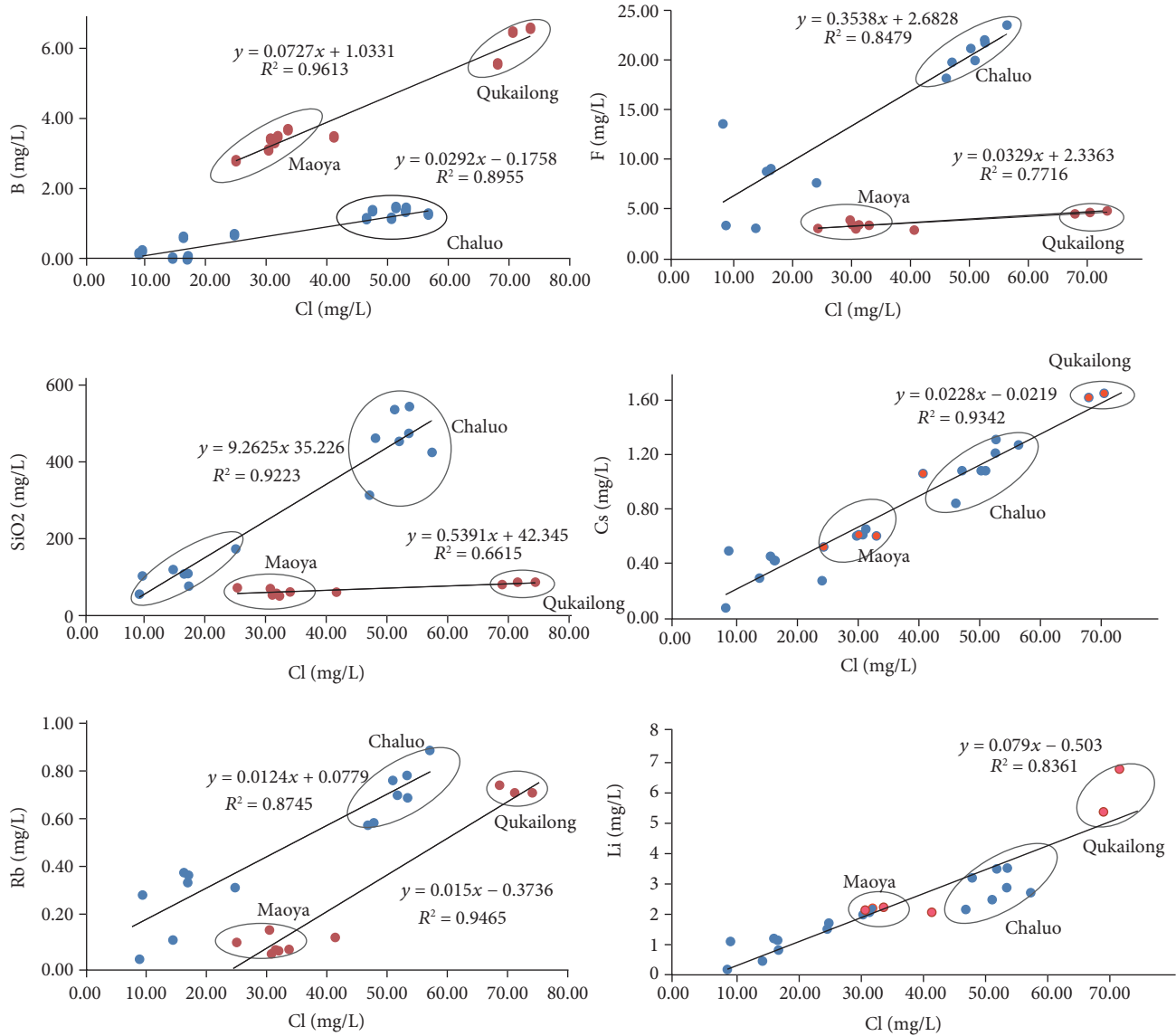


FIGURE 5: Plot of Cl versus B, Cl versus F, Cl versus SiO₂, Cl versus Cs, Cl versus Rb, and Cl versus Li of all hot spring samples. The blue points refer to the hot springs in the Yidun area, and red points refer to the hot springs in the Litang area.

water with old groundwater and groundwater having been subjected to radioactive decay [5, 19]. The tritium concentrations are less than 1 in number 1, number 4, number 8, number 2, number 13, number 12, number 21, number 15, and number 11 springs and are larger than 1 in the number 10 spring (Table 1).

5. Discussion

5.1. Hydrochemistry Evolution. According to the relationship between (Na + K)-Cl and (Ca + Mg)-(SO₄ + HCO₃) (Figure 4), the springs in the Qukailong and Maoya geothermal fields are falling on the $y = -x$ line, indicating that cation exchange is an important process that controls hydrochemical features in these two areas. For the springs in the Yidun area, most of them are located a little above the $y = -x$ line, indicating the possible dissolution of albite

origin from granite or diorites, together with cation exchange between Ca + Mg and Na, which are the dominant processes in the hydrochemical evolution. The high concentration of HCO₃ in hot springs of the Litang area may indicate a strong water-rock interaction with the limestone strata of the hydrothermal system when rising for discharge.

As the most conservative element in geothermal water, Cl is an important diagnostic solute and is frequently used in ratios with other elements in the interpretation of water chemistry. For the springs in the present study, we plot the ratios of Cl/B, Cl/F, Cl/SiO₂, Cl/Li, Cl/Rb, and Cl/Cs. A linear relationship could only be found in the relationship of Cl/Cs and Cl/Li for all the hot springs; others show a distinctly different linear relationship for the springs in Yidun and Litang areas (Figure 5). Furthermore, Na, K, HCO₃, and SO₄ behave differently from Li, Rb, Cs, and B, and no linear relationship

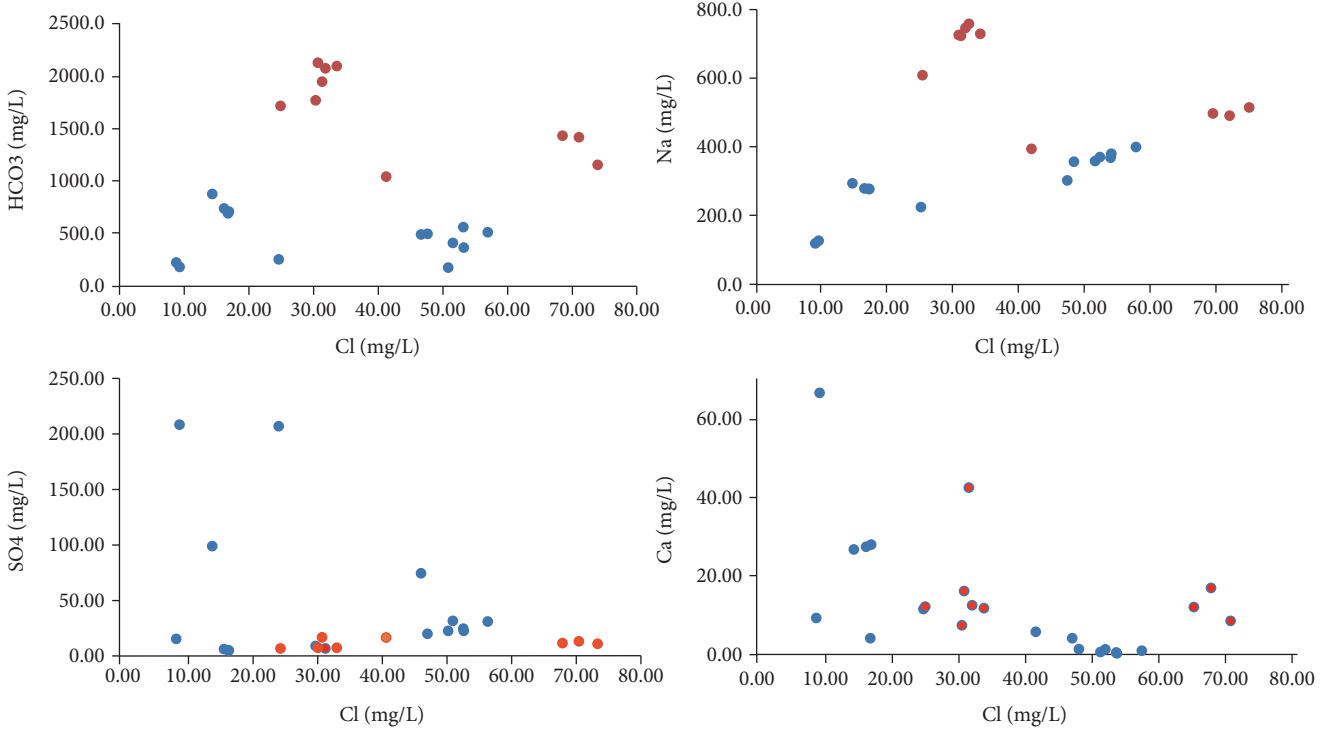


FIGURE 6: Plot of Cl versus HCO_3^- , Cl versus Na, Cl versus SO_4^{2-} , and Cl versus Ca of all hot spring samples. The blue points refer to the hot springs in the Yidun area, and red points refer to the hot springs in the Litang area.

can be found with Cl (Figure 6). The ratios of Cl/B, Cl/Li, Cl/Rb, Cl/Cs, and Cl/F are widely used to indicate a common reservoir source for water by the same ratios from different samples [20]. We calculated the ratios of Cl/B, Cl/Li, Cl/Rb, Cl/Cs, Cl/F, and Cl/SiO₂ for all of the 24 samples (Table 2). Most of the ratios in the Yidun and Litang areas show distinctly different values (i.e., Cl/B is around 40.12 (exclude anomalously high value) in the Chaluo area and 10.11 in the Litang area; Cl/F is around 2.4 in Chaluo and around 11.25 in the Litang area). Only the ration of Cl/Cs shows similarity for both areas; such similarity may be caused by the similar host rocks during the geothermal fluid rising to the surface as Cs may be incorporated into secondary, alternated mineral during migration to the surface. Thus, we infer that the hot springs in the two areas may derive from different heat sources.

5.2. Trace Element Geochemistry. Lithium (Li), rubidium (Rb), and cesium (Cs) generally act as less reactive and conservative elements in thermal waters and help to identify the existence of a common origin or of common deep processes shaping the composition of the surface water discharges [21]. The relative contents of Li, Rb, and Cs are plotted in the ternary plot (Figure 7). All the samples are falling close to the corner of Cs, indicating that all the thermal water discharges fall in the upflow region (low Li/Cs), but with different concentrations of the two areas. Furthermore, the data points of these hot springs are far removed from the compositional area of crustal rocks, pointing toward the existence of the secondary processes during the upflow process.

TABLE 2: Ratio between Cl and B, F, SiO₂, Li, Rb, and Cs.

Sample name	B/Cl	F/Cl	SiO ₂ /Cl	Cs/Cl	Rb/Cl	Li/Cl
1	0.0292	0.4188	9.3960	0.0229	0.0124	0.0663
2	0.0230	0.4205	10.2262	0.0214	0.0149	0.0482
3	0.0258	0.4183	8.6482	0.0229	0.0147	0.0534
4	0.0274	0.4116	9.9099	0.0248	0.0130	0.0653
5	0.0249	0.3929	6.5124	0.0182	0.0124	0.0456
6	0.0284	0.3139	6.8127	0.0114	0.0134	0.0604
7	0.0258	0.3677	10.7527	0.0538	0.0323	0.1172
8	0.0287	0.3906	8.5288	0.0211	0.0136	0.0669
9	0.0226	0.4167	7.2293	0.0225	0.0154	0.0470
10	0.0182	1.5609	6.1433	0.0091	0.0046	0.0205
11	0.0021	0.2187	8.0780	0.0209	0.0084	0.0313
12	0.0389	0.5501	6.4895	0.0284	0.0241	0.0735
13	0.0006	0.5363	6.3095	0.0256	0.0208	0.0673
14	0.0041	0.5422	4.3709	0.0254	0.0224	0.0478
15	0.1031	0.1304	2.2398	0.0201	0.0053	0.0646
16	0.1101	0.1095	1.5489	0.0207	0.0025	0.0681
17	0.1132	0.1248	2.8090	0.0213	0.0044	0.0678
18	0.1065	0.0982	1.7778	0.0198	0.0026	0.0650
19	0.1121	0.1140	1.6837	0.0202	0.0023	0.0687
20	0.1104	0.1026	1.7739	0.0181	0.0024	0.0655
21	0.0893	0.0662	1.1351	0.0227	0.0096	0.0896
22	0.0914	0.0665	1.1818	0.0234	0.0100	0.0943
23	0.0815	0.0670	1.1379	0.0238	0.0108	0.0775
24	0.0848	0.0715	1.4296	0.0259	0.0031	0.0494

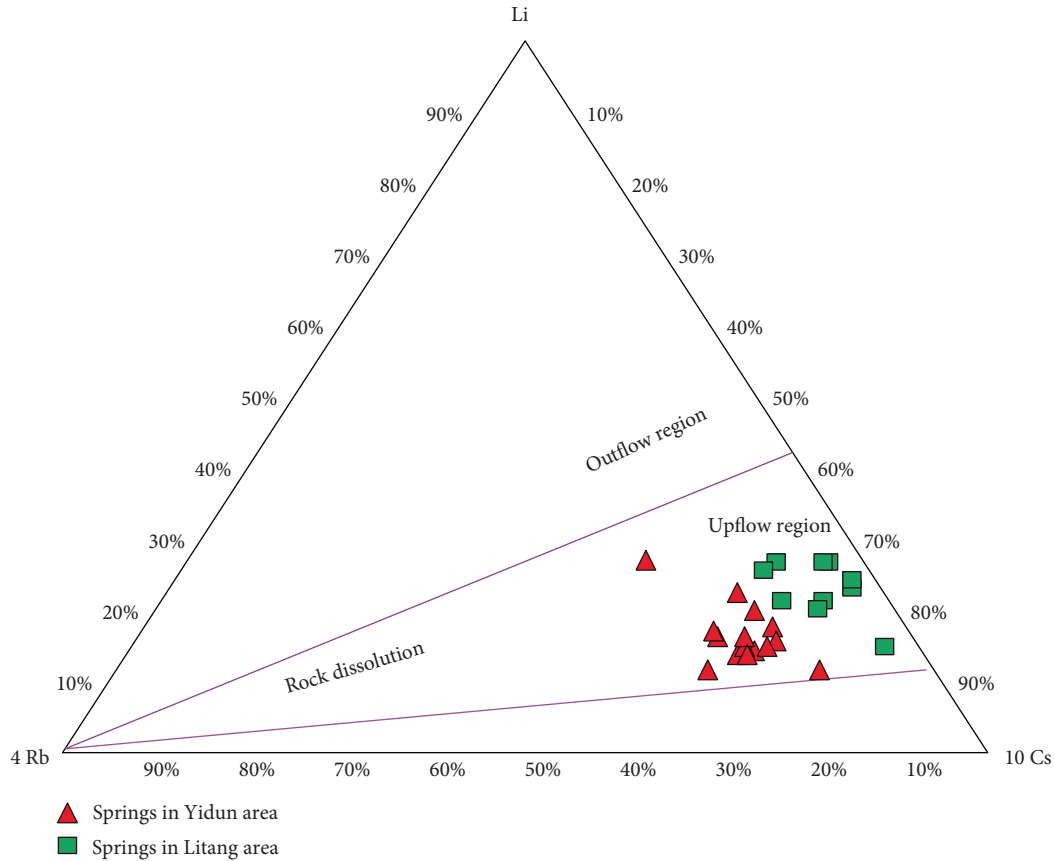


FIGURE 7: Li-Rb-Cs ternary diagram of the hot springs.

Li, as a good tracer for initial deep rocks, is used to evaluate the possible origin of boron and chloride (another two conservative constituents in hot water) [22]. In the Cl-Li-B ternary plot, most of the hot springs fall close to the compositional area of the crustal rocks, indicating that rock leaching is the main contributing factor for boron and lithium concentrations in these thermal waters (Figure 8). And it can be concluded that there is no absorption of magmatic vapour (low B/Cl or high B/Cl steam); thus, these hydrothermal systems have no association with any volcanic/magmatic activity. For the hot springs in Chaluo and Litang areas, although the concentrations of these elements are located in similar locations in Li-Rb-Cs and Cl-Li-B ternary plots, two distinct clusters could be found (Figures 7 and 8), again supporting that the hot springs of the two areas originate from different sources.

5.3. Origin of the Water by O and H Isotope. Although the hydrogen and oxygen stable isotope data of the hot springs show a meteoric source of groundwater, they do not originate from the local surface water as the stable isotope values are more negative than those of the local surface water (Figure 3) and may be recharged from the high mountains. The recharge location of these hot springs can be roughly estimated by using the isotope altitude effect [23]. Because of the significant ^{18}O shift and water-rock interaction in the hydrothermal systems, we choose deuterium as a trace to

estimate the recharge altitude. Taking the altitude effect of $-2.6\text{‰}/100\text{ m}$ for the deuterium isotope [24], we obtained the approximate recharge locations of number 5, number 12, number 16, and number 22 spring as 4300 m, 4640 m, 4750 m, and 5200 m, respectively. Thus, the recharge altitude of the hydrothermal system in the Yidun area (number 5, number 12) is lower than that of the Litang area (number 16, number 22). Both of them received recharges from the different high mountains nearby.

Furthermore, a good linear relationship of δD and $\delta^{18}\text{O}$ can be both found for hot springs in Yidun and Litang areas (with square correlation coefficients of 0.602 and 0.697, resp.). Such good linear relationship is likely caused by subsurface boiling when the high-temperature geothermal waters uprising towards the surface exceed the hydrostatic burden; the slope of such process is commonly slight [25]. Thus, the supply of hot water is primarily dependent on atmospheric precipitation and surface water infiltration along the fault zone; after being heated by the deep heat source, they return to the surface along different subfaults with different geochemical processes. The different isotope shift of springs in the Chaluo and Litang areas indicates the different subsurface properties of the reservoirs in the two areas.

The time that meteoric water spends in the geothermal system being heated, reacting with rocks, stored in the reservoir, and finally discharged at the surface can be estimated

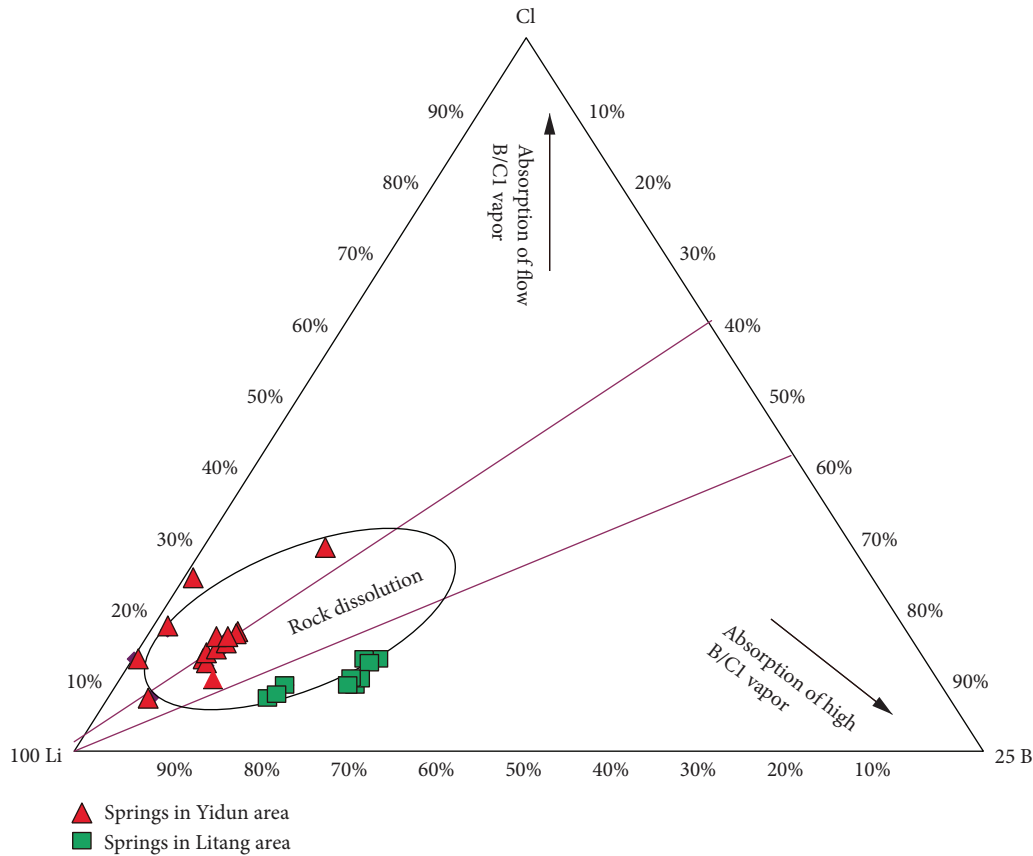


FIGURE 8: Cl-Li-B ternary diagram of the hot springs.

from the radioactive isotopes [20]. Although tritium can only be used for waters with short residence time, it is still insightful to estimate the geothermal fluid ages and identify the possible geothermal processes during the geothermal fluid evolution. In our samples, only the number 10 hot spring shows a tritium value larger than 1 (2.4 ± 1.4 TU), indicating that the number 10 spring is mixing with more modern water (shallow cold water) recharge and has a younger age than the other springs. Although no tritium is measured in the number 11 well, a similar low Li/Cl ratio with the number 10 well also indicates the mixing of shallow meteoric water (Table 2).

5.4. Geothermal Characteristic. Subsurface reservoir temperature is one of the most important characteristics in assessing the potential of geothermal resources. Several chemical geothermometers based on the chemical composition of thermal water can be used in calculating the reservoir temperature [21]. A temperature equation for a geothermometer is a temperature equation for a specific equilibrium constant referring to a specific mineral-solution reaction under specific conditions [26, 27]. The silica and cationic geothermometers (Na-K, Na-K-Ca, and K-Mg) are the most commonly applied [26]. Silica-quartz/chalcedony-based geothermometers are widely applied to calculate the temperature of low enthalpy reservoirs [28]. The Na-K geothermometer is mostly applicable to reservoir temperatures above 150°C and may yield erroneous values for low-temperature waters [29], while the

Na-K-Ca geothermometer is more suitable for waters with high Ca contents [30]. Thus, different chemical geothermometers applied to the same geothermal fluid yield appreciably different subsurface temperatures due to the lack of attainment of equilibrium between fluid and hydrothermal minerals or as a result of mixing with shallow groundwater or degassing during upflow [31], which can have important effects on geothermometry calculations—especially for silica geothermometers.

The reservoir temperatures estimated by chalcedony, quartz, Na-K-Ca, Na-K-Mg, Na-K, K-Mg, and Na-Li geothermometers are listed in Table 3. All the calculated reservoir temperatures are higher than the discharge temperature. Although the reservoir temperature varies with the different geothermometers, the estimated subsurface reservoir temperatures in the Yidun area (number 1~number 14 spring) are generally higher than that of the Litang area (number 15~number 24 spring) (Table 3). The silica geothermometers produced similar reservoir temperatures with the cation geothermometers in the Chaluo geothermal field (number 1~number 9). The low reservoir temperature in number 10 spring may be caused by the mixing of shallow cold water or other shallow surface processes as it shows local shallow water characteristics. For the other springs, the estimated reservoir temperatures by silica geothermometers and K-Mg geothermometers are lower than by other cation geothermometers. The good linear relationship between Cl

TABLE 3: Estimated reservoir temperature ($^{\circ}\text{C}$) for thermal waters.

Sample name	Chalcedony conductive	Quartz conductive	Quartz adiabatic	Na-K-Ca	Na-K-Ca Mg corr	Na/K [30]	K/Mg Giggenbach 1986	Na-Li
1	233	246	218	207	207	197	182	246
2	250	262	228	218	218	200	194	217
3	236	249	220	220	220	200	175	230
4	251	264	230	225	225	199	195	250
5	194	212	193	192	186	196	139	220
6	146	169	159	177	168	197	121	214
7	110	137	133	96	96	229	117	242
8	231	244	217	213	213	203	193	252
9	224	238	212	217	217	203	185	215
10	76	106	106	81	81	127	74	97
11	120	146	140	167	24	186	77	99
12	114	140	135	174	149	197	109	172
13	114	141	135	190	112	196	110	168
14	93	121	119	172	149	195	109	142
15	88	117	115	173	11	158	89	136
16	71	102	102	170	15	159	90	140
17	90	118	117	169	16	161	87	138
18	77	107	107	161	45	160	91	137
19	74	104	104	167	18	159	89	142
20	81	111	110	171	15	159	90	144
21	100	128	125	221	55	230	113	294
22	100	128	125	213	62	231	111	302
23	96	124	121	217	60	231	112	269
24	80	110	109	184	9	183	84	190

and the conservation species indicate the mixing processes and dilution for these hot springs (Figure 5); thus, it is expected that the silica geothermometers and K-Mg geothermometers will show lower reservoir temperature than the other cation geothermometers. The Na-K-Mg ternary diagram shows that these hot springs are located on the isothermal line of $220\sim 240^{\circ}\text{C}$ and shows a linear trend from full equilibrium to disequilibrium water area, especially for the hot springs in the Yidun area (Figure 9). Hot springs located in the Chaluo geothermal field are mostly located in the partial equilibrium area while other springs are located in the disequilibrium water area (Figure 9) [32]. Thus, the K-Mg geothermometer and silica geothermometer may not be appropriate for the reservoir temperature calculation as both will be largely affected by the dilution processes. The $10/(10\text{K} + \text{Na})$ versus $10\text{Mg}/(10\text{Mg} + \text{Ca})$ diagram proposed by Giggenbach [32] (Figure 10) also shows the deviation of hot springs from the full equilibrium line, and the high Ca + Mg concentration in the Litang area (numbers 15–24) may indicate the faster equilibration of K-Mg and mixing with Ca-Mg-rich shallow waters [33]. This also explains why the reservoir temperatures calculated by the silica and K-Mg geothermometer are much lower than the other cation geothermometer in the Litang area. Thus, the Na-K and Na-Li geothermometers tend to provide more reliable

reservoir temperatures since they are less influenced by SiO_2 reequilibration and mixing with Ca-Mg-rich shallow water than the other geothermometers in the Litang area.

According to the above discussion, hot springs in the Litang area are located in a nonequilibrium state and may be affected by the mixing (dilution) processes, which is also indicated by the good linear relationship of B/Cl, F/Cl, and SiO_2/Cl in Maoya and Qukailong (Figure 6). Here, we use the silica-enthalpy method [34] to evaluate the temperature of the hot water component before mixing. The temperature of cold water is assumed as 15°C and SiO_2 concentration of 10mg/L ; we use the average spring temperature of 50°C and SiO_2 of 51mg/L for the springs in the Maoya geothermal field. The calculated SiO_2 concentration in the reservoir is about 200mg/L , with temperature of 207°C . And a similar result could be obtained for the hot springs in the QKL geothermal field. The mixing ratio in this area is $0.6\sim 0.74$ for cold water. Thus, we can roughly get the conclusion that the reservoir temperature in the Yidun area is around 230°C and is around 200°C in the Litang area. Thus, the reservoir temperature also supports that the Yidun area and the Litang area should have different heat sources.

From the chemical and geothermal analysis, we propose a conceptual model for the genesis mechanism of the hydrothermal system in the Yidun and Litang areas.

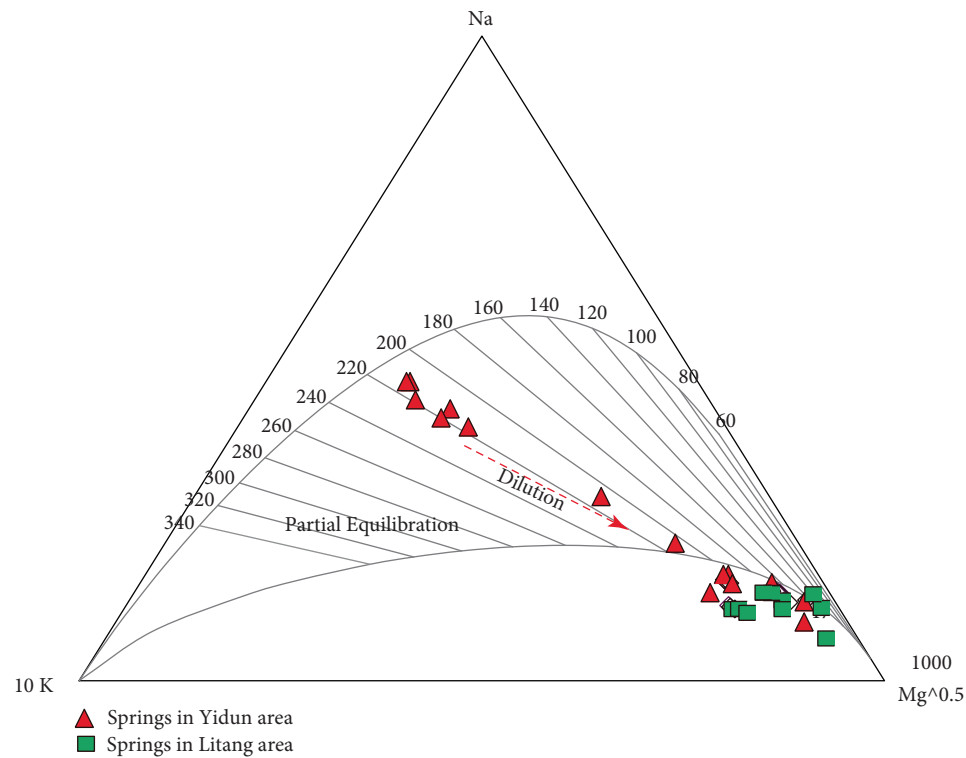


FIGURE 9: Na-K-Mg ternary diagram of the hot springs.

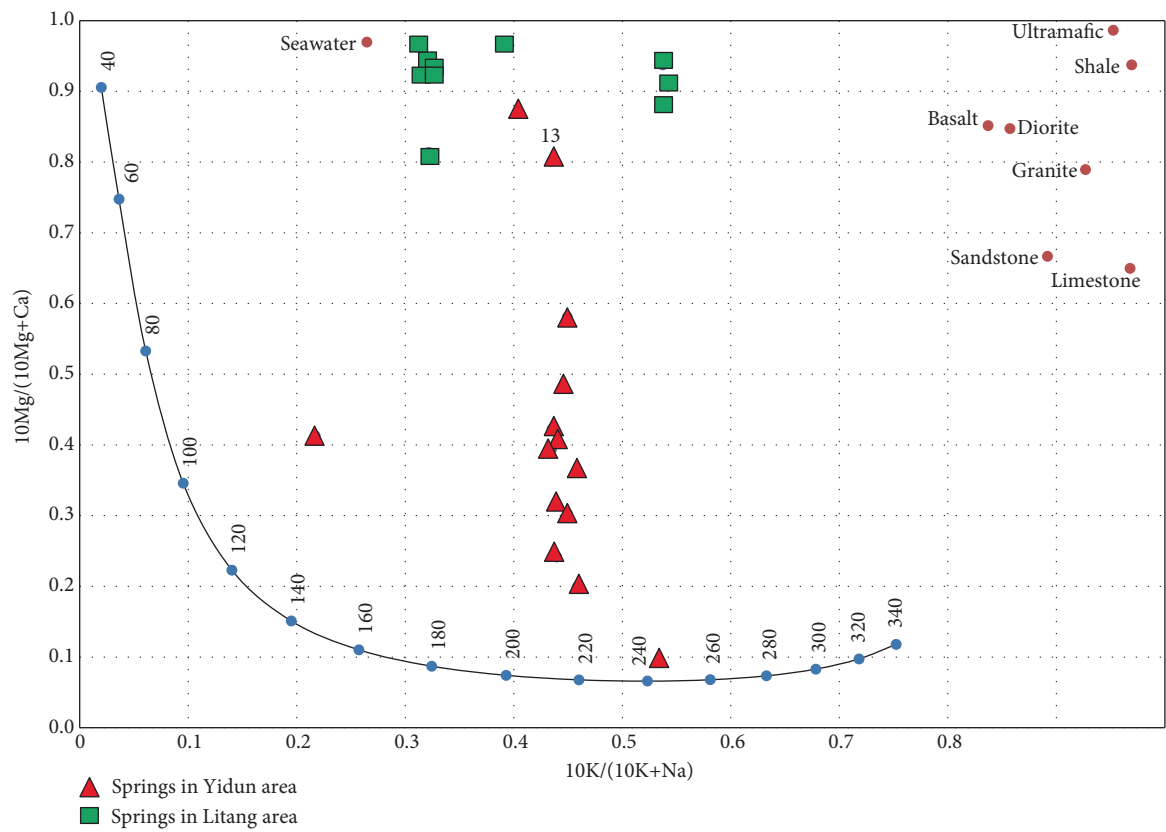


FIGURE 10: 10 Mg/(10 Mg + Ca) versus 10 K/(10 K + Na) binary diagram.

Meteoric precipitation penetrates into the crust, is heated by the different deep, thermally and topographically driven convection along faults, and undergoes subsurface boiling before going back to the surface. The same chemistries in the two areas may be caused by the same host rock in the different fault zones. Although the measured age of the magmatic rock revealed that the magmatic residual heat has disappeared [8], the residual radioactive decay in rock will continue to heat the water during the circulation [17].

6. Conclusions

The geochemical and geothermal characteristics of the fault zone hydrothermal system in the Yidun-Litang area are investigated in this paper. Na-HCO₃ water is the dominant water type in the Yidun-Litang area. Water-rock interaction and cation exchange are the dominant hydrogeochemical processes in the hydrothermal evolution. The D and ¹⁸O isotopes of all the hot springs show a linear shift from the GMWL, indicating that these springs have undergone subsurface boiling before rising to the surface. Different ratios of Cl to other conservation species can be found for the springs in the Litang and Yidun areas, suggesting the different heat sources of the two hydrothermal systems. The reservoir temperature in the Yidun area is around 230°C while the reservoir temperature in the Litang area is around 200°C. Both hydrothermal systems are recharged by the meteoric water and are heated by the different deep, thermally and topographically driven convection heat along faults and undergoing subsurface boiling before going back to the surface.

Conflicts of Interest

The authors declare that they have no conflicts of interest.

Acknowledgments

The authors greatly thank Xianhe Yang and Haijiang Niu for their help in the field. This work is supported by the National Natural Science Foundation of China (41602266 and U1602233), the Fok Ying Tung Education Foundation (161014) and partly support from the Engineering Research Center of Geothermal Resources Development Technology and Equipment, Ministry of Education, Jilin University.

References

- [1] C. Apollaro, G. Vespasiano, R. De Rosa, and L. Marini, "Use of mean residence time and flowrate of thermal waters to evaluate the volume of reservoir water contributing to the natural discharge and the related geothermal reservoir volume. Application to Northern Thailand hot springs," *Geothermics*, vol. 58, pp. 62–74, 2015.
- [2] Ö. Avşar, N. Güleş, and M. Parlaktuna, "Hydrogeochemical characterization and conceptual modeling of the Edremit geothermal field (NW Turkey)," *Journal of Volcanology and Geothermal Research*, vol. 262, pp. 68–79, 2013.
- [3] W. F. Giggenbach, "Variations in the chemical and isotopic composition of fluids discharged from the Taupo Volcanic Zone, New Zealand," *Journal of Volcanology and Geothermal Research*, vol. 68, no. 1–3, pp. 89–116, 1995.
- [4] Q. Guo and Y. Wang, "Geochemistry of hot springs in the Tengchong hydrothermal areas, Southwestern China," *Journal of Volcanology and Geothermal Research*, vol. 215–216, pp. 61–73, 2012.
- [5] T. Özen, A. Bülbül, and G. Tarcın, "Reservoir and hydro-geochemical characterizations of geothermal fields in Salihli, Turkey," *Journal of Asian Earth Sciences*, vol. 60, pp. 1–17, 2012.
- [6] D. M. Han, X. Liang, M. G. Jin, M. J. Currell, X. F. Song, and C. M. Liu, "Evaluation of groundwater hydrochemical characteristics and mixing behavior in the Daying and Qicun geothermal systems, Xinzhou Basin," *Journal of Volcanology and Geothermal Research*, vol. 189, no. 1–2, pp. 92–104, 2010.
- [7] Z. Shi, F. Liao, G. Wang, Q. Xu, W. Mu, and X. Sun, "Hydro-geochemical characteristics and evolution of hot springs in eastern Tibetan Plateau geothermal belt, western China: insight from multivariate statistical analysis," *Geofluids*, vol. 2017, Article ID 6546014, 11 pages, 2017.
- [8] X. Tang, J. Zhang, Z. Pang, S. Hu, Y. Wu, and S. Bao, "Distribution and genesis of the eastern Tibetan Plateau geothermal belt, western China," *Environmental Earth Sciences*, vol. 76, no. 1, p. 31, 2017.
- [9] W. Tong and M. Zhang, *Chorography of Spring in the Hengduan Mountainous District*, Science Press, Beijing, 1994.
- [10] D. Curewitz and J. A. Karson, "Structural settings of hydrothermal outflow: fracture permeability maintained by fault propagation and interaction," *Journal of Volcanology and Geothermal Research*, vol. 79, no. 3–4, pp. 149–168, 1997.
- [11] J. Fairley, J. Heffner, and J. Hinds, "Geostatistical evaluation of permeability in an active fault zone," *Geophysical Research Letters*, vol. 30, no. 18, 2003.
- [12] Z. Shi and G. Wang, "Evaluation of the permeability properties of the Xiaojiang Fault Zone using hot springs and water wells," *Geophysical Journal International*, vol. 209, no. 3, pp. 1526–1533, 2017.
- [13] R. Favara, F. Grassa, S. Inguaggiato, and M. Valenza, "Hydro-geochemistry and stable isotopes of thermal springs: earthquake-related chemical changes along Belice Fault (Western Sicily)," *Applied Geochemistry*, vol. 16, no. 1, pp. 1–17, 2001.
- [14] A. Skelton, M. Andrén, H. Kristmannsdóttir et al., "Changes in groundwater chemistry before two consecutive earthquakes in Iceland," *Nature Geoscience*, vol. 7, no. 10, pp. 752–756, 2014.
- [15] J. P. Toutain, M. Munoz, F. Poitrasson, and A. C. Lienard, "Springwater chloride ion anomaly prior to a M_L = 5.2 Pyrenean earthquake," *Earth and Planetary Science Letters*, vol. 149, no. 1–4, pp. 113–119, 1997.
- [16] X. Zhou, L. Liu, Z. Chen, Y. Cui, and J. Du, "Gas geochemistry of the hot spring in the Litang fault zone, Southeast Tibetan Plateau," *Applied Geochemistry*, vol. 79, pp. 17–26, 2017.
- [17] J. Zhang, W. Li, X. Tang et al., "Geothermal data analysis at the high-temperature hydrothermal area in Western Sichuan," *Science China Earth Sciences*, vol. 60, no. 8, pp. 1507–1521, 2017.
- [18] X. Xu, X. Wen, G. Yu, R. Zheng, H. Luo, and B. Zheng, "Average slip rate, earthquake rupturing segmentation and recurrence behavior on the Litang fault zone, western Sichuan Province, China," *Science in China Series D*, vol. 48, no. 8, pp. 1183–1196, 2005.

- [19] P. Ravikumar and R. K. Somashekar, "Environmental tritium (^3H) and hydrochemical investigations to evaluate groundwater in Varahi and Markandeya river basins, Karnataka, India," *Journal of Environmental Radioactivity*, vol. 102, no. 2, pp. 153–162, 2011.
- [20] K. Nicholson, *Geothermal Fluids: Chemistry and Exploration Techniques*, Springer-Verlag, Berlin, 1993.
- [21] S. Chatterjee, A. Sarkar, A. S. Deodhar et al., "Geochemical and isotope hydrological characterisation of geothermal resources at Godavari valley, India," *Environmental Earth Sciences*, vol. 76, no. 2, p. 97, 2017.
- [22] W. F. Giggenbach, *Collection and Analysis of Geothermal and Volcanic Water and Gas Discharges*, vol. 81, DSIR Chemisty, New Zealand, 1989.
- [23] W. G. Darling, A. H. Bath, and J. C. Talbot, "The O and H stable isotope composition of freshwaters in the British Isles. 2. Surface waters and groundwater," *Hydrology and Earth System Sciences*, vol. 7, no. 2, pp. 183–195, 2003.
- [24] Y. Guan and F. Xiao, "Isotope trace of water circulatory system in Jiuzhaigou Sichuan province," *Journal of Geographical*, vol. 55, no. 4, pp. 487–494, 2000.
- [25] W. F. Giggenbach and M. K. Stewart, "Processes controlling the isotopic composition of steam and water discharges from steam vents and steam-heated pools in geothermal areas," *Geothermics*, vol. 11, no. 2, pp. 71–80, 1982.
- [26] S. Arnórsson, *Isotopic and Chemical Techniques in Geothermal Exploration, Development and Use*, International Atomic Energy Agency, 2000.
- [27] J. Qi, M. Xu, C. An et al., "Characterizations of geothermal springs along the Moxi deep fault in the western Sichuan plateau, China," *Physics of the Earth and Planetary Interiors*, vol. 263, pp. 12–22, 2017.
- [28] R. O. Fournier, "Chemical geothermometers and mixing models for geothermal systems," *Geothermics*, vol. 5, no. 1–4, pp. 41–50, 1977.
- [29] S. Arnórsson, "Chemical equilibria in icelandic geothermal systems—implications for chemical geothermometry investigations," *Geothermics*, vol. 12, no. 2–3, pp. 119–128, 1983.
- [30] R. O. Fournier, "Geochemical and hydrologic considerations and the use of enthalpy-chloride diagrams in the prediction of underground conditions in hot-spring systems," *Journal of Volcanology and Geothermal Research*, vol. 5, no. 1–2, pp. 1–16, 1979.
- [31] M. I. M. Burgos, *Geochemical Interpretation of Thermal Fluid Discharge from Wells and Springs in Berlín Geothermal Field, El Salvador*, United Nations University, 1999.
- [32] W. F. Giggenbach, "Geothermal solute equilibria. Derivation of Na-K-Mg-Ca geothermometers," *Geochimica et Cosmochimica Acta*, vol. 52, no. 12, pp. 2749–2765, 1988.
- [33] Q. Guo, Z. Pang, Y. Wang, and J. Tian, "Fluid geochemistry and geothermometry applications of the Kangding high-temperature geothermal system in eastern Himalayas," *Applied Geochemistry*, vol. 81, pp. 63–75, 2017.
- [34] A. H. Truesdell and R. O. Fournier, "Procedure for estimating the temperature of a hot-water component in a mixed water by using a plot of dissolved silica versus enthalpy," *Journal of Research of the U. S. Geological Survey; (United States)*, vol. 5, p. 1, 1977.

Research Article

Investigation on the Relationship between Wellhead Injection Pressure and Injection Rate for Practical Injection Control in CO₂ Geological Storage Projects

Bing Bai , Haiqing Wu , and Xiaochun Li

State Key Laboratory of Geomechanics and Geotechnical Engineering, Institute of Rock and Soil Mechanics, Chinese Academy of Sciences, Wuhan 430071, China

Correspondence should be addressed to Bing Bai; bai_bing2@126.com

Received 31 January 2018; Accepted 3 April 2018; Published 25 June 2018

Academic Editor: Liangping Li

Copyright © 2018 Bing Bai et al. This is an open access article distributed under the Creative Commons Attribution License, which permits unrestricted use, distribution, and reproduction in any medium, provided the original work is properly cited.

The existing investigations on the maximum allowable wellhead injection pressure have found the upper limit of wellhead injection pressure, which, however, cannot provide a practical operational designing scheme of wellhead injection parameters for CO₂ geological storage projects. Therefore, this work firstly proposes the complete constraint conditions of wellbore injection to realize the whole process of forward and inverse calculations of wellbore pressure and then applies it to explore the relationship between wellhead injection pressure and injection rate. The results show that the wellhead injection pressure and the injection rate are a pair of mutually constrained physical quantities. For a certain injection project, the allowable wellhead injection pressure and injection rate separately form a continuous interval. Change of one quantity within its allowable interval will also change the other within its interval, both jointly forming a closed region. Thus, controlling the wellhead injection parameters in this closed region can simultaneously ensure the effectiveness and safety of injection. Subsequently, this work further studies the factors of impacting the relationship between wellhead injection pressure and injection rate and finds that all the temperature of injected fluid, the parameters of saturation, and the characteristic parameters of reservoirs only change their upper and lower limits to some extent but have no essential effects on their relationship. Application of this theory and method in Shenhua CCS demonstration project obtained the relationship diagram of wellhead injection pressure and injection rate, which found that its actual injection parameters just fall into the closed region of the relationship diagram, effectively verifying the reliability of this work.

1. Introduction

In the China-US joint announcement on climate change, 2014, China intended to achieve the peaking of CO₂ emissions around 2030 and to make best efforts to peak early [1]. To achieve this goal, carbon capture and storage (CCS), as one of the most effective approaches for greatly reducing CO₂ level in the atmosphere [2–5], is expected to gradually advance from demonstration project to commercialization. The general procedure of CO₂ geological storage includes site selection, well drilling, injection, monitoring, and evaluation [6, 7], among which the most key step is CO₂ injection. Therefore, it is very important to control wellbore injection parameters [8, 9]. Due to the great burial depth of the storage sites (means high temperature and high pressure),

CO₂ injection (resulting complex two-phase flow in pores and cracks), and the complexity and uncertainty of geological conditions, a great challenge to the effectiveness and safety of CO₂ injection is induced [2, 10].

Currently, it is widely accepted by engineers that controlling the maximum bottom hole pressure is practical and reliable to avoid the strata fracturing [11–13]. Based on that, the more convenient method is to control the wellhead injection pressure [13], which has been verified sufficiently in In Salah [14] and Ketzin and Shenhua CCS projects [13, 15]. To obtain the maximum allowable wellhead injection pressure for CCS projects, Carroll and Lui [16] and Hashim and Maloka [17] analyzed the main influential factors of wellhead pressure, and Streit and Hillis [18], Rutqvist et al. [10], and Gapillou et al. [19] proposed some approximate

estimation methods and engineering experience. Subsequently, Bai et al. [8] developed a new fast explicit finite difference method (FEFDM) for calculating the wellhead pressure under assumption of single reservoir, and Wu et al. [20] presented a new estimation method of wellbore pressure from the perspective of engineering. However, many CCS projects still use the typical approach referring from the field of enhanced oil recovery (EOR) and sour gas reinjection for the advantages of simplicity and extensive application experience [21], although there are four obvious shortcomings [13]. Therefore, Bai et al. [13] developed a methodology for determining the maximum allowable wellhead injection pressure based on the precious work recently, which includes the control conditions for bottom hole safety, the inversion method of wellhead pressure, and the design coefficients on the basis of engineering experience and analogy. It is available for multireservoirs injection simultaneously. However, it is worthy to concern that the above investigations are mainly focused on the wellhead injection pressure, especially on the maximum allowable wellhead injection pressure, which ignores the wellhead injection rate. Although the injection rate is usually set as the project target, it is also a significant parameter of injection control. What is more, no investigation has addressed the relationship between wellhead injection pressure and injection rate.

Thus, as to a determined target injection flow, the above methods of designing wellhead injection pressure can only provide the maximum allowable wellhead injection pressure. However, the actual wellhead injection pressure must be less than its maximum value in consideration of safety, so how much should the applicable wellhead injection pressure be? Could any wellhead injection pressure bellowing the maximum allowable wellhead injection pressure ensure that the target injection flow will enter the reservoirs completely? Of course, the answer is no. That is to say, the applicable wellhead injection pressure not only has an upper limit but also has a lower limit. Only the pressure of ranging from the lower limit to the upper limit can ensure that the target injection flow will enter the reservoirs completely. Another question is how does the applicable wellhead injection pressure change when the target injection flow changes? It would be transferred to the schema of constant pressure controlling; thus the problem is how to determine the applicable target injection flow under knowing the wellhead injection pressure. Apparently, to answer these questions exactly, it is necessary to investigate the wellhead injection pressure and the injection rate simultaneously and to master the internal relationship between wellhead injection pressure and injection rate clearly. In addition, to facilitate the application in projects, it is worthy to study their influential factors.

Therefore, this work will firstly improve the constraint conditions of wellbore injection from the perspective of flow rate to realize the whole process of forward and inverse calculations of wellbore pressure and then explore the relationship between wellhead injection pressure and injection rate and its influential factors. Finally, we apply this method to Shenhua CCS demonstration project to find the feasible ranges of wellhead injection pressure and injection rate and to verify the reliability of this work simultaneously.

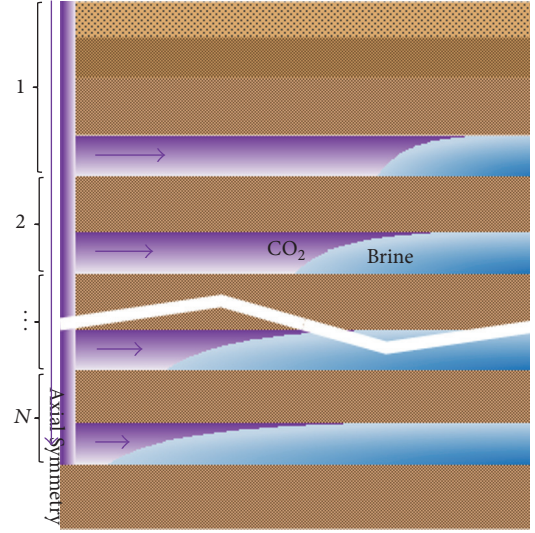


FIGURE 1: Schematic of the injection well and its related reservoirs.

2. Theory and Method

2.1. Constraint Conditions of Wellbore Injection. Figure 1 shows the schematic of injection wellbore and its related reservoirs. There is one injection well and N layers of reservoir-caprock combination units from top to bottom. The wellbore is divided into N segments by the reservoir-caprock unit. The reservoir-caprock units, reservoirs, caprocks, and well segments are numbered as $1, 2, \dots, N$ from top to bottom. In the following, the subscript i denotes the corresponding physical quantities of the i th reservoir-caprock unit, the superscript r indicates the physical quantities within the reservoir, and the superscript w marks the physical quantities within the well segments.

As described in Bai et al. [13], when CO_2 is injected at a given wellhead injection pressure P_{WH} [Pa] into the injection well, the flow not only should satisfy its related fluid dynamics equations but also should not damage the stratum. Moreover, the injection rate C_{WH} [kg/s] should reach the preset target injection flow. These are enough for the inverse calculation of wellhead injection parameters based on the bottom hole conditions, whereas for the forward calculation of wellbore pressure and flow rate distribution on the basis of wellhead injection parameters, they are not enough because the forward calculation is unable to ensure that the injected fluid will enter reservoirs completely only from the perspective of pressure. Therefore, to realize the process of forward calculation, C_{WH} must be less than the total available capacity of all the reservoirs and the actual flow rate of each reservoir also must be below its available capacity; then the effectiveness and safety of injection can be ensured.

Hence, the complete constraint conditions of wellbore injection are

$$\begin{aligned} P_{0i} + P_{bi} &< P_{ki} \leq [P_{ki}] \\ M_0 &\leq C_{\text{WH}} = \sum C_i \leq \sum [C_i] \\ C_i &\leq [C_i], \end{aligned} \quad (1)$$

where P_0 is the formation pressure (Pa), P_b is the capillary pressure (Pa), P_k is the pressure on the interface of wellbore and reservoir (Pa), $[P_k]$ is the maximum allowable pressure of reservoir (Pa), M_0 is the target injection flow rate (kg/s), C denotes the actual flow rate of the reservoir (kg/s), and $[C]$ denotes the available capacity of reservoir (kg/s).

The first inequality of (1) is the constraint condition about pressure. The maximum allowable pressure is a reduced value of fracturing pressure [22]; details can be found in Bai et al. [13]. The other two inequalities represent the constraint conditions about flow rate. And the second one is focused on the total flow rate, which requires the injection rate to be higher than the design target but lower than the total available capacity of all the reservoirs. The third one requires the actual flow rate of each reservoir to be within its available capacity. Obviously, when the third inequality is satisfied, the right half of the second one is met naturally, while the left half of the second one could be confirmed in the feasibility study of project. Therefore, the constraint conditions about flow rate are equivalent to the third inequality in essence. Furthermore, in the actual calculations, only the available capacity of the bottom reservoir needs to be checked because the capacity of the other reservoirs is just equal to their actual flow rate, which is calculated by the following calculation method. Therefore, they always satisfy (1). It should be noted that the above constraint conditions did not involve the caprocks, which are beyond our discussion.

2.2. Calculation Method. As mentioned above, inverting wellhead parameters based on the bottom hole conditions only can find their maximum value, which, however, can only be used as the upper limit of injection control. Therefore, in practical operation, it is necessary to directly calculate the wellbore pressure and flow rate distribution according to the given wellhead injection parameters and then to judge whether the injection is safe and effective. It is a forward calculation process. The fast explicit finite difference model (EFDM) from wellhead to bottom can be derived based on the continuity equation of steady flow, the motion equation of vertical wellbore, and the state equation of fluid [8, 9] as follows:

$$P_{j+1} = P_j + \frac{(\Delta x g (P_j^3 M / RT_j Z_j) - (\Delta x \gamma \bar{C}_j^2 RT_j / 2D) (Z_j P_j / M))}{(P_j^2 - (\bar{C}_j^2 RT_j / M) Z_j)}, \quad (2)$$

where P is the wellbore pressure (Pa); \bar{C} is the mass flow rate of wellbore cross section (kg/m²/s); Δx is the differential element (m); g is the acceleration of gravity (m/s²); D is the interior diameter of injection tube (m); M is the molar mass of gas (kg/mol); R is the universal gas constant; γ is the friction coefficient; Z is the compression factor; and T is the temperature (K). The subscript j is the number of differential elements within a certain well segment.

CO₂ is injected from wellhead through wellbore into the reservoirs; due to the presence of brine in the reservoir pores, the flow changes into two-phase flow [23–25]. In accordance

with the two-phase flow theory, the fluid-rock characters determine the relative permeability of each phase [26–29]. The functional relationship of the flow rate flowing into the i th reservoir and the pressure can be obtained under the assumption of steady flow [27], or

$$C_i^r = 2\pi k_i B_i \rho_i^w \cdot \frac{P_{ki} - P_{0i}}{(1/\lambda_{ci}) \ln(R_{ci}/r_0) + (1/\lambda_{wi} - 1/\lambda_{ci}) + (1/\lambda_{wi}) \ln(R_{0i}/R_{maxi})}, \quad (3)$$

where R_0 is the maximum influence radius of flow in the reservoir (m); R_c and R_{max} are the maximum radii of CO₂ plume at the bottom and top of the reservoir (m), respectively; r_0 is the tubing radius (m); k is the absolute permeability of the reservoir (m²); B is the thickness of the reservoir (m); φ is the porosity of the reservoir; ρ is the density of CO₂ (kg/m³); λ_c is the mobility of CO₂ (m·s/kg); and λ_w is the mobility of brine (m·s/kg).

On the basis of (2) and (3), to realize the multireservoir injection simultaneously, the equilibrium condition of flow at the reservoir node is still required. It could be simplified into the flow rate allocation under the condition of constant pressure because all junctions of reservoirs and wellbore are regarded as the equivalent nodes of flow rate allocation and the wellbore pressure between the top and bottom of the reservoir is assumed to be a constant in this work. Hence, the equilibrium condition of flow of the i th equivalent node is that the inflow amount of CO₂ equals the sum of outflow to the next well segment and inflow into the i th reservoir. Then, combined with (3), the flow rate allocation relationship at the equivalent node can be deduced as follows [13]:

$$\bar{C}_i^w = \frac{2k_i B_i \rho_i^w}{r_0^2} \cdot \frac{P_{ki} - P_{0i}}{(1/\lambda_{ci}) \ln(R_{ci}/r_0) + (1/\lambda_{wi} - 1/\lambda_{ci}) + (1/\lambda_{wi}) \ln(R_{0i}/R_{maxi})} + \frac{\rho_i^w}{\rho_{i+1}^w} \bar{C}_{i+1}^w. \quad (4)$$

When (4) is applied to the N th reservoir (the bottom reservoir), due to the absence of outflow, the second term of right hand should be considered as zero. Then, according to (4), the available capacity of the bottom reservoir can be determined. And the actual flow rate of the bottom reservoir is obtained by (4) with $i = N - 1$. So that when the latter is not more than the former, the constraint conditions about flow rate are satisfied.

2.3. Calculation Procedure. There are two basic control models on fluid injection, namely, the constant pressure and the constant flow rate. For constant pressure, the allowable interval of flow rate should be solved; and as for constant flow rate, the problem is how to obtain the allowable interval of pressure. However, the results under different control models are the same. Therefore, this work chooses the control model of constant pressure as an example to explore the relationship between wellhead injection pressure and injection rate. The calculation procedures of forward calculation process are listed as follows:

TABLE 1: The parameters of reservoir-caprock combination units.

Reservoir number	Reservoir thickness (m)	Caprock thickness (m)	Reservoir permeability ($\times 10^{-3} \mu\text{m}^2$)	Reservoir porosity (%)	Fracturing pressure (MPa)	Formation pressure (MPa)
1	10	1400	6	12	35	15
2	10	200	5	11	38	17
3	10	200	4	10	41	19
4	10	200	3	9	44	21

TABLE 2: The simulation injection design schemes.

Injection design schemes	(a)	(b)	(c)	(d)	(e)	(f)	(g)	(h)
P_{WH} (MPa)	15	14.49	14	13	6	5	4.83	4.5
C_{WH} (kg/s)	0~9	0~9	0~9	0~9	0~2.5	0~2.5	0~1.1	0~2.5

Notes. The calculation step of C_{WH} in (a), (b), (c), and (d) is 0.1 kg/s; for (g) it is 0.02 kg/s; for (e), (f), and (h) it is 0.05 kg/s.

- (1) Set P_{WH} .
- (2) Set the initial C_{WH} .
- (3) Compute the wellbore pressure according to (2); compute the flow rate of flow into the reservoir according to (3) and renew the flow rate of flow to the next well segment according to (4) when the calculation reaches to the reservoir.
- (4) Judge whether the computed results at the equivalent node meet the constraint condition of (1). If “Yes,” execute the subsequent calculation; if “No,” go to Step (5). After finishing all calculation process, if the calculated results meet all the corresponding inequality conditions in (1), the corresponding P_{WH} and C_{WH} are the feasible wellhead injection parameters.
- (5) Renew C_{WH} ; repeat Step (3) to Step (4) until both the upper and lower limits of feasible C_{WH} under the condition of P_{WH} are found; if there is no feasible C_{WH} (indicating that P_{WH} cannot achieve injection), go to Step (6).
- (6) Renew P_{WH} ; repeat Step (2) to Step (5) to find the upper and lower limits of feasible P_{WH} .
- (7) Plot the relationship diagram between P_{WH} and C_{WH} according to the results.

3. Relationship between Wellhead Injection Pressure and Injection Rate

3.1. Parameters and Injection Schemes. In the following, this work supposed an analysis case to explore the relationship between P_{WH} and C_{WH} . There are four reservoirs and one injection well with a depth of 2000 meters in this case. Table 1 lists the reservoir-caprock combination units and the characteristic parameters of the reservoirs. The values of thickness, permeability, and porosity of reservoirs are determined by engineering experience, which represent the typical characteristic (small thickness, low porosity, and low permeability) of reservoirs in China. They could be updated for research.

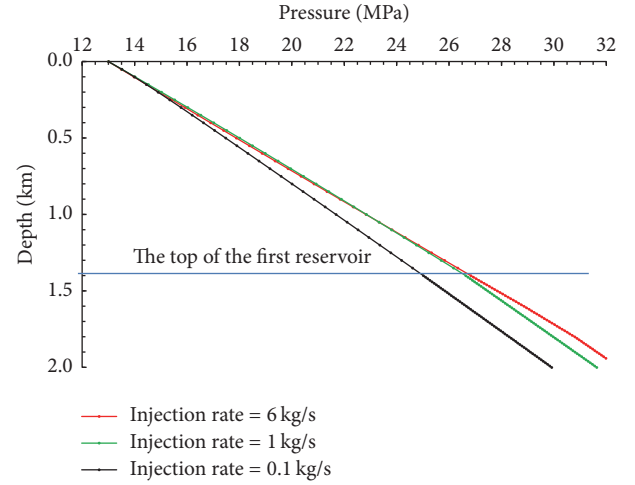


FIGURE 2: Distribution of wellbore pressure at different injection rates.

First, it is necessary to present the wellbore pressure distribution for a determined P_{WH} under different C_{WH} to analyze the characteristics of the wellbore pressure distribution, as shown in Figure 2. Here P_{WH} is given as 13 MPa, while C_{WH} are 0.1, 1, and 6 kg/s.

It is clear from Figure 2 that (1) the wellbore pressure increases approximately linearly with the well depth; the bigger C_{WH} is, the more obviously the pressure increases; when C_{WH} enlarges to a certain value, the wellbore pressure above the reservoirs barely changes with C_{WH} ; (2) the wellbore pressure distribution changes linearly and continuously with C_{WH} , showing no inflection point; thus it is appropriate to use the variation trend of wellbore pressure at one point to represent the variation trend of pressure in the whole wellbore. Therefore, in the following, the change in pressure on the interface of wellbore and reservoir is adopted to replace that of the whole wellbore.

Table 2 shows the simulation injection schemes. When P_{WH} is great enough, the lower limit of the constraint conditions about pressure expressed by the left part of the

first inequality in (1) is clearly met, so the four injection schemes (a), (b), (c), and (d) in Table 2 are adopted to study the variation rule of pressure on the interface of wellbore and reservoir with C_{WH} in the condition of no reservoir fracturing. The calculation results are shown in Figures 3(a)–3(d). Subsequently, with P_{WH} reducing, the constraint condition about pressure to prevent the reservoir from fracturing can be naturally satisfied and the lower limit of the constraint conditions about pressure should be considered. The four injection schemes (e), (f), (g), and (h) in Table 2 are adopted for that and the calculation results are shown in Figures 3(e)–3(h).

3.2. Results Analysis. There are two types of curves shown in Figures 3(a), 3(b), 3(c), and 3(d): the pressure curves and the flow rate curves. The former are used to analyze whether the calculated results meet the upper limit of the constraint conditions about pressure, and the latter are used to analyze whether the calculated results meet the constraint conditions about flow rate. The specific analyses are shown below.

(1) The dense data segments in the figure result from one-tenth of calculation step, which verified that no oscillation singularities existed in the calculations. It aims to accurately find the intersection and its corresponding C_{WH} .

(2) In Figures 3(a), 3(b), and 3(c), with C_{WH} changing, there is an interval that $P_{k1} > [P_{k1}]$; as for the other reservoirs, the similar intervals basically disappear or are included in the interval of the first reservoir, which indicates that the critical reservoir [13, 30] is the first one under the above described injection conditions. Hence, only the intersections of the curve P_{k1} and the curve $[P_{k1}]$ are shown in Figures 3(a)–3(d) as the basis for the following discussions.

(3) With C_{WH} changing, all the pressure curves P_{ki} show the same varying trend of upward convex parabola with obvious peak. Based on the above analysis and with Figure 3(a) as an example, the intersections P1 and P2 of the curve P_{k1} and the curve $[P_{k1}]$ divide C_{WH} into three intervals. It looks like C_{WH} smaller than P1 or greater than P2 would meet the upper limit of the constraint conditions about pressure. However, in fact, this is not true, because the calculations are based on the assumption that the flow in the wellbore reaches to steady state at 10 days after CO₂ injection; if greatly expanding the time, even a tiny C_{WH} will make the wellbore pressure exceed the allowable pressure at some points. Therefore, as for P_{WH} whose P1 is located before the peak point, C_{WH} less than P1 could not be used as the design scheme of the gas injection projects. Moreover, whether C_{WH} higher than P2 can be used as the design scheme still needs to be determined by the constraint conditions about flow rate, which can be judged by the flow rate curves of the last reservoir. Apparently, C_{WH} at the left side of intersection F1 of the flow rate curves meet this condition, while C_{WH} at the right side does not. Therefore, for determined P_{WH} , its corresponding C_{WH} that can be used as the design scheme of gas injection must belong to the interval of $[P2, F1]$. Among the above schemes, in Figure 3(a), F1 is smaller than P2, indicating that there is no feasible C_{WH} under this P_{WH} ; that is, this P_{WH} has exceeded the maximum allowable

wellhead injection pressure; in Figure 3(b), F1 is equal to P2, indicating that this P_{WH} is the maximum allowable wellhead injection pressure; in Figure 3(c), F1 is greater than P2, corresponding to the general cases; in Figure 3(d), only F1 exists but there is no intersection of pressure curves, revealing that no matter how C_{WH} changes, the constraint conditions about pressure will be always met under this P_{WH} ; therefore the corresponding interval of flow rate is $(0, F1]$. It is predictable that the feasible interval of C_{WH} remains $(0, F1]$ with continuous reduction of P_{WH} , although F1 will decrease with P_{WH} declining.

Figures 3(e)–3(h) are basically consistent with Figures 3(a)–3(d) except that the pressure curves in Figures 3(e)–3(h) show the lower limit of the constraint conditions about pressure. According to Figures 3(e)–3(h), (1) as for each injection scheme, the intersections of curve P_{k1} and curve P_{01} correspond to the minimum C_{WH} , indicating that the injection to the first reservoir is most easily realized. Therefore, the lower limit of the constraint conditions about pressure can be transferred into that as long as $P_{k1} > P_{01}$; the injection is achievable. (2) Similarly, conclusion (1) is only focused on the constraint conditions about pressure, and the constraint conditions about flow rate still need to be met. In summary, the feasible interval of C_{WH} is $[0, F1]$ in Figure 3(e), $[F1, F2]$ in Figure 3(f), and $F1$ in Figure 3(g) and does not exist in Figure 3(h), revealing that P_{WH} in Figure 3(g) is corresponding to the minimum achievable wellhead injection pressure. It is predictable that gradually increasing P_{WH} from the minimum achievable wellhead injection pressure will expand the feasible range of C_{WH} , which is consistent with the relationship between P_{WH} and C_{WH} in the consideration of no reservoir fracturing. In the process of one increasing with the other decreasing, they will coincide eventually.

The two above-mentioned types of injection schemes represent two limit zones in the relationship diagram between P_{WH} and C_{WH} , respectively. Similarly, the middle P_{WH} and C_{WH} can also be obtained, plotting them in one figure, that is, the relationship diagram between P_{WH} and C_{WH} , as shown in Figure 4, where the red and blue lines represent the upper and lower limits of the interval of flow rate under constant pressure injection, respectively; both of them jointly form a closed region. And the closed region forms the wellhead injection parameters domain of simultaneously meeting the constraint conditions about pressure and flow rate. Hence theoretically, as long as controlling the wellhead injection parameters falling in the closed region, the safe and effective injection can be achieved. In addition, the left intersection of curves represents the lower limit of constraint conditions about pressure, where the CO₂ fluid is just able to be injected into the reservoir completely. And the right one represents the upper limit of constraint conditions about pressure, in which just no reservoir would fracture. The feasible flow rate corresponding to these two intersections is unique and determined. Therefore, the wellhead injection parameters should be away from the intersections and close to the middle region as much as possible when designing the injection schemes, which will bring a greater allowable interval for pressure and flow rate, and then the projects will be safer.

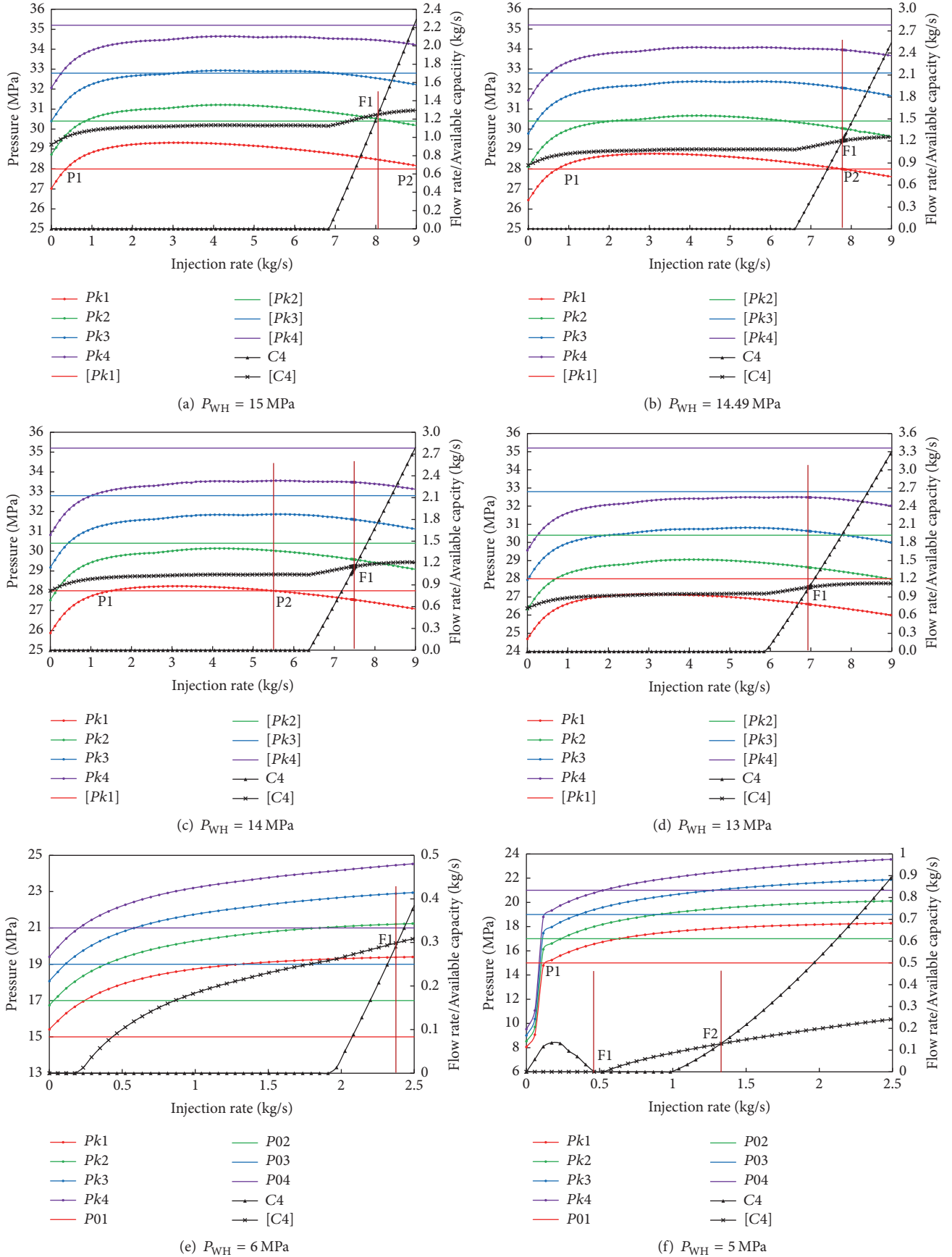


FIGURE 3: Continued.

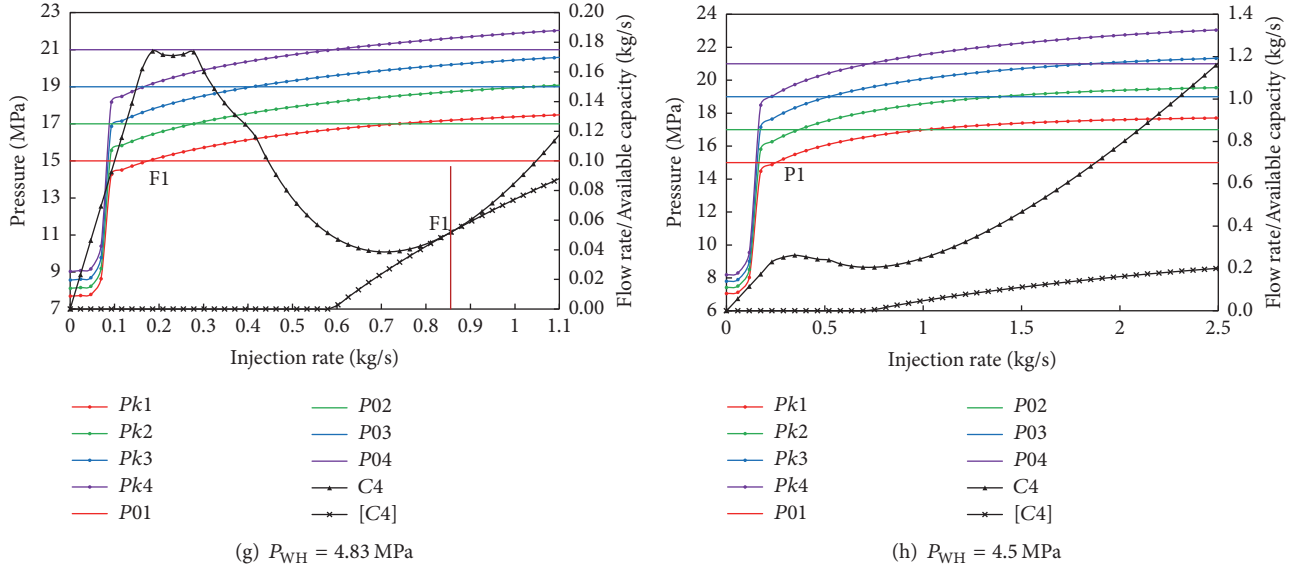


FIGURE 3: Curves of pressure and flow rate on the interface of wellbore and reservoir along with injection rate.

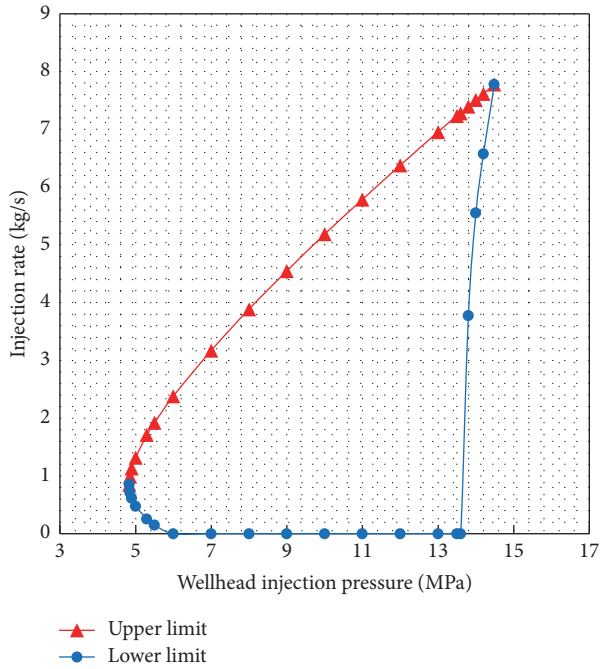


FIGURE 4: Relationship diagram between wellhead injection pressure and injection rate.

4. Influential Factors of Wellhead Injection Pressure and Injection Rate

4.1. Overview. The influential factors can be classified into two parts: the human-controllable factors and the engineering geological factors, as shown in Figure 5. The former mainly refer to the temperature of injected fluid T_0 determined by the engineers, and the latter include the factors of impacting wellbore heat transfer, impacting reservoir

capacity, and determining constraint conditions about pressure. And the last five in Figure 5 also can be considered as the characteristic parameters of reservoirs.

As for the geothermal gradient, it was studied by Lui et al. [31] in consideration of the single reservoir and they found that it affects the wellbore pressure distribution by impacting the wellbore heat transfer and only has slight effect when C_{WH} is small. Obviously, the impact of earth's surface temperature is weaker. Since the wellbore heat transfer has nothing to do with the number of reservoirs, it is acceptable that the effect of geothermal parameters on the wellbore pressure distribution can be neglected. Thereafter, the analysis case in Section 3.1 is used to study the effect of the other above-mentioned factors.

4.2. Temperature of Injected Fluid. Take the situation of $T_0 = -5^\circ\text{C}$ as the standard case, compared with the cases of $T_0 = -10, 0, 10,$ and 20°C , respectively, to study the influence of T_0 on the relationship of P_{WH} and C_{WH} with other parameters unchanged. Figure 6 shows the calculated results.

According to Figure 6, it is clear that the relationship diagrams of P_{WH} and C_{WH} under different T_0 are accordant in shape and the areas of different closed region are roughly equal. With T_0 increasing, the closed region only shows a tendency of uniformly shifting to the right. Therefore, it could be concluded that T_0 has no substantial impact on the relationship of P_{WH} and C_{WH} . Furthermore, with T_0 increasing, the allowable C_{WH} exhibits a linearly decreasing trend, and the allowable P_{WH} shows a linearly increasing trend. The reason is that a rise in T_0 causes the wellbore pressure to reduce, therefore leading to an increase in the allowable P_{WH} . Subsequently all the constraint conditions about pressure and flow rate changed, especially for the upper limit of constraint condition about pressure.

4.3. Saturation Parameters S_{lw} and S_{lc} . In the above cases, the saturation parameters S_{lc} and S_{lw} are set as 0.55 and 0.999,

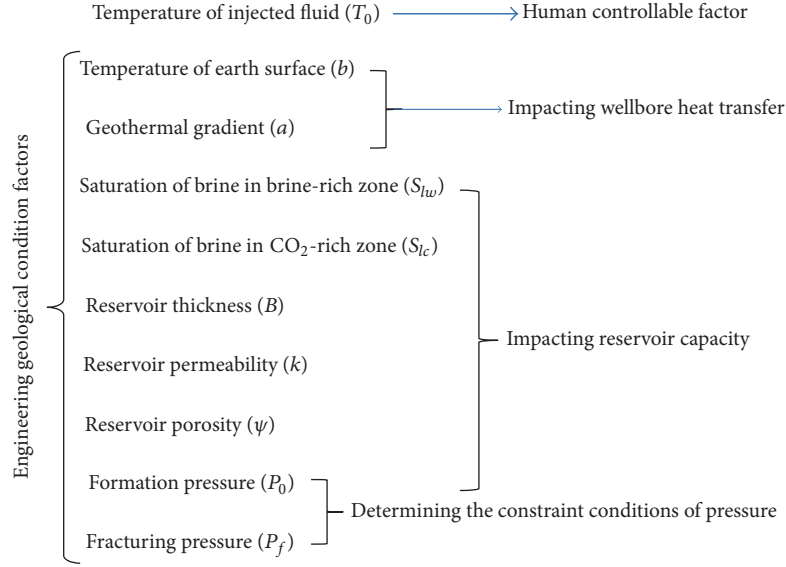


FIGURE 5: The influential factors of the relationship between wellhead injection pressure and injection rate.

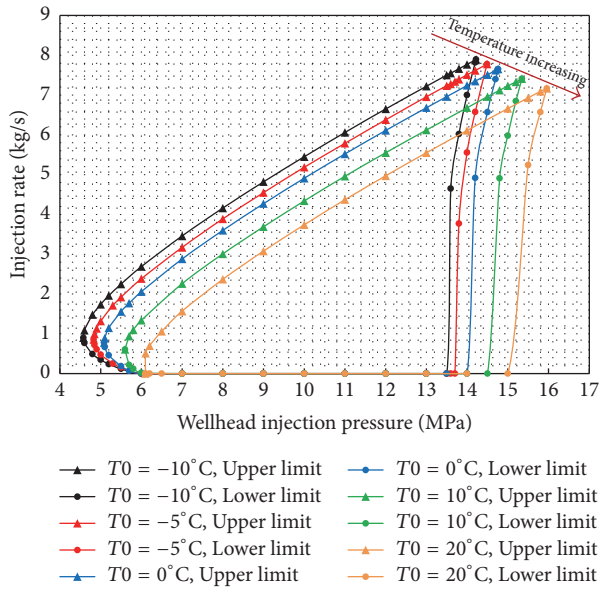


FIGURE 6: Relationship diagram between wellhead injection pressure and injection rate at different temperature of injected fluid.

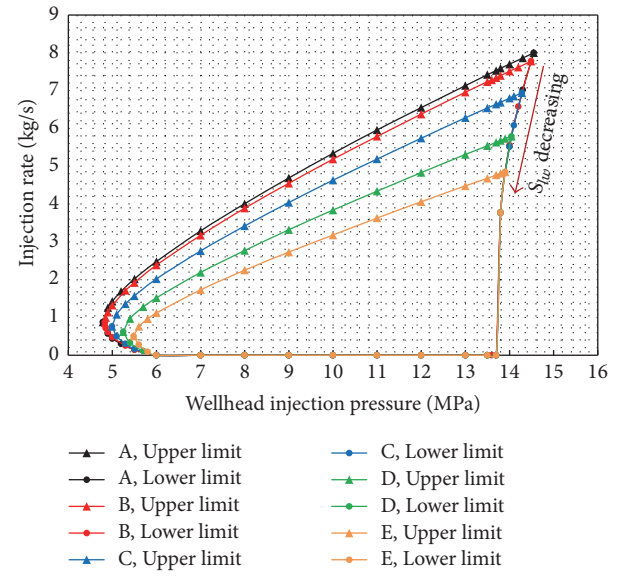


FIGURE 7: Relationship diagram between wellhead injection pressure and injection rate at different S_{lw} .

respectively. To analyze their impact on the relationship between P_{WH} and C_{WH} , firstly it is necessary to design different values of S_{lc} and S_{lw} . Here, the Van Genuchten-Mualem Model [32] was adopted to inversely derive the parameters S_{lc} and S_{lw} . Table 3 lists the design values of S_{lc} and S_{lw} and Figures 7 and 8 show the calculation results.

Figures 7 and 8 show that (1) the parameters S_{lc} and S_{lw} just change the ranges of allowable P_{WH} and C_{WH} to some extent and have no substantial effects on the relationship between P_{WH} and C_{WH} , which is similar to T_0 . (2) With the decrease of S_{lw} , the allowable P_{WH} and C_{WH} gradually reduce, the upper limit of C_{WH} gradually closes to its lower

limit, and the effects of S_{lc} are just contrary to those of S_{lw} because the CO_2 domain and brine domain of two-phase flow are mutually restrictive. (3) The changes of the right intersection of the upper and lower limits of C_{WH} in Figures 7 and 8 have a common feature; that is, the intersection moves strictly along the track of lower limit of C_{WH} with the variable changing. And it differs slightly from that of the left intersection, which suggested that the change of S_{lc} and S_{lw} just alters the constraint conditions about the flow rate and the lower limit of pressure; however, it has no impact on the constraint conditions about the upper limit of pressure.

TABLE 3: The values of parameters S_{lw} and S_{lc} .

	A	B	C	D	E	F	G	H	I	J
S_{lc}	0.55	0.55	0.55	0.55	0.55	0.40	0.50	0.55	0.60	0.70
S_{lw}	0.9999	0.999	0.99	0.97	0.95	0.999	0.999	0.999	0.999	0.999

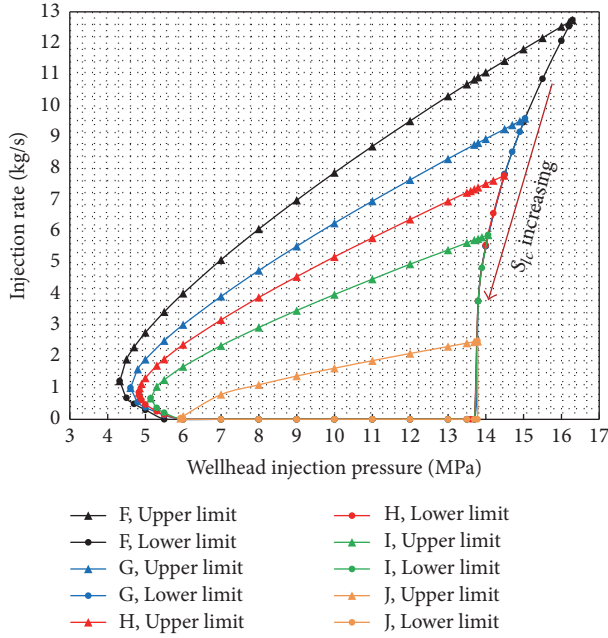
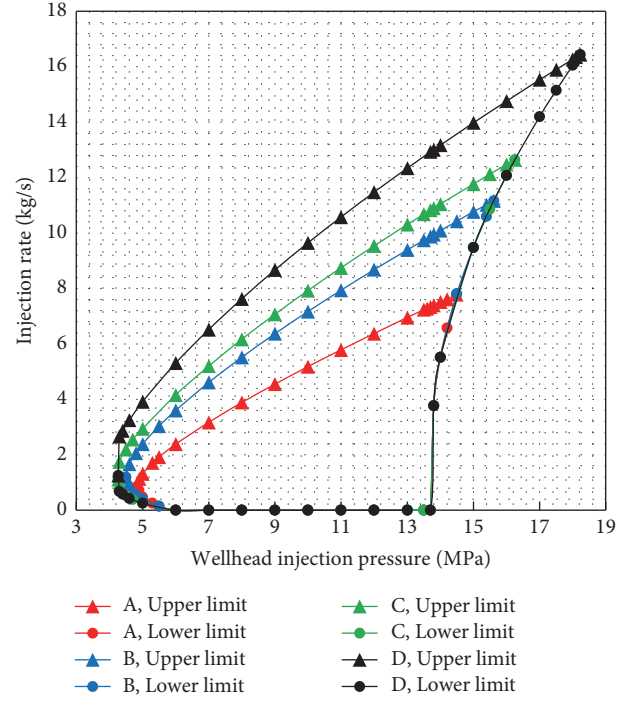
FIGURE 8: Relationship diagram between wellhead injection pressure and injection rate at different S_{lc} .

FIGURE 9: Relationship diagram between wellhead injection pressure and injection rate at different reservoir thickness.

4.4. Thickness, Permeability, and Porosity of Reservoirs. The thickness, permeability, and porosity of reservoirs as their inherent characteristic parameters are invariant for a given storage site, but they directly determine the capacity of the reservoir. Thus their influence that aims to generalize the above obtained conclusions to other projects is analyzed. Secondly, with CO_2 injected into the reservoir, this will cause a series of physical and chemical reactions. However, a change in load and chemical reactions with minerals will generally cause changes in the permeability and porosity of reservoirs [33–35]. Limited by the existing testing technology, the impacts of thickness, permeability, and porosity have not been taken into consideration. Tables 4–6 list the different design parameters of reservoirs, and the corresponding calculation results are shown in Figures 9–11.

On the basis of Figures 9 and 10, (1) the impacts of reservoir thickness and permeability on the relationship between P_{WH} and C_{WH} have common features: both only affect the range rather than the essence of P_{WH} and C_{WH} . With the thickness or permeability increasing, the allowable P_{WH} and C_{WH} increase at similar ratio, ascribed to their similar status in (3). (2) Of course, there are also some differences about the impact of reservoir thickness and permeability: curves B and C in the figures are not exactly the same, because the value of R_0 is also affected by the thickness but not by the permeability. (3) Curves B and C in Figure 9 do not overlap,

revealing that increase in thickness of the upper reservoir has greater effect on enlarging the allowable P_{WH} and C_{WH} in the multireservoir injection simultaneously, compared with increasing the thickness of the lower reservoir. It indicates that the injected fluid majorly enters the upper reservoirs, which is consistent with the conclusions of Rutqvist and Tsang [36], Liu et al. [31], and Xie et al. [37, 38] based on TOUGH2. Furthermore, as described above, the critical reservoir in this case is the first reservoir, which means that increase in thickness of the critical reservoir is most effective for the increase of total available capacity of the entire storage site. (4) The effect of reservoir porosity on P_{WH} and C_{WH} is limited and could be ignored according to Figure 11. (5) The traces of intersections of upper and lower limit of C_{WH} in Figures 9, 10, and 11 are in agreement with those in Figures 7 and 8, indicating that the changes caused by these five parameters are similar in essence; that is, they all indirectly change the constraint conditions about flow rate by changing the capacity of reservoirs.

4.5. Formation Pressure and Fracturing Pressure. The formation pressure in essence also affects the capacity of reservoirs; therefore it has some similarity to the five above-mentioned parameters. However, it is also different from

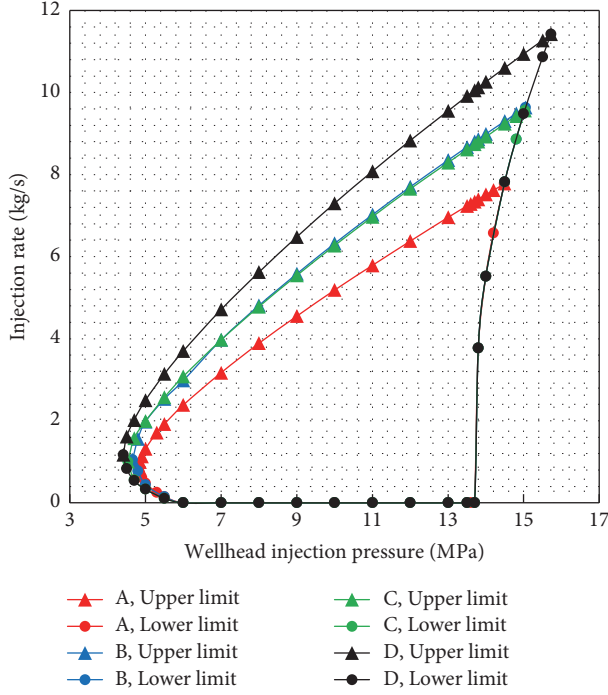


FIGURE 10: Relationship diagram between wellhead injection pressure and injection rate at different reservoir permeability.

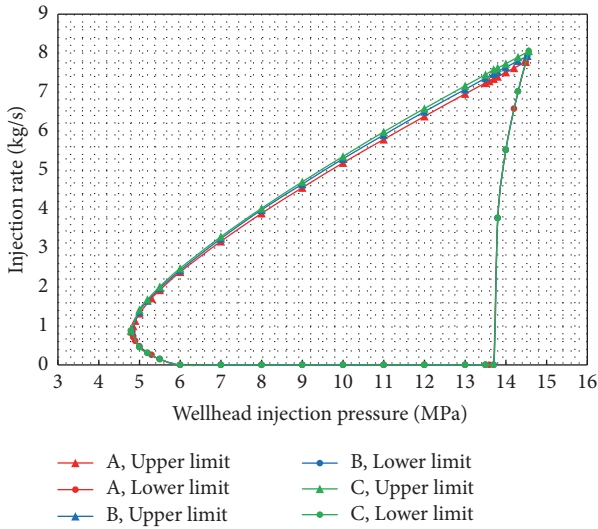


FIGURE 11: Relationship diagram between wellhead injection pressure and injection rate at different reservoir porosity.

them because it also determines the lower limit of constraint conditions about pressure. Thus, it is discussed together with the fracturing pressure. Table 7 lists the different pressure conditions and Figure 12 shows the corresponding calculation results.

Comparison of curves A, B, and C shows that, with the formation pressure increasing, both allowable P_{WH} and C_{WH} decline, and the right intersection of upper and lower limits of C_{WH} still moves along the lower limit of C_{WH} . It

TABLE 4: The values of reservoir thickness.

Reservoir number	Reservoir thickness (m)			
	A	B	C	D
1	10	10	20	20
2	10	13	16	20
3	10	16	13	20
4	10	20	10	20

TABLE 5: The values of reservoir permeability.

Reservoir number	Reservoir permeability ($\times 10^{-3} \mu m^2$)			
	A	B	C	D
1	6	6	8	8
2	5	5	7	7
3	4	6	4	6
4	3	5	3	5

TABLE 6: The values of reservoir porosity.

Reservoir number	Reservoir porosity (%)		
	A	B	C
1	12	17	22
2	11	16	21
3	10	15	20
4	9	14	19

TABLE 7: The values of formation pressure and fracturing pressure.

Reservoir number	Formation pressure (MPa)			Fracturing pressure (MPa)	
	A	B	C	D	E
1	15	15.5	16	35.5	36
2	17	17.5	18	38.5	39
3	19	19.5	20	41.5	42
4	21	21.5	22	44.5	45

indicates that the formation pressure also indirectly changes the constraint conditions about flow rate by affecting the capacity of reservoirs, so there is a same feature with the five aforementioned parameters with similar characteristics. Moreover, the left part of closed region shifts toward the right when the formation pressure increases, which embodies the fact that the formation pressure directly determines the lower limit of constraint conditions about pressure. Obviously, a rise in the lower limit of pressure will naturally increase the allowable P_{WH} . Comparison of curves A, D, and E shows that, with the fracturing pressure increasing, both allowable P_{WH} and C_{WH} will increase, and only the right boundary with the initial trend and shape extends to the right. It suggests that the fracturing pressure only changes the upper limit of constraint conditions about pressure and does not affect the other conditions and parameters.

TABLE 8: The parameters of reservoir-caprock combination units in Shenhua CCS project [13].

Reservoir number	Reservoir thickness (m)	Caprock thickness (m)	Logging permeability ($\times 10^{-3} \mu\text{m}^2$)	Logging porosity (%)	Fracturing pressure (MPa)	Formation pressure (MPa)
1	9	1699	2.81	10.6	35.29	17.45
2	5	57	5.47	12.4	37.53	17.89
3	40	191	1.431	9.7	38.95	20.15
4	8	43	6.58	12.9	42.60	21.43
5	4	119	5.99	12.6	47.00	22.94
6	26	114	2.738	12.5	43.47	23.1
7	8	52	5.1	11.9	46.03	23.84
8	12	178	0.039	5.2	45.68	22.75

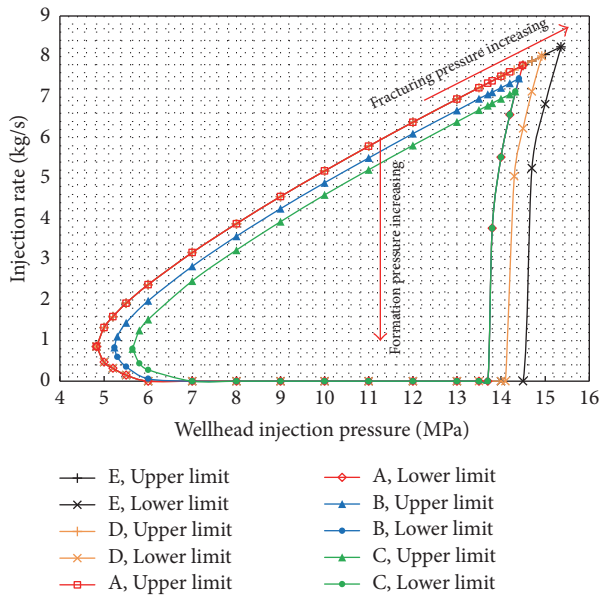


FIGURE 12: Relationship diagram between wellhead injection pressure and injection rate at different formation pressure and fracturing pressure.

5. Case Study: Shenhua CCS Demonstration Project

In Section 3, the relationship diagram between P_{WH} and C_{WH} was obtained through an analysis case; in Section 4, relevant factors affecting the relationship and their influential rules were found. All these indicate that the theory and method presented in this paper are scientific and effective in solving engineering problems. As follows, this work will apply the theory and method in Shenhua CCS demonstration project to obtain the ranges of P_{WH} and C_{WH} which simultaneously meet the constraint conditions of pressure and flow rate in the actual project.

The calculation parameters of the reservoir-caprock combination units in Shenhua CCS demonstration project are listed in Table 8, including 8 reservoir-caprock combination units from top to bottom and one injection well with a depth of 2450 meters. The parameters are mainly determined by

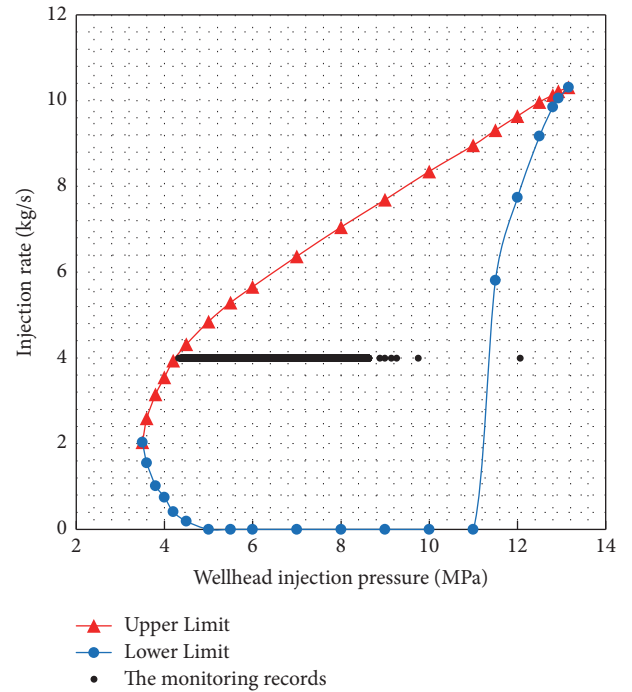


FIGURE 13: Relationship diagram between wellhead injection pressure and injection rate in Shenhua CCS project.

the logging interpretation data [13]. As mentioned above, the reservoirs are a kind of formation with small thickness, low porosity, and low permeability. The reservoirs are simplified into homogeneous and isotropous formation because we applied an analytical solution to describe the CO_2 -brine flow in the reservoirs, although the actual reservoirs have strong heterogeneity.

Figure 13 shows the calculation results. P_{WH} and C_{WH} of right intersection are 13.16 MPa and 10.31 kg/s, respectively. If the annual injection time is 300 days, the annual injection mass flow will reach 270,000 tons. Obviously, the preset annual injection of 100,000 tons for Shenhua project is achievable. The actual injection started in March 2011 and stopped in April 2015. Figure 14 shows the monitoring records of wellhead injection pressure during the formal injection

stage from March 2011 to April 2014, during which time CO_2 was injected at a constant injection rate about 4.0 kg/s. Inputting the actual injection parameters into Figure 13 finds that they all fall into the closed region except the records of initial loading process and the other two monitoring records. However, the other two abnormal pressures were induced by some unexpected circumstances, which was controlled by engineers immediately and returned to normal. Hence, it is convincing that the theory and method established by this work can withstand the practice test and are scientifically reliable. Moreover, it is necessary to note that the actual injection is very close to the upper limit curve of C_{WH} at the later period of formal injection. Although it improves the utilization efficiency of cost, any improper operation or uncontrollable factor could possibly lead to an abortive injection and subsequently a series of chain consequences. Therefore, according to the current preset annual injection target, this work recommends to control its P_{WH} at 5~7 MPa in the subsequent injection process.

In addition, according to the conclusions of Section 4 and considering the changes of relevant parameters with time, it is necessary to pay attention to the following points for the actual injection control of Shenhua CCS project. (1) T_0 is real-time measurable in the injection process. Thus if T_0 rises, it is necessary to properly reduce C_{WH} or increase P_{WH} ; if T_0 declines, it is necessary to increase C_{WH} or decrease P_{WH} . (2) Because the parameters of saturation and permeability and fracturing pressure are difficult to measure in operation, it is worthy to investigate the rules that they change with time by laboratorial experiments. Then the wellhead injection parameters should be modified based on the conclusions of experiments. (3) For a given project, the thickness of reservoirs generally does not change over time and the effect of the porosity is small enough and ignorable. As to the impacts of formation pressure, it is unnecessary to consider that because the distant boundary condition is constant pressure in this work.

6. Conclusions

To improve the control theory of the wellhead injection parameters, this work firstly developed the complete constraint conditions of wellbore injection and then studied the relationship and its influential factors between P_{WH} and C_{WH} by applying the EFDM in the vertical well segment and the analytical solution of two-phase flow in the horizontal reservoir and obtained the following conclusions.

(1) P_{WH} and C_{WH} are a pair of mutual constraint physical quantities. For a given injection project, the allowable P_{WH} and C_{WH} individually form a continuous interval. When one changes within its allowable range, the other correspondingly alters within its allowable range; both of them jointly form a closed region. Thus, controlling the wellhead injection parameters within this closed region can simultaneously ensure the effectiveness and safety of CO_2 injection.

(2) Analysis of the factors that affect the relationship between P_{WH} and C_{WH} found that all of them only change their allowable upper and lower limits to some extent but not the essence of their relationship. With the fracturing

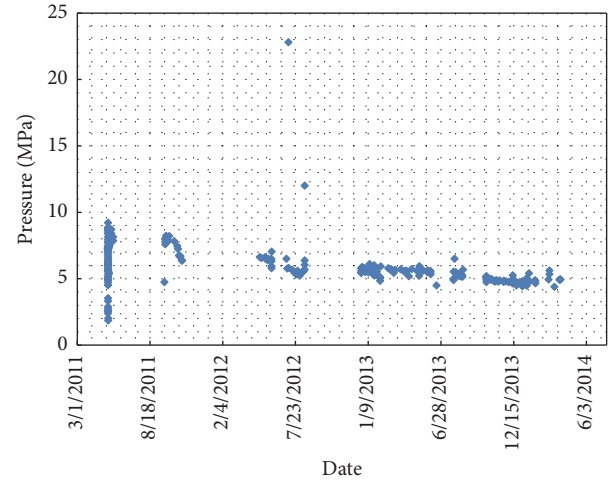


FIGURE 14: The monitoring records of wellhead injection pressure.

pressure increasing, their allowable upper limits increase and their lower limits remain unchanged. With the formation pressure increasing, the lower limit of P_{WH} increases and its upper limit remains unchanged; in contrast, the upper limit of C_{WH} decreases. With reservoir thickness and permeability increasing, the allowable upper limits of P_{WH} and C_{WH} significantly increase, and the lower limit of P_{WH} slightly decreases. As S_{lc} enlarges or S_{lw} reduces, the impacts on P_{WH} and C_{WH} are in agreement with that of reservoir thickness decreasing. The impact of reservoir porosity is ignorable. With T_0 increasing, the allowable upper and lower limits of P_{WH} enlarge, and those of C_{WH} reduce.

(3) Application of the above theory and method in Shenhua CCS demonstration project obtained the relationship diagram of P_{WH} and C_{WH} and found that its actual injection parameters are just located in the closed region, effectively verifying the reliability of the previous conclusions. Accordingly, it is recommended that if Shenhua project keeps the current annual target injection flow rate invariant, P_{WH} would better be controlled within 5~7 MPa in the subsequent injection process.

(4) Although this work only studies the relationship between P_{WH} and C_{WH} of the injection well, the above theory and method can be generalized to study the production well, which can obtain the similar relationship between wellbore pressure and production flow, and to further explore the effects of above-mentioned influential factors on the relationship.

(5) The constraint conditions of this paper do not involve the caprocks, so when including the caprocks, the entry pressure may have a strong impact on the maximum allowable pressure of reservoirs. Then the constraint conditions may change. Therefore, further study needs to address this occasion.

Data Availability

The data used to support the findings of this study are available from the corresponding author upon request.

Conflicts of Interest

The authors declare that they have no conflicts of interest.

Acknowledgments

This work was sponsored by the National Natural Science Foundation of China (Grant no. 41672252).

References

- [1] China-U.S. Joint Announcement on climate change, Beijing, China, 2014, http://www.china.org.cn/chinese/2014-12/09/content_34268965.htm.
- [2] S. Bachu, "Screening and ranking of sedimentary basins for sequestration of CO₂ in geological media in response to climate change," *Environmental Geology*, vol. 44, no. 3, pp. 277–289, 2003.
- [3] IPCC, "Carbon Dioxide Capture and Storage," in *Intergovernmental Panel on Climate Change*, WMO & UNEP, Cambridge University Press, New York, NY, USA, 2005.
- [4] S. Sun, "Geological problems of CO₂ underground storage and its significance on the mitigation of climate change," *China Basic Science*, no. 3, pp. 17–22, 2006.
- [5] M. Zhang and M. J. McSaveney, "Is air pollution causing landslides in China?" *Earth and Planetary Science Letters*, vol. 481, pp. 284–289, 2018.
- [6] S. Bachu, "CO₂ storage in geological media: role, means, status and barriers to deployment," *Progress in Energy and Combustion Science*, vol. 34, no. 2, pp. 254–273, 2008.
- [7] X. Li and Z. Fang, "Status quo of connection technologies of CO₂ geological storage in China," *Rock and Soil Mechanics*, vol. 28, no. 10, pp. 2229–2239, 2007 (Chinese).
- [8] B. Bai, X. Li, M. Liu, L. Shi, and Q. Li, "A fast explicit finite difference method for determination of wellhead injection pressure," *Journal of Central South University*, vol. 19, no. 11, pp. 3266–3272, 2012.
- [9] M. Liu, B. Bai, and X. Li, "A unified formula for determination of wellhead pressure and bottom-hole pressure," *Energy Procedia*, vol. 37, pp. 3291–3298, 2014.
- [10] J. Rutqvist, J. Birkholzer, F. Cappa, and C.-F. Tsang, "Estimating maximum sustainable injection pressure during geological sequestration of CO₂ using coupled fluid flow and geomechanical fault-slip analysis," *Energy Conversion and Management*, vol. 48, no. 6, pp. 1798–1807, 2007.
- [11] S. Mukhopadhyay, S.-Y. Yang, and H.-D. Yeh, "Pressure Buildup During Supercritical Carbon Dioxide Injection From a Partially Penetrating Borehole into Gas Reservoirs," *Transport in Porous Media*, vol. 91, no. 3, pp. 889–911, 2012.
- [12] A. Liebscher, F. Möller, A. Bannach et al., "Injection operation and operational pressure-temperature monitoring at the CO₂ storage pilot site Ketzin, Germany-Design, results, recommendations," *International Journal of Greenhouse Gas Control*, vol. 15, pp. 163–173, 2013.
- [13] B. Bai, X. Li, H. Wu, Y. Wang, and M. Liu, "A methodology for designing maximum allowable wellhead pressure for CO₂ injection: application to the Shenhua CCS demonstration project," *China. Greenhouse Gases Science Technology*, vol. 7, no. 1, pp. 158–181, 2017.
- [14] J. Rutqvist, "The Geomechanics of CO₂ Storage in Deep Sedimentary Formations," *Geotechnical and Geological Engineering*, vol. 30, no. 3, pp. 525–551, 2012.
- [15] H. Wu, B. Bai, X. Li, M. Liu, and Y. He, "An explicit finite difference model for prediction of wellbore pressure and temperature distribution in CO₂ geological sequestration," *Greenhouse Gases: Science and Technology*, vol. 7, no. 2, pp. 353–369, 2017.
- [16] J. J. Carroll and D. W. Lui, "Density, phase behavior keys to acid gas injection," *Oil & Gas Journal*, vol. 95, no. 25, pp. 63–72, 1997.
- [17] E. T. Hashim and I. E. Maloka, "Static bottom-hole pressures in wells," *Petroleum Science and Technology*, vol. 24, no. 1, pp. 113–116, 2006.
- [18] J. E. Streit and R. R. Hillis, "Estimating fault stability and sustainable fluid pressures for underground storage of CO₂ in porous rock," *Energy*, vol. 29, no. 9–10, pp. 1445–1456, 2004.
- [19] C. Gapillou, S. Thibeau, G. Mouronval, and M. Lescanne, "Building a geocellular model of the sedimentary column at rousse CO₂, geological storage site (aquitaine, france) as a tool to evaluate a theoretical maximum injection pressure," *Energy Procedia*, vol. 1, no. 1, pp. 2937–2944, 2009.
- [20] H. Wu, B. Bai, M. Liu, X. Li, and L. Wang, "The equivalent density method to estimate the wellbore pressure of CO₂ well," *Special Oil & Gas Reservoirs*, vol. 22, no. 3, pp. 114–117, 2015.
- [21] J. J. Carroll, *Acid Gas Injection and Carbon Dioxide Sequestration*, LLC, Salem, Massachusetts: Wiley-Scrivener press, Hoboken, NJ, USA, 2010.
- [22] M. Zhang and M. J. McSaveney, "Rock avalanche deposits store quantitative evidence on internal shear during runoff," *Geophysical Research Letters*, vol. 44, no. 17, pp. 8814–8821, 2017.
- [23] X. Li, K. Hitoshi, and O. Takashi, "CO₂ aquifer storage and the related rock mechanics issues," *Chinese Journal of Rock Mechanics & Engineering*, vol. 22, no. 6, pp. 989–994, 2003.
- [24] J. M. Nordbotten, M. A. Celia, and S. Bachu, "Injection and storage of CO₂ in deep saline aquifers: Analytical solution for CO₂ plume evolution during injection," *Transport in Porous Media*, vol. 58, no. 3, pp. 339–360, 2005.
- [25] A. Cihan, J. T. Birkholzer, and Q. Zhou, "Pressure Buildup and Brine Migration During CO₂ Storage in Multilayered Aquifers," *Groundwater*, vol. 51, no. 2, pp. 252–267, 2013.
- [26] C.-F. Tsang, J. Birkholzer, and J. Rutqvist, "A comparative review of hydrologic issues involved in geologic storage of CO₂ and injection disposal of liquid waste," *Environmental Geology*, vol. 54, no. 8, pp. 1723–1737, 2008.
- [27] H. Wu, B. Bai, X. Li, S. Gao, M. Liu, and L. Wang, "An explicit integral solution for pressure build-up during CO₂ injection into infinite saline aquifers," *Greenhouse Gases: Science and Technology*, vol. 6, no. 5, pp. 633–647, 2016.
- [28] H. Sidiq, R. Amin, and T. Kennaird, "The study of relative permeability and residual gas saturation at high pressures and high temperatures," *Advances in Geo-Energy Research*, vol. 1, no. 1, pp. 64–68, 2017.
- [29] S. Wang, X. Han, Y. Dong, and H. Shi, "Mechanisms of reservoir pore/throat characteristics evolution during long-term waterflooding," *Advances in Geo-Energy Research*, vol. 1, no. 3, pp. 148–157, 2017.
- [30] L. Shi, B. Bai, H. Wu, and X. Li, "Evaluating reservoir risks and their influencing factors during CO₂ injection into multilayered reservoirs," *Geofluids*, vol. 2017, Article ID 6059142, 2017.
- [31] H. Liu, Z. Hou, P. Were, Y. Gou, and X. Sun, "Simulation of CO₂ plume movement in multilayered saline formations through multilayer injection technology in the Ordos Basin, China," *Environmental Earth Sciences*, vol. 71, no. 10, pp. 4447–4462, 2014.

- [32] K. Pruess, C. Oldenburg, and G. Moridis, "TOUGH2 User's Guide Version 2," Tech. Rep. LBNL-43134, Lawrence Berkeley National Laboratory, Berkeley, Calif, USA, 1999.
- [33] B. R. Crawford, D. R. Faulkner, and E. H. Rutter, "Strength, porosity, and permeability development during hydrostatic and shear loading of synthetic quartz-clay fault gouge," *Journal of Geophysical Research: Solid Earth*, vol. 113, no. 3, Article ID B03207, 2008.
- [34] J. Cai, B. Yu, M. Zou, and M. Mei, "Fractal analysis of invasion depth of extraneous fluids in porous media," *Chemical Engineering Science*, vol. 65, no. 18, pp. 5178–5186, 2010.
- [35] Z. Zhang, J. Cai, F. Chen, H. Li, W. Zhang, and W. Qi, "Progress in enhancement of CO₂ absorption by nanofluids: A mini review of mechanisms and current status," *Journal of Renewable Energy*, vol. 118, pp. 527–535, 2018.
- [36] J. Rutqvist and C.-F. Tsang, "A study of caprock hydromechanical changes associated with CO₂ injection into a brine formation," *Environmental Geology*, vol. 42, no. 2-3, pp. 296–305, 2002.
- [37] J. Xie, K. Zhang, L. Hu, Y. Wang, and M. Chen, "Understanding the carbon dioxide sequestration in low-permeability saline aquifers in the Ordos Basin with numerical simulations," *Greenhouse Gases: Science and Technology*, vol. 5, no. 5, pp. 558–576, 2015.
- [38] J. Xie, K. Zhang, L. Hu, P. Pavelic, Y. Wang, and M. Chen, "Field-based simulation of a demonstration site for carbon dioxide sequestration in low-permeability saline aquifers in the Ordos Basin, China," *Hydrogeology Journal*, vol. 23, no. 7, pp. 1465–1480, 2015.

Research Article

Numerical Investigation into the Evolution of Groundwater Flow and Solute Transport in the Eastern Qaidam Basin since the Last Glacial Period

Qichen Hao ¹, Chuan Lu ¹, Yuchen Zhu ¹, Yong Xiao ², and Xiaomin Gu³

¹Institute of Hydrogeology and Environmental Geology of the Chinese Academy of Geological Sciences, Shijiazhuang 050061, China

²Faculty of Geosciences and Environmental Engineering, Southwest Jiaotong University, Chengdu 610031, China

³China University of Geosciences, Beijing 100083, China

Correspondence should be addressed to Yuchen Zhu; zhuyuchen413@163.com

Received 27 October 2017; Revised 9 April 2018; Accepted 15 May 2018; Published 7 June 2018

Academic Editor: Meijing Zhang

Copyright © 2018 Qichen Hao et al. This is an open access article distributed under the Creative Commons Attribution License, which permits unrestricted use, distribution, and reproduction in any medium, provided the original work is properly cited.

A complete understanding of groundwater circulation as well as the transport and distribution of solutes in arid-semiarid basin regions is a prerequisite for the safe use of groundwater resources. The distributions of the groundwater flow system and solutes are affected by the basin morphology, lithology, and climate variations; therefore, they can change over geologic time. In this study, we performed a case study of the Qaidam Basin in the northeastern Tibetan Plateau, in which we utilized reactive solute transport simulations to build a numerical model in TOUGHREACT for a typical section of the eastern Qaidam Basin since the last glacial period. The results show that the groundwater in the eastern Qaidam Basin developed into a three-level groundwater flow system and that the seepage velocity of the local water flow system is significantly higher than that of the intermediate and regional water flow systems. Although groundwater in the discharge region has been continuously concentrated and enriched since the last glacial period, the distributions of the groundwater flow system and solutes have been greatly affected by climate variations. During warm periods, the centres of groundwater discharge and solute concentration shifted to areas with more groundwater recharge; in contrast, both centres shifted to the central basin during drought periods. The groundwater in the basin mainly contains Na^+ and Cl^- ions, which vary significantly from the recharge region to the discharge region. Evaporation of groundwater results in increases in the concentrations of most of the components except HCO_3^- . The groundwater in the discharge region is currently in the stage of carbonate precipitation and is far from gypsum and halite precipitation.

1. Introduction

As an important component of water resources, groundwater is the main and sometimes only source of water in the arid and semiarid regions of China. More than 50% of the water supply of the major cities in northern and western China comes from the groundwater, and this percentage is as high as 80% in many cities [1]. The reasonable development and utilization of groundwater resources has become the main factor affecting the sustainable development of local economies, and water security is a significant issue that China urgently needs to address [2].

The Qaidam Basin is located in the arid and semiarid regions of China. It is one of the four major inland basins of China and contains abundant mineral resources, such as salt and borax. However, water resources are extremely scarce, which will seriously threaten the sustainable development of the economy and the ecological security of the Qaidam Basin. The development and utilization of water resources has not been prudent, which has caused environmental and geological problems, such as an expanding groundwater depression cone, saline water, and vegetation degradation [3]. In addition, in recent years, global climate warming has significantly influenced the Qaidam Basin,

making it the region experiencing the most significant climate changes in the Tibetan Plateau [4]. These changes have also considerably influenced the local water resources [4–6]. Therefore, a comprehensive understanding of the groundwater flow in the Qaidam Basin is key to the reasonable development and utilization of local water resources.

The movement and evolution of groundwater in a basin is controlled and affected by multiple factors. Tóth summarized two major classes of controlling factors: the geometric morphology of the basin and the geological conditions of the basin [7]. In addition, many scholars believe that the upper boundary conditions and the physical properties of the fluid are also important factors that affect the movement of groundwater in a basin [8–11]. Li and Hao [12] adopted a multidisciplinary research method to determine that inland basins can be roughly divided into four grades of flow systems and three characteristic zones of salt migration, and they explained the formation mechanism for the freshwater segment of an inland basin. Lin and Jin [13] began with the principles of the hydrologic cycle and considered the motion of water and salt as one entity to systematically study the characteristics of hydrologic circulation and salt migration and accumulation on different levels under the natural and human-influenced conditions of a basin.

Many studies have focused on the groundwater flow and saltwater migration in the Qaidam Basin [14–21]. For example, Ma et al. [19] performed an isotope study in the Golmud subdrainage basin and concluded that groundwater was the main source of the salt lakes. Ye et al. [21] investigated the hydrochemical characteristics and sources of brine in the Gasikule salt lake in the northwestern Qaidam Basin and concluded that the sources of the salt in the lake included stream water, the leaching of Pliocene salt-bearing host rocks, and Ca-Cl-type deep water. Chen et al. [14] used rare earth elements as tracers to study the dissolution of source rocks in different water bodies in the Qaidam Basin. Hu and Jiao [15] constructed a regional three-dimensional groundwater flow model for the Qaidam Basin that was calibrated using GRACE data from 2003 to 2012. However, these studies mainly focused on short time scales. Few studies have explored the groundwater flow and salt transport over long time scales, such as the 1000-year or 10,000-year scales. In addition, previous studies mainly focused on the western part of the Qaidam Basin, where the hydrogeologic conditions are different from those in the eastern part of the basin [22].

In this paper, we use TOUGHREACT [23] to perform a reactive solute transport simulation and consider the influence of water-soluble components on the fluid density. We take a typical cross section of the Qaidam Basin as an example and simulate the migration and evolution of the groundwater and salt in the eastern Qaidam Basin since the last glacial period. Based on the simulation results, we identify multiple levels of the groundwater flow system and present the distribution of the solutes in the groundwater during different geological periods. This information is important for the sustainable utilization of local groundwater resources and for coping with climate change.

2. Study Area

2.1. Geological and Hydrogeological Setting. The Qaidam Basin is a large closed intermountain fault basin in which the maximum thickness of the Quaternary sediments exceeds 3000 m [11]. From the piedmont to the central basin, the structural characteristics of the water-bearing media generally have zonal or semizonal distributions. In the vertical direction, from the piedmont to the central basin, the water-bearing unit changes from a single phreatic aquifer to a multilayer confined aquifer. The lithology of the aquifers changes from coarse to fine-grained, and the thickness decreases. The water yield and permeability change from high to low.

Piedmont alluvial plains are distributed around the basin. The aquifers in these plains are dominated by sand and gravel [22]. The aquifer thickness varies from tens of metres to one to two hundred metres, and the hydraulic conductivity varies from several metres per day to hundreds of metres per day [22]. These areas are the water-rich regions of the basin, and the daily single-well water yields vary from several tens of cubic metres to three thousand cubic metres [22]. Alluvial plains are located in the central basin. The aquifer changes from a single-layer structure to a multilayer structure, and the groundwater transitions from phreatic water to confined water. The aquifer is generally no more than 50 m thick, and the thinnest part is less than 10 m thick [22]. The lithology of the aquifer is generally moderately fine sand, coarse sand, and fine sand, and the aquiclude layers are mainly composed of impermeable sandy loam, loam, and clay. The hydraulic conductivity of the aquifer varies relatively significantly, which is generally less than one metre per day; however, the maximum value is tens of metres per day [22].

The climate of the Qaidam Basin is classified as an extremely arid inland climate. The basin is surrounded by high mountains (Figure 1), and the flow of warm and moist air is restricted. Therefore, precipitation is rare, and potential evaporation is significant. Based on an analysis of multiyear observational data at meteorological stations, the average rainfall in the basin is 16.09–189.73 mm, and the average potential evaporation in the plains area is 1973.62–3183.04 mm [17]. The potential evaporation rates are much higher than the precipitation rates; therefore, rainfall only slightly replenishes the groundwater. The groundwater mainly receives vertical infiltration from rivers in the alluvial fans as well as lateral supply from channel seepage, infiltration of irrigation water, and water from bedrock fissures [22]. The seepage conditions in the alluvial fans are good. The groundwater rapidly moves to the overflow zone at the front edge of the alluvial fans, and some of the groundwater flows to the surface in the groundwater spill belt to form rivers. A portion of the groundwater continuously seeps towards the central basin and eventually evaporates from phreatic water or is directly recharged to the terminal lake.

The distribution of chemical components in the groundwater in the basin is mainly controlled by the groundwater recharge and discharge conditions. The chemical components of the groundwater in the middle and upper parts of the alluvial fan are not significantly different from those of

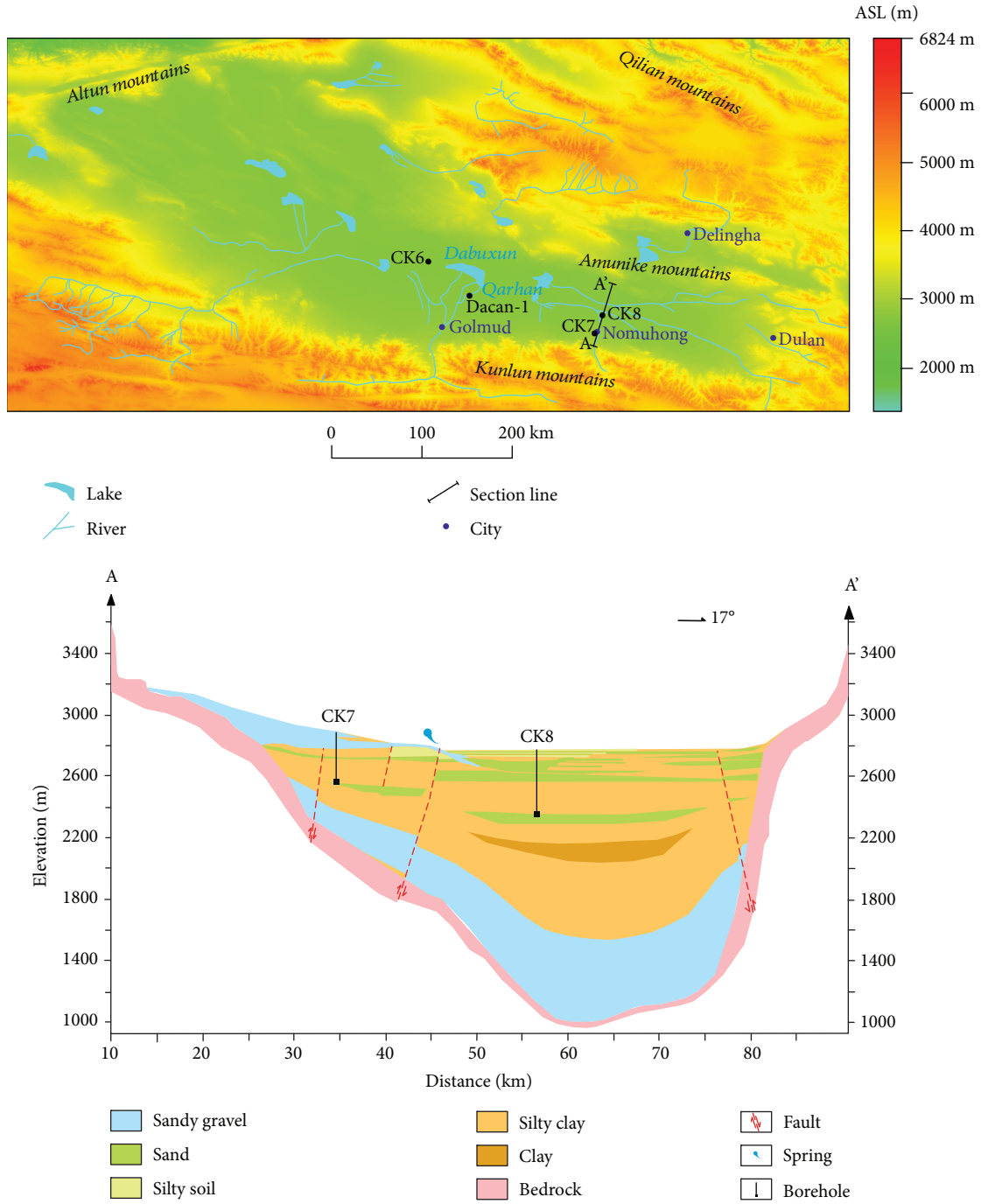


FIGURE 1: Location of the study area and the geological structure along a typical section.

the river water. Based on a chemical analysis of well CK7, which was drilled in the middle of the alluvial fan and sampled at several depths in 2013, the average total dissolved solids (TDS) of the groundwater is 403 mg/L. The TDS of the river water in the Nuomuhong mountain pass is 427 mg/L [24]. When the groundwater flows to the overflow zone, the concentrations of the chemical components in the groundwater rapidly increase by evaporation, and the TDS of the groundwater can reach the concentration of saline water. The TDS of the groundwater can exceed

the concentration of brine until it reaches the region adjacent to the terminal lake in the central basin.

2.2. Selected Cross Section and Salinization Period. The typical cross section selected in this study is located in the Nuomuhong area in the eastern Qaidam Basin. The cross section begins at the top of the Nuomuhong alluvial fan in the south and extends to the Amunike Mountain piedmont in the north. Because the Nuomuhong alluvial fan has a regular form and the surface runoff is relatively high, it is

suitable for studying the variations in the groundwater flow system caused by surface water [24]. From the top to the edge of the alluvial fan, the direction of the cross section is aligned with the slope gradient as well as the groundwater flow direction. In the central basin, the groundwater and surface water flow to the west. However, the groundwater seepage velocity in the east-west direction (perpendicular to the cross section) is extremely slow and does not have a significant influence on the flow simulation along the section [25].

The Nuomuhong area is located in the eastern Qaidam Basin, and it has not entered the salt precipitation stage until recently. Based on the analytical results of the Dacan-1 well on the eastern coast of Dabuxun Lake, the salinization zone and desalination zone from 3200 m to 45 m depth indicate that the Qarhan lake water at that time was in the transition between saline water and brackish water, and the lake was likely dominated by brackish water [26]. The age of the most recent appearance of a turf or humus soil layer inferred from a pore is 70 ka BP, which is close to the start of the last glacial period at 75 ka BP; this indicates that after 70 ka BP, the Qarhan Salt Lake began to develop. Therefore, the salinization period is determined to have extended from the beginning of the last glacial period at 70 ka to the present.

2.3. Paleohydrologic Reconstruction. Rainfall is sparse in the Qaidam Basin, and the river runoff from the mountainous area represents most of the groundwater recharge resources in the basin. Therefore, the key to determining the basin source and sink terms is to determine the river runoff and the potential evaporation. The river runoff is affected by the amount of rainfall in the catchment area, and the rainfall is affected by regional and global climate change. Therefore, we can approximate the rainfall rates under different climate conditions and further estimate the river runoff based on the rainfall rates. According to a hydrogeological survey in the Qaidam Basin, the variation in river runoff in this area is 60% of that of precipitation [22]. The period of 45–25 ka BP was a relatively warm period during the last glacial period, and the temperature reached that of an interglacial climate [27]. The temperature in the southwestern Tibetan Plateau was 3–4°C higher than at present, and the amount of rainfall was 40%–100% higher. The amount of rainfall in the Qinghai Lake region adjacent to the Qaidam Basin was 79% higher. The Qarhan Salt Lake was also three to seven times larger than its current area. The highest temperatures during the Holocene warm period occurred at 7.2–6.0 ka BP. The temperature in the Qinghai Lake area was 3°C higher than the current temperature, and the precipitation was 70%–80% higher [27]. The Golmud River flood event in 1989 caused the Qarhan Salt Lake area to expand by approximately 3.9 times [28]. Based on hydrological monitoring data, the average temperature in 1989 was approximately 2°C higher than the multiyear average. The rainfall in the Golmud River basin during that year was 3.2 times the multiyear average, and the river runoff was 2.1 times the multiyear average [22].

These data show that there is a positive correlation between changes in precipitation and temperature changes in the Qaidam area. Based on these data, we preliminarily infer the paleohydrological characteristics of the Qaidam

Basin since 70 ka by combining the characteristics of global climate change from the Late Pleistocene epoch to the Holocene (Figure 2). The current multiyear average temperature in the Qaidam Basin is approximately 4°C. Based on the global climate characteristics, the temperature during the first interglacial period was approximately 7–8°C. According to the results using the isotope and rare gas method in this research, the Pleniglacial temperature was approximately 1–2°C [25]. The first subsidiary glacial stage was warmer than the Pleniglacial stage, and it was colder than the first subsidiary interglacial stage, which is believed to be the same as today. As described above, the variation in precipitation is positively correlated with temperature. We use the current amount of rainfall as a reference to infer the variations in rainfall at other times. The river runoff is positively correlated with the rainfall, but the magnitude of the fluctuations in runoff is smaller than the magnitude of the rainfall variation. Based on the analysis of multiyear data, the magnitude of the variation in runoff in the Golmud region is approximately 60% of that of the rainfall [22]. The evaporation capacity is negatively correlated with both the amount of precipitation and the temperature. A temperature change of 2°C causes the evaporation to fluctuate by approximately 20%; based on this correlation, we can infer the evaporation at different times [22].

3. Simulation Approach

3.1. Conceptual Model. The horizontal distance of the cross section is 63 km. The vertical range of the simulation is from the ground surface to the Quaternary basement. The simulation thickness gradually increases from the top of the alluvial fan to the central basin, and the maximum simulation thickness is 1800 m. The bottom is defined as an impermeable boundary because the exchange between the Quaternary aquifer and the bedrock is minimal and can be ignored [22]. The upper boundary is defined as a flow boundary or Dirichlet boundary. The piedmont river infiltration is a given flow boundary, which is the only supply source in the simulation region. We determine the amounts and locations of infiltration based on the river infiltration distribution. The spring, river, and groundwater evaporation are defined as Dirichlet boundaries for the unidirectional discharge.

From the edge of the basin towards the centre, the sediment is mainly composed of sandy gravel, sand, silty soil, silty clay, and clay. Because limited data are available from in situ pumping tests along the cross section, the hydrogeological parameters of the different lithologies are based on empirical values [22]. The hydrogeological parameters were adjusted during the model calibration process by comparing the simulation results with observation data. The calibrated parameters are shown in Table 1. The discussion of the simulation results is based on the calibrated parameters.

Before the unconsolidated sediment entered the basin, it had undergone sufficient weathering and hydrolysis, and the soluble salt had been fully filtered. After entering the basin, most of the clastic sediments are composed of relatively insoluble minerals that are not easily weathered. A comparison of the chemical analysis of well CK7 with that

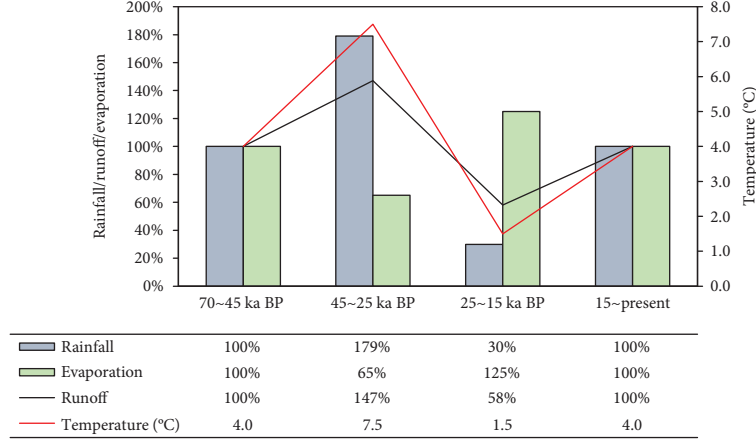


FIGURE 2: Paleohydrological characteristics of the Qaidam Basin since the last glacial period.

TABLE 1: Hydrogeological parameters of different lithologies.

Lithology	Porosity	Horizontal permeability (m/d)	Vertical permeability (m/d)
Sandy gravel	0.2	59.02	59.02
Sand	0.2	25.63	25.63
Silty soil	0.3	1.05	0.11
Silty clay	0.5	0.13	0.01
Clay	0.5	0.01	0.001

of the surface water demonstrated that the groundwater in the basin will not dissolve additional components. Therefore, we can ignore the soluble salt formed by mineral weathering in the basin. It is assumed that all of the soluble salt came from outside the basin by surface water recharge.

The movement of water-soluble components in an aquifer mainly includes convection and hydrodynamic dispersion. The hydrodynamic dispersion coefficient is replaced by the diffusion coefficient in TOUGHREACT [23]. The groundwater flow rate is relatively slow in the central basin, so it is reasonable to make the replacement. The value of the diffusion coefficient is set to $2.95 \times 10^{-6} \text{ m}^2/\text{s}$ [24]. The chemical reactions considered in the model mainly include mineral dissolution/precipitation, convective mixing, and cation exchange. The hydrochemical reactions are based on the local equilibrium model of water-soluble components. The ionic activity coefficient of high ionic strength is calculated based on the Pitzer model of ion interaction [23, 29].

The main ion components in the groundwater are the main variables in the hydrochemical model, including K^+ , Na^+ , Ca^{2+} , Mg^{2+} , Cl^- , SO_4^{2-} , and HCO_3^- . Due to intense evaporation, salt precipitation can occur in the groundwater; therefore, the possible mineral facies include calcite (CaCO_3), dolomite (CaMgCO_3), magnesite (MgCO_3), gypsum (CaSO_4), rock salt (NaCl), and potash (KCl) as shown in Table 2.

3.2. Governing Equations. The basic governing equations for solving the multicomponent motions (mass and energy

TABLE 2: Chemical components used in the simulations.

Primary aqueous species	Aqueous complexes	Minerals
H_2O	OH^-	Sylvite
H^+	$\text{NaHCO}_3 \text{ (aq)}$	Halite
Na^+	CaHCO_3^+	$\text{CaCl}_2 \cdot 2\text{H}_2\text{O}$
K^+	MgHCO_3^+	Gypsum
Ca^{2+}	$\text{CO}_2 \text{ (aq)}$	Calcite
Mg^{2+}	CO_3^{2-}	Magnesite
Cl^-	$\text{CaCO}_3 \text{ (aq)}$	Dolomite
SO_4^{2-}	$\text{MgSO}_4 \text{ (aq)}$	
HCO_3^-	$\text{CaSO}_4 \text{ (aq)}$	
	NaSO_4^-	
	KSO_4^-	
	NaCO_3^-	

conservation equations) can be written in the following general form [30]:

$$\frac{d}{dt} \int_{V_n} M^K dV_n = \int_{\Gamma_n} F^K \cdot n d\Gamma_n + \int_{V_n} q^K dV_n. \quad (1)$$

The integration is over an arbitrary subdomain V_n of the flow system under study, which is bounded by the closed surface Γ_n . The quantity M in the accumulation term (left-hand side) represents the mass or energy per volume, $\kappa = 1, \dots, \text{NK}$ labels the mass components (e.g., water, air, H_2 , and solutes), $\kappa = \text{NK} + 1$ denotes the heat “component,” F denotes the mass or heat flux, q denotes sinks and sources, and n is a normal vector of the surface element $d\Gamma_n$ that points into V_n .

The simulations were carried out using the reactive transport code TOUGHREACT [23], which introduces reactive geochemistry into the multiphase fluid and heat flow code TOUGH2 V2 [30]. TOUGHREACT is a thermal-physical-chemical code applicable to one-, two-, or three-dimensional geologic systems with physical and chemical heterogeneity. The numerical method for the fluid flow and chemical transport simulation is based on the

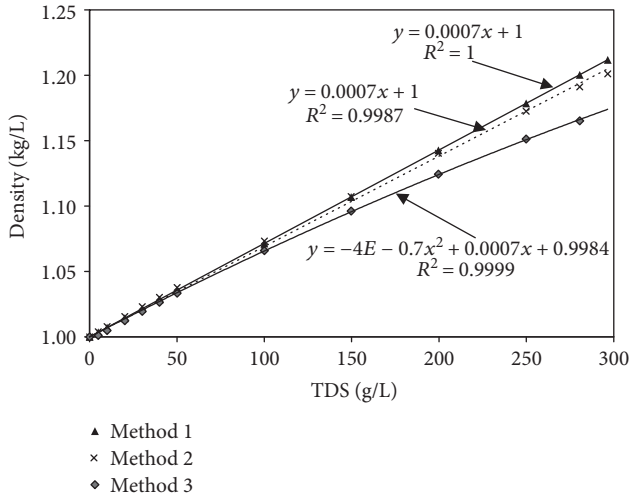


FIGURE 3: Relationship between the natural water densities calculated using different methods and TDS.

integral finite difference (IFD) method for space discretization. The system of chemical reaction equations is solved on a grid-block basis by Newton-Raphson iteration. The thermodynamic data used in the simulations were taken from the EQ3/6 database, which was derived using SUPCRT92 [31]. The local equilibrium constants and kinetic rates used in TOUGHREACT are given in Xu et al. [23].

The change in volume of the high concentration solution is related to many factors. Currently, there are three main methods to calculate the density of natural water based on the concentration [32–34]. The relationship between the variations in density and TDS under natural water evaporation is calculated using three methods as shown in Figure 3. There is a relatively significant difference between the results calculated using the third method and the results of the other two methods; in particular, the difference increases gradually when the TDS is greater than 50 g/L. The densities calculated using the first and second methods form essentially linear relationships with the TDS. However, the densities calculated using the third method indicate a nonlinear relationship with TDS. Because the third method calculates the density based on the partial molar volume of the solute and the results calculated using this method are closer to the actual values, they are more suitable for calculating the density of high-concentration brine [34]. In this study, the third method is used to calculate the density of fluids with high TDS concentrations.

3.3. Spatial and Temporal Discretization. We adopt the gradient mesh size method to divide the simulation domain. The mesh size increases gradually from the ground surface to the bottom. The thickness of the smallest cell grid is 0.1 m. The model is divided into 3150 computational units (Figure 4). The time discretization uses the automatic time step method. The minimum time step is 1 s, and the maximum time step is 1000 a. The numerical model will automatically set the time step based on the iterative situation.

3.4. Initial and Boundary Conditions. River infiltration is set as the only groundwater recharge. It is introduced into the model in the form of a specified flow. The infiltration at the piedmont is relatively high, and the infiltration in the lower reach gradually decreases. The spring is calculated using the DELV module, which is similar to the DRAIN module of MODFLOW. The EVAP module is used to simulate groundwater evaporation, and the value of groundwater evaporation is calculated based on the soil water content method [35]. The pressure distribution of the groundwater under stable conditions is taken as the initial pressure condition for the numerical model.

The solute concentrations of well CK7 are taken as the initial chemical conditions for the numerical model (Table 3). The sampling and chemical analysis of the groundwater in well CK7 was conducted in 2013. Its solute concentrations are similar to those of the other wells in the recharge region as well as the river water, even though the ages of the groundwater in these wells vary from thousands of years to 10,000 years. These observations indicate that the chemical components of the groundwater in the recharge region have not changed significantly over geologic time [25]. Therefore, it is reasonable to take the solute concentrations of well CK7 as the initial chemical conditions. Because the groundwater recharge is mainly from river water, the solutes from the river water are taken as the flux boundary conditions. In the discharge region, groundwater discharges by evaporation, but the solutes are left in the aquifer. Therefore, the chemical boundary condition in the discharge region is defined as a no-flux boundary.

4. Results and Discussion

4.1. Validation of the Simulation Model. The simulation results were validated by comparing the simulated groundwater levels with the observed groundwater levels and the simulated solute concentrations with the measured solute concentrations in the groundwater. The observed groundwater levels are from some wells including CK7 and CK8. And the measured solute concentrations are from well CK8. A comparison of the simulated and observed groundwater levels shows that they are similar (Figure 5). The simulated mean residual is 5 m, and the absolute residual is 5.7 m. The regions with relatively large errors are mainly located in the recharge area, where the variation in the groundwater levels is much larger than that in the discharge area. Figure 6 shows a comparison of the simulated TDS with the measured TDS in well CK8. Although the variation in the simulated TDS is smaller, they have the same trends from the shallow to the deep aquifers. The TDS of the groundwater decreases from the surface to a depth of 100 m and then increases. Overall, the simulation model of the groundwater flow and solute transport is reasonable.

4.2. Groundwater Flow System Distribution. Figure 7 shows the simulated distribution of the flow velocity under the present conditions. There are considerable differences in both the horizontal and vertical seepage velocities. In general, the velocity at the top of the basin is greater than that at the

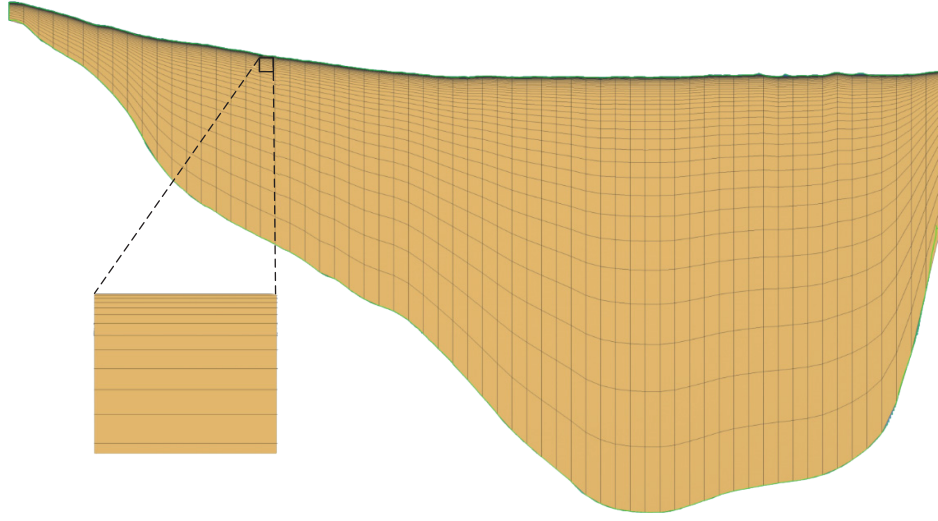


FIGURE 4: Schematic diagram of the model mesh.

TABLE 3: Initial component concentrations of the model.

Component	Concentration (mol/kg H ₂ O)
H ₂ O	1.000
H ⁺	5.754×10^{-9}
Na ⁺	4.622×10^{-3}
K ⁺	0.087×10^{-3}
Ca ²⁺	1.381×10^{-3}
Mg ²⁺	1.492×10^{-3}
Cl ⁻	2.822×10^{-3}
SO ₄ ²⁻	1.642×10^{-3}
HCO ₃ ⁻	3.127×10^{-3}

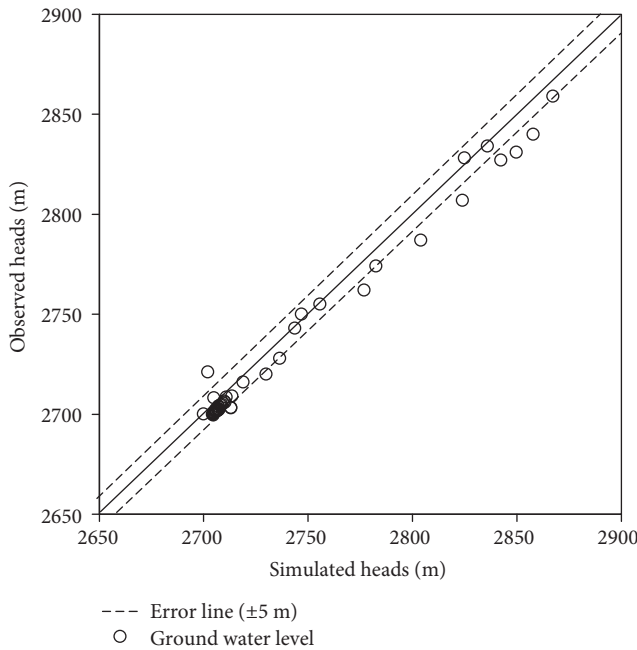


FIGURE 5: Comparison of the simulated groundwater heads with the observed heads.

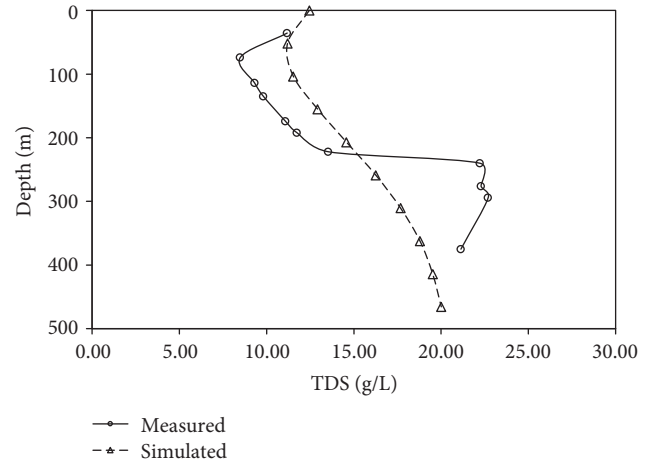


FIGURE 6: Comparison of the simulated TDS with the measured TDS in well CK8.

bottom of the basin, and the velocity at the basin margin is greater than that in the centre. The maximum difference in the flow velocity can reach several orders of magnitude. The shallow velocity at the margin of the basin is greater than 1×10^{-5} m/s. Groundwater is recharged at the piedmont and is then discharged in the form of springs or surface evaporation at the spill belt. The renewal rate of that groundwater is relatively fast, and it can be defined as the local groundwater flow system shown in Figure 7 (I_1 , I_2). The spring grows into a river, and a portion of the river water infiltrates into the groundwater to form a local flow system (I_3). The flow velocities below the local flow system are generally in the range of 1×10^{-6} m/s to 1×10^{-7} m/s, and they are significantly lower than those in the local flow system. Moreover, the seepage depth and seepage distance both increase significantly, although the groundwater still receives recharge from the piedmont. However, this water flows below two local water flow systems (I_1 , I_3) and is discharged via evaporation near

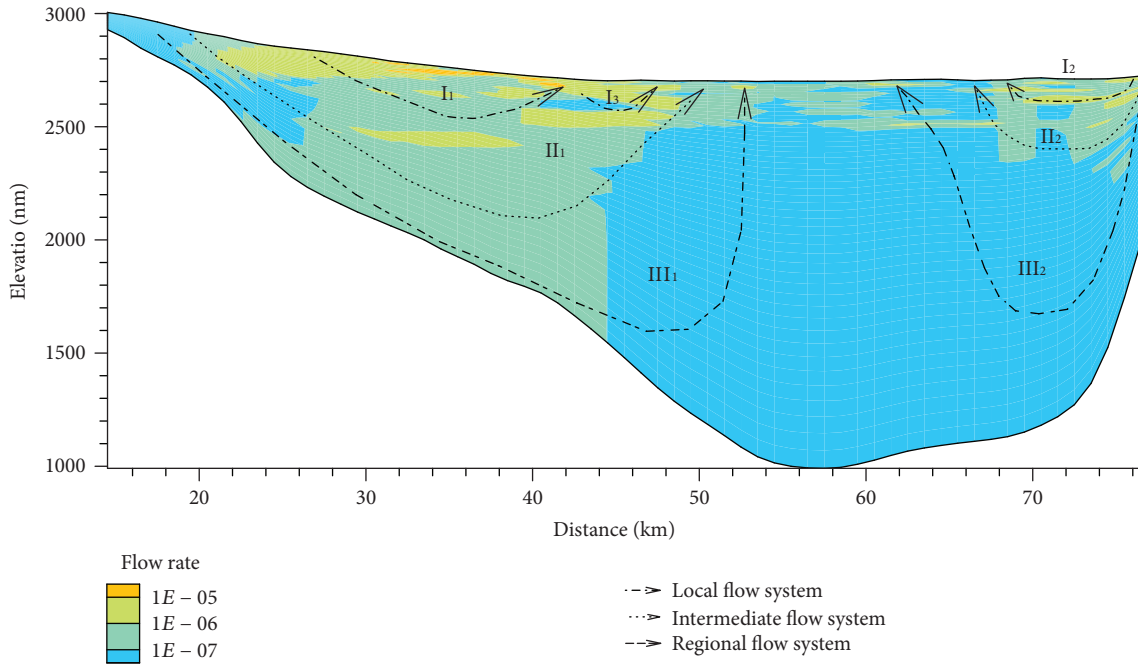


FIGURE 7: Simulated groundwater seepage velocities (m/s) and groundwater flow system distribution.

the central basin. There are relatively large differences in the flow path from those of the local water flow systems; therefore, it can be defined as the intermediate water current systems (II_1 , II_2). The seepage velocity of the deep groundwater in the central basin is less than 1×10^{-7} m/s, and the flow velocity is extremely slow. The groundwater is supplied from the piedmont and infiltrates to the bottom of the basin. It flows below the intermediate flow system and is discharged via evaporation in the central basin. In comparison to the intermediate flow system, the seepage depth is greater, and the seepage path is longer, so it can be defined as the regional flow systems (III_1 , III_2). In summary, the simulation results indicate that the groundwater in the Qaidam Basin under the present conditions forms a three-level groundwater flow system.

The distribution of these flow systems is controlled by the form of the basin, the sediment permeabilities, and the recharge and discharge conditions. The elevations decrease gradually from the piedmont to the central basin, and the main source for the Qaidam Basin is the river in the proluvial fan. These two factors cause the groundwater to accumulate more potential energy in the piedmont and drive the groundwater towards the lower reaches. The piedmont terrain on the southern side of the basin is higher than that on the northern side, and the recharge is also higher, which causes the development region of the water flow system on the southern side to be larger than that on the northern side. The permeability in the central basin is poor, which causes the groundwater to not be completely discharged from the central basin; instead, it is partially discharged in the form of an overflow spring in the spill belt between the piedmont and the central basin. The river formed by the overflow spring infiltrates again and forms the local water flow system, and it will eventually develop a multilevel flow system.

4.3. Solute Accumulation and Evolution. The simulation results indicate that the groundwater in the eastern region of the Qaidam Basin has been continually undergoing concentration and enrichment since 70 ka BP (Figure 8). However, with climate change, the distribution of the groundwater flow system and the solute distribution may change.

The climate conditions at 70–45 ka BP were similar to the current conditions. Due to the influence of evaporation, the hydrochemical components were first concentrated in the local flow system at the spill belt. This mainly occurred because of the large water circulation in the spill belt, where the water supply was adequate and the evaporation was high; therefore, the concentration first occurred in the spill belt, which resulted in salty and brackish water. However, the hydrochemical components concentrated in the spill belt did not remain in the spill belt. They were transported with the water towards the central basin and were eventually enriched in the central basin. Later, at 30 ka BP, the groundwater components continued to be enriched. By 45 ka BP, most of the groundwater in the central basin had evolved to saline water to form a distribution with salty water in the upper part of the overflow zone and freshwater in the lower part.

The time period of 45–25 ka BP was a minor interglacial period; it was the relatively warm time of the last glacial period. More rainfall fell than at present, and the potential evaporation was relatively low [26]. The reduction in evaporation resulted in greater groundwater discharge in the form of springs, and the local flow system was enhanced. The discharge centre of groundwater shifted towards Nuomuhong, and the enrichment centre of the water-soluble components also moved. The relative changes in the circulation of the different flow systems also caused the distributions of the shallow freshwater and deep salty

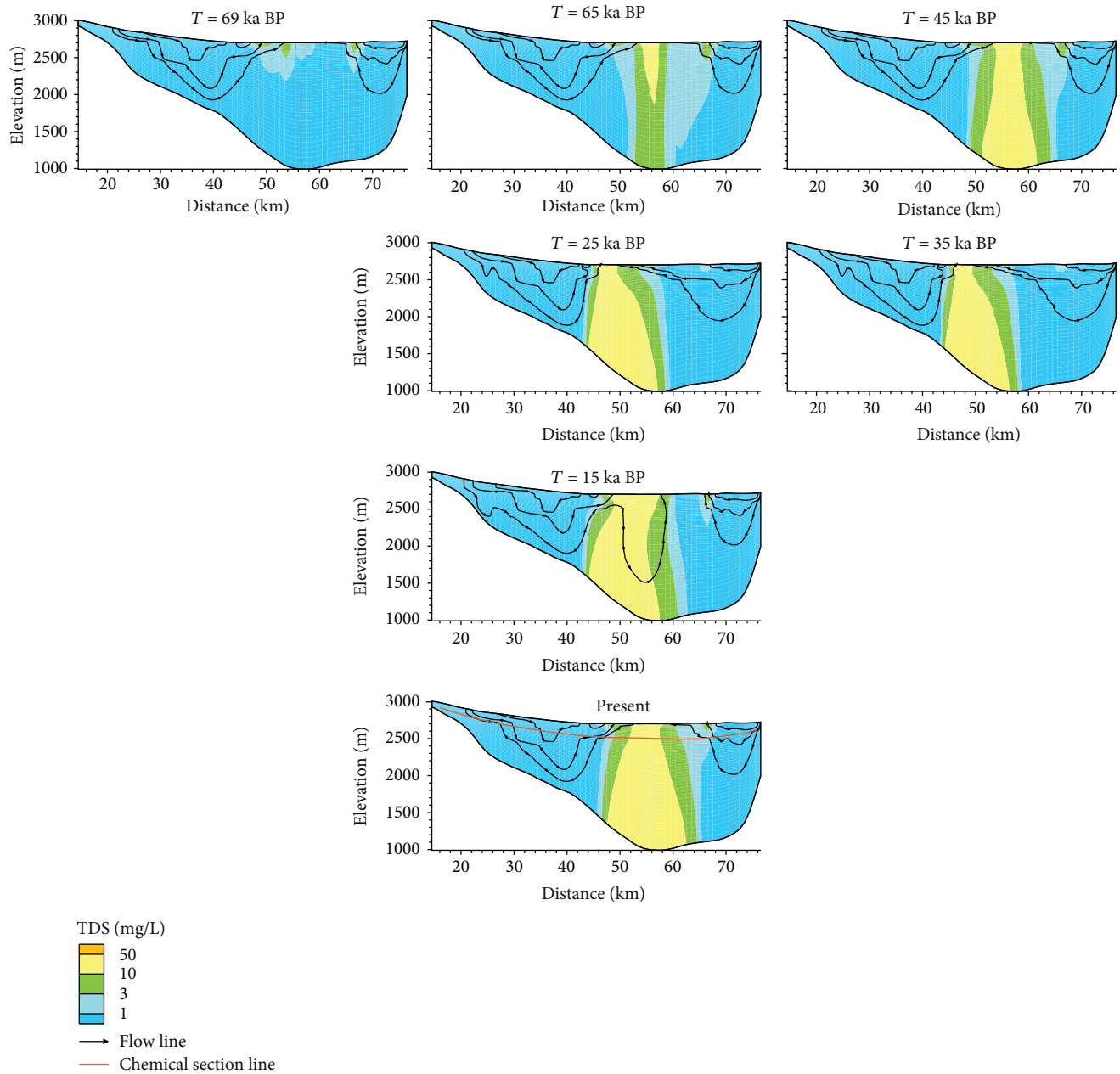


FIGURE 8: Evolution of the TDS concentrations during different geological periods (units: g/L).

water to expand; namely, some desalination of the shallow water occurred.

The time period of 25–15 ka BP was the Pleniglacial during the last glacial period, and the rainfall was only 30% of the present level. The abrupt reduction in recharge caused the enhancement of the regional water flow system, and the water and salt enrichment centres returned to the central basin. The variation in the density difference between the shallow water and deep water generated free convection of the groundwater in the central basin, and the groundwater with relatively low concentrations moved upward via buoyancy, whereas the groundwater with relatively high concentrations moved downward. However, the free convection caused by this density difference was only temporary over

geologic time, and the forced convection driven by gravity rapidly became a dominant factor.

The period from 15 ka BP to the present includes the late glacial period and postglacial period. The temperature gradually increased again, and the recharge and potential evaporation gradually changed to their present levels. The distributions of brackish and freshwaters were similar to those in the initial stage of the simulation. The distribution of saline water reached its maximum and formed a wedge of freshwater below the spill belt.

Currently, the groundwater in the central basin is mostly saline water with a concentration of 10–20 g/L. If there are no significant changes in the climate conditions in the future, the soluble components of the groundwater will continue to

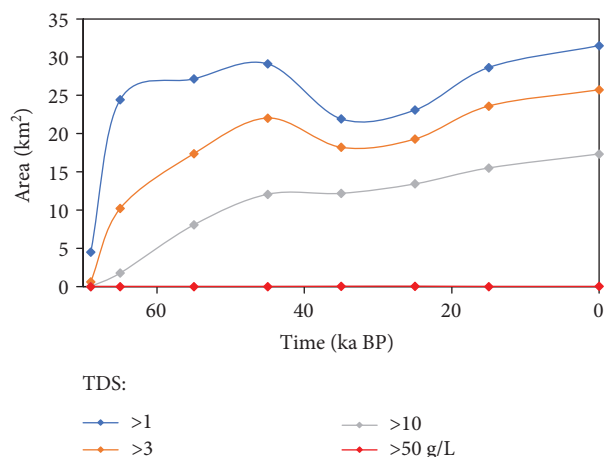


FIGURE 9: Areas of high TDS in different periods.

be concentrated and enriched. The calculated results of mineral saturation indicate that under the current conditions, except for dolomite, most minerals have not reached the saturated state. Currently, the groundwater is in the carbonate precipitation stage, and it is still far from precipitating gypsum and halite.

Due to the enrichment of salt in the central basin, the area of high TDS grew over time (Figure 9). Initially, the area of TDS > 1 g/L increased dramatically, which was caused by groundwater evaporation. The salt was transported from the surface of the central basin towards the bottom of the basin and from the centre of the basin towards the margin. After 65 ka BP, when the groundwater with high TDS occupied the largest area of the central basin, the area of TDS > 1 g/L continued to increase but at a relatively slow rate. This occurred because the salt transport from the central basin (discharge region) towards the margin of the basin (recharge region) was dominated by hydraulic dispersion; however, when the salt was transported close to the recharge region, hydraulic dispersion was prevented by the groundwater flow from the recharge region. The areas of higher TDS, such as TDS > 3 g/L and TDS > 10 g/L, increased much more slowly than the area of TDS > 1 g/L. Over time, larger areas became occupied by groundwater with higher TDS. Currently, the TDS in 81.7% of the area is higher than 3 g/L, and 55.0% of the area is higher than 10 g/L.

4.4. Variation in Chemical Composition. There are significant variations in the hydrochemical components and composition from the recharge region to the discharge region (Figure 10). The variations in the concentrations of different components were not large before 45 km and after 70 km (between the alluvial fan and the spill belt), which is consistent with the initial supply concentration. The main cation is Na^+ , and the main anion is Cl^- ; this is mainly because the chemical action in this region is dominated by leaching and mixing. The sediment has experienced sufficient filtration over geologic time; therefore, the hydrochemical components will no longer significantly increase. The components in the groundwater mainly come from surface water recharge. Between 45 km and 70 km (in the central basin), except for

the HCO_3^- concentration, which decreases, the concentrations of all the other components increase significantly. However, there are still differences in the rates of increase of the different components. The concentrations of Cl^- and Na^+ increase the most, and their maximum concentrations are 84 and 79 times higher than their initial concentrations, respectively. The concentrations of Ca^{2+} and Mg^{2+} increase moderately, and their maximum concentrations are 43 and 51 times higher than their initial concentrations, respectively. The evaporation and concentration mainly occur in the central basin. HCO_3^- reacts with Ca^{2+} and Mg^{2+} to generate dolomite, which causes a decrease in the HCO_3^- concentration. The formation of dolomite will generate H^+ , which increases the concentration of H^+ in the groundwater and eventually causes the pH of groundwater in the central basin to decrease from 7.7 to 7.2. In general, evaporation enhances the concentrations of most components, but there are no significant changes in the proportions of the different components. This occurs mainly because the concentration has not resulted in a period of significant diagenesis.

5. Conclusions

Using the reactive transport simulation technique, a vertical 2D numerical model was developed to simulate groundwater flow and solute transport since the last glacial period. The simulation was performed on a typical cross section across the Qaidam Basin, which is located in the northeastern Tibetan Plateau.

The Qaidam Basin generally receives recharge from the piedmont regions and is drained by evaporation. Due to the basin morphology, sediment lithology, and recharge and discharge conditions, a three-level nested groundwater flow system is developed. There are significant differences in the flow ranges and velocities of the different groundwater flow systems. In the local water flow system, the seepage path and seepage depth are relatively short, and the flow velocity is relatively fast. In the regional water flow system, the seepage path is relatively long and the seepage is relatively deep (it can extend to the bottom of the basin). The flow velocity in the regional is relatively slow, which can be many orders of magnitude slower than that in the local water flow system.

Since the last glacial period, the groundwater in the eastern part of the Qaidam Basin has experienced solute concentration and enrichment. In general, the solute is recharged with the groundwater in the piedmont regions and moves towards the central part of the basin. Due to intense evaporation and concentration, the solutes are concentrated and enriched in the central basin. During different geological periods, climate change affected the distribution of the groundwater flow system and the solute concentrations. During warm climate periods, the local flow system was enhanced, and the drainage centre of the groundwater and the solute concentration centre both shifted towards the side with the greater recharge. During periods of drought, the drainage centre and solute concentration centre shifted towards the central part of the basin. Currently, the groundwater is under conditions favourable for the precipitation of

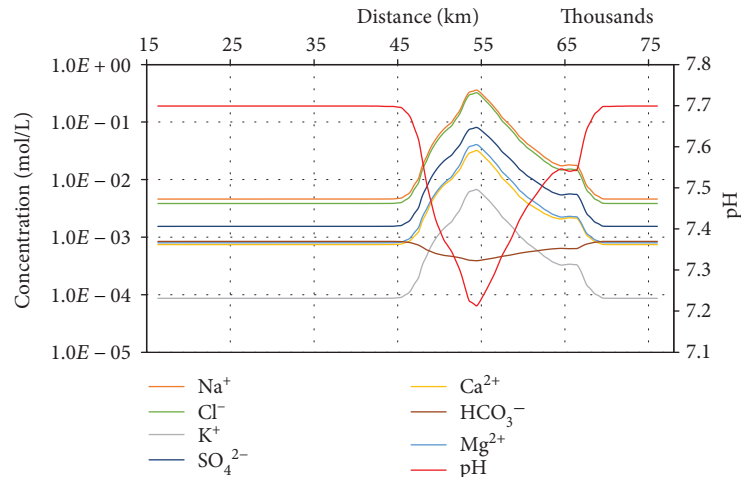


FIGURE 10: Concentrations (units in moles/L, except for pH) of primary components in the upper 100 m of the section.

carbonate but is still far from the precipitation of gypsum or halite.

Many parameters are involved in the coupled model of water flow and solute transport. In particular, for a large basin such as the Qaidam Basin, the hydrogeological parameters of the deep aquifer are not easy to obtain, and the hydrodynamic dispersion coefficient under large-scale conditions is also relatively difficult to determine. Therefore, further analysis of the numerical model parameters for the water flow and salt migration is necessary. In addition, the study did not take into account the influence of human activities on the groundwater flow and salt migration, which also need to be explored further.

Conflicts of Interest

The authors declare that they have no conflicts of interest.

Acknowledgments

This work was jointly supported by the Natural Science Foundation of China (no. 41702282), the Fundamental Research Funds for Central Public Research Institutes (no. YYWF201626), and a China Geological Survey Project (no. DD20160238).

References

- [1] Z. J. Zhang, Y. H. Fei, Z. Y. Chen et al., *Evaluation of Groundwater Sustainable Use in North China Plain*, Geological Publishing House, Beijing, 2009.
- [2] J. Qiu, "China faces up to groundwater crisis," *Nature*, vol. 466, no. 7304, p. 308, 2010.
- [3] Z. Y. Bao, X. F. Dong, S. Z. Guo, and W. C. Xu, "Main problem and solutions of Chaidamu basin groundwater resources exploitation," *Journal of Qinghai University (Nature Science)*, vol. 28, no. 1, pp. 54–59, 2010.
- [4] C. Jiang, "Qaidam basin has become the most significant warming area of the qinghai-tibet plateau," vol. 163, 2009, <http://news.163.com/09/1023/09/5MA5IT5T000120GU.html>.
- [5] E. Chongyi, H. Guangliang, W. Chengyong, Y. Ping, and L. Wenwen, "The analysis on air temperature variation characteristic in Qaidamu basin (1961–2011) under the background of global warming," *Journal of Arid Land Resources and Environment*, vol. 27, no. 10, pp. 94–99, 2013.
- [6] L. Xiang, H. Wang, H. Steffen et al., "Groundwater storage changes in the Tibetan Plateau and adjacent areas revealed from GRACE satellite gravity data," *Earth and Planetary Science Letters*, vol. 449, pp. 228–239, 2016.
- [7] J. Tóth, *Gravitational Systems of Groundwater Flow: Theory, Evaluation, Utilization*, Cambridge University Press, New York, NY, USA, 2009.
- [8] J. M. Sharp Jr and M. Shi, "Heterogeneity effects on possible salinity-driven free convection in low-permeability strata," *Geofluids*, vol. 9, no. 4, 274 pages, 2009.
- [9] X. Liang, R. Q. Zhang, and M. G. Jing, *Groundwater Flow System-Theory Application Investigation*, Geological Publishing House, Beijing, 2015.
- [10] J. Mádl-Sz_Nyi, S. Simon, and J. Tóth, "Hydrodynamic interaction between gravity-driven and over-pressured groundwater flow and its consequences on soil and wetland salinisation," in *Groundwater and Ecosystems*, p. 267, CRC Press, 2013.
- [11] J. W. Yang, Z. H. Feng, X. R. Luo, and Y. R. Chen, "Numerically quantifying the relative importance of topography and buoyancy in driving groundwater flow," *Science in China Series D: Earth Sciences*, vol. 53, no. 1, pp. 64–71, 2010.
- [12] W. P. Li and A. B. Hao, "The evolution model and significance of groundwater in the dry basin in northwest China," *Hydrogeology and Engineering Geology*, vol. 28, no. 4, pp. 28–32, 1999.
- [13] L. R. Lin and M. G. Jin, "Characteristics of hydrological cycle and salt migration in yanqi basin," *Yellow River*, vol. 28, no. 5, pp. 5–7, 2006.
- [14] L. Chen, T. Ma, Y. Du, and C. Xiao, "Dissolved rare earth elements of different waters in Qaidam Basin, northwestern China," *Procedia Earth and Planetary Science*, vol. 17, pp. 61–64, 2017.
- [15] L. Hu and J. J. Jiao, "Calibration of a large-scale groundwater flow model using GRACE data: a case study in the Qaidam

- Basin, China," *Hydrogeology Journal*, vol. 23, no. 7, pp. 1305–1317, 2015.
- [16] J. J. Jiao, X. Zhang, Y. Liu, and X. Kuang, "Increased water storage in the Qaidam Basin, the North Tibet Plateau from GRACE gravity data," *PLoS One*, vol. 10, no. 10, article e0141442, 2015.
 - [17] X. Jin, J. Liu, S. Wang, and W. Xia, "Vegetation dynamics and their response to groundwater and climate variables in Qaidam Basin, China," *International Journal of Remote Sensing*, vol. 37, no. 3, pp. 710–728, 2016.
 - [18] T. K. Lowenstein and F. Risacher, "Closed basin brine evolution and the influence of Ca–Cl inflow waters: Death Valley and Bristol Dry Lake California, Qaidam Basin, China, and Salar de Atacama, Chile," *Aquatic Geochemistry*, vol. 15, no. 1–2, pp. 71–94, 2009.
 - [19] H. Y. Ma, L. H. Yin, L. Guo, and J. Zhang, "Modeling the evaporation line of Lake water isotopes in Golmud Drainage Basin, P.R. China," *Advanced Materials Research*, vol. 518–523, pp. 4186–4193, 2012.
 - [20] H. Z. Wei, S. Y. Jiang, H. B. Tan, W. J. Zhang, B. K. Li, and T. L. Yang, "Boron isotope geochemistry of salt sediments from the Dongtai salt lake in Qaidam Basin: boron budget and sources," *Chemical Geology*, vol. 380, pp. 74–83, 2014.
 - [21] C. Ye, M. Zheng, Z. Wang et al., "Hydrochemical characteristics and sources of brines in the Gasikule salt lake, Northwest Qaidam Basin, China," *Geochemical Journal*, vol. 49, no. 5, pp. 481–494, 2015.
 - [22] Y. G. Wang, H. Y. Guo, J. Li, Y. Huang, Z. Y. Liu, and C. E. Liu, *Investigation and Assessment of Groundwater Resources and Their Environmental Issues in the Qaidam Basin*, Geological Publishing House, Beijing, 2008.
 - [23] T. Xu, N. Spycher, E. Sonnenthal, G. Zhang, L. Zheng, and K. Pruess, "TOUGHREACT Version 2.0: a simulator for subsurface reactive transport under non-isothermal multiphase flow conditions," *Computers & Geosciences*, vol. 37, no. 6, pp. 763–774, 2011.
 - [24] Q. C. Hao, *Coupled Modeling of Salt Movement and Groundwater Flow in Inland Basin—a Case Study in Qaidam Basin, China*, China University of Geosciences, Beijing, 2015.
 - [25] F. Liu, Y. L. Cui, G. Zhang, F. Q. Geng, and J. Liu, "Using the ^3H and ^{14}C dating methods to calculate the groundwater age in Nuomuhong, Qaidam Basin," *Geoscience*, vol. 28, no. 6, pp. 1322–1328, 2014.
 - [26] L. Huang and F. Q. Han, *The Evolution of Salt Lake in Qaidam Basin and Palaeoclimate Fluctuation*, Science Press, Beijing, 2007.
 - [27] M. Z. Tian and J. Cheng, *Quaternary Geology and Geomorphology*, Geological Publishing House, Beijing, 2009.
 - [28] D. S. Hu and K. Z. Chen, "The change of the salt lake in the modern times," *Chinese Science Bulletin*, vol. 35, no. 24, pp. 1888–1892, 1990.
 - [29] G. Zhang, N. Spycher, E. Sonnenthal, C. Steefel, and T. Xu, "Modeling reactive multiphase flow and transport of concentrated solutions," *Nuclear Technology*, vol. 164, no. 2, pp. 180–195, 2008.
 - [30] K. Pruess, C. M. Oldenburg, and G. J. Moridis, "TOUGH2 User's Guide Version 2," Lawrence Berkeley National Laboratory. Report LBNL-43134, 1999.
 - [31] J. W. Johnson, E. H. Oelkers, and H. C. Helgeson, "SUPCRT92: a software package for calculating the standard molal thermodynamic properties of minerals, gases, aqueous species, and reactions from 1 to 5000 bar and 0 to 1000°C," *Computers & Geosciences*, vol. 18, no. 7, pp. 899–947, 1992.
 - [32] G. P. Baxter and C. C. Wallace, "Changes in volume upon solution in water of the halogen salts of the alkali metals. II," *Journal of the American Chemical Society*, vol. 38, no. 1, pp. 70–105, 1916.
 - [33] X. Mao, H. Prommer, D. A. Barry, C. D. Langevin, B. Panteleit, and L. Li, "Three-dimensional model for multi-component reactive transport with variable density groundwater flow," *Environmental Modelling & Software*, vol. 21, no. 5, pp. 615–628, 2006.
 - [34] C. Monnin, "Density calculation and concentration scale conversions for natural-waters," *Computers & Geosciences*, vol. 20, no. 10, pp. 1435–1445, 1994.
 - [35] Q. C. Hao, J. L. Shao, Y. L. Cui, and Q. L. Zhang, "Development of a new method for efficiently calculating of evaporation from the phreatic aquifer in variably saturated flow modeling," *Journal of Groundwater Science and Engineering*, vol. 4, no. 1, pp. 26–34, 2016.

Research Article

Characterization of Microscopic Pore Structures of Rock Salt through Mercury Injection and Nitrogen Absorption Tests

Jianwen Chen,¹ Erbing Li,² and Jin Luo ^{1,3}

¹Faculty of Engineering, China University of Geosciences (Wuhan), Wuhan 430074, China

²College of Defense Engineering, Army Engineering University of PLA, Nanjing 210007, China

³Department of Civil and Environmental Engineering, University of California, Berkeley, Berkeley, CA 94720, USA

Correspondence should be addressed to Jin Luo; jinluo@cug.edu.cn

Received 5 March 2018; Accepted 12 April 2018; Published 15 May 2018

Academic Editor: Liangping Li

Copyright © 2018 Jianwen Chen et al. This is an open access article distributed under the Creative Commons Attribution License, which permits unrestricted use, distribution, and reproduction in any medium, provided the original work is properly cited.

Microscopic pore structure of rock salt plays a dominant role in its permeability. In this paper, microscopic pore structure of a set of rock salt samples collected from Yunying salt mine of Hubei province in China is investigated by high pressure mercury injection, rate-controlled mercury penetration, and nitrogen absorption tests. The pore size distribution is further evaluated based on fractal analysis. The results show that pore size of rock salt varies from 0.01 to 300 μm with major concentration of pore size smaller than 1.00 μm . The pore's radiuses are mainly distributed within a range between 15 and 50 nm. The research further reveals that the pore channel size of rock salt is randomly distributed, but the distribution of pore throat radius fits very well with fractal law. By analysis of permeability, it is found that the maximum and medium radius of the pore throat have significant impacts on permeability. Porosity is not apparently related to the permeability of rock salt. The higher the fractal dimension is, the higher the impacts on permeability of the small throat are detected and the lower the influence on permeability of the big throat is exhibited. It indicates that the small throat determines majorly the permeability of rock salt. The findings obtained from this study provide an insight into understanding the characteristics of microscopic pore structure of rock salt.

1. Introduction

Rock salt is an ideal underground medium to store energy (oil and natural gas) with 90% of the world's energy repository constructed in rock salt medium or deserted salt mines [1, 2]. The first rock salt natural gas repository went into operation in Jintan, Jiangsu Province, in 2007, and there will be more rock salt gas repository going into operation to address the cyclic operation needs of natural gas. Although rock salt gas repository is relatively safe, it is still possible that natural gas could leak from salt caverns and thus cause explosion accidents [3]. According to [4], till 2009, the rate for rock salt gas repository accidents was 11% worldwide, with 60% of the accidents causing blowout explosion disasters resulting from failure of gas repository leakproofness. Only with great leakproofness of salt caverns can natural gas in rock salt gas repository be prevented from leaking and pore structure of rock salt is the key element to evaluate the leakproofness of rock salt [5, 6]

As a polycrystalline polymer, rock salt features great leakproofness with a porosity rate of less than 0.5% for undisturbed rock salt and a permeability rate of 10^{-21} – 10^{-20} m^2 [7]. However, rock salt dilatancy behavior will lead to remarkable increase in permeability rate. For instance, with a dilatancy rate of 0.1–0.2%, rock salt's permeability rate would increase by 4 to 5 orders of magnitude [8], indicating the interrelation between porosity rate and permeability rate [9, 10] and that study of pore structure is a significant aspect for the research of rock salt permeability. Cuevas [11] adopted mercury intrusion method, gas adsorption, and saturated hydrocarbon to test the pore structure of Cardona Saline Fm rock salt and divided rock salt pores into mesoscopic pores, microscopic pores, and macroscopic pores. Wu et al. [12] found that, with a porosity rate of 0.3–3.0%, the permeability rate would be about 10^{-20} m^2 . Ji et al. [13] employed mercury intrusion method to test the average porosity rate of rock salt in Qianjiang, China, and found it to be 2.7%.

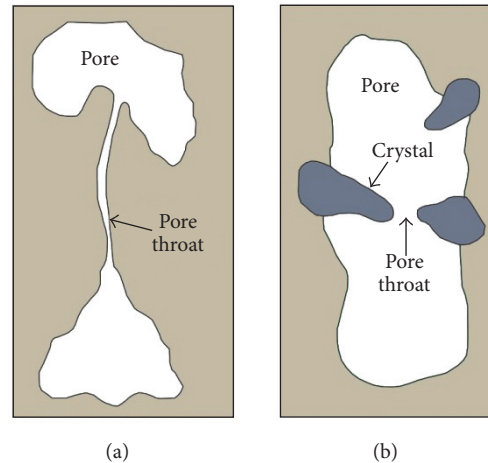


FIGURE 1: A sketch diagram of pore and pore throat in rock salt. (a) demonstrates two pores connecting with a pore throat; (b) displays a pore throat within a single pore.

Gueguen and Dienes [14] did some theoretical research into the relationship between rock microfracture and permeability rate based on statistics and percolation theory. Spangenberg et al. [15] made artificial rock salt with a porosity rate of 5–42% and results show apparent relationship between permeability and porosity rates in samples. Afterwards, Popp and Kern [16], Popp et al. [17], Kissling [18], and Hampel and Schulze [19] consecutively tested the porosity and permeability rates of undisturbed rock salt and results show that there is certain relationship between porosity rate and permeability rate of rock salt and moreover, based on this, Lebensohn et al. [20] set up the gas permeation equation for rock salt.

However, Stormont and Daemen [21] experimented on the relationship between porosity and permeability rates in rock salt's force process and results show that permeability rate increases with the increase of porosity rate, but when confining pressure reaches 7.6 MPa, the increase of permeability rate with porosity rate is no longer apparent. Ji et al. [13] used mercury intrusion experiment to test rock salt in Qianjiang and found that there could be highly porous rock salt with low permeability rate. Therefore, the relationship between rock salt's permeability and porosity rates is very complicated. Apart from porosity rate, pore's channel, throat, connectivity between pores, and other structural features also have great influence on permeability rate, as a schematic diagram shown in Figure 1.

In order to better understand the influences of pore structure on permeability of rock salt, the present research implements mercury intrusion and gas adsorption testing methods to test the pore structure of rock salt in Yunying mine of China and analyze the porosity rate of rock salt, average pore throat ratio, average pore radius, size of pore, and the influence distribution geometry has on permeability rate so as to provide physical basis for the research on permeability rate.

2. Sampling and Testing

2.1. Sampling. The rock salt samples are collected from Yunying salt mine of Hubei province in China. Surface of

samples are first cleaned and cut to be cubically shaped with size of $8 \times 8 \times 8 \text{ mm}^3$. Then, the samples are covered perfectly using ethyl alcohol. Ten samples are grouped into two categories: group one contains Samples No. 1–No. 4 being tested by deploying high pressure injection and group two includes Samples No. 5–No. 10 being examined by rate-controlled penetration. The principle and testing setups mercury injection method is showed in Cuevas [11] and Zhu et al. [22]. Furthermore, the other four samples XF-01, XF-02, XF-03, and XF-04 are tested by nitrogen absorption method. The detailed process of this test has been reported in [23]. All tests are carried out using NOVA multifunction-physical adsorption analyzer in the Geological Engineering Experiment Center, China University of Geosciences (Wuhan).

2.2. Testing Process. The setup of mercury injection test is organized as follows:

- (i) Dry the samples by putting samples in vacuum oven with the temperature 80°C lasting for 4 hours; weigh the sample when this process is completed.
- (ii) Open nitrogen pressure relief valve and set the outlet pressure of 0.28 MPa and then open vacuum pump to start test, and simultaneously switch on the data logging system.
- (iii) Put samples into NOVA to start first with low pressure test; then test the samples with deploying high pressure; the parameters including the accumulative volume of the mercury, mercury rate, and porosity are automatically recorded.
- (iv) Shut down testing facilities and take the samples out of the devices.

The nitrogen absorption tests are set as follows: put samples into vacuum drying oven at 150°C and they are vacuumed for 10 hours and then put the samples into device NOVA to determine the adsorption-desorption curve.

TABLE 1: Classification of the pore size of rock salt.

Sample number	Total porosity (%)	Macroporosity (%)	microporosity (%)	Subporosity (%)
No. 1	3.0660	18.90%	22.56%	58.54%
No. 2	0.9900	15.98%	26.32%	57.64%
No. 3	2.4099	16.70%	25.10%	58.20%
No. 4	2.9468	10.81%	37.06%	53.04%
No. 5	0.9343	51.74%	12.17%	86.09%
No. 6	0.9526	0%	30.52%	63.48%
No. 7	3.743	10.56%	29.18%	60.26%
No. 8	0.4742	52.73%	18.18%	29.09%
No. 9	0.5526	10.4%	28.64%	61.22%
No. 10	0.6339	8.46%	21.18%	70.36%

TABLE 2: Porosity and the average throat radius.

Sample number	No. 5	No. 6	No. 7	No. 8	No. 9	No. 10
Porosity (%)	0.9343	0.9526	3.743	0.4742	0.5526	0.6339
Average throat radius (μm)	0.0155	0.0143	0.0141	0.0169	0.0168	0.0185

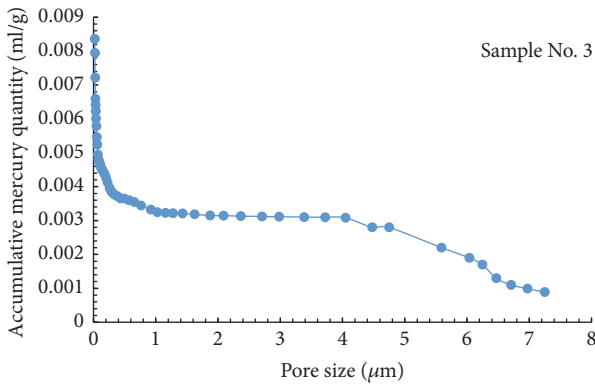


FIGURE 2: Accumulative mercury quantity versus pore size curve of Sample No. 3.

3. Results and Discussion

3.1. Pore of Rock Salt

3.1.1. Pore Size Distribution. The pore size distribution of the rock salt is determined based on high pressure mercury injection tests. Figure 2 shows the accumulative mercury quantity varies with pore size of Sample No. 3. According to previous studies [24, 25], the pore size of rock salt can be classified into three categories as follows: macroscopic pore with size larger than $8 \mu\text{m}$, microscopic pore with a size varying between $1 \mu\text{m}$ and $8 \mu\text{m}$, and subpore with pore size that is smaller than $1.0 \mu\text{m}$. Among these three types of pore, macroscopic pore is generally flat-shaped, the microscopic pores form often network, and subpore is connected as pore throat, as displayed in Figure 1.

The testing results show that the porosity of the rock salt samples collected from Yuying mine varies between 0.26% and 3.0%, as shown in Table 1. These findings fit very well with the results reported by Wu et al. [12]. On the other hand, the pore size is determined to be ranged from 2.0 to $300 \mu\text{m}$. And the subpore accounts for 60% of the total pores in the samples. The curve of mercury injection pressure-increase mercury rate shows a singlet, indicating that the pore size is intensively concentrated. Furthermore, the pore size was determined to be concentrated within 15 nm to 35 nm, implying a subpore dominated porous mediums of the rock salt.

3.1.2. Pore Throat Radius. Both pore volume and pore throat volume can be precisely determined by rate-controlled penetration experiments. Thus, the pore structure is investigated very specifically. In this study, six samples including Nos. 5–10 are tested by rate-controlled penetration experiment. Table 2 lists the determined porosity and the average throat radius of the samples. The average throat radius varies from 14 nm to 18 nm based on this method; it is verified that the pores majorly consist of subpores.

Considering that nitrogen absorption experiment can test the pore size from 0.35 nm to 100 nm and the rate-controlled penetration test can test pore size ranging from 7 nm to $200 \mu\text{m}$, the nitrogen absorption experiment is applied to investigate the pore size characteristics in the present study. Three samples are prepared and tested and the obtained results are listed in Table 3. The throat radiuses for these samples are 6.04 nm, 13.54 nm, and 38.07 nm, with void volume per weight being $80 \text{ cm}^3 \text{ g}^{-1}$, $100 \text{ cm}^3 \text{ g}^{-1}$, and $1400 \text{ cm}^3 \text{ g}^{-1}$, respectively.

By analysis, the samples XF-02, XF-03, and XF-04 exhibit obviously peaks in their BJH (Barrett Joyner and Halenda)

TABLE 3: The determined specific surface area and pore size using nitrogen absorption method.

Sample number	XF-01	XF-02	XF-03
Average pore throat radius (nm)	6.04	13.54	38.07
Specific surface area ($\text{m}^2 \text{g}^{-1}$)	13.3×10^3	7.16×10^3	0.3×10^3
Micropore volume ($\text{cm}^3 \text{g}^{-1}$)	80	100	1400

TABLE 4: Major parameters for the distribution of pore throat.

Sample number	No. 5	No. 6	No. 7	No. 8	No. 9	No. 10
Average throat radius (μm)	0.0155	0.0143	0.0141	0.0169	0.0168	0.0185
Sorting coefficient	0.5802	0.6187	0.7113	0.5537	0.9104	0.6979
Fractal dimension (D , -)	2.47	2.38	2.53	2.23	2.19	2.62
Fractal coefficient (a , -)	4.086	22.420	11.821	16.900	11.900	9.071
Relation coefficient (R^2 , -)	0.997	0.955	0.995	0.874	0.932	0.985

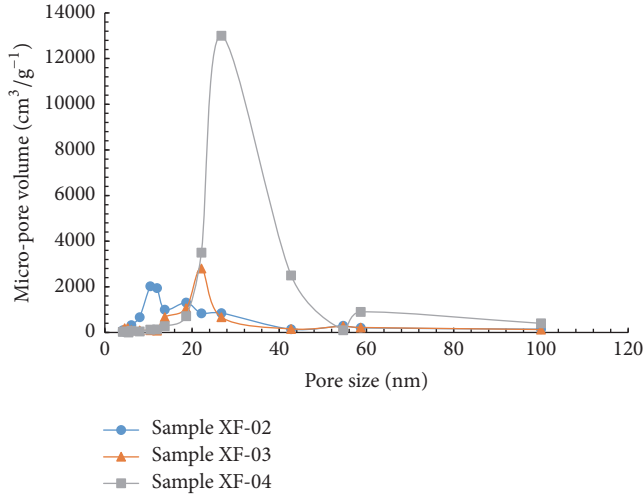


FIGURE 3: The BJH distribution of pore size of the rock salt samples.

distribution curve, as shown in Figure 3. The corresponding pore sizes to the peak values are 10.4 nm, 22.1 nm, and 26.7 nm, showing that the pore sizes are mainly distributed among 10 nm and 30 nm.

3.1.3. The Pore Size Distribution of Channel and Pore Throat.

Figure 4 shows the pores channels and pore throats determined by rate-controlled penetration test. It can be seen that the pore throats are mainly concentrated with the size smaller than $2.0 \mu\text{m}$. By fitting the curve, it is found that the distribution of pore exhibits an exponential relationship with quantity of the pores percentage.

The study above revealed that the pore throats have a size generally smaller than $2.0 \mu\text{m}$. According to fractal theory [26], the number of pore throats can be derived as follows in case of the distribution of pore throat fit with fractal theory:

$$N(r) = ar^{-D}. \quad (1)$$

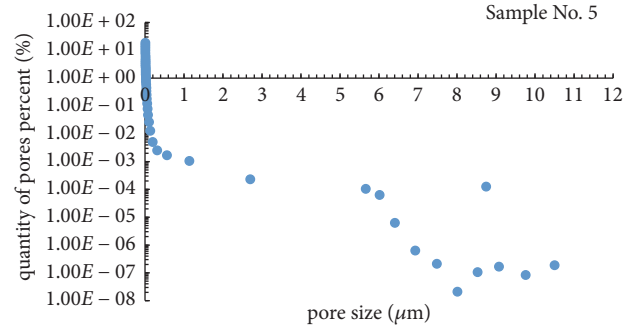


FIGURE 4: The pore size distribution of Sample No. 3.

Similarly, the function for the distribution of pore throat can be formulated as follows:

$$P(r) = aDr^{-D-1}, \quad (2)$$

where N is quantity of pore throat; $P(r)$ is the function on pore throat radius density distribution; r is the pore throat radius, in μm ; a is the fractal coefficient; and D is the fractal dimension of the pore throat distribution.

Taking Samples No. 5–No. 10, for example, the pore channels are analyzed by following fractal theory for the size both smaller and bigger than $2.0 \mu\text{m}$. Table 4 shows the results for the pore channel. The fractal dimensions of these six samples are varied between 2.19 to 2.62 with correlation coefficient of 0.874–0.997. According to the fractal theory, the three-dimensional pore should range from 2.0 to 3.0. The finding indicates that the pore channel distribution fits very well with the fractal theory. Therefore, the microscopic structure of the pore throat can be quantitatively estimated by fractal dimensions.

On the other hand, pore channel is also analyzed using the fractal dimensions, as shown in Table 5. The fractal dimensions are determined to be ranged from 3.75 to 6.29, implying that the distribution of pore channel does not fit the fractal law.

TABLE 5: The pore channel distribution and fractal dimensions.

Sample number	No. 5	No. 6	No. 7	No. 8	No. 9	No. 10
Fractal dimension D	6.29	3.75	6.04	4.54	4.87	5.95
Fractal coefficient a	19.00	8.50	6.90	6.84	8.40	12.30
Relation coefficient R^2	0.451	0.684	0.705	0.948	0.922	0.811

TABLE 6: Relationship of throat microgeometrical parameters with porosity and permeability.

Microgeometrical parameters	Maximum	Minimum	Correlation with porosity	Correlation with permeability
Skewness	1.08	0.39	$y = 0.831x^{-1.18}$ $R^2 = 0.382$	$y = 0.008x^{-0.97}$ $R^2 = 0.136$
Sorting coefficient	1.3449	0.3023	$y = 1.374x^{0.233}$ $R^2 = 0.017$	$y = 0.005x^{1.648}$ $R^2 = 0.139$
Variation coefficient	0.797	0.5006	$y = 3.462x^{1.978}$ $R^2 = 0.166$	$y = 0.501x^{9.991}$ $R^2 = 0.663$
Median pore throat radius (μm)	1.115	0.0086	$y = 1.647x^{0.192}$ $R^2 = 0.136$	$y = 0.015x^{1.106}$ $R^2 = 0.775$
Median pressure (MPa)	36.293	0.3871	$y = 3.552x^{-0.53}$ $R^2 = 0.739$	$y = 0.028x^{-0.46}$ $R^2 = 0.400$
Displacement pressure (MPa)	0.07176	0.0471	$y = 3.458x^{0.796}$ $R^2 = 0.715$	$y = 0.022x^{0.749}$ $R^2 = 0.837$
Maximum mercury saturation (%)	96.04	71.43	$y = 5E - 10x^{4.919}$ $R^2 = 0.722$	$y = 9E - 16x^{6.792}$ $R^2 = 0.540$

3.2. Relationship of Throat Microgeometrical Parameters with Porosity and Permeability. Pore throat reveals the connection among the pores which is considered to be crucially important to the permeability of rock mass. The parameters including average capillary pressure, P_d , the displacement pressure, the median pressure, P_{C50} , the mean capillary pressure, \bar{p}_c , mean value, \bar{X} , sorting coefficient, σ , variation coefficient, vc , and skewness, S_k , can be determined by mercury injection test. These parameters are useful in quantitatively determining the pore's structure. Among all the parameters, S_k represents the distribution of pore throat radius.

Ten samples are tested by the capillary tests and the obtained parameters are displayed in Table 6. It shows that P_d , P_{C50} and the maximum mercury saturation have good correlation with porosity of the rock salt. P_d represents the minimum pressure for the mercury entering into the pores, corresponding to the maximum pore throat radius. Similarly, P_{C50} denotes the median pressure that is accordance with the median radius. In general, the bigger the pore size is the lower displacement pressure is. The maximum mercury saturation represents a peak pressure for the injection test. The larger the volume of mercury entering the pore means the better the connectivity of the pores, and the higher the porosity detected.

Table 6 shows that the displacement pressure, P_d , and median pressure are strongly related to porosity of rock salt, with the correlation coefficient $R^2 = 0.837$ and $R^2 = 0.775$. In addition, the variation coefficients show a weak correlation with porosity, $R^2 = 0.166$. A low correlation

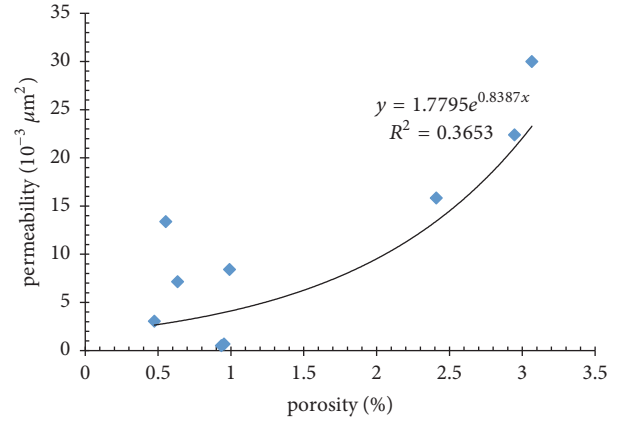


FIGURE 5: Relationship between porosity and permeability of rock salt.

coefficient is shown when fitting porosity with permeability, as it is also verified in Figure 5. Therefore, the porosity has no obvious effects on permeability of the rock salt. Conclusively, the microstructures of the pore throat such as shape, size, connectivity, and distribution are the important factors to the permeability of the rock salt

3.3. Influences of Pore Throat on Permeability. The low permeable medium has generally small throat radius, but with big pore size. The throat has larger number than pore and thus the throat plays determining role in the permeability of rock salt [27]. As this study revealed above that distribution

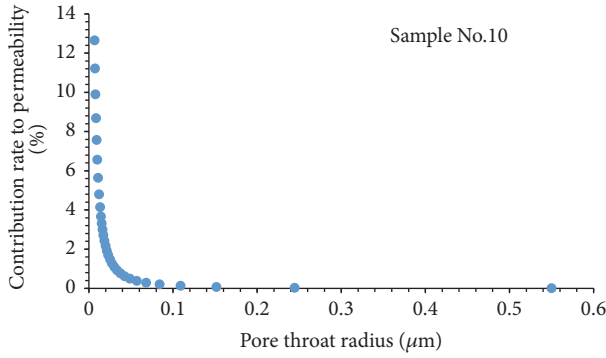


FIGURE 6: Pore throat radius and its contribution rate to permeability.

of pore size conforms very well with fractal theory. According to Hagen-Poiseuille's approach, the contribution of a single throat to permeability can be formulated as follows:

$$\Delta K_i = \frac{r_i^{1-D}}{\sum_{i=1}^n r_i^{1-D}}, \quad (3)$$

where ΔK_i is the contribution rate to permeability of a single pore throat radius; r represents the radius (μm).

Figure 6 shows that pore throat radius versus with contribution rate to permeability of rock salt Sample No. 10. It is observed that the small pore throat contributes mainly the permeability. The effect of throat radius on permeability becomes negligible when the radius is larger than $0.1 \mu\text{m}$.

4. Conclusions

In this paper, the microscopic pore structure and its influences on permeability of rock salt samples collected from Yunying salt mine in China are studied. High pressure mercury injection, rate-controlled mercury penetration, and nitrogen absorption experiments are carried out to determine the pore size and its distribution. The impact of pore size and structure on permeability is then analyzed. Major findings of this study include the following:

- (i) The porosity of rock salt is determined to be varying between 0.26% and 3.00%. The pore size covers a range from 0.01 to $300 \mu\text{m}$, which can be categorized into macroscopic pore with pore size larger than $8 \mu\text{m}$, microscopic pore ($1 \mu\text{m}$ – $8 \mu\text{m}$), and subpore ($<1 \mu\text{m}$). The void of rock salt mainly consists of subpore, accounting for 60% of the total pores. The pore size is estimated to range mainly from 15 nm to 50 nm based on Wash-Born approach. The pore throat radius is determined to be within 10 nm to 30 nm by nitrogen absorption tests.
- (ii) Pore channel size of the rock salt is distributed randomly, but the pore throat radius conforms with the law of fractal theory and the fractal dimension is determined to vary between 2.19 and 2.62. The displacement pressure, P_d , the median pressure, P_{C50} ,

and the maximum mercury saturation are found to be strongly correlated with porosity.

- (iii) The porosity of the rock salt is observed to be not correlated obviously with its permeability. On the other hand, maximum pore and median pore throat radius are both related to permeability of the rock salt. The variation coefficient of pore throat distribution is estimated to be 0.663, indicating they are strongly correlated. Thus, pore throat radius plays dominated role in permeability of rock salt. The further research shows that the influences of big throat radius on permeability of rock salt become lower and the contribution of small throat radius on permeability increases drastically with increasing the fractal dimension.

Data Availability

The data used to support the findings of this study are available from the corresponding author upon request.

Conflicts of Interest

The authors declare that they have no conflicts of interest.

Acknowledgments

The project was also supported by the National Natural Science Foundation of China (no. 51474259) and Fundamental Research Funds for the Central Universities, China University of Geosciences (Wuhan) no. CUGL150818 and no. CUGL 150610. The funding provided by China Scholarship Council (CSC) during the visit at University of California, Berkeley, is deeply appreciated.

References

- [1] C. H. Yang, W. G. Liang, D. H. Wei et al., "Investigation on possibility of energy storage in salt rock in China," *Chinese Journal of Rock Mechanics and Engineering*, vol. 24, no. 24, pp. 4409–4417, 2005.
- [2] J. Cai, B. Yu, M. Zou, and L. Luo, "Fractal characterization of spontaneous co-current imbibition in porous media," *Energy & Fuels*, vol. 24, no. 3, pp. 1860–1867, 2010.
- [3] M. Zhang and M. J. McSaveney, "Rock avalanche deposits store quantitative evidence on internal shear during runout," *Geophysical Research Letters*, vol. 44, no. 17, pp. 8814–8821, 2017.
- [4] L. H. Xie, H. L. Li, X. W. Zhao et al., "Statistics and risk analysis of underground gas storage accident in salt caverns," *China Safety Science Journal*, vol. 19, no. 9, pp. 125–132, 2009.
- [5] S. Wang, X. Han, Y. Dong, and H. Shi, "Mechanisms of reservoir pore/throat characteristics evolution during long-term waterflooding," *Advances in Geo-Energy Research*, vol. 1, no. 3, pp. 148–157, 2017.
- [6] Y. Xia, J. Cai, W. Wei, X. Hu, X. Wang, and X. Ge, "A new method for calculating fractal dimensions of porous media based on pore size distribution," *Fractals*, vol. 26, no. 1, Article ID 1850006, 2018.

- [7] P. Berest, J. Bergues, B. Brouard et al., "A salt cavern abandonment test," *International Journal of Rock Mechanics & Mining Sciences*, vol. 38, pp. 357–368, 2001.
- [8] O. Schulze, T. Popp, and H. Kern, "Development of damage and permeability in deforming rock salt," *Engineering Geology*, vol. 61, no. 3, pp. 163–180, 2001.
- [9] W. Liu, N. Muhammad, Y. Li, C. J. Spiers, C. Yang, and H. Ma, "Experimental study of permeability of salt rock and its application to deep underground gas storage," *Chinese Journal of Rock Mechanics and Engineering*, vol. 33, no. 10, pp. 1953–1961, 2014.
- [10] S. Huang, Y. Wu, X. Meng, L. Liu, and W. Ji, "Recent advances on microscopic pore characteristics of low permeability sandstone reservoirs," *Advances in Geo-Energy Research*, vol. 2, no. 2, pp. 122–134, 2018.
- [11] C. D. L. Cuevas, "Pore structure characterization in rock salt," *Engineering Geology*, vol. 47, no. 1, pp. 17–30, 1997.
- [12] Z. Wu, H. Zhou, J. Ding, L. Ran, and H. Yi, "Research on permeability testing of rock salt under different permeability pressures," *Chinese Journal of Rock Mechanics and Engineering*, vol. 31, no. S2, pp. 3740–3746, 2012.
- [13] W. Ji, C. H. Yang, W. Liu, and M. Li, "Experimental investigation on meso-pore structure properties of bedded salt rock," *Chinese Journal of Rock Mechanics and Engineering*, vol. 32, no. 10, pp. 2036–2044, 2013.
- [14] Y. Gueguen and J. Dienes, "Transport properties of rocks from statistics and percolation," *Mathematical Geology*, vol. 21, no. 1, pp. 1–13, 1989.
- [15] E. Spangenberg, U. Spangenberg, and C. Heindorf, "An experimental study of transport properties of porous rock salt," *Physics and Chemistry of the Earth*, vol. 23, no. 3, pp. 367–371, 1998.
- [16] T. Popp and H. Kern, "Monitoring the state of microfracturing in rock salt during deformation by combined measurements of permeability and P- and S-wave velocity," *Physics and Chemistry Earth*, vol. 25, no. 2, pp. 149–154, 2000.
- [17] T. Popp, H. Kern, and O. Schulze, "Evolution of dilatancy and permeability in rock salt during hydrostatic compaction and triaxial deformation," *Journal of Geophysics*, vol. 106, no. B3, pp. 4061–4078, 2001.
- [18] W. Kissling, "Transport of three-phase hyper-saline brines in porous media: theory and code complementation," *Transport Porous Medium*, vol. 61, pp. 25–44, 2005.
- [19] A. Hampel and O. Schulze, "The composite dilatancy model: a constitutive model for the mechanical behavior of rock salt," in *Proceedings of the 6th Conference on The Mechanical Behavior of Salt-Understanding of THMC Process in Salt*, M. Wallner, K.-H. Lux, W. Minkley, and H. R. Hardy Jr., Eds., pp. 99–107, Taylor & Francis Group, London, UK, 2007.
- [20] R. A. Lebensohn, P. R. Dawson, H. M. Kern, and H.-R. Wenk, "Heterogeneous deformation and texture development in halite polycrystals: Comparison of different modeling approaches and experimental data," *Tectonophysics*, vol. 370, no. 1–4, pp. 287–311, 2003.
- [21] J. C. Stormont and J. J. K. Daemen, "Laboratory study of gas permeability changes in rock salt during deformation," *International Journal of Rock Mechanics and Mining Sciences & Geomechanics Abstracts*, vol. 29, no. 2, pp. 325–342, 1992.
- [22] Y. X. Zhu, W. Sun, and Y. U. Feng, "Application of high pressure injection and rate-controlled penetration experimental technique to studying reservoir microscopic pore structure," *Natural Gas Geoscience*, vol. 19, no. 4, p. 553, 2008.
- [23] T. X. Zhong, "Characteristics of pore structure of marine shales in South China," *Natural Gas Industry*, vol. 32, no. 9, pp. 1–4, 2012.
- [24] H. H. Yuan and B. F. Swanson, "Resolving pore space characteristics by rate-controlled porosimetry," *SPE Formation Evaluation*, vol. 4, article no. 14892, no. 01, pp. 167–175, 1986.
- [25] M. Zhang, Y. Yin, and R. Hu, "Mechanisms of rainfall-induced landslides in gently inclined red beds in the eastern Sichuan," *Landslides*, vol. 12, no. 5, pp. 973–983, 2015.
- [26] B. B. Mandelbrot, *Fractals: Form, Chance and Dimension*, Freeman, San Francisco, Calif, USA, 1977.
- [27] J. B. Yu, D. J. Guo, and X. Q. Wang, "Study of microscopic behavior of low permeable reservoir through constant velocity mercury injection technique," *Journal of Daqing Petroleum Institute*, vol. 30, no. 2, pp. 22–25, 2006.

Research Article

Interaction between Vetiver Grass Roots and Completely Decomposed Volcanic Tuff under Rainfall Infiltration Conditions

Ling Xu ¹, Chongyang Gao,¹ and Dongdong Yan²

¹Department of Civil Engineering, School of Human Settlements and Civil Engineering, Xi'an Jiaotong University, Xi'an 710049, China

²Department of Geotechnical and Tunnel Engineering, School of Highway, Chang'an University, Xi'an 710064, China

Correspondence should be addressed to Ling Xu; suyu820@163.com

Received 28 January 2018; Revised 30 March 2018; Accepted 8 April 2018; Published 14 May 2018

Academic Editor: Liangping Li

Copyright © 2018 Ling Xu et al. This is an open access article distributed under the Creative Commons Attribution License, which permits unrestricted use, distribution, and reproduction in any medium, provided the original work is properly cited.

The important role of vetiver grass roots in preventing water erosion and mass movement has been well recognized, though the detailed influence of the grass roots on soil has not been addressed. Through planting vetiver grass at the Kadoorie Farm in Hong Kong and leaving it to grow without artificial maintenance, the paper studies the influence of vetiver grass roots on soil properties and slope stability. Under the natural conditions of Hong Kong, growth of the vetiver grass roots can reach 1.1 m depth after one and a half year from planting. The percentage of grain size which is less than 0.075 mm in rooted soil is more than that of the nonrooted soil. Vetiver grass roots can reduce soil erosion by locking the finer grain. The rooted soil of high finer grain content has a relatively small permeability. As a result, the increase in water content is therefore smaller than that of nonrooted soil in the same rainfall conditions. Shear box test reveals that the vetiver grass roots significantly increased the peak cohesion of the soil from 9.3 kPa to 18.9 kPa. The combined effects of grass roots on hydrological responses and shearing strength significantly stabilize the slope in local rainfall condition.

1. Introduction

The use of vetiver grass for various applications in erosion and sediment control was developed by the World Bank for soil and water conservation in India in the 1980s [1]. Many literatures reviewed or studied the characteristics of vetiver grass and its application in preventing soil erosion and mass movement [2–9]. Rainfall infiltration is a key factor to control slope stability [10, 11]. In all, the effects of vetiver grass roots on erosion control and mass movement can be summarized as follows: (1) preventing surface erosion through the soil-binding properties of roots, (2) reducing effects of splash erosion through rainfall interception of vegetation canopy, (3) reducing the incidence of shallow slope instability through the anchoring properties of roots, (4) channeling run-off to alter slope hydrology, and (5) providing support to the base of the slope and trapping material moving down the slope.

Hong Kong is a small place and is densely populated; urban development has been carried out over the decades,

which has led to enormous pressures on the fragile mountain environment. Most of Hong Kong's crucial rain is brought by the monsoon, which falls in just a few weeks between May and September (Figure 1). In combination with the monsoon climate, very steep slopes, and inherently weak geological conditions, these factors make Hong Kong highly susceptible to erosion and landslides [12–17]. So, vetiver grass, as an important species used for soil bioengineering, is selected in this research to deal with erosion problems and shallow landslides in Hong Kong (Figure 2).

The paper focused on the influence of vetiver grass roots on physical and mechanical properties of soil which has not been addressed, though the important role of vetiver grass roots in preventing water erosion and mass movement has been recognized in recent years. Because the majority of published literatures are based on practical experience or not under such local nature conditions of Hong Kong, there is still a clear need for scientific research concerning the influence of vetiver grass roots on physical and mechanical

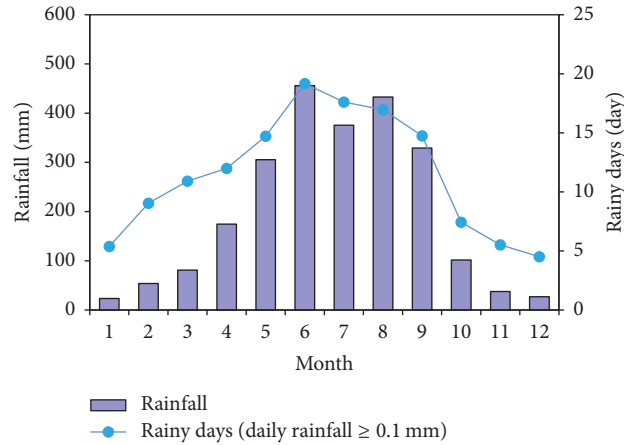


FIGURE 1: The monthly average of rainfall and rainfall days recorded by the observatory in 1981–2010.

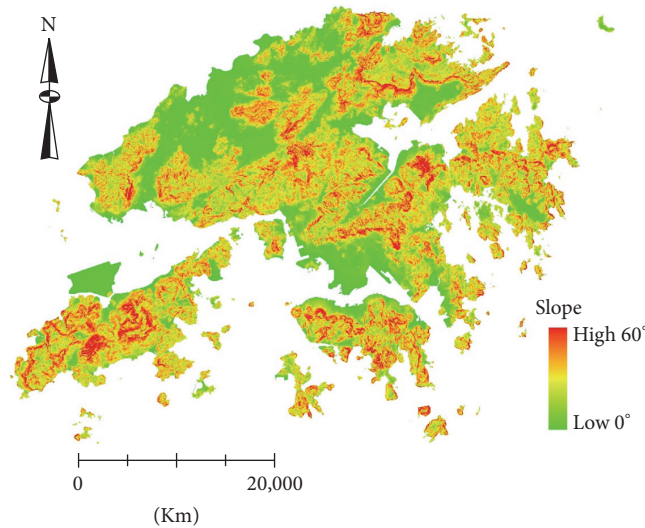


FIGURE 2: The site and DEM of Hong Kong.

prosperities. In this study, the in situ water content was tested by moisture probe in field. Tests consisting of water content, soil density, grain-size distribution, permeability, and direct shearing were carried out in the laboratory. All items were conducted on rooted and nonrooted soil, respectively.

2. Planting Site and Vetiver Grass Growth

Vetiver grass used in this research has been planted at the Kadoorie Farm of Hong Kong in June. Vetiver grass was planted at spacing of 1 m on a steep slope surface (Figure 3). The slope is 10 m long and has a maximum height of about 10 m. The slope was formed to an angle of 60° by cutting into completely decomposed volcanic tuff.

In order to test its survivability, no water and nutrients were artificially given to the grass during its growth. In 3 months after planting, the grass had grown up to 1.0 m high (Figure 4(a)). Figure 4(b) shows a typical grass roots system. The maximum root depth is 1.1 m and the root diameter ranges from 0.05 mm to 4 mm. Main roots were mostly found

within the 25 cm below the ground surface, and for the depth greater than 25 cm from the surface, fibrous roots were mostly found.

Figure 5 shows the development of the grass stem length against time. At the time of field sampling and testing in January, the grass had grown to about 1.8 m tall in a very healthy condition despite the fact that it had been exposed to heavy rain in the summer and a very dry winter.

3. Field and Laboratory Test Results

3.1. Physical Properties. Herein, physical properties include water content, soil density, grain-size distribution, and permeability. All these items were conducted on both rooted soil and nonrooted soil to explore the influences of vetiver grass roots on soil's physical properties.

Water Content. Firstly, soil water content was studied in field on nonrooted and rooted soil. The ML2X moisture probe and data logger produced by detaT company in UK were used



FIGURE 3: Panorama of research site (a) before grass planting and (b) during field testing.

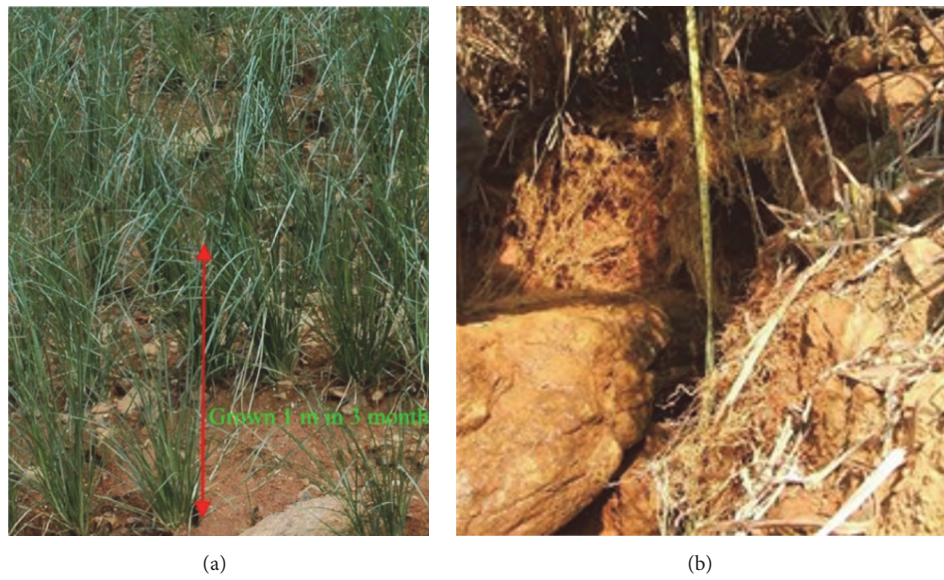


FIGURE 4: (a) Vetiver stem growth in 3 months after planting. (b) Typical grass root system.

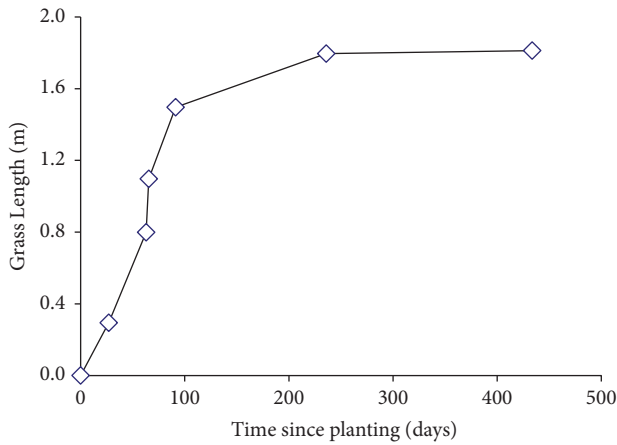


FIGURE 5: The development of the grass stems length against time.

in this test. The selected testing locations and the measured output voltage value are shown in Figure 6. According to the

calibration curves of measured voltage and water content, the mass water content was obtained as shown in Table 1. Soil water content was also tested in laboratory. The soil tested was taken from the sample surface when the sample box was opened in laboratory. The water content was measured by drying method. The results are shown in Table 2.

From the results of the in situ and laboratory water content shown in Table 3, it is observed that vetiver grass roots increased the average soil water content by about 11.63% in field. The increase scale in laboratory testing is 8.26%. It is less than that obtained in field and may be because of the difference of two types of samples in water loss.

Soil Density. The soil used for density testing was taken from the block sample surface when opening the box in laboratory. Ring-knife method was used in this test. Inner diameter of the ring-knife is 61.8 mm and height is 20 mm. Test results are shown in Table 4. It can be found that the average density of soil with roots is 1.81 g/cm^3 , which is higher than that of the soil without roots, 1.67 g/cm^3 . Using the laboratory water

TABLE 3: In situ and laboratory water content of soil samples.

	Soil without roots	Soil with roots	Increase in percentage
Average in situ water content	13.33%	14.88%	11.63%
Average laboratory water content taken from sample surface	18.7%	19.8%	8.26%

TABLE 4: Laboratory soil density and calculated dry density.

Sample number	Laboratory soil density (%)	Average natural soil density (g/cm^3)	Calculated dry density (g/cm^3)
Rootedsample_1	1.81	1.81	1.51
Rootedsample_2	1.85		
Rootedsample_3	1.86		
Rootedsample_4	1.79		
Rootedsample_5	1.74		
Nonrooted sample_1	1.70	1.67	1.41
Nonrooted sample_2	1.66		
Nonrooted sample_3	1.66		

TABLE 5: Grain-size distribution of different samples.

Sample number	Grain size (mm)						
	10~5	5~2	2~0.5	0.5~0.25	0.25~0.075	0.075~0.005	<0.005
Nonrooted sample_1	2.7	32.7	12.8	1.9	20.7	19.7	9.5
Nonrooted sample_2	3.7	38.2	12.5	2	16.1	17.2	10.3
Nonrooted sample_3	7.4	25.7	5.3	0.9	10.9	25.9	23.9
Rooted sample_1	2.2	36.1	8.9	1.2	10.5	21	20.1
Rooted sample_2	2	25.6	10.6	1.5	15.8	26.1	18.4
RootedSample_3	1.1	22.2	8.1	1.1	13.3	30.7	23.5
RootedSample_4	3.6	26.3	10	1.7	13.4	25.4	19.6
RootedSample_5	2.7	37.8	7.6	1.1	10.6	20.5	19.7

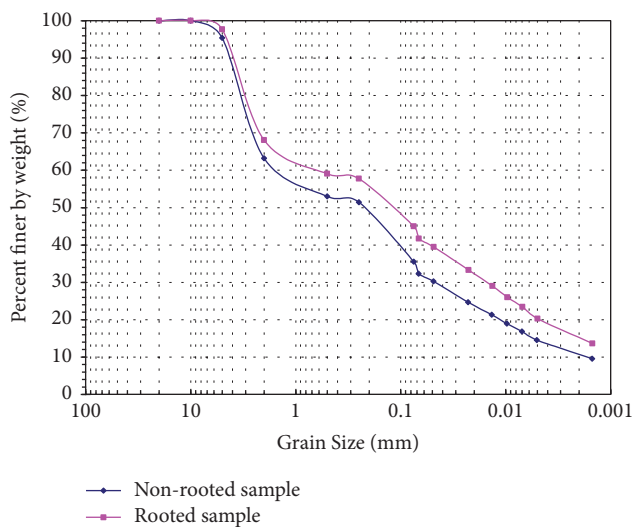


FIGURE 7: Average grain-size distribution of rooted and nonrooted properties.

TABLE 6: Densities and moisture content of the soil samples.

Sample	Moisture content	Moist density (kg/m^3)	Dry density (kg/m^3)
Rooted soil	14.9%	1800	1500
Nonrooted soil	13.3%	1700	1400

3.2. Mechanical Properties

Shear Box Test Results. Eight samples, each of dimensions $600 \text{ mm} \times 600 \text{ mm} \times 600 \text{ mm}$, were retrieved at location shown in Figure 3. Five samples were matrix of soil containing vetiver grass roots, whereas the remaining three were “bare” soil.

The soil was identified to be completely decomposed tuff. The densities and moisture content were tabulated in Table 6. Furthermore, the particle-size distribution of each sample was determined by taking samples, and the results are

TABLE 7: Results of large-scale direct shear test.

Sample number	Designed normal stress/kPa	Displacement/mm	Peak state		Residual state		Root area ratio
			Normal stress/kPa	Shear stress/kPa	Normal stress/kPa	Shear stress/kPa	
Rooted_1	20	16	22.4	32.2	24.5	19.8	1.98%
Rooted_2	40	18	51.3	39.5	42.9	25.4	0.88%
Rooted_3	60	32	71.5	46.6	67.5	41	1.60%
Rooted_4	80	22	82.9	54.4	84.6	41.4	2.45%
Rooted_5	120	16	124.2	76.1	128.4	62.2	2.11%
Nonrooted_1	10	15	10.7	14	9.6	10.4	---
Nonrooted_2	80	29	80	45.5	79	34	---
Nonrooted_3	120	36	120	63	120.3	54	---

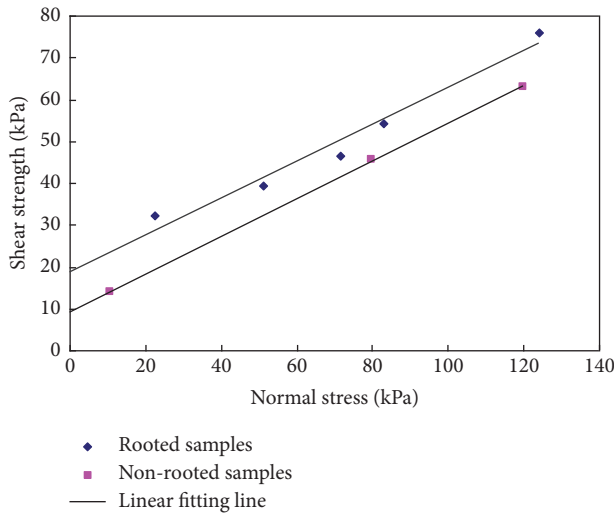


FIGURE 8: Peak shear strength against normal stress of rooted and nonrooted sample.

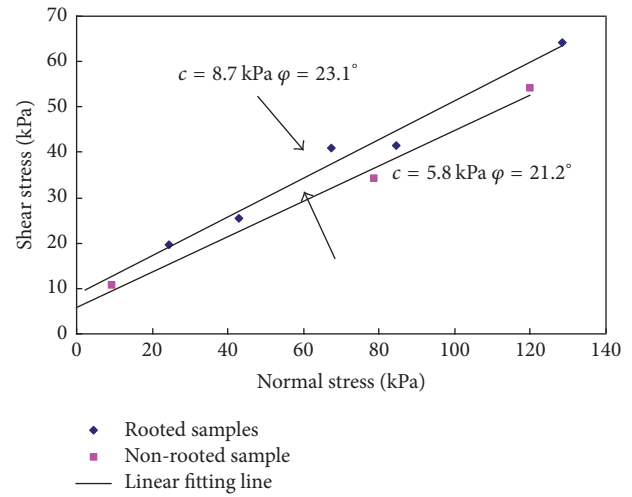


FIGURE 9: Residual shear strength against normal stress of rooted and nonrooted sample.

depicted in Figure 7. The soil is rather fine with some gravel. The coefficient of uniformity is approximately 5.

The shear strength obtained is plotted on the y -axis with the corresponding normal stress on the x -axis. Based on the test results (Table 7), the soil cohesion and frictional angle were obtained (Figures 8 and 9).

As shown in Figure 8, the peak cohesion of rooted soil is 18.9 kPa and the nonrooted soil is 9.3 kPa. Vetiver grass roots increased the cohesion by 103% in this study. The peak friction angles of rooted and nonrooted soils are nearly the same, which are 23.7° and 24.2° , respectively. The results of residual strength are shown in Figure 9. The residual cohesions of the rooted and nonrooted soils are 8.7 kPa and 5.8 kPa and their corresponding friction angles are 23.1° and 21.2° .

3.3. Application to Slope Safety. Vetiver grass was used to stabilize the slope. The effect of roots on slope stability is therefore analysed here. As revealed by shearing box testing,

the grass roots can increase the soil strength. On the other hand, vetiver grass also changed the soil permeability. Finer particles were well reserved in the rooted soil in case of rainfall conditions. This will certainly influence the soil water characteristic curve (SWCC). In this study, the SWCC is evaluated using the soil's particle-size distribution. Soil permeability function is generated for rooted and nonrooted soils. As a result, the soil water contents in slope under the same rainfall conditions are different. The slope stability will therefore be different for rooted soil and nonrooted soil.

A slope is selected in this study. The slope angle is 45° . This is mainly because the 45° slope is mostly distributed in Hong Kong (Figure 2). The vetiver grass rooted soil is 3 m deep in vertical direction. The particle-size distribution of rooted and nonrooted soils as shown in Figure 7 is adopted to evaluate SWCC (Figure 10) for grass slope and nongrass slope, respectively. The soil strength as presented in Figure 8 is adopted for the rooted and nonrooted soils. The rainfall intensity of $7.62 \times 10^{-7} \text{ m/s}$ was used in the model. The preset

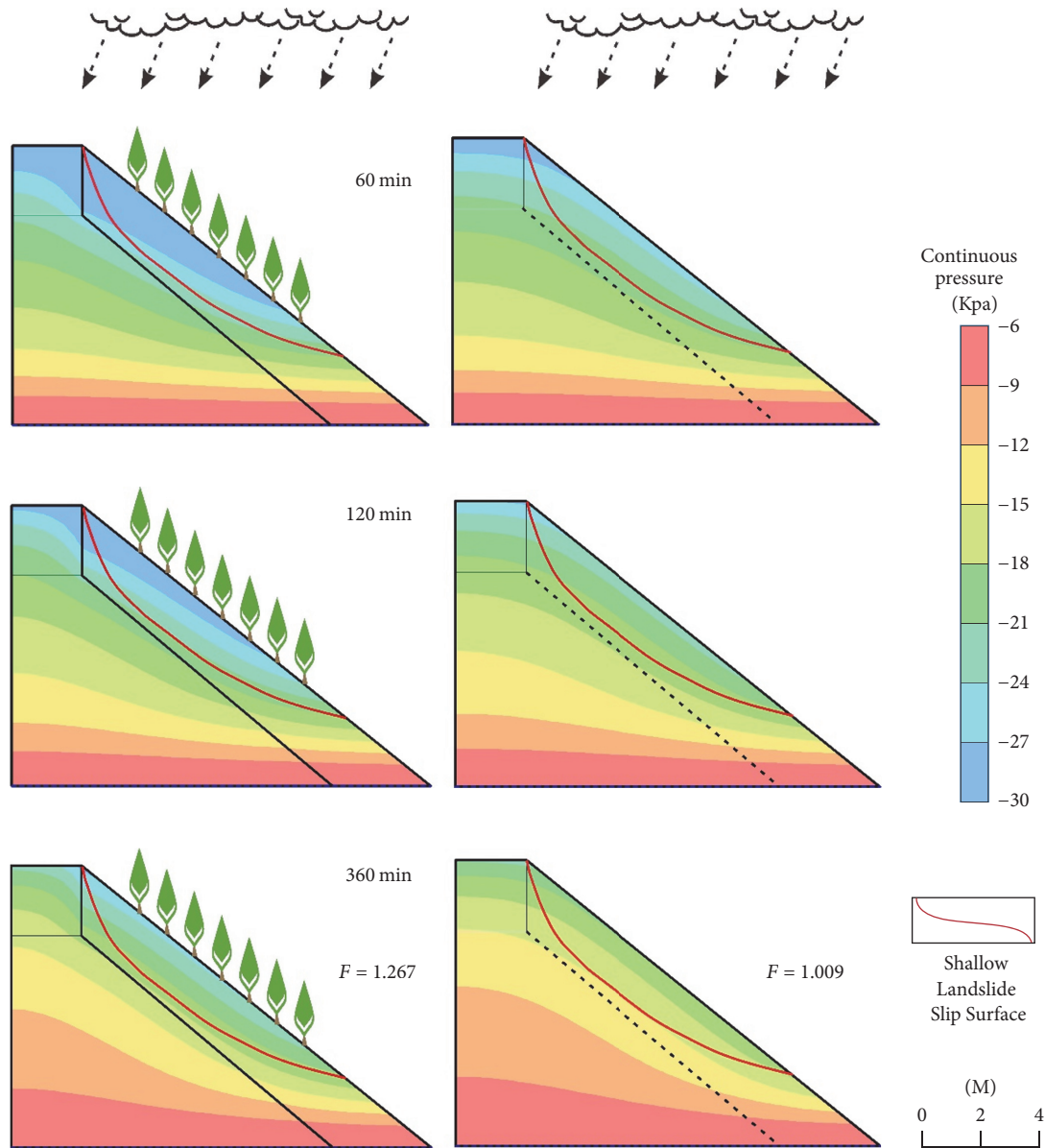


FIGURE 10: Hydrological responses to rainfall and slope stability for nonrooted and rooted slopes.

slip surface was defined in the slope to constitute the base of the comparison between nonrooted and rooted slopes.

Figure 10 shows the results of rooted and nonrooted slopes under rainfall conditions. The rainfall intensity used in this study is calculated from the monthly average of rainfall and rainfall days recorded by the observatory in 1981–2010 (Figure 1). It was found that the rainfall firstly infiltrated into the nonrooted slope is quicker than the rooted slope. It causes the soil in the nonrooted slope to be higher in water content than the rooted slope. The metric suction was evolved in the slope stability analysis. With increasing the soil water content, the soil strengths decrease. The grass root can enhance the soil strength. In this model, the peak strength for nonrooted and rooted soil was adopted in the slope. The data results clearly show that the grass root can increase the slope's stability.

4. Conclusions

This study highlights the influence of vetiver grass on soil properties and associated slope stability. It was firstly found that, under the natural conditions of Hong Kong, growth of the vetiver grass roots can reach 1.1 m depth after one and a half year from planting. Vetiver grass roots can increase the soil water content and density. The vetiver grass roots can reduce soil erosion by locking the finer grain. Grain-size distribution analysis shows that the percentage of grain size of 0.075–0.005 mm and that less than 0.005 mm in rooted soil is higher than those of nonrooted soil by 18.2% and 39.1%, respectively.

Shear box test results do show that the vetiver grass roots significantly increased the peak cohesion of completely

decomposed volcanic tuff by 103% from 9.3 kPa to 18.9 kPa. To evaluate the effect of grass roots on slope stability, a numerical modeling was performed. It illustrates that the grass roots can prevent the rainfall water infiltration by locking the finer grain, which is of benefit for slope stabilizing. It was therefore demonstrated that the combined effects of grass roots on hydrological responses and shearing strength can stabilize the slope.

Conflicts of Interest

The authors declare that they have no conflicts of interest.

Acknowledgments

The first author thanks Professor L. G. Tham and A. K. L. Kwong from the Hong Kong University. They funded the first author to work at HKU and joined in the research group of vetiver grass project. The authors thank Hong Min from the Institute of Rock and Soil Mechanics, Chinese Academy of Sciences, who carried out some of the laboratory tests. The financial support of the Research Grants Council, the HKSAR Government (Project no. HKU7138/07E), is acknowledged.

References

- [1] P. N. V. Truong and R. Loch, "Vetiver system for erosion and sediment control," in *Proceeding of the 13th International Soil Conservation Organization Conference*, 2004.
- [2] O. Babalola, S. C. Jimba, O. Maduako, and A. O. Dada, "Use of vetiver grass strips for soil and water conservation in Nigeria," in *Proceedings of the Third International Conference on Vetiver and Exhibition: Vetiver and Water*, China Agriculture Press, Guangzhou, China, October, 2003.
- [3] N. Dudai, E. Putievsky, D. Chaimovitch, and M. Ben-Hur, "Growth management of vetiver (*Vetiveria zizanioides*) under Mediterranean conditions," *Journal of Environmental Management*, vol. 81, no. 1, pp. 63–71, 2006.
- [4] O. Babalola, S. O. Oshunsanya, and K. Are, "Effects of vetiver grass (*Vetiveria nigritana*) strips, vetiver grass mulch and an organomineral fertilizer on soil, water and nutrient losses and maize (*Zea mays*, L) yields," *Soil & Tillage Research*, vol. 96, no. 1–2, pp. 6–18, 2007.
- [5] S. Donjadee and T. Tingsanchali, "Soil and water conservation on steep slopes by mulching using rice straw and vetiver grass clippings," *Agriculture and Natural Resources*, vol. 50, no. 1, pp. 75–79, 2016.
- [6] E. Gnansounou, C. M. Alves, and J. K. Raman, "Multiple applications of vetiver grass—a review," *International Journal of Environmental Sciences*, vol. 2, pp. 125–141, 2017.
- [7] C. Ghosh and S. Bhattacharya, "Landslides and erosion control measures by vetiver system," in *Disaster Risk Governance in India and Cross Cutting Issues, Disaster Risk Reduction (Methods, Approaches and Practices)*, I. Pal and R. Shaw, Eds., pp. 387–413, Springer Singapore, Singapore, 2018.
- [8] H. Liu, L. Yao, C. Lin, X. Wang, W. Xu, and H. Wang, "18-year grass hedge effect on soil water loss and soil productivity on sloping cropland," *Soil & Tillage Research*, vol. 177, pp. 12–18, 2018.
- [9] J. K. Raman and E. Gnansounou, "A review on bioremediation potential of vetiver grass," in *Waste Bioremediation, Energy, Environment, and Sustainability*, S. Varjani, E. Gnansounou, B. Gurunathan, D. Pant, and Z. Zakaria, Eds., Singapore, 2018.
- [10] M. Zhang, Y. Yin, and B. Huang, "Mechanisms of rainfall-induced landslides in gently inclined red beds in the eastern Sichuan Basin, SW China," *Landslides*, vol. 12, no. 5, pp. 973–983, 2015.
- [11] M. Zhang and M. J. McSaveney, "Is air pollution causing landslides in China?" *Earth and Planetary Science Letters*, vol. 481, pp. 284–289, 2018.
- [12] E. W. Brand, "Landslides in Hong Kong," in *Proceedings of the Eighth Southeast Asian Geotechnical Conference*, 1985.
- [13] S. W. C. Au, "Rain-induced slope instability in Hong Kong," *Engineering Geology*, vol. 51, no. 1, pp. 1–36, 1998.
- [14] F. C. Dai, C. F. Lee, J. Li, and Z. W. Xu, "Assessment of landslide susceptibility on the natural terrain of Lantau Island, Hong Kong," *Environmental Geology*, vol. 40, no. 3, pp. 381–391, 2001.
- [15] K. T. Chau, Y. L. Sze, M. K. Fung, W. Y. Wong, E. L. Fong, and L. C. P. Chan, "Landslide hazard analysis for Hong Kong using landslide inventory and GIS," *Computers & Geosciences*, vol. 30, no. 4, pp. 429–443, 2004.
- [16] K. K. S. Ho, "Managing the uncertainties of natural terrain landslides and extreme rainfall in Hong Kong," in *Landslide Science and Practice*, pp. 285–302, Springer Berlin Heidelberg, Berlin, Germany, 2013.
- [17] L. Gao, L. M. Zhang, and R. W. M. Cheung, "Relationships between natural terrain landslide magnitudes and triggering rainfall based on a large landslide inventory in Hong Kong," *Landslides*, pp. 1–14, 2017.

Research Article

A Measured Method for In Situ Viscosity of Fluid in Porous Media by Nuclear Magnetic Resonance

Zhengming Yang ^{1,2}, Zhuangzhi Ma,^{1,2} Yutian Luo ^{1,2}, Yapu Zhang,^{1,2}
Hekun Guo,^{1,2} and Wei Lin ^{1,2}

¹Department of Porous Flow & Fluid Mechanics, Research Institute of Petroleum Exploration & Development, PetroChina Company Limited, Beijing 100083, China

²University of Chinese Academy of Sciences, Beijing 100493, China

Correspondence should be addressed to Zhengming Yang; yzhm69@petrochina.com.cn

Received 22 January 2018; Revised 11 March 2018; Accepted 26 March 2018; Published 30 April 2018

Academic Editor: Ming Zhang

Copyright © 2018 Zhengming Yang et al. This is an open access article distributed under the Creative Commons Attribution License, which permits unrestricted use, distribution, and reproduction in any medium, provided the original work is properly cited.

At present, the existing measuring methods for viscosity of fluid can only obtain the viscosity of bulk fluid, while the in situ viscosity of fluid in porous media cannot be acquired. In this paper, with the combination of nuclear magnetic resonance (NMR) and physical simulation experiment, a testing method for in situ viscosity of fluid in porous media is established, and the in situ viscosity spectra of water in tight cores under different displacement conditions is obtained. The experimental results show that the in situ viscosity distribution of water in porous media is inhomogeneous, and it is not a constant but is related to the distance between water and rock walls. When the distance between fluid and rock walls is close enough (e.g., T_2 relaxation time is less than 1 ms), the viscosity of fluid increases rapidly, and the in situ viscosity is greater than the bulk viscosity. Moreover, after the rock samples are saturated with water, the in situ viscosity of water is distributed as a double-peak structure. The left peak is characterized mainly by the in situ viscosity distribution of movable fluid, whose in situ viscosity is smaller, and the right peak mainly represents the in situ viscosity distribution characteristics of immovable fluid, whose in situ viscosity is larger and increases gradually. Under a relatively large driving force, the in situ viscosity amplitude of movable fluid decreases greatly, and the average in situ viscosity of residual water in the core is much higher than that of saturated water in initial state.

1. Introduction

Viscosity is an embodiment of physical properties for fluid [1–3]. It affects the law of subsurface fluid flow, reservoir development mode, and hydrocarbon reservoir evaluation [4–16]. Therefore, accurate measurement of fluid viscosity is of great significance. The studies indicate that the viscosity of fluid is affected mainly by the pressure, temperature, and molecular force at liquid-solid interface, and the viscosity of the same fluid behaves variously under different conditions [16–25]. At present, the influence of pressure and temperature on fluid viscosity has been much more studied [16–23]. However, little is known about the influence on the fluid viscosity of molecular force at the fluid-solid interface in porous media.

With the development of low permeability oilfields, understanding of the effect of microstructure on fluid properties in porous media becomes more and more significant,

which requires people to pay more attention to the influence of the properties of porous media on fluid viscosity [24–33]. In low permeability porous media, the molecular force at the liquid-solid interface is more obvious because of its large specific surface [24, 25, 30]. Under the influence of the molecular force, liquid molecules near the liquid-solid interface will form an orderly distribution, forming a boundary layer on the liquid-solid interface. The property of the fluid in this boundary layer is different from that of the bulk fluid and its viscosity will be greater than the viscosity of the bulk fluid [24, 25]. Marrhassing [34] found that the resin and asphaltene in crude oil were orderly distributed in pore channels. For the same crude oil sample, the viscosity of crude oil is smaller in large gaps, and the viscosity of crude oil is greater in small gaps. It was also believed that the share of the boundary layer in the small gap is larger than that in the large gap. However,

the results of these studies still remain on the qualitative and semiquantitative description, and the viscosity distribution of the fluid in porous media cannot be quantified. On this basis, Huang et al. [24, 25] proposed a new concept of percolation fluid and the physical model of percolation fluid in porous media. It is considered that percolation fluid is a kind of fluid in porous media and includes bulk fluid and boundary fluid. Bulk fluid refers to the fluid whose properties are not affected by the interface and distributes in the middle axis of porous media channel. Accordingly, boundary fluid is a kind of fluid whose properties are influenced by the interface phenomenon, which is close to the pore wall to form a boundary layer. The formula for calculating the viscosity of percolation fluid is also given [25], but it is difficult to be applied directly because the thickness of the boundary layer and the average viscosity involved in this formula are difficult to be measured. Currently, there are many kinds of conventional viscosity testing methods, which are generally divided into three categories: capillary method [35, 36], rotation method [37–39], and vibration method [40–43]. These methods can only measure the viscosity by direct contact with the fluid, and it is impossible to test the viscosity of the fluid in the porous media: that is, the in situ viscosity of fluid in porous media cannot be measured, whereas the in situ viscosity of the fluid in porous media is more capable of characterizing the transport capacity of the fluid, so it is especially necessary to develop the method of testing the in situ viscosity of fluid in porous media.

Viscosity measurement using nuclear magnetic resonance (NMR) is a novel viscosity test method developed in recent years, which has the advantages of noncontact and wide application range and so on and has broad application prospects in in situ viscosity measurement of fluid in rock porous media. Scholars from all over the world have done a great deal of work in studying the fluid viscosity of reservoirs by using NMR technology. In 1994, Morriss et al. [44] carried out NMR test on 31 groups of bulk crude oil. It was found that the movement of hydrogen atom was restricted with the increase of hydrogen chain, resulting in shorter relaxation time and increased viscosity. And the relationship between relaxation time and the viscosity of crude oil was also given. In 1996, Kleinberg and Vinegar [45] proposed an improved formula for measuring the viscosity of crude oil by NMR, and the temperature was introduced into the viscosity formula. In 1998, LaTorraca et al. [46] used NMR to measure the viscosity of high-viscosity crude oil. The conclusion was drawn that the geometric mean value of T_2 is more sensitive to the change of viscosity than the geometric mean value of T_1 , and the meaning of the relative hydrogen index HI was put forward. In 2001, Freedman et al. [47] employed the magnetorheological fluid (MRF) method to invert the NMR data through the MRF multifluid relaxation model and studied NMR relaxation characteristics under gradient magnetic field of the sandstone, limestone, and dolomite saturated with different oil phases. Studies suggest that, under gradient magnetic field, the NMR experiment can identify different fluids in the rock pores and can also get the fluid saturation and oil-water phase viscosity and rock porosity. In 2005, Bryan et al. [4] used low-field NMR methods to

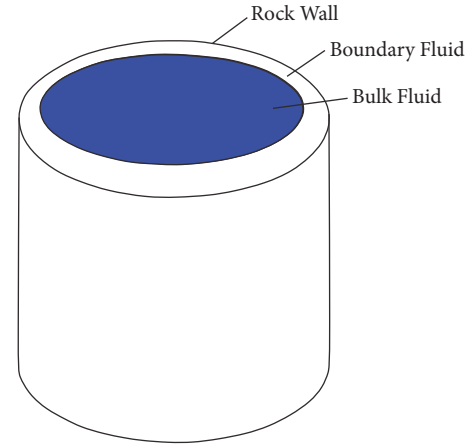


FIGURE 1: Physical model of percolation fluid in porous media.

measure crude oil viscosity. It was found that the higher the viscosity of the oil sample is, the lower the relative hydrogen index (RHI) is, a new NMR formula for viscosity of crude oil was put forward, and the T_2 gm and RHI of the crude oil were associated with the viscosity. In 2011, Zhang et al. [48] determined the relationship between viscosity and NMR relaxation properties through theoretical derivation and clarified the feasibility of using nuclear magnetic resonance to distinguish reservoir fluid properties. In general, at present, a relatively mature experimental method for measuring the viscosity of bulk fluid in rock pores by NMR technique has been formed, and a method for testing the viscosity of oil-water mixed phase was also initially formed. However, an effective experimental method for quantitatively measuring in situ viscosity of fluid in porous media using NMR has not yet been established.

In this paper, NMR and physical simulation experiment are combined to establish a method for in situ viscosity measurement of percolation fluid in porous media and obtain the in situ viscosity spectra of water in the tight rocks under different displacement conditions.

2. Method and Principle

2.1. The Nonconstant Liquid Viscosity in Rocks. Here we verify the inference that the liquid viscosity in porous media is not constant by fluid viscosity testing in different plate spacing using rheometer. According to the new concept of percolation fluid and the physical model of percolation fluid in porous media (Figure 1) proposed by Huang et al. [24, 25], we designed the viscosity experiment of the fluid at different plate spacing to verify the variation of fluid viscosity with the wall distance in the porous media. The results of constant speed mercury pressure testing of low permeability cores show that the average pore radius is generally more than $50\ \mu\text{m}$, and the average throat radius is generally less than $5\ \mu\text{m}$ [49]. Therefore, the designed plate spacing is the same as the pore and throat radius of low permeability rocks, which are $3\ \mu\text{m}$, $4\ \mu\text{m}$, $5\ \mu\text{m}$, $6\ \mu\text{m}$, $7\ \mu\text{m}$, $8\ \mu\text{m}$, $10\ \mu\text{m}$, $30\ \mu\text{m}$, $50\ \mu\text{m}$, and $124\ \mu\text{m}$, respectively. The experimental

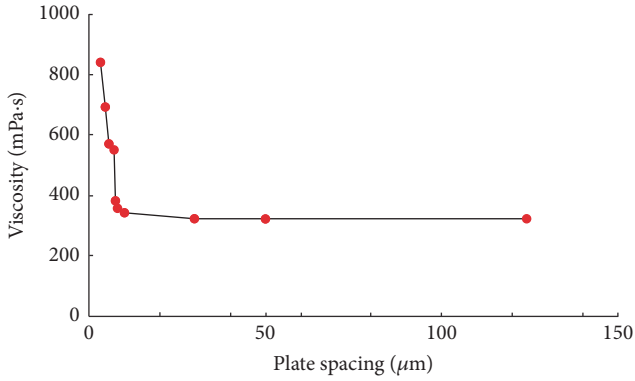


FIGURE 2: Viscosity variation of glycerol with different plate spacing.

equipment for measuring the viscosity of fluid is Anton Paar's MCR rheometer, the experimental fluid is glycerol (the viscosity in the test tube at 25°C is 320 mPa·s), and the test temperature is 25°C. The experimental results are shown in Figure 2.

As can be seen from Figure 2, when the plate spacing is greater than 8 μm, the test viscosity of glycerol is constant and does not change with the variation of plate spacing. To the contrary, when the plate spacing is less than 8 μm, with the narrowing of the plate spacing, the viscosity of glycerol increases rapidly. Furthermore, when the plate spacing is reduced to 3 μm, the viscosity of glycerol reaches 740 mPa·s, which is 2.3 times bulk viscosity of glycerol.

The experiment results verify the percolation fluid model proposed by Huang et al. [24, 25] and show that, in low permeability porous media, the viscosity of the fluid is no longer a constant. There is a boundary fluid near the solid wall, whose viscosity is much larger than that of the bulk fluid. Therefore, in the low permeability porous media, the in situ viscosity of the fluid is larger than that measured in the laboratory. Hence, it is so necessary to study the in situ viscosity of fluid in porous media, in order to help us understand the actual viscosity of the fluid in the ground.

2.2. Testing Principle for Fluid Viscosity by NMR. The principle of NMR is to measure the signal of hydrogen atoms in the magnetic field. There is a certain amount of hydrogen atoms in the oil and water, and when a magnetic pulse signal is applied, these hydrogen atoms will produce a strong attenuation response [45, 46]. If NMR is performed on oil-bearing or water-bearing rocks, due to the absence of paramagnetic elements in the rocks, there is no signal response in the rocks, and the measured signals are only from the oil and water in the rock pores [47]. In nuclear magnetic resonance experiments, hydrogen atoms are polarized by the external magnetic field, and the energy acts on hydrogen atoms in the form of radio frequency pulses, causing the hydrogen atoms to absorb energy and undergo energy level transitions. After the hydrogen atom absorbs energy, it transfers energy to other rotating atoms or solid surfaces to restore to the original state of equilibrium [4]. Because the measurement time of the longitudinal attenuation signal is longer and is easily

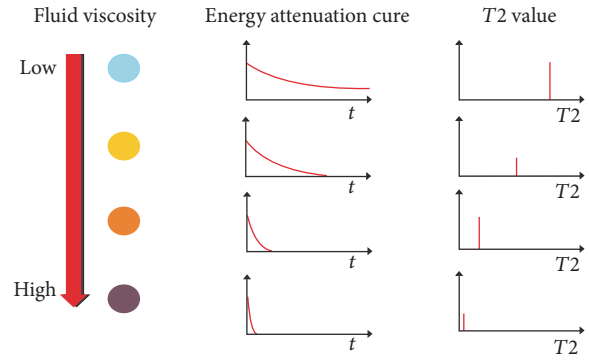


FIGURE 3: Relationship between fluid viscosity and energy attenuation rate and T_2 value.

affected by the external environment, the NMR measurement signal is a transverse attenuation signal. The attenuation signals can be converted to the attenuation curve, which is the superposition of the attenuation signals of different fluid phases. The fluid components are different, so the attenuation signals and the attenuation curves are different, and the attenuation curve functions conform to the single index or multiexponential function [48–51].

Eyring viscosity theory shows [50, 51] that the viscosity is related to the diffusion conductivity. Even if fluid does not flow, its viscosity can also be measured, and NMR technology can be used to measure the diffusion conduction characteristics of fluids. NMR can be used to measure the attenuation response of liquid hydrogen atom in magnetic field under the action of external magnetic field. Prammer [52] presented the relation between the amplitude attenuation of NMR and the transverse relaxation time (T_2) and pointed out that the fluid viscosity is correlated positively with the attenuation rate of fluid amplitude. The smaller the fluid viscosity is, the slower the amplitude attenuation rate is, and the greater the relaxation time T_2 is. Instead, the larger the fluid viscosity is, the faster the amplitude attenuation rate is, and the smaller the relaxation time T_2 is. Its principle is shown in Figure 3 and (1).

The equation of energy attenuation curve in magnetic field is as follows [52]:

$$M(t) = M_0 e^{-t/T_2}, \quad (1)$$

where $M(t)$ is the macroscopic magnetization at moment t , M_0 is the equilibrium magnetization, T_2 is the transverse relaxation time, and t is time, ms.

From the energy attenuation curve equation, it can be seen as follows: the greater the T_2 value is, the smoother the energy attenuation curve is. The smaller the T_2 value is, the faster the energy attenuation curve falls. The transverse relaxation time T_2 is related to the properties of fluid itself and the interaction between fluid and rock pore surface, and so on. Therefore, NMR T_2 value can be used to characterize the viscosity of fluid.

2.3. Relationship between Fluid Viscosity and T_2 Peak. The purpose of this section is to find the empirical formula of

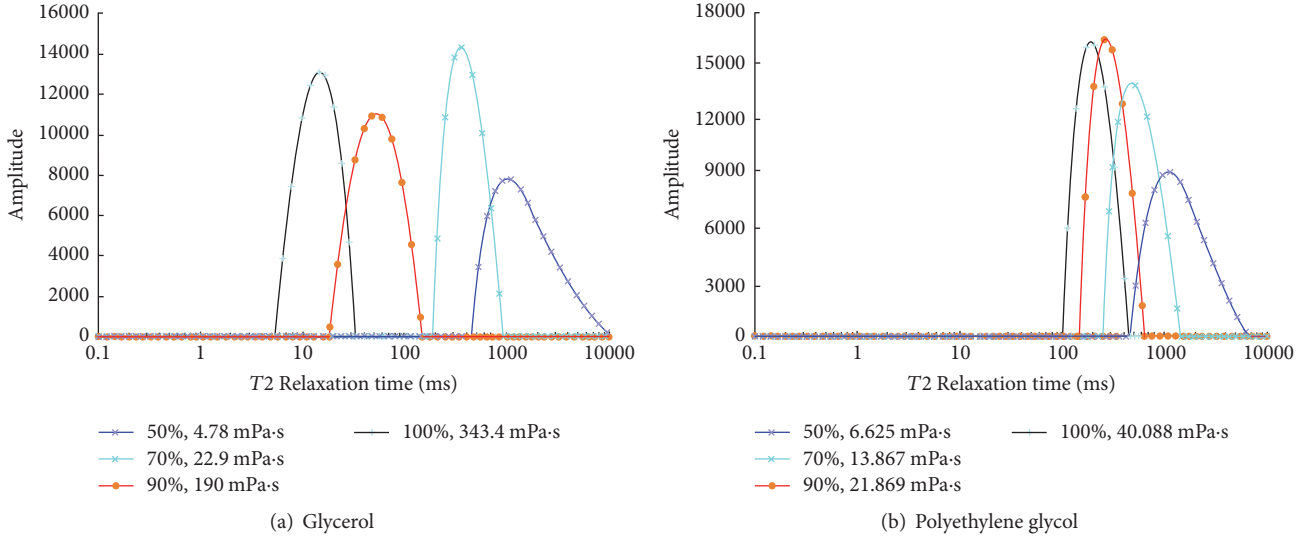


FIGURE 4: T_2 spectra of solutions at different concentrations.

fluid viscosity and NMR T_2 values by conducting NMR experiments on different kinds of fluids with different viscosity, providing a basis for testing in situ fluid viscosity in porous media.

The experimental instrument is the RecCore4 NMR equipment developed independently by China Petroleum Exploration and Development Research Institute Langfang Branch. Its operating frequency is 2 MHz, the echo time T_E is adjustable, and the minimum time is $2\mu\text{s}$. Glycerol and polyethylene glycol are selected as test fluid, prepared into experimental solutions with different concentrations (10%~90%), and placed in the test tubes.

The experimental steps are as follows: first, Ubbelohde viscometer is used to measure the viscosity of different concentration solutions, and then the NMR spectra of different concentration solutions are obtained with the RecCore4 NMR equipment; finally, we analyze and process the data to get the experimental results shown in Figures 3 and 4.

It can be seen from Figures 4 and 5 that there is a good correlation between viscosity and T_2 peak value (T_{2f}). The relationship is as follows:

$$\mu = 23938T_{2f}^{-1.236}, \quad (2)$$

$$R^2 = 0.983.$$

Equation (2) indicates that the greater the T_2 peak value is, the smaller the fluid viscosity is. Contrarily, the smaller the T_2 peak value is, the greater the fluid viscosity is.

The above experimental results demonstrate that NMR method can be used to test the viscosity of different liquid. The relationship between fluid viscosity and T_2 peak of NMR is clearly defined as follows:

$$\mu = \frac{a}{T_{2f}^b}, \quad (3)$$

where μ is the viscosity, T_{2f} is the T_2 peak, and a and b are the parameters related to the properties of the solution.

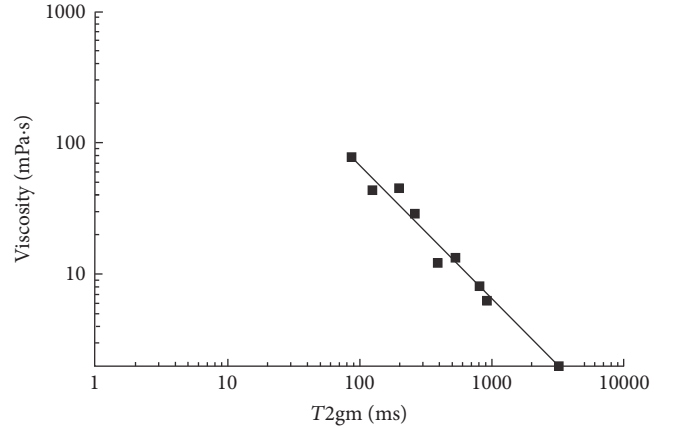


FIGURE 5: Relationship between fluid viscosity and T_2 relaxation time.

3. In Situ Viscosity Measurement of Fluid in Porous Media

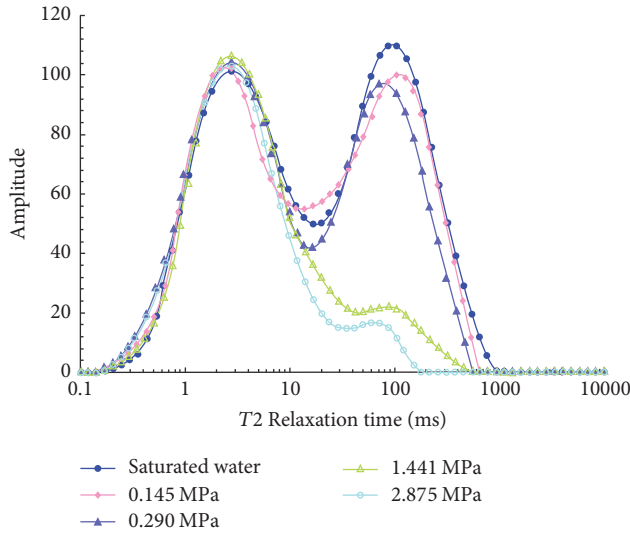
Taking the water in porous media as an example, the in situ viscosity of fluid in porous media is measured here. The T_2 relaxation spectrum of water in rock sample can be obtained by NMR technology. By (3), the T_2 spectra of fluid can be converted into the in situ viscosity spectra of fluid in different pores and throats of porous media.

In order to test the in situ viscosity of fluid in porous media, five tight cores in Changqing and Jilin were selected, and their petrophysical parameters are shown in Table 1. The experimental steps are as follows.

Firstly, the above five cores were completely saturated with water; at the same time, the NMR spectra were tested. Then, different centrifugal experiments of 0.145 MPa, 0.290 MPa, 0.717 MPa, 1.441 MPa, 2.069 MPa, and 2.876 MPa

TABLE 1: Petrophysical parameters of 5 tight rock cores.

Core number	Oil block	Length (cm)	Diameter (cm)	Gas measurement porosity (%)	Gas measurement permeability (mD)
1	Jilin	2.664	2.438	8.08	0.130
2		3.236	2.503	9.42	0.673
3	Changqing	3.225	2.514	12.30	0.058
4		3.076	2.515	10.30	0.116
5		3.206	2.513	9.40	0.710

FIGURE 6: T_2 spectra of 0.130 mD rock core after centrifugation with different centrifugal pressures.

were carried out for each core (different centrifugal pressures represent different displacement pressures), and NMR T_2 spectra under each centrifugal pressure were captured. Finally, the experimental data was analyzed and processed to obtain the experimental results as shown in Figures 6–9.

4. Results and Discussion

Figure 6 is a NMR spectrum of 0.130 mD rock sample in Jilin oilfield. When the centrifugal pressure is 0.145 MPa and 0.290 MPa, the yield of water centrifuged out of rock core is only 4.49% and 7.38%, respectively. When the centrifugal pressure increases to 1.441 MPa, the yield of water centrifuged out of rock core is 41.18%. However, when the centrifugal pressure is increased from 1.441 MPa to 2.876 MPa, the production increment of water centrifuged out of rock core is only 5.13%.

According to (3), NMR spectra of 0.130 mD tight rock sample under saturated water condition in Figure 6 are treated, and we obtain the relationship of in situ viscosity and T_2 relaxation time in porous media under saturated water condition (Figure 7). Studies show that [45] T_2 relaxation time can represent the distance between fluid and rock wall. The

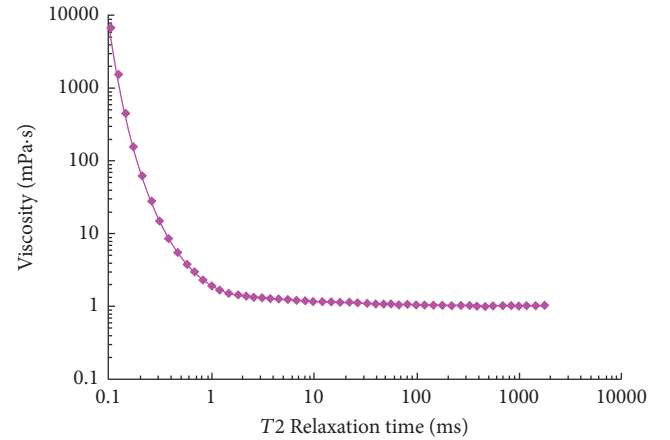
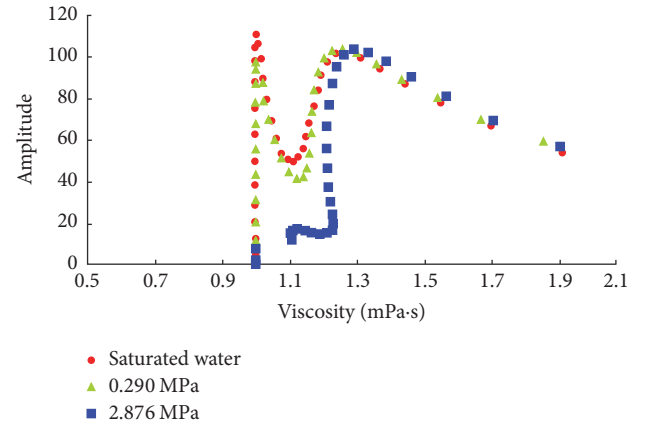
FIGURE 7: Relationship between in situ viscosity and T_2 relaxation time of 0.130 mD rock core after saturated water.

FIGURE 8: In situ viscosity spectrum of 0.130 mD rock sample under different displacement conditions.

larger the T_2 relaxation time, the greater the distance between the fluid and the rock wall. So it can be found from Figure 7 that the in situ viscosity of water in porous media is not a constant, and it is related to the distance between water and rock wall. When water is closer to wall, its in situ viscosity is greater than its bulk fluid viscosity. What is more, when T_2 relaxation time is less than 1 ms, that is, the closer the fluid is to rock wall, the higher the in situ viscosity is. At the

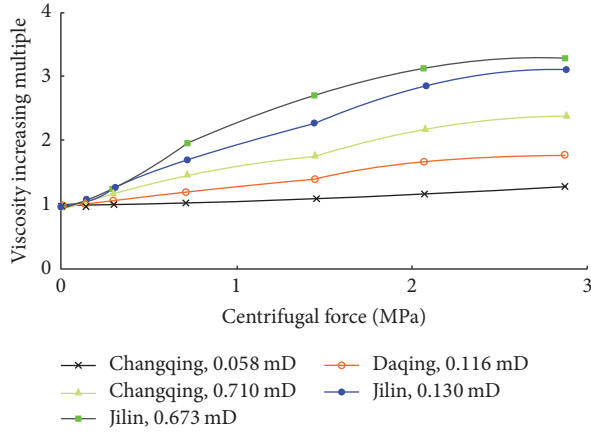


FIGURE 9: Variation of average in situ viscosity of water in tight rock under different centrifugal pressures.

same time, this result also indicates that the interface force between fluid and rock is stronger, and it is extremely difficult to develop the fluid with T_2 time less than 1 ms.

Figure 8 shows the in situ viscosity spectra of 0.130 mD rock samples under different displacement conditions. We realize from Figure 8 that the in situ viscosity of fluid is distributed unevenly in porous media. Under the saturated water state of rock sample, the in situ viscosity spectrum of water presents a double-peak structure. For the left peak of in situ viscosity spectrum, the viscosity of fluid is smaller, which mainly characterizes the in situ viscosity distribution characteristics of movable fluid at the right peak of NMR T_2 spectrum. This part of fluid is distributed mainly in the middle of pores and throats. For the right peak of in situ viscosity spectrum, the viscosity increases greatly, which mainly characterizes the in situ viscosity distribution characteristics of nonmovable fluid at the left peak of NMR T_2 spectrum. This part of fluid is distributed mainly in the boundary layer of pores and throats or nearby the wall. Furthermore, as the in situ viscosity is greater than 1.3 mPa·s, the proportion of nonmovable fluid decreases sharply with the increase of viscosity. At a relatively lower driving force (e.g., 0.290 MPa), the in situ viscosity amplitude of movable fluid decreases smaller, and the in situ viscosity amplitude of nonmovable fluid coincides basically with the curve under the saturated water condition. This indicates that only some movable fluid can be exploited in tight cores under the small pressure difference, but the boundary fluid cannot be developed basically. Under the larger driving force (e.g., 2.876 MPa), the in situ viscosity amplitude of movable fluid drops greatly, which indicates the movable fluid is produced more. However, the fluid with the viscosity more than 1.3 mPa·s is harvested less, which indicates that it is very difficult to exploit the boundary fluid. Hence, findings also include that the production degree of fluid in tight rock is lower under a small pressure gradient. Only under a high pressure gradient, the production degree of fluid is relatively higher.

Figure 9 shows the variation of the average in situ viscosity of residual water in rock cores with different permeability under different centrifugal pressures. The longitudinal coordinate is the increasing multiple of viscosity, which is the ratio of the average in situ viscosity of the residual water in rock cores and the average in situ viscosity of the water in rock cores with saturated water state under a centrifugal pressure.

It can be seen from Figure 9 that the increasing multiple of viscosity in rock core is small under relatively low centrifugal pressure (e.g., 0.145 MPa and 0.290 MPa). This is because the amount of yield water centrifuged out of rock core under a smaller centrifugal pressure is small, and large amounts of water still exist in the large pores, which has little influence on the average in situ viscosity of water in rock core. Only when the centrifugal pressure increases to a certain value (e.g., 0.717 MPa, 1.441 MPa, and 2.069 MPa), the increasing multiple of viscosity in rock core increases rapidly. This is because that, with the centrifugal pressure increases, the amount of water centrifuged out of rock core increases, and the production of water in the large channel increases, the proportion of the boundary fluid thus rises, which has great influence on the average in situ viscosity of water in rock core. When the centrifugal pressure is once increased from 2.069 MPa to 2.876 MPa, the increasing multiple of viscosity in core increases slowly, because the amount of water produced is less, which has a little effect on the average in situ viscosity of the water in rock core. For rock samples in the same block (Changqing or Jilin), under the same centrifugal pressure, the viscosity increasing multiple of water in rock increases with the increase of permeability. This phenomenon can be interpreted as, under the same centrifugal pressure, the higher the permeability, the more the amount of water centrifuged out of rock core. Under the same centrifugal pressure, the viscosity increasing multiple of water in Jilin is higher than that in Changqing, which can be ascribed to the different reservoir characteristics of Changqing and Jilin tight cores reported by Yang et al. [49].

5. Conclusions

An approach to test in situ viscosity of fluid in porous media by NMR is reported in this work. Studies have shown that there is a better correlation between fluid viscosity and T_2 peak value and the in situ viscosity of fluid is distributed unevenly in porous media. In saturated water state, the in situ viscosity of water in rock samples is distributed as a double-peak structure. Moreover, for the tight rocks with saturated water, after a small amount of water is centrifuged, the average in situ viscosity of water in rocks has little difference with that of initial status. However, when more water is separated from the rocks, the average in situ viscosity of water in rocks is significantly higher than that of initial status. Furthermore, under the same centrifugal pressure, the ratio of the average in situ viscosity of water in rocks to that of initial status increases with the increase of permeability, and the average in situ viscosity increasing multiple of water in Jilin is higher than that in Changqing, which is due to the different reservoir characteristics of Changqing and Jilin tight rocks. The paper first proposes the method for measuring the in situ viscosity

of fluid in porous media, which can provide guidance for the development of movable oil in oil field. At the same time, the accuracy and application range of the method will be improved after a large number of tests of different fluids.

Conflicts of Interest

The authors declare that they have no conflicts of interest.

Acknowledgments

The authors gratefully acknowledge financial support from the National Science and Technology Major Project (2017ZX05013-001).

References

- [1] A. Roszkowski, M. Bogdan, W. Skoczynski, and B. Marek, "Testing viscosity of MR fluid in magnetic field," *Measurement Science Review*, vol. 8, no. 3, pp. 58–60, 2008.
- [2] T. Schäfer, "Fluid dynamics and viscosity in strongly correlated fluids," *Annual Review of Nuclear and Particle Science*, vol. 64, no. 1, pp. 125–148, 2014.
- [3] D. Bonn, H. Kellay, M. Bräunlich, M. B. Amar, and J. Meunier, "Viscous fingering in complex fluids," *Physica A: Statistical Mechanics and its Applications*, vol. 220, no. 1-2, pp. 60–73, 1995.
- [4] J. Bryan, A. Kantzas, and C. Bellehumeur, "Oil-viscosity predictions from low-field NMR measurements," *SPE Reservoir Evaluation and Engineering*, vol. 8, no. 1, pp. 44–52, 2005.
- [5] H. Singh, F. Javadpour, A. Ettehadvakkol, and H. Darabi, "Nonempirical apparent permeability of shale," *SPE Reservoir Evaluation and Engineering*, vol. 17, no. 3, pp. 414–424, 2014.
- [6] H. Singh and F. Javadpour, "Langmuir slip-Langmuir sorption permeability model of shale," *Fuel*, vol. 164, pp. 28–37, 2016.
- [7] H. Singh and J. Cai, "Screening improved recovery methods in tight-oil formations by injecting and producing through fractures," *International Journal of Heat and Mass Transfer*, vol. 116, pp. 977–993, 2018.
- [8] H. Singh, "A critical review of water uptake by shales," *Journal of Natural Gas Science and Engineering*, vol. 34, pp. 751–766, 2016.
- [9] R. Song, M. Cui, and J. Liu, "Single and multiple objective optimization of a natural gas liquefaction process," *Energy*, vol. 124, pp. 19–28, 2017.
- [10] A. F. Li Petroleum University Press, Dongying, China, 2011.
- [11] W. Lin, Z. Yang, X. Li et al., "A method to select representative rock samples for digital core modeling," *Fractals. Complex Geometry, Patterns, and Scaling in Nature and Society*, vol. 25, no. 4, Article ID 1740013, 1740013, 9 pages, 2017.
- [12] R. Song, M. Cui, and J. Liu, "A correlation for heat transfer and flow friction characteristics of the offset strip fin heat exchanger," *International Journal of Heat and Mass Transfer*, vol. 115, pp. 695–705, 2017.
- [13] W. Lin, X. Li, Z. Yang et al., "A new improved threshold segmentation method for scanning images of reservoir rocks considering pore fractal characteristics," *Fractals*, vol. 26, article 1840003, no. 2, 2018.
- [14] R. Song, J. Liu, and M. Cui, "Single- and two-phase flow simulation based on equivalent pore network extracted from micro-CT images of sandstone core," *SpringerPlus*, vol. 5, no. 1, article no. 817, 2016.
- [15] M. Zhang, Y. Yin, and B. Huang, "Mechanisms of rainfall-induced landslides in gently inclined red beds in the eastern Sichuan Basin, SW China," *Landslides*, vol. 12, no. 5, pp. 973–983, 2015.
- [16] W. Lin, Z. Yang, J. Wang, T. Chen, and X. Shi, "Wormlike micelles with pH-induced rheological property formed by cationic surfactant/anthranilic acid mixed aqueous solution," *Journal of Molecular Liquids*, vol. 224, pp. 333–337, 2016.
- [17] W. Wei, J. Cai, X. Hu et al., "A numerical study on fractal dimensions of current streamlines in two-dimensional and three-dimensional pore fractal models of porous media," *Fractals*, vol. 23, no. 1, Article ID 1540012, 2015.
- [18] M. Zhang and M. J. McSaveney, "Is air pollution causing landslides in China?" *Earth and Planetary Science Letters*, vol. 481, pp. 284–289, 2018.
- [19] J. Wang, S. Wang, W. Lin, Z. Kang, and Q. You, "Formula optimization and rheology study of clean fracturing fluid," *Journal of Molecular Liquids*, vol. 241, pp. 563–569, 2017.
- [20] T. Watanabe and A. Higuchi, "A new apparatus for measuring elastic wave velocity and electrical conductivity of fluid-saturated rocks at various confining and pore-fluid pressures," *Geofluids*, vol. 14, no. 3, pp. 372–378, 2014.
- [21] D. Zhu, Q. Meng, Z. Jin, and W. Hu, "Fluid environment for preservation of pore spaces in a deep dolomite reservoir," *Geofluids*, vol. 15, no. 4, pp. 527–545, 2015.
- [22] C. Huber and Y. Su, "A pore-scale investigation of the dynamic response of saturated porous media to transient stresses," *Geofluids*, vol. 15, no. 1-2, pp. 11–23, 2015.
- [23] R. Song, M. Cui, J. Liu, P. G. Ranjith, and Y. Lei, "A Pore-Scale Simulation on Thermal-Hydrromechanical Coupling Mechanism of Rock," *Geofluids*, vol. 2017, pp. 1–12, 2017.
- [24] Y. Z. Huang, *Percolating Flow Mechanism of Low Permeability Reservoir*, Petroleum Industry Press, Beijing, China, 1998.
- [25] Y. Huang, Z. Yang, Y. He, and X. Wang, "An overview on nonlinear porous flow in low permeability porous media," *Theoretical & Applied Mechanics Letters*, vol. 3, no. 2, p. 022001, 2013.
- [26] G. J. Hirasaki and J. B. Lawson, "Mechanisms of foam flow in porous media: apparent viscosity in smooth capillaries," *SPE Journal*, vol. 25, no. 2, pp. 176–190, 1985.
- [27] Y. Xia, J. Cai, W. Wei et al., "A new method for calculating fractal dimensions of porous media based on pore size distribution," *Fractals*, vol. 26, article 1850006, no. 1, 2018.
- [28] Y.-L. Feng, Y. Zhang, B.-Y. Ji, and W.-Z. Mu, "Micro-acting force in boundary layer in low-permeability porous media," *Chinese Physics Letters*, vol. 28, no. 2, Article ID 024703, 2011.
- [29] J. C. Cai and B. M. Yu, "A discussion of the effect of tortuosity on the capillary imbibition in porous media," *Transport in Porous Media*, vol. 89, no. 2, pp. 251–263, 2011.
- [30] W. Lin, X. Li, Z. Yang et al., "Construction of Dual Pore 3-D Digital Cores with a Hybrid Method Combined with Physical Experiment Method and Numerical Reconstruction Method," *Transport in Porous Media*, vol. 120, no. 1, pp. 227–238, 2017.
- [31] J. G. Celauro, V. A. Torrealba, Z. T. Karpyn, K. A. Klise, and S. A. McKenna, "Pore-scale multiphase flow experiments in bead packs of variable wettability," *Geofluids*, vol. 14, no. 1, pp. 95–105, 2014.
- [32] J. Liu, M. Wu, Z. Zhu, and Z. Shao, "A study on the mechanical properties of the representative volume element in fractal porous media," *Geofluids*, vol. 2017, Article ID 7905218, 10 pages, 2017.

- [33] R. Song, J. Liu, and M. Cui, "A new method to reconstruct structured mesh model from micro-computed tomography images of porous media and its application," *International Journal of Heat and Mass Transfer*, vol. 109, pp. 705–715, 2017.
- [34] H. Marrhassing, *Mechanism of petrophysics and petrochemical*, Petroleum Industry Press, Beijing, China, 1987.
- [35] E. Hatschek, *The Viscosity of Liquids*, D. Van Nostrand Co., New York, NY, USA, 1963.
- [36] X. Y. Liu, M. G. He, and Y. Zhang, "Viscosity of water in the region around the critical point," *The Journal of Supercritical Fluids*, vol. 63, pp. 150–154, 2012.
- [37] A. Colafigli, L. Mazzei, P. Lettieri, and L. Gibilaro, "Apparent viscosity measurements in a homogeneous gas-fluidized bed," *Chemical Engineering Science*, vol. 64, no. 1, pp. 144–152, 2009.
- [38] L. A. Belfiore, "Dynamic shear in continuous-flow rotating-disk catalytic reactors with stress-sensitive kinetics based on Curie's theorem in non-equilibrium thermodynamics," *Chemical Engineering Science*, vol. 65, no. 2, pp. 680–691, 2010.
- [39] M. Iguchi, Y. Hiraga, K. Kasuya et al., "Viscosity and density of poly(ethylene glycol) and its solution with carbon dioxide at 353.2 K and 373.2 K at pressures up to 15 MPa," *The Journal of Supercritical Fluids*, vol. 97, pp. 63–73, 2015.
- [40] M. J. Assael, C. P. Oliveira, M. Papadaki, and W. A. Wakeham, "Vibrating-wire viscometers for liquids at high pressures," *International Journal of Thermophysics*, vol. 13, no. 4, pp. 593–615, 1992.
- [41] X. Meng, P. Zheng, J. Wu, and Z. Liu, "Density and viscosity measurements of diethyl adipate from (303 to 373) K and up to 20 MPa," *Journal of Chemical & Engineering Data*, vol. 53, no. 7, pp. 1474–1478, 2008.
- [42] J. C. F. Diogo, F. J. P. Caetano, and J. M. N. A. Fareleira, "Viscosity and density measurements of compressed liquid dimethyl adipate using oscillating body techniques," *Fluid Phase Equilibria*, vol. 367, pp. 85–94, 2014.
- [43] S. V. D. Freitas, J. J. Segovia, M. Carmen Martín et al., "Measurement and prediction of high-pressure viscosities of biodiesel fuels," *Fuel*, vol. 122, pp. 223–228, 2014.
- [44] C. E. Morriss, R. Freedman, C. Straley, M. Johnston, H. J. Vinegar, and P. N. Tutunjian, "Hydrocarbon saturation and viscosity estimation from NMR logging in the Belridge diatomite," *Log Analyst*, vol. 38, no. 2, pp. 44–59, 1997.
- [45] R. L. Kleinberg and H. J. Vinegar, "NMR properties of reservoir fluids," *Log Analyst*, vol. 37, no. 6, pp. 20–32, 1996.
- [46] G. A. LaTorraca, K. J. Dunn, P. R. Webber, and R. M. Carlson, "Low-field NMR determinations of the properties of heavy oils and water-in-oil emulsions," *Magnetic Resonance Imaging*, vol. 16, no. 5–6, pp. 659–662, 1998.
- [47] R. Freedman, N. Heaton, and M. Flaum, "Field applications of a new nuclear magnetic resonance fluid characterization method," *SPE Reservoir Evaluation and Engineering*, vol. 5, no. 6, pp. 455–464, 2002.
- [48] Z. P. Zhang, P. J. Li, and D. P. Jiang, "Study on NMR fluid identification method," *nner Mongolia Petrochemical Industry*, vol. 37, no. 3, pp. 29–30, 2011.
- [49] Z. M. Yang, H. K. Guo, and X. W. Liu, *Characteristic Experimental Technology of an Extra-Ultra Low Permeability Reservoir*, Petroleum Industry Press, Beijing, China, 2012.
- [50] H. Eyring, "Viscosity, plasticity, and diffusion as examples of absolute reaction rates," *The Journal of Chemical Physics*, vol. 4, no. 4, pp. 283–291, 1936.
- [51] Z. Liu, Y. Yang, J. Yao, Q. Zhang, J. Ma, and Q. Qian, "Pore-scale remaining oil distribution under different pore volume water injection based on CT technology," *ADvances in Geo-Energy Research*, vol. 1, no. 3, pp. 171–181, 2017.
- [52] M. G. Prammer, "NMR logging-while-drilling (1995–2000)," *Concepts in Magnetic Resonance*, vol. 13, no. 6, pp. 409–411, 2001.

Research Article

Stability Analysis of Partially Submerged Landslide with the Consideration of the Relationship between Porewater Pressure and Seepage Force

Yang Wang¹ ,¹ Le Yu,¹ Tianci Yin,¹ Lanbing Yu,¹ and Zhitao Huo²

¹Engineering Faculty, China University of Geosciences, Wuhan, Hubei 430074, China

²China Institute of Geo-Environment Monitoring, Beijing 100081, China

Correspondence should be addressed to Yang Wang; wangyangcug@126.com

Received 25 October 2017; Accepted 11 March 2018; Published 12 April 2018

Academic Editor: Liangping Li

Copyright © 2018 Yang Wang et al. This is an open access article distributed under the Creative Commons Attribution License, which permits unrestricted use, distribution, and reproduction in any medium, provided the original work is properly cited.

For partially submerged landslides, hydrostatic and hydrodynamic pressures, related to water level fluctuation and rainfall, are usually expressed in the form of porewater pressure, seepage force, and buoyancy. There are some connections among them, but it is very easy to confuse one force with another. This paper presents a modified mathematical expression for stability analysis of partially submerged landslide and builds the relationship between porewater pressures and buoyancy acting on the underwater zone of partially submerged landslide and the relationship among porewater pressures, seepage force, and buoyancy acting on partially submerged zone. The porewater pressures acting on the underwater slice are calculated using hydrostatic forces, and the porewater pressures acting on the partially submerged slice are estimated by an approximation of equipotential lines and flow lines under the steady state seepage condition. The resultant of the porewater pressures acting on the underwater slice equals the buoyancy, and that acting on the partially submerged slice is equivalent to the vector sum of seepage force and the buoyancy. The result shows there are two equivalent approaches for considering the effect of water on landslide stability in the limit equilibrium method. One is based on total unit weight and porewater pressures, and the other is in terms of the buoyant weight and the seepage force. The study provides a modified model for simplifying the complex boundary porewater pressures in limit equilibrium analysis for the stability of the partially submerged landslide.

1. Introduction

Water, including groundwater and reservoir water, has long been considered as one of the most significant factors responsible for landslide failures, which is affected by water level fluctuation and rainfall in partially submerged landslides [1–5]. Statistics data from He et al. [6] showed that about 94% of landslides are triggered by rain and water storage in the TGR Region. The combined seepage-slope stability analyses in Mountain Toc of Italy by Paronuzzi et al. [7] demonstrated that the decreases in safety factors caused by filling and drawdown of the Vajont reservoir and heavy rainfall were about 12% and 3%. The significant examples related to the water level fluctuation and rainfall have been recorded and discussed by researchers, such as rainfall-induced landslides of the Iva Valley in Southeastern Nigeria [8], landslides

triggered by the July 2011 intense rainstorm in Korea, the June 2013 extreme rainfall in India and the October 2013 heavy rainfall associated with the typhoon in Japan [9–11], and landslide events associated with the water level fluctuation and rainfall [12–19].

Forces acting on landslide, related to water level fluctuation and rainfall, mainly include hydrostatic and hydrodynamic pressures. For partially submerged landslides, these forces are usually expressed in the form of porewater pressure, seepage force, and buoyancy. Some studies show that there are some connections between one force and another. The porewater pressure is considered as internal force and has the effect of reducing internal energy dissipation for a given collapse mechanism. However it may also be regarded as external forces, and its contribution can be included in the virtual work equations through the seepage force and buoyant

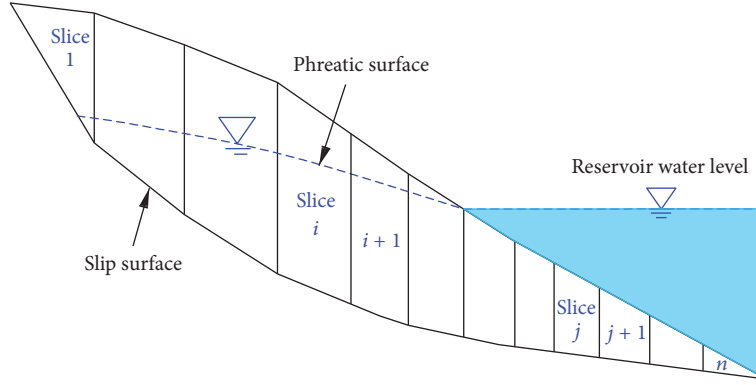


FIGURE 1: Division of a partially submerged landslide into vertical slices.

terms [20–22]. Water pressures on the face of a partially submerged landslide can be replaced by forces and moments which are directly added to slices or by a strengthless soil layer with self-weight equivalent to water weight or by an end force on slip surface at the toe of the landslide [23].

In some previous studies about the limit equilibrium methods of landslide stability, there are still some differences in analysing and using these forces related to hydrostatic and hydrodynamic pressures. Yamin and Liang [24] developed a limiting equilibrium method of slices for calculating global factor of safety of a slope and accounted for porewater pressure at the slice base related to its effective stress. However, they did not discuss the porewater pressure acting on the vertical boundaries of the slice. Li and Liang [25] only considered porewater pressure at the slice base when applying the limit equilibrium method to the interslice forces of a drilled shaft slope system. Zhou et al. [26] used the limiting equilibrium method to calculate the lateral force acting on the piles and considered the effect of the porewater pressure on the lateral forces of stabilizing piles in terms of the seepage force and the buoyant weight. Some used the porewater pressure on the base of the landslide [24, 25, 27–29], some others allowed for boundary water pressures of slices [30], and others accounted for the seepage pressure [26, 31, 32]. Therefore, it is very easy to confuse one force with another.

This paper presents a modified expression for stability analysis of partially submerged landslide based on considering hydrostatic and hydrodynamic pressures acting on the underwater zone and partially submerged zone of the partially submerged landslides. Two relationships, including the relationship between porewater pressures and buoyancy acting on the underwater zone of partially submerged landslide and the relationship among porewater pressures, seepage force, and buoyancy acting on partially submerged zone, are clarified in detail. Two equivalent approaches are proposed to consider the effect of water on landslide stability in the limit equilibrium method of slices. One is based on the total unit weight and the porewater pressures, and the other is in terms of the buoyant weight and the seepage force. The latter is simpler to determine the safety factor of partially submerged landslide.

2. Porewater Pressures of a Partially Submerged Landslide

2.1. Porewater Pressures Acting on an Underwater Slice. A partially submerged landslide can be divided into the underwater zone and partially submerged zone. A typical cross section of a partially submerged landslide is shown in Figure 1. Two types of slices, underwater slice (Slice j) and partially submerged slice (Slice i), are bounded by the reservoir water surface.

When analysing forces acting on an underwater slice (Figure 2), we posit that reservoir water is under static condition, and the boundary porewater pressures can be calculated as

$$P_1 = 0.5r_w(h_A + h_D)l_{AD}, \quad (1a)$$

$$P_2 = 0.5r_w(h_D + h_C)l_{CD}, \quad (1b)$$

$$P_3 = 0.5r_w(h_B + h_C)l_{BC}, \quad (1c)$$

$$P_4 = 0.5r_w(h_A + h_B)l_{AB}, \quad (1d)$$

where P_1 , P_2 , P_3 , and P_4 are the porewater pressures acting on its four sides of slice j , l_{AD} , l_{CD} , l_{BC} , and l_{AB} are the lengths of four sides, and r_w is the unit weight of water.

2.2. Porewater Pressures Acting on a Partially Submerged Slice. When a phreatic surface of the partially submerged zone is defined, the porewater pressures are calculated for the steady state seepage condition by drawing a flow net (Figure 3). The actual pressure head at point C can be obtained by drawing an equipotential line (CD) through that point. But the actual seepage and porewater pressures are complex; it is necessary to use simple approximations [33–35]. One approximation is to define the porewater pressures using a line MN that represents a phreatic surface (AB) and to approximate the equipotential line as a straight line CE which is perpendicular to the straight line MN [33]. The porewater pressure can be represented as a function of the hydraulic head. Under the steady state seepage conditions, the hydraulic head of the line CE can be described by

$$h = \frac{u_C}{\gamma_w} + z_C = \frac{u_E}{\gamma_w} + z_E, \quad (2)$$

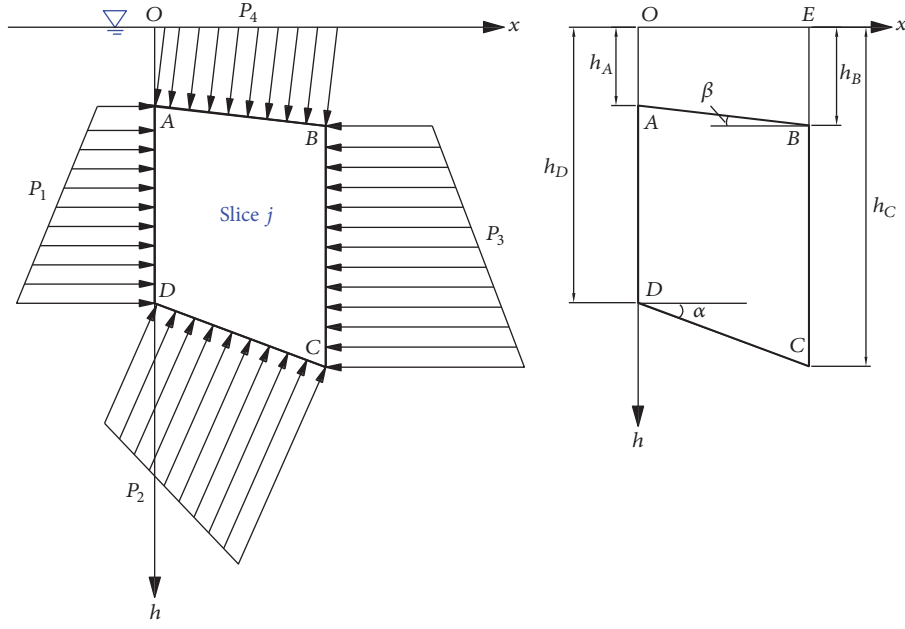


FIGURE 2: Porewater pressures acting on four sides of an underwater slice.

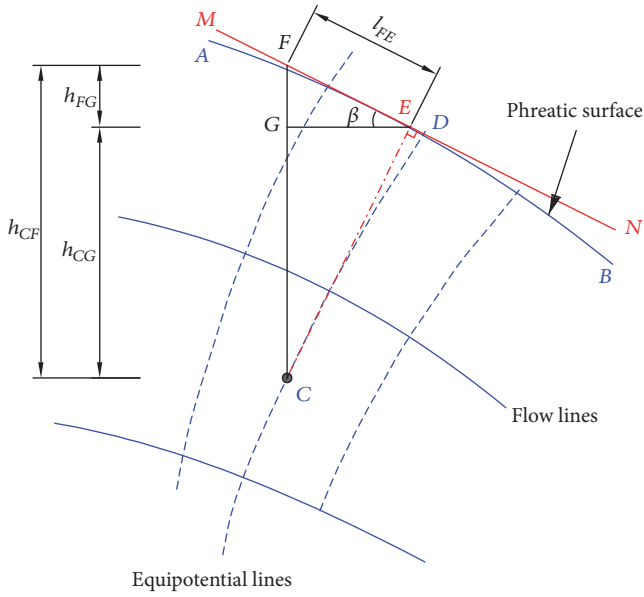


FIGURE 3: Approximation of the porewater pressure from flow net.

where h is the hydraulic head, u_C and u_E are the porewater pressures of the point C and point E, respectively, and z_C and z_E are the elevation heads of the point C and point E, respectively.

The phreatic surface is considered to be a flow line and a line of the atmospheric pressure or zero pressure, and (2) can be written as

$$u_C = \gamma_w (z_E - z_C) = h_{CF} \cos^2 \beta. \quad (3)$$

The hydraulic gradient of the seepage can be approximately estimated by examining the hydraulic head difference between point F and point E on the phreatic surface

$$i_{EF} = \frac{h_{FG}}{l_{FE}} = \sin \beta. \quad (4)$$

The porewater pressures acting on a partially submerged slice are shown in Figure 4. According to (3), these forces can be calculated as

$$P_1 = 0.5 r_w l_{AD}^2 \cos^2 \beta, \quad (5a)$$

$$P_2 = 0.5 r_w (l_{AD} + l_{BC}) l_{CD} \cos^2 \beta, \quad (5b)$$

$$P_3 = 0.5 r_w l_{BC}^2 \cos^2 \beta. \quad (5c)$$

3. Relationship between Porewater Pressures and Seepage Force

3.1. Resultant of the Porewater Pressures Acting on the Underwater Slice. The porewater pressures, acting on four sides of the underwater slice (Figure 2), are resolved into two directions which are parallel and perpendicular to the slice base. The resultants of these forces acting on the slice can be derived as

$$N_P = P_2 + (P_1 - P_3) \sin \alpha - P_4 \cos (\alpha - \beta), \quad (6)$$

$$T_P = (P_1 - P_3) \cos \alpha + P_4 \sin (\alpha - \beta),$$

where N_P is the resultant of the porewater pressures in direction perpendicular to the slice base, T_P is the their resultant in direction parallel to the slice base, α is the inclination of the slice base of slice j , and β is the inclination of top slide of slice j .

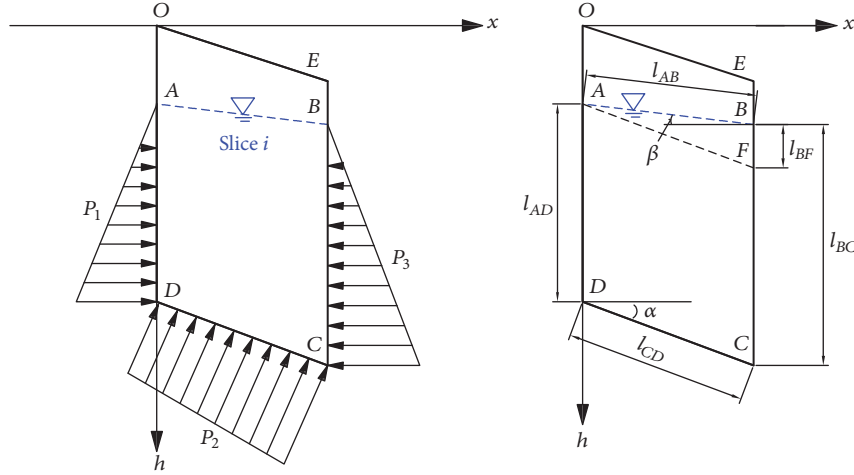


FIGURE 4: Porewater pressures acting on three sides of a partially submerged slice.

By substituting (1a), (1b), (1c), and (1d) into (6), we obtain

$$\begin{aligned} \frac{N_P}{0.5r_w} &= \frac{h_C^2 - h_D^2}{\sin \alpha} + (h_D^2 - h_A^2 - h_C^2 + h_B^2) \sin \alpha \\ &\quad - \frac{h_B^2 - h_A^2}{\sin \beta} (\cos \alpha \cos \beta + \sin \alpha \sin \beta), \\ \frac{T_P}{0.5r_w} &= (h_D^2 - h_A^2 - h_C^2 + h_B^2) \cos \alpha \\ &\quad + \frac{h_B^2 - h_A^2}{\sin \beta} (\sin \alpha \cos \beta - \cos \alpha \sin \beta). \end{aligned} \quad (7)$$

By rearranging the above two equations, the following expressions can be written as

$$N_P = 0.5r_w \cos \alpha \left[\frac{h_C^2 - h_D^2}{\tan \alpha} - \frac{h_B^2 - h_A^2}{\tan \beta} \right] = r_w V \cos \alpha, \quad (8)$$

$$T_P = 0.5r_w \sin \alpha \left[\frac{h_D^2 - h_C^2}{\tan \alpha} + \frac{h_B^2 - h_A^2}{\tan \beta} \right] = -r_w V \sin \alpha, \quad (9)$$

where V is the volume of slice j in Figure 2.

3.2. Resultant of the Porewater Pressures Acting on the Partially Submerged Slice. All porewater pressures acting on the partially submerged slice, which are shown in Figure 4, are also decomposed into two directions which are parallel and perpendicular to the slice base, which can be expressed as

$$\begin{aligned} N_P &= P_2 + (P_1 - P_3) \sin \alpha, \\ T_P &= (P_1 - P_3) \cos \alpha. \end{aligned} \quad (10)$$

By substituting (5a), (5b), and (5c) into (10), we obtain

$$\begin{aligned} N_P &= 0.5r_w [(l_{AD} + l_{BC}) l_{CD} - (l_{AD} + l_{BC}) l_{BF} \sin \alpha] \\ &\quad \cdot \cos^2 \beta, \\ T_P &= -0.5r_w (l_{AD} + l_{BC}) l_{BF} \cos \alpha \cos^2 \beta. \end{aligned} \quad (11)$$

Based on the Law of Sines, an equation relating the lengths of the sides of the triangle ABF to the Sines of its angles can be given by

$$\frac{l_{BF}}{\sin(\alpha - \beta)} = \frac{l_{AF}}{\sin(90^\circ + \beta)} = \frac{l_{CD}}{\cos \beta}. \quad (12)$$

By substituting (12) into (11), the following expressions can be derived as

$$\begin{aligned} N_P &= 0.5r_w (l_{AD} + l_{BC}) \\ &\quad \cdot l_{CD} [\cos^2 \beta - \sin(\alpha - \beta) \sin \alpha \cos \beta], \end{aligned} \quad (13)$$

$$T_P = -0.5r_w (l_{AD} + l_{BC}) l_{CD} \sin(\alpha - \beta) \cos \alpha \cos \beta.$$

Trigonometric functions using functional equations in terms of properties like the sum and difference formulas of two angles are applied to transformation of equations. The expressions above can be written as

$$\begin{aligned} N_P &= 0.5r_w (l_{AD} + l_{BC}) \\ &\quad \cdot l_{CD} [\cos^2 \alpha + \sin(\alpha - \beta) \cos \alpha \sin \beta] \\ &= r_w V_d [\cos \alpha + \sin(\alpha - \beta) \sin \beta], \\ T_P &= 0.5r_w (l_{AD} + l_{BC}) \\ &\quad \cdot l_{CD} [\cos \alpha \cos(\alpha - \beta) \sin \beta - \cos \alpha \sin \alpha] \\ &= r_w V_d [\cos(\alpha - \beta) \sin \beta - \sin \alpha], \end{aligned} \quad (14)$$

where V_d is the volume of the section $ABCD$ below the phreatic surface of slice i in Figure 4.

3.3. Relationship between Porewater Pressures and Seepage Force. The seepage force is directly proportional to the hydraulic gradient and the soil volume below the phreatic surface [26, 31], which can be defined as

$$P = r_w V_d i = r_w V_d \sin \beta. \quad (15)$$

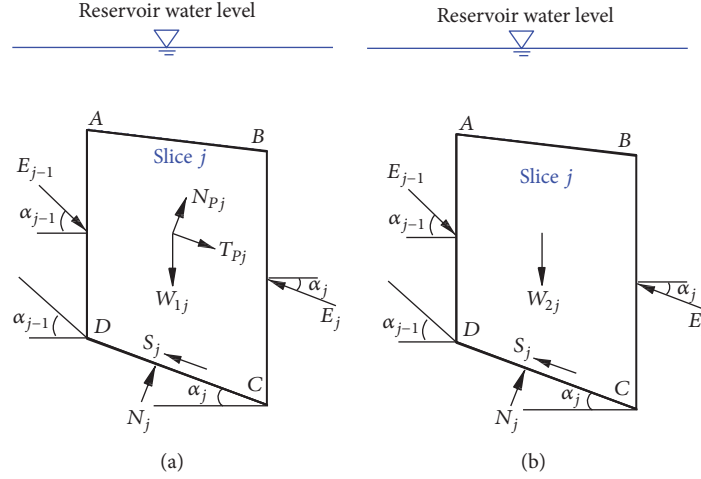


FIGURE 5: Forces acting on the underwater slice: (a) the porewater pressures based on (6) and (7); (b) substituting the buoyant weight for the porewater pressures and the total weight of the slice.

By substituting (15) into (14), the following expressions can be derived as

$$N_P = r_w V_d \cos \alpha + P \sin (\alpha - \beta), \quad (16)$$

$$T_P = P \cos (\alpha - \beta) - r_w V_d \sin \alpha. \quad (17)$$

According to (8) and (9), the resultant of the porewater pressures acting on four sides of the underwater slice equals the buoyancy. Based on (16) and (17), the resultant of the porewater pressures acting on three sides acting on the partially submerged slice is equivalent to the vector sum of the buoyancy and the seepage force.

4. Stability Analysis of Partially Submerged Landslide

The following assumptions were applied to limit equilibrium method for the landslide stability [25, 26]. (1) The landslide is divided into a series of vertical slices. (2) Each slice is assumed to be rigid. (3) The FOS is considered to be identical for all slices. (4) The thrust line of the interslice force on a lower slice is assumed to be parallel to the current slice base. (5) If the interslice force is negative, the value is assumed to be zero.

4.1. Limit Equilibrium Equations of the Underwater Slice. One approach, considering the effect of water on the underwater slices of partially submerged landslides in the limit equilibrium analysis, is based on porewater pressures. The resultant of the porewater pressures is based on (8) and (9). All forces are resolved into both the parallel and perpendicular directions to the slice base (Figure 5(a)), resulting in the following equations:

$$W_{1j} \cos \alpha_j - N_{Pj} - N_j + E_{j-1} \sin (\alpha_{j-1} - \alpha_j) = 0, \quad (18)$$

$$W_{1j} \sin \alpha_j + T_{Pj} + E_{j-1} \cos (\alpha_{j-1} - \alpha_j) - E_j - S_j = 0. \quad (19)$$

The other approach directly uses the buoyancy. All forces are resolved into both directions (Figure 5(b)), and we obtain

$$W_{2j} \cos \alpha_j - N_j + E_{j-1} \sin (\alpha_{j-1} - \alpha_j) = 0, \quad (20)$$

$$W_{2j} \sin \alpha_j + E_{j-1} \cos (\alpha_{j-1} - \alpha_j) - E_j - S_j = 0, \quad (21)$$

where W_{1j} is the total weight of the slice j , which is calculated using saturated unit weight, W_{2j} is the buoyant weight of the slice, which is calculated using buoyant unit weight, N_j is the normal force at the base of the slice, E_{j-1} is the interslice force of slice $j - 1$ acting on slice j at the vertical boundary, E_j is the interslice force of slice j acting on slice $j + 1$ at the vertical boundary, and S_j is the mobilized shear strength along the base of the slice, which can be determined using the Mohr–Coulomb yield criterion:

$$S_j = \frac{c_j \cdot l_j + N_j \tan \varphi_j}{F_s}, \quad (22)$$

where c is the cohesion of the slip surface, l is the length of the slip surface, φ is the friction angle of the slip surface, and F_s is the safety factor.

In fact, substituting (8) into (18), (20) can be obtained, and substituting (9) into (19), (21) can be obtained. Therefore, there are two equivalent approaches for considering the effect of water on the underwater zone of the partially submerged landslide in limit equilibrium analysis. One is based on porewater pressures, and the other uses the buoyant weight, without considering any porewater pressures.

4.2. Limit Equilibrium Equations of the Partially Submerged Slice. For the partially submerged slice, all forces, including the resultant of the porewater pressures in terms of (16) and (17), are also resolved into the same directions with the underwater slice as follows (Figure 6(a)):

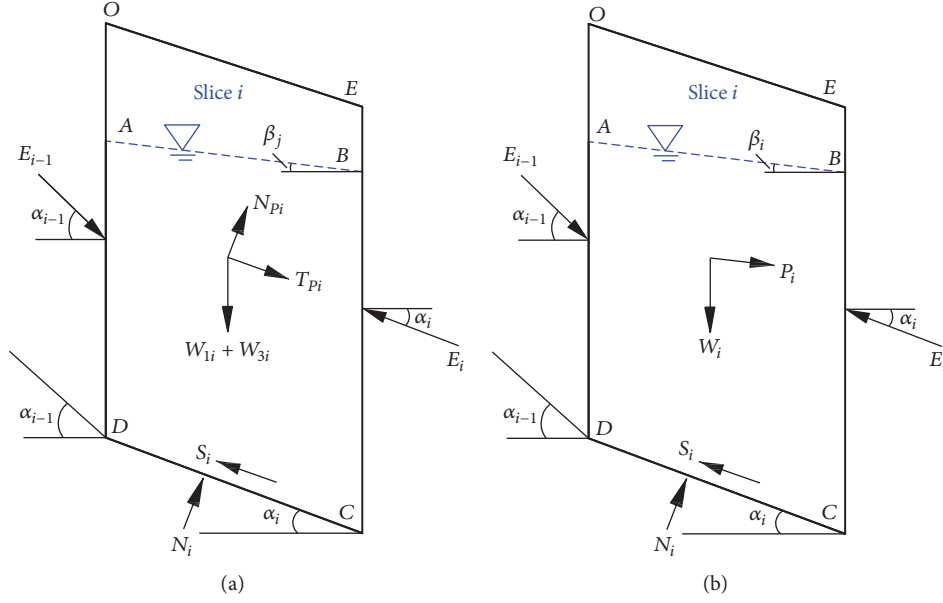


FIGURE 6: Forces acting on the partially submerged slice. (a) The porewater pressures based on (16) and (17); (b) substituting the seepage force and buoyant weight for the porewater pressures and the total weight of the slice.

$$(W_{1i} + W_{3i}) \cos \alpha_i - N_{Pi} - N_i + E_{i-1} \sin (\alpha_{i-1} - \alpha_i) = 0, \quad (23)$$

$$(W_{1i} + W_{3i}) \sin \alpha_i + T_{Pi} + E_{i-1} \cos (\alpha_{i-1} - \alpha_i) - E_i - S_i = 0. \quad (24)$$

The other approach directly uses the buoyancy and the seepage force. All forces are resolved into both directions (Figure 6(b)), and we obtain

$$W_i \cos \alpha_i - P_i \sin (\alpha_i - \beta_i) - N_i + E_{i-1} \sin (\alpha_{i-1} - \alpha_i) = 0, \quad (25)$$

$$W_i \sin \alpha_i + P_i \cos (\alpha_i - \beta_i) + E_{i-1} \cos (\alpha_{i-1} - \alpha_i) - E_i - S_i = 0, \quad (26)$$

where W_{1i} is the total weight of the section ABCD below the surface phreatic, W_{2i} is the buoyant weight of the section ABCD, W_{3i} is the weight of the section ABEO above the surface phreatic, and W_i is the sum of W_{2i} and W_{3i} .

If we substitute (16) into (23), (25) can be obtained, and substituting (17) into (24), (26) can be obtained. Therefore, there are also two equivalent approaches for considering the effect of water on the partially submerged zone. One is based on the porewater pressures and total weight, and the other uses the seepage force and buoyant weight, without considering any porewater pressures.

4.3. The Safety Factor of the Partially Submerged Landslide. It can be seen that both of (20) and (25) have the same forms, but (25) differs from (20) in two ways. One is that the weight term in (20) is the buoyant weight of the slice, while it is the

sum of the weight of the section above the phreatic surface and buoyant weight of the section below the surface phreatic. The other is that there is the seepage force term in (25), not in (20). It is the same for (21) and (26). Thus, (25) and (26) are used not only for the partially submerged zone, but also for the underwater zone by regarding the seepage force as zero.

By adding the effect of the porewater pressure to the formula proposed by Yamin and Liang [24], we obtain a modified expression for calculating the safety factor of the partially submerged landslide stability using the seepage force and the buoyant weight terms, which is written as

$$Fs = \frac{\sum_{i=1}^{n-1} (R_i \prod_{j=i}^{n-1} \psi_j) + R_n}{\sum_{i=1}^{n-1} (T_i \prod_{j=i}^{n-1} \psi_j) + T_n} \quad (27)$$

with

$$R_i = [W_i \cos \alpha_i - P_i \sin (\alpha_i - \beta_i)] \tan \varphi_i + c_i l_i,$$

$$T_i = W_i \sin \alpha_i + P_i \cos (\alpha_i - \beta_i),$$

$$W_i = V_{di} \gamma' + V_{ui} \gamma,$$

$$P_i = \gamma_w V_{di} \sin \beta_i, \quad (28)$$

$$\prod_{j=i}^{n-1} \psi_j = \psi_i \cdot \psi_{i+1} \cdot \psi_{i+2} \cdots \psi_{n-1},$$

$$\psi_{i-1} = \cos (\alpha_{i-1} - \alpha_i) - \sin \cos (\alpha_{i-1} - \alpha_i) \frac{\tan \varphi_i}{Fs},$$

where W_i is the weight of any slice i , P_i is the seepage force, which is zero for an underwater slice, V_{di} is the volume of slice i below the surface phreatic, γ' is buoyant unit weight of slice i , V_{ui} is the volume of slice i above the surface phreatic,

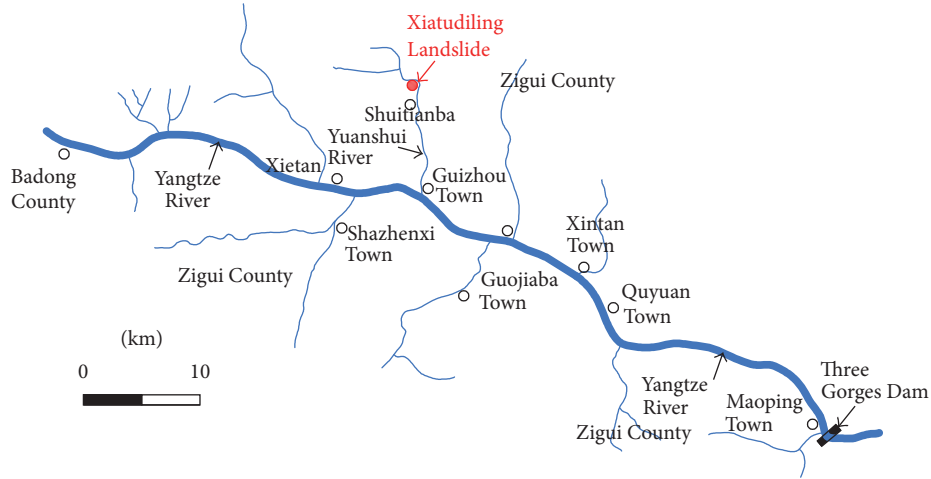


FIGURE 7: Location of the Xiatudiling landslide.



FIGURE 8: A panorama of the Xiatudiling landslide.

which is zero for an underwater slice, r is the unit weight of slice i above the surface phreatic, and n is the slice number of a landslide.

5. Case Study

5.1. Characteristics of Xiatudiling Landslide. Xiatudiling landslide is located in Zigui County, Hubei Province, China (Figure 7). The elevations of the top and toe of the landslide are 205 m and 155 m, respectively. The water level of the Three Gorges Reservoir fluctuates between 145 m and 175 m; thus this landslide is a partially submerged slope. The landslide is about 170 m long and 14 m thick, with a volume of $25 \times 10^4 \text{ m}^3$. The width of the landslide is between 70 m and 150 m in the middle part and back part, with the biggest width of 210 m in the front part (Figures 8 and 9).

The Xiatudiling landslide is composed of loose rubble soil with a clay content of 15% ~40%, the rubbles, which consist of sandstone and mudstone. Slip surface is mainly formed in the strongly weathered mudstone. Slip surface has a dip direction of 342° and a dip angle of 8° . The exposed bedrock of the landslide is mainly red Jurassic Penglaizhen Formation (J_3P), and the lithologies are mainly composed of purple mudstone, purple pelitic siltstone, and gray feldspar-quartz sandstone [36].

The Xiatudiling landslide is divided into 64 vertical slices (Figure 10). The cohesion of slip surface is 10 kN, and the

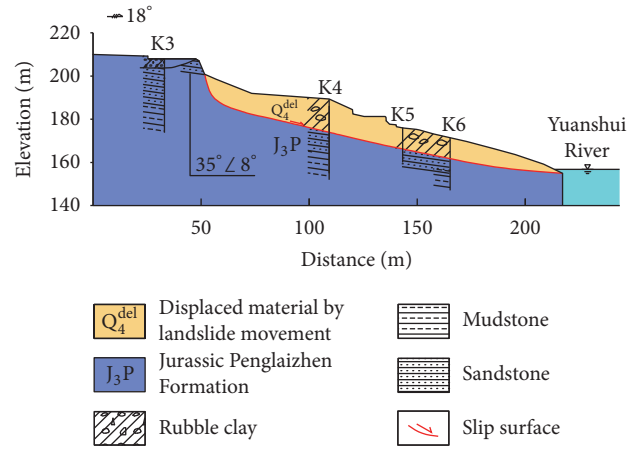


FIGURE 9: Longitudinal section of Xiatudiling landslide.

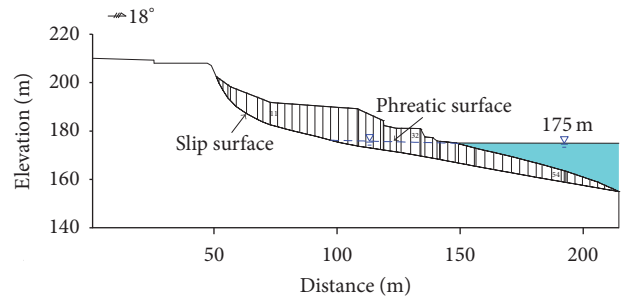


FIGURE 10: Division of the Xiatudiling landslide into slices.

friction angle is 11.8° . The dry unit weight of landslide material is 21.5 kN/m^3 , and the saturated unit weight is 23.5 kN/m^3 . The permeability coefficient of slide mass is 1.141 m/d , and the saturated water content of rubble soil is 26.20%.

5.2. Results and Discussion. The safety factors of the Xiatudiling landslide are calculated by four models, Janbu,

TABLE 1: The safety factors calculated by four models.

Model	Janbu	Morgenstern-Price	Spencer	This study
Factor of safety	1.110	1.097	1.100	1.130

Morgenstern-Price, Spencer, and the method proposed by us. When the level of reservoir water is 175 m, the safety factor calculated by the method proposed in this study, Janbu, Morgenstern-Price, and Spencer is 1.130, 1.110, 1.097, and 1.100, respectively (Table 1). The safety factor proposed in this study is slightly larger than that by other models. The maximum difference is 0.033 and the rate of deviation is 2.92%.

The difference is caused by the different assumption of interslice resultant force. Our method assumes the vector of interslice resultant force is parallel to slice base, while Janbu assumes the position of interslice horizontal force, Morgenstern-Price assumes a function relationship between interslice horizontal force and shear force, and Spencer assumes the dip of interslice resultant force is a constant.

6. Conclusions

The influences of water on the stability of the partially submerged landslide are usually expressed in the form of porewater pressure and seepage force in limit equilibrium analysis. This study builds the relationship between the porewater pressures and the seepage force by decomposition and composition of all boundary porewater pressures into two directions that are parallel and perpendicular to the slice base.

A partially submerged landslide is divided into many vertical slices that include underwater slices and partially submerged slices. A hydrostatic force approach is applied to calculate the boundary porewater pressure acting on an underwater slice, and a flow net approach is used to obtain the porewater pressures acting on a partially submerged slice. The resultant of the porewater pressures acting on the underwater slice equals the buoyancy, and that acting on the partially submerged slice is equivalent to the vector sum of the seepage force and the buoyancy.

There are two approaches for considering the effect of water on landslide stability in the limit equilibrium method of slices. One is based on total unit weight and porewater pressures acting, and the other is in terms of the buoyant weight and the seepage force. Both approaches are equivalent. The approach including the total unit weight and porewater pressures is complex. The porewater pressures of the underwater slice consist of four terms corresponding to the four sides, and those of the partially submerged slice are comprised of three terms corresponding to the three sides below the phreatic surface, while the other approach including the seepage force and buoyancy is simpler. Therefore, we choose the latter to consider the effect of water on the partially submerged landslide stability in limit equilibrium analysis, which offers a simple solution to complex boundary porewater pressures of slices in determining the factor of safety.

The proposed simplified method is used to calculate the safety factors of Xiatudiling landslide and is compared with that by Janbu, Morgenstern-Price, and Spencer model. The safety factor of this study is slightly larger than that by other models. The maximum difference is 0.033 and the rate of deviation is 2.92%.

Conflicts of Interest

The authors declare that they have no conflicts of interest.

Acknowledgments

This research work was funded by the National Natural Science Foundation of China (no. 41572289, no. 41572292) and the follow-up work of geological disaster prevention projects in Three Gorges Reservoir (no. 000121 2015C C60 005).

References

- [1] L. Cascini, S. Cuomo, M. Pastor, and G. Sorbino, "Modeling of rainfall-induced shallow landslides of the flow-type," *Journal of Geotechnical and Geoenvironmental Engineering*, vol. 136, no. 1, pp. 85–98, 2010.
- [2] J. Du, K. Yin, and S. Lacasse, "Displacement prediction in colluvial landslides, Three Gorges Reservoir, China," *Landslides*, vol. 10, no. 2, pp. 203–218, 2013.
- [3] D. Li, K. Yin, and C. Leo, "Analysis of Baishuihe landslide influenced by the effects of reservoir water and rainfall," *Environmental Earth Sciences*, vol. 60, no. 4, pp. 677–687, 2010.
- [4] C. Liang, M. B. Jaksa, B. Ostendorf, and Y. L. Kuo, "Influence of river level fluctuations and climate on riverbank stability," *Computers & Geosciences*, vol. 63, pp. 83–98, 2015.
- [5] M. Zhang, Y. Yin, and B. Huang, "Mechanisms of rainfall-induced landslides in gently inclined red beds in the eastern Sichuan Basin, SW China," *Landslides*, vol. 12, no. 5, pp. 973–983, 2015.
- [6] K. He, X. Li, X. Yan, and G. Dong, "The landslides in the Three Gorges Reservoir Region, China and the effects of water storage and rain on their stability," *Environmental Geology*, vol. 55, no. 1, pp. 55–63, 2008.
- [7] P. Paronuzzi, E. Rigo, and A. Bolla, "Influence of filling-drawdown cycles of the Vajont reservoir on Mt. Toc slope stability," *Geomorphology*, vol. 191, pp. 75–93, 2013.
- [8] O. Igwe, "The study of the factors controlling rainfall-induced landslides at a failure-prone catchment area in Enugu, South-eastern Nigeria using remote sensing data," *Landslides*, vol. 12, no. 5, pp. 1023–1033, 2015.
- [9] T. R. Martha, P. Roy, K. B. Govindharaj, K. V. Kumar, P. G. Diwakar, and V. K. Dadhwal, "Landslides triggered by the June 2013 extreme rainfall event in parts of Uttarakhand state, India," *Landslides*, vol. 12, no. 1, pp. 135–146, 2015.
- [10] S. Jeong, Y. Kim, J. K. Lee, and J. Kim, "The 27 July 2011 debris flows at Umyeonsan, Seoul, Korea," *Landslides*, vol. 12, no. 4, pp. 799–813, 2015.
- [11] Y. Miyabuchi, F. Maeno, and S. Nakada, "The October 16, 2013 rainfall-induced landslides and associated lahars at Izu Oshima Volcano, Japan," *Journal of Volcanology and Geothermal Research*, vol. 302, pp. 242–256, 2015.

- [12] L. Müller, "The rock slide in the Vajont Valley," *Rock Mechanics and Rock Engineering*, vol. 2, pp. 148–212, 1964.
- [13] F.-W. Wang, Y.-M. Zhang, Z.-T. Huo, T. Matsumoto, and B.-L. Huang, "The July 14, 2003 Qianjiangping landslide, three gorges reservoir, China," *Landslides*, vol. 1, no. 2, pp. 157–162, 2004.
- [14] A. Panizzo, P. De Girolamo, M. Di Risio, A. Maistri, and A. Petaccia, "Great landslide events in Italian artificial reservoirs," *Natural Hazards and Earth System Sciences*, vol. 5, no. 5, pp. 733–740, 2005.
- [15] G.-Q. Chen, R.-Q. Huang, Q. Xu, T.-B. Li, and M.-L. Zhu, "Progressive modelling of the gravity-induced landslide using the local dynamic strength reduction method," *Journal of Mountain Science*, vol. 10, no. 4, pp. 532–540, 2013.
- [16] X. Hu, M. Zhang, M. Sun, K. Huang, and Y. Song, "Deformation characteristics and failure mode of the Zhujiadian landslide in the three gorges Reservoir, China," *Bulletin of Engineering Geology and the Environment*, vol. 74, no. 1, pp. 1–12, 2015.
- [17] G. Xu, W. Li, Z. Yu, X. Ma, and Z. Yu, "The 2 September 2014 Shanshucao landslide, Three Gorges Reservoir, China," *Landslides*, vol. 12, no. 6, pp. 1169–1178, 2015.
- [18] Y. Yin, H. Wang, Y. Gao, and X. Li, "Real-time monitoring and early warning of landslides at relocated Wushan Town, the Three Gorges Reservoir, China," *Landslides*, vol. 7, no. 3, pp. 339–349, 2010.
- [19] Y.-P. Yin, B. Huang, X. Chen, G. Liu, and S. Wang, "Numerical analysis on wave generated by the qianjiangping landslide in Three Gorges Reservoir, China," *Landslides*, vol. 12, no. 2, pp. 355–364, 2015.
- [20] T. W. Miller and J. M. Hamilton, "New analysis procedure to explain a slope failure at the Martin Lake mine," *Géotechnique*, vol. 39, no. 1, pp. 107–123, 1989.
- [21] R. L. Michalowski, "Slope stability analysis: A kinematical approach," *Géotechnique*, vol. 45, no. 2, pp. 283–293, 1995.
- [22] J. Kim, R. Salgado, and H. S. Yu, "Limit analysis of soil slopes subjected to pore-water pressures," *Journal of Geotechnical and Geoenvironmental Engineering*, vol. 125, no. 1, pp. 49–58, 1999.
- [23] E. N. Bromhead, A. J. Harris, and P. D. J. Watson, "Influence of pore water pressures in partly submerged slopes on the critical pool level," in *Proceedings of the International Symposium on Slope Stability Engineering*, N. Yagi, T. Yamagami, and J. C. Jiang, Eds., pp. 411–416, Matsuyama, Japan, 1999.
- [24] M. Yamin and R. Y. Liang, "Limiting equilibrium method for slope/drilled shaft system," *International Journal for Numerical and Analytical Methods in Geomechanics*, vol. 34, no. 10, pp. 1063–1075, 2010.
- [25] L. Li and R. Y. Liang, "Limit equilibrium based design approach for slope stabilization using multiple rows of drilled shafts," *Computers & Geosciences*, vol. 59, pp. 67–74, 2014.
- [26] C. Zhou, W. Shao, and C. J. van Westen, "Comparing two methods to estimate lateral force acting on stabilizing piles for a landslide in the three gorges reservoir, China," *Engineering Geology*, vol. 173, pp. 41–53, 2014.
- [27] A. W. Bishop, "The use of the slip circle in the stability analysis of slopes," *Géotechnique*, vol. 5, pp. 7–17, 1955.
- [28] N. R. Morgenstern and V. E. Price, "The analysis of the stability of general slip surfaces," *Géotechnique*, vol. 15, no. 1, pp. 79–93, 1965.
- [29] A. G. Razdolsky, "Slope stability analysis based on the direct comparison of driving forces and resisting forces," *International Journal for Numerical and Analytical Methods in Geomechanics*, vol. 33, no. 8, pp. 1123–1134, 2009.
- [30] Y. Zheng, W. Shi, and W. Kong, "Calculation of seepage forces and phreatic surface under drawdown conditions," *Chinese Journal of Rock Mechanics and Engineering*, vol. 23, pp. 3203–3210, 2004 (Chinese).
- [31] B. D. Collins and D. Znidarcic, "Stability analyses of rainfall induced landslides," *Journal of Geotechnical and Geoenvironmental Engineering*, vol. 130, no. 4, pp. 362–372, 2004.
- [32] H. Ghiassian and S. Ghareh, "Stability of sandy slopes under seepage conditions," *Landslides*, vol. 5, no. 4, pp. 397–406, 2008.
- [33] J. Kim, R. Salgado, and J. Lee, "Stability analysis of complex soil slopes using limit analysis," *Journal of Geotechnical and Geoenvironmental Engineering*, vol. 128, no. 7, pp. 546–557, 2002.
- [34] J. M. Duncan and S. G. Wright, *Soil Strength and Slope Stability*, John Wiley & Sons, Inc., New York, NY, USA, 2005.
- [35] L. Abramson, T. Lee, S. Sharma, and G. Boyce, *Slope Stability and Stabilization Methods*, John Wiley & Sons, Inc., New York, NY, USA, 2nd edition, 2002.
- [36] S. Yan, Y. Wang, H. Du, L. Yu, and S. Zheng, "Evaluation of the lateral forces acting on stabilizing piles considering the resistance of the lower zone of a landslide in the three Gorges Reservoir, China," *Journal of Engineering Science and Technology Review*, vol. 9, no. 6, pp. 170–177, 2016.

Research Article

CO₂ Leakage-Induced Contamination in Shallow Potable Aquifer and Associated Health Risk Assessment

Chan Yeong Kim ¹, Weon Shik Han ¹, Eungyu Park,² Jina Jeong,² and Tianfu Xu ³

¹Department of Earth System Sciences, Yonsei University, Seoul, Republic of Korea

²College of Earth System Science, Kyungpook National University, Daegu, Republic of Korea

³Key Laboratory of Groundwater Resources and Environment, Ministry of Education, Jilin University, Jilin, China

Correspondence should be addressed to Weon Shik Han; hanw@yonsei.ac.kr

Received 29 November 2017; Accepted 31 January 2018; Published 5 April 2018

Academic Editor: Liangping Li

Copyright © 2018 Chan Yeong Kim et al. This is an open access article distributed under the Creative Commons Attribution License, which permits unrestricted use, distribution, and reproduction in any medium, provided the original work is properly cited.

Leakage of stored CO₂ from a designated deep reservoir could contaminate overlying shallow potable aquifers by dissolution of arsenic-bearing minerals. To elucidate CO₂ leakage-induced arsenic contamination, 2D multispecies reactive transport models were developed and CO₂ leakage processes were simulated in the shallow groundwater aquifer. Throughout a series of numerical simulations, it was revealed that the movement of leaked CO₂ was primarily governed by local flow fields within the shallow potable aquifer. The induced low-pH plume caused dissolution of aquifer minerals and sequentially increased permeabilities of the aquifer; in particular, the most drastic increase in permeability appeared at the rear margin of CO₂ plume where two different types of groundwater mixed. The distribution of total arsenic ($\sum As$) plume was similar to the one for the arsenopyrite dissolution. The breakthrough curve of $\sum As$ monitored at the municipal well was utilized to quantify the human health risk. In addition, sensitivity studies were conducted with different sorption rates of arsenic species, CO₂ leakage rates, and horizontal permeability in the aquifer. In conclusion, the human health risk was influenced by the shape of $\sum As$ plume, which was, in turn, affected by the characteristics of CO₂ plume behavior such as horizontal permeability and CO₂ leakage rate.

1. Introduction

Carbon capture and storage are considered to be one of the mitigating strategies for reducing CO₂ emissions to the atmosphere [1–3]. Among various carbon capture and storage technologies, CO₂ can be injected into geologically stable formations, which typically have large storage capacities and are capped by low-permeability sealing formations. However, during CO₂ injection activity, injection-induced pressure builds up within the storage formation [4–6]. If any unwanted pathways exist within the sealing formation, CO₂ is able to migrate to the shallow aquifer through these pathways while experiencing phase change from supercritical to gaseous CO₂ [7–10]. Especially in this study, the leakage of gaseous CO₂ into a shallow confined aquifer was considered. Leaked gaseous CO₂ dissolves in the potable groundwater and develops a low-pH plume [11, 12], which induces secondary contamination within the aquifer by enhancing the mobility of toxic heavy metals [13–16].

Released toxic heavy metals are able to migrate with the ambient groundwater induced by natural hydraulic gradient or influenced by enforced gradient due to any active municipal wells nearby. If the contaminated groundwater produced from the municipal well is directly distributed without proper treatment (disinfection or chlorination processes) to residents who use it daily for the purpose of drinking, bathing, cleaning, or other household uses, these residents can be exposed to adverse carcinogenic health risks. The World Health Organization's (WHO) International Agency for Research on Cancer classified various dissolved heavy metals (e.g., arsenic and lead) and other radioactive metals (e.g., uranium and cesium) as toxic substances hazardous to human health [17]. Among these carcinogenic heavy metals, this study focused on arsenic [18]. According to the US Agency for Toxic Substances and Disease Registry, who ranked hazardous substances based on their occurrence, toxicity, and potential for human exposure, arsenic was ranked the first in their Substance Priority List in 2013 and 2015 [19].

Moreover, arsenic contamination and its detrimental impacts have been reported by various countries such as China [20], Bangladesh [21], Vietnam [22], and India [23] in recent years.

Mobilization of arsenic in a shallow groundwater aquifer due to CO_2 leakage has been investigated at one of the natural analog sites, Chimayó, New Mexico, where CO_2 -saturated brackish water was leaked into the shallow aquifer along the fault [7, 13, 24, 25]. At this site, decreased pH and the resulting mobilization of trace metals, including arsenic, were observed. Even if their adverse effects had been alleviated due to the high buffering capacity of the local groundwater aquifer, Keating et al. [7] reported significantly elevated trace metal concentrations at a number of local wells due to the influx of brackish waters. Later, both Keating et al. [13] and Viswanathan et al. [24] integrated the field dataset into a multiphase reactive transport model to understand the behavior of arsenic, since some wells in Chimayó exceeded the maximum contamination level (MCL). In addition to studies targeting natural CO_2 release sites, several experiments have been conducted at field-scale CO_2 injection sites to determine secondary contamination caused by the injected CO_2 [11, 26–28]. Decreased pH, increased HCO_3^- concentrations, and subsequent changes in groundwater chemistry such as increased Fe^{2+} , Mn^{2+} , Mg^{2+} , and Ca^{2+} concentrations were observed at both Frio-I brine pilot injection [11, 27] and ZERT field tests [12, 28].

In addition to field-oriented research, several studies have focused on the implementation of numerical simulations to evaluate geochemical behaviors associated with arsenic contamination. For example, Zhang et al. [29] and Xiao et al. [30] utilized the reactive transport simulation and investigated the complex chemical change induced by CO_2 leaked into a shallow aquifer. In contrast to these studies which presented detailed geochemical interactions, Siirila et al. [31] simplified the geochemical processes by solving the advection-dispersion equation with a linear sorption. Without full assessment of geochemical reactions, they were able to account for the movement of toxic elements in complex 3D heterogeneous systems as well as for groundwater contamination-induced carcinogenic health risks with a probabilistic approach. Later, Navarre-Sitchler et al. [32] utilized PFLOTRAN and simulated the mobilization of lead in a complex heterogeneous system by assuming that released gaseous CO_2 instantaneously dissolved in the groundwater aquifer. The proposed work in this study was built upon the framework of the previous studies mentioned above. Certain approaches accounted for the detailed geochemical behavior of toxic heavy metals (e.g., complexation, sorption, mineral dissolution, and precipitation) in the groundwater aquifer, whereas other approaches relied on either simplified chemical reactions (e.g., advection-dispersion equation) or multiphase fluid migration (e.g., gaseous CO_2 leakage into the groundwater aquifer) while accounting for carcinogenic health risks or complex 3D heterogeneous systems. Therefore, the goal of this study was to integrate these two approaches and delineate the multiphase behavior of leaked gaseous CO_2 to a shallow potable aquifer. Moreover, leaked CO_2 -induced geochemical changes, such as evolution of water quality and mobility of toxic trace metals

(e.g., arsenic), were characterized by adapting the multispecies reactive transport model. Finally, the simulated concentration of arsenic species observed from the assigned municipal well was used to quantify the carcinogenic health risk for chronically exposed humans.

2. Behavior of Arsenic in Subsurface Environment

Arsenic in natural water typically originates from arsenic-bearing minerals that frequently possess sulfur, oxygen, and iron [33]. Generally, these naturally occurring arsenic-bearing minerals include arsenopyrite (FeAsS), realgar (AsS), enargite (CuAsS_4), scorodite ($\text{FeAsO}_4 \cdot 2\text{H}_2\text{O}$), and tennantite ($\text{Cu}_6[\text{Cu}_4(\text{Fe,Zn})_2]\text{As}_4\text{S}_{13}$) [29, 34, 35]. When these minerals dissolve, various forms of arsenic species such as H_3AsO_4^0 , H_2AsO_4^- , HAsO_4^{2-} , AsO_4^{3-} , H_3AsO_3^0 , and H_2AsO_3^- can be released into groundwater. As seen in Figure 1, arsenic species can be present in several valence states (−3, 0, +3, and +5), but in natural groundwater, it is mostly found in oxyanions of trivalent arsenite (As(III)) or pentavalent arsenate (As(V)), depending on reducing or oxidizing conditions, respectively. Typically, the mobility and toxicity of As(III) are considered to be much higher than those of As(V) [36–38]. Under the reducing condition, uncharged As(III) species, such as H_3AsO_3^0 , is dominant below pH 9.2 (Figure 1). However, under the oxidizing condition, H_2AsO_4^- is dominant at pH < 6.9, while HAsO_4^{2-} is dominant at higher pH (pH > 6.9). Moreover, H_3AsO_4^0 and AsO_4^{3-} could exist under extremely acidic and alkaline conditions, respectively. In this study, when injected CO_2 leaked into the shallow potable groundwater aquifer, the dissolution of leaked CO_2 induced the acidification of the ambient groundwater to $4 < \text{pH} < 6$ [11], where H_3AsO_3^0 and H_2AsO_4^- were dominant under reducing and oxidizing conditions, respectively [33, 39]. Here, the shallow aquifer was considered to be under the reducing condition, and thus, H_3AsO_3^0 was chosen as the most dominant species.

3. Work Flow: Numerical to Probabilistic Quantification

The following study comprised two major parts, namely, numerical prediction of CO_2 transport from a leakage point to a municipal well (numerical simulation) and probabilistic quantification of health risks to humans who have been chronically exposed to a certain toxic heavy metal (health risk assessment), in sequence (Figure 2). Processes for both numerical simulation and probabilistic risk quantification were designed in three steps: “Data,” “Process,” and “Result.” During the “Data” step, input parameters were chosen selectively, and the sampling scheme was determined either deterministically or randomly. Subsequently, a series of calculations using either numerical or probabilistic approaches were conducted in the “Process” step. Finally, in the “Result” step, simulation outputs, such as CO_2 plume distribution, maximum concentrations of selected toxic heavy metals, and human health risk, were analyzed. The link between

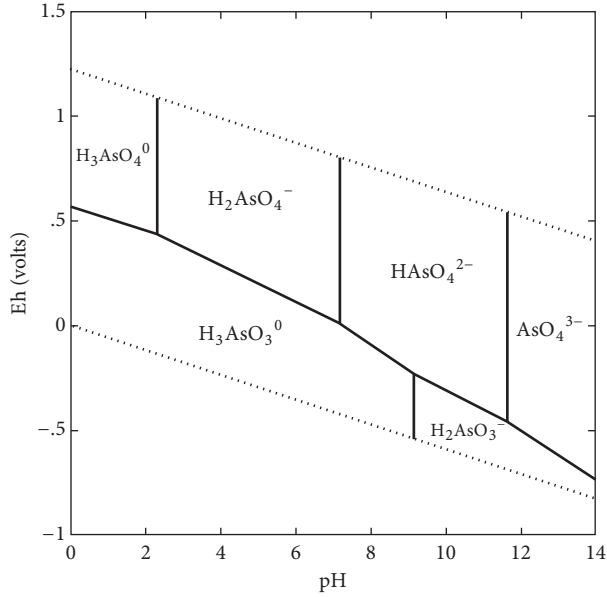


FIGURE 1: Eh-pH diagram for arsenic species under H-O-As system at 1 bar and 25°C.

“numerical simulation” and “health risk assessment” was the profile of arsenic concentration monitored at the municipal well; throughout complex spatial and temporal movements of the CO₂ plume predicted from numerical simulations, a time series of arsenic concentration was observed at the municipal well, which was then used to assess carcinogenic human health risk.

4. Numerical Approach

The multiphase and multicomponent reactive transport simulator, TOUGHREACT, was used to simulate secondary contamination processes in a shallow confined aquifer induced by CO₂ leakage [44] in conjunction with the ECO2N module, which was used to predict the fluid properties of H₂O, NaCl, and gaseous CO₂ [45]. For this study, the original thermodynamic database incorporated in TOUGHREACT was not adequate for delineating the complex chemical reactions associated with arsenic species. Therefore, the revised EQ3/6V7.2b database was specifically adopted to account for chemical reactions of arsenic and related chemical species [43]. In detail, the modified thermodynamic database adopted arsenite (H₃AsO₃⁰) as a primary species and incorporated associated aqueous complexes (e.g., H₂AsO₃⁻, H₂AsO₄⁻, H₃AsO₄(aq), HAsO₂(aq), HAsO₄²⁻, and HAsS₂(aq)), while accounting for their activity coefficients from the extended Debye-Hückel equation [46]. Moreover, solubility products of arsenic-bearing minerals such as arsenopyrite were included in this thermodynamic database.

Precipitation and dissolution of minerals were simulated kinetically by following the rate law, which was coupled with the equation representing the kinetic rate constant (see (1)).

In this equation, the kinetic rate constant is dependent not only on temperature but also on the pH as shown below [47]:

$$r_n = \pm \left\{ k_{25}^{\text{nu}} \exp \left[-\frac{E_a^{\text{nu}}}{R} \left(\frac{1}{T} - \frac{1}{298.15} \right) \right] + k_{25}^{\text{H}} \exp \left[-\frac{E_a^{\text{H}}}{R} \left(\frac{1}{T} - \frac{1}{298.15} \right) \right] a_{\text{H}}^{n_{\text{H}}} + k_{25}^{\text{OH}} \exp \left[-\frac{E_a^{\text{OH}}}{R} \left(\frac{1}{T} - \frac{1}{298.15} \right) \right] a_{\text{OH}}^{n_{\text{OH}}} \right\} A_n \left| 1 - \Omega_n^{\theta} \right|^{\eta}, \quad (1)$$

where E_a (J/mol) is the activation energy and k_{25} (mol/m²/s) is the rate constant at 25°C with superscripts nu, H, and OH representing neutral, acid, and base mechanisms, respectively. R (J/mol/K) is the gas constant, T (K) is temperature, a is the activity of dissolved species under acid or base conditions, and n is the power term. A_n is the specific reactive surface area (cm²/g), and Ω_n is the kinetic mineral saturation ratio of the n th mineral. Finally, both θ and η are assumed to be unity.

5. Conceptual Model

5.1. Model Description. The model designed for this study delineates the CO₂ leakage process throughout undetected and unexpected pathways in the sealing formation. In order to understand such processes, the 2D cross-sectional potable aquifer model was designed as shown in Figure 3. The potable aquifer was assumed to be relatively deep (300 m with a reducing condition), where the municipal or high-capacity wells produced a large amount of groundwater, which was then distributed for residential purposes [48, 49]. In addition, the width and thickness of the potable aquifer were assigned as 200 m and 40 m, respectively, with the size of grid blocks of 2 m; the total number of grid blocks was 2,000 (100 × 20). Assuming that the aquifer is located at a depth of 300 m, the initial formation pressure and temperature were assigned as 3 MPa and 25°C, respectively. Top and bottom boundaries of the model were assigned as no-flow conditions assuming that the upper and lower confining formations act as nearly impermeable sealing units. Lateral boundaries (purple-colored grid blocks) were assigned as the Dirichlet condition, where the left and right pressure were 3.2 MPa and 2.8 MPa, respectively. The difference of pressure in lateral boundaries in addition to aquifer properties ($k_h = 10^{-13}$ m²) results in 1.94 cm/day of the ambient groundwater flow in the aquifer. The leakage point for gaseous CO₂ was located at a 50 m distance from the left boundary where CO₂ was leaked at a rate of 0.05 kg/s (Figure 3). The CO₂ leakage was maintained for 1 year. Furthermore, the municipal well with a continuous pumping rate of 0.5 kg/s was located 100 m away from the CO₂ leakage point and penetrated a depth of 30 m from the upper confining seal. Finally, the simulation was conducted for 100 years.

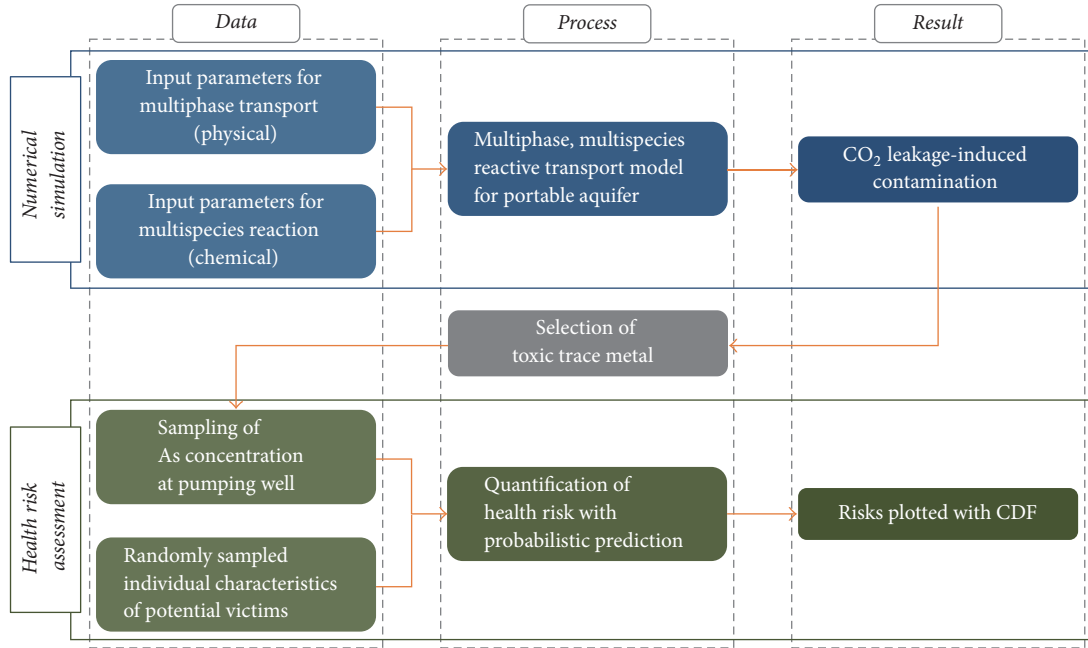


FIGURE 2: Flow chart explaining the sequence of both numerical simulation and probabilistic health risk assessment. Numerical simulation composed of multiphase and multispecies reactive transport modeling required both physical and chemical parameters within the shallow aquifer. Subsequently, the output of numerical simulation was utilized for calculating probabilistic health risk for carcinogenic effect.

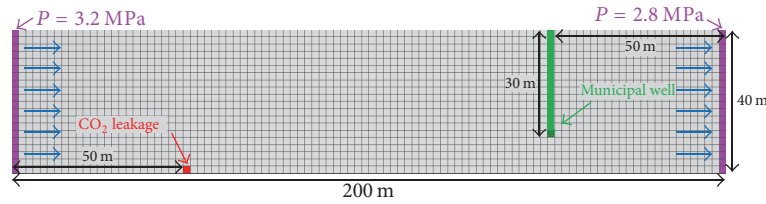


FIGURE 3: Conceptual model representing the shallow potable aquifer with a length and thickness of 200 m and 40 m, respectively. Blue arrows represent ambient groundwater flow with the rate of 2 cm/day. The grid blocks with the purple color stand for constant pressure boundaries; left and right boundary are 3.2 MPa and 2.8 MPa, respectively. Both upper and lower boundaries are assumed to be the no-flow boundary. CO₂ leakage point (red) is located at 50 m away from the left boundary. In addition, the municipal well (green) located at 50 m away from the right boundary penetrates 30 m deep from the upper seal while the pumping activity was only conducted through the screened section.

5.2. Physical and Chemical Parameters. The aquifer was assumed to be homogeneous with its horizontal permeability (k_h) and porosity (ϕ) to be 10^{-13} m^2 and 0.2, respectively (Table 1); the anisotropy ratio (k_v/k_h) was assumed to be 0.1. In addition, delineation of gaseous CO₂ transport through the groundwater-saturated aquifer required constitutive relations such as relative permeability and capillary pressure. In this study, Van Genuchten's functions were adapted, and the relevant parameters are shown in Table 1 [40].

The mineralogical composition of the designated aquifer materials was assumed to be sandstone, which is the typical hosting formation for geological CO₂ sequestration [50, 51] and natural analog CO₂ leakage sites [52, 53]. As an example, Kampman et al. [54] analyzed the mineralogical assemblage of Navajo Sandstone, which was considered to be the primary sourcing aquifer for CO₂-charged brine [55]. Chemical analyses of Navajo Sandstone fluids collected either from adjacent geysers or from springs revealed elevated

concentrations of both arsenic and other toxic heavy metals [54, 56–58]. Due to this reason, mineralogical composition in this study was adopted from the composition of Navajo Sandstone while assuming that arsenopyrite is the primary source of arsenic species in the ambient groundwater. A total of 7 primary minerals, that is, quartz, kaolinite, illite, K-feldspar, arsenopyrite, calcite, and magnesite, were chosen, and another 5 secondary minerals (chlorite, dolomite, goethite, oligoclase, and smectite-Ca) were expected to be precipitated (Table 2).

Mineral volume fraction of each primary mineral was chosen from a similar quantity of Navajo Sandstone with the addition of 1% arsenopyrite; quartz was predominant (81%), and kaolinite accounted for the second-largest amount (16%). Due to the small proportion of carbonate minerals, fluid chemistry possessed less buffering capacity against CO₂ dissolution. With the chosen mineral composition, the batch reaction was conducted to determine a list of primary species

TABLE 1: Input parameters for shallow groundwater aquifer materials. Relative permeability and capillary pressure follow equations developed by van Genuchten [40].

Aquifer characteristic	
Permeability	
Horizontal	10^{-13}
Vertical	10^{-14}
Porosity	0.2
Density (kg/m^3)	2600
Tortuosity	0.3
Compressibility	10^{-8}
Diffusivity (m^2/s)	10^{-9}
Relative permeability	
$k_{rl} = \sqrt{S} \{1 - (1 - [\bar{S}]^{1/m})^m\}^2$	$\bar{S} = \frac{S_l - S_{lr}}{1 - S_{lr} - S_{gr}}$
$k_{rg} = (1 - \bar{S})^2 (1 - \bar{S}^2)$	
S_{lr} : irreducible water saturation	0.20
S_{gr} : irreducible gas saturation	0.05
m : exponent	0.457
Capillary pressure	
$p_{\text{cap}} = -P_0([S^*]^{-1/m} - 1)^{1-m}$	$S^* = \frac{S_l - S_{lr}}{1 - S_{lr}}$
S_{lr} : irreducible water saturation	0.20
m : exponent	0.457
P_0 : strength coefficient	19.59 kPa

TABLE 2: Mineral volume fractions for shallow groundwater aquifer materials. A total of 7 primary and 5 secondary minerals were selected.

Primary mineral		Vol. fraction
Quartz	SiO_2	8.10×10^{-1}
Kaolinite	$\text{Al}_2\text{Si}_2\text{O}_5(\text{OH})_4$	1.58×10^{-1}
Illite	$\text{K}_{0.6}\text{Mg}_{0.25}\text{Al}_{1.8}(\text{Al}_{0.5}\text{Si}_{3.5}\text{O}_{10})(\text{OH})_2$	1.28×10^{-2}
K-feldspar	KAlSi_3O_8	9.43×10^{-3}
Arsenopyrite	FeAsS	9.00×10^{-3}
Calcite	CaCO_3	3.38×10^{-4}
Magnesite	MgCO_3	2.12×10^{-4}
Secondary mineral		Vol. fraction
Chlorite	$\text{Mg}_{2.5}\text{Fe}_{2.5}\text{Al}_2\text{Si}_3\text{O}_{10}(\text{OH})_8$	0.00
Dolomite	$(\text{CaMg}(\text{CO}_3)_2)$	0.00
Goethite	$\text{FeO}(\text{OH})$	0.00
Oligoclase	$\text{CaNa}_4\text{Al}_6\text{Si}_{14}\text{O}_{40}$	0.00
Smectite-Ca	$\text{Ca}_{0.145}\text{Mg}_{0.26}\text{Al}_{1.77}\text{Si}_{3.97}\text{O}_{10}(\text{OH})$	0.00

and their initial concentrations. As a result, AlO_2^- , Ca^{2+} , Cl^- , Fe^{2+} , H^+ , H_2O , $\text{H}_3\text{AsO}_3(\text{aq})$, HCO_3^- , HSO_4^{2-} , HS^- , K^+ , Mg^{2+} , Na^+ , $\text{O}_2(\text{aq})$, $\text{SiO}_2(\text{aq})$, and SO_4^{2-} were selected as primary species, and associated aqueous complexes were chosen as secondary species (Table 3).

As described by Keating et al. [7] and Zheng et al. [43], the concentration of arsenic species in the aquifer media was significantly controlled by both adsorption and desorption processes. Due to this reason, many researchers

TABLE 3: The 16 primary species and 39 secondary species are selected after the batch-reaction simulation.

Primary species (16)			
AlO_2^-	H^+	HSO_4^{2-}	Na^+
Ca^{2+}	H_2O	HS^-	$\text{O}_2(\text{aq})$
Cl^-	$\text{H}_3\text{AsO}_3(\text{aq})$	K^+	$\text{SiO}_2(\text{aq})$
Fe^{2+}	HCO_3^-	Mg^{2+}	SO_4^{2-}
Secondary species (39)			
$\text{Al}(\text{OH})_2^+$	$\text{CO}_2(\text{aq})$	$\text{H}_2\text{S}(\text{aq})$	MgHCO_3^+
$\text{Al}(\text{OH})_3(\text{aq})$	CO_3^{2-}	$\text{H}_3\text{AsO}_4(\text{aq})$	$\text{MgSO}_4(\text{aq})$
Al^{3+}	Fe^{3+}	H_3SiO_4^-	$\text{NaCl}(\text{aq})$
AlOH^{2+}	FeCl^+	$\text{HAlO}_2(\text{aq})$	NaCO_3^-
$\text{CaCl}_2(\text{aq})$	FeCl_4^{2-}	$\text{HAsO}_4(\text{aq})$	$\text{NaHCO}_3(\text{aq})$
$\text{CaCO}_3(\text{aq})$	FeCO_3^+	HAsO_4^{2-}	$\text{NaOH}(\text{aq})$
CaHCO_3^+	FeHCO_3^+	$\text{HAsS}_2(\text{aq})$	NaSO_4^-
CaOH^+	$\text{H}_2(\text{aq})$	HS^-	OH^-
$\text{CaSO}_4(\text{aq})$	H_2AsO_3^-	HSO_3^-	$\text{SO}_2(\text{aq})$
$\text{CH}_4(\text{aq})$	H_2AsO_4^-	MgCl^+	

experimentally measured sorption values (K_d) for arsenic species under various conditions (e.g., different minerals and pH) and revealed that K_d of As(III) and As(V) varied from 1.47 L/kg to 275 L/kg within geologic media including sub-surface soil and aquifers [39, 59, 60]. In this study, a shallow sandstone aquifer was targeted, composed of over 90% quartz and kaolinite (Table 2). Previous experimental measurements revealed that K_d for quartz and kaolinite was measured at 2 and 19 L/kg, respectively [39]. Therefore, the K_d value was assigned as 10 L/kg.

The multiple parameters required to address the kinetic rates for mineral reactions following (1) are listed in Table 4. In addition, the calculation of reactive surface area for minerals was followed by both Xu et al. [27] and Sonnenthal et al. [61], who assumed that a mineral is a cubic array of truncated spheres, in which the radius of the sphere is assumed to be 0.001 m. In this study, the surface roughness-based area predicted from the spherical radius was reduced by two orders to reasonably represent the reactive surface area. Typically, chemical reactions only occur at selected sites on the mineral surface, and furthermore, only a small fraction of mineral surface is involved in this reaction due to grain coating and armoring. Therefore, the reactive surface areas of most silicate and carbonate minerals were chosen to be approximately $10 \text{ cm}^2/\text{g}$, similar to those chosen by Knauss et al. [62] and Zerai et al. [63]. Finally, reactive surface areas of clay minerals such as kaolinite, illite, chlorite, and smectite were selected for larger values because of their smaller grain sizes [43].

Porosity was associated with changes in volume due to mineral dissolution or precipitation [64]. The porosity in this study was simulated by the following equation:

$$\phi = 1 - \sum_{m=1}^{n_m} (f_{rm} - f_{ru}), \quad (2)$$

where n_m is the number of minerals and f_{rm} and f_{ru} are the volume fractions of m th mineral in the rock and nonreactive

TABLE 4: Kinetic data for selected primary and secondary minerals. Only calcite was treated similar to the equilibrium reaction, and the rest of the minerals were kinetically treated with consideration of neutral, acid, and base mechanisms.

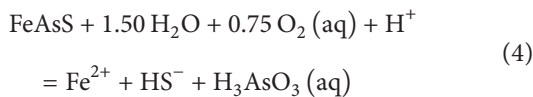
Mineral	A_n (cm ² /g)	Neutral mechanism		Acid mechanism			Base mechanism			References
		k_{25} (mol/m ² ·s)	E_a (kJ/mol)	k_{25} (mol/m ² ·s)	E_a (kJ/mol)	n (H ⁺)	k_{25} (mol/m ² ·s)	E_a (kJ/mol)	n (H ⁺)	
Quartz	9.8	1.02×10^{-14}	87.7							[41]
Kaolinite	1.95×10^5	6.91×10^{-14}	22.2	4.89×10^{-12}	65.9	0.78	8.91×10^{-18}	17.9	-0.47	[42]
Illite	6.68×10^5	1.66×10^{-13}	35.0	1.05×10^{-14}	23.6	0.34	3.02×10^{-17}	85.9	-0.40	Set to smectites
K-feldspar	9.8	3.89×10^{-13}	38.0	8.71×10^{-11}	51.7	0.50	6.31×10^{-12}	94.1	-0.82	[42]
Arsenopyrite	12.9	2.52×10^{-12}	62.8							[43]
Calcite				Equilibrium reaction						
Magnesite	9.8	4.57×10^{-10}	23.5	4.17×10^{-7}	14.4	1.00				[42]
Chlorite	9.8	3.02×10^{-13}	88.0	7.76×10^{-12}	88.0	0.50				[42]
Dolomite	12.9	2.52×10^{-12}	52.2	2.34×10^{-7}	43.5	0.50				[27]
Goethite	9.8	2.52×10^{-12}	62.8							[43]
Oligoclase	9.8	1.44×10^{-12}	69.8	2.13×10^{-10}	65.0	0.46				[42]
Smectite-Ca	5.64×10^5	1.66×10^{-13}	35.0	1.05×10^{-14}	12.6	0.34	3.02×10^{-17}	58.9	-0.40	[42]

rock, respectively. Finally, permeability change was calculated using the porosity changes with cubic law [65]:

$$k = k_i \left(\frac{\phi}{\phi_i} \right)^3, \quad (3)$$

where k and ϕ are permeability and porosity, respectively, with subscript i representing the initial value.

Even if the proposed approach was capable of simulating water-rock interaction, it would still have some limitations. Firstly, in this study, the sorption effect of arsenic onto the surface of clay minerals was simulated with a linear K_d approach instead of surface complexation. Although the linear K_d approach had limitations in terms of delineating chemical heterogeneities on both temporal and spatial scales, this approach was effective for application to a large-scale simulation by reducing computation [66–68]. Secondly, arsenopyrite is a solid solution of pyrite (FeS₂), in which the ratio of arsenic and sulfur varies depending on their mole fractions. However, in this study, for simplification in predicting the thermodynamic properties, it was assumed that 1 mole fraction of arsenic replaced the sulfur (FeAsS). Finally, it was assumed that arsenopyrite oxidatively dissolves in the presence of common geologic oxidants such as dissolved O₂, NO₃⁻, and Fe³⁺. Under acidic conditions, Fe³⁺ quickly oxidizes, and sequential dissolution of arsenopyrite releases arsenic species (H₃AsO₄⁰ and H₃AsO₃⁰) by following (4). Therefore, the stoichiometric reaction for arsenopyrite dissolution, which was used in this numerical simulation, involved the reduction of Fe³⁺ to Fe²⁺ [43].



5.3. Probabilistic Health Risk Approach. Carcinogenic effects on humans who have been chronically exposed to arsenic

species through multiple pathways were probabilistically quantified based on individual exposure rate and toxicity, which were suggested by the “Guidelines for Carcinogenic Risk Assessment” of the US Environmental Protection Agency (EPA) [69], Siirila et al. [31], and the EPA Superfund Risk Assessment [70]. In general, three different uptake pathways, namely, ingestion, dermal sorption, and inhalation, were considered. Among these, ingestion and dermal sorption were considered to be major pathways, because humans are often exposed to risk by drinking dissolved toxic species in tap water or showering. Uptake through inhalation was not considered in this study, as it is unlikely that the concentration of vaporized trace metals was high enough to cause carcinogenic effects indoors under normal conditions. Therefore, following Siirila et al. [31], only two exposure pathways (ingestion and dermal sorption) were considered for quantifying exposure rate and toxicity of arsenic.

$$\text{Risk} = e^{1-(\text{ADD}_i \times \text{CPF}_i)} \approx \text{ADD}_i \times \text{CPF}_i. \quad (5)$$

Arsenic toxicity was predicted from the product of cancer potency factor (CPF) (kg·day/mg) and average daily dose (ADD) (mg/kg·day). Typically, the CPF is different at the individual pathway even for the same toxic metal; in this study, the CPF for ingestion and dermal sorption of arsenic were assumed to be 1.5 and 1.6 kg·day/mg by following IRIS [71] and EPA [72], respectively. Subsequently, ADD was used to assess the individual exposure rate with the following equation:

$$\text{ADD} = \bar{C} \left[\frac{\text{IN}}{\text{BW}} \right] \frac{\text{ED} \times \text{EF}}{\text{AT}}, \quad (6)$$

where [IN/BW] is the individual intake per body weight (L/kg/day), AT is the average lifetime, which was assumed to be 25,550 days (70 years), and EF is the standard exposure frequency during 1 year, which was assumed to be 350 (days/year) [73]. The most significant term in (6) is \bar{C} , which is

the maximum average of arsenic concentration (mg/L) monitored at the municipal well during the exposure duration (ED) (years). In this study, the ED was assumed to be 30 years following the EPA guideline [74]. Accordingly, \bar{C} , calculated from concentration profiles ($C(t)$) of arsenic species at the municipal well in the numerical simulation can be represented as follows:

$$\bar{C} = \max \left[\sum_t^{t+ED} C(t) \right]_{-\infty}^{+\infty}. \quad (7)$$

Specific to ADD, exposure pathways through both ingestion and dermal sorption are defined as follows:

$$ADD_{\text{ingestion}} = \bar{C} \left[\frac{IR}{BW} \right] \frac{ED \times EF}{AT}, \quad (8)$$

$$ADD_{\text{dermal}} = \bar{C} \left[\frac{SA}{BW} \right] \frac{ED \times EF}{AT} K_p f_{\text{skin}} ED_{\text{shower}} CF, \quad (9)$$

where $[SA/BW]$ is the skin surface area per body weight (m^2/kg), K_p is the dermal permeability coefficient for arsenic in water, designated as 1.0×10^{-5} m/hour, f_{skin} is the fraction of skin in contact with water (-), ED_{shower} is exposure time of shower per day (hours/day), and CF is the unit conversion factor ($0.001 \text{ L}/\text{m}^3$). Finally, the total risk is the summation of individual risks representing each exposure pathway as shown below:

$$\begin{aligned} \text{Total Risk} &= \text{Risk}_{\text{ingestion}} + \text{Risk}_{\text{dermal}} \\ &= \left(ADD_{\text{ingestion}} \times CPF_{\text{ingestion}} \right) \\ &\quad + \left(ADD_{\text{dermal}} \times CPF_{\text{dermal}} \right). \end{aligned} \quad (10)$$

In this study, the calculation of the total risk was repeated 100,000 times to account for variability, which stands for probabilistic quantification in human health risk. Except for \bar{C} (the concentration of arsenic species obtained from the result of numerical simulation), individual parameters considered in the quantification of total risk were randomly sampled within each intrinsic distribution (Table 5) [31, 75]. Finally, the calculated total health risks were plotted as a cumulative density function, which enables the estimation of the probability exceeding the risk level of concern (10^{-4}) [76, 77].

6. Model Scenarios

Case 1 (base case) was designed to delineate CO_2 leakage processes associated water-rock interactions and secondary contamination caused by arsenic species (Table 6). Subsequently, sensitivity studies were conducted with different K_d , CO_2 leakage rates, and horizontal permeability of the aquifer (k_h). First, the degree of sorption intensity was evaluated by varying K_d between 25, 50, and $100 \text{ L}/\text{kg}$ (Cases 2–4). Second, in Cases 5–7, the effect of CO_2 leakage rate was evaluated by varying its rate between 0.020, 0.025, and $0.030 \text{ kg}/\text{s}$. Different CO_2 leakage rates could induce the development of CO_2

plumes with different sizes. For example, as the size of a CO_2 plume increases, larger areas expect to experience water-rock interactions and more dissolution of arsenic species. Consequently, the municipal well captures dissolved arsenic species more when the size of the CO_2 plume is greater, which eventually increases the carcinogenic health risk on humans. Finally, in Cases 8–10, k_h varied ($k_h = 0.2 \times 10^{-13}$, 1.0×10^{-13} , and $5.0 \times 10^{-13} \text{ m}^2$) while maintaining the vertical permeability ($1.0 \times 10^{-14} \text{ m}^2$); increased k_h accelerates the horizontal velocity of ambient groundwater while reducing buoyancy forces on the CO_2 plume.

7. Results and Discussion

7.1. Base Case

7.1.1. Migration of Leaked CO_2 Plume within the Shallow Potable Aquifer. Figures 4(a)–4(e) represent the evolution of the leaked CO_2 plume at designated times of 120, 240, 360, 480, and 600 days. The mass centers of the CO_2 plume, shown as red, black, and yellow circles, were calculated and plotted every 120 days; black circles represent the present time of the mass center, and red and yellow circles represent past and future times, respectively. From the leakage point, CO_2 continuously leaked at a rate of $0.05 \text{ kg}/\text{s}$ only until 365 days. During this period, three flow systems induced by ambient groundwater, CO_2 leakage, and pumping activity interacted with each other (Figure 4(c)), which developed two mixing zones for geochemically different types of groundwater at both the front and the rear margins of the CO_2 plume. The ambient groundwater flow (orange arrows) was developed from the left to the right boundaries at an approximate rate of $1.94 \text{ cm}/\text{day}$. Additionally, the CO_2 plume gradually expanded from the leakage point where CO_2 saturation remained at 0.3; the rate of CO_2 flux was approximately $2.1 \times 10^{-5} \text{ kg}/(\text{s} \cdot \text{m}^2)$ (black arrows) adjacent to the leakage point. At the rear margin of the CO_2 plume, two chemically different types of groundwater (ambient groundwater and CO_2 -dissolved groundwater) flowed in opposite directions, inducing the development of a vigorous geochemical mixing zone. Subsequently, the CO_2 plume migrated together with the ambient groundwater until it was captured by the municipal well (Figure 4(c)).

After CO_2 leakage had stopped at 365 days, the size of the CO_2 plume gradually decreased due to both dissolution to ambient groundwater and extraction from the municipal well (Figures 4(d) and 4(e)); CO_2 solubility predicted by Duan and Sun [78] was $0.83 \text{ mol}/\text{kg}$ water in this aquifer (3 MPa and 25°C). After movable CO_2 was captured by the municipal well, residually trapped CO_2 governed by irreducible CO_2 saturation (shown in Table 1) remained until complete dissolution to the ambient groundwater; residually trapped CO_2 eventually vanished approximately 5 years after CO_2 leakage had stopped.

The calculated mass center was located close to the plume center while the CO_2 plume migrated toward the municipal well. The migration rate of the CO_2 plume estimated from the mass center locations was approximately $12.5 \text{ cm}/\text{day}$ until

TABLE 5: Parameters for health risk assessment. Each parameter is randomly sampled within the designated value range and distributions to represent individual characteristics of potential victims.

Parameter	Symbol	Unit	Distribution	Values
Exposure duration	ED	[yr]	Constant	30
Exposure frequency	EF	[d/yr]	Constant	350
Averaging time	AT	[d]	Constant	25,550
Ingestion rate per unit body weight	IR/BW	[L·kg/d]	Lognormal	$(3.3 \times 10^{-2}, 1.3 \times 10^{-2})$
Skin surface area per unit body weight	SA/BW	[m ² /kg]	Lognormal	$(2.7 \times 10^{-2}, 2.5 \times 10^{-3})$
Fraction skin in contact with water	f_{skin}	[-]	Uniform	$(4.0 \times 10^{-1}, 9.0 \times 10^{-1})$
Shower exposure duration	ED _{shower}	[h/d]	Lognormal	$(1.3 \times 10^{-1}, 9.0 \times 10^{-2})$
Unit conversion factor	CF	[L/m ³]	Constant	1.0×10^{-3}
Cancer potency factor	CPF _{ingestion}	[kg·day/mg]	Constant	1.5
	CPF _{dermal}			1.6

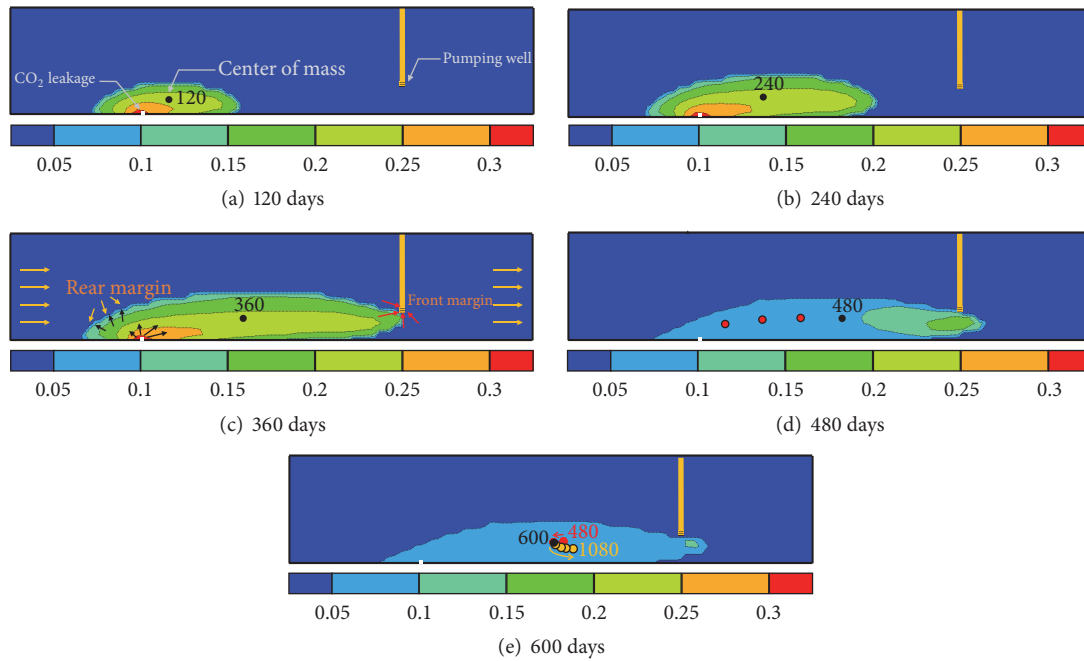


FIGURE 4: Saturation of leaked CO₂ at different times (120, 240, 360, 480, and 600 days). Red, black, and yellow circles with labels indicate the locations of mass center for CO₂ plume. Red circles in (d) and (e) stand for the evolution of the mass center in multiple times; yellow circles in (e) express the mass center from 600 to 1,080 days.

480 days (Figures 4(a)–4(d)), indicating that the migration rate of the CO₂ plume was faster than the ambient groundwater flow (1.94 cm/day). This is because the pumping activity developed an additional head gradient, which was greater than ambient groundwater flow. After 480 days, the mass center slightly moved back until 600 days (Figure 4(e)), implying that all movable CO₂, which was weighted CO₂ mass at the plume front, was pumped out. After 600 days, continuous CO₂ dissolution occurred at the plume rear, and the pumping activity at the front induced the movement of the mass center slowly.

7.1.2. Induced Geochemical Reactions. The dissolution of gaseous CO₂ into ambient groundwater increased HCO₃[−] concentration from 0.2 to 1 mol/L while decreasing the pH

from 8.0 to 5.5 within the CO₂ plume (Figures 5(a) and 5(d)). Concurrently, both carbonate and silicate minerals were either dissolved or precipitated. In particular, dramatic changes in minerals were localized at both rear and front margins of the CO₂ plume where the vigorous advective mixing of chemically different types of groundwater occurred.

Dissolutions in calcite (CaCO₃) and magnesite (MgCO₃) were distinct (Figures 5(b) and 5(c)). Such dissolution released HCO₃[−] into the ambient groundwater and subsequently induced positive feedback to lower pH. Calculation of the saturation index (SI) using the initial concentration of ambient groundwater indicated that calcite (SI_{calcite} = −3.1) was more saturated than magnesite (SI_{magnesite} = −12.4); the initial concentrations of Ca²⁺ and Mg²⁺ were 3.3×10^{-3} mol/L and 4.2×10^{-12} mol/L, respectively, in the ambient

TABLE 6: Different parameters for sensitivity studies. Three groups except Case 1 (base case) are designed for sorption rate (K_d) (Cases 2–4), gaseous CO_2 leakage rate (Q_L) (Cases 5–7), and horizontal permeability (k_h) (Cases 8–10), respectively.

Case name	Sorption rate (K_d)	CO_2 leakage rate (Q_L)	Horizontal permeability (k_h)
Case 1 (base case)	10	0.050 kg/s	$1.0 \times 10^{-13} \text{ m}^2$
Case 2	25	0.050 kg/s	$1.0 \times 10^{-13} \text{ m}^2$
Case 3	50	0.050 kg/s	$1.0 \times 10^{-13} \text{ m}^2$
Case 4	100	0.050 kg/s	$1.0 \times 10^{-13} \text{ m}^2$
Case 5	50	0.020 kg/s	$1.0 \times 10^{-13} \text{ m}^2$
Case 6	50	0.025 kg/s	$1.0 \times 10^{-13} \text{ m}^2$
Case 7	50	0.030 kg/s	$1.0 \times 10^{-13} \text{ m}^2$
Case 8	50	0.050 kg/s	$0.2 \times 10^{-13} \text{ m}^2$
Case 9	50	0.050 kg/s	$1.0 \times 10^{-13} \text{ m}^2$
Case 10	50	0.050 kg/s	$5.0 \times 10^{-13} \text{ m}^2$

groundwater. Due to this reason, when CO_2 was leaked, dissolution of magnesite (-6 mol/m^3) was greater than that of calcite (-4 mol/m^3) within the CO_2 plume. However, even if overall magnesite dissolution was greater than that of calcite, the greatest change in mineral dissolution appeared in calcite (-8 mol/m^3), focusing at the rear margin of the CO_2 plume (Figure 5(b)). This implies that the localized dissolution of calcite was primarily induced by the mixing of two chemically different types of groundwater, such as the ambient and CO_2 -dissolved groundwater. Initially, the Ca^{2+} concentration in the ambient groundwater was $3.3 \times 10^{-3} \text{ mol/L}$ (Figure 5(e)). Inside the CO_2 plume, calcite was dissolved and increased Ca^{2+} concentration 10-fold to $2.5 \times 10^{-2} \text{ mol/L}$. At the rear margin of the CO_2 plume, Ca^{2+} concentration was increased even more (to $3.1 \times 10^{-2} \text{ mol/L}$). Overall, the distribution of Ca^{2+} was similar to that of calcite (Figures 5(b) and 5(e)), and distributions of both Mg^{2+} and HCO_3^- were similar to that of magnesite (Figures 5(c), 5(d), and 5(f)).

Patterns of dissolution and precipitation in silicate minerals were more complex than those of carbonate minerals (Figures 6(a)–6(c)). CO_2 leakage primarily induced the dissolution of K-feldspar (KAlSi_3O_8) (Figure 6(a)); the greatest dissolution ($3.5 \times 10^{-2} \text{ mol/m}^3$) occurred at the rear of the CO_2 plume, and the degree of dissolution gradually decreased as the plume approached the municipal well. Dissolution of K-feldspar increased concentrations of K^+ , $\text{SiO}_2(\text{aq})$, and AlO_2^- in the groundwater (Figures 6(d)–6(f)). Nevertheless, distributions of such species did not imitate the dissolution pattern of K-feldspar. Rather, $\text{SiO}_2(\text{aq})$ and K^+ showed the highest concentrations at the rear and front margins of the CO_2 plume with values of $1.8 \times 10^{-4} \text{ mol/L}$ and $3.5 \times 10^{-4} \text{ mol/L}$, respectively (Figures 6(d) and 6(e)), but the decrease in AlO_2^- concentration occurred uniformly throughout the CO_2 plume (Figure 6(f)). The discrepancy in patterns between K-feldspar and other dissolved species was presumably caused by a combination of both dissolution and precipitation

among various silicate minerals such as illite, kaolinite, and chlorite as described below.

For the distribution of illite ($\text{K}_{0.6}\text{Mg}_{0.25}\text{Al}_{1.8}(\text{Al}_{0.5}\text{Si}_{3.5}\text{O}_{10})(\text{OH})_2$), a small amount ($3.3 \times 10^{-2} \text{ mol/m}^3$) was precipitated throughout the CO_2 plume (Figure 6(b)). However, at the rear margin and immediately adjacent to the municipal well, a relatively large degree of illite dissolution was predicted (-9.1×10^{-3} and $-7.4 \times 10^{-2} \text{ mol/m}^3$, resp.). In contrast to illite, a small amount ($-2.9 \times 10^{-2} \text{ mol/m}^3$) of kaolinite was dissolved within the plume, and reversely, a small amount of precipitation was predicted at the rear and front margins (1.9×10^{-2} and $4.8 \times 10^{-2} \text{ mol/m}^3$, resp.) (Figure 6(c)). Presumably, the dissolution and precipitation of illite and kaolinite would influence the distribution of $\text{SiO}_2(\text{aq})$ and K^+ in addition to K-feldspar dissolution (Figures 6(d) and 6(e)). Finally, the behavior of individual silicate mineral influenced the distribution of AlO_2^- , the concentration of which within the plume was lower than that outside (Figure 6(f)). Overall, CO_2 leakage induced dissolution or precipitation of both carbonate and silicate minerals and ultimately changed both the porosity and the permeability of the shallow aquifer. The dissolution of carbonate minerals primarily caused an increase in permeability; permeability increased to 0.43% ($k'(\%) = (k_{\text{changed}} - k_{\text{initial}})/k_{\text{initial}} \times 100$) within the CO_2 plume, and the most drastic increase (0.77%) occurred at the rear margin of the CO_2 plume (Figure 7).

Dissolution of arsenopyrite, which was the primary reaction for predicting carcinogenic health risk, occurred only within the CO_2 plume with a dissolved amount of $4.84 \times 10^{-5} \text{ mol/m}^3$ (Figure 8(a)). Similar to that of carbonate minerals, the greatest amount of arsenopyrite dissolution ($8.57 \times 10^{-5} \text{ mol/m}^3$) occurred at the rear margin of the plume due to the vigorous mixing of two chemically different types of groundwater. Following (4), oxidative dissolution of arsenopyrite consumed 0.75 moles of $\text{O}_2(\text{aq})$ and 1 mole of H^+ while increasing the concentrations of total arsenic ($\sum \text{As}$), Fe^{2+} , and HS^- (Figures 8(b)–8(e)). In this study, $\sum \text{As}$ represents the summation of primary species such as arsenite ($\text{H}_3\text{AsO}_3^0(\text{aq})$), which is the by-product of arsenopyrite dissolution, as well as other arsenic species such as H_2AsO_3^- , $\text{H}_3\text{AsO}_4(\text{aq})$, H_2AsO_4^- , $\text{H}_2\text{AsO}_4^{2-}$, HAsO_4^{2-} , $\text{HAsO}_2(\text{aq})$, and $\text{HAsS}_2(\text{aq})$. Distribution of $\sum \text{As}$ concentration mimics that of arsenopyrite (Figures 8(a) and 8(b)); generally, $\sum \text{As}$ concentration within the CO_2 plume was greater than that outside, while the rear margin revealed the highest concentration. However, the other associated species such as Fe^{2+} , HS^- , and $\text{O}_2(\text{aq})$ revealed relatively uniform distribution (Figures 8(c)–8(e)). The difference between arsenopyrite-produced species such as $\sum \text{As}$ and other associated species (e.g., Fe^{2+} , HS^- , and $\text{O}_2(\text{aq})$) presumably occurred due to the sorption effect, which was accounted with the linear K_d approach. K_d was designated for arsenic species only, and thus, as shown in Figure 8(b), enrichment of $\sum \text{As}$ concentration occurred at the rear of the CO_2 plume. In summary, the greatest concentration of $\sum \text{As}$ was $4.9 \times 10^{-7} \text{ mol/L}$ at the rear margin of the plume and the average concentration of $\sum \text{As}$ within the plume was 2.9 mol/L (Figure 8(b)). The average

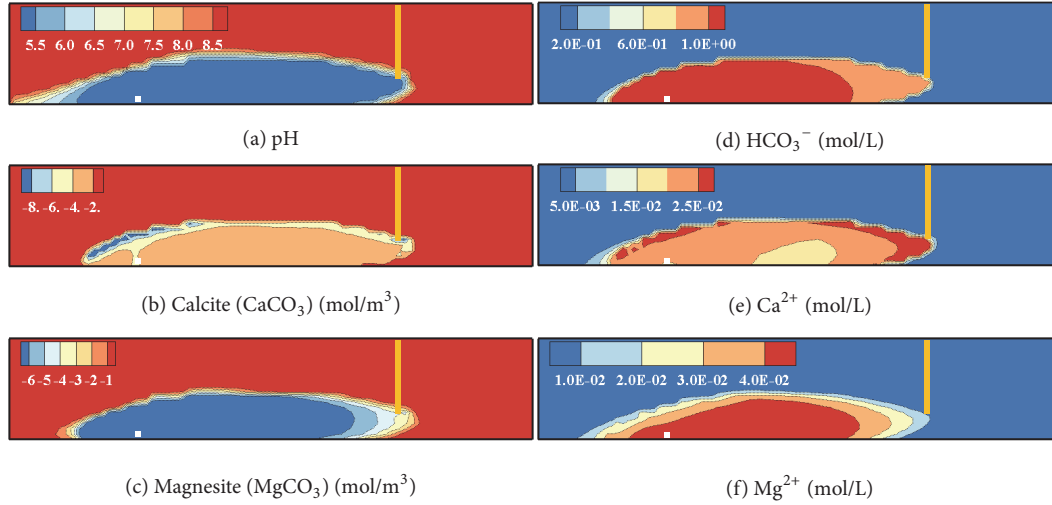


FIGURE 5: Distribution of pH, carbonate minerals (calcite and magnesite), and associated dissolved species (HCO_3^- , Ca^{2+} , and Mg^{2+}) after 365 days.

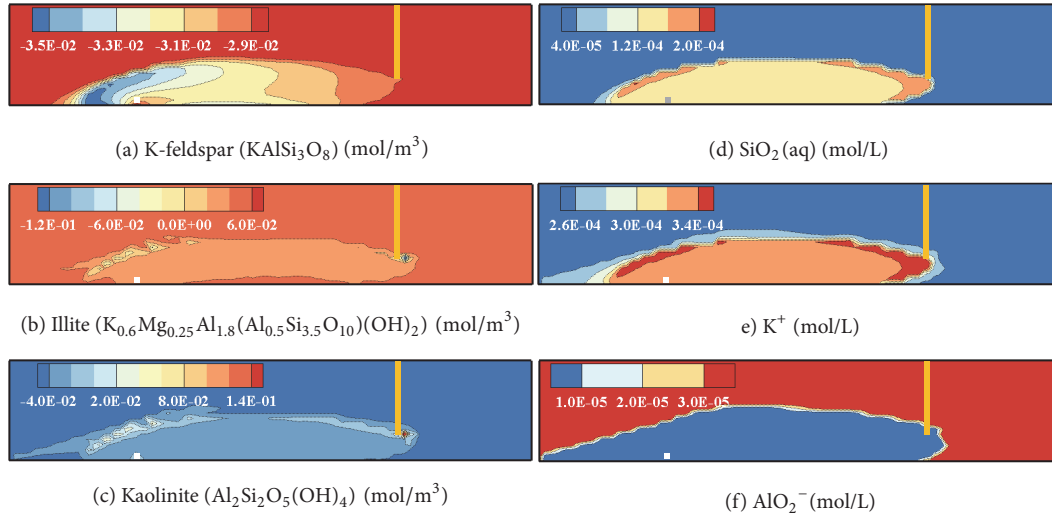


FIGURE 6: Distribution of silicate minerals (K-feldspar, illite, chlorite, and kaolinite) and associated dissolved species ($\text{SiO}_2(\text{aq})$, K^+ , and AlO_2^-) after 365 days.

concentrations of other species such as Fe^{2+} and HS^- were 3.9×10^{-7} mol/L and 3.6×10^{-7} mol/L, respectively (Figures 8(c) and 8(d)).

7.1.3. Health Risk Assessment of Carcinogenic Effect. To account for carcinogenic health risk, selected species such as pH, $\sum \text{As}$, and arsenite ($\text{H}_3\text{AsO}_3^0(\text{aq})$) concentrations were monitored at the municipal well for 100 years (Figure 9(a)). Dramatic changes in gaseous CO_2 saturation (S_g), pH, and mass fraction of CO_2 dissolved in groundwater (X_{CO_2}) predicted during 10 years were magnified at the small window (Figure 9(a)). Depending on the profiles of both pH and dissolved arsenic species, two stages (Stages I and II) were characterized. During Stage I (0–6.3 years), the leaked CO_2 plume, which existed as either gaseous CO_2 (S_g , black dotted line) or dissolved CO_2 (X_{CO_2} , purple dotted line), arrived at

the municipal well approximately after 360 days. Once the CO_2 plume arrived at the well, immediate reduction of pH from 8.8 to 5.2 was observed, while $\sum \text{As}$ and $\text{H}_3\text{AsO}_3^0(\text{aq})$ concentrations sharply increased to 2.93×10^{-7} and 1.32×10^{-7} mol/L, respectively, exceeding the maximum contaminant level ($\text{MCL} = 1.33 \times 10^{-7}$ mol/L, red dotted line) [79]. After 2.1 years, S_g decreased to 0 at the municipal well, implying that all movable gaseous CO_2 was pumped out. Even after all gaseous CO_2 had been diminished due to the pumping activity, residually trapped CO_2 remained within the pores while dissolving into the groundwater. Due to the dissolution of residually trapped CO_2 , the mass fraction of dissolved CO_2 (X_{CO_2}) was invariant at 0.035 until 5 years; in this shallow aquifer, flow caused by both ambient fresh groundwater and pumping activity accelerated CO_2 dissolution. Therefore, complete dissolution of residually trapped CO_2

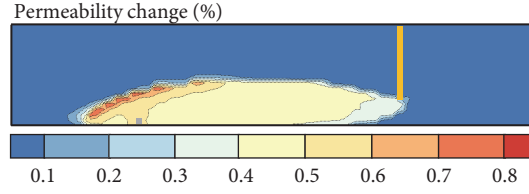


FIGURE 7: Distribution of altered permeability (%) after 365 days. The changes in permeability were predicted from the following equation ($k'(\%) = (k_{\text{changed}} - k_{\text{initial}})/k_{\text{initial}} \times 100$) because its variation was too small. Here, k_{initial} and k_{changed} indicate the initial permeability and altered permeability at designated time, respectively.

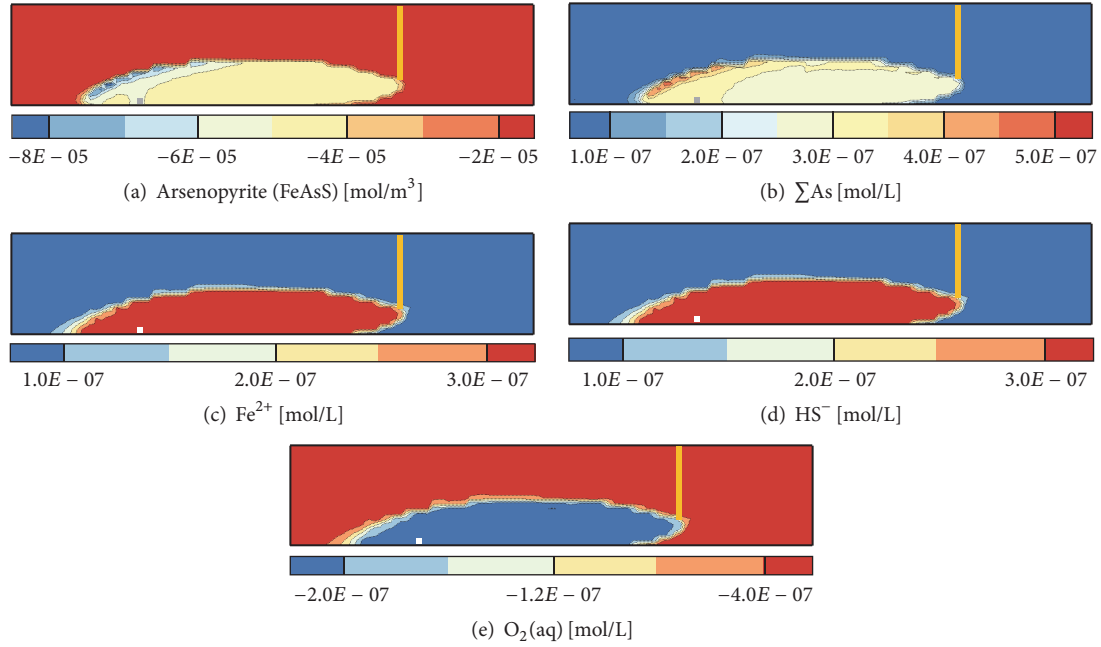


FIGURE 8: Distribution of arsenopyrite dissolution and associated dissolved species (ΣAs , Fe^{2+} , HS^- , and $\text{O}_2(\text{aq})$) after 365 days.

appeared at 6.3 years when X_{CO_2} became 0 and pH returned to 8.2. In addition, concentrations of ΣAs and $\text{H}_3\text{AsO}_3^0(\text{aq})$ reached 3.77×10^{-7} and 1.70×10^{-7} mol/L, respectively. Immediately beginning with Stage II (6.3–100 years), elevated pH (8.2) of groundwater inhibited the dissolution of arsenopyrite, the reaction of which requires the consumption of H^+ (see (4)). Due to decreased arsenopyrite dissolution, concentrations of both ΣAs and $\text{H}_3\text{AsO}_3^0(\text{aq})$ were stabilized and gradually decreased due to sorption on aquifer media. The pH continuously decreased until 90 years. However, concentrations of ΣAs and $\text{H}_3\text{AsO}_3^0(\text{aq})$ reached the background level (6.60×10^{-8} and 3.01×10^{-8} mol/L, resp.) at 62 years.

Based on the simulated profiles of both ΣAs and $\text{H}_3\text{AsO}_3^0(\text{aq})$, \bar{C} , which is the maximum average concentration calculated from (7), was predicted, and the carcinogenic health risk was quantified following the method described in Section 5.3. Figure 9(b) shows histograms representing calculated frequencies of carcinogenic risk for both ΣAs (blue bar) and $\text{H}_3\text{AsO}_3^0(\text{aq})$ (green bar). The carcinogenic risk predicted from $\text{H}_3\text{AsO}_3^0(\text{aq})$ profile, which revealed relatively low concentrations, showed a mean, median, and standard

deviation of 4.00×10^{-4} , 4.30×10^{-4} , and 1.69×10^{-4} , respectively. For risk predicted from ΣAs concentration profile, the mean, median, and standard deviation were 8.94×10^{-4} , 9.60×10^{-4} , and 3.77×10^{-4} , respectively. Cumulative density functions (blue and green lines) were also plotted together with the risk level of concern (10^{-4}) [77, 80]. From the cumulative density functions, the risk, which exceeds the risk level of concern, can be considered to have carcinogenic potential after chronic exposure to arsenic-contaminated groundwater. As shown, the risk level predicted from both ΣAs and $\text{H}_3\text{AsO}_3^0(\text{aq})$ exceeded the risk level (red dotted line) of concern.

7.2. Sensitivity Studies

7.2.1. Effect of Sorption Intensity (K_d) (Cases 2–4). In this sensitivity study, the intensity of the sorption effect (K_d of 25, 50, and 100 L/kg) on ΣAs was evaluated while gaseous CO_2 was leaked into the shallow aquifer (Table 6). As shown in Figure 4, once gaseous CO_2 was leaked from unidentifiable pathways, it migrated with the ambient groundwater. Here, characteristics of gaseous CO_2 plume such as its size, shape,

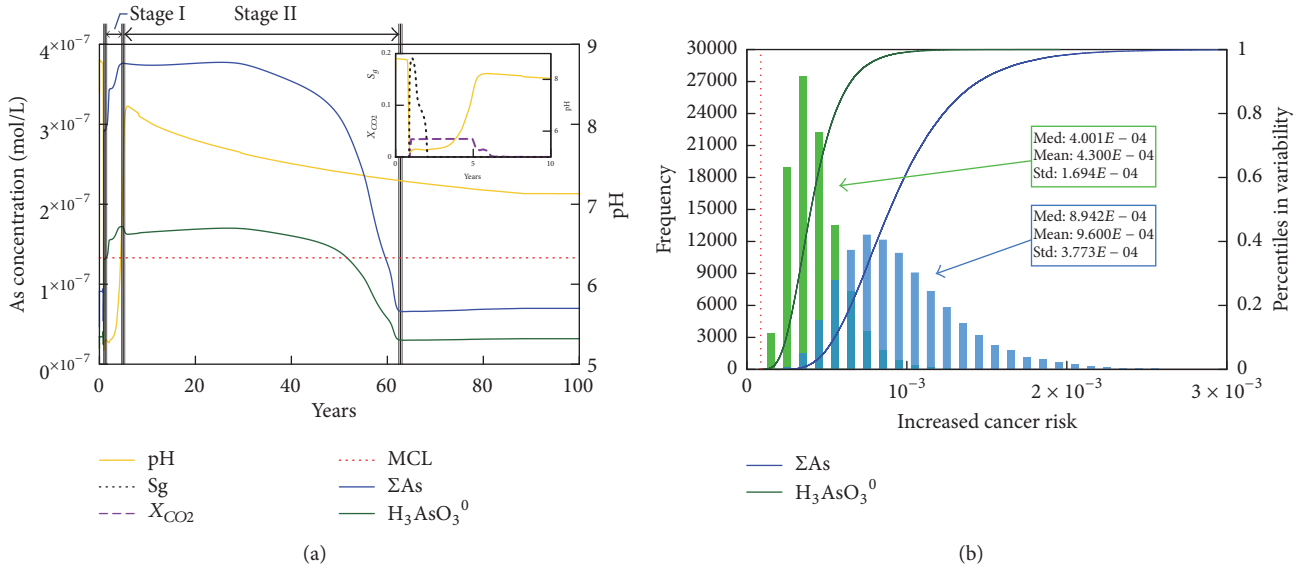


FIGURE 9: (a) Changes in pH, total arsenic (ΣAs), and arsenite ($H_3AsO_3^0$) concentrations monitored at the municipal well. The maximum contaminant level (MCL) of arsenic species is 1.33×10^{-7} mol/L. Gaseous CO_2 saturation (S_g) and pH for 10 years were also plotted at the magnified window. Two stages were characterized based on the behavior of CO_2 plume. (b) Frequency of predicted health risk accounting for both ΣAs and $H_3AsO_3^0$ and cumulative density functions representing probabilistic health risk. The bin size of both histograms was designated to be 10^{-4} , and thus the number of bins was 10 and 20, respectively. Finally, the threshold of risk or the risk level of concern was 10^{-4} (red dotted line).

migrating velocity, and gas saturation (S_g) were influenced by multiphase parameters such as capillary pressure and relative permeability (Table 1); the role of K_d in gaseous CO_2 transport was minimal because the sorption typically accounted for the movement of dissolved species within geologic media. Due to this reason, regardless of the variation in K_d , the distribution and behavior of gaseous CO_2 plume were not affected, and therefore the CO_2 plume remained essentially the same in all cases as shown in Figure 4. However, within the gaseous CO_2 plume, various geochemical processes occurred, including reductions in pH, dissolution of arsenopyrite, and interactions between dissolved species. In particular, variation in K_d was anticipated to affect the behavior of dissolved arsenic species after all gaseous CO_2 was pumped out or dissolved into the groundwater.

In Stage I, the gaseous CO_2 plume arrived at the municipal well after 350 days (0.95 years) for all cases (Figure 10(a)). The elevated concentration (2.9×10^{-7} mol/L) of ΣAs occurred simultaneously in all cases because the source of arsenic species was the dissolution of arsenopyrite, which resulted from CO_2 dissolution. Despite the variation in K_d , the arrival times of ΣAs at the municipal well were the same because the sorption did not affect the migration of the gaseous CO_2 plume. Therefore, the ΣAs profiles evolved similarly until approximately 30 years (the middle of Stage II) when its concentration reached a maximum (3.9×10^{-7} mol/L). After the arrival of the ΣAs peak, the differences between ΣAs profiles were amplified until the ΣAs concentration reached the background level (6.7×10^{-8} mol/L). In detail, differences in the slopes of ΣAs profiles were small immediately after the arrival of the ΣAs peak

(30–40 years), but the discrepancy was amplified from 40 years while the slopes for ΣAs profiles sharply dropped. Differences in ΣAs profiles were attributed to the degree of K_d , which determined the amount of arsenic adsorbed to aquifer media, especially at the rear margin of the CO_2 plume; at this location, the highest ΣAs concentration occurred due to the mixing of two chemically different types of groundwater as shown in Figure 8(b).

In these simulations, with increasing K_d , more arsenic was adsorbed to the aquifer media, and the migration of ΣAs was therefore retarded. In other words, stronger retardation caused ΣAs concentration to be maintained higher and longer in the aquifer, and therefore the arrival of ΣAs concentration at the background level was delayed. For example, in Case 2 ($K_d = 25$ L/kg), ΣAs concentration revealed the earliest recovery (69.3 years) at the municipal well (Figure 10(a)). As K_d increased to 50 and 100 L/kg, the recovery time was delayed to 72.1 and 73.9 years, respectively.

Figure 10(b) represents the predicted probabilistic health risk for Cases 2–4. While calculating the health risk, \bar{C} , the peak calculated from the moving average of ΣAs concentration by adopting the designated interval of ED (30 years), influenced the health risk most significantly based on (8), (9), and (10). Since ΣAs profiles revealed similar patterns with the same peak values while the only difference being the recovery time, the calculated \bar{C} values for Cases 2–4 were almost the same (3.9×10^{-7} mol/L). Consequently, predicted carcinogenic health risk for humans was almost identical to variation in K_d . This result implies that variation in K_d was a less influential parameter for assessing health risk for arsenic species. This was because variation in K_d did not affect the

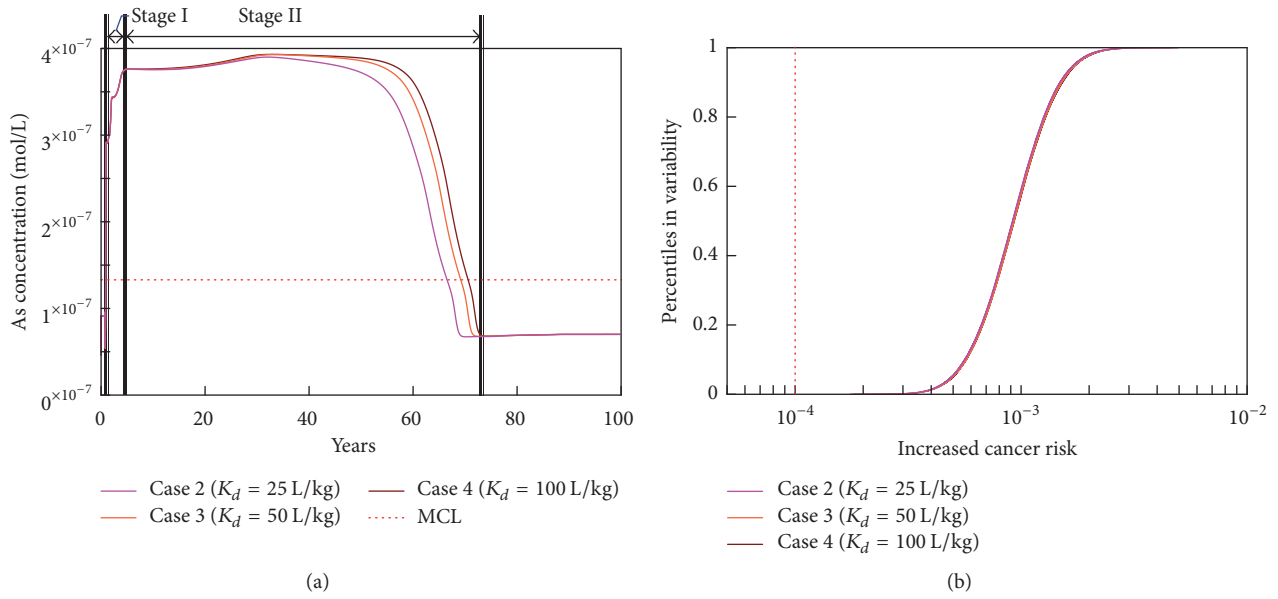


FIGURE 10: (a) Σ As profiles with different K_d of 25, 50, and 100 L/kg^{-1} (Cases 2–4) and (b) probabilistic health risk plotted as cumulative density functions. The red dotted line represents the risk level of concern (10^{-4}).

characteristics of the CO_2 plume such as size, shape, and migration velocity, which determined the dissolved amount or reaction rate for arsenic sources such as arsenopyrite. Due to this reason, additional simulations were conducted and described in the following section after varying parameters (CO_2 leakage rate and aquifer permeability), which directly affected the size of the CO_2 plume and its migration rate.

7.2.2. Effect of CO_2 Leakage Rate (Q_L) (Cases 5–7). In Cases 5–7, the effect of CO_2 leakage rate (Q_L) on the quantification of carcinogenic health risk was evaluated. Figures 11(a)–11(c) show the distribution of the gaseous CO_2 plume after CO_2 leakage was stopped at 1 year, and Figures 11(d)–11(f) present the distribution of Σ As concentration after 20 years. As Q_L increased from 0.020 to 0.025 to 0.030 kg/s , the CO_2 plume approached the municipal well more closely; the calculated mass center of the CO_2 plume, plotted as black circles at a 120-day interval, moved rapidly as Q_L increased. In addition, adjacent to the CO_2 leakage point, CO_2 saturation was elevated from 0.27 to 0.30, implying occurrence of active dissolution of gaseous CO_2 . As described before, although the movable gaseous CO_2 plume was pumped out after approximately 2 years, residually trapped CO_2 still remained in the pores, concurrently dissolving into the ambient groundwater until 8 years. Increases in dissolved CO_2 concentration due to dissolution of residually trapped CO_2 and resulting low-pH groundwater influenced the distribution of Σ As concentration even after all gaseous CO_2 was pumped out (Figures 11(d)–11(f)). For example, the intensity of Q_L governed the size of the CO_2 plume where the active dissolution of arsenopyrite, the source of Σ As, primarily occurred. Therefore, as Q_L increased from 0.020 to 0.025 to 0.030 kg/s , the size of Σ As plume expanded at 20 years. Additionally, the effects of dispersion, diffusion, and sorption

were amplified while the Σ As plume migrated in the ambient groundwater.

The Σ As profiles monitored at the municipal well revealed the drastic increase in Σ As concentration immediately after the arrival of the Σ As plume at 1.31, 1.07, and 0.98 years for Cases 5, 6, and 7, respectively (Figure 12(a)). The arrival time of the Σ As plume coincided with that of the gaseous CO_2 plume, implying that multiphase migration of CO_2 governed the movement of dissolved Σ As. The size of the Σ As peaks, all of which were over the MCL, increased with Q_L (1.56×10^{-7} , 2.75×10^{-7} , and $4.07 \times 10^{-7} \text{ mol/L}$ for Cases 5, 6, and 7, resp.). In addition, its peak was maintained for a longer time with increased Q_L (13.5, 16.6, and 23.0 years for Cases 5, 6, and 7, resp.). Figure 12(b) shows the calculated probabilistic health risk. While calculating the health risk using (9) and (10), an important parameter was \bar{C} , which was the maximum average of arsenic concentration monitored at the municipal well (see (7)). The size of Q_L varied with \bar{C} as shown in Figure 12(a), which directly affected the risk prediction. Therefore, as the Σ As concentration increased, the health risk for humans increased accordingly. In particular, the medians of Cases 5, 6, and 7, located at the half percentile in variability, were 3.39×10^{-4} , 6.53×10^{-4} , and 9.56×10^{-4} , respectively, all of which exceeded the risk level of concern (10^{-4}).

7.2.3. Effect of Horizontal Permeability (k_h) (Cases 8–10). From two previous sensitivity studies, it was revealed that the driving force of the Σ As plume was essentially the movement of the gaseous CO_2 plume; depending on the size of the CO_2 plume, the amount of dissolved Σ As was determined. In this study, the magnitude of horizontal permeability (k_h), which altered the velocity of ambient groundwater flow, varied

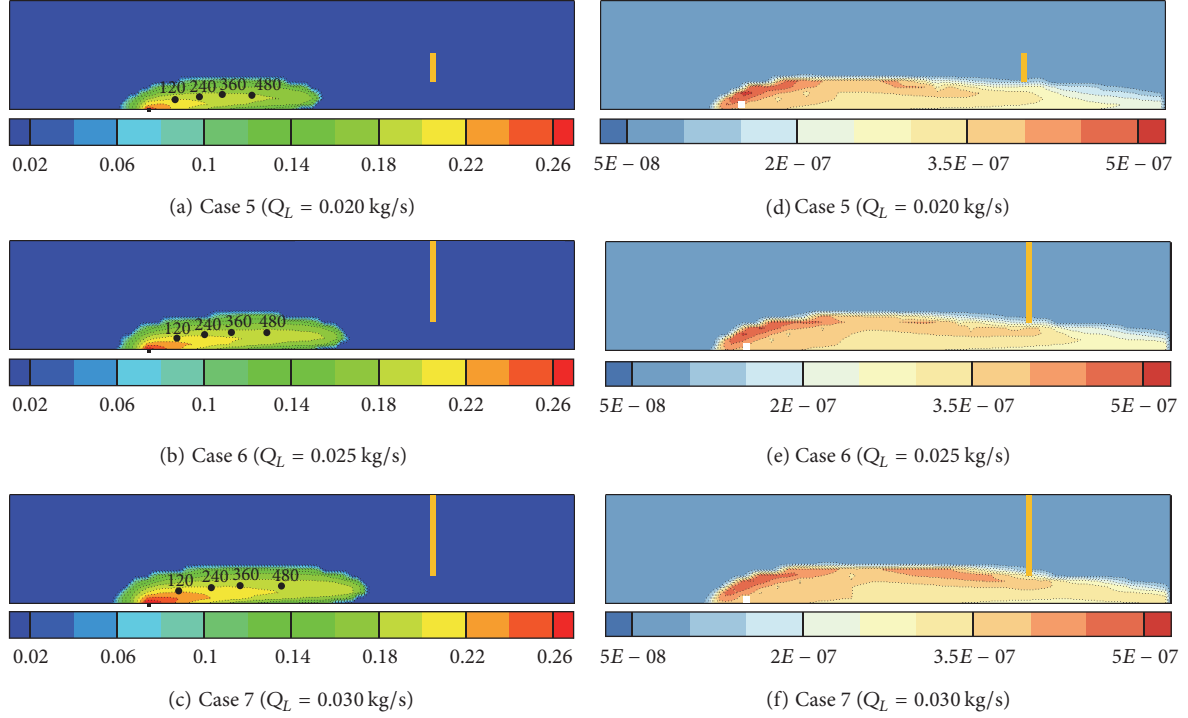


FIGURE 11: Saturation of leaked CO_2 at different leakage rates after 1 year (365 days). (a) Case 5, (b) Case 6, and (c) Case 7. Black circles with labels indicate the locations of mass center for CO_2 plume. Distribution of ΣAs concentration induced by leaked CO_2 at different leakage intensities (Q_L) after 20 years. (d) Case 5, (e) Case 6, and (f) Case 7.

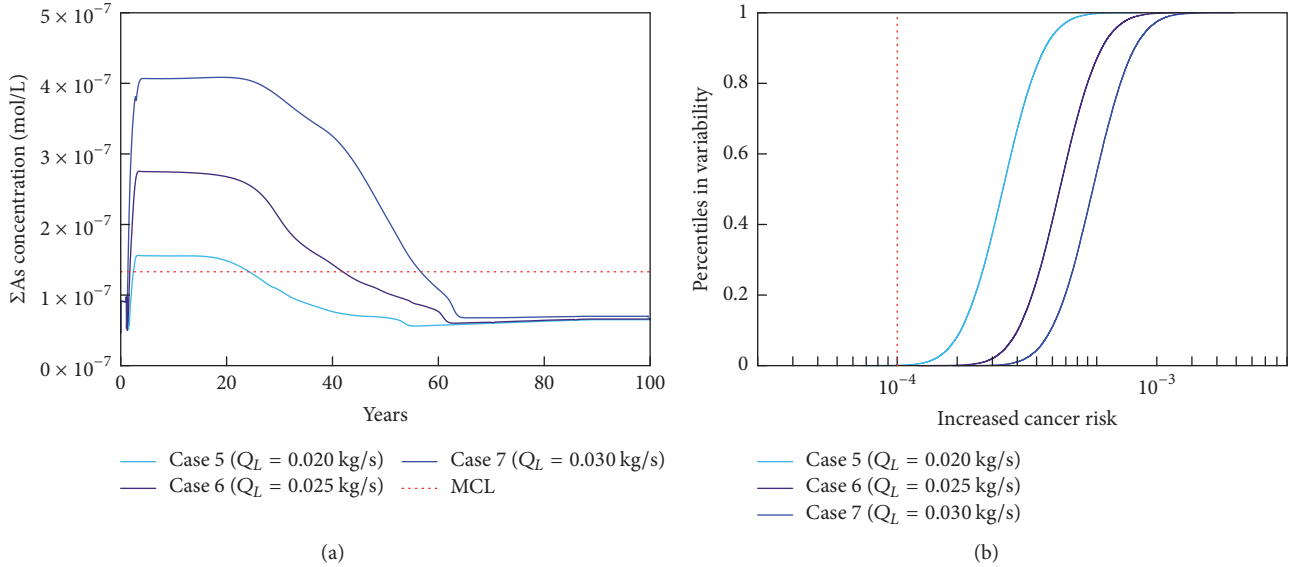


FIGURE 12: (a) ΣAs profiles with different leakage intensities (Q_L) of 0.01, 0.02, and 0.03 kg/s (Cases 5–7) and (b) probabilistic health risk for Cases 5–7 plotted as cumulative density functions (CDF). The red dotted line represents the risk level of concern (10^{-4}).

between 0.2×10^{-13} , 1.0×10^{-13} , and $5.0 \times 10^{-13} \text{ m}^2$ (Cases 8–10, resp.). As k_h increased, the ambient groundwater rate increased from 0.39 to 1.94 to 9.71 cm/day, which induced a change in the shape of the CO_2 plume from oval to flat (Figures 13(a)–13(c)).

Typically, the shape and movement of the gaseous CO_2 plume within the groundwater aquifer are governed by

the balance between buoyancy and viscous forces due to the density contrast of these two fluids. Even the density contrast is amplified as CO_2 leaks into the shallower aquifer, because CO_2 density radically decreases while approaching the surface. The magnitude of the buoyancy number ($N_b = k_v L \Delta \rho g / H \nu \mu$) reflects the change in CO_2 plume shape, where g is gravitational acceleration, L and H are the length and

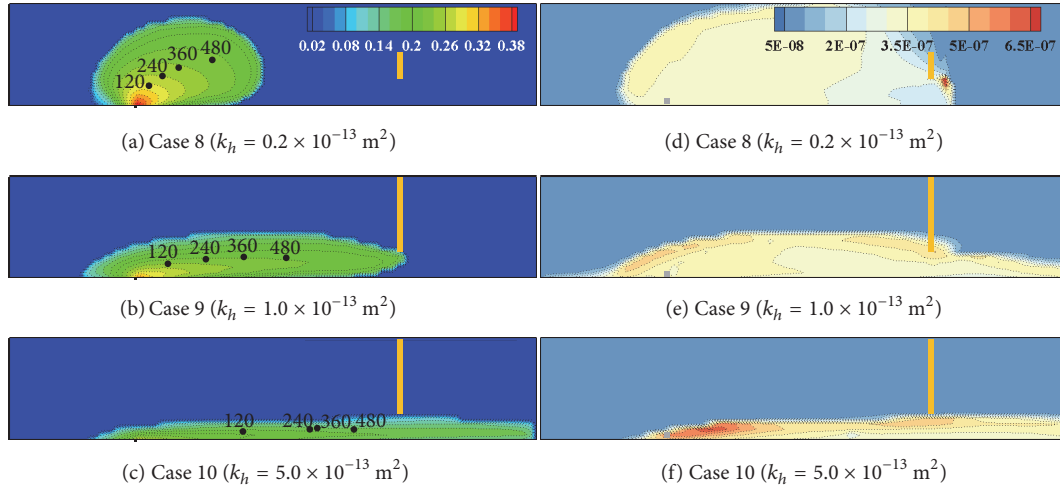


FIGURE 13: Saturation of leaked CO₂ at different horizontal permeabilities (k_h) after 1 year (365 days). (a) Case 8, (b) Case 9, and Case 10. Black circles with labels indicate the locations of mass center for CO₂ plume. Distribution of ΣAs Concentration induced by leaked CO₂ at different horizontal permeabilities (k_h) after 20 years: Cases 8, 9, and 10.

height of the model domain, respectively, v is the ambient groundwater flow rate, and μ is dynamic viscosity of CO₂ (1.47×10^{-5} Pa·s). Finally, $\Delta\rho$ is the density difference between groundwater ($1,000 \text{ kg/m}^3$) and CO₂ (1.842 kg/m^3) [81]. The calculated N_b of Cases 8, 9, and 10 was 740.30, 148.06, and 29.61, respectively, implying that the buoyancy force acting on CO₂ plume increased as k_h decreased.

Even if the velocity of the CO₂ plume was the lowest in Case 8 (or the largest N_b), the CO₂ plume swept the largest area, covering the entire thickness of the aquifer; the calculated mass center moved to the middle height of the aquifer (Figure 13(a)). Due to large coverage of the CO₂ plume, the size of the corresponding ΣAs plume was the largest in Case 8 (Figure 13(d)). In contrast, Case 10 with high k_h accelerated the advective groundwater flow and dispersion, resulting in the flattened shape of the CO₂ plume sinking to the bottom of the aquifer (Figure 13(c)). Due to the poor sweeping efficiency of the CO₂ plume, the ΣAs plume only migrated beneath the municipal well.

The ΣAs concentrations at the municipal well for Cases 8–10 are plotted in Figure 14(a). The arrival time of ΣAs concentration was the latest (4.95 years) in Case 8 due to a low k_h . However, due to large coverage of the ΣAs plume, the ΣAs concentration at the municipal well continuously increased to $3.77 \times 10^{-7} \text{ mol/L}$ until 190 years. In contrast, for Case 10, the arrival time of the ΣAs plume was the shortest (0.95 years), reaching a peak of $1.73 \times 10^{-7} \text{ mol/L}$. However, due to dominance of high advective flow, the ΣAs plume was flattened below the municipal well. Therefore, the amount of ΣAs captured from the municipal well decreased soon, reaching the background level ($0.67 \times 10^{-7} \text{ mol/L}$) only after 25 years. These results imply that the location of the wellbore (e.g., fully or partially penetrating well, the location of screen interval) and the size of the capture zone (e.g., the pumping capacity) are important characteristics for governing ΣAs concentration at the well.

The calculated health risk for each case is plotted in Figure 14(b). As expected, Case 10, which showed the smallest breakthrough of the ΣAs concentration (e.g., the smallest \bar{C}), revealed the lowest risk. Both Cases 8 and 9 showed almost equivalent high-risk prediction even if the profile of the ΣAs concentration appeared differently at the municipal well (Case 8: ~ 80 years; Case 9: ~ 180 years). While accounting for the risk assessment, the exposure duration (ED) was chosen to be 30 years in this work [74]. Following (7), \bar{C} calculated from the ΣAs concentration profile is typically dependent on the duration of ED [31, 82, 83]. For example, \bar{C} can decrease when the breakthrough of ΣAs concentration is shorter than the ED. However, when the breakthrough of the ΣAs concentration is sufficiently longer than the chosen ED, \bar{C} does not change. Similarly, in both Cases 8 and 9, the profiles of ΣAs concentration at the municipal well were sufficiently longer than the chosen ED (Figure 14(a)). Due to this reason, \bar{C} for these two cases were similar to each other, and subsequently the predicted risk levels only showed a slight difference.

8. Conclusion

Even if there is no direct evidence showing that the stored CO₂ has leaked to the shallow aquifers from any major CO₂ injection demonstration sites [50, 84, 85], there exist a few natural analog sites indicating that naturally stored CO₂ has leaked through preexisting fault systems [25, 86–88]. These natural sites where CO₂ leakage is primarily driven by geothermal or tectonic activities are typically less populated with lack of concern in potable groundwater resources. However, as the number of CO₂ injection demonstration activities is growing, the secondary contamination of leaked CO₂ to the shallow potable aquifer becomes an important issue. In this study, with the presence of arsenic-bearing minerals in the aquifer, it is suggested that water-rock interactions induced by CO₂ leakage could mobilize arsenic species to

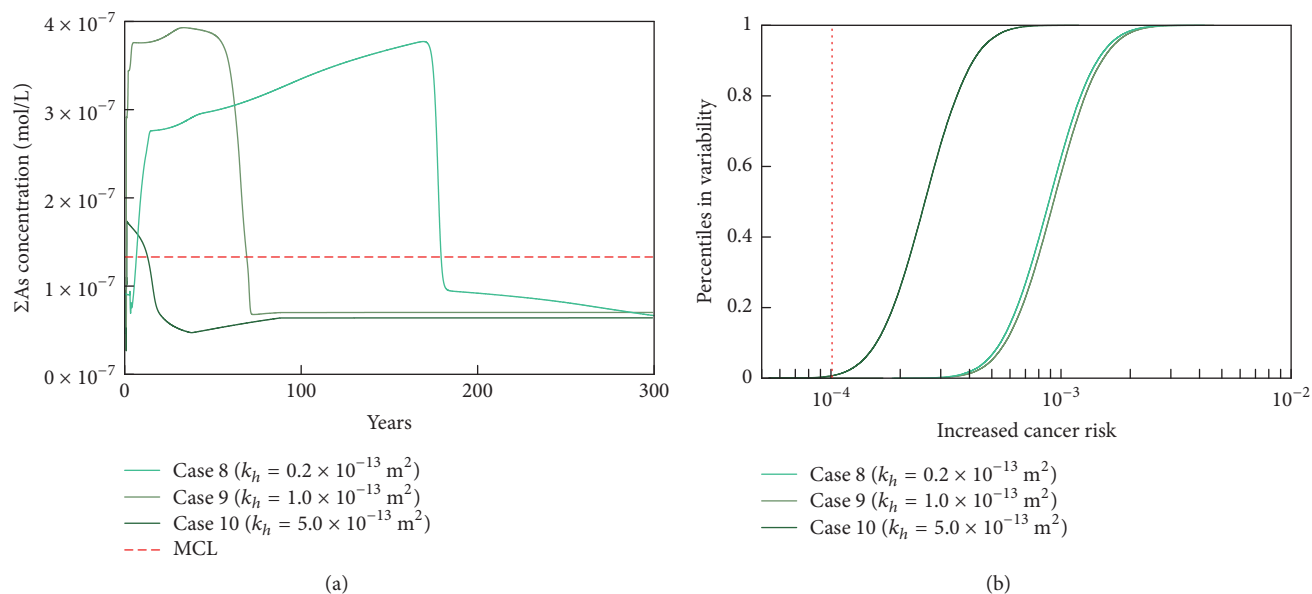


FIGURE 14: (a) Σ As profiles with different horizontal permeabilities (k_h) of 0.2×10^{-13} , 1.0×10^{-13} , and 5.0×10^{-13} m² (Cases 8–10) and (b) probabilistic health risk for Cases 8–10 plotted as cumulative density functions (CDF). The red dotted line represents the risk level of concern (10^{-4}).

the shallow potable aquifer. Therefore, without proper treatments, any residents who continuously utilize these groundwater resources could have great probability of exposure to cancer-related diseases.

Throughout this study, we developed a 2D confined aquifer model where gaseous CO₂ was leaked, and a nearby municipal well concurrently pumped out both leaked CO₂ and groundwater. Immediately after a leaked CO₂ plume arrived at the municipal well, concentrations of As species increased together, indicating occurrence of active arsenopyrite dissolution in the aquifer media. Subsequently, by analyzing As concentration from the municipal well, the carcinogenic health risk was quantified. The processes characterizing the movement of gaseous CO₂ and associated CO₂-water-rock reactions were simulated with the multiphase, multispecies reactive transport model, and subsequent carcinogenic health risks were predicted with probabilistic approach. The simulation results revealed that the movement of leaked CO₂ plume was governed by local flow fields within the shallow potable aquifer; three driving forces, that is, ambient groundwater flow, CO₂ leakage-driven flow, and pumping-driven flow, were characterized. This complex flow field governed chemical reactions, resulting in the most drastic increase (0.77%) in permeability occurring at the rear margin of the CO₂ plume where the vigorous mixing between the ambient groundwater and CO₂-dissolved fluid accelerated dissolution of the minerals. Additionally, sensitivity studies were conducted while varying the sorption intensity, leakage rate of CO₂, and horizontal permeability.

In summary, key factors that exacerbate the secondary contamination of arsenic species at the municipal well were physical characteristics of CO₂ plume such as shape, size, and migration velocity of CO₂ plume; these physical characteristics govern the area where arsenopyrite dissolves,

subsequently affecting As concentration. Furthermore, the size of capture zone (e.g., screen interval, pump capacity) also governed the As concentration in the municipal well. Therefore, when the secondary contamination occurs within the shallow potable aquifer, it is suggested that the aquifer characteristics as well as the amount of leaked CO₂ and its plume size should be evaluated to develop a proper remediation protocol. Additionally, the prompt shutdown of any nearby municipal wells could minimize any potential hazards.

Disclosure

A primitive version of this research was presented at the 2016 Fall General Assembly of the American Geophysical Union.

Conflicts of Interest

The authors declare that there are no conflicts of interest regarding the publication of this paper.

Acknowledgments

The research was partially supported by multiple programs including R&D Project on Environmental Management of Geologic CO₂ Storage offered by the Korea Environmental Industry & Technology Institute (Project no. 201700180004), the R&D Convergence Program of National Research Council of Science & Technology in Korea (Grant no. CAP-15-07-KICT), and, finally, the Yonsei University Future-Leading Research Initiative of 2017-22-0044.

References

- [1] D. Reichle, J. Houghton, B. Kane, and J. Ekmann, *Carbon Sequestration Research and Development*, Oak Ridge National Lab., Oak Ridge, Tenn, USA; National Energy Technology Lab., Pittsburgh, Pa, USA; National Energy Technology Lab., Morgantown, WV, USA, 1999.
- [2] B. Metz, O. Davidson, H. de Coninck, M. Loos, and L. Meyer, *IPCC Special Report on Carbon Dioxide Capture and Storage*, Intergovernmental Panel on Climate Change, 2005.
- [3] NETL, *United States 2012 Carbon Utilization and Storage Atlas*, National Energy Technology Laboratory, 2013.
- [4] J. T. Birkholzer, Q. Zhou, and C.-F. Tsang, "Large-scale impact of CO₂ storage in deep saline aquifers: a sensitivity study on pressure response in stratified systems," *International Journal of Greenhouse Gas Control*, vol. 3, no. 2, pp. 181–194, 2009.
- [5] C. W. Strandli and S. M. Benson, "Identifying diagnostics for reservoir structure and CO₂ plume migration from multilevel pressure measurements," *Water Resources Research*, vol. 49, no. 6, pp. 3462–3475, 2013.
- [6] E. Guyant, W. S. Han, K.-Y. Kim, E. Park, and S.-T. Yun, "Leakage and pressurization risk assessment of CO₂ reservoirs: a metamodelling approach," *International Journal of Greenhouse Gas Control*, vol. 54, part 1, pp. 345–361, 2016.
- [7] E. H. Keating, J. Fessenden, N. Kanjorski, D. J. Koning, and R. Pawar, "The impact of CO₂ on shallow groundwater chemistry: observations at a natural analog site and implications for carbon sequestration," *Environmental Earth Sciences*, vol. 60, no. 3, pp. 521–536, 2010.
- [8] K. Pruess, "Leakage of CO₂ from geologic storage: role of secondary accumulation at shallow depth," *International Journal of Greenhouse Gas Control*, vol. 2, no. 1, pp. 37–46, 2008.
- [9] C. M. Oldenburg, C. Doughty, C. A. Peters, and P. F. Dobson, "Simulations of long-column flow experiments related to geologic carbon sequestration: Effects of outer wall boundary condition on upward flow and formation of liquid CO₂," *Greenhouse Gases: Science and Technology*, vol. 2, no. 4, pp. 279–303, 2012.
- [10] S. Bachu, "Legal and regulatory challenges in the implementation of CO₂ geological storage: an Alberta and Canadian perspective," *International Journal of Greenhouse Gas Control*, vol. 2, no. 2, pp. 259–273, 2008.
- [11] Y. K. Kharaka, D. R. Cole, S. D. Hovorka, W. D. Gunter, K. G. Knauss, and B. M. Freifeld, "Gas-water-rock interactions in Frio Formation following CO₂ injection: implications for the storage of greenhouse gases in sedimentary basins," *Geology*, vol. 34, no. 7, pp. 577–580, 2006.
- [12] J. A. Apps, L. Zheng, N. Spycher et al., "Transient changes in shallow groundwater chemistry during the MSU ZERT CO₂ injection experiment," *Energy Procedia*, vol. 4, pp. 3231–3238, 2011.
- [13] E. H. Keating, J. A. Hakala, H. Viswanathan et al., "CO₂ leakage impacts on shallow groundwater: field-scale reactive-transport simulations informed by observations at a natural analog site," *Applied Geochemistry*, vol. 30, pp. 136–147, 2013.
- [14] S. A. Carroll, E. Keating, K. Mansoor et al., "Key factors for determining groundwater impacts due to leakage from geologic carbon sequestration reservoirs," *International Journal of Greenhouse Gas Control*, vol. 29, pp. 153–168, 2014.
- [15] S. Wang and P. R. Jaffe, "Dissolution of a mineral phase in potable aquifers due to CO₂ releases from deep formations; effect of dissolution kinetics," *Energy Conversion and Management*, vol. 45, no. 18–19, pp. 2833–2848, 2004.
- [16] L. Zheng, N. Spycher, C. Varadharajan et al., "On the mobilization of metals by CO₂ leakage into shallow aquifers: exploring release mechanisms by modeling field and laboratory experiments," *Greenhouse Gases: Science and Technology*, vol. 5, no. 4, pp. 403–418, 2015.
- [17] WHO, *Chemical Agents and Related Occupations—A Review of Human Carcinogens*, International Agency for Research on Cancer, Lyon, France, 2012.
- [18] J. Matschullat, "Arsenic in the geosphere—a review," *Science of the Total Environment*, vol. 249, no. 1–3, pp. 297–312, 2000.
- [19] ATSDR, *Support Document to the 2015 Priority List of Hazardous Substances That Will Be Candidates for Toxicological Profiles*, Agency for Toxic Substances and Disease Registry, Atlanta, Ga, USA, 2015.
- [20] L. Rodríguez-Lado, G. Sun, M. Berg et al., "Groundwater arsenic contamination throughout China," *Science*, vol. 341, no. 6148, pp. 866–868, 2013.
- [21] U. K. Chowdhury, B. K. Biswas, T. R. Chowdhury et al., "Groundwater arsenic contamination in Bangladesh and West Bengal, India," *Environmental Health Perspectives*, vol. 108, no. 5, pp. 393–397, 2000.
- [22] A. A. Meharg and M. M. Rahman, "Arsenic contamination of Bangladesh paddy field soils: implications for rice contribution to arsenic consumption," *Environmental Science & Technology*, vol. 37, no. 2, pp. 229–234, 2003.
- [23] J. M. Hebbar Annapoorna, "Arsenic contamination in groundwater of the areas surrounding Ingaldhal, Chitradurga district, Karnataka state," *International Journal of Geology, Earth & Environmental Science*, vol. 6, pp. 1–7, 2016.
- [24] H. Viswanathan, Z. Dai, C. Lopano et al., "Developing a robust geochemical and reactive transport model to evaluate possible sources of arsenic at the CO₂ sequestration natural analog site in Chimayo, New Mexico," *International Journal of Greenhouse Gas Control*, vol. 10, pp. 199–214, 2012.
- [25] E. H. Keating, D. L. Newell, H. Viswanathan, J. W. Carey, G. Zyvoloski, and R. Pawar, "CO₂/brine transport into shallow aquifers along fault zones," *Environmental Science & Technology*, vol. 47, no. 1, pp. 290–297, 2013.
- [26] R. C. Trautz, J. D. Pugh, C. Varadharajan et al., "Effect of dissolved CO₂ on a shallow groundwater system: a controlled release field experiment," *Environmental Science & Technology*, vol. 47, no. 1, pp. 298–305, 2013.
- [27] T. Xu, Y. K. Kharaka, C. Doughty, B. M. Freifeld, and T. M. Daley, "Reactive transport modeling to study changes in water chemistry induced by CO₂ injection at the Frio-I Brine Pilot," *Chemical Geology*, vol. 271, pp. 153–164, 2010.
- [28] Y. K. Kharaka, J. J. Thordsen, E. Kakouros et al., "Changes in the chemistry of shallow groundwater related to the 2008 injection of CO₂ at the ZERT field site, Bozeman, Montana," *Environmental Earth Sciences*, vol. 60, no. 2, pp. 273–284, 2010.
- [29] L. Zhang, H. Parthasarathy, and A. Karamalidis, "Investigation on arsenopyrite dissolution and As (III) migration under geologic carbon storage conditions: A numerical simulation approach," *Greenhouse Gases: Science and Technology*, vol. 7, no. 3, pp. 460–473, 2017.
- [30] T. Xiao, Z. Dai, H. Viswanathan et al., "Arsenic mobilization in shallow aquifers due to CO₂ and brine intrusion from storage reservoirs," *Scientific Reports*, vol. 7, no. 1, article 2763, 2017.

- [31] E. R. Siirila, A. K. Navarre-Sitchler, R. M. Maxwell, and J. E. McCray, "A quantitative methodology to assess the risks to human health from CO₂ leakage into groundwater," *Advances in Water Resources*, vol. 36, pp. 146–164, 2012.
- [32] A. K. Navarre-Sitchler, R. M. Maxwell, E. R. Siirila, G. E. Hammond, and P. C. Lichtner, "Elucidating geochemical response of shallow heterogeneous aquifers to CO₂ leakage using high-performance computing: Implications for monitoring of CO₂ sequestration," *Advances in Water Resources*, vol. 53, pp. 45–55, 2013.
- [33] P. Lu and C. Zhu, "Arsenic Eh-pH diagrams at 25°C and 1 bar," *Environmental Earth Sciences*, vol. 62, no. 8, pp. 1673–1683, 2011.
- [34] P. Bhattacharya, D. Chatterjee, and G. Jacks, "Occurrence of arsenic-contaminated groundwater in alluvial aquifers from delta plains, eastern India: options for safe drinking water supply," *International Journal of Water Resources Development*, vol. 13, no. 1, pp. 79–92, 1997.
- [35] P. Bose and A. Sharma, "Role of iron in controlling speciation and mobilization of arsenic in subsurface environment," *Water Research*, vol. 36, no. 19, pp. 4916–4926, 2002.
- [36] C. K. Jain and I. Ali, "Arsenic: occurrence, toxicity and speciation techniques," *Water Research*, vol. 34, no. 17, pp. 4304–4312, 2000.
- [37] G. A. Cutter, "Kinetic controls on metalloid speciation in seawater," *Marine Chemistry*, vol. 40, no. 1-2, pp. 65–80, 1992.
- [38] E. Berman, *Toxic Metals and Their Analysis*, John Wiley & Sons, 1980.
- [39] P. L. Smedley and D. G. Kinniburgh, "A review of the source, behaviour and distribution of arsenic in natural waters," *Applied Geochemistry*, vol. 17, no. 5, pp. 517–568, 2002.
- [40] M. T. van Genuchten, "A closed-form equation for predicting the hydraulic conductivity of unsaturated soils," *Soil Science Society of America Journal*, vol. 44, no. 5, pp. 892–898, 1980.
- [41] J. W. Tester, W. G. Worley, B. A. Robinson, C. O. Grigsby, and J. L. Feerer, "Correlating quartz dissolution kinetics in pure water from 25 to 625°C," *Geochimica et Cosmochimica Acta*, vol. 58, no. 11, pp. 2407–2420, 1994.
- [42] J. L. Palandri and Y. K. Kharaka, "A compilation of rate parameters of water-mineral interaction kinetics for application to geochemical modeling," DTIC Document, 2004.
- [43] L. Zheng, J. A. Apps, Y. Zhang, T. Xu, and J. T. Birkholzer, "On mobilization of lead and arsenic in groundwater in response to CO₂ leakage from deep geological storage," *Chemical Geology*, vol. 268, no. 3-4, pp. 281–297, 2009.
- [44] T. Xu, E. Sonnenthal, N. Spycher, and K. Pruess, "TOUGH-REACT—a simulation program for non-isothermal multiphase reactive geochemical transport in variably saturated geologic media: applications to geothermal injectivity and CO₂ geological sequestration," *Computers & Geosciences*, vol. 32, pp. 145–165, 2006.
- [45] K. Pruess and N. Spycher, "ECO2N—a fluid property module for the TOUGH2 code for studies of CO₂ storage in saline aquifers," *Energy Conversion and Management*, vol. 48, no. 6, pp. 1761–1767, 2007.
- [46] H. C. Helgeson, D. H. Kirkham, and G. C. Flowers, "Theoretical prediction of the thermodynamic behavior of aqueous electrolytes at high pressures and temperatures: IV. Calculation of activity coefficients, osmotic coefficients, and apparent molal and standard and relative partial molal properties to 600°C and 5 kb," *American Journal of Science*, vol. 291, no. 10, pp. 1249–1516, 1981.
- [47] L. André, M. Azaroual, C. Bernstone, and A. Wittek, "Modeling the geochemical impact of an injection of CO₂ and associated reactive impurities (SO₂ and O₂) into a saline reservoir," *Transport in Porous Media*, vol. 108, no. 1, pp. 185–205, 2015.
- [48] R. A. Renken, K. J. Cunningham, M. R. Zygnerski et al., "Assessing the vulnerability of a municipal well field to contamination in a karst aquifer," *Environmental and Engineering Geoscience*, vol. 11, no. 4, pp. 319–331, 2005.
- [49] D. Larsen, R. W. Gentry, and D. K. Solomon, "The geochemistry and mixing of leakage in a semi-confined aquifer at a municipal well field, Memphis, Tennessee, USA," *Applied Geochemistry*, vol. 18, no. 7, pp. 1043–1063, 2003.
- [50] R. J. Finley, S. M. Frailey, H. E. Leetaru, O. Senel, M. L. Couëslan, and M. Scott, "Early operational experience at a one-million tonne CCS demonstration project, Decatur, Illinois, USA," *Energy Procedia*, vol. 37, pp. 6149–6155, 2013.
- [51] C. Doughty, B. M. Freifeld, and R. C. Trautz, "Site characterization for CO₂ geologic storage and vice versa: the Frio brine pilot, Texas, USA as a case study," *Environmental Geology*, vol. 54, no. 8, pp. 1635–1656, 2008.
- [52] B. Dockrill and Z. K. Shipton, "Structural controls on leakage from a natural CO₂ geologic storage site: Central Utah, U.S.A.," *Journal of Structural Geology*, vol. 32, no. 11, pp. 1768–1782, 2010.
- [53] Z. K. Shipton, J. P. Evans, D. Kirschner, P. T. Kolesar, A. P. Williams, and J. Heath, "Analysis of CO₂ leakage through 'low-permeability' faults from natural reservoirs in the Colorado Plateau, east-central Utah," *Geological Society, London, Special Publications*, vol. 233, pp. 43–58, 2004.
- [54] N. Kampman, M. J. Bickle, A. Maskell et al., "Drilling and sampling a natural CO₂ reservoir: implications for fluid flow and CO₂-fluid-rock reactions during CO₂ migration through the overburden," *Chemical Geology*, vol. 369, pp. 51–82, 2014.
- [55] W. T. Parry, C. B. Forster, J. P. Evans, B. B. Bowen, and M. A. Chan, "Geochemistry of CO₂ sequestration in the Jurassic Navajo Sandstone, Colorado Plateau, Utah," *Environmental Geosciences*, vol. 14, no. 2, pp. 91–109, 2007.
- [56] N. Kampman, M. Bickle, J. Becker, N. Assayag, and H. Chapman, "Feldspar dissolution kinetics and Gibbs free energy dependence in a CO₂-enriched groundwater system, Green River, Utah," *Earth and Planetary Science Letters*, vol. 284, no. 3-4, pp. 473–488, 2009.
- [57] W. S. Han, Z. T. Watson, N. Kampman, T. Grundl, J. P. Graham, and E. H. Keating, "Periodic changes in effluent chemistry at cold-water geyser: Crystal geyser in Utah," *Journal of Hydrology*, vol. 550, pp. 54–64, 2017.
- [58] C. I. A. Carruthers, *Metal Mobility in Sandstones and the Potential Environmental Impacts of Offshore Geological CO₂ Storage*, The University of Edinburgh, 2016.
- [59] M. Sakata, "Relationship between adsorption of arsenic(III) and boron by soil and soil properties," *Environmental Science & Technology*, vol. 21, no. 11, pp. 1126–1130, 1987.
- [60] Q. H. Hu, G. X. Sun, X. B. Gao, and Y. G. Zhu, "Conversion, sorption, and transport of arsenic species in geological media," *Applied Geochemistry*, vol. 27, no. 11, pp. 2197–2203, 2012.
- [61] E. Sonnenthal, A. Ito, N. Spycher et al., "Approaches to modeling coupled thermal, hydrological, and chemical processes in the drift scale heater test at Yucca Mountain," *International Journal of Rock Mechanics and Mining Sciences*, vol. 42, no. 5-6, pp. 698–719, 2005.
- [62] K. G. Knauss, J. W. Johnson, and C. I. Steefel, "Evaluation of the impact of CO₂, co-contaminant gas, aqueous fluid and

- reservoir rock interactions on the geologic sequestration of CO₂,” *Chemical Geology*, vol. 217, no. 3–4, pp. 339–350, 2005.
- [63] B. Zerai, B. Z. Saylor, and G. Matisoff, “Computer simulation of CO₂ trapped through mineral precipitation in the Rose Run Sandstone, Ohio,” *Applied Geochemistry*, vol. 21, no. 2, pp. 223–240, 2006.
- [64] T. Xu, *TOUGHREACT User’s Guide: A Simulation Program for Non-isothermal Multiphase Reactive Geochemical Transport in Variably Saturated Geologic Media*, V1.2.1, 2008.
- [65] C. I. Steefel and A. C. Lasaga, “A coupled model for transport of multiple chemical species and kinetic precipitation/dissolution reactions with application to reactive flow in single phase hydrothermal systems,” *American Journal of Science*, vol. 294, no. 5, pp. 529–592, 1994.
- [66] C. M. Bethke and P. V. Brady, “How the K_d approach undermines ground water cleanup,” *Groundwater*, vol. 38, no. 3, pp. 435–443, 2000.
- [67] A. J. Valocchi, “Describing the transport of ion-exchanging contaminants using an effective K_d approach,” *Water Resources Research*, vol. 20, no. 4, pp. 499–503, 1984.
- [68] J. A. Davis, J. A. Coston, D. B. Kent, and C. C. Fuller, “Application of the surface complexation concept to complex mineral assemblages,” *Environmental Science & Technology*, vol. 32, no. 19, pp. 2820–2828, 1998.
- [69] U. S. EPA, *Guidelines for Carcinogen Risk Assessment*, Risk Assessment Forum, Washington, DC, USA, 2005.
- [70] B. Means, *Risk-Assessment Guidance for Superfund. Vol 1. Human Health Evaluation Manual. (Part A Interim Report (Final))*, Environmental Protection Agency, Office of Solid Waste and Emergency Response, Washington, DC, USA, 1989.
- [71] I. R. I. S. IRIS, “Chemical assessment summary, arsenic, inorganic,” CASRN 7440-38-2, U.S. Environmental Protection Agency, 1991.
- [72] U. S. EPA, *Risk Assessment Guidance for Superfund*, U.S. Environmental Protection Agency, Washington, DC, USA, 2004.
- [73] S. Fahrner, D. Schäfer, F. Dethlefsen, and A. Dahmke, “Reactive modelling of CO₂ intrusion into freshwater aquifers: current requirements, approaches and limitations to account for temperature and pressure effects,” *Environmental Earth Sciences*, vol. 67, no. 8, pp. 2269–2283, 2012.
- [74] U. S. EPA, *Risk Assessment Guidance for Superfund*, U.S. Environmental Protection Agency, Washington, DC, USA, 1989.
- [75] R. M. Maxwell, S. D. Pelmulder, A. F. B. Tompson, and W. E. Kastenber, “On the development of a new methodology for groundwaterdriven health risk assessment,” *Water Resources Research*, vol. 34, no. 4, pp. 833–847, 1998.
- [76] U. S. EPA, *Risk Assessment Guidance for Superfund*, U.S. Environmental Protection Agency, Washington, DC, USA, 2001.
- [77] K. E. McSarrow, *National Oil and Hazardous Substances Pollution Contingency Plan*, United States Environmental Protection Agency, JSTOR, 1991.
- [78] Z. Duan and R. Sun, “An improved model calculating CO₂ solubility in pure water and aqueous NaCl solutions from 273 to 533 K and from 0 to 2000 bar,” *Chemical Geology*, vol. 193, no. 3–4, pp. 257–271, 2003.
- [79] U. S. EPA, *National Primary Drinking Water Regulations*, United States Environmental Protection Agency, 2008.
- [80] U. S. EPA, *Risk Assessment Guidance for Superfund, Vol. 3 (Part A Process for Conduction of Probabilistic Risk Assessment)*, EPA, Washington, DC, USA, 2001.
- [81] R. Span and W. Wagner, “A new equation of state for carbon dioxide covering the fluid region from the triple-point temperature to 1100 K at pressures up to 800 MPa,” *Journal of Physical and Chemical Reference Data*, vol. 25, no. 6, pp. 1509–1596, 1996.
- [82] R. M. Maxwell, S. F. Carle, and A. F. B. Tompson, “Contamination, risk, and heterogeneity: On the effectiveness of aquifer remediation,” *Environmental Geology*, vol. 54, no. 8, pp. 1771–1786, 2008.
- [83] E. R. Siirila and R. M. Maxwell, “A new perspective on human health risk assessment: Development of a time dependent methodology and the effect of varying exposure durations,” *Science of the Total Environment*, vol. 431, pp. 221–232, 2012.
- [84] T. A. Torp and J. Gale, “Demonstrating storage of CO₂ in geological reservoirs: the Sleipner and SACS projects,” *Energy*, vol. 29, no. 9–10, pp. 1361–1369, 2004.
- [85] A. Mathieson, J. Midgely, I. Wright, N. Saoula, and P. Ringrose, “In Salah CO₂ storage JIP: CO₂ sequestration monitoring and verification technologies applied at Krechba, Algeria,” *Energy Procedia*, vol. 4, pp. 3596–3603, 2011.
- [86] W. S. Han, M. Lu, and B. J. Mcpherson, “Characteristics of CO₂-driven cold-water geyser, Crystal Geyser in Utah: Experimental observation and mechanism analyses,” *Geofluids*, vol. 13, no. 3, pp. 283–297, 2013.
- [87] C. D. Farrar, M. L. Sorey, W. C. Evans et al., “Forest-killing diffuse CO₂ emission at mammoth mountain as a sign of magmatic unrest,” *Nature*, vol. 376, no. 6542, pp. 675–678, 1995.
- [88] G. W. Kling, M. A. Clark, H. R. Compton et al., “The 1986 Lake Nyos gas disaster in Cameroon, West Africa,” *Science*, vol. 236, no. 4798, pp. 169–175, 1987.

Research Article

Hydrochemical Characteristics and Evolution of Geothermal Fluids in the Chabu High-Temperature Geothermal System, Southern Tibet

X. Wang,¹ G. L. Wang ,¹ H. N. Gan,¹ Z. Liu,² and D. W. Nan³

¹Institute of Hydrogeology and Environmental Geology, Chinese Academy of Geological Sciences, Shijiazhuang, Hebei 050061, China

²School of Water Resources and Environment, Hebei GEO University, Shijiazhuang, Hebei 050031, China

³The Geothermal Geological Team of Tibet, Tibet Bureau of Exploration & Development of Geology and Mineral Resources, Lhasa 850032, China

Correspondence should be addressed to G. L. Wang; guilingw@yeah.net

Received 28 October 2017; Revised 29 January 2018; Accepted 18 February 2018; Published 21 March 2018

Academic Editor: Ming Zhang

Copyright © 2018 X. Wang et al. This is an open access article distributed under the Creative Commons Attribution License, which permits unrestricted use, distribution, and reproduction in any medium, provided the original work is properly cited.

This study defines reasonable reservoir temperatures and cooling processes of subsurface geothermal fluids in the Chabu high-temperature geothermal system. This system lies in the south-central part of the Shenzha-Xietongmen hydrothermal active belt and develops an extensive sinter platform with various and intense hydrothermal manifestations. All the geothermal spring samples collected systematically from the sinter platform are divided into three groups by cluster analysis of major elements. Samples of group 1 and group 3 are distributed in the central part and northern periphery of the sinter platform, respectively, while samples of group 2 are scattered in the transitional zone between groups 1 and 3. The hydrochemical characteristics show that the geothermal waters of the research area have generally mixed with shallow cooler waters in reservoirs. The reasonable reservoir temperatures and the mixing processes of the subsurface geothermal fluids could be speculated by combining the hydrochemical characteristics of geothermal springs, calculated results of the chemical geothermometers, and silica-enthalpy mixing models. Contour maps are applied to measured emerging temperatures, mass flow rates, total dissolved solids of spring samples, and reasonable subsurface temperatures. They indicate that the major cooling processes of the subsurface geothermal fluids gradually transform from adiabatic boiling to conduction from the central part to the peripheral belt. The geothermal reservoir temperatures also show an increasing trend. The point with the highest reservoir temperature (256°C) appears in the east-central part of the research area, which might be the main up-flow zone. The cooling processes of the subsurface geothermal fluids in the research area can be shown on an enthalpy-chloride plot. The deep parent fluid for the Chabu geothermal field has a Cl⁻ concentration of 290 mg/L and an enthalpy of 1550 J/g (with a water temperature of 369°C).

1. Introduction

As a part of the Mediterranean-Himalayan geothermal belt, Tibet has abundant geothermal resources. There are a series of S-N-trending normal faults distributed in the Tibetan Plateau, which are the result of the collision between the India and Eurasian plates [1]. These S-N-trending normal fault systems crosscut the Yarlung Zangbo River and Pangong Tso-Nu River suture belts, forming the famous hydrothermal active belt of the Tibetan Plateau [2, 3]. From west to east, there are four major hydrothermally active belts: Tangrayumco-Gucuo, Shenzha-Xietongmen, Yadong-Gulu,

and Sangri-Cuona (Figure 1). Yadong-Gulu is the most active hydrothermal belt and has the most concentrated geothermal reserves, followed by the Shenzha-Xietongmen hydrothermal belt. The Chabu high-temperature geothermal system lies in the south-central part of the Shenzha-Xietongmen hydrothermally active belt and has developed an extensive sinter platform with various and intense hydrothermal manifestations.

The heat source for the high-temperature geothermal system in the research area is a partially melted crustal layer, as is seen in most high-temperature geothermal fields [4–14]. A high-temperature geothermal system with a magmatic

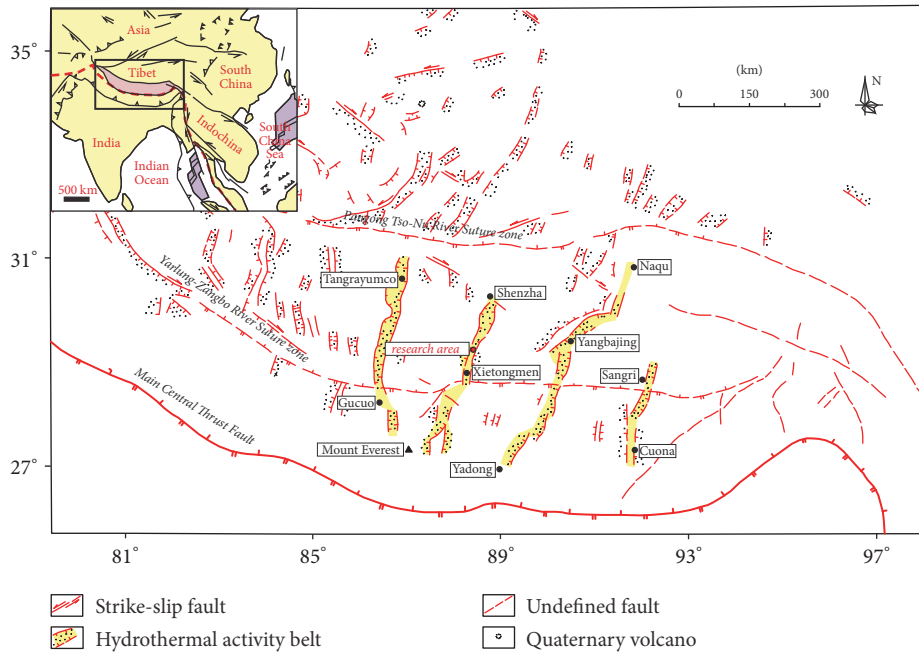


FIGURE 1: Distribution of hydrothermally active belts on the Tibetan Plateau [22–24].

heat source usually hosts deep parent fluids that remain in equilibrium with the surrounding rock. The pH of these fluids is near neutral; the principal anion and cation are Cl^- and Na^+ , respectively [15–17]. This type of deep geothermal fluid ascending in a geothermal system may cool by (1) conduction of heat to the surrounding rock, (2) adiabatic boiling, (3) mixing with cooler water, or (4) a combination of these [18–21].

Except for some fundamental geological investigations (stratum, structure, and magmatite) and some preliminary resource assessment, there are very few studies on this research area, especially on the hydrochemical characteristics, temperatures, and cooling processes of geothermal fluids. Thus, the aim of this work is to fill this gap by combining the hydrochemical characteristics of hot spring waters with cluster analysis, chemical geothermometers, and mixing models (silica-enthalpy and enthalpy-chloride). This work could provide valuable guidance for further assessment, exploitation, and utilization of geothermal resources of the Chabu geothermal field.

2. Geological Setting

The research area lies in the Lhasa–Gangdise block between the Yarlung Zangbo River suture belt and the Pangong Tso–Nu River suture belt and is largely bounded by the Pangong Tso–Nu River deep fracture in the north and Yaluzangbu River deep fracture in the south, both of which trend approximately E–W. Extension fractures are well developed in the research area, and the major faults extend in S–N and SW–NE directions forming the main heat-controlling structures.

The strata exposed in the research area are Paleogene and Quaternary units. Paleogene rocks are mainly lithic tuff and are distributed to the south of the research area and

appear as strip belts along a NE or NW direction. Quaternary unconsolidated sediments are found throughout the area. Quaternary sinters are distributed in the central part of the Chabu geothermal field and are mainly composed of siliceous minerals. The sinter platform contains approximately 80 thermal springs and imbricated deposits from NE to SW.

The magmatic rocks exposed in the research area are primarily biotite alkali-feldspar granite and biotite granite of Paleogene age, as well as porphyritic biotite monzonitic granite and two-mica adamellite of Neogene age (Figure 2).

3. Materials and Methods

In this study, 36 geothermal spring samples are collected systematically from the north-central part of the sinter platform which holds the most concentrated and intense hydrothermal manifestations (Figure 3). Table 1 includes the sample ID, concentration of major ions and some trace ions, measured emerging temperatures, mass flow rates, and charge imbalance for all the geothermal spring samples.

The temperature (T) and pH values of the geothermal water samples were measured with hand-held meters on-site prior to sampling. All geothermal water samples were filtered through $0.45\ \mu\text{m}$ membranes and stored in three 200 mL polyethylene bottles that had been rinsed with water from the sample source twice before sample collection. For SiO_2 analyses, the geothermal water samples were diluted to 10% of their initial concentration using deionized water. For metallic and cation element analyses, samples were acidified with HNO_3 to pH 1. No reagents were added to the samples for inorganic anion analysis. All water samples were analyzed at the Key Laboratory for Groundwater Science and Engineering of the Ministry of Land and Resources with the Determination Method for Underground Water published by

TABLE 1: Hydrochemical characteristics of geothermal spring samples from the research area (in mg/L, except for pH in standard pH units, mass flow rate in L/min, T in $^{\circ}\text{C}$, and charge imbalance in %). Sample H1 is the cold groundwater of the research area. The samples are listed in the order of the results of cluster analysis mentioned in "Cluster Analysis."

Group	Sample ID	T	Mass flow rate	pH	TDS	K	Na	Ca	Mg	Cl	SO_4	HCO_3	CO_3	Li	F	SiO_2	B	Charge imbalance	Hydrochemical type
	H1	11	-	7.34	62.35	1.02	3.27	8.61	0.69	0.68	0.74	377	0	0.0098	0.31	13.79	0.022	-0.96	Ca- Na-HCO_3
1	C31	87.3	1842.6	8.4	1933.04	52.38	403.14	2.47	3.25	303.18	89.96	478.71	60.99	7.83	11	309.58	48.84	-1.18	Na- Cl-HCO_3
	C34	87.2	1311.6	8.42	1731.81	47.48	382.1	1.65	5.5	282.08	98.85	513.44	35.37	7.92	10	143.82	47.92	-1.58	Na- Cl-HCO_3
	C35	78.6	70.3	8.6	1648.91	46.28	371.32	1.65	3.5	277.85	92.92	453.91	51.23	7.98	9.9	123.74	47.46	-1.53	Na- Cl-HCO_3
	C6	81.4	172.8	8.64	1832.81	47.54	385.2	2.42	1.96	281.08	99.54	458.34	53.18	8.37	9.8	294.12	47.46	-0.87	Na- Cl-HCO_3
	C32	87	98.2	8.82	1784.5	48.08	391.2	1.24	4	287.7	97.86	410.5	90.26	7.92	10.4	287.84	47.96	-1.64	Na- Cl-HCO_3
	C3	80.8	21.6	8.73	1691.54	46.4	385.2	2.42	2.45	286.02	103.4	406.84	83.57	8.95	9.84	162.32	48.38	-1.61	Na- Cl-HCO_3
	C33	87.3	173	8.9	1593.57	44.56	378.25	1.65	4.5	279.97	92.92	311.29	129.29	7.38	9.5	135.06	47.54	-1.63	Na- Cl-HCO_3
	C5	81.8	151.2	8.82	1769.56	43.2	379.5	2.42	3.91	276.84	89.87	375.94	98.76	8.21	9.62	289.94	47.46	-1.03	Na- Cl-HCO_3
	C19	78.7	324.0	8.51	1800.12	53.22	378.25	1.61	0.98	282.49	76.34	388.81	96.23	7.47	9.82	312.14	48.38	-1.56	Na- Cl-HCO_3
	C20	83.2	496.8	8.55	1854.85	58.62	384.94	1.61	1.47	286.73	78.28	435.16	73.44	8.13	10	321.9	48.38	-0.53	Na- $\text{HCO}_3\text{-Cl}$
	C18	79.2	64.8	8.48	1848.79	58.94	397.98	1.61	0.98	284.61	74.41	383.66	96.23	7.96	9.43	345.36	46.54	1.4	Na- Cl-HCO_3
2-1	C1	70.4	6.5	8.25	1850.07	41.68	420	4.83	1.96	292.38	89.87	538.15	43.05	8.37	10	153.6	49.30	0.1	Na- Cl-HCO_3
	C26	76	0.0	8.21	1864.55	39.58	393.6	4.84	2.45	282.49	86.01	533.01	20.25	7.89	10.2	296.22	46.54	0.01	Na- $\text{HCO}_3\text{-Cl}$
	C23	81.6	0.0	8.25	1923.22	39.78	407.36	4.03	2.45	290.96	78.28	517.56	45.58	8.41	10.4	305.64	52.99	-0.09	Na- $\text{HCO}_3\text{-Cl}$
	C36	77.6	432.0	8.22	1798.58	39.43	397.94	4.03	1.47	278.25	76.34	468.63	53.18	8.14	9.06	270.64	49.30	1.13	Na- $\text{HCO}_3\text{-Cl}$
	C11	80.6	216.0	8.24	1843.16	41.2	396.54	4.03	1.47	279.66	72.48	509.83	40.52	8.24	9.9	284.64	48.38	0.47	Na- $\text{HCO}_3\text{-Cl}$
	C25	77.2	43.2	8.22	1894.08	48.42	407.08	6.45	1.96	281.08	89.87	538.16	22.79	8.11	10.4	285.6	48.38	1.65	Na- Cl-HCO_3
	C4	72.2	0.2	8.6	1702.44	44.96	385.4	2.42	2.93	276.84	86.01	489.23	37.99	7.98	9.44	174.18	45.61	0.11	Na- $\text{HCO}_3\text{-Cl}$
	C21	77.4	43.2	8.34	1796.67	43.2	395.86	6.45	0.98	269.07	87.94	471.21	45.58	8.18	9.22	275.18	45.61	1.94	Na- $\text{HCO}_3\text{-Cl}$
	C7	80	0.0	8.5	1783.32	46.2	401.29	4.83	1.47	272.6	86.01	435.16	65.84	8.04	9.4	261.4	47.46	1.17	Na- $\text{HCO}_3\text{-Cl}$
	C24	66	6.5	7.5	1878.5	39.85	372.36	15.32	2.93	264.83	76.34	605.11	0	7.94	9.3	295.68	46.54	-0.26	Na- $\text{HCO}_3\text{-Cl}$
2-2	C28	71	21.6	7.53	1950.27	44.7	400.91	20.97	2.45	278.25	78.28	669.48	0	7.94	9.91	239.22	49.30	0	Na- $\text{HCO}_3\text{-Cl}$
	C22	78.8	43.2	8.21	1830.68	44.5	383.68	10.48	1.47	264.13	78.28	592.23	20.25	7.71	9.62	227.74	47.46	0.03	Na- $\text{HCO}_3\text{-Cl}$
	C30	57.6	2.2	6.89	1915.04	43.8	397.84	17.74	0.98	280.05	84.07	581.93	0	7.92	9	302.5	46.54	1.17	Na- $\text{HCO}_3\text{-Cl}$
	C27	70	0.0	7.38	1929.03	42	390	11.03	2.2	271.9	79.24	569.06	0	7.49	9.96	362.15	47.46	1.74	Na- $\text{HCO}_3\text{-Cl}$
	C29	62.6	43.2	7.4	1980.45	37.84	399.6	20.97	2.93	272.6	76.34	623.13	0	7.89	9.42	344.34	45.61	1.93	Na- $\text{HCO}_3\text{-Cl}$
	C2	77.6	86.4	8.1	1922.72	40.18	399	11.4	1.47	272.6	70.2	587.08	0	8.11	9.63	328.86	48.38	1.43	Na- $\text{HCO}_3\text{-Cl}$
3	C14	70	2.2	7.62	1828.63	40.6	387.28	22.58	5.65	272.6	123.69	589.66	0	8.09	10.6	227.13	48.00	0.37	Na- $\text{HCO}_3\text{-Cl}$
	C16	66.2	21.6	7.6	1943.51	38.42	397.62	12.9	7.82	272.6	115.96	636	0	7.49	9.8	243.98	49.76	-0.96	Na- $\text{HCO}_3\text{-Cl}$
	C15	62	2.2	7.7	1865.26	38.7	355.9	22.58	5.86	254.24	96.63	602.53	0	7.42	9.45	276.96	47.96	-1.05	Na- $\text{HCO}_3\text{-Cl}$
	C8	67.8	2.2	7.3	1925.16	37.6	375.98	19.35	10.76	262.72	104.37	641.15	0	7.66	9.43	261.76	47.92	-0.78	Na- $\text{HCO}_3\text{-Cl}$
	C12	68.8	21.6	7.28	1878.22	40.2	384.12	11.29	8.8	268.37	98.57	620.56	0	7.93	10.4	225.94	49.76	-0.43	Na- $\text{HCO}_3\text{-Cl}$
	C9	58.8	21.6	6.6	1931.58	39.2	372.1	17.74	7.82	266.95	92.77	610.26	0	7.14	9.8	307.31	49.76	-0.59	Na- $\text{HCO}_3\text{-Cl}$
	C17	61.4	21.6	7.17	1914.32	41.5	370.9	11.29	5.86	262.72	104.37	593.52	0	7.78	10.8	312.17	47.92	-1.32	Na- $\text{HCO}_3\text{-Cl}$
	C13	74.6	32.4	7.42	1881.16	36.4	377.82	19.35	7.82	266.95	108.23	626.99	0	7.29	10.2	228.16	47.92	-1.41	Na- $\text{HCO}_3\text{-Cl}$
	C10	73	0.0	7.18	1965.03	38.2	375.78	16.13	6.85	269.78	105.1	602.53	0	4.12	9.8	325.78	51.60	-1.29	Na- $\text{HCO}_3\text{-Cl}$

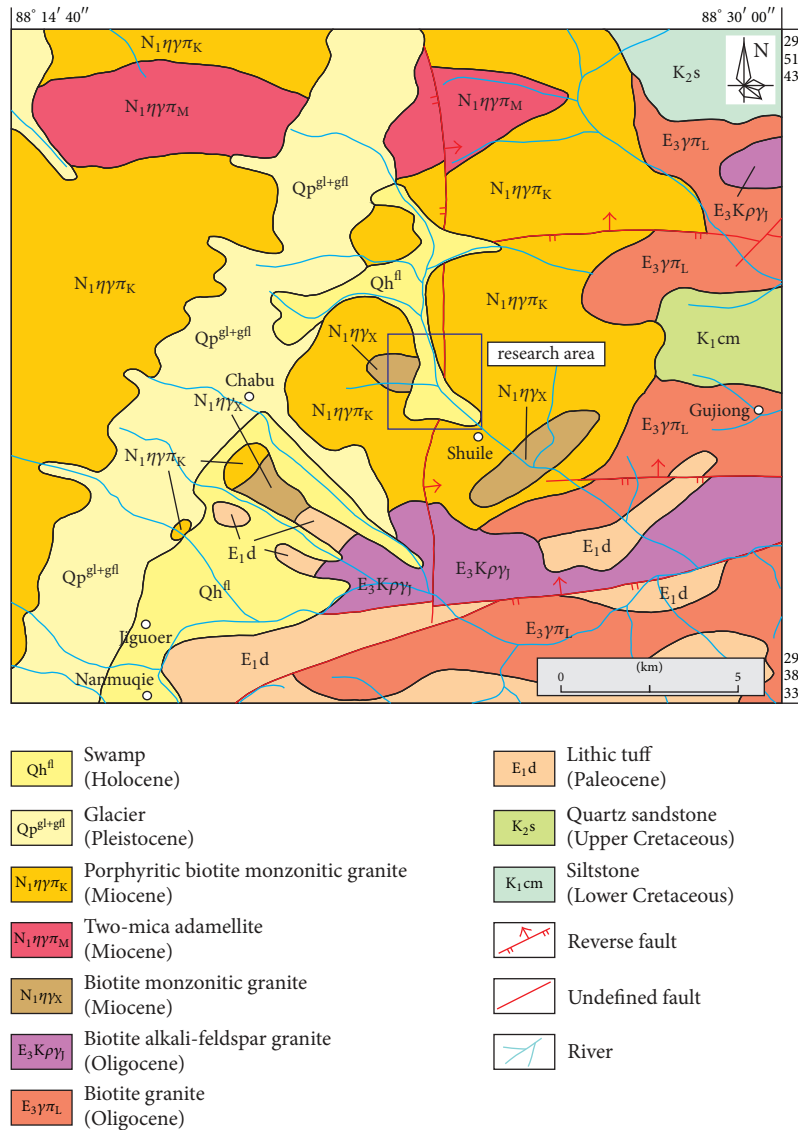


FIGURE 2: Geological map of the research area.

the Chinese government (DZ/T 0064-1993). The concentrations of major cations and trace elements were detected using inductively coupled plasma atomic emission spectroscopy (ICP-AES) (ICAP-6300) and inductively coupled plasma mass spectrometry (ICP-MS 7500C), respectively, while the concentrations of major anions were measured using ion chromatography (DX-120).

The ion charge imbalances for the water samples were calculated using the program AquaChem, and the results showed that all of the samples have a charge imbalance less than $\pm 5\%$ (Table 1). Values in this range are usually accepted as valid and can support the reliability of the data used in this work [25–27].

In this work, all the samples were divided into three groups by cluster analysis of the major elements; then the hydrochemical characteristics, emerging temperatures, and mass flow rate of each group were compared. The

temperatures of the geothermal reservoirs were estimated using silica and cation geothermometers, and the optimum temperature of each sample was selected by taking into account the measured emerging temperature and the mass flow rate of the corresponding spring. To verify the reliability of the chemical geothermometers, the silica-enthalpy mixing models were applied to estimate the geothermal reservoir temperatures and identify mixing processes. The varying pattern of geothermal reservoir temperatures was explored and the major ascending zone was delineated using contour maps. Based on the aforementioned work, different cooling processes of ascending geothermal fluids were speculated, and the temperature of the deep parent fluid was estimated by integrating the hydrochemical characteristics with an enthalpy-chloride graph. The methodologies of the main methods and models applied in this work are described as follows.

TABLE 2: Calculation formulas of chemical geothermometers used in this work.

Geothermometer	Calculation formula	Reference
Chalcedony (no loss of steam)	$t = 1032/(4.69 - \log \text{SiO}_2) - 273.15$	Fournier (1977)
Chalcedony (maximum steam loss)	$t = 1264/(5.31 - \log \text{SiO}_2) - 273.15$	
Quartz (no loss of steam)	$t = 1309/(5.19 - \log \text{SiO}_2) - 273.15$	
Quartz (maximum steam loss)	$t = 1522/(5.75 - \log \text{SiO}_2) - 273.15$	
Na-K-Ca	$t = 1647/(\log(\text{Na}/\text{K}) + \beta(\log(\sqrt{\text{Ca}}/\text{Na}) + 2.06) + 2.47) - 273.15$ $\beta = 4/3$ (when $t < 100^\circ\text{C}$) or $\beta = 1/3$ (when $t > 100^\circ\text{C}$)	Fournier (1981)
Na/K	$t = 1217/(\log(\text{Na}/\text{K}) + 1.483) - 273.15$	Giggenbach (1988)
K/Mg	$t = 4410/(13.95 - \log(K^2/\text{Mg})) - 273.15$	

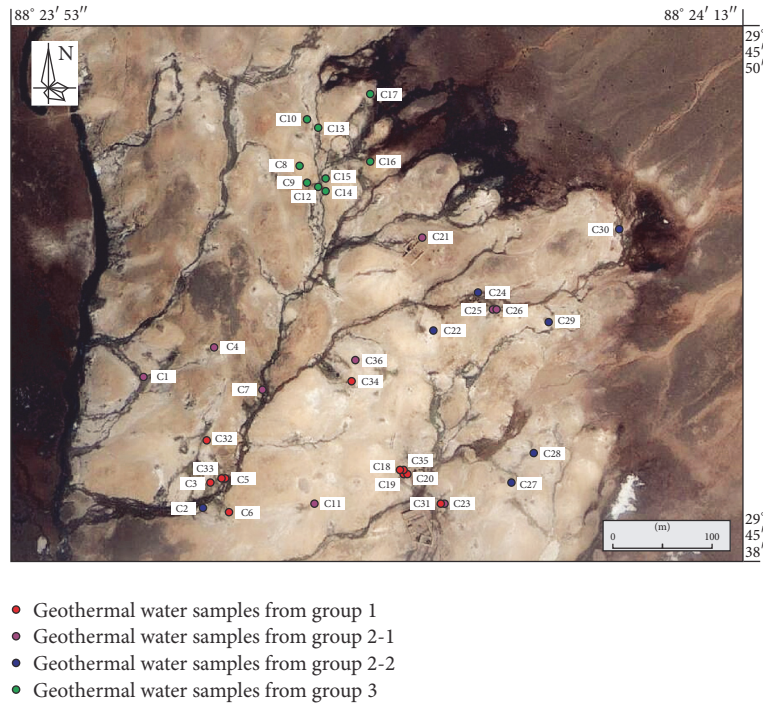


FIGURE 3: Sampling locations in the research area. The samples are colored according to the results of cluster analysis mentioned in “Cluster Analysis.”

3.1. Cluster Analysis. As one of the multivariate statistical methods, cluster analysis (CA) is a convenient and effective means to explore geochemical patterns and interpret hydrochemical characteristics [28]. Cluster analysis was used as an analysis of variance approach (hierarchical cluster) to measure the distance between variable clusters, attempting to minimize the sum of squares of any two clusters that could be formed at each step (square euclidean distance) [29]. Hydrochemical data with similar properties were clustered in a group. In this study, the contents of the major elements, including K, Na, Ca, Mg, Cl, SO_4 , HCO_3 , and CO_3 , were considered to evaluate the characteristics of the geothermal spring samples using the average linkage hierarchical method, which is designed to optimize the minimum variance within groups. The similarities among samples were measured using the squared euclidean distance method [30]. To avoid misclassifications arising from the different orders

of magnitude of the variables, the variances for each variable were sourced from a previous study [31, 32].

3.2. Chemical Geothermometer. Chemical geothermometers were applied to estimate the temperatures of the geothermal reservoirs, including a silica geothermometer (the solubility of silica changes as a function of temperature and pressure) and a cation geothermometer (the equilibrium constants for exchange and alteration reactions are temperature-dependent). The formulas for the calculations used in this research are listed in Table 2.

3.3. Mixing Models. The silica-enthalpy mixing model was applied in this research to estimate the temperatures of geothermal reservoirs and identify mixing processes [19, 33, 34]. In this model, enthalpy is used as a coordinate rather than a temperature, because the combined heat contents of

two waters at different temperatures are conserved when the waters are mixed, but the combined temperatures are not [35]. In the silica-enthalpy model, the silica concentrations of the analyzed samples are plotted against their corresponding on-site enthalpies. The enthalpy values are determined using international steam tables [36]. For application to emerging geothermal samples, two end-member fluids were considered: a cold groundwater sample and an initial deep geothermal water. The point of the initial deep geothermal water can be obtained using two different methods. For the situation in which no steam is lost before mixing, one plots the silica and heat contents (enthalpies) of the cold and emerging spring waters as two points and then draws a straight line through these points to intersect the quartz solubility curve; intersection A_1 then provides the original silica content and enthalpy of the deep hot water. For the situation in which the maximum amount of steam is lost from the hot water before mixing, one plots the silica and heat contents of the cold and emerging spring waters as two points, draws a straight line through the points, and extends that line to intersect the vertical line from the enthalpy values of 419 J/g (corresponding to 100°C, the boiling point of water) and subsequently from this intersection point moves horizontally to the maximum steam loss curve and then moves vertically to intersect the quartz solubility curve. The original silica content and enthalpy of the deep hot-water component are provided by point A_2 [18].

The enthalpy-chloride model was first proposed by [19] to describe the cooling processes of geothermal fluids during ascent and to estimate the temperature and Cl^- concentration of the deep parent fluid. As in the silica-enthalpy mixing model, in this model enthalpy is also used as a coordinate rather than a temperature. In brief, the Cl^- concentrations of the cold water, steam, and emerging spring waters can be plotted against their corresponding on-site enthalpies. Lines from the emerging spring waters towards the steam point represent the variation in enthalpy and Cl^- content of the liquid water fraction caused by the process of steam separation during passage to the surface. Lines from the emerging spring waters towards the cold water represent the variation in enthalpy and Cl^- content caused by mixing with shallow colder waters during ascent. For samples that are mainly cooled by conduction during ascent, their chloride contents generally will be nearly the same as those of waters from aquifers feeding the springs. By combining the cooling processes of the subsurface geothermal fluids and the reasonable reservoir temperatures, the temperature and salinity of the deep parent fluid can be predicted.

4. Results and Discussion

4.1. Hydrochemical Characteristics

4.1.1. Cluster Analysis. The dendrogram constructed by the software SPSS17.0 shows that all the geothermal samples are divided into three clusters, groups 1, 2, and 3, and group 2 can be further divided into two subclusters (Figure 4). From the sampling location map (Figure 3), it can be seen that the samples of group 1 and group 3 are distributed

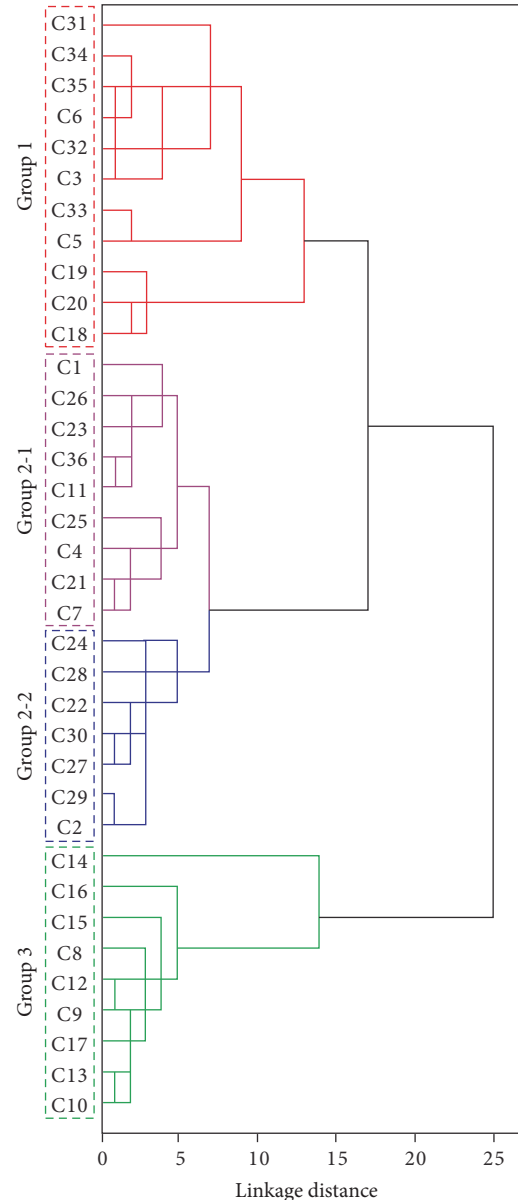


FIGURE 4: Dendrogram showing the results of the cluster analysis performed on the geothermal spring samples from the research area.

in the central part and northern periphery of the sinter platform, respectively. Samples of group 2 are scattered in the transitional zone between groups 1 and 3, with subgroup 2-1 distributed closer to the central part, where its hydrochemical characteristics are more similar to those of group 1.

4.1.2. Indicative Significance of Geothermal Fluid Composition.

The hydrochemical characteristics of all water samples are summarized in Table 1. Cold groundwater in the research area is of the HCO_3 -Ca-Na type. All the geothermal spring samples contain Na^+ as the predominant cation, while the proportions of Na^+ contents decrease from groups 1, 2, and 3 to the ambient cold groundwater. The predominant anions of the geothermal spring samples from different groups

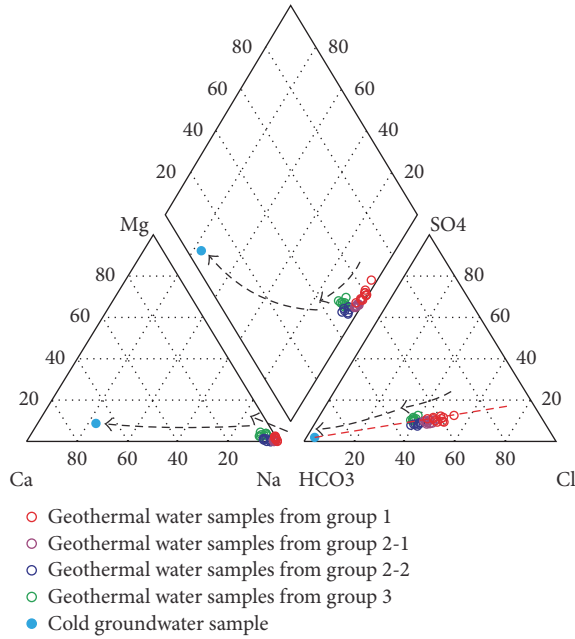


FIGURE 5: Piper diagram of geothermal spring samples in the research area.

differ from each other. Samples of group 1 contain Cl^- and HCO_3^- as the predominant and subordinate anions, while the opposite is found in group 3. As the transitional group between groups 1 and 3, most samples of group 2 contain HCO_3^- as the predominant anion and Cl^- as the subordinate anion (Figure 5).

On the triangular plot of $\text{Cl}-\text{SO}_4-\text{HCO}_3 + \text{CO}_3$ (Figure 5) and the $\text{Na}-\text{K}-\text{Mg}$ diagram (Figure 6), a linear relationship of all the samples is presented and was found to be one main indicator of mixing between geothermal fluids and shallow cooler waters. Furthermore, samples of groups 1, 2, and 3 draw near to cold groundwater, indicating that there is a gradually increasing mixture of geothermal waters and cooler shallow water from group 1 to group 2 to group 3.

Figure 6 shows that almost all the samples can be classified as immature waters. According to [15], high-temperature well discharges plot on the full equilibrium line and somewhat above actually measured deep temperatures, while the associated spring waters are off the full equilibrium line and shift to lower temperatures in the $\text{Na}-\text{K}-\text{Mg}$ diagram. This indicates acquisition of Mg by spring waters in response to decreasing temperatures is faster than that of Na . Therefore, on the premise of insufficient information, calculation results of geothermal spring samples based on the $\text{Na}-\text{K}-\text{Mg}$ system still bear a certain significance.

4.2. Temperatures of Geothermal Reservoirs

4.2.1. Geothermometric Applications. The temperatures of the geothermal reservoirs were estimated using a silica geothermometer [18], $\text{Na}-\text{K}-\text{Ca}$ and Na/K geothermometers [37], and K/Mg geothermometer [15]. The calculation results are listed in Table 3.

4.2.2. Quartz Geothermometer. Silica geothermometers contain quartz and chalcedony geothermometers which are based on the solubility of silica changing as a function of temperature and pressure. The quartz geothermometer is more applicable than is the chalcedony geothermometer in the research area because quartz controls the dissolved silica concentration at temperatures higher than 150°C [18, 38, 39], which is the case in the research area where all of the quartz results and most of the chalcedony results are above 150°C . Therefore, the calculation results of the quartz geothermometer are adopted in this research.

The temperatures of the geothermal reservoirs estimated using the quartz geothermometer were selected for the optimum temperature of each sample (i.e., the calculated temperatures were chosen between the values of the maximum steam loss and no loss of steam) taking into account the measured emerging temperature and the mass flow rate of the corresponding spring [40]. Waters that flow at relatively large mass rates directly to the surface will cool adiabatically, and the emerging spring water will be at or slightly above the boiling temperature for the prevailing atmospheric pressure [41]. For these waters, the quartz geothermometer with the maximum steam loss was applied. Boiling generally occurs when the water temperatures reach 80°C at high altitudes in the research area [42, 43], and, following [44], 30 L/min is subjectively considered as a large mass flow rate for the spring systems. For the geothermal spring samples, of which the emerging temperatures are above 70°C and the mass flow rates are higher than 30 L/min, the calculated results from the quartz geothermometer with maximum steam loss were adopted. Otherwise, the calculated results from the quartz geothermometer with no loss of steam were adopted, as waters that flow to the surface at relatively slow rates of mass movement and that show emerging spring temperatures much lower than the maximum temperature in the convecting hydrothermal system are generally cooled by conduction. The high mass flow rates usually keep pace with the high emerging temperatures; therefore, for a small part of samples that lack mass flow rate data, the optimum temperatures were only selected by the measured emerging temperature. The optimum temperature of each spring sample selected from the quartz geothermometers is in bold font in Table 3. The adoption rates of the results from the quartz geothermometer with maximum steam loss gradually decreased from group 1 to group 3.

4.2.3. Cation Geothermometer. The $\text{Na}-\text{K}-\text{Ca}$, Na/K , and K/Mg geothermometers were also used to estimate geothermal reservoir temperatures. When the $\text{Na}-\text{K}-\text{Ca}$ geothermometer is used to estimate subsurface temperatures, $\log(\sqrt{\text{Ca}}/\text{Na})$ first needs to be calculated. When all the results from the water samples are negative, geothermal reservoir temperatures can be calculated using the β value of 1/3 [45]. These results are listed in Table 3.

For the samples of group 1, the results from the Na/K geothermometer are consistent with those from the $\text{Na}-\text{K}-\text{Ca}$ geothermometer, as the Ca contents are generally lower than 3 mg/L. For the samples of groups 2 and 3, the results from the Na/K geothermometer are increasingly higher

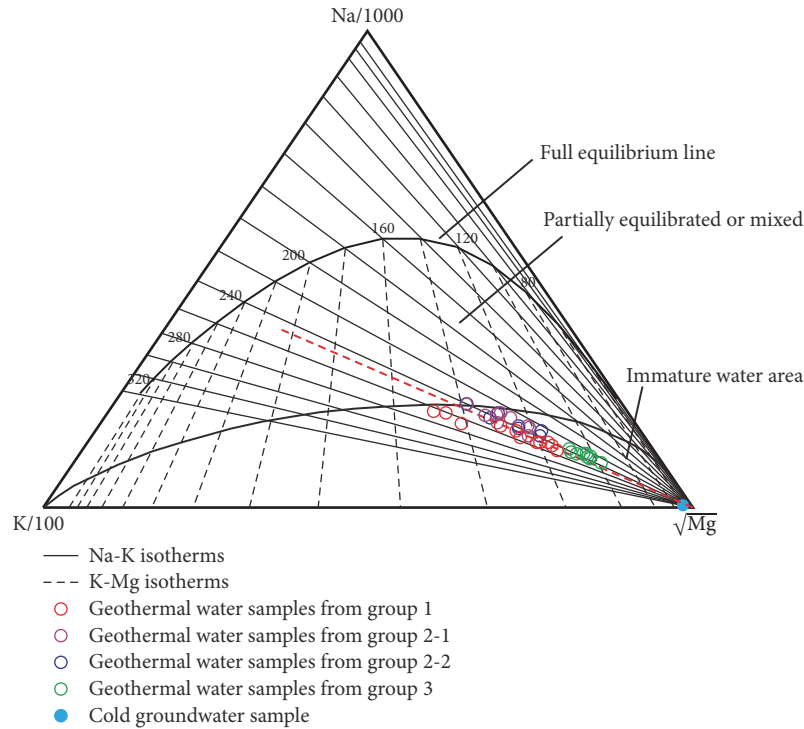


FIGURE 6: Na-K-Mg diagram for all the geothermal spring samples in the research area [15].

than those from the Na-K-Ca geothermometer, as the Ca contents of groups 2 and 3 are relatively higher, especially for the samples of subgroup 2-2 and group 3, where the Ca contents reach 10–23 mg/L. The Na-K-Ca geothermometer makes a correction for the Ca content of the water, thereby removing some ambiguity; thus, the results from the Na-K-Ca geothermometer for the Ca-rich samples of groups 2 and 3 could be adopted.

4.2.4. Silica-Enthalpy Mixing Model. In the silica-enthalpy mixing model, except for samples C3, C33, C34, and C35 from group 1, the extrapolations of the lines through other data points of the cold and emerging spring waters have no intersection point with the quartz solubility curve, indicating that most of the geothermal fluids in the research area have not mixed with shallow cooler water during ascent to the surface (Figure 7). Regarding the deep geothermal waters that are not mixed with shallow cooler water during ascent, the connection lines of the sampling points and the steam point are extended to intersect the quartz solubility curve at points B and C (the upper and lower limits). The corresponding temperatures of the geothermal reservoirs are 176–205°C; however, this method underestimated the temperatures of some geothermal samples from group 2 and group 3, as they are mainly cooled by conduction during ascent to the surface. The results calculated using the quartz geothermometer with no loss of steam and the Na-K-Ca geothermometer listed in Table 3 are more optimal.

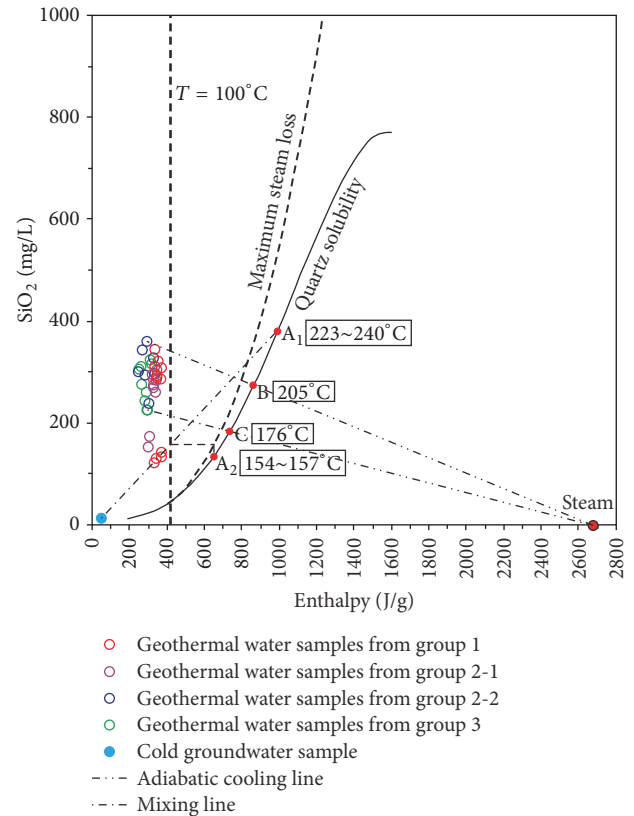


FIGURE 7: Silica-enthalpy mixing models of geothermal spring samples in the research area.

TABLE 3: Calculation results of geothermal reservoir temperatures in the research area (T in $^{\circ}\text{C}$, except for mass flow rate in L/min). The results in bold font are the optimum temperatures selected from the quartz geothermometers taking into account the measured emerging temperatures and the mass flow rates of the spring samples.

Group	Sample ID	Emerging temperature	Mass flow rate	Quartz (maximum steam loss)	Quartz (no loss of steam)	Na-K-Ca	Na/K	K/Mg
1	C31	87.3	1842.6	193.83	211.80	235.20	240.51	126.90
	C34	87.2	1311.6	152.31	160.68	235.52	236.34	115.83
	C35	78.6	70.32	142.98	149.45	235.08	236.62	121.90
	C6	81.4	172.8	190.67	207.84	230.93	235.71	131.88
	C32	87	98.16	189.34	206.19	238.57	235.32	121.02
	C3	80.8	21.6	146.32	153.46	229.30	233.48	127.54
	C33	87.3	17.34	147.35	154.70	231.68	231.45	116.93
	C5	81.8	151.2	189.79	206.74	225.24	228.35	118.11
	C19	78.7	324	194.34	212.45	244.19	248.12	147.29
	C20	83.2	496.8	196.27	214.87	250.26	255.90	143.63
	C18	79.2	64.8	200.74	220.49	249.05	253.13	150.87
2-1	C1	70.4	-	153.95	162.66	211.32	216.33	127.67
	C26	76	-	191.10	208.39	210.78	217.46	122.57
	C23	81.6	-	193.04	210.81	211.57	214.96	122.73
	C36	77.6	432	185.61	201.54	211.98	216.20	130.49
	C11	80.6	216	188.66	205.34	214.87	220.28	131.90
	C25	77.2	-	188.87	205.59	219.03	232.32	132.47
	C4	72.2	0.216	160.59	170.73	227.19	230.56	123.75
	C21	77.4	-	186.62	202.78	213.01	224.59	140.15
	C7	80	-	183.54	198.95	219.72	229.37	135.64
2-2	C24	66	6.48	190.99	208.25	201.80	222.87	120.04
	C28	71	21.6	178.32	192.49	202.59	226.49	126.36
	C22	78.8	43.2	191.42	208.78	205.34	230.03	134.41
	C30	57.6	2.16	192.40	210.01	203.34	225.37	140.61
	C27	70	-	203.80	224.36	206.39	223.42	126.09
	C29	62.6	43.2	200.55	220.25	192.97	212.35	118.47
	C2	77.6	86.4	197.62	216.56	202.48	217.58	131.09
	C14	70	2.16	175.32	188.79	197.54	221.06	96.58
3	C16	66.2	21.6	179.47	193.91	198.74	214.06	104.61
	C15	62	2.16	187.00	203.27	198.03	224.27	108.92
	C8	67.8	2.16	183.62	199.06	195.72	216.99	99.59
	C12	68.8	21.6	175.02	188.41	204.12	220.91	104.22
	C9	58.8	21.6	193.37	211.23	199.40	221.49	105.18
	C17	61.4	21.6	194.35	212.45	207.46	226.81	110.94
	C13	74.6	32.4	195.54	213.95	193.66	213.81	103.10
	C10	73	-	197.03	215.82	198.43	218.39	106.32

For samples C3, C33, C34, and C35 from group 1, different intersections were provided by the two methods mentioned in “Materials and Methods” (Figure 7). If there is no steam separation before mixing, the intersection point A_1 provides the temperature range of 223–240 $^{\circ}\text{C}$; however, if steam separation occurs before mixing, the intersection point A_2 lies within the temperature range of 154–157 $^{\circ}\text{C}$. Obviously, the geothermal reservoir temperatures obtained at intersection point A_1 (223–240 $^{\circ}\text{C}$) are more comparable to

those calculated using the Na/K geothermometer. The mixing ratio of cold water with initial deep geothermal water could be calculated by dividing the distance of point A_1 to the cold water by that of point A_1 to the measured emerging water (Table 4).

Therefore, the results of the silica-enthalpy mixing model indicate that most of the geothermal fluids in the research area do not mix with shallow cooler water during ascent to the surface. A few samples from group 1 experience mixing

TABLE 4: Parameters of geothermal spring samples that experience mixing during ascent obtained from silica-enthalpy mixing models (T in $^{\circ}\text{C}$).

Sample ID	Na/K	Maximum steam loss	No loss of steam	Mixture ratio of cold water (%)
C34	236.34	240.76	156.61	66.9
C35	236.62	232.68	154.71	69.7
C3	233.48	240.29	155.90	69.7
C33	231.45	227.21	154.23	64.8

during ascent and the mixture ratios of cold water with initial deep geothermal water are approximately 65%–70%. The temperatures of the geothermal reservoirs are approximately 223–240 $^{\circ}\text{C}$ with no steam separation before mixing, which are consistent with the corresponding Na/K results.

4.2.5. Selected Reservoir Temperatures. The calculated results from the K/Mg geothermometer for groups 1, 2, and 3 are 115.83–150.87 $^{\circ}\text{C}$, 96.58–110.94 $^{\circ}\text{C}$, and 118.47–140.61 $^{\circ}\text{C}$, respectively, which are significantly lower than those of the quartz and Na/K (Na-K-Ca) results (Table 3). The system K-Mg approaches mineral-fluid equilibrium at low temperatures because of the obviously rapid response to variations in temperature, which reinforce the view that the subsurface geothermal fluids in the research area generally mix with cooler water in the reservoirs [46, 47].

The spring samples from group 1 and subgroup 2-1 fall significantly below the “equal temperature” line of Figure 8, especially for the samples from group 1, of which the results estimated from Na/K geothermometer are much higher than that from the quartz geothermometer. The Na/K (Na-K-Ca) results of group 1 and subgroup 2-1 are 228–256 $^{\circ}\text{C}$ and 215–232 $^{\circ}\text{C}$. Except for a few samples that mixed with considerable amount of shallow cold water during ascent, the quartz results of group 1 and subgroup 2-1 are 189–201 $^{\circ}\text{C}$ and 184–193 $^{\circ}\text{C}$, respectively. When initial temperatures are above approximately 210–230 $^{\circ}\text{C}$, silica is likely to precipitate during ascent owing to relatively rapid rates of reaction at higher temperatures and the attainment of supersaturation with respect to amorphous silica as the solution cools. This silica precipitation may coat the channels and prevent other water–rock reactions, particularly those involving Na, K, and Ca. In this situation, the Na/K(Na-K-Ca) geothermometer could provide higher and more reliable results than those of the silica geothermometer [19, 48].

The quartz results of samples C3, C33, C34, and C35 are 143–155 $^{\circ}\text{C}$, which are significantly lower than those of the other samples in the same group. According to the silica-enthalpy mixing models, the temperatures of deep initial fluids are consistent with the corresponding Na/K results, and the mixture ratios of cold water with initial deep geothermal water are approximately 65%–70%. Therefore, it can be speculated that, before significant precipitation of silica, these samples mixed with a considerable amount of shallow cold water during ascent leading to lower quartz results, which could be corrected using the silica-enthalpy mixing model.

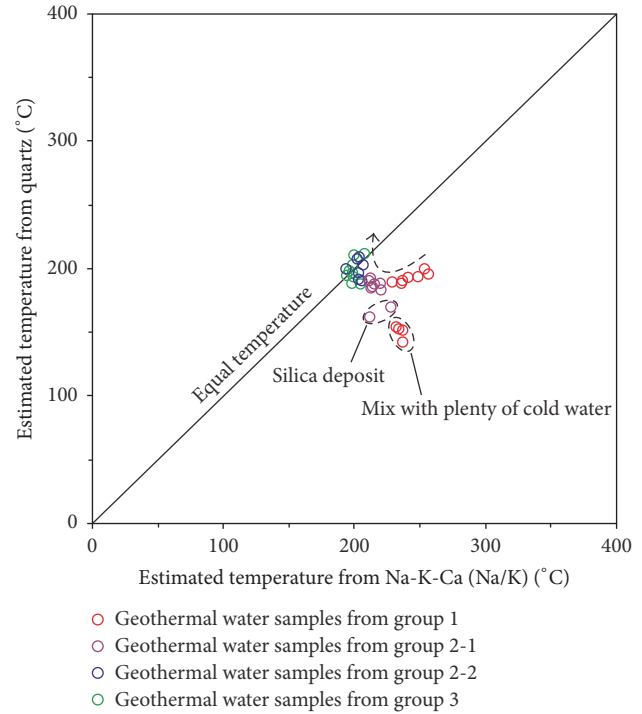


FIGURE 8: Comparison of geothermal reservoir temperatures estimated using quartz and Na/K (Na-K-Ca) geothermometers in the research area. Na/K results were applied to samples of group 1, and Na-K-Ca results were applied to samples of groups 2 and 3.

The quartz results of samples C1 and C4 from subgroup 2-1 are obviously lower than those of the other samples in the same group, while their Na-K-Ca temperatures are comparable to the others. The lower quartz results are a result of mixing with cold water as shown in the silica-enthalpy mixing models. The measured emerging temperatures and mass flow rates of these two samples are much lower than those of other samples in the same group, which indicate that they mainly experienced conductive cooling during ascent. Therefore, the lower SiO_2 contents are probably due to silica deposition in the case of high initial temperatures and relatively slower mass flow rates of the geothermal fluids.

The spring samples from group 3 and subgroup 2-2 plot near the “equal temperature” line. The results of the quartz geothermometer (188–212 $^{\circ}\text{C}$) agree well with those of the Na-K-Ca geothermometer (193–207 $^{\circ}\text{C}$), suggesting that the geothermal waters of group 3 and subgroup 2-2 reached a fluid–rock chemical equilibrium during ascent to the surface [15, 49]. Some samples plot slightly above the “equal temperature” line which might be a result of the effects of slight evaporation. Samples from group 3 and subgroup 2-2 generally featured low measured emerging temperatures, slow mass flow rates, and high TDS, indicating they mainly undergo conductive cooling during ascent to the surface (Figure 9). Therefore, both the quartz and Na-K-Ca geothermometers could provide reasonable temperatures of geothermal reservoirs.

In summary, for most samples from group 1 and subgroup 2-1, an Na/K or Na-K-Ca geothermometer could be used to

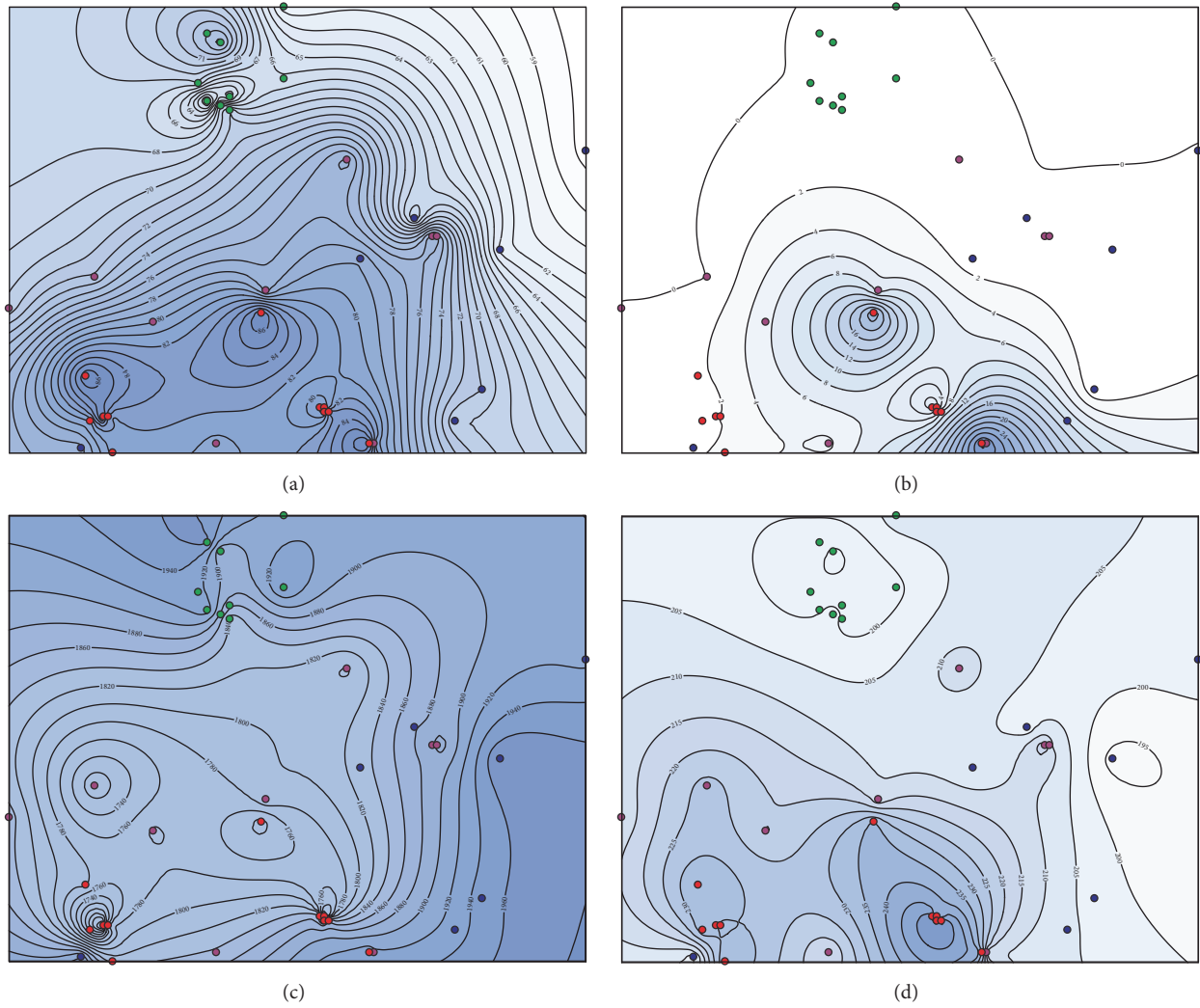


FIGURE 9: Contour maps of the geothermal spring samples in the research area. Figures 9(a), 9(b), and 9(c) are the contour maps of measured emerging temperatures, mass flow rates, and TDS of the spring samples, respectively; Figure 9(d) is the contour map of reasonable temperatures of geothermal reservoirs determined in “Selected Reservoir Temperatures.”

estimate reasonable temperatures of geothermal reservoirs, while, for the samples from group 1 mixing with a considerable amount of shallow cold water during ascent, a silica-enthalpy plot could also be applied to obtain reasonable temperatures. For samples from group 3 and subgroup 2-2, both the quartz and Na-K-Ca geothermometers could provide reasonable results for the geothermal reservoirs.

4.3. Variation Characteristics of Geothermal Reservoir Temperatures. Contour maps were applied to measure emerging temperatures, mass flow rates, and TDS of the spring samples and the reasonable temperatures of geothermal reservoirs as determined in “Selected Reservoir Temperatures.” This shows that the measured emerging temperatures and mass flow rates gradually decrease from the central part to the peripheral belt (Figures 9(a) and 9(b)), while the opposite change is found with TDS (Figure 9(c)). This indicates that, from the central part to the peripheral belt, the major cooling

processes of the subsurface geothermal fluids gradually transform from adiabatic boiling to conduction. Figure 9(d) shows an increasing trend of geothermal reservoir temperatures from the center to the periphery. The point with the highest temperature (256°C) appears in the east-central part of the research area, of which the emerging temperature and mass flow rate are relatively high, and the TDS is obviously lower. Therefore, this point might be the main up-flow zone of the subsurface geothermal fluids.

On the whole, the measured emerging temperatures, mass flow rates, and TDS of the spring samples and the reasonable temperatures of geothermal reservoirs change regularly from the central part to the peripheral belt, which are consistent with the distribution of the sinter platform and are mainly controlled by the north-south trending fracture.

4.4. Cooling Process of Subsurface Geothermal Fluids. As shown in the piper diagram (Figure 5), the Na-K-Mg triangular plot (Figure 6), and contour maps (Figure 9), from

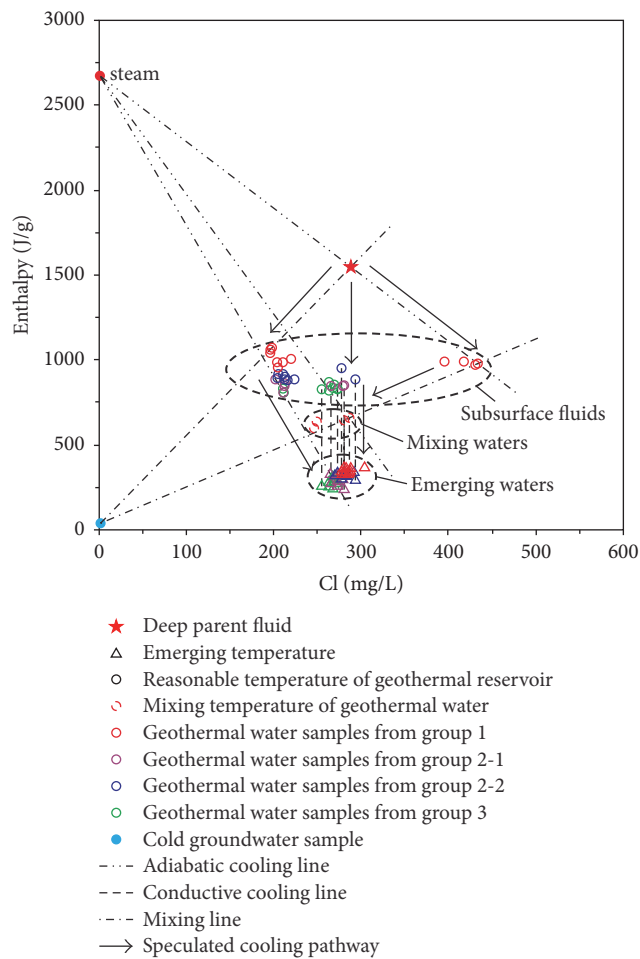


FIGURE 10: Enthalpy-chloride plot for the geothermal spring samples of the research area.

the central part (represented by group 1) to the peripheral belt (represented by group 3), the major cooling processes of the subsurface geothermal fluids gradually transform from adiabatic to conductive. Furthermore, most of the geothermal fluids in the research area do not mix with shallow cooler water during ascent to the surface, except for a few samples from group 1. Therefore, on the enthalpy-chloride plot of geothermal water samples from the research area (Figure 10), for most of the geothermal spring samples from group 1 and subgroup 2-1, an Na-K-Ca or Na/K geothermometer was used to estimate the subsurface temperatures. In addition, the results of the quartz geothermometers were used to represent mixing temperatures for the mixed samples from group 1, which could differentiate the various processes interfering with the evolution of deep fluids. For the geothermal spring samples from group 3 and subgroup 2-2, although both the quartz and Na-K-Ca geothermometers could provide reasonable temperatures of the geothermal reservoirs, the subsurface temperatures were uniformly provided by the Na-K-Ca geothermometer, as the cation geothermometer is barely affected by mixing with cold water or boiling.

The major cooling process of each sample was determined using the measured emerging temperature and the mass flow

rate of the corresponding spring, just as the selection process of optimal temperature was estimated using quartz geothermometers. For samples that mainly experienced adiabatic cooling while ascending, straight lines were extended from the sampling points to S (the steam point at zero chloride), marking the enthalpies of the subsurface geothermal fluids along the corresponding lines to obtain the locations of subsurface geothermal fluids on the enthalpy-chloride plot. For the samples that are mainly cooled by conduction during ascent, their chloride contents generally will be nearly the same as that of the waters in the aquifers feeding the springs [18, 50, 51]. The reasonable temperatures of the geothermal reservoirs are plotted directly above the sampling points. For the samples from group 1 that mixed with a considerable amount of shallow colder water during ascent, their sampling and mixing temperatures were estimated using the quartz geothermometer, and they are used to mark the temporary points on the graph. Then, these points are connected to the cold groundwater point and combined with the Na/K temperatures to obtain the locations of subsurface geothermal fluids on the enthalpy-chloride plot.

According to the enthalpy-chloride plot, the deep parent fluid of the Chabu geothermal field is estimated to have a Cl^- concentration of 290 mg/L and an enthalpy of 1550 J/g (water temperature of 369°C). The deep parent fluid mainly experienced adiabatic boiling, conduction, or mixing with cooler water, to form the subsurface geothermal fluids in the reservoirs. Most of the subsurface geothermal fluids emerging on the surface as hot or boiling springs are mainly cooled by adiabatic boiling or conduction. In addition to adiabatic or conductive cooling, a few subsurface geothermal fluids mix with a considerable amount of shallow colder water during ascent and emerge with unsaturated quartz.

5. Conclusions

In this study, the geothermal spring samples were collected systematically from the north-central part of the sinter platform, which holds the most concentrated and intense hydrothermal manifestations in the Chabu high-temperature geothermal system. All the geothermal spring samples were divided into three groups (group 2 could be further divided into two subgroups) using cluster analysis of major elements. Samples of group 1 and group 3 were distributed in the central part and northern periphery of the sinter platform, respectively, while samples of group 2 were scattered in the transitional zone between groups 1 and 3. On the triangular plot of $\text{Cl-SO}_4\text{-HCO}_3 + \text{CO}_3$ and the Na-K-Mg diagram, a linear relationship of all the samples was presented, which was found to be the one main indicator of mixing between geothermal fluids and shallow cooler waters in the geothermal reservoirs. Furthermore, samples of groups 1, 2, and 3 draw near to cold groundwater, indicating that there is a gradually increasing mixture of geothermal waters and shallow cooler water from group 1 to group 2 to group 3.

The optimal quartz temperature of each sample was selected by considering the measured emerging temperature and the mass flow rate of the corresponding spring. Then, the reasonable reservoir temperatures and the mixing processes

of the subsurface geothermal fluids in the research area were defined by combining the calculated results of the quartz and cation geothermometers with the silica-enthalpy mixing models. For most samples from group 1 and subgroup 2-1, the Na/K or Na-K-Ca geothermometer could be used to estimate reasonable reservoir temperatures, as silica is likely to precipitate during ascent owing to relatively rapid rates of reaction at high temperatures ($>210^{\circ}\text{C}$). For the samples from group 1 mixing with shallow cold water during ascent, a silica-enthalpy plot could also be applied to obtain reasonable reservoir temperatures. For samples from group 3 and subgroup 2-2, both the quartz and Na-K-Ca geothermometers could provide reasonable results for the geothermal reservoirs. Contour maps were applied to measure emerging temperatures, mass flow rates, and TDS of the spring samples and reasonable reservoir temperatures. These indicated that, from the central part to the peripheral belt, the major cooling processes of the subsurface geothermal fluids gradually transform from adiabatic boiling to conduction. These also showed an increasing trend of geothermal reservoir temperatures from the center to the periphery. The point with the highest temperature (256°C) appears in the east-central part of the research area, which might be the main up-flow zone for the subsurface geothermal fluids.

The cooling processes of the subsurface geothermal fluids in the research area can be shown on an enthalpy-chloride plot. The deep parent fluid for the Chabu geothermal field has a Cl^{-} concentration of 290 mg/L and an enthalpy of 1550 J/g (water temperature of 369°C). The deep parent fluid ascends to high-temperature geothermal reservoirs and forms subsurface geothermal fluids mainly cooled by adiabatic boiling, conduction, or mixing with cooler water. Most of the subsurface geothermal fluids emerging on the surface as hot or boiling springs are mainly cooled by conduction or adiabatic cooling, though some fraction of the geothermal waters mixed with a considerable amount of shallow colder water during ascent and emerged with unsaturated quartz.

Conflicts of Interest

The authors declare that they have no conflicts of interest.

Acknowledgments

This work was financially supported by the Basal Research Fund from the Institute of Hydrogeology and Environmental Geology, Chinese Academy of Geological Sciences (no. SK201501, no. SK201606) and the National Natural Science Foundation of China (no. 41672249, no. 41502249). The manuscript benefited from numerous constructive comments by Nvdawa and Chuanlu.

References

- [1] P. Tapponnier and P. Molnar, "Active faulting and tectonics in China," *Journal of Geophysical Research: Atmospheres*, vol. 82, no. 20, pp. 2905–2930, 1977.
- [2] Z. Q. Hou and Z. Q. Li, "Possible location for underthrusting front of the Indus continent: constraints from helium isotope of the geothermal gas in southern Tibet and eastern Tibet," *Acta Geologica Sinica*, vol. 78, no. 4, pp. 482–493, 2004 (Chinese).
- [3] Z. Q. Li, Z. Q. Hou, F. J. Nie, and X. J. Meng, "Characteristic and distribution of the partial melting layers in the upper crust: evidence from active hydrothermal fluid in south Tibet," *Acta Geologica Sinica*, vol. 79, no. 1, pp. 68–76, 2005 (Chinese).
- [4] L. D. Brown, W. Zhao, K. D. Nelson et al., "Bright spots, structure, and magmatism in southern Tibet from INDEPTH seismic reflection profiling," *Science*, vol. 274, no. 5293, pp. 1688–1690, 1996.
- [5] P. Zhao, J. Jin, H. Z. Zhang, J. Duo, and T. Liang, "Chemical composition of thermal water in the Yangbajing geothermal field, Tibet," *Scientia Geologica Sinica*, vol. 33, no. 1, pp. 61–72, 1998 (Chinese).
- [6] L. Hoke, S. Lamb, D. R. Hilton, and R. J. Poreda, "Southern limit of mantle-derived geothermal helium emissions in Tibet: Implications for lithospheric structure," *Earth and Planetary Science Letters*, vol. 180, no. 3–4, pp. 297–308, 2000.
- [7] Z. Q. Hou, Z. Q. Li, X. M. Qu et al., "Qinghai-Tibet plateau uplift process since 0.5 Ma—evidence from hydrothermal activity of Gangdise belt," *Science in China Series D*, vol. 44, no. S1, pp. 35–44, 2001 (Chinese).
- [8] P. Zhao, E. J. Xie, J. Dor et al., "Geochemical characteristics of geothermal gases and their geological implications in Tibet," *Acta Petrologica Sinica*, vol. 18, no. 4, pp. 539–550, 2002 (Chinese).
- [9] J. A. Becker, M. J. Bickle, A. Galy, and T. J. B. Holland, "Himalayan metamorphic CO_2 fluxes: quantitative constraints from hydrothermal springs," *Earth and Planetary Science Letters*, vol. 265, no. 3–4, pp. 616–629, 2008.
- [10] W. Zhao, P. Kumar, J. Mechie et al., "Tibetan plate overriding the Asian plate in central and northern Tibet," *Nature Geoscience*, vol. 4, no. 12, pp. 870–873, 2011.
- [11] Q. Guo, "Hydrogeochemistry of high-temperature geothermal systems in China: A review," *Applied Geochemistry*, vol. 27, no. 10, pp. 1887–1898, 2012.
- [12] Q. Guo, D. K. Nordstrom, and R. B. McCleskey, "Towards understanding the puzzling lack of acid geothermal springs in Tibet (China): insight from a comparison with Yellowstone (USA) and some active volcanic hydrothermal systems," *Journal of Volcanology and Geothermal Research*, vol. 288, pp. 94–104, 2014.
- [13] Z. Liu, W. Lin, M. Zhang, E. Xie, Z. Liu, and G. Wang, "Geothermal fluid genesis and mantle fluids contributions in Nimu-Naqu, Tibet," *Earth Science Frontiers*, vol. 21, no. 6, pp. 356–371, 2014 (Chinese).
- [14] P. Stelling, L. Shevenell, N. Hinz, M. Coolbaugh, G. Melosh, and W. Cumming, "Geothermal systems in volcanic arcs: Volcanic characteristics and surface manifestations as indicators of geothermal potential and favorability worldwide," *Journal of Volcanology and Geothermal Research*, vol. 324, pp. 57–72, 2016.
- [15] W. F. Giggenbach, "Geothermal solute equilibria. Derivation of Na-K-Mg-Ca geoindicators," *Geochimica et Cosmochimica Acta*, vol. 52, no. 12, pp. 2749–2765, 1988.
- [16] M. Afsin, D. M. Allen, D. Kirste, U. G. Durukan, A. Gurel, and O. Oruc, "Mixing processes in hydrothermal spring systems and implications for interpreting geochemical data: A case study in the Cappadocia region of Turkey," *Hydrogeology Journal*, vol. 22, no. 1, pp. 7–23, 2014.
- [17] J. X. Li, Q. H. Guo, and Y. X. Wang, "Evaluation of temperature of parent geothermal fluid and its cooling processes during

- ascent to surface: a case study in Rehai geothermal field, Tengchong,” *Earth Science*, vol. 40, no. 9, pp. 1576–1584, 2015 (Chinese).
- [18] R. O. Fournier, “Chemical geothermometers and mixing models for geothermal systems,” *Geothermics*, vol. 5, pp. 41–50, 1977.
 - [19] R. O. Fournier, “Geochemical and hydrologic considerations and the use of enthalpy-chloride diagrams in the prediction of underground conditions in hot-spring systems,” *Journal of Volcanology and Geothermal Research*, vol. 5, no. 1–2, pp. 1–16, 1979.
 - [20] M. P. Asta, M. J. Gimeno, L. F. Auqué, J. Gómez, P. Acero, and P. Lapuente, “Hydrochemistry and geothermometrical modeling of low-temperature Panticosa geothermal system (Spain),” *Journal of Volcanology and Geothermal Research*, vol. 235–236, pp. 84–95, 2012.
 - [21] Ö. Avşar, N. Güleç, and M. Parlaktuna, “Hydrogeochemical characterization and conceptual modeling of the Edremit geothermal field (NW Turkey),” *Journal of Volcanology and Geothermal Research*, vol. 262, pp. 68–79, 2013.
 - [22] Z. M. Zhang, X. Dong, M. Santosh, and G. C. Zhao, “Metamorphism and tectonic evolution of the Lhasa terrane, Central Tibet,” *Gondwana Research*, vol. 25, no. 1, pp. 170–189, 2014.
 - [23] T. L. Han, *Evolution on the Lithospheric Deformation of the Himalayan: Tibetan Active Tectonics*, 1987 (Chinese), Geological Publishing House.
 - [24] Y. Y. Zhao, X. T. Zhao, and Z. B. Ma, “Study on chronology for hot spring typed Cs-deposit of Targjia, Tibet,” *Acta Petrologica Sinica*, vol. 22, no. 3, pp. 717–724, 2006 (Chinese).
 - [25] D. K. Nordstrom, J. W. Ball, R. J. Donahoe, and D. Whittemore, “Groundwater chemistry and water-rock interactions at Stripa,” *Geochimica et Cosmochimica Acta*, vol. 53, no. 8, pp. 1727–1740, 1989.
 - [26] E. Dotsika, D. Poutoukis, and B. Raco, “Fluid geochemistry of the Methana Peninsula and Loutraki geothermal area, Greece,” *Journal of Geochemical Exploration*, vol. 104, no. 3, pp. 97–104, 2010.
 - [27] M. Blasco, L. F. Auqué, M. J. Gimeno, P. Acero, and M. P. Asta, “Geochemistry, geothermometry and influence of the concentration of mobile elements in the chemical characteristics of carbonate-evaporitic thermal systems. The case of the Tiermas geothermal system (Spain),” *Chemical Geology*, vol. 466, pp. 696–709, 2017.
 - [28] J. Wang, R. Zuo, and J. Caers, “Discovering geochemical patterns by factor-based cluster analysis,” *Journal of Geochemical Exploration*, vol. 181, pp. 106–115, 2017.
 - [29] Y.-H. Kao, S.-W. Wang, S. K. Maji et al., “Hydrochemical, mineralogical and isotopic investigation of arsenic distribution and mobilization in the Guandu wetland of Taiwan,” *Journal of Hydrology*, vol. 498, pp. 274–286, 2013.
 - [30] J. C. Davis, *Statistics and Data Analysis in Geology*, John Wiley & Sons, Inc., New York, NY, USA, 2nd edition, 1990.
 - [31] L. S. Kalkstein, G. Tan, and J. A. Skindlov, “An evaluation of three clustering procedures for use in synoptic climatological classification,” *Journal of Climate and Applied Meteorology*, vol. 26, no. 6, pp. 717–730, 1987.
 - [32] M. Zou, B. Yu, J. Cai, and P. Xu, “Fractal model for thermal contact conductance,” *Journal of Heat Transfer*, vol. 130, no. 10, Article ID 101301, 9 pages, 2008.
 - [33] A. H. Truesdell and R. O. Fournier, “Procedure for estimating the temperature of a hot-water component in a mixed water by using a plot of dissolved silica versus enthalpy,” *Journal of Research of the U. S. Geological Survey*, vol. 5, no. 1, pp. 49–52, 1977.
 - [34] Q. Guo, Z. Pang, Y. Wang, and J. Tian, “Fluid geochemistry and geothermometry applications of the Kangding high-temperature geothermal system in eastern Himalayas,” *Applied Geochemistry*, vol. 81, pp. 63–75, 2017.
 - [35] M. Burgos, “Geothermal interpretation of thermal fluid discharge from wells and springs in Berlin Geothermal Field, El Salvador,” *The United Nations University Reports*, vol. 7, no. 7, pp. 165–191, 1999.
 - [36] W. Wagner and H. J. Kretzschmar, *International Steam Tables, Properties of Water and Steam Based on the Industrial Formulation IAPWS-IF97*, Springer-Verlag, Berlin, Germany, 2nd edition, 2008.
 - [37] R. O. Fournier, “Application of water geochemistry to geothermal exploration and reservoir engineering,” in *Geothermal Systems: Principles and Case Histories*, pp. 109–143, John Wiley and Sons, New York, NY, USA, 1981.
 - [38] H. Saibi and S. Ehara, “Temperature and chemical changes in the fluids of the Obama geothermal field (SW Japan) in response to field utilization,” *Geothermics*, vol. 39, no. 3, pp. 228–241, 2010.
 - [39] G. Schettler, H. Oberhänsli, G. Stulina, and J. H. Djumanov, “Hydrochemical water evolution in the Aral Sea Basin. Part II: confined groundwater of the Amu Darya Delta—evolution from the headwaters to the delta and SiO₂ geothermometry,” *Journal of Hydrology*, vol. 495, pp. 285–303, 2013.
 - [40] S. Arnórsson, “Chemical equilibria in icelandic geothermal systems—Implications for chemical geothermometry investigations,” *Geothermics*, vol. 12, no. 2–3, pp. 119–128, 1983.
 - [41] R. O. Fournier and A. H. Truesdell, “Chemical indicators of subsurface temperature applied to hot spring waters of Yellowstone National Park, Wyoming, U.S.A.,” *Geothermics*, vol. 2, no. 1, pp. 529–535, 1970.
 - [42] J. Duo, “The basic characteristics of the Yangbajing geothermal field—a typical high temperature geothermal system,” *Engineering Science*, vol. 5, pp. 42–47, 2003 (Chinese).
 - [43] H. L. Sun, F. Ma, W. Lin, Z. Liu, G. Wang, and D. Nan, “Geochemical characteristics and geothermometer application in high temperature geothermal field in Tibet,” *Geological Science and Technology Information*, vol. 3, pp. 171–177, 2015 (Chinese).
 - [44] R. O. Fournier and A. H. Truesdell, “Geochemical indicators of subsurface temperature—part 2, estimation of temperature and fraction of hot water mixed with cold water,” *Journal of Research of the U. S. Geological Survey*, vol. 2, pp. 263–270, 1974.
 - [45] R. O. Fournier and A. H. Truesdell, “An empirical NaKCa geothermometer for natural waters,” *Geochimica et Cosmochimica Acta*, vol. 37, no. 5, pp. 1255–1275, 1973.
 - [46] N. Majumdar, A. L. Mukherjee, and R. K. Majumdar, “Mixing hydrology and chemical equilibria in Bakreswar geothermal area, Eastern India,” *Journal of Volcanology and Geothermal Research*, vol. 183, no. 3–4, pp. 201–212, 2009.
 - [47] Y. Liu, X. Zhou, Z. Deng et al., “Hydrochemical characteristics and genesis analysis of the Jifei hot spring in Yunnan, southwestern China,” *Geothermics*, vol. 53, pp. 38–45, 2015.
 - [48] S. Arnórsson, “The use of mixing models and chemical geothermometers for estimating underground temperatures in geothermal systems,” *Journal of Volcanology and Geothermal Research*, vol. 23, no. 3–4, pp. 299–335, 1985.
 - [49] S. Chatterjee, S. Sharma, M. A. Ansari et al., “Characterization of subsurface processes estimation of reservoir temperature in

- Tural Rajwadi geothermal fields, Maharashtra, India,” *Geothermics*, vol. 59, pp. 77–89, 2016.
- [50] M. R. Carvalho, V. H. Forjaz, and C. Almeida, “Chemical composition of deep hydrothermal fluids in the Ribeira Grande geothermal field (São Miguel, Azores),” *Journal of Volcanology and Geothermal Research*, vol. 156, no. 1-2, pp. 116–134, 2006.
- [51] T. Özen, A. Bülbül, and G. Tarcan, “Reservoir and hydro-geochemical characterizations of geothermal fields in Salihli, Turkey,” *Journal of Asian Earth Sciences*, vol. 60, pp. 1–17, 2012.

Research Article

Impact of Redox Condition on Fractionation and Bioaccessibility of Arsenic in Arsenic-Contaminated Soils Remediated by Iron Amendments: A Long-Term Experiment

Quan Zhang,^{1,2} Lixin Pei,¹ Chunyan Liu,¹ Mei Han,¹ and Wenzhong Wang¹ 

¹*Institute of Hydrogeology and Environmental Geology, Chinese Academy of Geological Sciences, Shijiazhuang, China*

²*China University of Geosciences, Beijing, China*

Correspondence should be addressed to Wenzhong Wang; wwenzhong2005@163.com

Received 25 October 2017; Accepted 8 January 2018; Published 11 March 2018

Academic Editor: Meijing Zhang

Copyright © 2018 Quan Zhang et al. This is an open access article distributed under the Creative Commons Attribution License, which permits unrestricted use, distribution, and reproduction in any medium, provided the original work is properly cited.

Iron-bearing amendments, such as iron grit, are proved to be effective amendments for the remediation of arsenic- (As-) contaminated soils. In present study, the effect of redox condition on As fractions in As-contaminated soils remediated by iron grit was investigated, and the bioaccessibility of As in soils under anoxic condition was evaluated. Results showed that the labile fractions of As in soils decreased significantly after the addition of iron grit, while the unlabile fractions of As increased rapidly, and the bioaccessibility of As was negligible after 180 d incubation. More labile fractions of As in iron-amended soils were transformed into less mobilizable or unlabile fractions with the contact time. Correspondingly, the bioaccessibility of As in iron-amended soils under the aerobic condition was lower than that under the anoxic condition after 180 d incubation. The redistribution of loosely adsorbed fraction of As in soils occurred under the anoxic condition, which is likely ascribed to the reduction of As(V) to As(III) and the reductive dissolution of Fe-(hydr)oxides. The stabilization processes of As in iron-amended soils under the anoxic and aerobic conditions were characterized by two stages. The increase of crystallization of Fe oxides, decomposition of organic matter, molecular diffusion, and the occlusion within Fe-(hydr)oxides cocontrolled the transformation of As fractions and the stabilization process of As in iron-amended soils under different redox conditions. In terms of As bioaccessibility, the stabilization process of As in iron-amended soils was shortened under the aerobic condition in comparison with the anoxic condition.

1. Introduction

The widespread contamination of soils with arsenic (As), caused by human activities, is a high environmental and toxicological concern. Several technologies, such as in situ chemical stabilization, phytoremediation, and soil washing, can be used to decrease As pollution in soils [1, 2]. Among them, the in situ chemical stabilization implies the application of stabilizing amendments, which by chemical means reduces As mobility and bioaccessibility [3] and refer to the portion of As that can reach into groundwater [4]. Nowadays, iron-bearing amendments, such as iron oxides, iron salts, zero-valent irons, and iron-rich industrial byproducts, are proved to be effective in remediating As-contaminated soils [2, 5–7].

Among zero-valent irons, nanoscale zero-valent iron and iron grit are the two most prevalent soil remediation agents [4].

The remediation efficiency of iron amendments such as iron grit to As-contaminated soils is commonly dependent on the proportions of labile and unlabile As fractions accounting for the total As in soils. Thus, it is essential to understand the stabilization/aging processes of As related to the change of As fractions in soils. And the stabilization/aging processes of As in soils not only depended on the properties of amendments but also were affected by some environmental conditions, such as temperature and redox conditions [5, 8–10]. For instance, the crystallization of Fe (hydr)oxides and the diffusion of As in micropores from the outer layers into the inner complex are accelerated after the temperature

TABLE 1: Physicochemical properties of the experimental soil.

pH	7.67
Organic matter (g/kg)	28.7
Total Fe (g/kg)	43.1
Free iron oxides (g/kg)	17.0
Amorphous iron oxides (g/kg)	6.7
Total Al (g/kg)	93.7
Total Mn (g/kg)	0.627
CEC (cmol/kg)	12.7
Particle size (%)	
Sand (>0.05 mm)	31.8
Silt (0.002–0.05 mm)	55.6
Clay (<0.002 mm)	12.6
As fractions (mg/kg)	
F1	0.045
F2	0.082
F3	0.199
F4	2.59
F5	1.77
F6	16.5

elevated, resulting in the transformation of labile fractions of As into unlabile fractions [5, 9]. The forms of As and Fe-hydroxides in soils are commonly affected by the redox conditions [10, 11]. However, the effect of redox condition on the stabilization processes and bioaccessibility of As in soils amended by iron grit are little known.

The present study aims to (1) investigate the effect of redox condition on As fractions in As-contaminated soils remediated by iron grit in a long term and (2) evaluate the bioaccessibility of As in remediated (iron grit) soils and unremediated soils. Fractions of As in soils were extracted by the sequential extraction procedure (SEP). The results will be beneficial to understanding of the stabilization processes and remediation efficiency of As in soils amended by iron grit under different redox conditions.

2. Materials and Methods

2.1. Soil and Amendment Characteristics. The soils were collected from the upper 10 cm of an agricultural land irrigated by sewage in South China. Soil samples were air-dried, ground, and passed through a 0.9 mm sieve after discarding debris and finally homogenized in advance of analysis. The detailed physicochemical properties of the experiment soil are shown in Table 1, and the related analytical methods have been discussed in our previous publication [11]. The iron grit used for soil additive was purchased from Tianjin evergreen chemical reagent manufacturing Co., Ltd. (China).

2.2. Soil Preparation and Handling. Three samples were taken from the above composite soil with 300 g each. The first and the second ones were spiked by Na_3AsO_4 solution and made the concentrations of As in soils up to 100 mg/kg and then added with 6 g of iron grit (2%, w/w) and mixed immediately.

The first one was added with relatively small volume and high concentration of As solution to make the soil moisture equal to field capacity, which is labeled as S_{IA} . The second one was spiked with relatively big volume and low concentration of As solution to make the soil supersaturated, which is denoted as S_{IN} . The third one was treated with the same process of S_{IN} but with no addition of iron grit and is denoted as S_N . S_N and S_{IN} represent soils under the anoxic condition, and the latter one added iron grit. By contrast, S_{IA} with the addition of iron grit represents soils under the aerobic condition. All samples were incubated in an artificial climate chamber with a temperature of 25°C and a humidity of 65%. S_{IA} was opened and maintained at the soil moisture of field capacity, while S_N and S_{IN} were sealed and maintained a supersaturated condition. At different times (0 d, 3 d, 10 d, 30 d, 60 d, 120 d, and 180 d) after incubation, soil samples were collected and freeze-dried for 24 h in a vacuum before the extraction of As fractions [12].

2.3. Sequential Extraction Procedure and Quality Control. The dried samples were ground and mixed after being collected, and 1.00 g of samples was weighted into acid-washed 50 ml centrifuge tubes. All sample analyses were performed in duplicate. The fractionation of As in soils was determined by one modified Tessier's SPE [11]. Six fractions are denoted as F1, F2, F3, F4, F5, and F6 and are corresponding to water soluble fraction, exchangeable fraction, loosely adsorbed fraction, strongly adsorbed and organically bound fraction, Fe and Mn/Al oxides bound fraction, and the residual fraction. The details are shown in our previous study [11]. In this study, all reagents were analytical grade or better. The concentrations of As in the extractions were determined using an atomic fluorescence spectrophotometer (AFS-610A model, Beijing, China). A standard reference soil GSS-16 (National Center for Standard Reference Material, Beijing, China) was used for quality control of the acid digestion. The recovery for As in the standard reference soil GSS-16 was 98.7%. The errors for the sum of As measured in all six fractions to a single total As determination were within $\pm 18.5\%$.

3. Results and Discussion

3.1. Influence of Iron Grit Amendment on As Fractions in Soils. As shown in Figure 1, there was significant difference for all As fractions between iron grit amended soils (S_{IN}) and unamended soils (S_N) at initial time (0 d). It is worth mentioning that the determination of As fractions at initial time was after 24 h freeze-drying in this study. The labile fractions such as F1, F2, and F3 in S_N accounted for 32%, 14%, and 27% of the total As, respectively, and were far higher than that in S_{IN} . In contrast, the less mobilizable fractions such as F4 and F5 in S_N accounted for 11% and 4% of the total As, respectively, and were far lower than that in S_{IN} . This indicates that iron grit has a rapid effect on the decrease of labile fractions of As in soils and a large proportion of labile fractions of As in soils transformed rapidly into less mobilizable fractions after the addition of iron grit. This is likely to be ascribed to the rapidly increase of iron oxides in

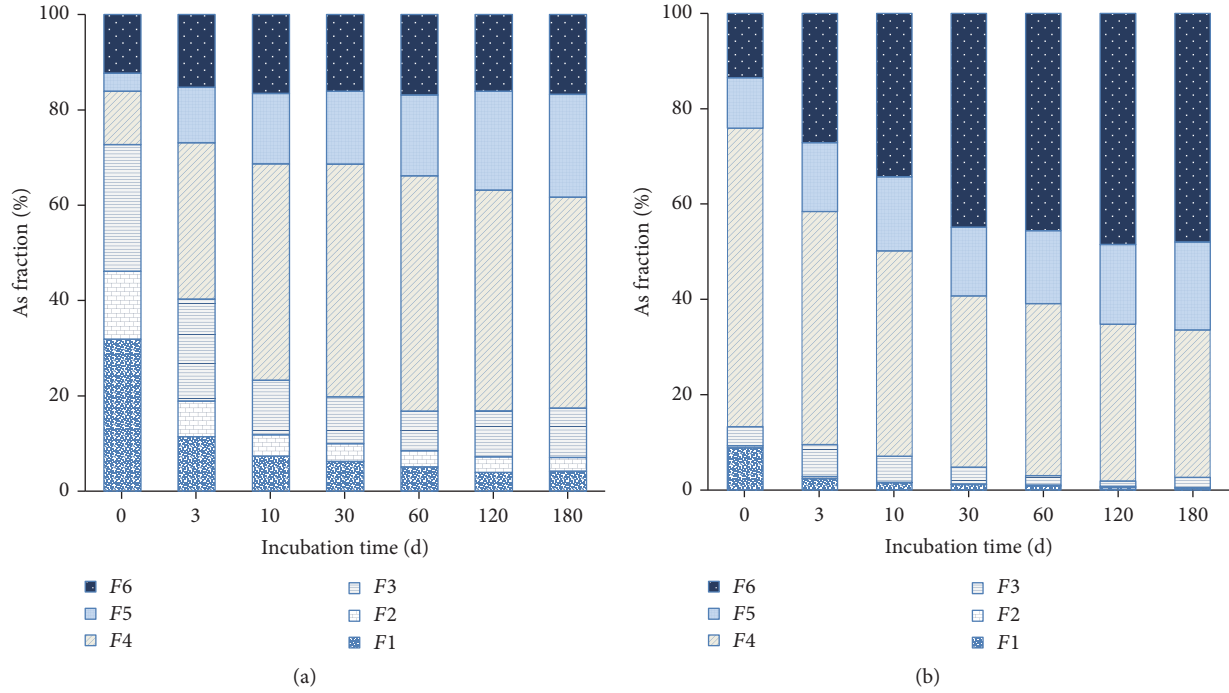


FIGURE 1: The fractions of As in iron grit amended and unamended soils at different time under the anoxic condition ((a) S_N , (b) S_{IN} ; F1—water soluble fraction, F2—exchangeable fraction, F3—loosely adsorbed fraction, F4—strongly adsorbed and organically bound fraction, F5—Fe and Mn/Al oxides bound fraction, and F6—residual fraction).

soils after the addition of iron grit, because iron oxides have strong adsorbed ability on water soluble As [13, 14]. After the incubation, F1 in both of S_N and S_{IN} decreased significantly within 120 d and were from 32% and 9% of the total As to 4% and less than 1%, respectively. F2 in S_N decreased from 14% to 3% and reached a steady state within 60 d, while it in S_{IN} was negligible during the whole incubation period. F3 in S_N decreased from 27% to about 10% and reached a steady state within 30 d, while it was increased firstly from 4% to 7% within 3 d and then decreased to 2% within 60 d in S_{IN} . F4 increased from 11% to about 49% within 30 d and then decreased slowly to 44% in the later incubation (60 d–180 d) in S_N . By contrast, F4 in S_{IN} was shown a remarkable decrease from 63% to 31% within 180 d. F5 in both of S_N and S_{IN} increased within 180 d and were from 4% and 11% of the total As to 22% and 18%, respectively. F6 in S_N increased from 12% to 17% and reached a steady state within 60 d, while in S_{IN} a remarkable increase from 13% to 48% within 180 d was exhibited. Compared to As fractions in S_N , the proportions of F1, F2, F3, F4, and F5 in S_{IN} were lower, while the proportion of F6 in S_{IN} was higher after the incubation. This indicates that iron grit is an effective amendment to stabilize As fractions in soils.

The sum of weakly bound fractions of As after amended is usually used to assess the effectiveness of amendments reducing As bioaccessibility in soils [15, 16]. In this study, the sum of F1, F2, and F3 to the total As, denoted as F_M , represents the bioaccessibility of As in soils [9]. F_M in both of S_N and S_{IN} showed a significant decrease from 73% and 13% to 17% and 2%, respectively, and reached a steady state within 60 d (Figure 2). Therefore, in terms of the As bioaccessibility,

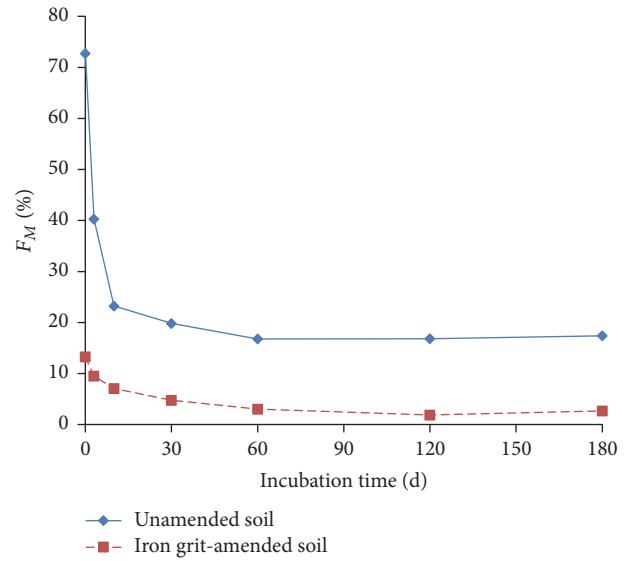


FIGURE 2: Changes of As bioaccessibility in soils under anoxic conditions (unamended soil, S_N ; iron grit amended, S_{IN}).

the stabilization/aging processes of As in both of S_N and S_{IN} occur and end within 60 d, and the addition of iron grit is more effective on the stabilization of As in soils.

3.2. Effect of Redox Conditions on As Fractions in Iron-Amended Soils. F1 in both of S_{IA} and S_{IN} decreased markedly within the first 10 d following the addition of water soluble As and iron grit (Figure 3). By contrast, in the incubation

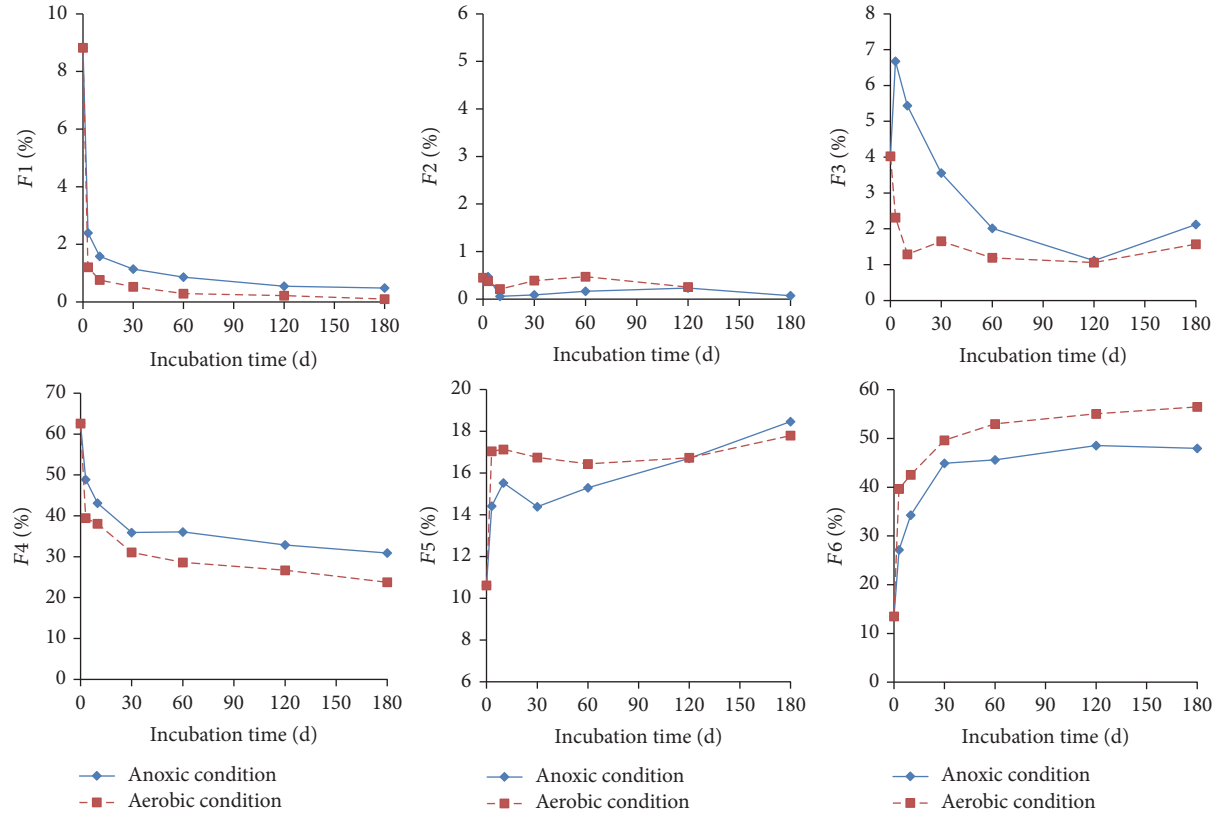


FIGURE 3: Changes of As fractions in iron grit amended soils under different redox conditions over time (anoxic condition, S_{IN} ; aerobic condition, S_{IA}).

time of 60 d to 180 d, the changes of $F1$ in these two soils were distinct; in this period, $F1$ exhibited further decreases at slow rates and the tendency was not complete at the end of incubation in S_{IN} , while $F1$ in S_{IA} had no significant change in 60 d–180 d. This indicates that the transformation of $F1$ into less mobilizable fractions in iron-amended soils under the anoxic condition is a long-term (>180 d) process, while it is a short-term (<60 d) process in iron-amended soils under the aerobic condition. Moreover, in the whole incubation period, the proportion of $F1$ in S_{IN} was higher than that in S_{IA} , indicating that more soluble As in iron-amended soils transformed into less mobilizable fractions under aerobic condition in comparison with under anoxic condition. This is likely to be attribute to the ongoing reduction of As(V) to As(III) in soils under anoxic condition and the higher adsorption of As(V) than As(III) onto soil components [10, 11, 17, 18].

Different from $F1$, there was no significant difference of $F2$ in both S_{IA} and S_{IN} , and the proportion of $F2$ exhibited a negligible level during the whole incubation time (Figure 3). So it could be speculated that $F2$ was converted to less mobilizable fractions at an extremely fast rate following the addition of iron grit to soils whether in an oxidizing environment or in a reducing environment. This may be ascribed to the rapidly formed Fe oxides after the addition of iron grit into soils, because the rapid adsorption of added As on the surface of newly formed amorphous iron oxides has been found [19].

$F3$ in S_{IA} showed a marked decrease and reached a steady state quickly within the first 10 d (Figure 3). By contrast, $F3$ in S_{IN} exhibited a significant increase within the first 3 d and then decreased, indicating that the redistribution of $F3$ in iron-amended soils under anoxic conditions occurred. The reason for the increase of $F3$ in S_{IN} within the first 3 d may be as follows: on the one hand, pH in S_{IN} may increase within the first 3 d, because soil pH increased slightly after the flood while pH in nonflooded soil showed little change [20]; on the other hand, the reduction of As(V) to As(III) often occurs in soils under anoxic conditions [12], both leading to the increase of $F3$ in S_{IN} within the first 3 d, because As(III) is preferentially nonspecific adsorbed to Fe-hydroxides at alkaline condition [2]. As on external surface of soil minerals gradually diffuses into inner surface and mineral lattice and forms relatively immobilizable surface complexes and insoluble secondary solid phases [10, 21], which may be responsible for the decrease of $F3$ in iron-amended soils with the contact time. The change of $F3$ in S_{IA} ended in the first 10 d while in S_{IN} it ended within 60 d, indicating that the transformation of $F3$ into other fractions in iron-amended soils under the anoxic condition is more lasting than that under the aerobic condition.

Similar to $F1$ in soils, $F4$ also showed a significant decrease in both S_{IA} and S_{IN} , and the decrease of $F4$ was not complete within the incubation time in both S_{IA} and S_{IN} (Figure 3). This indicates that effect of redox conditions on the tendency of $F4$ in iron-amended soils is negligible. The

decomposition of organic matter and the increase of crystallization of Fe oxides with the contact time may be responsible for the decrease of F_4 in iron-amended soils [10, 22, 23]. In addition, the proportion of F_4 in S_{IN} was significantly higher than that in S_{IA} during the whole incubation period. This may be attributed to the more As(V) reduction to As(III) and less decomposition of dissolved organic matters in soils under anoxic condition than that under aerobic condition [8, 11].

Contrary to the four former fractions, F_5 in both S_{IA} and S_{IN} increased promptly within the first 10 d after the addition of water soluble As and iron grit (Figure 3). In contrast, during the later incubation period (10 d–180 d), the changes of F_5 in these two soils were distinct: F_5 in S_{IA} reached the equilibrium within the first 10 d, while in S_{IN} it exhibited a further increase in the later incubation period (10 d–180 d). This indicates that the transformation of F_5 into other fractions in iron-amended soils under the anoxic condition is a long-term (>180 d) process, while it is a short-term (<10 d) process in iron-amended soils under the aerobic condition. The reductive dissolution and reproduction of As-Fe phases in soils occur under reducing conditions, but it is inhibited at oxidative conditions, which may be responsible for the different tendency of F_5 in S_{IA} and S_{IN} [17, 24]. It is worth mentioning that the proportion of F_5 in S_{IN} was significantly lower than that in S_{IA} during the incubation period of 3 d–60 d. This may be ascribed to the reduction of As(V) into As(III) and the poor crystallization of Fe oxides in soils under the anoxic condition [10].

F_6 in both S_{IA} and S_{IN} increased markedly within the first 30 d following the addition of As and iron grit (Figure 3). The changes of F_6 in these two soils in the later incubation period (30 d–180 d) were distinct: F_6 in S_{IN} reached the equilibrium within the first 30 d, while in S_{IA} it showed a further increase at slow rates and the tendency was not complete within 180 d. This indicates that aerobic condition is likely to prolong the formation of F_6 in iron-amended soils in comparison with anoxic condition. This may be attributed to the lasting well crystallization of Fe oxides in iron-amended soils under the aerobic condition. The proportion of F_6 in S_{IN} was significantly lower than that in S_{IA} during the whole incubation period. This indicates that the aerobic condition likely leads to the more increase of F_6 in iron-amended soils over time in comparison with the anoxic condition. Reduction of As(V) to As(III) under the anoxic condition over time may be also responsible for the above effect, because a higher proportion of labile fraction of As(V) commonly transforms into less mobilizable fractions, such as F_6 , in soils over time in comparison with As(III) [10].

3.3. Impact of Redox Conditions on As Bioaccessibility in Iron-Amended Soils. As shown in Figure 4, F_M in both S_{IA} and S_{IN} decreased rapidly within the first 10 d following the addition of As(V) and iron grit into the soils. In contrast, the changes of F_M in these two soils in the later incubation period (10 d–180 d) were distinct: F_M in S_{IA} reached the equilibrium within the first 10 d, while in S_{IN} it showed a further decrease and reached the equilibrium within 120 d. This indicates that anoxic condition would lead to the tendency of F_M in iron-amended soils reaching equilibrium

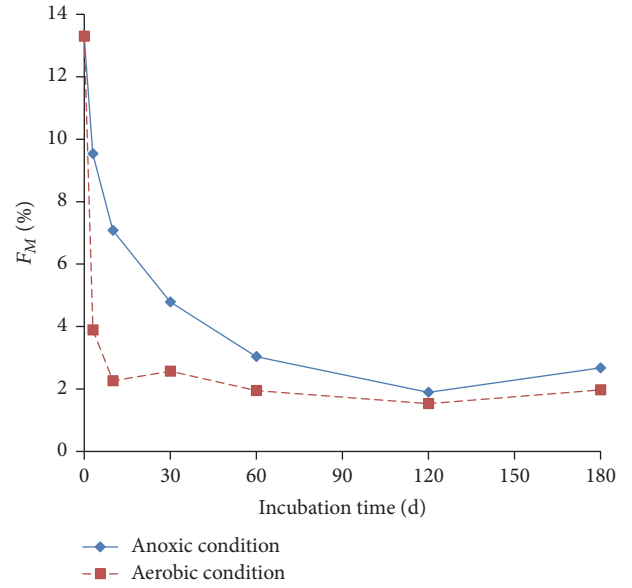


FIGURE 4: Changes of As bioaccessibility in soils under different redox conditions after the addition of iron grit over time (anoxic condition, S_{IN} ; aerobic condition, S_{IA}).

later in comparison with aerobic condition. In terms of As bioaccessibility, the stabilization process ended within 10 d in S_{IA} , but it was complete within 120 d in S_{IN} , indicating that the anoxic condition would prolong the stabilization process of As in iron-amended soils. In addition, over the whole incubation period, the proportion of F_M in S_{IN} was higher than that in S_{IA} , which demonstrates that the aerobic condition tended to be more conducive to reduced bioaccessibility of As than anoxic condition. It is likely to be coaffected by the reductive dissolution of Fe (hydr)oxides and the reduction of As(V) to As(III) at anoxic condition [25, 26], because As which was coprecipitated and adsorbed on Fe-(hydr)oxides surface could be released due to the reductive dissolution of the Fe oxides and the lower adsorption of As(III) onto the surface of soil minerals than that of As(V) [27].

3.4. Effect of Redox Conditions on the Stabilization Processes of As in Iron-Amended Soils. The stabilization process of As in S_{IN} had two distinct stages in the whole incubation period (Figure 5(a)). The first stage was from 0 d to 3 d, where F_1 and F_4 decreased and, in contrast, F_3 , F_5 , and F_6 increased, while other fractions exhibited no marked change, indicating that F_1 and F_4 transformed into F_3 , F_5 , and F_6 in S_{IN} within the first 3 d, and the main transformation was from F_1 and F_4 to F_6 due to their large variations. In this stage, transformation of F_1 to F_6 in S_{IN} was likely to be affected by the molecular diffusion in micropores of the soil minerals [9, 10]. Transformation of F_4 to F_6 in S_{IN} was coaffected by the decomposition of organic matter and molecular diffusion in the surface of soil minerals [22], because As occluded within organic matters would be released again after the decomposition of arganic matter by microbial respiration under the anoxic condition and then diffused into the mineral

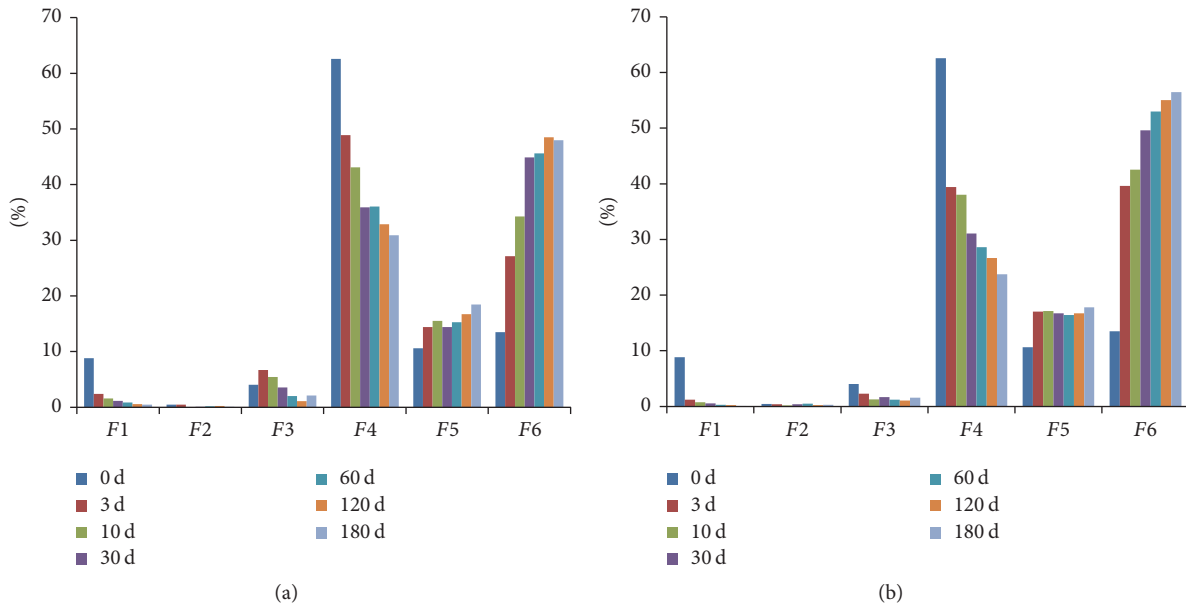


FIGURE 5: The stabilization processes of As in soils at different redox conditions ((a) S_{IN} and (b) S_{IA}).

lattice [10]. The second stage in S_{IN} was from 3 d to 180 d; $F1$, $F3$, and $F4$ decreased and, in contrast, $F5$ and $F6$ increased, while $F2$ was without significant change. This indicates that three more mobilizable fractions transformed into two less mobilizable or immobilizable fractions in the later incubation time in S_{IN} . The main transformation in S_{IN} in the second stage was also from $F4$ to $F6$ due to their large variations, and the decomposition of organic matter and molecular diffusion in the surface of soil minerals should be responsible for this transformation.

Similar to the iron-amended soils under anoxic condition, the stabilization process of As in iron-amended soils under aerobic condition also had two distinct stages in the whole incubation period (Figure 5(b)). The first stage was also within the first 3 d, where $F1$, $F3$, and $F4$ decreased and, in contrast, $F5$ and $F6$ increased, while $F2$ was without significant change. This indicates that three more labile fractions transformed into two unlabile fractions in S_{IA} within the first 3 d. The main transformation in S_{IA} in the first stage was from $F1$ to $F5$ and $F4$ to $F6$ due to their large variations. In this stage, the transformation of $F1$ to $F5$ in S_{IA} may be ascribed to the well crystallization of Fe oxides and As occluded within Fe-(hydr)oxides, because the crystallization of Fe oxides in soils under aerobic conditions would occur rapidly [28]. The transformation of $F4$ to $F6$ in S_{IA} is also likely to be attributed to the decomposition of organic matter and molecular diffusion in the surface of soil minerals. The second stage in S_{IA} was also from 3 d to 180 d; $F1$ and $F4$ decreased and, in contrast, $F6$ increased, while other fractions showed no significant change, indicating the transformation of $F1$ and $F4$ into $F6$ in S_{IA} in the later incubation period. In this stage, the main transformation in S_{IA} was $F4$ to $F6$, and the reason was discussed as in the above.

4. Conclusions

The present study demonstrated that water soluble and loosely adsorbed As was the primary fractions in soils spiked As(V). After the addition of iron grit, the primary fractions of As in soils were characterized by strongly adsorbed and organically bound fractions (~63%), while the water soluble and loosely adsorbed As only account for a small proportion. More labile fractions transformed into immobilizable fractions in iron-amended soils under aerobic conditions in comparison with under anoxic conditions. The redistribution of $F3$ in iron-amended soils under anoxic conditions occurs, as a result of the reduction of As(V) to As(III) and the reductive dissolution of Fe-(hydr)oxides.

The stabilization processes of As in iron-amended soils under the anoxic and aerobic conditions were characterized by two stages. The increase of crystallization of Fe oxides, decomposition of organic matter, molecular diffusion, and the occlusion within Fe-(hydr)oxides cocontrolled the transformation of As fractions and the stabilization process of As in iron-amended soils under different redox conditions. In terms of As bioaccessibility, the stabilization process of As in iron-amended soils was shortened under the aerobic condition in comparison with under the anoxic condition.

Conflicts of Interest

The authors declare that they have no conflicts of interest.

Acknowledgments

This research was supported by the Natural Science Foundation of Hebei Province of China (D2015504004), the Fundamental Research Funds for Central Public Welfare Research







Institutes, CAGS (SK201611, SK201410), China Geological Survey project (DD20160309), and the National Natural Science Foundation of China (41472264, 41772334).

References

- [1] C. N. Mulligan, R. N. Yong, and B. F. Gibbs, "Remediation technologies for metal-contaminated soils and groundwater: an evaluation," *Engineering Geology*, vol. 60, no. 1–4, pp. 193–207, 2001.
- [2] P. Miretzky and A. F. Cirelli, "Remediation of arsenic-contaminated soils by iron amendments: A review," *Critical Reviews in Environmental Science and Technology*, vol. 40, no. 2, pp. 93–115, 2010.
- [3] B. Song, G. Zeng, J. Gong et al., "Evaluation methods for assessing effectiveness of in situ remediation of soil and sediment contaminated with organic pollutants and heavy metals," *Environment International*, vol. 105, pp. 43–55, 2017.
- [4] C. Tiberg, J. Kumpiene, J. P. Gustafsson et al., "Immobilization of Cu and As in two contaminated soils with zero-valent iron - Long-term performance and mechanisms," *Applied Geochemistry*, vol. 67, pp. 144–152, 2016.
- [5] M. Komárek, A. Vaněk, and V. Ettler, "Chemical stabilization of metals and arsenic in contaminated soils using oxides - A review," *Environmental Pollution*, vol. 172, pp. 9–22, 2013.
- [6] T. Makino, K. Nakamura, H. Katou et al., "Simultaneous decrease of arsenic and cadmium in rice (*Oryza sativa* L.) plants cultivated under submerged field conditions by the application of iron-bearing materials," *Soil Science & Plant Nutrition*, vol. 62, no. 4, pp. 340–348, 2016.
- [7] J. Kumpiene, A. Lagerkvist, and C. Maurice, "Stabilization of As, Cr, Cu, Pb and Zn in soil using amendments—a review," *Waste Management*, vol. 28, no. 1, pp. 215–225, 2008.
- [8] S. M. Shaheen, J. Rinklebe, T. Frohne, J. R. White, and R. D. DeLaune, "Redox effects on release kinetics of arsenic, cadmium, cobalt, and vanadium in Wax Lake Deltaic freshwater marsh soils," *Chemosphere*, vol. 150, pp. 740–748, 2016.
- [9] G. Huang, Z. Chen, J. Wang, Q. Hou, and Y. Zhang, "Impact of temperature on the aging mechanisms of arsenic in soils: fractionation and bioaccessibility," *Environmental Science and Pollution Research*, vol. 23, no. 5, pp. 4594–4601, 2016.
- [10] G. Huang, Z. Chen, Y. Zhang, F. Liu, J. Wang, and Q. Hou, "Changes of arsenic fractionation and bioaccessibility in wastewater-irrigated soils as a function of aging: Influence of redox condition and arsenic load," *Geoderma*, vol. 280, pp. 1–7, 2016.
- [11] Q. Hou, Y. Zhang, L. Li, and S. Song, "Effects of particle size and redox potential on arsenic fractionation in soils irrigated with arsenate-rich water," *Soil and Sediment Contamination: An International Journal*, vol. 26, no. 4, pp. 391–403, 2017.
- [12] G. Huang, Z. Chen, J. Sun, F. Liu, J. Wang, and Y. Zhang, "Effect of sample pretreatment on the fractionation of arsenic in anoxic soils," *Environmental Science and Pollution Research*, vol. 22, no. 11, pp. 8367–8374, 2015.
- [13] G. Huang, Z. Chen, F. Liu, J. Sun, and J. Wang, "Impact of human activity and natural processes on groundwater arsenic in an urbanized area (South China) using multivariate statistical techniques," *Environmental Science and Pollution Research*, vol. 21, no. 22, pp. 13043–13054, 2014.
- [14] M. Vítková, S. Rákosová, Z. Micháľková, and M. Komárek, "Metal(loid)s behaviour in soils amended with nano zero-valent iron as a function of pH and time," *Journal of Environmental Management*, vol. 186, pp. 268–276, 2017.
- [15] J.-Y. Kim, A. P. Davis, and K.-W. Kim, "Stabilization of available arsenic in highly contaminated mine tailings using iron," *Environmental Science & Technology*, vol. 37, no. 1, pp. 189–195, 2003.
- [16] M. Simón, V. González, S. de Haro, and I. García, "Are soil amendments able to restore arsenic-contaminated alkaline soils?" *Journal of Soils and Sediments*, vol. 15, no. 1, pp. 117–125, 2014.
- [17] S. Matsumoto, J. Kasuga, N. Taiki, T. Makino, and T. Arai, "Inhibition of arsenic accumulation in Japanese rice by the application of iron and silicate materials," *Catena*, vol. 135, pp. 328–335, 2015.
- [18] N. Bolan, A. Kunhikrishnan, R. Thangarajan et al., "Remediation of heavy metal(loid)s contaminated soils—to mobilize or to immobilize?" *Journal of Hazardous Materials*, vol. 266, pp. 141–166, 2014.
- [19] S. C. Wilson, P. V. Lockwood, P. M. Ashley, and M. Tighe, "The chemistry and behaviour of antimony in the soil environment with comparisons to arsenic: a critical review," *Environmental Pollution*, vol. 158, no. 5, pp. 1169–1181, 2010.
- [20] S. Das, M.-L. Chou, J.-S. Jean, C.-C. Liu, and H.-J. Yang, "Water management impacts on arsenic behavior and rhizosphere bacterial communities and activities in a rice agro-ecosystem," *Science of the Total Environment*, vol. 542, pp. 642–652, 2016.
- [21] S. Hafeeznezhad, A. G. Zimmer-Faust, D. Jun et al., "Remediation of groundwater contaminated with arsenic through enhanced natural attenuation: Batch and column studies," *Water Research*, vol. 122, pp. 545–556, 2017.
- [22] C. T. Parsons, R.-M. Couture, E. O. Omoregie et al., "The impact of oscillating redox conditions: Arsenic immobilisation in contaminated calcareous floodplain soils," *Environmental Pollution*, vol. 178, pp. 254–263, 2013.
- [23] J. Kumpiene, J. P. Fitts, and M. Mench, "Arsenic fractionation in mine spoils 10 years after aided phytostabilization," *Environmental Pollution*, vol. 166, pp. 82–88, 2012.
- [24] P. Hu, Y. Ouyang, L. Wu, L. Shen, Y. Luo, and P. Christie, "Effects of water management on arsenic and cadmium speciation and accumulation in an upland rice cultivar," *Journal of Environmental Sciences*, vol. 27, no. C, pp. 225–231, 2015.
- [25] A. Neumann, R. Kaegi, A. Voegelin, A. Hussam, A. K. M. Munir, and S. J. Hug, "Arsenic removal with composite iron matrix filters in Bangladesh: a field and laboratory study," *Environmental Science & Technology*, vol. 47, no. 9, pp. 4544–4554, 2013.
- [26] Z. Zhao, S. Wang, and Y. Jia, "Effect of sulfide on As(III) and As(V) sequestration by ferrihydrite," *Chemosphere*, vol. 185, pp. 321–328, 2017.
- [27] J. Beiyuan, Y. M. Awad, F. Beckers, D. C. W. Tsang, Y. S. Ok, and J. Rinklebe, "Mobility and phytoavailability of As and Pb in a contaminated soil using pine sawdust biochar under systematic change of redox conditions," *Chemosphere*, vol. 178, pp. 110–118, 2017.
- [28] A. Thompson, O. A. Chadwick, D. G. Rancourt, and J. Chorover, "Iron-oxide crystallinity increases during soil redox oscillations," *Geochimica et Cosmochimica Acta*, vol. 70, no. 7, pp. 1710–1727, 2006.

Research Article

Effects of Dissolved Organic Matter on Sorption of Oxytetracycline to Sediments

Zongzhou Wang ^{1,2}, Qianli Jiang ³, Runze Wang,^{1,2} Xiaoyu Yuan ^{1,2},
Shengke Yang ^{1,2}, Wenke Wang ^{1,2} and Yaqian Zhao ⁴

¹Key Laboratory of Subsurface Hydrology and Ecological Effects in Arid Region, Chang'an University, Ministry of Education, Xi'an, Shaanxi 710054, China

²School of Environmental Science and Engineering, Chang'an University, Xi'an, Shaanxi 710054, China

³Weinan Institute of Environmental Science, Weinan, Shaanxi 714000, China

⁴Dooge Centre for Water Resource Research, School of Civil Engineering, University College Dublin, Belfield, Dublin 4, Ireland

Correspondence should be addressed to Shengke Yang; ysk110@126.com

Received 25 October 2017; Revised 12 January 2018; Accepted 7 February 2018; Published 8 March 2018

Academic Editor: Meijing Zhang

Copyright © 2018 Zongzhou Wang et al. This is an open access article distributed under the Creative Commons Attribution License, which permits unrestricted use, distribution, and reproduction in any medium, provided the original work is properly cited.

The effects of two representative dissolved organic matters (DOMs) (derived from corrupt plants (PDOM) and chicken manure (MDOM)) on sorption characteristic of oxytetracycline to three typical sediments (first terrace (FT), river floodplain (RF), and riverbed (RB) sediments collected from the Weihe River) were investigated. Results showed that both DOMs can make the adsorption equilibrium time advance about 6 hours. The presence of DOMs changed the sorption kinetics model and the spontaneous degree of the reaction but did not change the sorption isotherm models. The adsorption of oxytetracycline (OTC) could be promoted by adding PDOM, and its maximum adsorption amount increased by 23.8% for FT, 38.0% for RB, and 28.3% for RF, respectively, whereas MDOM could inhibit the adsorption and maximum adsorption amount decreased by 23.3% for FT, 11.6% for RB, and 16.1% for RF, respectively. In addition, the DOM concentration also affected the adsorption. Overall, this study suggests that the humus-like DOM can promote the adsorption of OTC while the protein-like DOM can inhibit the adsorption of OTC to sediments, which is determined by the aromaticity, hydrophilicity, and polarity of the DOMs.

1. Introduction

Antibiotics are widely used in aquaculture, poultry breeding, food processing, and pharmaceutical. However, they can not only cause organic pollution, but also threaten the safety of microbial communities, triggering resistance genes after being released into the environment. Lately the resistance genes have been detected in environmental media such as river water, sediment, groundwater, and soil [1–3]. Therefore, the study of environmental behavior of antibiotics to achieve risk prediction and management is of great significance.

The fate of antibiotics in the soil is mainly through adsorption, migration, transformation, and degradation. Among them, adsorption is one of the processes that profoundly affected the behavior of the antibiotics in soil and sediments. It was reported that the adsorption behavior of antibiotics was influenced by the soil type, composition

and properties, pH, and temperature conditions [4, 5]. In addition, the interaction of antibiotics with some other coexistences, such as dissolved organic matter (DOM) and metal oxides, is also an important factor affecting the adsorption of antibiotics on soil [6]. A large number of studies have shown that the main substance to adsorb antibiotics in soil and sediments is its organic constituents. In other words, it is DOM that plays an important role in the migration of antibiotics. Therefore, identification of the effect of DOM on the adsorption of antibiotics in sediments will facilitate better understanding the mechanism of antibiotic adsorption and its transformation in unsaturated zone.

Previous studies reported that the source of DOM apparently influences the magnitude of sorption. Oh et al. [7] found that, for the effect of DOMs on ibuprofen sorption, citrate concentration increased and the K_d value decreased

but urea did not interrupt the ibuprofen sorption. The concentration of DOM also showed a different adsorption behavior of antibiotics to soil. Kulshrestha et al. [8] observed an increased sorption at a lower concentration of dissolved humic acid (1 mg/L), while a higher concentration of humic acid (10 mg/L) resulted in an opposite effect. Moreover, the variety of antibiotics can make significant influence on their adsorption behavior due to the difference of their properties [4, 9]. So there should be some essential mechanism to dominate these apparently different results. It has been clearly demonstrated that DOM can form complexation with relatively polar pesticides or uptake hydrophobic organic contaminants, which increases the apparent aqueous solubility and potentially decreases the sorption [10–15]. However, it has been found that the presence of cow dung DOM promotes the adsorption of OTC on black soil and with the increasing of DOM concentration, the promoting effect is more evident. In addition, the presence of DOM will mask the adsorption sites to inhibit the adsorption of soil on oxytetracycline [16], while Ling et al. [17] reported that the binding of DOM to sediment particles also increased the organic carbon content and changed its surface morphology, resulting in an increase in the adsorption sites on the surface of the sediment and an increase in the adsorption of oxytetracycline. It has been demonstrated that the most important compositions of DOM include three categories: humic substances, polysaccharides, and proteins [18], while these substances should play an essential role on the adsorption of antibiotics by their hydrophobicity, aromaticity, and functionality properties. However, to our knowledge, very few studies showed solicitude or comparison to the distinct adsorption behavior caused by the humic and protein substances on the adsorption. At least, the effect on the adsorption of OTC still deserves investigation. The study of the mechanism of these kinds of DOMs affecting soil adsorption of antibiotics is obviously insufficient.

In this study, with the aim of investigating the effect of DOM on the sorption of OTC to sediments, three typical sediments (first terrace sediment, river floodplain sediment, and riverbed sediment) were collected from the Weihe River, Northwest China, and subjected for testing. Two typical DOMs were derived from corrupt plants and chicken manure. Elemental analysis and three-dimensional fluorescence were deployed to elucidate the mechanism of the effect of DOM on the adsorption of OTC to sediments.

2. Materials and Methods

2.1. Sample Collection and Analysis

2.1.1. Sample Collection and Pretreatment. The sampling sites are located at Guanzhong basin, middle reaches of the Weihe River. To make the study more representative, three sediments were collected from first terrace (FT), river floodplain (RF), and riverbed (RB) along the Weihe River crosswise. Sediment samples were naturally air-dried, then sealed, and low temperature stored before use. Quartz, feldspar, mica, and other minerals can be found in the FT and RF sediment by SEM. Their characterization of sediments is showed in

Table 1. Corrupt plants were collected from the litters through natural corruption at the Weihe River bank, while chicken manure was obtained from a local poultry farming (with no use of antibiotics). All of the samples were detected with no OTC.

After collection, corrupt plants and chicken manure were subjected for DOMs extraction. To do so, 40 g of corrupt plants and chicken manure were placed in 400 mL distilled water, respectively, shaking at 200 rpm and $25 \pm 1^\circ\text{C}$ for 12 hrs. The suspensions were then centrifuged at 12000 rpm and 4°C for 10 min. Finally, the supernatant was filtered through a $0.45 \mu\text{m}$ membrane and stored in the dark environment at a low temperature (4°C) [19, 20].

2.1.2. Analysis. Elemental (C, H, N) analyses were conducted via a Vario ELIII elemental analyzer. The oxygen content was calculated by the mass difference. To assess the polarity and aliphatic characteristics of the sorbents, $(\text{O} + \text{N})/\text{C}$ and H/C atomic ratios were calculated. The fluorescence spectra of DOM samples were also recorded at room temperature with a 700-V Xe lamp and a 1 cm quartz cell (F-7000; Hitachi, Japan). The excitation wavelengths (Ex) ranging from 220 to 600 nm and emission (Em) wavelengths ranging from 250 to 600 nm were used. The scan rate was 1200 nm/min.

2.2. Sorption Experiments. The sorption experiments were performed using an Organization for Economic Co-operation and Development (OECD) method. OTC was used as a representative antibiotic for adsorption experiments.

2.2.1. Sorption Kinetics. A preequilibrium kinetic experiment was carried out to determine the equilibrium time for batch reactions in order to study sorption isotherms. The reaction solutions in 10 mL centrifuge tubes containing three sediments (0.25 g) and 5 mL of OTC (10 mg/L) were initiated by spiking 1 mL of the following solutions, respectively: distilled water (without DOM) and the TOC concentration of 100 mg/L of PDOM and MDOM solution. The tubes were stirred continuously at a constant temperature of 25°C (298 K). At time intervals of 2, 4, 8, 16, 20, 24, 30, 36, 48, 60, and 72 hrs, three replicates were centrifuged at 10000 rpm for 20 min. The obtained supernatants were analyzed using UPLC to quantify the concentration of unabsorbed OTC. Control experiments without sediments were also conducted under the same conditions as blank.

2.2.2. Sorption Isotherms and Thermodynamics. In the batch experiments, sediments and DOMs were added in the same amount as sorption kinetics experiments described in Section 2.2.1, while the initial concentration of OTC ranged from 5.0 mg/L to 25.0 mg/L. All samples were allowed to equilibrate in the tubes at a constant room temperature. After equilibrium was reached, 5 mL of the solutions from each tube was collected and centrifuged at 10,000 rpm for 20 min. The obtained supernatants were used to quantify the concentration of OTC. Reactions were conducted in duplicate for each sample.

TABLE 1: Basic composition of first terrace (FT), river floodplain (RF), and riverbed (RB) sediments.

Samples	TOC (%)	Silt <0.25 mm	Granulometric composition (%)		
			Fine sand 0.25–0.35 mm	Medium sand 0.35–0.5 mm	Coarse sand >0.5 mm
FT	6.032	7.5 ± 4.7	43.3 ± 7.6	42.6 ± 5.8	6.6 ± 4.3
RB	4.184	5.3 ± 1.4	43.9 ± 9.7	42.9 ± 4.2	7.9 ± 3.1
RF	1.575	21.7 ± 3.8	47.5 ± 4.5	23.1 ± 6.2	7.7 ± 4.7

The sorption thermodynamics experiments were conducted at the temperature ranging from 25°C (298 K) to 45°C (318 K), and the initial concentration of OTC ranged from 5.0 mg/L to 25.0 mg/L. Other steps were the same as the sorption isotherms described in Section 2.2.2.

2.2.3. Effect of DOM Concentration on Sorption. Edge experiments were conducted to investigate the effect of DOM concentration on sorption. Briefly, 0.25 g sediments were weighed into a 10 mL centrifuge tubes and 1 mL of PDOM and 1 mL of MDOM with a series of DOM concentration (50, 100, 150, 200, and 300 mg TOC/L) were spiked. Then, 5 mL of OTC (10 mg/L) solution was added, stirring continuously at a constant temperature of 25°C for 30 hrs, and then centrifuged at 10000 rpm for 20 min; the obtained supernatants were used to quantify the concentration of OTC. The experiment without DOM was also conducted as blank.

2.3. Oxytetracycline Measurement. Ultrahigh performance liquid chromatography fitted with waters TUV detector (Waters UPLC H-Class) and ACQUITY UPLC BEH C18 1.7 μ m 2.1 \times 150 mm Column was employed for detection and quantification of OTC. Column temperature was 40°C \pm 0.1°C and sample 10°C \pm 0.1°C. Injection volumes of 5 μ L, a retention time of 1.530 \pm 0.003 min, and a mobile phase of 60% acetonitrile/40% water with a flow rate of 0.1 mL/min were used. OTC was measured at 260 nm.

3. Results and Discussion

3.1. Adsorption Characteristics of OTC to Sediments. Data obtained from the sorption experiments of OTC to three sediments showed that the adsorption amount gradually increased with time till equilibrium is reached (Figure 1). The equilibrium time of FT sediment is in 24 hrs which is shorter than other two sediments. The maximum adsorption amount of three sediments followed the order: RF > FT > RB. According to the basic characteristics presented in Table 1, the TOC content of FT is greater than RB, which also means that the organic matter content of FT sediment is greater than RB. That is why the adsorption amount of FT is larger than RB. Chen et al. [21] reported that there is a positive correlation between organic matter content and sediment adsorption capacity. However, the amount of OTC adsorbed by the RF sediment is larger than that of the other two sediments because of its high content of silt in the sediment particle size distribution [22]. Laak et al. reported that the higher content of silt contains more clay minerals, more metal ions, and a

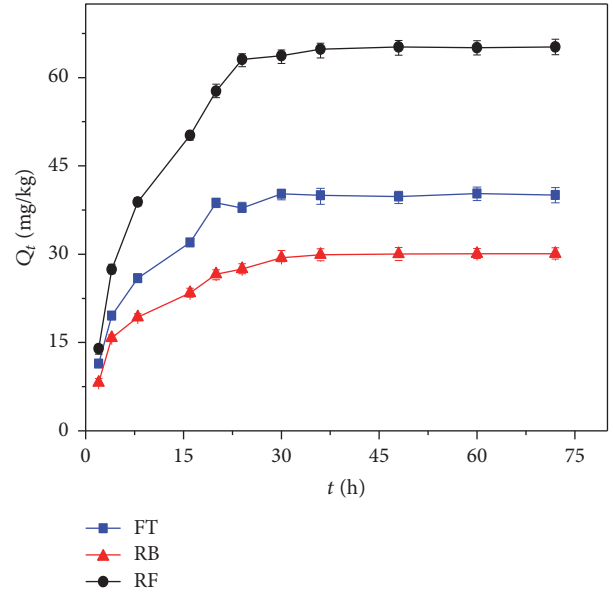


FIGURE 1: Adsorption characteristic of OTC to sediments.

larger cation exchange capacity. Interactions of exchangeable salt-based ions through the hydroxyl or dihydroxy sites with the cation in soil surface could enhance soil adsorption of OTC [23].

3.2. Effect of DOM on the Adsorption of OTC to Sediments

3.2.1. Effect on Sorption Kinetics. The adsorption kinetics of OTC to three sediments plotted in Figure 2 apparently showed that, before DOMs were added, the adsorption for three sediments is mainly divided into two phases, that is, the first phase for rapid adsorption in the first 8 hrs and the second phase for slow adsorption; the equilibrium time is about in 30 hrs. After the DOMs were added, the rapid phase is still in the first 8 hrs, while the equilibrium time is significantly accelerated in 24 hrs, indicating that the presence of DOMs can promote the adsorption equilibrium time, which may be due to the activation of the adsorption sites of sediment particles, reduction of the activation energy, and increasing of the adsorption rate when the DOMs were added.

To investigate the adsorption reaction process of OTC to sediments, pseudo-first-order model and pseudo-second-order model were used to fit the sorption kinetics data of OTC to sediments [5, 24, 25]. The adsorption trends are showed in Figure 2, while the corresponding fitting parameters are

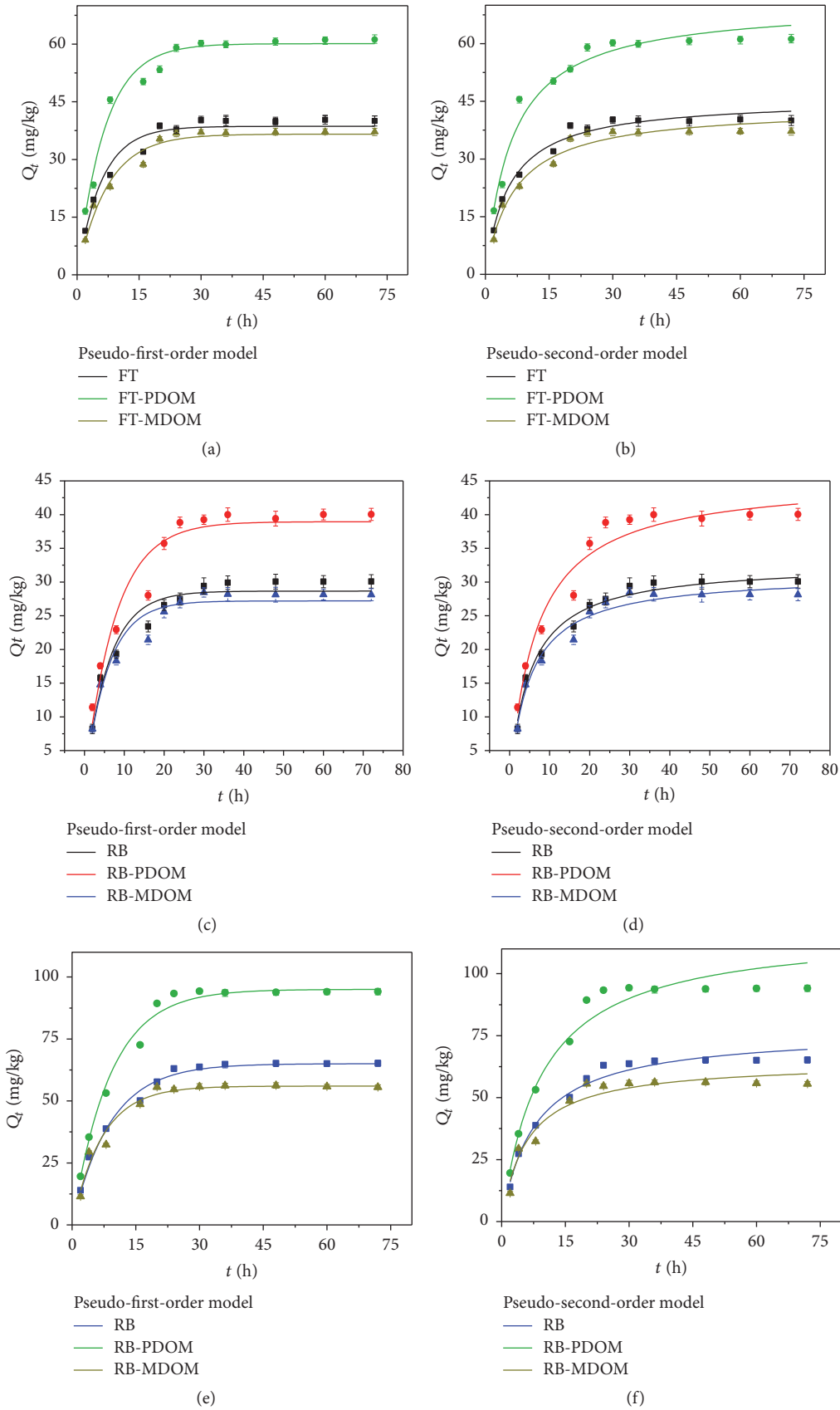


FIGURE 2: Effects of dissolved organic matter (DOM) on sorption kinetics of oxytetracycline to first terraces (FT) (a, b), riverbed (RB) (c, d), and river floodplain (RF) (e, f) sediment. FT-PDOM, RF-PDOM, and RB-PDOM refers to the sorption with the presence of corrupt plant derived DOM (PDOM). FT-MDOM, RF-MDOM, and RB-MDOM refers to the sorption with the presence of chicken manure derived DOM (MDOM).

TABLE 2: Pseudo-first-order and pseudo-second-order model fitted parameters for oxytetracycline sorption to three sediments with the presence of DOMs.

Samples	$Q_{e,exp}$	Pseudo-first-order model				Pseudo-second-order model			
	(mg/kg)	R^2	k_1 (1/h)	$Q_{e,cal}$ (mg/kg)	RSS/dof	R^2	k_2 (kg/mg·h)	$Q_{e,cal}$ (mg/kg)	RSS/dof
FT	40.027	0.9738	0.1695	38.618	101.663	0.9858	0.0040	45.684	55.278
FT-PDOM	61.209	0.9868	0.1695	60.121	118.341	0.9814	0.0023	70.417	166.769
FT-MDOM	37.190	0.9750	0.1502	36.588	101.698	0.9772	0.0034	43.441	93.081
RB	30.089	0.9410	0.1644	28.652	49.604	0.9789	0.0061	32.802	17.755
RB-PDOM	40.027	0.9453	0.1311	38.943	145.568	0.9683	0.0033	45.400	84.239
RB-MDOM	28.133	0.9458	0.1701	27.193	63.592	0.9729	0.0065	31.157	31.771
RF	65.208	0.9846	0.1121	65.024	61.865	0.9828	0.0017	76.862	68.885
RF-PDOM	94.121	0.9905	0.1129	95.029	266.481	0.9839	9.12E-4	117.880	450.348
RF-MDOM	55.521	0.9420	0.1423	55.988	221.475	0.9337	0.0027	64.432	252.881

TABLE 3: Langmuir isotherm model and Freundlich isotherm model fitted parameters for oxytetracycline sorption to three sediments with the presence of DOMs.

Samples	Langmuir isotherm model				Freundlich isotherm model				
	Q_m (mg/kg)	K_L (L/mg)	R^2	RSS/dof	R_L	K_F	$1/n$	R^2	RSS/dof
FT	454.919	0.0152	0.9883	27.1564	(0.759, 0.940)	8.1760	0.8628	0.9896	24.0104
FT-PDOM	563.141	0.0225	0.9889	57.3752	(0.681, 0.914)	14.2079	0.8551	0.9825	98.5720
FT-MDOM	323.665	0.0198	0.9898	60.8960	(0.708, 0.924)	7.5841	0.8411	0.9662	63.3506
RB	207.996	0.0257	0.9779	24.3801	(0.651, 0.903)	6.7888	0.7898	0.9789	23.2086
RB-PDOM	287.087	0.0237	0.9945	10.1586	(0.669, 0.910)	8.2462	0.8162	0.9926	13.6067
RB-MDOM	174.721	0.0334	0.9469	58.8434	(0.590, 0.878)	7.5521	0.7537	0.9445	61.3908
RF	536.867	0.0165	0.9701	179.9477	(0.744, 0.936)	14.6219	0.8530	0.9589	247.1996
RF-PDOM	688.969	0.0352	0.9549	567.9393	(0.577, 0.872)	26.4432	0.8302	0.9395	760.5967
RF-MDOM	426.129	0.0244	0.9625	149.7934	(0.663, 0.908)	11.1970	0.8354	0.9570	171.7898

listed in Table 2. The results showed that the sorption kinetic of OTC to RF sediments (without DOM) was fitted well to pseudo-first-order model for the greater value of R^2 and lower value of residual sum of squares (RSS/dof). The fitted theoretical equilibrium adsorption capacity ($Q_{e,cal}$) is also closer to the actual equilibrium adsorption capacity ($Q_{e,exp}$), while FT and RB sediments were fitted well to pseudo-second-order model. After the PDOM was added, R^2 of pseudo-first-order model was higher than that of pseudo-second-order model. $Q_{e,cal}$ of the pseudo-first-order model was 60.121, which was closer to the $Q_{e,exp}$ value of 61.209 than that of the value of 70.417 obtained by the pseudo-second-order model. The RSS/dof value of the former was 118.341, lower than that of the latter value of 166.769, so the sorption kinetic of OTC to FT sediments fitted better with pseudo-first-order with the addition of PDOM. Comparing to the sorption process without PDOM, the kinetic changed from pseudo-second-order to pseudo-first-order model. Similarly, after MDOM addition, the sorption kinetic of OTC to RF sediments was also changed from pseudo-second-order to pseudo-first-order model. This suggests that the adsorption process of these two sediments was controlled by binary factors (may be the surface active sites of the adsorbent and the solution concentration) changed to mono controlling (the

sites or the solution concentration only), after the DOM was added.

3.2.2. Effect on Sorption Isotherms. Freundlich and Langmuir isotherm models, which can be applicable to describe heterogeneous systems and reversible adsorption, and monolayer adsorption on a homogeneous surface, respectively, were employed to fit the experimental data of OTC [26]. Both Freundlich and Langmuir isotherm models fitted well to sorption isotherms of OTC with regression coefficients $R^2 > 0.93$ (Figure 3, Table 3) whether the DOMs were added or not, indicating that the addition of DOMs would not change the isotherm models.

With the increasing of OTC equilibrium concentration (C_e), the saturated adsorption capacity (Q_e) of the three sediments was also increased (Figure 3). However, there is a significant difference for the effects of the maximum adsorption amount of three sediments with two kinds of DOMs. After the PDOM was added, the adsorption capacity of FT sediment increased by 23.8%, and this value is 38.0% for RB sediment and 28.3% for RF, respectively (Table 3). While the MDOM was added, the adsorption capacity of FT sediment decreased by 23.3%, with similar decrease of 11.6% for RB sediment and 16.1% for RF sediment, respectively,

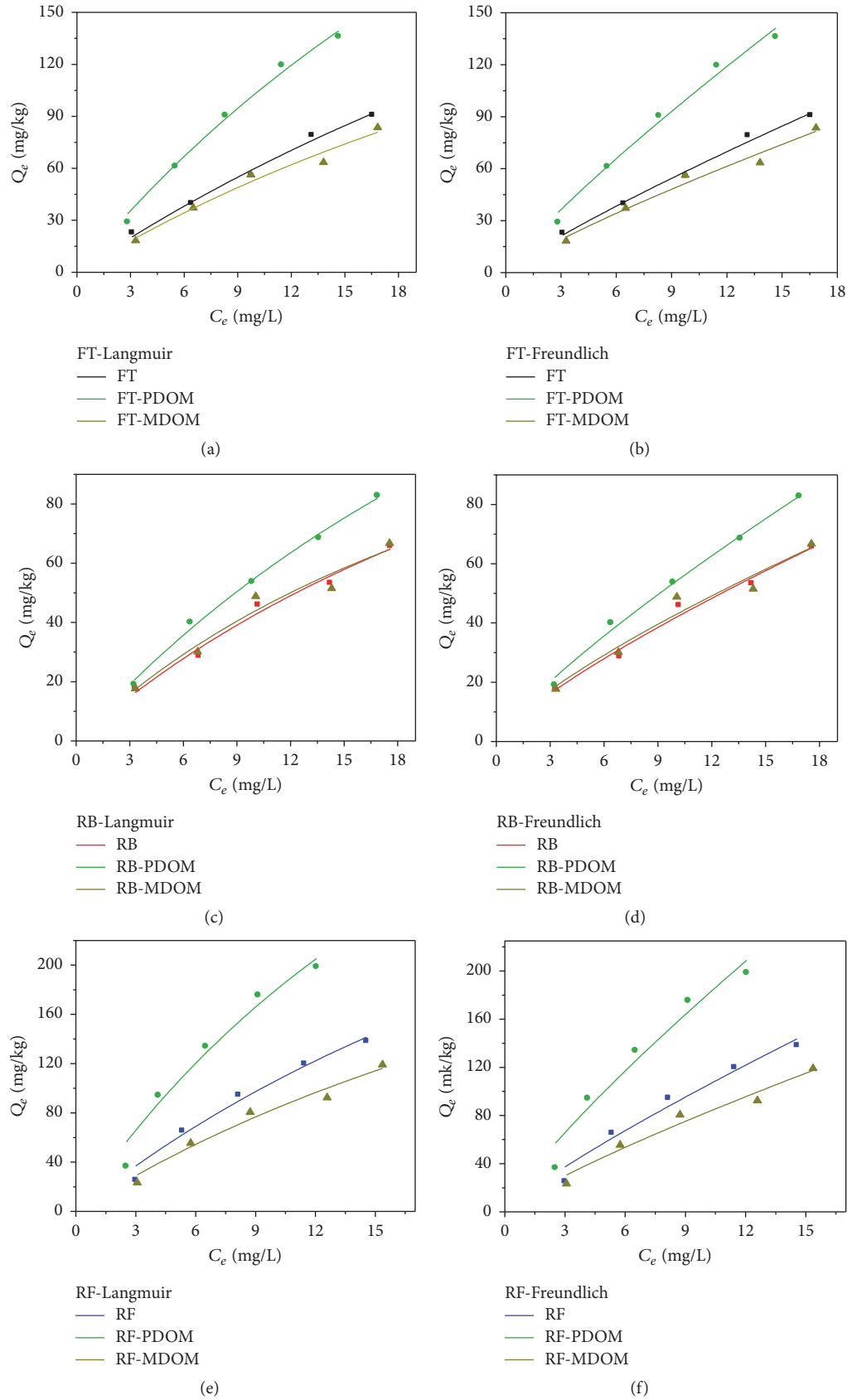


FIGURE 3: Effects of dissolved organic matter (DOM) on sorption isotherms of oxytetracycline to first terrace sediments (FT) (a, b), riverbed (RB) (c, d), and river floodplain (RF) (e, f).

TABLE 4: The parameters of sorption thermodynamics of oxytetracycline to three sediments with the presence of DOMs.

Samples	T (K)	K	ΔG (kJ/mol)	ΔH (kJ/mol)	ΔS (J·mol ⁻¹ ·K ⁻¹)
FT	298	5.1985	-4.084	39.417	0.146
	308	9.6358	-5.801		
	318	14.1700	-7.009		
FT-PDOM	298	9.1670	-5.489	35.796	0.139
	308	15.217	-6.971		
	318	22.761	-8.262		
FT-MDOM	298	4.5200	-3.737	38.559	0.141
	308	6.3480	-4.733		
	318	11.9860	-6.567		
RB	298	3.3407	-2.988	38.568	0.139
	308	5.1806	-4.212		
	318	8.8799	-5.774		
RB-PDOM	298	4.5150	-3.735	33.599	0.125
	308	6.7050	-4.873		
	318	10.584	-6.238		
RB-MDOM	298	3.2920	-2.952	38.280	0.138
	308	5.0800	-4.162		
	318	8.6850	-5.715		
RF	298	9.4643	-5.568	31.838	0.125
	308	13.0460	-6.577		
	318	21.1930	-8.073		
RF-PDOM	298	16.4380	-6.936	33.751	0.136
	308	23.6930	-8.105		
	318	38.6570	-9.663		
RF-MDOM	298	7.1801	-4.884	13.376	0.061
	308	8.3985	-5.449		
	318	10.0790	-6.109		

indicating that the adsorption of OTC could be promoted by adding PDOM, whereas the addition of MDOM could inhibit the adsorption.

3.2.3. Effect on Sorption Thermodynamics. The effects of temperature on the adsorption behavior were plotted in Figure 4. The adsorption capacity of OTC was consistent with the increase of temperature whether the DOM is added or not; that is, with the increase of temperature, the adsorption capacity increased, and at 318 K, the adsorption amount was the highest. The sorption capacity of the sediments followed the order: RF > FT > RB sediments at three temperatures. The maximum adsorption capacity of FT, RB, and RF sediment without DOMs fitted Langmuir models reached 776.015 mg/kg, 437.020 mg/kg, and 1182.468 mg/kg, respectively, at 318 K, which is increased by 1.203 times, 1.101 times, and 0.705 times for FT, RB, and RF, respectively, at 298 K. When the PDOM was added, the maximum adsorption capacity of three sediments of FT, RB, and RF reached 1056.176 mg/kg, 549.200 mg/kg, and 1350.031 mg/kg, respectively, at 318 K, which is increased by 0.876, 0.913, and

0.960 times compared to that at 298 K, respectively. When the MDOM was added, the maximum adsorption capacity of FT, RB, and RF in turn reached 538.410 mg/kg, 404.072 mg/kg, and 673.726 mg/kg at 318 K, which also increased by 0.663 times, 1.313 times, and 0.581 times compared to that at 298 K. Overall, the adsorption behavior of OTC to sediments responding to temperatures was changed with the addition of DOMs.

The thermodynamic parameters shown in Table 4 apparently displayed that the value of ΔG ranged from -9.663 kJ/mol to -2.952 kJ/mol for the adsorption process under three temperatures (298 K, 308 K, and 318 K) with the addition of DOMs. Jaycock et al. [27, 28] reported that the change of free energy for physical adsorption is smaller than that for chemisorption. The former is in the range of -20 kJ/mol~0, and the latter is in the range of -80 to -400 kJ/mol. So the adsorption process of OTC to sediments in this study is spontaneous, which was dominated mainly by physical adsorption. All the values of $\Delta H > 0$ indicated that the adsorption process is endothermic. With the increase of temperature, the value of ΔG gradually decreases, indicating

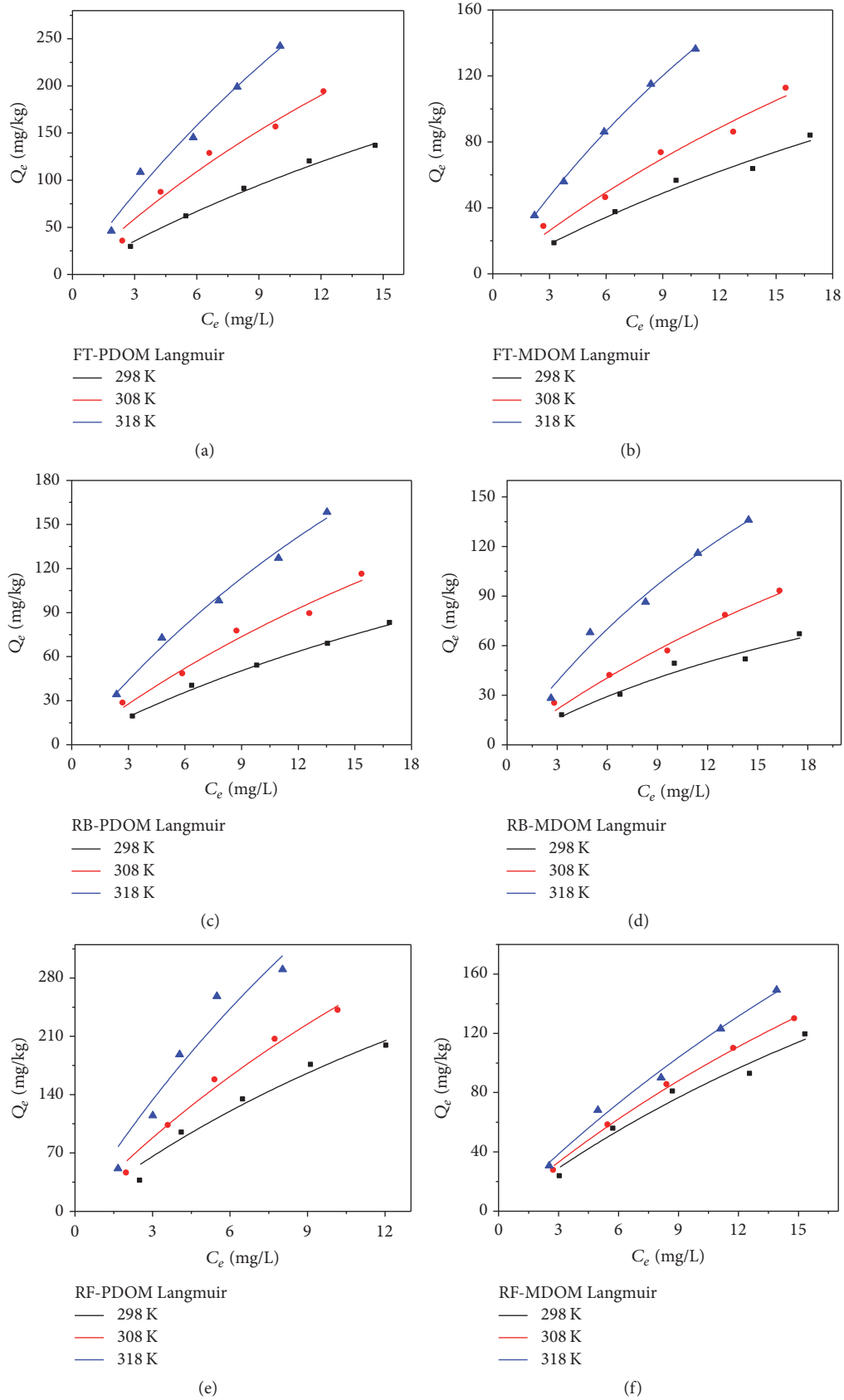


FIGURE 4: Effects of dissolved organic matter (DOM) on sorption thermodynamics of oxytetracycline to first terrace (FT) (a, b), riverbed (RB) (c, d), and river floodplain (RF) (e, f) sediments.

TABLE 5: The locations of five kinds of peaks and their significance.

Peaks	F_{\max} -Ex/Em (nm)	Significance	Main source and properties
P1	270/315	Protein-like	Site production, anthropogenic effluent-biodegradable
P2	285/350	Protein-like	Site production, anthropogenic effluent-biodegradable
H1	315(250)/400	Humus-like	Agricultural land, sewage-easy photolysis, poor bioavailability
	230/430		
	280/380–460		
H2	350(280)/460	Humus-like	Land-based, easy photodegradation, poor bioavailability
	320/366		
	420/480		
H3	350/450–485	Humus-like	Land-based, the degree of degradation is relatively abundant, widely spread in the water, photodegradable

$F_{\max}()$ refers to the wavelength of secondly high fluorescence peaks.

that the higher temperature reflects a higher spontaneous degree of reaction; that is, the elevated temperature is favorable for the adsorption. In addition, the values of ΔG for the sorption process followed the order: the process of MDOM > without DOMs > PDOM, indicating that the spontaneous degree of the adsorption was PDOM > without DOMs > MDOM, which also means that the adsorption of OTC could be promoted by adding PDOM, whereas the addition of MDOM could inhibit the adsorption.

3.2.4. Effect of DOM Concentration on Adsorption. To further explore the role of DOM on the sorption of OTC to sediments, single point sorption experiments were conducted under different concentration of DOM ranging from 0 to 300 mg TOC/L. The results showed that the presence of PDOM enhanced the adsorption of OTC to sediments in all examined concentrations, and the concentration ranging from 100 to 200 mg TOC/L related to a more obvious enhancement (Figure 5), indicating that the appropriate concentration of PDOM promoted a better effect; Jia et al. [5] reported that humic acid could be adsorbed by the sediments through π - π interaction. The excessive adsorbed PDOM could block pores and compete with OTC for adsorption sites on sediments, so the promotion was no more obvious. However, the adsorption amount of OTC adsorbed to three sediments decreased with increasing concentration of MDOM, and the inhibition to RF sediments is more obvious than FT and RB sediments.

3.3. Analysis for the Mechanism of the Adsorption

3.3.1. 3D Fluorescence Characteristics of DOMs. Two different peaks were identified in the three-dimensional fluorescence spectra of the two DOMs (Figure 6). Actually, many studies have investigated the location and significance of fluorescence peaks (Table 5) [29–34]. The PDOM can promote the adsorption of OTC to sediments, because it has a high-intensity H3 peak at Ex/Em = 340/430, which was assigned

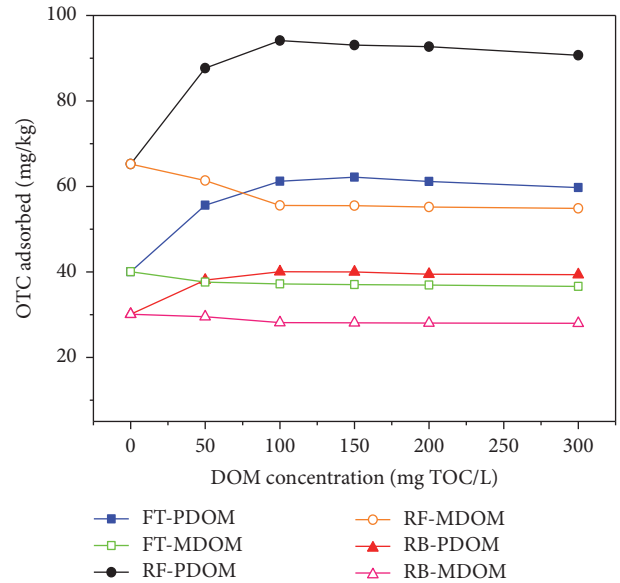


FIGURE 5: Effects of the presence of dissolved organic matters (DOM) on the sorption of oxytetracycline to first terrace (FT), river floodplain (RF), and riverbed (RB) sediments.

to a large number of humus-like substances. The result was consistent with our previous study that the humic acid could accelerate the adsorption of OTC to sediment [35], as well as its effect of tetracycline to montmorillonite reported by Zhao et al. [36], while the MDOM can inhibit the adsorption, because it has two P2 peaks at Ex/Em = 280/320 and a high-intensity peak at Ex/Em = 230/320, which were denoted as a large amount of protein-like substances. These results were in agreement with the effect of pig slurry on the sorption of sulfonamide antibiotics to soil [16] and chicken manure on the sorption of OTC [37].

3.3.2. Elemental Analysis. To investigate the characterization of two DOMs, the elemental analysis was conducted. The

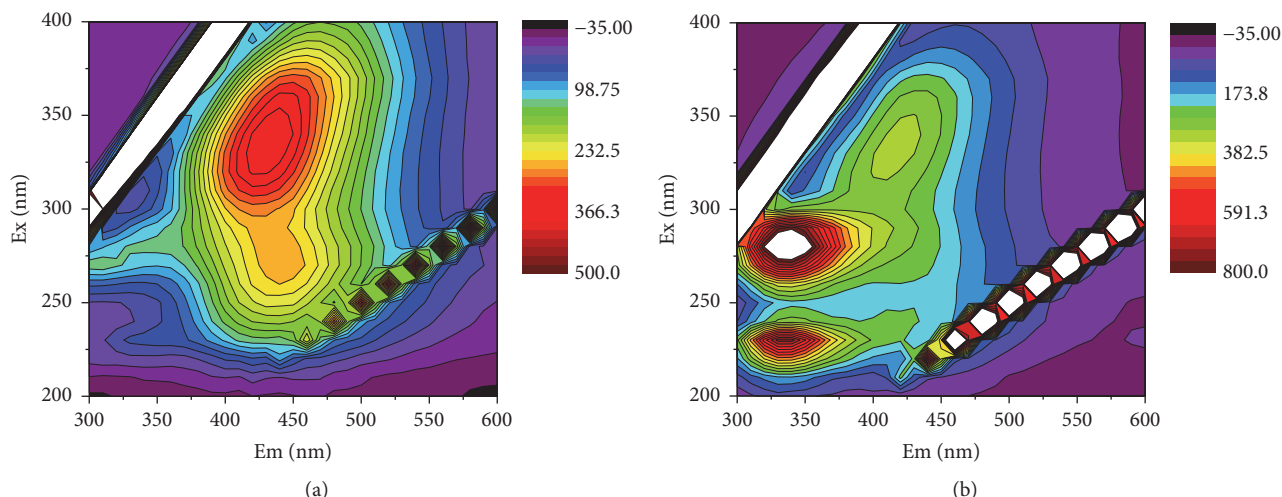


FIGURE 6: The 3D fluorescence spectra of (a) corrupt plant derived DOM (PDOM); (b) chicken manure derived DOM (MDOM).

TABLE 6: Elemental composition of corrupt plant derived DOM (PDOM) and chicken manure derived DOM (MDOM).

Samples	N (%)	C (%)	H (%)	O (%)	H/C	(N + O)/C	O/C
PDOM	1.706	23.483	2.905	0.256	0.124	0.084	0.011
MDOM	1.977	9.490	1.951	0.122	0.206	0.152	0.013

larger value of $(N + O)/C$ reflects the samples with higher polarity, while larger value of H/C indicates a lower aromaticity. The larger value of O/C reflects a higher hydrophilicity. Two samples contained a large amount of C content while O content is relatively small (Table 6). Compared with the MDOM, the PDOM has the higher C, H contents, whereas the content of N is low, which is consistent with the source of this kind of DOM.

Considering that the H/C value of the PDOM is smaller, its high aromaticity leads to an easier combination with the sediment, so as to increase the number of adsorption sites and promote the adsorption of OTC. For the chicken manure, it has a higher value of $(N + O)/C$, O/C . Its hydrophilicity and polarity are higher, which can not only promote the dissolution of pollutants in the water, but also improve its mobility, suggesting that the chicken manure DOM inhibits the adsorption of OTC to sediments.

4. Conclusions

The following conclusions can be drawn from the current study:

(1) The presence of DOMs can reduce the adsorption equilibrium time about 6 hrs and can change the sorption kinetics. Both Freundlich and Langmuir isotherm models fitted to sorption isotherms of OTC well and the addition of DOMs would not change the isotherm models. The adsorption of OTC could be promoted by adding PDOM, whereas the addition of MDOM could inhibit the adsorption. The adsorption processes are all endothermic, spontaneous, and mainly physical adsorption. The spontaneous degree of

the adsorption process followed the order: PDOM > without DOMs > MDOM.

(2) Comparing the adsorption mechanism of the two kinds of DOM, it was found that the PDOM has high aromaticity, low hydrophilicity, and polarity because it consists of humus-like substances, leading to an easier combination with the sediment, so as to increase the number of adsorption sites and promote the adsorption of OTC. The MDOM has high hydrophilicity and polarity because it consists of protein-like substances, which can promote the dissolution of pollutants in the water and improve its mobility. It suggested that the chicken manure DOM inhibits the adsorption of OTC to sediments; that is, the humus-like dominated DOM can promote the adsorption of OTC, while the protein-like dominated DOM can inhibit the adsorption of OTC to sediments.

Conflicts of Interest

The authors declare that there are no conflicts of interest regarding the publication of this article.

Acknowledgments

The work was financially supported by National Natural Science Foundation of China (no. 41372259 and no. 41672224), the National Key Research and Development Program of China (no. 2016YFC0400701), the Fundamental Research Funds for the Central Universities (no. GK201703052), China Postdoctoral Science Foundation (no. 2017M613048), and Shaanxi postdoctoral research funding project in China (no. 2017BSHTDZZ03).

References

- [1] A. K. Sarmah, M. T. Meyer, and A. B. A. Boxall, "A global perspective on the use, sales, exposure pathways, occurrence, fate and effects of veterinary antibiotics (VAs) in the environment," *Chemosphere*, vol. 65, no. 5, pp. 725–759, 2006.
- [2] S. Q. Zhang, F. D. Zhang, and X. M. Liu, "Determination and analysis on main harmful composition in excrement of scale livestock and poultry feedlots," *Plant Nutrition Fertilizing Science*, vol. 11, no. 6, pp. 822–829, 2005.
- [3] R. Wang, T.-Z. Liu, and T. Wang, "The fate of antibiotics in environment and its ecotoxicology: A review," *Acta Ecologica Sinica*, vol. 26, no. 1, pp. 265–269, 2006 (Chinese).
- [4] Y.-Y. Bao, Q.-X. Zhou, Y. Wan, Q. Yu, and X.-J. Xie, "Adsorption and desorption of three tetracycline antibiotics in cinnamon soils of China," *China Environmental Science*, vol. 30, no. 10, pp. 1383–1388, 2010 (Chinese).
- [5] M. Jia, F. Wang, Y. Bian et al., "Sorption of sulfamethazine to biochars as affected by dissolved organic matters of different origin," *Bioresource Technology*, 2017.
- [6] M. Kühne, D. Ihnen, G. Möller, and O. Agthe, "Stability of Tetracycline in Water and Liquid Manure," *Journal of Veterinary Medicine Series A: Physiology Pathology Clinical Medicine*, vol. 47, no. 6, pp. 379–384, 2000.
- [7] S. Oh, W. S. Shin, and H. T. Kim, "Effects of pH, dissolved organic matter, and salinity on ibuprofen sorption on sediment," *Environmental Science and Pollution Research*, vol. 23, no. 22, pp. 22882–22889, 2016.
- [8] P. Kulshrestha, R. F. Giese Jr., and D. S. Aga, "Investigating the molecular interactions of oxytetracycline in clay and organic matter: Insights on factors affecting its mobility in soil," *Environmental Science & Technology*, vol. 38, no. 15, pp. 4097–4105, 2004.
- [9] K.-L. Chen, L.-C. Liu, and W.-R. Chen, "Adsorption of sulfamethoxazole and sulfapyridine antibiotics in high organic content soils," *Environmental Pollution*, vol. 231, pp. 1163–1171, 2017.
- [10] C. T. Chiou, R. L. Malcolm, T. I. Brinton, and D. E. Kile, "Water solubility enhancement of some organic pollutants and pesticides by dissolved humic and fulvic acids," *Environmental Science & Technology*, vol. 20, no. 5, pp. 502–508, 1986.
- [11] S. D. Nelson, J. Letey, W. J. Farmer, C. F. Williams, and M. Ben-Hur, "Facilitated transport of napropamide by dissolved organic matter in sewage sludge-amended soil," *Journal of Environmental Quality*, vol. 27, no. 5, pp. 1194–1200, 1998.
- [12] C. F. Williams, M. Agassi, J. Letey, W. J. Farmer, S. D. Nelson, and M. Ben-Hur, "Facilitated transport of napropamide by dissolved organic matter through soil columns," *Soil Science Society of America Journal*, vol. 64, no. 2, pp. 590–594, 2000.
- [13] X. Huang and L. S. Lee, "Effects of dissolved organic matter from animal waste effluent on chlorpyrifos sorption by soils," *Journal of Environmental Quality*, vol. 30, no. 4, pp. 1258–1265, 2001.
- [14] S. Yang, L. Gao, Y. Y. Liu, Y. Zhao, H. Li, and Y. Zhou, "The influence of Humic Acid Colloid on adsorption behaviors of acetaminophen onto sediment," *Fresenius Environmental Bulletin*, vol. 24, no. 11B, pp. 4042–4049, 2015.
- [15] C. Gao, S. Yang, W. Wang, and L. Gao, "Influence of humic acid colloid on adsorption of ddt in the riverbed sediments," *Asian Journal of Chemistry*, vol. 26, no. 9, pp. 2637–2642, 2014.
- [16] S. Thiele-Bruhn and M.-O. Aust, "Effects of pig slurry on the sorption of sulfonamide antibiotics in soil," *Archives of Environmental Contamination and Toxicology*, vol. 47, no. 1, pp. 31–39, 2004.
- [17] W. Ling, J. Xu, Y. Gao, and H. Wang, "Influence of dissolved organic matter (DOM) on environmental behaviors of organic pollutants in soils," *Chinese Journal of Applied Ecology*, vol. 15, no. 2, pp. 326–330, 2004 (Chinese).
- [18] A. Nebbioso and A. Piccolo, "Molecular characterization of dissolved organic matter (DOM): a critical review," *Analytical and Bioanalytical Chemistry*, vol. 405, no. 1, pp. 109–124, 2013.
- [19] Y. Zielesny, J. Groeneweg, H. Vereecken, and W. Tappe, "Impact of sulfadiazine and chlorotetracycline on soil bacterial community structure and respiratory activity," *Soil Biology & Biochemistry*, vol. 38, no. 8, pp. 2372–2380, 2006.
- [20] P. K. Jjemba, "The potential impact of veterinary and human therapeutic agents in manure and biosolids on plants grown on arable land: a review," *Agriculture, Ecosystems & Environment*, vol. 93, no. 1–3, pp. 267–278, 2002.
- [21] M. Chen, W. Tang, C. Ge, and L. Peng, "Effects of biochar made from bagasse on adsorption behavior of ofloxacin in latosols," *Chinese Journal of Environmental Engineering*, vol. 9, no. 10, pp. 5083–5090, 2015 (Chinese).
- [22] R.-H. Qi, Z.-J. Li, J. Long, F.-F. Fan, and Y.-C. Liang, "Effects of soil trituration size on adsorption of oxytetracycline on soils," *Environmental science*, vol. 32, no. 2, pp. 589–595, 2011 (Chinese).
- [23] T. L. Laak, W. A. Gebbink, and J. Tolls, "Estimation of soil sorption coefficients of veterinary pharmaceuticals from soil properties," *Environmental Toxicology and Chemistry*, vol. 25, no. 4, pp. 933–941, 2006.
- [24] J. Lin, Y. Zhan, Z. Zhu, and Y. Xing, "Adsorption of tannic acid from aqueous solution onto surfactant-modified zeolite," *Journal of Hazardous Materials*, vol. 193, pp. 102–111, 2011.
- [25] J. Y. Zhang, L. P. Liang, L. J. Pu, and et al., "Adsorption characteristics of Cr(VI) by wheat straw including kinetic and thermodynamics analysis," *Research of Environmental Sciences*, vol. 23, no. 12, pp. 1547–1552, 2010.
- [26] M. A. Wahab, S. Jellali, and N. Jedidi, "Ammonium biosorption onto sawdust: FTIR analysis, kinetics and adsorption isotherms modeling," *Bioresource Technology*, vol. 101, no. 14, pp. 5070–5075, 2010.
- [27] M. J. Jaycock and G. D. Parfitt, *Chemistry of Interfaces*, Ellis Horwood Limited Publisher, 1981.
- [28] Y. Yu, Y.-Y. Zhuang, Z.-H. Wang, and M.-Q. Qiu, "Adsorption of water-soluble dyes onto modified resin," *Chemosphere*, vol. 54, no. 3, pp. 425–430, 2004.
- [29] P. G. Coble, "Marine optical biogeochemistry: The chemistry of ocean color," *Chemical Reviews*, vol. 107, no. 2, pp. 402–418, 2007.
- [30] C. A. Stedmon and S. Markager, "Resolving the variability in dissolved organic matter fluorescence in a temperate estuary and its catchment using PARAFAC analysis," *Limnology and Oceanography*, vol. 50, no. 2, pp. 686–697, 2005a.
- [31] C. A. Stedmon and S. Markager, "Tracing the production and degradation of autochthonous fractions of dissolved organic matter by fluorescence analysis," *Limnology and Oceanography*, vol. 50, no. 5, pp. 1415–1426, 2005b.
- [32] L. Jørgensen, C. A. Stedmon, T. Kragh, S. Markager, M. Middelboe, and M. Søndergaard, "Global trends in the fluorescence characteristics and distribution of marine dissolved organic matter," *Marine Chemistry*, vol. 126, no. 1–4, pp. 139–148, 2011.
- [33] S. K. L. Ishii and T. H. Boyer, "Behavior of reoccurring parafac components in fluorescent dissolved organic matter in natural

- and engineered systems: A critical review,” *Environmental Science & Technology*, vol. 46, no. 4, pp. 2006–2017, 2012.
- [34] C. A. Stedmon, B. Seredyńska-Sobecka, R. Boe-Hansen, N. Le Tallec, C. K. Waul, and E. Arvin, “A potential approach for monitoring drinking water quality from groundwater systems using organic matter fluorescence as an early warning for contamination events,” *Water Research*, vol. 45, no. 18, pp. 6030–6038, 2011.
- [35] L. Gao, S. Yang, D. Wang, C. Gao, and G. Wang, “Influence of humic acid colloid on adsorption of oxytetracycline in sediment,” *Asian Journal of Chemistry*, vol. 26, no. 24, pp. 8303–8308, 2014.
- [36] Y. Zhao, X. Gu, S. Gao, J. Geng, and X. Wang, “Adsorption of tetracycline (TC) onto montmorillonite: Cations and humic acid effects,” *Geoderma*, vol. 183–184, pp. 12–18, 2012.
- [37] Q. Kang, S. Bao, H. Wang, and et al., “Adsorption of tetracycline and zine on the soil in the dissolved organic matter-tetracycline-zinc coexistence system,” *Science Technology and Engineering*, vol. 16, no. 14, pp. 69–73, 2016 (Chinese).

Research Article

A Regional Scale Investigation on Groundwater Arsenic in Different Types of Aquifers in the Pearl River Delta, China

Qinxuan Hou,¹ Jichao Sun,¹ Jihong Jing,¹ Chunyan Liu,¹ Ying Zhang,¹
Jingtao Liu ,¹ and Mengjian Hua²

¹*Institute of Hydrogeology and Environmental Geology, Chinese Academy of Geological Sciences, Shijiazhuang, China*

²*Tsinghua University High School, Beijing, China*

Correspondence should be addressed to Jingtao Liu; 728881944@qq.com

Received 10 October 2017; Revised 4 December 2017; Accepted 14 January 2018; Published 18 February 2018

Academic Editor: Meijing Zhang

Copyright © 2018 Qinxuan Hou et al. This is an open access article distributed under the Creative Commons Attribution License, which permits unrestricted use, distribution, and reproduction in any medium, provided the original work is properly cited.

Nearly 400 groundwater samples were collected from different types of aquifers in the Pearl River Delta (PRD), and the concentrations of groundwater arsenic (As) and other 22 hydrochemical parameters in different types of aquifers were then investigated. Results showed that groundwater As concentration was up to hundreds $\mu\text{g/L}$ in granular aquifers, while those in fissured aquifers and karst aquifers were only up to dozens and several $\mu\text{g/L}$, respectively. Correspondingly, about 9.4% and 2.3% samples with high concentrations ($>0.01\text{ mg/L}$) of As were in granular and fissured aquifers, respectively, but no samples with high concentration of As were in karst aquifers. The source and mobilization of groundwater As in granular aquifers are likely controlled by the following mechanism: organic matter in marine strata was mineralized and provided electrons for electron acceptors, resulting in the release of NH_4^+ and I^- and the reduction of Fe/Mn and NO_3^- , and was accompanied with the mobilization of As from sediments into groundwater. By contrast, both natural processes including the competitive adsorption between As anions and $\text{F}^-/\text{PO}_4^{3-}/\text{HCO}_3^-$ and anthropogenic processes including industrialization were responsible for high concentrations of groundwater As in fissured aquifers.

1. Introduction

Arsenic (As) is discovered as one of the most common toxic elements in environments. Groundwater with high concentrations of As is a major environmental and public health problem on a global scale. According to the World Health Organization [1], the acceptable value of As in groundwater for drinking purpose is $10\text{ }\mu\text{g/l}$. High concentrations of As ($>10\text{ }\mu\text{g/L}$) in aquifers have been reported in many countries, such as Bangladesh [2], India [3], China [4], and the United States [5], and granular aquifers are paid the most attention due to the common occurrence of high levels of As.

Pearl River Delta (PRD) is one of the most important economic regions in China. On the one hand, urbanization has accelerated the contamination and deterioration of surface water quality in this region [6]. On the other hand, abundant groundwater is stored in aquifers and it is free of charge in this region. As a consequence, it is essential to investigate the distribution of As in aquifers of the whole PRD, in

order to improve groundwater management in this region and increase the availability of groundwater for sustainable development of the PRD. Although a couple of studies had already reported the occurrence of high levels of As in granular aquifers of Xijiang river basin and Guangzhou area (both of them within the PRD) [7, 8], the distribution of As in karst aquifers and other areas within the PRD is little known.

The present study therefore aims to (1) investigate the concentrations of groundwater As in different types of aquifers in the whole PRD on a regional scale and (2) discuss the influence factors on the distribution of groundwater As in aquifers. Multivariate statistical techniques such as principal components analysis (PCA) have been used in this study, because PCA can not only help to understand the hydrochemical processes but also provide information about which factors are responsible for high levels of groundwater As in aquifers [7]. The results obtained from this study can be a useful reference on the groundwater management of this region.

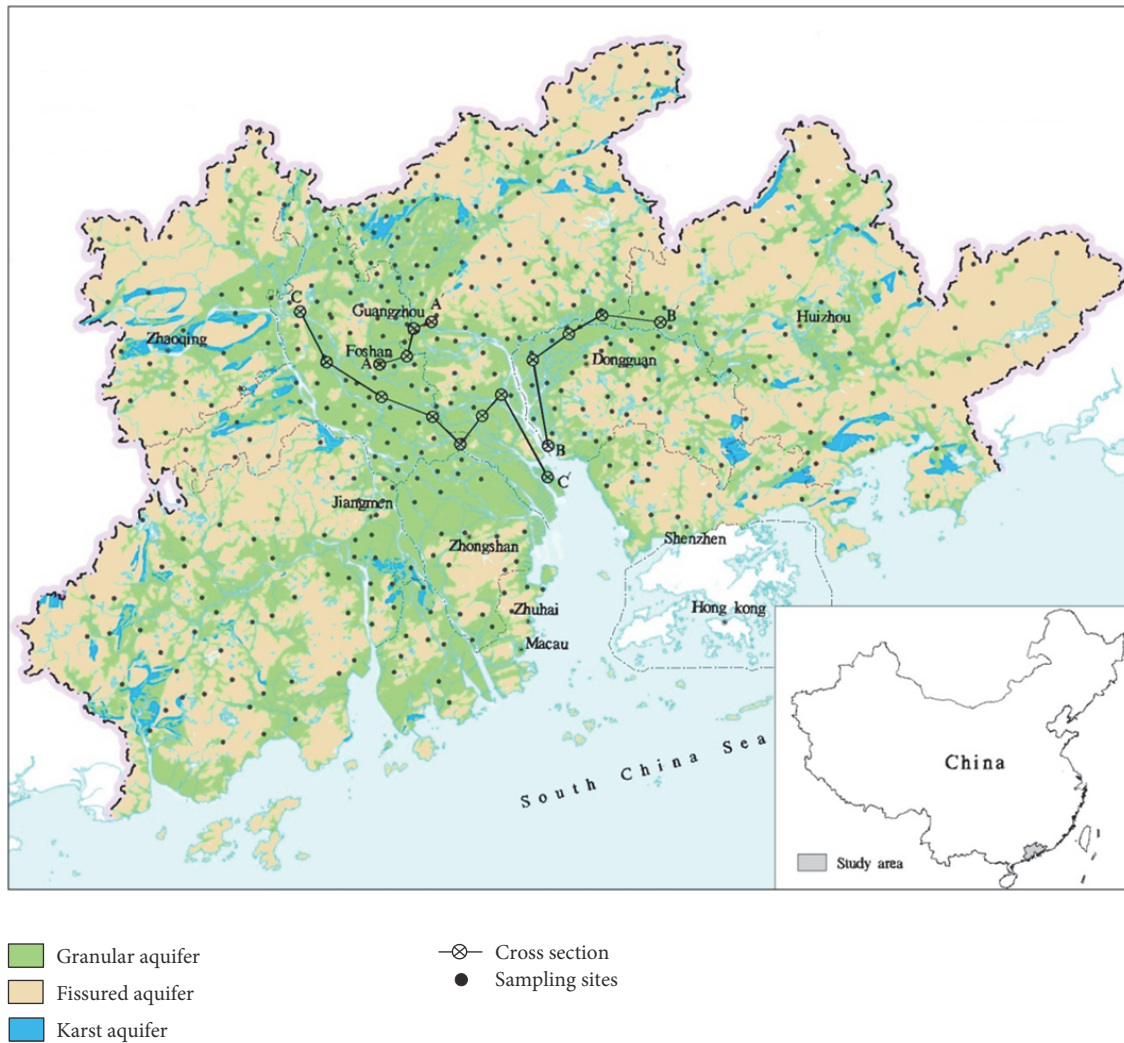


FIGURE 1: Hydrogeological setting and sampling sites in the PRD.

2. Study Area

2.1. Geographical Conditions. The PRD ($111^{\circ}59' - 115^{\circ}25'E$, $21^{\circ}17' - 23^{\circ}55'N$) is formed as a result of uplift of the Tibetan Plateau during the Tertiary and Quaternary Periods, locating in southern China (Figure 1). It is with the boundaries of hills in the east, west, and north and the South China Sea in the south, and the topography of PRD also inclines from the east, west, and north to the south. The total area is $41,698 \text{ km}^2$, including Guangzhou, Shenzhen, Huizhou, Dongguan, Foshan, Zhaoqing, Zhongshan, Zhuhai, and Jiangmen city in district. The total population of the area is 43.15 million in 2005. The climate is typically subtropical monsoon, characterized by hot and wet summer and autumn and relatively cold and dry winter and spring. The annual average temperature is 21.9°C , and the mean annual precipitation is 1800–2200 mm. The PRD belongs to the drainage basin of Pearl River. East River, West River, and North River merge in the south of the area and compose the Pearl River and discharge into the South China Sea [9].

2.2. Geological and Hydrogeological Settings. The central and southern parts of the PRD are mostly covered by Quaternary sediments. Quaternary sediments consist of two terrestrial sequences and two marine sequences by the mode of overlaying each other [10]. The younger marine sequence is recorded at altitudes above -20 m , and the older marine sequence is recorded at altitudes between -15 m and -40 m (Figure 2). The younger terrestrial sequence can be sandy fluvial deposits or clayed silt weathered from the in situ materials during the last glacial period and becomes a local intermediate aquifer when it is sandy. The older terrestrial sequence is dominated by sand and gravel and becomes the basal aquifer. In many places, the older marine sequence and the younger terrestrial sequence are missing or decomposed into clay when the sea-level regressed during the last glacial period [10]. Groundwater is mainly recharged by vertical infiltration from precipitation and agricultural irrigation and during the floodtime and wet season by the lateral flow from rivers. The bedrocks include shale, sandstone, limestone, dolomite, granite, and gneiss ranging in age from Cambrian to Tertiary

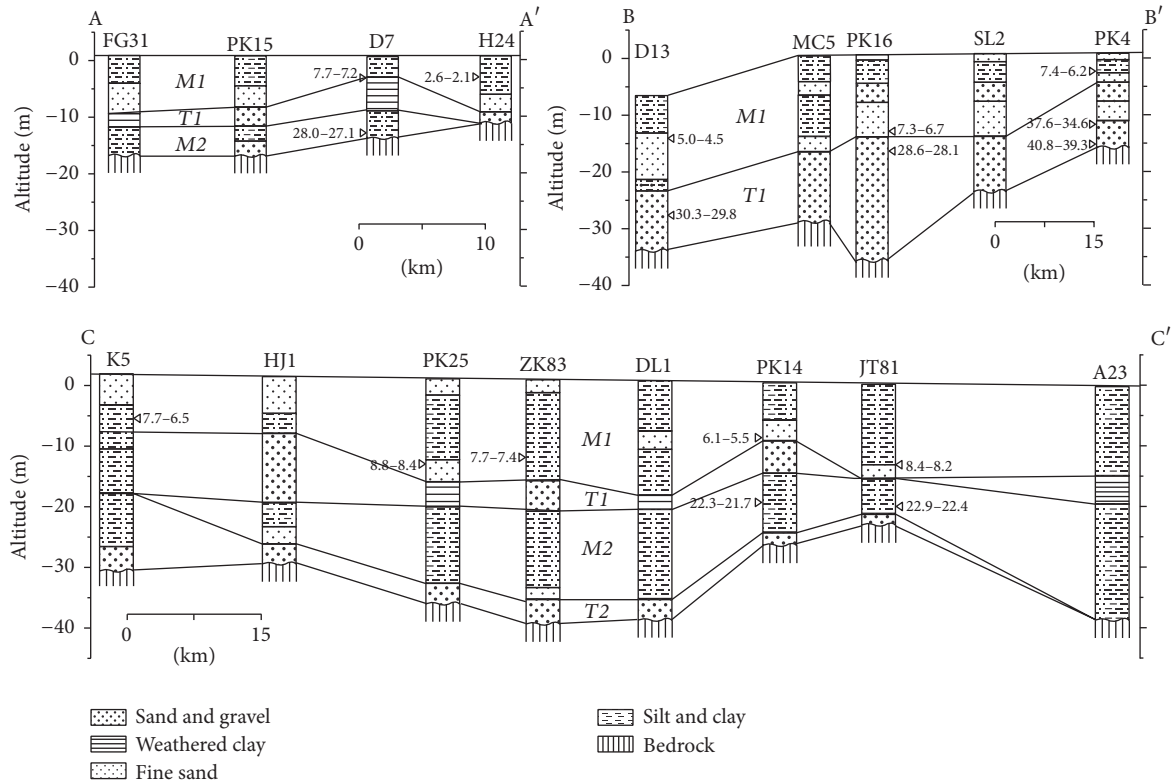


FIGURE 2: Cross sections in the PRD (from Zong et al. [10]).

and crop out around and within the PRD. Aquifers in this area are mainly associated with fractures and with springs yield up to hundreds m^3/d . Karst aquifers are less than 10% of the total area and around the PRD plain, and the groundwater yield can be as high as $1000 \text{ m}^3/\text{d}$. The general direction of regional groundwater flow in the aquifers of the PRD is northwest and northeast toward the coast [11].

3. Materials and Methods

3.1. Sample Collection. Groundwater samples were collected from 399 wells (256, 132, and 11 wells in granular aquifers, fissured aquifers, and karst aquifers, respectively), and the sampling densities were 30–50 samples and 5–10 samples of 1000 km^2 in plain and hilly areas, respectively. In order to ensure that the groundwater samples were representative of the in situ conditions, samples were collected after purging at least 2 borehole volumes. Two 250 mL polyethylene bottles were used to store filtered ($1.2 \mu\text{m}$ filter membrane) groundwater for trace elements and major ions analysis. One bottle was acidified with nitric acid to a pH less than 2 for trace elements determination. The other bottle for major ions analysis was unacidified. All samples were stored at 4°C until laboratory procedures could be performed.

3.2. Analytical Techniques. Electrical conductivity (EC), pH, electrode potential (Eh), and dissolved oxygen (DO) were measured in situ using WTW Multi 340i/SET multiparameters instrument (Germany), which was previously calibrated. All analyses were carried out at the Groundwater Mineral

Water and Environmental Monitoring Center of the Institute of Hydrogeology and Environmental Geology, Chinese Academy of Geological Sciences. Metal ions and trace elements (K, Na, Ca, Mg, Fe, Mn, As, and Al) were measured by inductively coupled plasma-mass spectrometry (ICP-MS) (Agilent 7500ce ICP-MS, Tokyo, Japan). Total dissolved solids (TDS) and total hardness (TH) were measured by gravimetric and EDTA titration method, respectively. HCO_3^- was measured by acid-base titration, and NH_4^+ and other anions (NO_3^- , SO_4^{2-} , Cl^- , NO_2^- , F^- , Br^- , I^- , and PO_4^{3-}) were carried out on ion chromatography (IC) (Shimadzu LC-10ADvp, Japan). The relative errors were less than $\pm 6\%$ for all analyzed parameters.

3.3. Principal Components Analysis (PCA). PCA was useful for data reduction [6, 7]. In this study, PCA was used to reduce the parameters and extract the main influence factors which are responsible for high concentrations of As in groundwater. In the PCA, the rotation of principal components (PCs) was carried out using the varimax method. The SPSS® release 23.0 (SPSS Inc., Chicago, USA) was used to analyze the groundwater chemical data.

4. Results and Discussion

4.1. Hydrochemical Characteristics. The descriptive statistics for the parameters analyzed in the groundwater samples are summarized in Table 1. Groundwater pH was predominantly acidic to near neutral in the PRD and similar range of pH in different types of aquifers. EC value was in a wide range

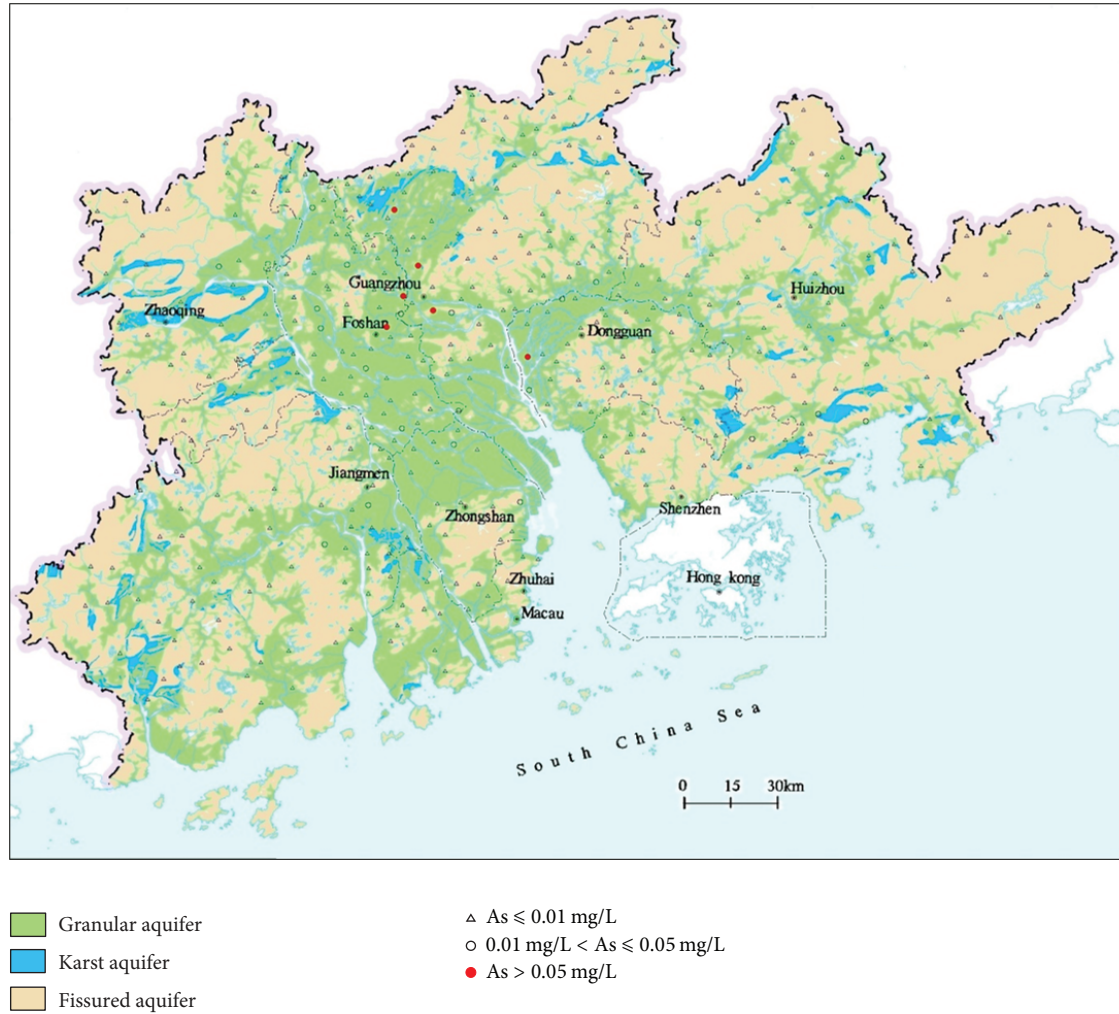


FIGURE 3: As concentrations in different types of aquifers in the PRD.

of $22 \mu\text{S}/\text{cm}$ to $6510 \mu\text{S}/\text{cm}$, and the mean and maximum values of EC in granular aquifers were far higher than that in fissured aquifers and karst aquifers. This may be attributed to the occurrence of sea water intrusion in granular aquifers, because sea water is characterized by high EC value and granular aquifers in the PRD are close to South China Sea while fissured and karst aquifers are relatively far from the sea [6]. DO and Eh values were also in a wide range. The mean value of Eh in karst aquifers was far higher than that in granular and fissured aquifers, indicating that the oxidability of karst aquifers in the PRD was commonly stronger than other two types of aquifers. TDS and TH values showed similar rules of the EC value in different types of aquifers in the PRD, which may also be ascribed to the occurrence of sea water intrusion in granular aquifers. The major cations of groundwater dominated with Na^+ and Ca^{2+} , while the major anions dominated with HCO_3^- and Cl^- in the whole PRD. It is worth mentioning that groundwater NO_3^- was also a major ion in aquifers in the whole PRD, not only in granular aquifers but also in fissured and karst aquifers, and the concentration of groundwater NO_3^- was up to hundreds mg/L in both granular aquifers and fissured aquifers. Correspondingly, the

concentrations of other two nitrogen compounds in aquifers of the PRD were up to dozens mg/L, and the mean and maximum values of both groundwater NO_3^- and NH_4^+ in granular aquifers were far higher than that in fissured and karst aquifers. No distinct difference of concentrations of groundwater PO_4^{3-} and F^- in different types of aquifers in the PRD was found. The concentration of groundwater I^- in granular and fissured aquifers was commonly higher than that in karst aquifers. The concentration of groundwater Fe in different types of aquifers showed a significant difference with the highest mean value in granular aquifers and lowest mean value in karst aquifers. The concentrations of groundwater Mn and Al in granular and fissured aquifers were generally higher than those in karst aquifers. The concentration of groundwater As in different types of aquifers also showed a significant difference. The concentration of groundwater As in granular aquifers was up to hundreds $\mu\text{g}/\text{L}$, while those in fissured aquifers and karst aquifers were only up to dozens and several $\mu\text{g}/\text{L}$, respectively (Table 1).

4.2. Spatial Distribution of As in Aquifers of the PRD. As it can be seen from Figure 3, the highest proportion of groundwater

TABLE 2: Principal component (PC) loadings for groundwater samples in granular aquifers.

Item	PC1	PC2	PC3	PC4	PC5	PC6	PC7
pH	0.105	0.755	0.163	0.174	0.025	-0.011	-0.043
EC	0.766	0.432	0.196	0.102	0.386	-0.053	0.003
DO	-0.274	-0.206	-0.163	-0.134	-0.045	0.500	-0.312
Eh	-0.015	-0.248	-0.051	-0.055	0.069	0.707	0.219
K ⁺	0.314	0.286	0.046	-0.044	0.804	-0.035	0.038
Na ⁺	0.942	0.151	0.065	0.053	0.107	-0.085	0.027
Ca ²⁺	0.324	0.753	0.239	0.158	0.314	-0.233	-0.043
Mg ²⁺	0.812	0.277	0.079	0.067	0.100	0.174	-0.059
NH ₄ ⁺	0.240	0.186	0.571	0.519	-0.113	0.260	-0.072
Fe	0.125	0.060	0.244	0.672	-0.141	-0.324	0.123
HCO ₃ ⁻	0.363	0.712	0.431	0.272	-0.026	-0.109	-0.048
Cl ⁻	0.945	0.092	0.010	0.039	0.178	-0.057	0.030
SO ₄ ²⁻	0.399	0.541	-0.131	0.064	0.420	-0.168	0.026
F ⁻	0.135	0.717	-0.098	-0.100	-0.223	-0.031	0.203
NO ₃ ⁻	0.236	-0.174	-0.072	-0.157	0.814	0.068	-0.048
TDS	0.675	0.530	0.294	0.138	0.350	-0.129	-0.026
TH	0.535	0.692	0.217	0.148	0.283	-0.125	-0.054
I ⁻	-0.021	0.136	0.361	0.684	0.088	0.039	0.186
PO ₄ ³⁻	0.048	0.203	0.900	0.064	0.031	0.016	0.023
Al	-0.034	0.019	-0.011	0.047	-0.018	0.096	0.905
Mn	0.058	0.075	-0.127	0.851	-0.070	0.044	-0.116
NO ₂ ⁻	0.252	0.338	0.218	0.376	-0.156	0.541	0.063
As	0.101	0.022	0.890	0.116	-0.021	-0.147	-0.004
Eigenvalue	4.6	3.9	2.7	2.3	2.1	1.4	1.1
Explained variance (%)	19.9	17.1	11.7	10.1	9.2	6.2	4.8
Cumulative% of variance	19.9	37.0	48.8	58.9	68.1	74.3	79.1

samples with high concentrations of As was in Foshan city, and it was 16.7%, which was followed by Zhongshan (10.5%), Dongguan (7.3%), Shenzhen (6.7%), Guangzhou (6.6%), Huizhou (4.8%), Zhaoqing (3.6%), Jiangmen (3.3%), and Zhuhai city (0%) in district. In granular aquifers, the occurrence of groundwater with high concentrations of As in West River and North River Delta plain was more frequent than that in East River Delta plain. Correspondingly, only one sample with extremely high concentrations of As (>0.05 mg/L) was in the East River Delta plain, while others were in the West River and North River Delta plain. According to the guideline value of As by the WHO (2011), approximately 6.8% and 9.4% samples exceeded the guideline value in aquifers of the whole PRD and granular aquifers, while only about 2.3% and no samples exceeded the guideline value in fissured aquifers and karst aquifers, respectively (Figure 3). Therefore, the following discussion will focus on the factors which are responsible for high concentrations of As in granular and fissured aquifers.

4.3. As in Granular Aquifers. According to our in situ investigation, groundwater samples with high As concentrations in granular aquifers were commonly of no significant potential source of As which is caused by human activities [9]. Thus, we concluded that the occurrence of high concentrations of

As in granular aquifers was mainly ascribed to the geologic origin. PCA was used to reduce the parameters and evaluate the relationships between As and other hydrochemical parameters [7]. In granular aquifers, the rotation of PCs was carried out using the varimax method, and seven PCs were extracted from the PCA method. The PC1, PC2, PC3, PC4, PC5, PC6, and PC7 explained 19.9%, 17.1%, 11.7%, 10.1%, 9.2%, 6.2%, and 4.8% of the total variance, respectively, and the cumulative variance by the seven PCs was 79.1% (Table 2). PC3, consisting of NH₄⁺, PO₄³⁻, and As, indicates that the occurrence of groundwater As in granular aquifers was closely related to NH₄⁺ and PO₄³⁻. It is known that high concentration of groundwater NH₄⁺ in granular aquifers was mainly originated from the overlying Holocene–Pleistocene aquitard and entered the granular aquifers by groundwater transport and diffusion, because much organic nitrogen remained in the aquitard available for conversion to NH₄⁺ [12, 13]. It is also known that the microbially mediated mobilization of As with the organic nutrient (including organic nitrogen) as an electron donor is strongly associated with the exchangeable As [14]. Therefore, NH₄⁺ and As in the same PC indicate that NH₄⁺ and As have the same origin in granular aquifers, because organic nitrogen in the aquitard was converted to NH₄⁺ and accompanied by the mobilization of As in the aquitard, and finally As entered the granular

aquifers by groundwater transport. To our knowledge, PO_4^{3-} and As in water have competitive relationship [15], which should be responsible for PO_4^{3-} and As in the same PC in granular aquifers.

After the PCs were reduced from seven PCs to two PCs, we found groundwater As in granular aquifers was not only closely related to NH_4^+ and PO_4^{3-} but also related to Fe, I^- , NO_2^- , and Mn (Figure 4). The good relationship of As and Fe/Mn indicates that As would be associated with Fe/Mn oxide minerals in the granular aquifers, which generally have strong affinity for both As(III) and As(V) [16, 17]. This is confirmed by the aging experiments and the sequential extraction method [18]. In addition, good correspondence between As and Fe/Mn has been observed in the Quaternary sediments of the PRD [8] which also supports the above conclusion. The good relationship between As and NO_2^- indicates that the mobilization of As in granular aquifers would be accompanied by the reduction of NO_3^- to NO_2^- . It is known that rich dissolved organic carbon (DOC) occurs in the Quaternary sediments of the PRD and is the trigger for the formation of reducing condition [12]. High concentrations of DOC provide electrons for electron acceptors, which commonly leads to the reduction of NO_3^- . This is further confirmed by the hydrochemical data in granular aquifers of the PRD. Because high concentrations ($>0.01 \text{ mg/L}$) of As in granular aquifers of the PRD were accompanied by the relatively low concentrations of NO_3^- (mean value of 9.9 mg/L) and high levels of NO_2^- (mean value of 0.97 mg/L), by contrast, low concentrations of As in granular aquifers were accompanied by the relatively high concentrations of NO_3^- (mean value of 34.9 mg/L) and low levels of NO_2^- (mean value of 0.58 mg/L). I^- and As have the same origin in granular aquifers which may be responsible for the good correspondence between As and I^- in granular aquifers of the PRD because I^- is generally derived from I-rich organic matter in marine strata [19], and two of the Quaternary sediments in the PRD are marine strata with rich organic matter [10, 12]. In addition, as mentioned above, mineralization of sedimentary organic matter is contributed to the occurrence of high concentrations of As in granular aquifers of the PRD [8].

To sum up, the main mechanism controlling the source and mobilization of groundwater As in granular aquifers of the PRD may be as follows: organic matter in marine strata was mineralized and provided electrons for electron acceptors, resulting in the release of NH_4^+ and I^- and the reduction of Fe/Mn and NO_3^- , and was accompanied with the mobilization of As from sediments into groundwater.

4.4. As in Fissured Aquifers. On the one hand, groundwater samples with high concentrations of As in fissured aquifers were located at the construction land, where many factories run and generally discharge their wastewater without treatment according to our investigation [9]. On the other hand, the sediments above the fissured aquifers were commonly characterized by coarse particles, leading to the weak ability for the prevention of contaminants from ground surface into aquifers. Therefore, anthropogenic source should be one of the factors for high concentrations of groundwater As in

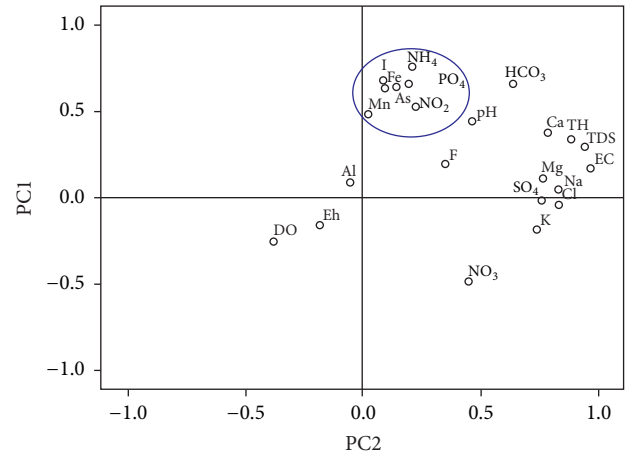


FIGURE 4: The relationship of hydrochemical parameters in two main PCs in granular aquifers.

fissured aquifers of the PRD. Six PCs were extracted from the groundwater samples in fissured aquifers by the PCA method. The PC1, PC2, PC3, PC4, PC5, and PC6 explained 36.3%, 12.7%, 8.5%, 8.1%, 6.3%, and 5.3% of the total variance, respectively, and the cumulative variance by the six PCs was 77.1% (Table 3). PC2, consisting of HCO_3^- , F^- , PO_4^{3-} , and As, indicates that the occurrence of groundwater As in fissured aquifers was closely related to HCO_3^- , F^- , and PO_4^{3-} . On the one hand, to our knowledge, the presence of HCO_3^- would alter the surface charge properties of Fe oxides via inner-sphere monodentate mononuclear surface species, and the HCO_3^- readily competes with As anions for adsorption sites on the Fe oxides at concentration $> 61 \text{ mg/L}$, which has been evidenced by some experiments [4]. Correspondingly, the mean concentration of HCO_3^- in fissured aquifers was more than 61 mg/L (Table 1). On the other hand, it is known that carbonate rocks commonly contain higher content of As than other rocks such as igneous rocks, indicating that the dissolution of carbonate rocks would accompany the release of As and HCO_3^- [7]. These two mechanisms may be responsible for the good relationship between As and HCO_3^- in fissured aquifers. To our knowledge, the competition for adsorption sites of the minerals between $\text{F}^-/\text{PO}_4^{3-}$ and As anions occurs [15, 20, 21], which may be responsible for the good correspondence between $\text{F}^-/\text{PO}_4^{3-}$ and As in fissured aquifers. In conclusion, high concentrations of groundwater As in fissured aquifers of the PRD are attributed to the coupling effects of anthropogenic and natural processes such as anion exchange of $\text{F}^-/\text{PO}_4^{3-}$ and As anions.

5. Conclusions

The concentration of groundwater As in different types of aquifers in the PRD showed a significant difference. In granular aquifers, groundwater As concentration was up to hundreds $\mu\text{g/L}$, while those in fissured aquifers and karst aquifers were only up to dozens $\mu\text{g/L}$ and several $\mu\text{g/L}$, respectively. Correspondingly, about 9.4% and 2.3% samples with high concentration of As were in granular and fissured

TABLE 3: Principal component loadings for groundwater samples in fissured aquifers.

Item	PC1	PC2	PC3	PC4	PC5	PC6
pH	0.237	0.237	0.754	−0.108	−0.211	−0.120
EC	0.944	0.138	0.044	0.079	−0.025	0.040
DO	−0.399	−0.140	−0.033	−0.350	−0.505	0.018
Eh	0.037	−0.354	−0.531	−0.056	−0.156	−0.242
K ⁺	0.876	0.011	0.055	−0.051	−0.171	−0.077
Na ⁺	0.846	0.166	−0.072	0.197	0.146	0.220
Ca ²⁺	0.788	0.474	0.250	0.063	0.067	0.067
Mg ²⁺	0.758	0.130	−0.049	0.103	0.163	−0.021
NH ₄ ⁺	−0.010	0.115	0.053	0.902	−0.093	0.162
Fe	−0.146	−0.076	0.024	−0.054	0.831	0.104
HCO ₃ [−]	0.563	0.619	0.357	0.161	0.214	−0.043
Cl [−]	0.893	0.003	−0.132	0.118	0.065	0.240
SO ₄ ^{2−}	0.832	0.076	0.212	0.036	−0.153	−0.200
F [−]	0.046	0.434	0.225	−0.298	−0.019	0.006
NO ₃ [−]	0.818	−0.146	−0.243	−0.097	−0.145	0.274
TDS	0.930	0.300	0.127	0.076	0.073	0.073
TH	0.840	0.433	0.202	0.076	0.093	0.053
I [−]	0.292	0.232	0.050	0.572	0.361	−0.130
PO ₄ ^{3−}	0.276	0.865	−0.003	0.060	0.043	−0.119
Al	0.077	0.074	−0.817	−0.075	−0.090	−0.021
Mn	0.499	−0.289	−0.065	0.433	0.234	−0.291
NO ₂ [−]	0.250	−0.058	0.051	0.065	0.092	0.865
As	0.085	0.797	0.044	0.402	−0.147	0.050
Eigenvalue	8.3	2.9	2.0	1.9	1.4	1.2
Explained variance (%)	36.3	12.7	8.5	8.1	6.3	5.3
Cumulative% of variance	36.3	48.9	57.5	65.6	71.8	77.1

aquifers, respectively, but no samples with high concentration of As was in karst aquifers. In granular aquifers, the occurrence of groundwater with high concentrations of As in West River and North River Delta plain was more frequent than that in East River Delta plain.

In granular aquifers, groundwater As was closely related to NH₄⁺, PO₄^{3−}, Fe, I[−], NO₂[−], and Mn. The source and mobilization of groundwater As in granular aquifers are likely to be controlled by the following mechanism: organic matter in marine strata was mineralized and provided electrons for electron acceptors, resulting in the release of NH₄⁺ and I[−] and the reduction of Fe/Mn and NO₃[−], and was accompanied with the mobilization of As from sediments into groundwater. By contrast, not only were the natural processes such as the competitive adsorption between As anions and F[−]/PO₄^{3−}/HCO₃[−] an important factor, but the anthropogenic processes were also responsible for high concentrations of groundwater As in fissured aquifers.

Conflicts of Interest

The authors declare that they have no conflicts of interest.

Acknowledgments

This research was supported by the Fundamental Research Funds for Central Public Welfare Research Institutes, CAGS (SK201611), China Geological Survey project (DD20160309, DD20179609, and DD20160308), and the National Natural Science Foundation of China (41472264, 41772334).

References

- [1] World Health Organization (WHO), *Guidelines for Drinking-Water Quality*, Geneva, Switzerland, 4th edition edition, 2011.
- [2] A. H. M. Selim Reza, J.-S. Jean, H.-J. Yang et al., “Occurrence of arsenic in core sediments and groundwater in the Chapai-Nawabganj District, northwestern Bangladesh,” *Water Research*, vol. 44, no. 6, pp. 2021–2037, 2010.
- [3] S. Kar, J. P. Maity, J.-S. Jean et al., “Arsenic-enriched aquifers: Occurrences and mobilization of arsenic in groundwater of Ganges Delta Plain, Barasat, West Bengal, India,” *Applied Geochemistry*, vol. 25, no. 12, pp. 1805–1814, 2010.
- [4] H. Guo, D. Wen, Z. Liu, Y. Jia, and Q. Guo, “A review of high arsenic groundwater in Mainland and Taiwan, China: distribution, characteristics and geochemical processes,” *Applied Geochemistry*, vol. 41, pp. 196–217, 2014.

- [5] L. M. Camacho, M. Gutiérrez, M. T. Alarcón-Herrera, M. D. L. Villalba, and S. Deng, "Occurrence and treatment of arsenic in groundwater and soil in northern Mexico and southwestern USA," *Chemosphere*, vol. 83, no. 3, pp. 211–225, 2011.
- [6] G. Huang, J. Sun, Y. Zhang, Z. Chen, and F. Liu, "Impact of anthropogenic and natural processes on the evolution of groundwater chemistry in a rapidly urbanized coastal area, South China," *Science of the Total Environment*, vol. 463–464, pp. 209–221, 2013.
- [7] G. Huang, Z. Chen, F. Liu, J. Sun, and J. Wang, "Impact of human activity and natural processes on groundwater arsenic in an urbanized area (South China) using multivariate statistical techniques," *Environmental Science and Pollution Research*, vol. 21, no. 22, pp. 13043–13054, 2014.
- [8] Y. Wang, J. J. Jiao, and J. A. Cherry, "Occurrence and geochemical behavior of arsenic in a coastal aquifer-aquitard system of the Pearl River Delta, China," *Science of the Total Environment*, vol. 427–428, pp. 286–297, 2012.
- [9] J. Sun, J. Jing, G. Huang, J. Liu, X. Chen, and Y. Zhang, "Report on the investigation and assessment of groundwater contamination in the Pearl River delta area," in *The Institute of Hydrogeology and Environmental Geology*, Chinese Academy of Geological Sciences, Shijiazhuang, China, 2009.
- [10] Y. Zong, W. W.-S. Yim, F. Yu, and G. Huang, "Late Quaternary environmental changes in the Pearl River mouth region, China," *Quaternary International*, vol. 206, no. 1–2, pp. 35–45, 2009.
- [11] Guangdong Hydrogeological Second Team (GHST), "Regional hydrogeological survey report," Guangdong Hydrogeological Second Team, Guangzhou, China, 1981 (Chinese).
- [12] J. J. Jiao, Y. Wang, J. A. Cherry et al., "Abnormally high ammonium of natural origin in a coastal aquifer-aquitard system in the pearl river delta, China," *Environmental Science & Technology*, vol. 44, no. 19, pp. 7470–7475, 2010.
- [13] G. Huang, C. Liu, J. Sun, M. Zhang, J. Jing, and L. Li, "A regional scale investigation on factors controlling the groundwater chemistry of various aquifers in a rapidly urbanized area: A case study of the Pearl River Delta," *Science of the Total Environment*, vol. 625, pp. 510–518, 2018.
- [14] H. Guo, X. Tang, S. Yang, and Z. Shen, "Effect of indigenous bacteria on geochemical behavior of arsenic in aquifer sediments from the Hetao Basin, Inner Mongolia: Evidence from sediment incubations," *Applied Geochemistry*, vol. 23, no. 12, pp. 3267–3277, 2008.
- [15] G. Huang, Z. Chen, J. Wang, J. Sun, J. Liu, and Y. Zhang, "Adsorption of arsenite onto a soil irrigated by sewage," *Journal of Geochemical Exploration*, vol. 132, pp. 164–172, 2013.
- [16] G. Huang, Z. Chen, J. Sun, F. Liu, J. Wang, and Y. Zhang, "Effect of sample pretreatment on the fractionation of arsenic in anoxic soils," *Environmental Science and Pollution Research*, vol. 22, no. 11, pp. 8367–8374, 2015.
- [17] G. Huang, Z. Chen, Y. Zhang, F. Liu, J. Wang, and Q. Hou, "Changes of arsenic fractionation and bioaccessibility in wastewater-irrigated soils as a function of aging: Influence of redox condition and arsenic load," *Geoderma*, vol. 280, pp. 1–7, 2016.
- [18] G. Huang, Z. Chen, J. Wang, Q. Hou, and Y. Zhang, "Impact of temperature on the aging mechanisms of arsenic in soils: fractionation and bioaccessibility," *Environmental Science and Pollution Research*, vol. 23, no. 5, pp. 4594–4601, 2016.
- [19] D. Wen, F. Zhang, E. Zhang, C. Wang, S. Han, and Y. Zheng, "Arsenic, fluoride and iodine in groundwater of China," *Journal of Geochemical Exploration*, vol. 135, pp. 1–21, 2013.
- [20] R. P. Liu, W. X. Gong, H. C. Lan, T. M. Yang, H. J. Liu, and J. H. Qu, "Simultaneous removal of arsenate and fluoride by iron and aluminum binary oxide: competitive adsorption effects," *Separation and Purification Technology*, vol. 92, pp. 100–105, 2012.
- [21] Q. Yang, H. B. Jung, R. G. Marvinney, C. W. Culbertson, and Y. Zheng, "Can arsenic occurrence rates in bedrock aquifers be predicted?" *Environmental Science & Technology*, vol. 46, no. 4, pp. 2080–2087, 2012.

Research Article

A Coupled One-Dimensional Numerical Simulation of the Land Subsidence Process in a Multilayer Aquifer System due to Hydraulic Head Variation in the Pumped Layer

Ye Wang ¹, Mao-sheng Zhang,² Fu-sheng Hu ¹, Ying Dong,² and Kun Yu¹

¹School of Water Resources and Environment, China University of Geosciences (Beijing), Beijing, China

²Xi'an Center of Geological Survey, CGS, Xi'an, China

Correspondence should be addressed to Fu-sheng Hu; 1991010439@cugb.edu.cn

Received 25 October 2017; Accepted 27 December 2017; Published 23 January 2018

Academic Editor: Liangping Li

Copyright © 2018 Ye Wang et al. This is an open access article distributed under the Creative Commons Attribution License, which permits unrestricted use, distribution, and reproduction in any medium, provided the original work is properly cited.

After exploitation of groundwater had been reduced and the groundwater level of the confined aquifer had risen, land subsidence was observed to continue rather than cease for several years according to the layer-wise mark monitoring data in Xi'an. To analyze the phenomena, a numerical model of a coupled one-dimensional multilayer aquifer system is developed to represent land subsidence due to hydraulic head variation in the pumped layer. The numerical simulation results show that the pressure head in other layers does not rise immediately when the hydraulic head in the pumped layer starts to recover after pumping ceases. In addition, after the pumping is stopped, a dividing point can be found in aquitards next to the pumped layer, with the aquitards being divided into two parts: a compressed part and a rebounding part. The dividing points move toward the side and away from the pumped layer with the transferring of pore pressure in the aquitard. The results of the simulation also show that there is a transition period between land subsidence and rebound. In this transition period, land could continue to subside even though the hydraulic head in the pumped layer begins to recover.

1. Introduction

Land subsidence resulting from overexploitation of groundwater has become a major concern all over the world. In China, land subsidence mainly occurs in the 17 provinces in the eastern and central regions, including Xi'an, Shanghai, and the Su-Xi-Chang area [1]. After the exploitation of groundwater had been reduced and the groundwater level of the confined aquifer had risen, land subsidence was observed to continue rather than cease according to the layer-wise mark monitoring data in Xi'an [2, 3]. The same phenomenon also occurred in Shanghai. While groundwater withdrawal in Shanghai had been controlled, the land continued to subside since the 1990s [4]. However, reasons, such as additional stresses caused by building loads and the reduction of recharged groundwater volume, cannot explain the continuous deformation mechanism [5]. It is, therefore, necessary to study the process of land subsidence for analyzing the phenomenon.

The hydraulic head variation in the pumped layer has a significant effect on the process of land subsidence. Therefore, it is necessary to simulate the deformation process of each aquifer in a multilayer aquifer system due to the hydraulic head variation in the pumped layer by applying a numerical model. Several multilayer aquifer system models and numerical analyses have been developed for the analysis of land subsidence. Bear and Corapcioglu [6] presented a variety of analytical solutions to evaluate groundwater flow and solid skeleton deformation due to groundwater withdrawal from aquifer systems. The simulation of multiaquifer systems was carried out using a quasi-three-dimensional model consisting of a three-dimensional hydrologic model coupled with a one-dimensional consolidation model [7–9]. Malama et al. [10] presented a semianalytical solution for the problem of leakage in multiaquifer systems. Considering the effect of the body force and the porosity variation on consolidation, the poroelastic consolidation model of a multilayer aquifer system was developed [11, 12]. The multiscale finite element method

(MsFEM) was applied to solve the model of the multilayer aquifer system successfully during the consolidation process [13]. Considering the multiaquifer-aquitard hydrogeological condition, a numerical model was established to analyze relationships among land subsidence, groundwater withdrawal volume, and groundwater level [14]. Lin et al. [15] proposed a distributed model comprised of an analytical quasi-three-dimensional groundwater model and a one-dimensional deformation model to simulate the groundwater flow and deformation for a multilayer aquifer system. Although the study of the process of groundwater flow and deformation in multilayer aquifer systems is extensive, those numerical simulations did not represent the variation state in each layer of the multilayer system during land subsidence. Several experiments of soil consolidation caused by water release have shown that the deformation of the clay layer lags behind the hydraulic head variation. The results from a viscoelastic model developed to simulate one-dimensional consolidation showed that land subsidence obviously lags behind pore pressure disappearance [16]. In addition, the lag time of the clay layer deformation was in direct proportion to the thickness of the layer [17, 18]. The delay index is only dependent on the properties and thickness of the aquitard in response to the sudden change in groundwater level in adjacent confined aquifers according to experimental studies [19].

In this study, a numerical model for a coupled one-dimensional multilayer aquifer system is developed to present the process of land subsidence due to hydraulic head variation in the pumped layer. The variations in pressure head and soil deformation in each layer of the system are simulated to analyze the process of land subsidence along with an analysis of the dividing point that appears in aquitards adjacent to the pumped layer when the hydraulic head in the pumped layer recovers gradually. The movement of the dividing point as a critical part of land subsidence is also explained in this study. There is a transition period between land subsidence and rebound during the hydraulic head recovery in the pumped layer. The transition period could be interpreted as the phenomenon in which land subsidence lags behind the variation in hydraulic head.

2. Methodology

A general mathematical model describing a coupled multilayer aquifer system due to hydraulic head variation in the pumped layer may be formulated by applying Biot's consolidation theory [20].

The governing differential equations can be derived based on the following basic assumptions: (1) the soil particles are incompressible, (2) the water is slightly compressible, (3) water flow follows saturated Darcy's law, and (4) the inertial force is neglected in the force equation.

The fluid transport is described by Darcy's law:

$$q_i = -k_{ij}\hat{k}\frac{\partial}{\partial x_j}\left[p - \rho_f x_j g_j\right], \quad (1)$$

where q_i (m/s) is the specific discharge vector, p (Pa) is fluid pore pressure, k_{ij} (1/Pa·s) is the tensor of permeability tensor

of the medium, \hat{k} (m²) is the relative mobility coefficient, ρ_f (kg/m³) is the fluid density, g_k (m/s²) is the gravity vector, and x_k (m) is the position.

The fluid mass balance may be expressed as

$$\frac{\partial \zeta}{\partial t} = -\frac{\partial q_i}{\partial x_i} + q_v, \quad (2)$$

where q_v (1/s) is the volumetric fluid source intensity and ζ is the variation of fluid volume per unit volume of porous material due to diffusive fluid mass transport, as introduced by Biot [21].

The constitutive equation is formulated as

$$\frac{1}{M}\frac{\partial p}{\partial t} = \frac{\partial \zeta}{\partial t} - \alpha\frac{\partial \varepsilon}{\partial t}, \quad (3)$$

where M (Pa) is Biot modulus, α is Biot coefficient, and ε is the mechanical volumetric strain. The Biot modulus M is related to the drained bulk modulus K (Pa) and fluid bulk modulus K_f (Pa):

$$M = \frac{K_f}{n + (\alpha - n)(1 - \alpha)(K_f/K)}, \quad (4)$$

where n is porosity. If α is equal to unity, the grains are considered to be incompressible, and the Biot modulus M is equal to K_f/n .

The relationship between strain rate and velocity gradient is

$$\dot{\varepsilon}_{ij} = \frac{1}{2}\left[\frac{\partial \dot{u}_i}{\partial x_j} + \frac{\partial \dot{u}_j}{\partial x_i}\right], \quad (5)$$

where $\dot{\varepsilon}_{ij}$ (1/s) is the strain rate, \dot{u}_i (m/s) and \dot{u}_j (m/s) are the rate direction of i and j , respectively.

3. Descriptions of the Multilayer Aquifer System

An ideal seven-layer aquifer system is established to apply the proposed model. The purpose of the numerical model is to simulate the coupling process of pressure head variations and soil deformation in each layer of the multilayer aquifer system subjected to hydraulic head variations in the pumped layer, which is located in confined aquifer II as shown in Figure 1. For such a case, a 300 m thick homogeneous and isotropic multilayer system consisting of confined aquifers I, II, and III, aquitards I, II, and III, and a phreatic aquifer is considered as shown in Figure 1. All the confined aquifers of the model comprise a 40 m thick layer, both aquitard I and aquitard II comprise a 35 m thick layer, the thickness of aquitard III is 25 m, and the phreatic aquifer is 70 m in thickness. The confined aquifers are more permeable and less compressible than the aquitards. In this study, the groundwater of the entire system is assumed to flow only in a vertical direction, and the soil is also assumed to deform vertically.

To describe the relationship between the layer positions and the hydraulic head distinctly, the bottom boundary and

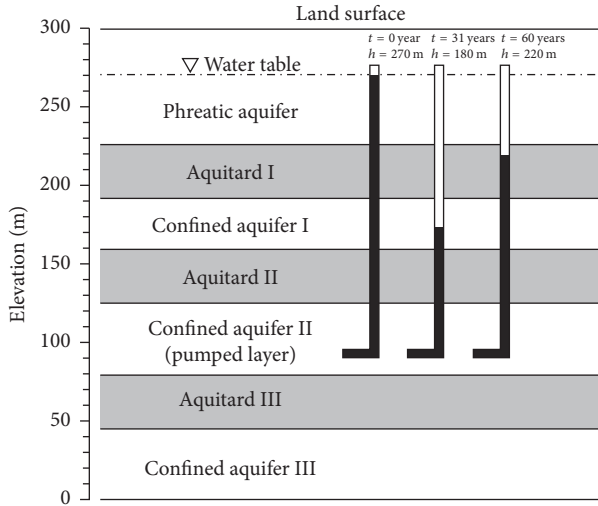


FIGURE 1: Conceptual model of the multilayer aquifer system and the variation in hydraulic head of the confined aquifer II (pumped layer).

land surface of the numerical model are set equal to 0 m and 300 m, respectively. The initial hydraulic head in the saturated zone of the numerical model is set equal to 270 m. It is assumed that the phreatic water table level is constant during all periods so that the vertical downward seepage from the phreatic aquifer recharges each layer directly or indirectly when the hydraulic head in the pumped layer drops. The land surface, also called the top boundary, is free to move vertically. At the bottom boundary, the soil is restrained from vertical movements. Additionally, the no-flow boundary condition is assigned to the bottom side of the model region. The initial displacement and velocity are equal to 0 throughout the model. As a vertical one-dimensional simulation, there is no need to set the lateral boundary. Table 1 lists the hydraulic parameters of each layer implemented, which include the phreatic aquifer, aquitards, and confined aquifers. As mentioned, these parameters are obtained from the references [22] but also are based on average values found in the literature for the Xi'an area undergoing land subsidence.

4. Results and Analyses

4.1. Characteristics and Development of the Land Subsidence Process. A 60-year coupled simulation is distributed in three stages as indicated in Figure 2 based on land surface vertical displacement and hydraulic head in the pumped layer. In addition, the soil is defined as being in compression when the soil vertical displacement is a positive value in this study.

The first stage (Stage I), from the first to the thirty-first year of the entire simulation period, is designed to simulate the fact that the hydraulic head of the pumped layer drops drastically from 270 m to 180 m. The decline of the hydraulic head level induces the land subsidence to begin. In addition, the hydraulic head has been observed to reach the minimum value of 180 m at the end of the first stage. However, the

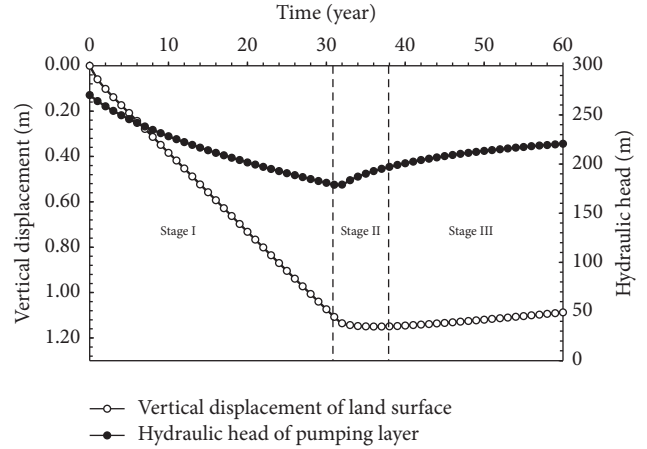


FIGURE 2: Simulated land surface vertical displacement corresponds to changes in hydraulic head of the confined aquifer II. In Stage I, the hydraulic head in the pumped layer drops and the land surface subsides. In Stage II, the hydraulic head in the pumped layer recovers rapidly and the land subsidence ceases gradually and reaches a stable state. In Stage III, the hydraulic head in the pumped layer recovers slowly and the land surface rebounds.

land subsidence did not cease at this stage. The hydraulic head in the pumped layer recovers rapidly in the second stage (Stage II) from the thirty-first to the thirty-eighth year. In contrast to the first stage, the land continues to subside at the beginning of the second stage, and then the land subsidence ceases gradually and reaches a stable state. The vertical displacement reaches the maximum value of 1.16 m at the end of the second stage. The results of the simulation show that the maximum land subsidence lags behind the minimum hydraulic head in the second stage. This indicates that, in the multilayer aquifer system, land subsidence cannot immediately respond to the temporal variation in hydraulic head. The land surface rebounds gradually in the third stage (Stage III) from the thirty-eighth to the sixtieth year. The land surface begins to smoothly rebound at the beginning of the third stage because of aquifer storage and hydraulic head recovery. The hydraulic head recovery occurs smoothly and slowly at the end of the third stage, while the land surface vertical displacement increases rapidly. Notice that the changes in hydraulic head in the pumped layer can only instantaneously influence the deformation of the pumped layer rather than the other aquifers.

4.2. Analysis for Each Aquifer in the Multilayer System. The distribution of pressure head and soil displacement in each layer of the multilayer aquifer system at different stages are shown in Figures 3–8. The head equation, a simplified form of the Bernoulli Principle for incompressible fluids, can be expressed as

$$\psi = h - z, \quad (6)$$

where ψ (m) is the pressure head, h (m) is the hydraulic head, and z (m) is the elevation head.

TABLE 1: Material properties of the multilayer aquifer system used in the numerical simulation.

Property	Layered aquifer			
	Phreatic aquifer	Aquitard I	Confined aquifer I	Aquitard II
Solid density, ρ_s [kg/m ³]	2.00×10^3	1.85×10^3	2.00×10^3	1.90×10^3
Elastic modulus, E [MPa]	200	100	200	150
Poisson's ratio, ν [dimensionless]	0.25	0.35	0.25	0.35
Internal friction angle, φ [°]	28	23	28	16
Cohesion, c [MPa]	0	0.3	0	0.6
Hydraulic conductivity, K [10 ⁻⁴ cm/s]	7200	368.4	5000	53.58
Porosity, n [dimensionless]	0.25	0.4	0.25	0.4
Property	Layered aquifer			
	Confined aquifer II	Aquitard III	Confined aquifer III	
Solid density, ρ_s [kg/m ³]	2.00×10^3	1.90×10^3	2.00×10^3	
Elastic modulus, E [MPa]	250	200	300	
Poisson's ratio, ν [dimensionless]	0.25	0.3	0.25	
Internal friction angle, φ [°]	30	19	34	
Cohesion, c [MPa]	0	0.8	0	
Hydraulic conductivity, K [10 ⁻⁴ cm/s]	3200	9.91	620	
Porosity, n [dimensionless]	0.25	0.38	0.3	

The pressure head generally declines and the soil displacement gradually increases in aquitard I during all periods as shown in Figure 3. During Stage I, when the pressure head in the pumped layer (i.e., the confined aquifer II) declines rapidly, the pressure head in aquitard I also declines to recharge the underlying aquifer (see Figure 3(a)). Following the drop in the hydraulic head, the soil displacement in the aquitard I continues to increase in Stage I (see Figure 3(b)). The pressure head in confined aquifer II recovers promptly with groundwater pumping ceasing in Stage II, but none of the pressure head and soil displacement in aquitard I responds to the changes in confined aquifer II (see Figures 3(c) and 3(d)). The pressure head continues to decrease and soil displacement continues to increase with time in aquitard I during Stage III even though the hydraulic head recovery has been maintained for about 30 years in the pumped layer. However, the rates of the pressure head drawdown and soil displacement increase slow (see Figures 3(e) and 3(f)). It is noticed that the variations in the pressure head drawdown and soil displacement initially occur in the lower part of aquitard I. In addition, the soil displacement in the lower part of aquitard I decreases abruptly (see Figures 3(b), 3(d), and 3(f)). The variation in the underlying confined aquifer I could influence first the lower part of aquitard I.

Similarly, the pressure head drops and the soil displacement increases in confined aquifer I at all stages as shown in Figure 4. In other words, the confined aquifer I recharges the underlying aquifer and is in compression all the time. The upper and lower parts of confined aquifer I, which are influenced by the neighboring aquitards, become more compressible. Therefore, the soil displacement in both the upper and lower parts of confined aquifer I is larger than in the middle part (see Figures 4(b), 4(d), and 4(f)).

Aquitard II is the overlying aquifer adjacent to the pumped layer. Large variations in both pressure head and soil displacement initially occur at the bottom of the layer

(see Figure 5). The pressure head declines following the hydraulic head drawdown in the pumped layer during Stage I. Meanwhile, the soil displacement increases with respect to the pressure head drop in the aquitard II (see Figures 5(a) and 5(b)). During Stage II, the pressure head decreases gradually with time in the upper part of the layer and increases slightly with time in the lower part of the layer (see Figure 5(c)). In other words, there is a dividing point separating aquifer II into two parts: the upper compressed part and lower rebounding part, with respect to the variation in the pressure head (see Figure 5(d)). It is obvious that the upper compressed part (around 22 meters thick) is thicker than the lower rebounding part (around 18 meters thick) from Figure 5(d). Therefore, aquitard II can be treated as in compression at Stage II. The dividing points of both the pressure head and soil displacement move upward and to the side away from the pumped layer during Stage III (see Figures 5(e) and 5(f)). Because of the upward movement of the dividing point, it is observed from Figure 5(d) that the lower rebounding part (around 30 meters thick) finally becomes thicker than the upper compressed part (around 10 meters thick). Therefore, aquitard II rebounds at Stage III.

As the pumped layer, the confined aquifer II is compressed corresponding to the pressure head drawdown during Stage I (see Figures 6(a) and 6(b)). The upper and lower aquifers recharge confined aquifer II due to pumping being stopped during Stage II. As a result, confined aquifer II rebounds immediately, corresponding to the pressure head rise (see Figure 6(d)). The difference in the pressure head among confined aquifer II and other aquifers becomes smaller with time, and the rate of the pressure head rise and layer rebound becomes smaller.

Aquitard III is the underlying aquifer adjacent to the pumped layer. Large variations in both pressure head and soil displacement initially appear at the top of the layer (see Figure 7). With the pressure head drawdown in the

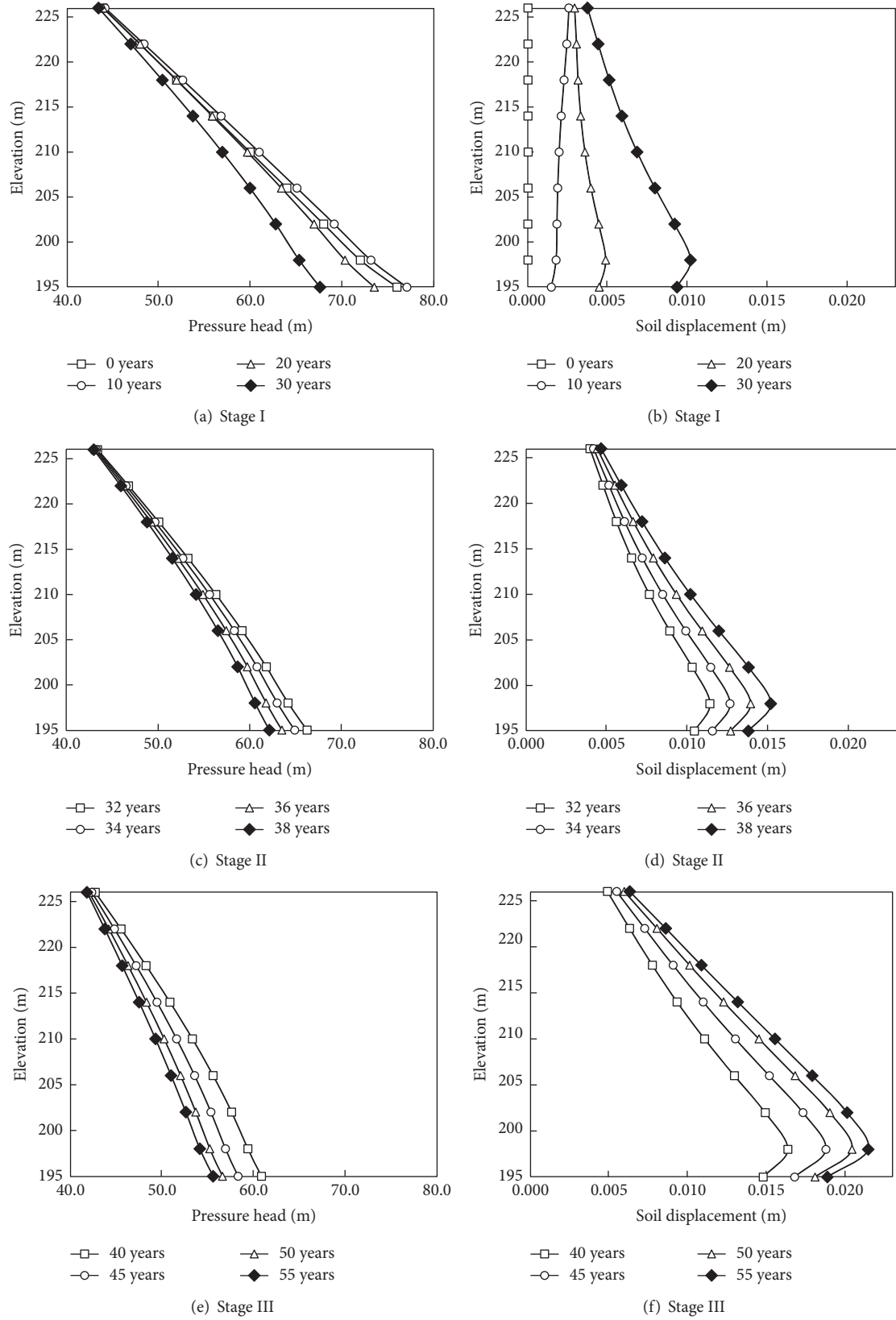


FIGURE 3: Distribution of pressure head and soil displacement in aquitard I during different stages.

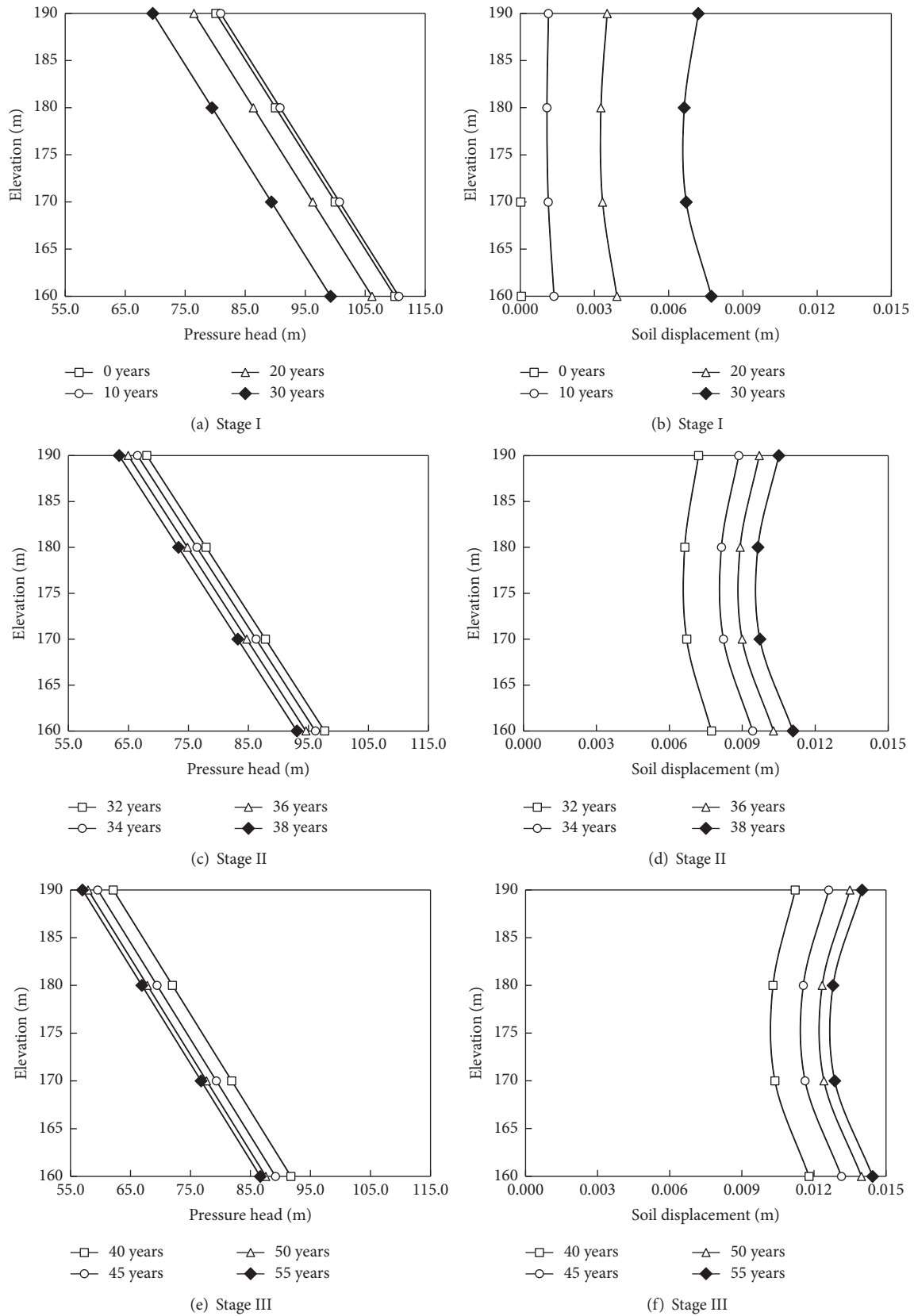


FIGURE 4: Distributions of pressure head and soil displacement in confined aquifer I during different stages.

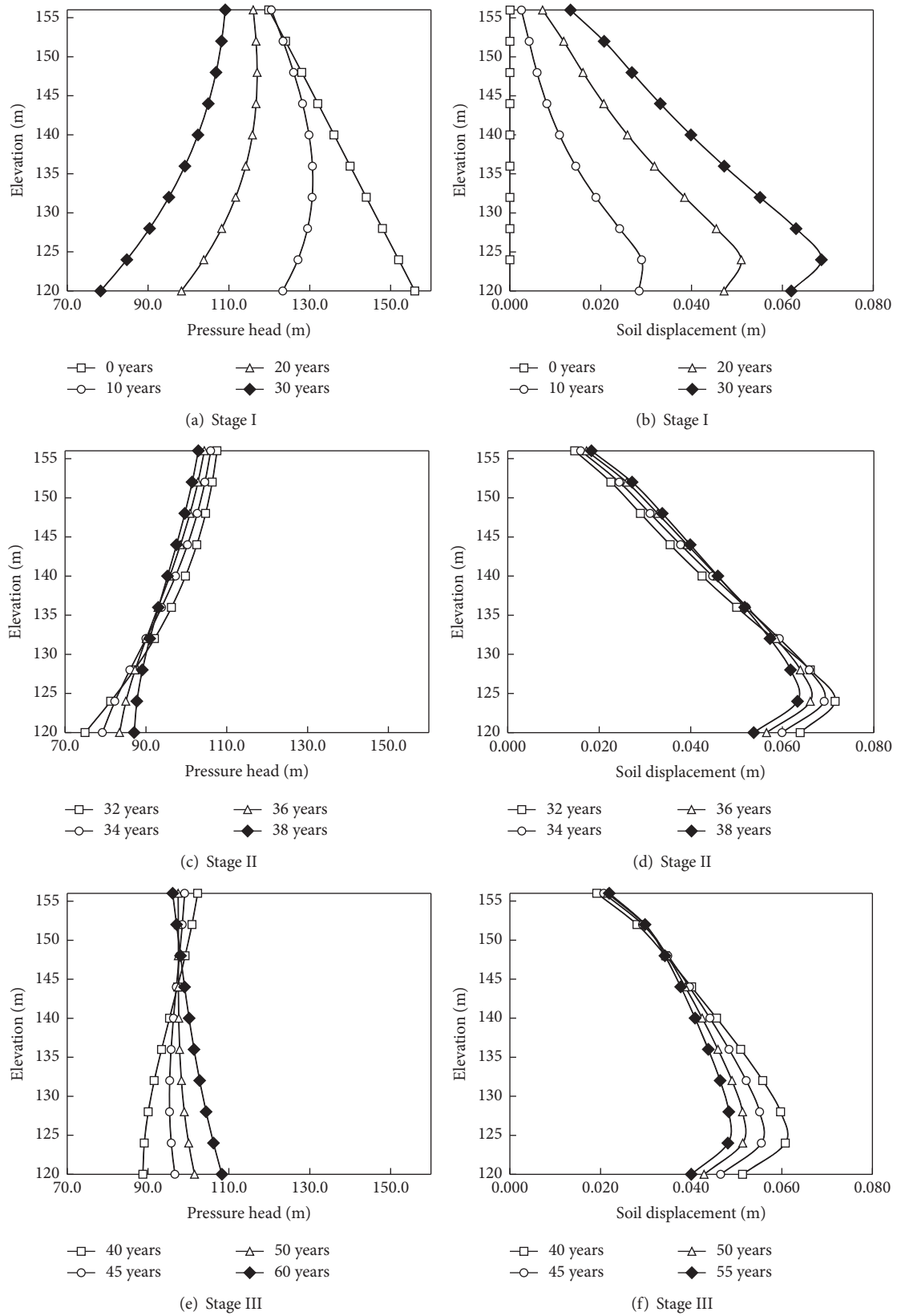


FIGURE 5: Distributions of pressure head and soil displacement in aquitard II during different stages.

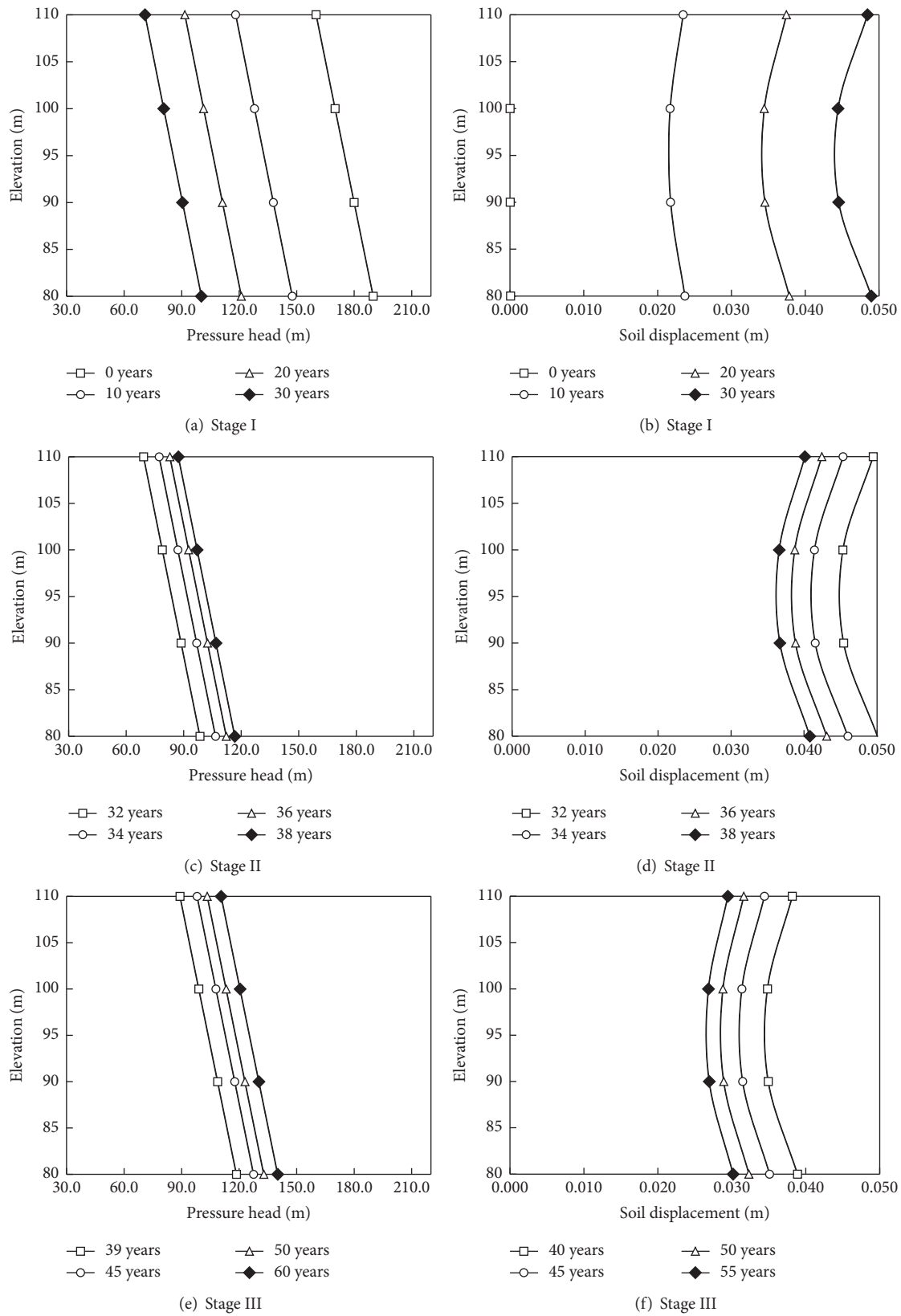


FIGURE 6: Distributions of pressure head and soil displacement in confined aquifer II during different stages.

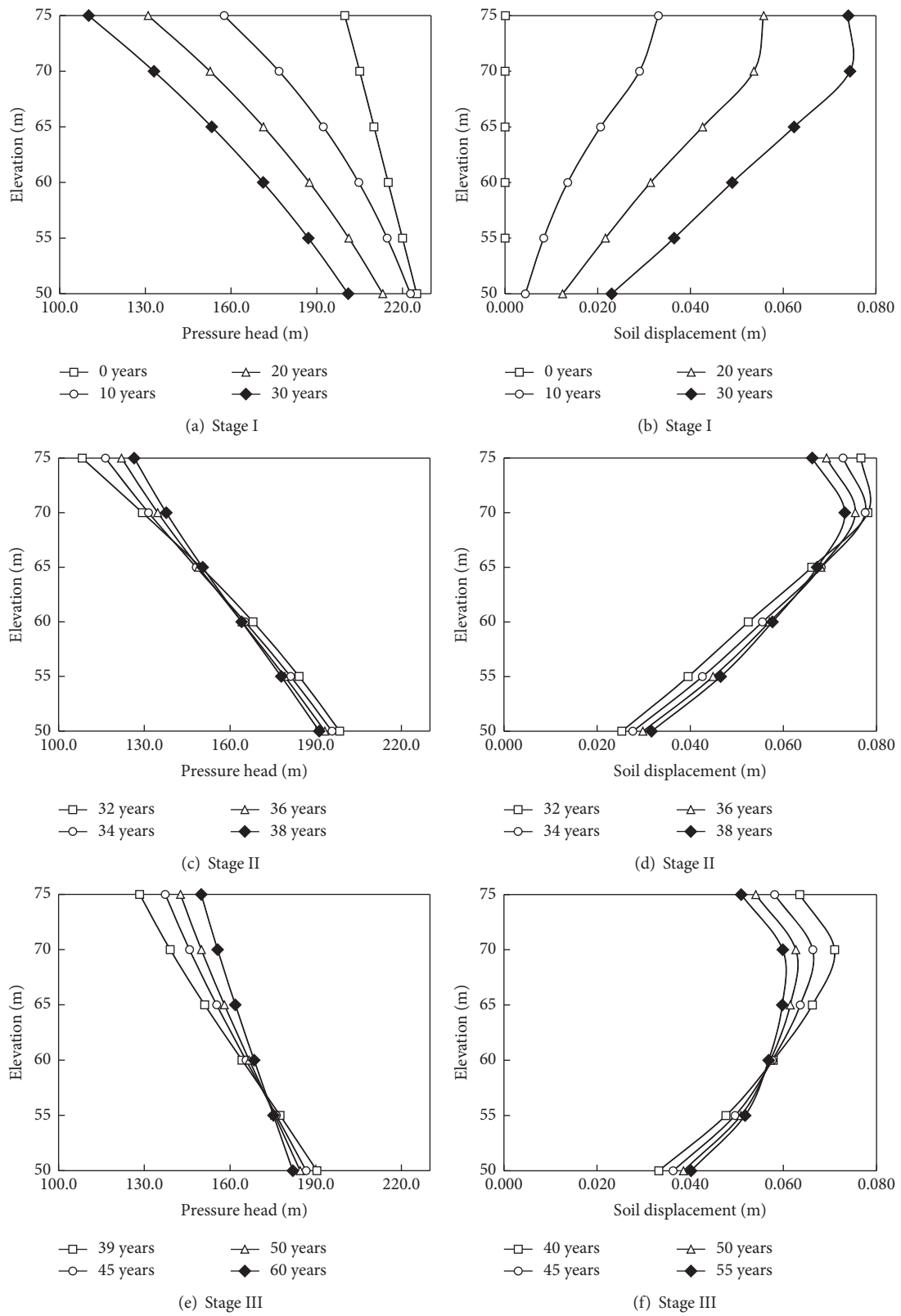


FIGURE 7: Distributions of pressure head and soil displacement in aquitard III during different stages.

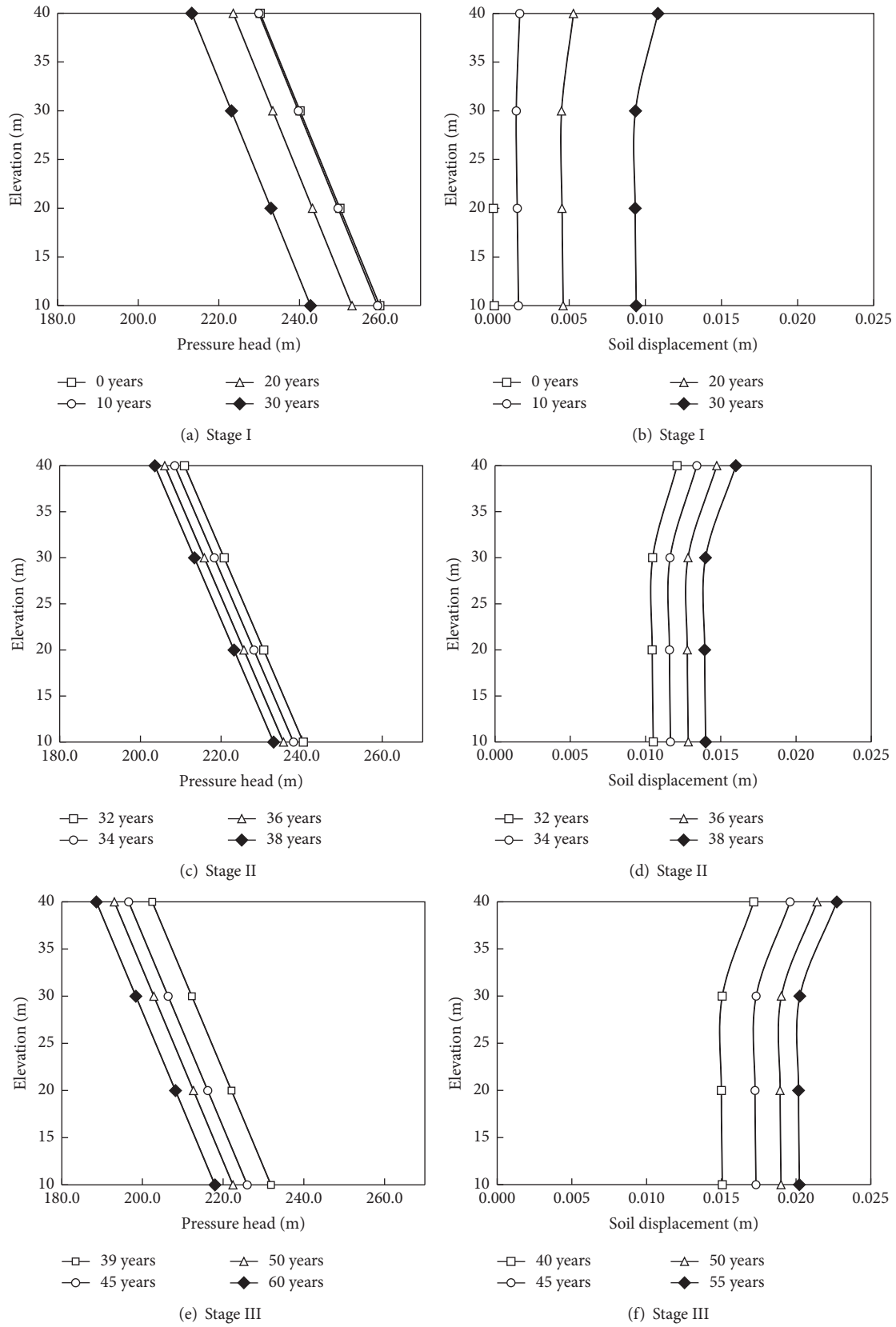


FIGURE 8: Distributions of pressure head and soil displacement in confined aquifer III during different stages.

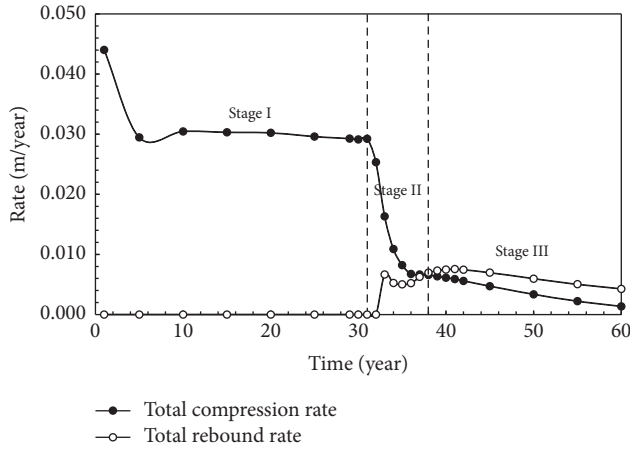


FIGURE 9: The total rate of compression and rebound during different stages.

pumped layer, the pressure head declines during Stage I. Meanwhile, aquitard III is compressed (see Figures 7(a) and 7(b)). In contrast to aquitard II, during Stage II, the hydraulic head recovers gradually with time in the upper part of the layer and declines slightly with time in the lower part of the layer (see Figure 7(c)). In other words, there is also a dividing point separating aquifer III into two parts: the upper compressed part and lower rebounding part, with respect to the variation of pressure head (see Figure 7(d)). Aquitard III could be in compression during Stage II because the lower compressed part (around 15 meters thick) is thicker than the upper rebounding part (around 10 meters thick) as shown in Figure 7(d). The dividing points of both the pressure head and soil displacement move downward and to the side away from the pumped layer during Stage III (see Figures 7(e) and 7(f)). The upper rebounding part (around 15 meters thick) finally becomes thicker than the lower compressed part (around 10 meters thick) due to the downward movement of the dividing point so that aquitard III could rebound during Stage III.

As with confined aquifer I, the pressure head declines and the soil displacement increases in confined aquifer III during all stages as shown in Figure 8. Confined aquifer III recharges the overlying aquifer and stays in compression all the time. The upper part of the layer gets more and more compressible influenced by the neighboring aquitard. Therefore, the soil displacement in the upper part of confined aquifer III is larger (see Figures 8(b), 8(d), and 8(f)). Note that the pressure head and soil displacement could not be recorded at elevation of 0 m because the bottom boundary of confined aquifer III is restrained from displacement.

Stage II is a transition period between land subsidence and rebound. As shown in Figure 9, the total compression rate of the entire system decreases rapidly and the total rebound rate increases during Stage II. At the end of Stage II, the total compression rate is equal to the total rebound rate. After that, the land surface starts to rebound. As mentioned above, each layer of the multilayer aquifer system is in compression during Stage I. During Stage II, the performance is different among the aquifers. Confined aquifer II rebounds at once, aquitard I, confined aquifer I, and confined aquifer

III are compressed, and both aquitard II and aquitard III are separated into a rebounding part and compressed part by the dividing point. In addition, at the beginning of Stage II, when the total compression deformation is larger than the total rebounding deformation, the land continues to subside even though the hydraulic head in the pumped layer begins to recover. The displacement of the land surface becomes stable (see Figure 2) until the total deformation between compression and rebounding gradually reaches equilibrium at the end of Stage II. The dividing point in aquitard II and aquitard III moves toward the side away from confined aquifer II during Stage III, and the total rebounding deformation is gradually larger than the total compressed deformation. Therefore, the land surface rebounds during Stage III as shown in Figure 2. It appears that the dividing point movement has significant impact on the land subsidence process. The poorly permeable aquitard cannot transfer the pore pressure rapidly relative to the sandy aquifer, which can be observed in Figures 3–8, so that the variation in pressure head could be transferred from one side to the other side in the aquitard for a long period. Therefore, there are different performances between the upper and lower sides of the aquitard. Once one side of the aquitard presents an opposite distribution, the dividing point will appear and move toward the other side with the transference of pore pressure in the aquitard similar to the movement of the dividing points in aquifer II and aquifer III.

5. Conclusions

Pressure head and soil displacement in a seven-layer aquifer system respond to the variation in hydraulic head of the pumped layer during different stages as indicated by a coupled one-dimensional numerical model. The numerical simulation results of the multilayer aquifer system show that the pressure head in other layers will not rise immediately when the pressure head in the pumped layer begins to recover after pumping ceases because the aquitards adjacent to the pumped layer are poorly permeable so that the recovery in pressure head from the pumped layer is transferred to other layers over a long time. The numerical simulation results also show that there will be a dividing point in aquitards adjacent to the pumped layer after pumping ceases. The aquitards adjacent to the pumped layer are divided into a compressed part and rebounding part by the dividing points. The dividing points move toward the side away from the pumped layer over time since the poorly permeable aquitard cannot transfer the pore pressure rapidly relative to the sandy aquifer, and the variation in pressure head can be transferred from one side to the other side of the aquitard for a long period. Therefore, there are different reactions in the upper and lower sides of the aquitard. If one side of the aquitard presents an opposite distribution, the dividing point will appear and move toward the other side with the transference of the pore pressure in the aquitard. The results of the numerical simulation also show that there is a transition period between land subsidence and rebound. In this transition period, land could continue to subside even though the hydraulic head in the pumped layer begins to recover, because, at the beginning of the transition period, the compressed parts are thicker than the rebounding

part in the aquitards separated by dividing points adjacent to the pumped layer so that the total compression rate is larger than total rebounding rate in the entire system. At the end of this period, the total compression rate is equal to the total rebounding rate. With the movement of the dividing points, the rebounding parts gradually become thicker than the compressed parts, and the total compression rate is larger than the total rebounding rate. The land surface starts to rebound after the transition period. The conclusions of this study may be helpful in understanding the phenomenon referred to in some studies in which land subsidence lags the hydraulic head in the pumped layer. A fully coupled three-dimensional groundwater flow and land deformation model will be developed to analyze the relationship between the pressure head and soil displacement in future work.

Conflicts of Interest

The authors declare that there are no conflicts of interest regarding the publication of this paper.

Acknowledgments

This study was supported by Xi'an Center of Geological Survey Project "1:50,000 Hydrogeological and Engineering geological survey about major district of Guanzhong Basin" (12120113004800).

References

- [1] Y.-Q. Xue, Y. Zhang, S.-J. Ye, J.-C. Wu, and Q.-F. Li, "Land subsidence in China," *Environmental Geology*, vol. 48, no. 6, pp. 713–720, 2005.
- [2] Q. Y. Wang, J. B. Peng, Z. W. Jiang et al., "Numerical simulation and layerwise mark monitoring of land subsidence and ground fissures of typical section in Xi'an," *Rock & Soil Mechanics*, vol. 35, no. 11, pp. 3298–3302, 3309, 2014.
- [3] J. B. Peng, X. H. Sun, W. Wang, and G. C. Sun, "Characteristics of land subsidence, earth fissures and related disaster chain effects with respect to urban hazards in Xi'an, China," *Environmental Earth Sciences*, vol. 75, no. 16, article no. 1190, 2016.
- [4] Y.-S. Xu, S.-L. Shen, and Y.-J. Du, "Geological and hydrogeological environment in Shanghai with geohazards to construction and maintenance of infrastructures," *Engineering Geology*, vol. 109, no. 3–4, pp. 241–254, 2009.
- [5] Y. Yuan, Y. S. Xu, S. L. Shen et al., "Investigation of alternative mechanisms of aquifer-system compaction and land subsidence in Shanghai," *Proceedings of the International Association of Hydrological Sciences*, vol. 372, pp. 13–15, 2015.
- [6] J. Bear and M. Y. Corapcioglu, "Mathematical model for regional land subsidence due to pumping: 1. Integrated aquifer subsidence equations based on vertical displacement only," *Water Resources Research*, vol. 17, no. 4, pp. 937–946, 1981.
- [7] S. Honma and M. Inada, "Land Subsidence Analysis for Multi-Aquifer-Aquitard System due to Pumping," in *Proceedings of the Faculty of Engineering of Tokai University*, vol. 17, pp. 15–29, 1991.
- [8] S. K. Mishra, R. P. Singh, and S. Chandra, "Prediction of subsidence in the Indo-gangetic basin carried by groundwater withdrawal," *Engineering Geology*, vol. 33, no. 3, pp. 227–239, 1993.
- [9] P. R. Onta and A. D. Gupta, "Regional management modeling of a complex groundwater system for land subsidence control," *Water Resources Management*, vol. 9, no. 1, pp. 1–25, 1995.
- [10] B. Malama, K. L. Kuhlman, and W. Barrash, "Semi-analytical solution for flow in leaky unconfined aquifer-aquitard systems," *Journal of Hydrology*, vol. 346, no. 1–2, pp. 59–68, 2007.
- [11] C.-M. Tseng, T.-L. Tsai, and L.-H. Huang, "Effects of body force on transient poroelastic consolidation due to groundwater pumping," *Environmental Geology*, vol. 54, no. 7, pp. 1507–1516, 2008.
- [12] T.-L. Tsai and W.-S. Jang, "Deformation effects of porosity variation on soil consolidation caused by groundwater table decline," *Environmental Earth Sciences*, vol. 72, no. 3, pp. 829–838, 2014.
- [13] J.-C. Wu, X.-Q. Shi, S.-J. Ye, Y.-Q. Xue, Y. Zhang, and J. Yu, "Numerical simulation of land subsidence induced by groundwater overexploitation in Su-Xi-Chang area, China," *Environmental Geology*, vol. 57, no. 6, pp. 1409–1421, 2009.
- [14] S.-L. Shen and Y.-S. Xu, "Numerical evaluation of land subsidence induced by groundwater pumping in Shanghai," *Canadian Geotechnical Journal*, vol. 48, no. 9, pp. 1378–1392, 2011.
- [15] P. L. Lin, K. C. Hsu, C. W. Lin et al., "Modeling compaction of multi-layer-aquifer system due to groundwater withdrawal," *Engineering Geology*, vol. 187, pp. 143–155, 2015.
- [16] J.-C. Liu, G.-G. Lei, and G.-X. Mei, "One-dimensional consolidation of visco-elastic aquitard due to withdrawal of deep-groundwater," *Journal of Central South University of Technology (English Edition)*, vol. 19, no. 1, pp. 282–286, 2012.
- [17] X. Haiyang, Z. Zhou, and Z. Gao, "Experimental Research of Hysteresis Effect of Land Subsidence Caused by Water Releasing," *Chinese Journal of Rock Mechanics & Engineering*, vol. 30, pp. 3595–3601, 2011.
- [18] Z. Zhou, Q. Guo, and Z. Dou, "Delayed drainage of aquitard in response to sudden change in groundwater level in adjacent confined aquifer: Analytical and experimental studies," *Chinese Science Bulletin*, vol. 58, no. 25, pp. 3060–3069, 2013.
- [19] H. A. Loáiciga, "Consolidation Settlement in Aquifers Caused by Pumping," *Journal of Geotechnical & Geoenvironmental Engineering*, vol. 139, no. 7, pp. 1191–1204, 2013.
- [20] M. A. Biot, "General theory of three-dimensional consolidation," *Journal of Applied Physics*, vol. 12, no. 2, pp. 155–164, 1941.
- [21] M. A. Biot, "General solutions of equations of elasticity and consolidation for a porous material," *Journal of Applied Physics*, vol. 23, pp. 91–96, 1956.
- [22] N. Li, M. Li, F. Zhao et al., "Numerical simulation analysis of Xi'an land subsidence by FLAC~(2D)," *Journal of Catastrophology*, vol. 28, no. 3, pp. 211–214, 2013.